PhD

3rd CYCLE

FCUP
2025

U.PORTO

Effect of Structure on the Thermodynamic and Transport Properties of Ionic Liquids

Carlos Filipe Pesqueira Miranda

FC

U.PORTO

FACULDADE DE CIÊNCIAS
UNIVERSIDADE DO PORTO

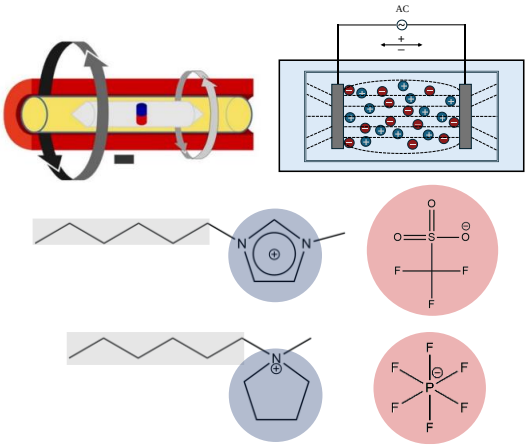
PhD

# Effect of Structure on the Thermodynamic and Transport Properties of Ionic Liquids

Carlos Filipe Pesqueira Miranda
Doctorate in Chemistry
Department of Chemistry and Biochemistry
Faculty of Sciences of the University of Porto
2025

U.PORTO
FACULDADE DE CIÊNCIAS
UNIVERSIDADE DO PORTO

PhD




# Effect of Structure on the Thermodynamic and Transport Properties of Ionic Liquids

Carlos Filipe Pesqueira Miranda
Thesis carried out as part of the Doctorate in Chemistry
Department of Chemistry and Biochemistry
2025

**Luís Manuel das Neves Belchior Faia dos Santos**
Associate Professor with Aggregation
Faculty of Sciences of the University of Porto

All the corrections determined by the jury, and only those, were made.

The Supervisor, 

Porto, 27 / 05 / 2025

# Acknowledgments

Gostaria de agradecer às pessoas que me apoiaram no meu percurso académico durante estes últimos quatros anos e que possibilitaram a elaboração desta dissertação.

Ao meu orientador, Professor Luís Belchior Santos, agradeço pelo apoio e orientação dados ao logo destes quatro anos. Agradeço ainda pelas discussões científicas que proporcionou e que muito contribuíram para o meu desenvolvimento pessoal e profissional durante esta etapa.

Ao Senhor Carlos Torres e ao Fernando Silva agradeço a enorme ajuda no desenvolvimento do ILDEM. Ao Óscar Fernandes também pelo apoio e também pelos conhecimentos que me transmitiu na área da eletrónica.

Aos meus colegas de grupo, Alexandre Alves, Ana Lobo Ferreira, Artur Farinha, Bruno Pinheiro, Carlos Lima, Inês Vaz, José Costa, e Rodrigo Silva, agradeço pela amizade, ajuda, disponibilidade e boa disposição. Agradeço também pelos conhecimentos que me transmitiram.

Aos meus amigos da Faculdade de Ciências da Universidade do Porto gostaria de agradecer pelo apoio e companheirismo ao logo deste percurso.

Aos meus restantes amigos agradeço pelo apoio e pelos momentos de descontração que me proporcionaram.

Agradeço à minha família, nomeadamente à minha mãe Aurora, pelo amor, apoio incondicional, confiança, compreensão e paciência.

Por fim agradeço à Fundação para a Ciência e Tecnologia (FCT) pelo financiamento da minha bolsa de doutoramento (2020.05717.BD).

# Resumo

Neste trabalho foi explorado o efeito da natureza e estrutura dos iões nas propriedades de transporte de líquidos iónicos (LIs) com base num estudo de alta precisão da dependência da viscosidade (273 – 373 K) e condutividade elétrica com a temperatura (283 – 333 K). Este estudo incluiu mais de 60 líquidos iónicos abrangendo uma grande variedade de estruturas catiónicas e aniónicas, assim como o tamanho da cadeia alquílica. A equação de Vogel-Fulcher-Tammann (VFT) foi utilizada para descrever o efeito da temperatura e derivar a energia de barreira associada aos processos de transporte e também a fragilidade do líquido.

O efeito do tamanho da cadeia alquílica do catião foi estudado para sete séries homólogas de líquidos iónicos. Com base nos resultados, verificou-se que o aumento da cadeia alquílica leva a um aumento da viscosidade, da energia de barreira e a uma diminuição na condutividade elétrica. A dependência das propriedades de transporte com o número de átomos de carbono na cadeia alquílica revela uma alteração de tendência próximo de $n = 6$, refletindo a intensificação da nanoestruturação dos líquidos iónicos com o aumento da região apolar.

O estudo com diferentes iões revelou que as propriedades de transporte são afetadas por diversos fatores associados com a natureza dos iões, nomeadamente tamanho, forma, distribuição de carga e basicidade/acidez. Os coeficientes pré-exponenciais ($A_\Lambda$ e $A_\eta$) e energias de barreira derivados com base na equação de VFT foram apresentados como viáveis indicadores de forma/tamanho/dinâmica e energia coesiva/distribuição de carga dos iões estudados. Valores mais altos de energia de barreira foram obtidos para iões com uma distribuição de carga mais localizada, em linha com a maior energia coesiva destes líquidos. De modo geral, $A_\Lambda$ mais baixos e $A_\eta$ mais elevados foram obtidos para aniões de maiores dimensões e com um maior impedimento estérico. Alterações da estrutura catiónica, como a metilação na posição C2 do anel de imidazólio e a isomerização do anel piridínico, afetam também a energia de barreira. Com base nos resultados a metilação em C2 leva a um pronunciado aumento de viscosidade e diminuição da condutividade molar. Em relação aos isómeros de piridínio dissubstituídos foi observado que a proximidade entre as duas cadeias resulta numa limitação da mobilidade do líquido que é refletida num aumento de viscosidade e diminuição de condutividade molar.

No âmbito deste projeto de Doutoramento foi desenvolvido um novo sistema/método de medição com alta precisão de condutividade elétrica de fluídos iónicos . Este sistema é baseado num medidor LCR de alta precisão e num conjunto de células condutimétricas desenhadas para garantir a estanqueidade do compartimento da amostra. Foi desenhado e construído um sistema de termostatização de alta precisão para a célula de medição do tipo banho de ar com um sistema de aquecimento e arrefecimento de Peltier que garante um controlo de temperatura com a precisão de (± 0.005 K). Durante este trabalho foram construídas duas células condutimétricas: uma célula de imersão (dip-in cell) baseada numa sonda comercial da Metrohm e uma célula “moeda” (coin cell). A maioria do trabalho apresentado foi elaborado utilizando a dip-in cell, enquanto que a coin cell foi desenvolvida com o objetivo de reduzir o volume de amostra necessário (~0,140 $cm^3$). A coin cell foi testada com diferentes tipos de elétrodos (SS316, SS316 revestido TiN, Pt, and Ni) e os resultados obtidos são coerentes com as medições com a dip-in cell. Os resultados experimentais foram extrapolados para frequência infinita de modo a mitigar o efeito da polarização da solução. A precisão e resolução do sistema foram avaliadas medindo o líquido iónico de referência $[^1C_6{}^3C_1im][NTf_2]$. Os resultados obtidos estão de acordo com os valores recomendados.

**Palavras-chave:** Líquidos Iónicos, Condutividade Molar, Viscosidade, Estrutura, Energia de Barreira, Nanoestruturação, Tamanho Alquílio Crítico, Energia Coesiva, Dinâmica, Impedância, Polarização, Célula Condutimétrica, Dependência com a Temperatura.

# Abstract

The effect of the ion structure on the transport properties of ionic liquids was explored by a high-precision study of the temperature dependence of viscosity (273 – 373 K) and electrical conductivity (283 – 333 K). This study included over 60 ILs covering different cationic headgroups, anions, and alkyl chain lengths. The Vogel-Fulcher-Tammann (VFT) equation was used to fit the temperature dependency and to derive the energy barriers associated with the viscous flow and ionic conduction, as well as liquid fragility.

The effect of the alkyl chain length of the cation was explored for seven IL homologue series. The increase of the alkyl chain length was found to lead to an increase in viscosity and energy barrier (cohesive energy) and a decrease in molar conductivity and fragility. A trendshift was observed around $n$ = 6 (CAS) in the dependence of the transport properties and derived parameter with the number of carbons on the alkyl side chain. This is a reflection of the intensification of the nanostructuration of ionic liquids with the increase of the nonpolar region.

The study with different ions highlighted that the transport properties are dependent on different factors, including size, shape, charge dispersion, and basicity/acidity. The pre-exponential coefficients ($A_\Lambda$ e $A_\eta$) and energy barrier derived from the VFT equation were found to correlate well with the shape/size/dynamics and cohesive energy/charge localization of the studied ions. Systems with more centralized charge regions were found to yield higher energy barriers, highlighting the higher cohesive energy of these liquids. Overall, lower $A_\Lambda$ and higher $A_\eta$ values were obtained for larger and more sterically hindered anions. Changes of cationic structures, namely the C2 methylation of the imidazolium ring and isomerization of the pyridinium ring, were also found to be reflected on the derived energy barriers. The results showed that C2 methylation dramatically increases the viscosity and decreases the molar conductivity. For the disubstituted pyridinium isomers, it was found that the proximity between the two alkyl chains limits the mobility of the liquid, resulting in higher viscosities and lower molar conductivities.

During this PhD work, a new system/methodology for the high-precision measurement of the electrical conductivity of ionic fluids, ILDEM, was designed and developed. The measuring system is based on a high-precision LCR meter and a conductivity cell system designed to ensure the vacuum and gastightness of the sample container. The high-precision temperature control is ensured by a customized air bath thermal chamber

based on a heating and cooling Peltier system. Two conductivity cells were developed during this work: a dip-in cell adapted from a commercial Metrohm probe and a PEEK-based coin cell. The majority of the work was conducted using the dip-in cell, while the coin cell was developed with the objective of reducing the sample volume. (~0.140 $cm^3$). The coin cell was tested with different electrode materials (SS316, SS316 coated with TiN, Pt, and Ni), and the results were found to be in agreement with the experiments using the dip-in cell. The electrical conductivity data were corrected for the effect of solution polarization by extrapolating the resistance to infinite frequency. The accuracy and resolution of the system were evaluated by measuring the conductivity of the reference ionic liquid, $[^1C_6{}^3C_1im][NTf_2]$, which was found to be in excellent agreement with the recommended data.

**Keywords:** Ionic Liquids, Molar Conductivity, Viscosity, Structural Effects, Energy Barrier, Nanostructuration, Critical Alkyl Size, Cohesive Energy, Dynamics, Impedance; Polarization, Conductivity Cell, Temperature Dependence.

# Table of Contents

**Acknowledgments** ..... **i**

**Resumo** ..... **iii**

**Abstract** ..... **v**

**Table of Contents** ..... **vii**

**List of Tables** ..... **xii**

**List of Figures** ..... **xxiv**

**List of Symbols and Abbreviations** ..... **xlii**

Symbols and Abbreviations of Physical Properties and Constants ..... xlii

Methodologies and Software ..... xlv

Ionic Liquids Abbreviation Nomenclature ..... xlvi

Other Materials ..... xlvii

**Units and Constants** ..... **xlviii**

**Organization of the Thesis** ..... **l**

**Chapter 1 − Introduction** ..... **1**

1. Introduction ..... 3

1.1. Structuration and Organization of Ionic Liquids ..... 5

1.2. Effect of Nanostructuration on the Physicochemical Properties of ILs ..... 10

1.2.1. Solid-Liquid Equilibria ..... 10

1.2.2. Heat Capacity ..... 12

1.2.3. Volatility and Vaporization Thermodynamics ..... 14

1.2.4. Transport Properties ..... 16

1.2.5. Surface Properties ..... 19

1.2.6. Summary ..... 21

1.3. Ionic Liquids in Energy Storage Applications ..... 21

1.3.1. Ionic Liquids as Electrolytes ..... 24

1.3.2. Effect of the Addition of Alkaline Cations ..... 25

1.4. Transport Properties of Ionic Liquids ..... 27
1.4.1. Anion Effect ..... 28
1.4.2. Effect of the Cation ..... 29
1.4.3. Effect of the Alkyl Chain Length ..... 31
1.5. Motivation, Aim and Strategy ..... 32
References ..... 33

**Chapter 2 − Methods, Theory and Fundamentals……..43**

2. Methods, Theory and Fundamentals ..... 45
2.1. Density of Liquids ..... 45
2.1.1. Measuring Principle ..... 46
2.1.2. Dependency of Density with Temperature ..... 47
2.2. Viscosity of Liquids ..... 48
2.2.1. Theory ..... 50
2.2.2. Measuring Principle ..... 52
2.3. Electrical Conductivity of Liquids ..... 54
2.3.1. Theory ..... 55
2.3.2. Measurement of Electrical Conductivity ..... 56
2.4. Effect of Temperature on the Transport Properties ..... 66
2.4.1. Arrhenius Relation ..... 67
2.4.2. Non-Arrhenius Behavior in Glassformers: VFT Equation ..... 68
2.4.3. Non-Arrhenius Behavior in Glassformers: Other Models ..... 79
2.5. Viscosity - Electrical Conductivity Relation ..... 83
2.6. Experimental Methodologies ..... 91
2.6.1. Density and Viscosity Measurements ..... 91
2.6.2. Electrical Conductivity Measurements ..... 97
References ..... 101

**Chapter 3 − Materials and Sample Preparation……..……..109**

3. Materials and Sample Preparation ..... 111

3.1. Ionic Liquids ..... 111

3.2. Purification of Ionic Liquids ..... 121

3.3. Other Materials ..... 122

3.3.1. Preparation of Potassium Chloride Solutions ..... 122

References ..... 124

**Chapter 4 − Development of an Impedance Measurement Apparat……125**

4. Ionic Liquid Dynamics and Electrical Mobility Measuring System ..... 127

4.1. LCR Meter ..... 128

4.1.1. Auto-balance Bridge ..... 129

4.1.2. Compensation and Correction ..... 132

4.2. Cell Design ..... 134

4.2.1. Dip-in Cell ..... 134

4.2.2. Coin Cell ..... 140

4.3. Vacuum/Gas line ..... 149

4.4. Air Bath Thermal Chamber ..... 149

4.4.1. Description ..... 150

4.4.2. Air Bath Control Box ..... 157

4.4.3. Temperature Measurements and Thermal Stability ..... 160

4.5. ILDEM Software (ILDEMSoft) ..... 165

4.5.1. Data Acquisition Module ..... 166

4.5.2. Signal Monitoring Module ..... 169

4.5.3. Air Bath Regulation Module ..... 170

4.5.4. Data Analysis Module ..... 172

4.6. Accuracy and Performance ..... 173

4.6.1. Dip-in Cell ..... 174

4.6.2. Coin Cell ..... 182
4.6.3. Comparison between the Dip-in and Coin Cell ..... 184
References ..... 185

**Chapter 5 − Results and Discussion: Structure-Property Relationship...187**

5. Results and Discussion: Structure-Property Relationship ..... 189
5.1. Effect of the Cation's Alkyl Chain Length ..... 194
5.1.1. $[^1C_n{}^3C_1im]BF_4$ Series ..... 195
5.1.2. $[^1C_n{}^3C_1im]PF_6$ Series ..... 208
5.1.3. $[^1C_n{}^3C_1im][OTf]$ Series ..... 220
5.1.4. $[^1C_n{}^3C_1im][NTf_2]$ Series ..... 232
5.1.5. $[^1C_n{}^3C_1im][FAP]$ Series ..... 238
5.1.6. $[^1C_npy][NTf_2]$Series ..... 249
5.1.7. $[^1C_nC_1pyr][NTf_2]$ Series ..... 261
5.1.8. Discussion Alkyl Chain Effect ..... 272
5.2. Effect of the Anion Nature ..... 280
5.2.1. Density ..... 281
5.2.2. Viscosity ..... 284
5.2.3. Electrical Conductivity ..... 287
5.2.4. Molar Conductivity ..... 288
5.3. Effect of the Cation Nature ..... 296
5.3.1. Effect of the Nature of the Cationic Ring ..... 296
5.3.2. C2-Methylation on the Imidazolium Ring ..... 309
5.3.3. Isomerization of the Pyridinium Ring ..... 322
References ..... 333

**Chapter 6 − Conclusions and Achievments……..……349**

6. Conclusions and Achievements..... 349

6.1. ILDEM ..... 349

6.2. Structure Effect on the Transport Properties of Ionic Liquids ..... 351

6.3. Reflections and Future Perspectives ..... 353

References..... 354

**Appendix……..……..357**

Appendix A: Pinout and Electric Configuration ..... 357

Appendix B: Experimental Results ..... 360

# List of Tables

## Chapter 2 – Methods, Theory, and Fundamentals

**Table 2.1.** Summary of analytical methods commonly applied to Determine polarization-corrected resistance. 66

## Chapter 3 – Materials and Sample Purification

**Table 3.1.** Summary of the ionic liquids studied in this work. 111

**Table 3.2.** Molecular structures of the ionic liquids studied in this work. 114

**Table 3.3.** List of compounds used in the testing and calibration of ILDEM and SVM 3001. 122

## Chapter 4 – Development of an Impedance Measuring Apparatus

**Table 4.1.** Specifications of the coin cell electrode discs 144

**Table 4.2.** Coefficients of the Pt100 calibration curve. 163

**Table 4.3.** Derived VFT coefficients, using different polarization correction models, applied experimental electrical conductivity data for $[^1C_6{}^3C_1im][NTf_2]$. 180

## Chapter 5 – Results and Discussion: Structure-property relationships

**Table 5.1.** Summary of ionic liquids measurements performed in this work. 191

**Table 5.2.** Fitting coefficients of the temperature dependence of density of the studied $[^1C_n{}^3C_1im]BF_4$ homologue series. 196

**Table 5.3.** Density, thermal expansion coefficient, and molar volume at the reference temperature, $T$ = 298.15 K for the studied $[^1C_n{}^3C_1im]BF_4$ homologue series. 196

**Table 5.4.** Fitting coefficients used to describe the temperature dependence of viscosity of the studied $[^1C_n{}^3C_1im]BF_4$ homologue series. 199

**Table 5.5.** Viscosity and derived energy barrier of the studied $[^1C_n{}^3C_1im]BF_4$ homologue series at the reference temperature ($T$ = 298.15 K), together with the strength parameter. 200

**Table 5.6.** Fitting coefficients used to describe the temperature dependence of electrical conductivity of the studied $[^1C_n{}^3C_1im]BF_4$ homologue series. 203

**Table 5.7.** Fitting coefficients used to describe the temperature dependence of molar conductivity of the studied $[^1C_n{}^3C_1im]BF_4$ homologue series. 206

**Table 5.8.** Molar conductivity and derived energy barrier of the studied $[^1C_n{}^3C_1im]BF_4$ homologue series at the reference temperature ($T$ = 298.15 K), together with the strength parameter. 207

**Table 5.9.** Fitting coefficients used to describe the temperature dependence of density of the studied $[^1C_n{}^3C_1im]PF_6$ homologue series. 209

**Table 5.10.** Density, thermal expansion coefficient, and molar volume at the reference temperature ($T$ = 298.15 K) for the studied $[^1C_n{}^3C_1im]PF_6$ homologue series. 209

**Table 5.11.** Fitting coefficients used to describe the temperature dependence of viscosity of the studied $[^1C_n{}^3C_1im]PF_6$ homologue series. 212

**Table 5.12.** Viscosity and derived energy barrier of the studied $[^1C_n{}^3C_1im]PF_6$ homologue series at the reference temperature ($T$ = 298.15 K), together with the strength parameter. 213

**Table 5.13.** Fitting coefficients used to describe the temperature dependence of electrical conductivity of the studied $[^1C_n{}^3C_1im]PF_6$ homologue series. 215

**Table 5.14.** Fitting coefficients used to describe the temperature dependence of molar conductivity of the studied $[^1C_n{}^3C_1im]PF_6$ homologue series. 218

**Table 5.15.** Molar conductivity and derived energy barrier of the studied $[^1C_n{}^3C_1im]PF_6$ homologue series at the reference temperature ($T$ = 298.15 K), together with the strength parameter. 219

**Table 5.16.** Fitting coefficients used to describe the temperature dependence of density of the studied $[^1C_n{}^3C_1im][OTf]$ homologue series. 221

**Table 5.17.** Density, thermal expansion coefficient, and molar volume at the reference temperature ($T$ = 298.15 K) for the studied $[^1C_n{}^3C_1im][OTf]$ homologue series. 221

**Table 5.18.** Fitting coefficients used to describe the temperature dependence of viscosity of the studied $[^1C_n{}^3C_1im][OTf]$ homologue series. 224

**Table 5.19.** Viscosity and derived energy barrier of the studied $[^1C_n{}^3C_1im][OTf]$ homologue series at the reference temperature ($T$ = 298.15 K), together with the strength parameter. 225

**Table 5.20.** Fitting coefficients used to describe the temperature dependence of electrical conductivity of the studied [$^1C_n{}^3C_1$im][OTf] homologue series. 227

**Table 5.21.** Fitting coefficients used to describe the temperature dependence of molar conductivity of the studied [$^1C_n{}^3C_1$im][OTf] homologue series. 230

**Table 5.22.** Molar conductivity and derived energy barrier of the [$^1C_n{}^3C_1$im][OTf] homologue series at the reference temperature ($T$ = 298.15 K), together with the strength parameter. 231

**Table 5.23.** Fitting coefficients used to describe the temperature dependence of electrical conductivity of the studied [$^1C_n{}^3C_1$im][$NTf_2$] homologue series. 233

**Table 5.24.** Fitting coefficients used to describe the temperature dependence of molar conductivity of the studied [$^1C_n{}^3C_1$im][$NTf_2$] homologue series. 236

**Table 5.25.** Molar conductivity and derived energy barrier of the studied [$^1C_n{}^3C_1$im][$NTf_2$] homologue series at the reference temperature ($T$ = 298.15 K), together with the strength parameter. 237

**Table 5.26.** Fitting coefficients used to describe the temperature dependence of density of the studied [$^1C_n{}^3C_1$im][FAP] homologue series. 239

**Table 5.27.** Density, thermal expansion coefficient, and molar volume at the reference temperature ($T$ = 298.15 K) for the studied [$^1C_n{}^3C_1$im][FAP] homologue series. 239

**Table 5.28.** Fitting coefficients used to describe the temperature dependence of viscosity of the studied [$^1C_n{}^3C_1$im][FAP] homologue series. 242

**Table 5.29.** Viscosity and derived energy barrier of the studied [$^1C_n{}^3C_1$im][FAP] homologue series at the reference temperature ($T$ = 298.15 K), together with the strength parameter. 243

**Table 5.30.** Fitting coefficients used to describe the temperature dependence of electrical conductivity of the studied [$^1C_n{}^3C_1$im][FAP] homologue series. 245

**Table 5.31.** Fitting coefficients used to describe the temperature dependence of molar conductivity of the studied [$^1C_n{}^3C_1$im][FAP] homologue series. 247

**Table 5.32.** Molar conductivity and derived energy barrier of the studied [$^1C_n{}^3C_1$im][FAP] homologue series at the reference temperature ($T$ = 298.15 K), together with the strength parameter. 248

**Table 5.33.** Fitting coefficients used to describe the temperature dependence of density of the studied [$^1C_n$py][$NTf_2$] homologue series. 250

**Table 5.34.** Density, thermal expansion coefficient, and molar volume at the reference temperature ($T$ = 298.15 K) for the studied [$^1C_n$py][$NTf_2$] homologue series. 250

**Table 5.35.** Fitting coefficients used to describe the temperature dependence of viscosity of the studied [$^1C_n$py][$NTf_2$] homologue series. 253

**Table 5.36.** Viscosity and derived energy barrier of the studied [$^1C_n$py][$NTf_2$] homologue series at the reference temperature ($T$ = 298.15 K), together with the strength parameter. 254

**Table 5.37.** Fitting coefficients used to describe the temperature dependence of electrical conductivity of the studied [$^1C_n$py][$NTf_2$] homologue series. 256

**Table 5.38.** Fitting coefficients used to describe the temperature dependence of molar conductivity of the studied [$^1C_n$py][$NTf_2$] homologue series. 259

**Table 5.39.** Molar conductivity and derived energy barrier of the studied [$^1C_n$py][$NTf_2$] homologue series at the reference temperature ($T$ = 298.15 K), together with the strength parameter. 260

**Table 5.40.** Fitting coefficients used to describe the temperature dependence of density of the studied [$^1C_n{}^1C_1$pyr][$NTf_2$] homologue series. 261

**Table 5.41.** Density, thermal expansion coefficient, and molar volume at the reference temperature ($T$ = 298.15 K) for the studied [$^1C_n{}^1C_1$pyr][$NTf_2$] homologue series. 262

**Table 5.42.** Fitting coefficients used to describe the temperature dependence of viscosity of the studied [$^1C_n{}^1C_1$pyr][$NTf_2$] homologue series. 264

**Table 5.43.** Viscosity and derived energy barrier of the studied [$^1C_n{}^1C_1$pyr][$NTf_2$] homologue series at the reference temperature ($T$ = 298.15 K), together with the strength parameter. 265

**Table 5.44.** Fitting coefficients used to describe the temperature dependence of electrical conductivity of the studied [$^1C_n{}^1C_1$pyr][$NTf_2$] homologue series. 267

**Table 5.45.** Fitting coefficients used to describe the temperature dependence of molar conductivity of the studied $[^1C_n{}^1C_1pyr][NTf_2]$ homologue series. 270

**Table 5.46.** Molar conductivity and derived energy barrier of the studied $[^1C_n{}^1C_1pyr][NTf_2]$homologue series at the reference temperature ($T$ = 298.15 K), together with the strength parameter. 271

**Table 5.47.** Dependence of molar volume per methylene group for each homologue ionic liquid series. 272

**Table 5.48.** Fitting coefficients used to describe the temperature dependence of density of the studied $[^1C_4{}^3C_1im][X]$ ILs. 282

**Table 5.49.** Density, thermal expansion coefficient, and molar volume at the reference temperature ($T$ = 298.15 K) for the studied $[^1C_4{}^3C_1im][X]$ ILs. 282

**Table 5.50.** Fitting coefficients used to describe the temperature dependence of viscosity of the studied $[^1C_4{}^3C_1im][X]$ ILs. 284

**Table 5.51.** Viscosity and derived energy barrier of the studied $[^1C_4{}^3C_1im][X]$ ILs at the reference temperature ($T$ = 298.15 K), together with the strength parameter. 285

**Table 5.52.** Fitting coefficients used to describe the temperature dependence of electrical conductivity of the studied $[^1C_4{}^3C_1im][X]$ ILs. 287

**Table 5.53.** Fitting coefficients used to describe the temperature dependence of molar conductivity of the studied $[^1C_4{}^3C_1im][X]$ ILs. 288

**Table 5.54.** Molar conductivity and derived energy barrier of the studied $[^1C_4{}^3C_1im][X]$ ILs at the reference temperature ($T$ = 298.15 K), together with the strength parameter. 289

**Table 5.55.** Fitting coefficients used to describe the temperature dependence of density of $[^1C_4py][OTf]$, $[^1C_4{}^1C_1pyr][OTf]$, and $[^1C_4{}^1C_1pyr][FAP]$. 299

**Table 5.56.** Density, thermal expansion coefficient, and molar volume at the reference temperature($T$ = 298.15 K) of $[^1C_4py][OTf]$, $[^1C_4{}^1C_1pyr][OTf]$, and $[^1C_4{}^1C_1pyr][FAP]$. 299

**Table 5.57.** Fitting coefficients used to describe the temperature dependence of viscosity of [$^1C_4$py][OTf], [$^1C_4{}^1C_1$pyr][OTf], and [$^1C_4{}^1C_1$pyr][FAP]. 299

**Table 5.58.** Viscosity and derived energy barrier of [$^1C_4$py][OTf], [$^1C_4{}^1C_1$pyr][OTf], and [$^1C_4{}^1C_1$pyr][FAP] ILs at the reference temperature ($T$ = 298.15 K), together with the strength parameter. 300

**Table 5.59.** Fitting coefficients used to describe the temperature dependence of electrical conductivity of [$^1C_4$py][OTf], [$^1C_4{}^1C_1$pyr][OTf], and [$^1C_4{}^1C_1$pyr][FAP]. 302

**Table 5.60.** Fitting coefficients used to describe the temperature dependence of molar conductivity of [$^1C_4$py][OTf], [$^1C_4{}^1C_1$pyr][OTf], and [$^1C_4{}^1C_1$pyr][FAP]. 303

**Table 5.61.** Molar conductivity and derived energy barrier of [$^1C_4$py][OTf], [$^1C_4{}^1C_1$pyr][OTf], and [$^1C_4{}^1C_1$pyr][FAP] at the reference temperature ($T$ = 298.15 K), together with the strength parameter. 303

**Table 5.62.** Fitting coefficients used to describe the temperature dependence of density of the studied C2-methylated [$^1C_n{}^2C_1{}^3C_1$im][$NTf_2$] ILs. 310

**Table 5.63.** Density, thermal expansion coefficient, and molar volume at the reference temperature ($T$ = 298.15 K) for the studied C2-methylated [$^1C_n{}^2C_1{}^3C_1$im][$NTf_2$] ILs and the respective non-methylated analogues. 310

**Table 5.64.** Fitting coefficients used to describe the temperature dependence of viscosity of the studied C2-methylated [$^1C_n{}^2C_1{}^3C_1$im][$NTf_2$] ILs and the respective non-methylated analogues. 312

**Table 5.65.** Viscosity and derived energy barrier of the studied C2-methylated [$^1C_n{}^2C_1{}^3C_1$im][$NTf_2$] ILs and the respective non-methylated analogues at the reference temperature ($T$ = 298.15 K), together with the strength parameter. 312

**Table 5.66.** Fitting coefficients used to describe the temperature dependence of electrical conductivity of the studied [$^1C_n{}^2C_1{}^3C_1$im][$NTf_2$] ILs. 314

**Table 5.67.** Fitting coefficients used to describe the temperature dependence of molar conductivity of the studied C2-methylated [$^1C_n{}^2C_1{}^3C_1$im][$NTf_2$] ILs and the respective non-methylated analogues. 315

**Table 5.68.** Molar conductivity and derived energy barrier of the studied C2-methylated [$^{1}C_{n}{}^{2}C_{1}{}^{3}C_{1}$im][$NTf_2$] ILs and the respective non-methylated analogues at the reference temperature ($T$ = 298.15 K), together with the strength parameter. 316

**Table 5.69.** Fitting coefficients used to describe the temperature dependence of density of the studied pyridinium isomers ILs. 324

**Table 5.70.** Density, thermal expansion coefficient, and molar volume at the reference temperature ($T$ = 298.15 K) for the studied pyridinium isomers ILs. 324

**Table 5.71.** Fitting coefficients used to describe the temperature dependence of viscosity of the studied pyridinium isomers. 324

**Table 5.72.** Viscosity and derived energy barrier of the studied pyridinium isomers at the reference temperature ($T$ = 298.15 K), together with the strength parameter. 325

**Table 5.73.** Fitting coefficients used to describe the temperature dependence of electrical conductivity of the studied pyridinium isomers. 326

**Table 5.74.** Fitting coefficients used to describe the temperature dependence of molar conductivity of the studied pyridinium isomers. 327

**Table 5.75.** Molar conductivity and derived energy barrier of the studied pyridinium isomers at the reference temperature ($T$ = 298.15 K), together with the strength parameter. 328

## Appendix

**Table B.1.** Experimental values for electrical conductivity and molar conductivity for [$^{1}C_{1}{}^{3}C_{1}$im][$NTf_2$]. 360

**Table B.2.** Experimental values for electrical conductivity and molar conductivity for [$^{1}C_{2}{}^{3}C_{1}$im][$NTf_2$]. 360

**Table B.3.** Experimental values for electrical conductivity and molar conductivity for [$^{1}C_{1}{}^{3}C_{3}$im][$NTf_2$]. 361

**Table B.4.** Experimental values for electrical conductivity and molar conductivity for $[^1C_4{}^3C_1im][NTf_2]$. 361

**Table B.5.** Experimental values for electrical conductivity and molar conductivity for $[^1C_1{}^3C_5im][NTf_2]$. 362

**Table B.6.** Experimental values for electrical conductivity and molar conductivity for $[^1C_6{}^3C_1im][NTf_2]$. 362

**Table B.7.** Experimental values for electrical conductivity and molar conductivity for $[^1C_7{}^3C_1im][NTf_2]$. 363

**Table B.8.** Experimental values for electrical conductivity and molar conductivity for $[^1C_1{}^3C_8im][NTf_2]$. 363

**Table B.9.** Experimental values for electrical conductivity and molar conductivity for $[^1C_1{}^3C_9im][NTf_2]$. 364

**Table B.10.** Experimental values for electrical conductivity and molar conductivity for $[^1C_{10}{}^3C_1im][NTf_2]$. 364

**Table B.11.** Experimental values for electrical conductivity and molar conductivity for $[^1C_1{}^3C_{11}im][NTf_2]$. 365

**Table B.12.** Experimental values for electrical conductivity and molar conductivity for $[^1C_{12}{}^3C_1im][NTf_2]$. 365

**Table B.13.** Experimental values for density, viscosity, electrical conductivity, and molar conductivity for $[^1C_2{}^2C_1{}^3C_1im][NTf_2]$. 366

**Table B.14.** Experimental values for density, viscosity, electrical conductivity, and molar conductivity for $[^1C_1{}^2C_1{}^3C_3im][NTf_2]$. 367

**Table B.15.** Experimental values for density, viscosity, electrical conductivity, and molar conductivity for $[^1C_4{}^2C_1{}^3C_1im][NTf_2]$. 368

**Table B.16.** Experimental values for density, viscosity, electrical conductivity, and molar conductivity for $[^1C_2{}^3C_1im]BF_4$. 369

**Table B.17.** Experimental values for density, viscosity, electrical conductivity, and molar conductivity for $[^1C_1{}^3C_3im]BF_4$. 370

**Table B.18.** Experimental values for density, viscosity, electrical conductivity, and molar conductivity for $[^1C_4{}^3C_1im]BF_4$. 371

**Table B.19.** Experimental values for density, viscosity, electrical conductivity, and molar conductivity for $[^1C_1{}^3C_5im]BF_4$. 372

**Table B.20.** Experimental values for density, viscosity, electrical conductivity, and molar conductivity for $[^1C_6{}^3C_1im]BF_4$. 373

**Table B.21.** Experimental values for density, viscosity, electrical conductivity, and molar conductivity for $[^1C_7{}^3C_1im]BF_4$. 374

**Table B.22.** Experimental values for density, viscosity, electrical conductivity, and molar conductivity for $[^1C_1{}^3C_8im]BF_4$. 375

**Table B.23.** Experimental values for density, viscosity, electrical conductivity, and molar conductivity for $[^1C_1{}^3C_9im]BF_4$. 376

**Table B.24.** Experimental values for density, viscosity, electrical conductivity, and molar conductivity for $[^1C_{10}{}^3C_1im]BF_4$. 377

**Table B.25.** Experimental values for density, viscosity, electrical conductivity, and molar conductivity for $[^1C_{12}{}^3C_1im]BF_4$. 378

**Table B.26.** Experimental values for density, viscosity, electrical conductivity, and molar conductivity for $[^1C_1{}^3C_3im]PF_6$. 378

**Table B.27.** Experimental values for electrical conductivity and molar conductivity for $[^1C_4{}^3C_1im]PF_6$. 379

**Table B.28.** Experimental values for electrical conductivity and molar conductivity for $[^1C_1{}^3C_5im]PF_6$. 379

**Table B.29.** Experimental values for electrical conductivity and molar conductivity for $[^1C_6{}^3C_1im]PF_6$. 380

**Table B.30.** Experimental values for electrical conductivity and molar conductivity for $[^1C_7{}^3C_1im]PF_6$. 380

**Table B.31.** Experimental values for electrical conductivity and molar conductivity for $[^1C_1{}^3C_8im]PF_6$. 381

**Table B.32.** Experimental values for electrical conductivity and molar conductivity for $[^1C_1{}^3C_9im]PF_6$. 381

**Table B.33.** Experimental values for density, viscosity, electrical conductivity, and molar conductivity for $[^1C_{10}{}^3C_1im]PF_6$. 382

**Table B.34.** Experimental values for density, viscosity, electrical conductivity, and molar conductivity for $[^1C_2{}^3C_1im][OTf]$. 383

**Table B.35.** Experimental values for density, viscosity, electrical conductivity, and molar conductivity for $[^1C_4{}^3C_1im][OTf]$. 384

**Table B.36.** Experimental values for density, viscosity, electrical conductivity, and molar conductivity for $[^1C_6{}^3C_1im][OTf]$. 385

**Table B.37.** Experimental values for density, viscosity, electrical conductivity, and molar conductivity for $[^1C_1{}^3C_8im][OTf]$. 386

**Table B.38.** Experimental values for density, viscosity, electrical conductivity, and molar conductivity for $[^1C_{10}{}^3C_1im][OTf]$. 387

**Table B.39.** Experimental values for density, viscosity, electrical conductivity, and molar conductivity for $[^1C_{12}{}^3C_1im][OTf]$. 387

**Table B.40.** Experimental values for density, viscosity, electrical conductivity, and molar conductivity for [$^1C_2{}^3C_1$im][FAP]. 388

**Table B.41.** Experimental values for density, viscosity, electrical conductivity, and molar conductivity for [$^1C_4{}^3C_1$im][FAP]. 389

**Table B.42.** Experimental values for density, viscosity, electrical conductivity, and molar conductivity for [$^1C_6{}^3C_1$im][FAP]. 390

**Table B.43.** Experimental values for density, viscosity, electrical conductivity, and molar conductivity for [$^1C_4{}^3C_1$im][FSI]. 391

**Table B.44.** Experimental values for density, viscosity, electrical conductivity, and molar conductivity for [$^1C_4{}^3C_1$im][BETI]. 392

**Table B.45.** Experimental values for density, viscosity, electrical conductivity, and molar conductivity for [$^1C_4{}^3C_1$im][Ac]. 393

**Table B.46.** Experimental values for density, viscosity, electrical conductivity, and molar conductivity for [$^1C_4{}^3C_1$im][TFA]. 394

**Table B.47.** Experimental values for density, viscosity, electrical conductivity, and molar conductivity for [$^1C_4{}^3C_1$im][DCA]. 395

**Table B.48.** Experimental values for density, viscosity, electrical conductivity, and molar conductivity for [$^1C_3$py][$NTf_2$]. 396

**Table B.49.** Experimental values for density, viscosity, electrical conductivity, and molar conductivity for [$^1C_4$py][$NTf_2$]. 396

**Table B.50.** Experimental values for density, viscosity, electrical conductivity, and molar conductivity for [$^1C_5$py][$NTf_2$]. 397

**Table B.51.** Experimental values for density, viscosity, electrical conductivity, and molar conductivity for [$^1C_6$py][$NTf_2$]. 398

**Table B.52.** Experimental values for density, viscosity, electrical conductivity, and molar conductivity for [$^1C_7$py][$NTf_2$]. 399

**Table B.53.** Experimental values for density, viscosity, electrical conductivity, and molar conductivity for [$^1C_8$py][$NTf_2$]. 400

**Table B.54.** Experimental values for density, viscosity, electrical conductivity, and molar conductivity for [$^1C_9$py][$NTf_2$]. 401

**Table B.55.** Experimental values for density, viscosity, electrical conductivity, and molar conductivity for [$^1C_3{}^2C_1$py][$NTf_2$]. 402

**Table B.56.** Experimental values for density, viscosity, electrical conductivity, and molar conductivity for [$^1C_3{}^3C_1$py][$NTf_2$]. 403

**Table B.57.** Experimental values for density, viscosity, electrical conductivity, and molar conductivity for [$^1C_4$py][OTf]. 404

**Table B.58.** Experimental values for density, viscosity, electrical conductivity, and molar conductivity for [$^1C_3{}^1C_1$pyr][$NTf_2$]. 405

**Table B.59.** Experimental values for density, viscosity, electrical conductivity, and molar conductivity for [$^1C_4{}^1C_1$pyr][$NTf_2$]. 406

**Table B.60.** Experimental values for density, viscosity, electrical conductivity, and molar conductivity for [$^1C_6{}^1C_1$pyr][$NTf_2$]. 407

**Table B.61.** Experimental values for density, viscosity, electrical conductivity, and molar conductivity for [$^1C_8{}^1C_1$pyr][$NTf_2$]. 408

**Table B.62.** Experimental values for density, viscosity, electrical conductivity, and molar conductivity for [$^1C_4{}^1C_1$pyr][OTf]. 408

**Table B.63.** Experimental values for density, viscosity, electrical conductivity, and molar conductivity for [$^1C_4{}^1C_1$pyr][FAP]. 410

# List of Figures

## Chapter 1 – Introduction

**Figure 1.1.** Schematic illustration comparing the structure and packing of conventional salts and ionic liquids. 4

**Figure 2.2.** Molecular structures of the most common anions and cations of ion liquids. 5

**Figure 1.3.** Schematic representation of the types of intermolecular interactions of an ionic liquid. 7

**Figure 1.4.** Schematic representation of the intensification of ionic liquid nanostructuration with the increases of the cation´s alkyl chain. 8

**Figure 1.5.** Schematic diagram of the interaction potentials present in the ionic liquids as a function of the cation alkyl chain size. 10

**Figure 1.6.** Effect of the cation's alkyl chain on the solid-liquid equilibrium of ionic liquids. 12

**Figure 1.7.** Effect of the cation's alkyl chain length on the isobaric heat capacity ionic liquids. 14

**Figure 1.8.** Effect of the cation's alkyl chain length on the vaporization properties of ionic liquids. 16

**Figure 1.9.** Effect of the cation's alkyl chain length on the viscosity of ionic liquids. 18

**Figure 1.10.** Effect of the cation's alkyl chain length on the speed of sound of ionic liquids. 19

**Figure 1.11.** Effect of the cation's alkyl chain length on the surface properties of ionic liquids. 20

**Figure 1.12.** Summary of three regions/behaviors typically observed by increasing the length of the cation's alkyl chain. 21

**Figure 1.13.** Summarized comparison between conventional electrolytes and ionic liquids electrolytes. 23

**Figure 1.14.** Commonly used ions in ionic liquid electrolytes. 24

**Figure 1.15.** Correlation between the Lithium coordination and electrical conductivity on an ionic liquid - lithium salt mixture. 26

**Figure 1.16.** Variation profiles for dynamic viscosity, lithium self-diffusion coefficients, and lithium transport number with lithium-ion content. 27

**Figure 1.17.** Effect of the nature of the anion on the electrical conductivity of ionic liquids based on common cationic groups. 28

**Figure 1.18.** Effect of the nature of the cation head charge group on the electrical conductivity of bistriflimide and dicyanamide ionic liquids 30

## Chapter 2 – Methods, Theory, and Fundamentals

**Figure 2.1.** Schematic representation of the measuring principle of a vibrating U-tube densimeter. 47

**Figure 2.2.** Schematic representation of the simple shear of a liquid film. 49

**Figure 2.3.** Schematic representation of the different fluid behaviors. 50

**Figure 2.4.** Schematic representation of the Couette measuring principle for the viscosity of liquids. 53

**Figure 2.5.** Schematic representation of a Stabinger viscometer. 54

**Figure 2.6.** Schematic representation of ion conduction when DC and AC are applied to an electrolyte. 57

**Figure 2.7.** Ideal frequency dependency for resistive, capacitive, and inductive elements. 59

**Figure 2.8.** Typical representation of current and voltage as a function of the angular frequency time product for ideal resistive, capacitive, and inductive systems. 60

**Figure 2.9.** Graphical representation of the impedance complex plane. 60

**Figure 2.10.** Typical resistance-frequency dependence for a conductive liquid/solution. 61

**Figure 2.11.** Example of the extrapolation of resistance to infinite frequency 62

**Figure 2.12.** Typical Nyquist Plot and Randel circuit. 64

**Figure 2.13.** Schematic representation of the charge-transfer process 64

**Figure 2.14.** Schematic representation of the Arrhenius temperature dependence on the viscosity and electrical conductivity. 67

**Figure 2.15.** Schematic representation of the heat capacity change at the glass transition temperature for fragile and strong glassformers.. 69

**Figure 2.16.** Characteristic energy potential surfaces for fragile and strong glassformers. 70

**Figure 2.17.** Representation of the Arrhenius relation for the temperature dependence of viscosity and electrical conductivity for the $[^1C_6{}^3C_1im][NTf_2]$ ionic liquid. 72

**Figure 2.18.** Schematic representation of the VFT temperature dependence on the viscosity and electrical conductivity. 73

**Figure 2.19.** Summary of the application of the VFT equation at different temperatures. 73

**Figure 2.20.** Graphical representation of the impact of the *B* and *C* coefficients on the energy barrier. 75

**Figure 2.21.** Simulated Angell plots for compounds with varying fragilities. 78

**Figure 2.22.** Schematic representation of types of ion distribution in the liquid phase/solution: free ions, ionic pairs, and ionic aggregates. 84

**Figure 2.23.** Schematic representation of types of ion distribution in a typical ionic liquid. 85

**Figure 2.24.** Schematic representation of the Walden plot as a tool to evaluate the ionicity of ionic liquids. 86

**Figure 2.25.** Schematic representation of the ion cross-correlations in an IL. 89

**Figure 2.26.** Anton Paar SVM 3001 viscometer-densimeter, used for simultaneous viscosity and density measurements. 91

**Figure 2.27.** Schematic representation of the density and viscosity cells inside the Anton Paar SVM 3001 apparatus. 92

**Figure 2.28.** Images of the viscosity cell of the Anton Paar SVM 3001 apparatus. 92

**Figure 2.29.** Deviation of the experimental results to the density values recommended by Anton Paar. 93

**Figure 2.30.** Deviation of the experimental results to the viscosity values recommended by Anton Paar. 94

**Figure 2.31.** Deviation of the available density literature data to the experimental results of $[^1C_6{}^3C_1im][NTf_2]$. 95

**Figure 2.32.** Deviation of the available viscosity literature data to the experimental results of $[^1C_6{}^3C_1im][NTf_2]$. 96

**Figure 2.33.** Ionic Liquid Dynamics and Electrical Mobility (ILDEM) measuring system: in laboratory image and features 98

**Figure 2.34.** Schematic representation of the complete experimental procedure of an ILDEM experiment. 99

## Chapter 3 – Materials and Sample Purification

**Figure 3.1.** Schematic representation of the drying/degassing system used for the purification of ionic liquids. 121

## Chapter 4 – Development of an Impedance Measuring Apparatus

**Figure 4.1.** In laboratory image of the Ionic Liquid Dynamics and Electrical Mobility (ILDEM) measuring system. 127

**Figure 4.2.** Schematic representation of the Ionic Liquid Dynamics and Electrical Mobility (ILDEM) measuring system. 128

**Figure 4.3.** Schematic representation of the intensification of ionic liquid nanostructuration with the increases of the cation´s alkyl chain. 129

**Figure 4.4.** Schematic representation of the measuring principle of the auto-balance bridge method. 129

**Figure 4.5.** Representation of the voltage complex quantities measured in the vector ratio section of the auto-balance bridge. 131

**Figure 4.6.** Schematic representation and in-laboratory images of the open and short compensation on an LCR circuit. 134

**Figure 4.7.** Images of the conductivity cell with specific detail on a schematic representation of the specially designed PEEK holder. 135

**Figure 4.8.** Exploded view of the dip-in conductivity cell, including the Metrohm conductivity probe, the PEEK holder, the PTFE connections to the vacuum/gas lines, and the glass tube sample vessel. 136

**Figure 4.9.** Drawings of the customized conductivity cell and the cell holder. 136

**Figure 4.10.** Images of the first setup of the dip-in cell – LCR cable connection. 137

**Figure 4.11.** Spectra obtained using the wiring configuration based on the commercial dip-in cell cable setup 138

**Figure 4.12.** Second and definitive setup for the Dip-in cell – LCR 4-wire connection. 139

**Figure 4.13.** Spectra obtained using the wiring configuration based on the customized cable/connection system 139

**Figure 4.14.** Images and schematic representation of the complete coin cell and the individual components. 141

**Figure 4.15.** Exploded view of the coin conductivity cell 141

**Figure 4.16.** Drawings of the coin cell and the individual components. 142

**Figure 4.17.** Schematic representation of the coin cell (2D cut and geometry) and the measuring chamber (3D perspective), 143

**Figure 4.18.** Drawings of the dedicated support for the coin cell. 143

**Figure 4.19.** Image of the in-laboratory setup of the Coin Cell. 144

**Figure 4.20.** Images of the coin cell electrode discs. 145

**Figure 4.21.** Characterization of the stainless-steel discs 145

**Figure 4.22.** Characterization of discs of stainless steel coated with titanium nitride 146

**Figure 4.23.** Characterization of the nickel discs. 146

**Figure 4.24.** Characterization of the platinum discs. 147

**Figure 4.25.** Images of the coin cell electric connections. 148

**Figure 4.26.** Coin cell – LCR connection. Images of the installation in the laboratory and schematic representation 148

**Figure 4.27.** Schematic representation of the ILDEM vacuum/gas line. 149

**Figure 4.28.** Images of the air bath thermal chamber. 150

**Figure 4.29.** Image of the fully connected Air Bath Thermal Chamber. 151

**Figure 4.30.** Images of aluminum plates of the air bath thermal chamber. 151

**Figure 4.31.** Exploded view of the air bath thermal chamber. 152

**Figure 4.32.** Detailed drawing of the air bath thermal chamber. 153

**Figure 4.33.** Detailed drawings of the core structure of the air bath thermal chamber 153

**Figure 4.34.** Detailed drawings of the front panel of the air bath thermal chamber. 154

**Figure 4.35.** Detailed drawings of the back panel of the air bath thermal chamber. 154

**Figure 4.36.** Detailed drawings of the lateral panels of the air bath thermal chamber. 155

**Figure 4.37.** Detailed drawings of the circular bottom/base of the air bath thermal chamber. 155

**Figure 4.38.** Detailed drawings of the lid of the air bath thermal chamber (Dip-in Cell setup). 156

**Figure 4.39.** Detailed drawings of the lid of the air bath thermal chamber (Coin Cell setup). 156

**Figure 4.40.** Images of the front (above) and rear (below) panels of the air bath control box. 157

**Figure 4.41.** Schematic representation of the electrical configuration of the air bath control box. 158

**Figure 4.42.** Image of the inside of the air bath control box. 158

**Figure 4.43.** Image of the TEC controller (TEC-1089-SV). 159

**Figure 4.44.** Schematic representation of the wiring configuration of the temperature sensor connector (CAB-6154). 159

**Figure 4.45.** Schematic representation of the conductivity cells on the air bath thermal box. 161

**Figure 4.46.** Images of the temperature sensors and the respective placement on the air bath thermal chamber 162

**Figure 4.47.** Residuals associated with the Pt100 calibration. 163

**Figure 4.48.** Long-term thermal stability on the air bath thermal chamber. 164

**Figure 4.49.** Schematic summary of the ILDEMSoft application. 165

**Figure 4.50.** Screenshot of the Data Acquisition Module interface. 166

**Figure 4.51.** Schematic representation of the features and operational procedure of the Data Acquisition Module. 168

**Figure 4.52.** Screenshot of the Signal Monitoring Module interface. 169

**Figure 4.53.** Schematic representation of the features and operational procedure of the Signal Monitoring Module. 170

**Figure 4.54.** Screenshot of the Air Bath Regulation Module interface. 170

**Figure 4.55.** Schematic representation of the features and operational procedure of the Air Bath Regulation Module. 171

**Figure 4.56.** Screenshot of the Data Analysis Module interface. 172

**Figure 4.57.** Schematic representation of the features and operational procedure of the Data Analysis Module. 173

**Figure 4.58.** Representation of the typical resistance/reactance spectra and procedure for the extrapolation of $R_\infty$ for the standard aqueous 0.1000 mol·kg$^{-1}$ KCl solution. 175

**Figure 4.59.** Residuals associated with the cell constant determination of the dip-in cell derived from the electrical resistance measurement of a standard aqueous 0.1000 mol·kg$^{-1}$ KCl solution. 176

**Figure 4.60.** Typical impedance spectra for [$^1C_6{}^3C_1$im][$NTf_2$] at different experimental temperatures (283 – 333 K). 177

**Figure 4.61.** Representation of the typical resistance/reactance spectra and procedure for the extrapolation of $R_\infty$ for the [$^1C_6{}^3C_1$im][$NTf_2$] 179

**Figure 4.62.** Evaluation of the precision and accuracy evaluation of the dip-in cell with the reference ionic liquid [$C_6C_1$im][$NTf_2$]. 181

**Figure 4.63.** Representation of the impact of air bubbles inside the measuring region on the electrical resistance. 182

**Figure 4.64.** Residuals associated with the cell constant determination of the coin cell derived from the electrical resistance measurement of a standard aqueous 0.1000 mol·kg$^{-1}$ KCl solution. 183

**Figure 4.65.** Evaluation of the precision and accuracy evaluation of the coin cell with the reference ionic liquid [$C_6C_1$im][$NTf_2$].**.** 183

**Figure 4.66.** Comparative summary of the main features of the dip-in and coin electrical conductivity cells. 184

## Chapter 5 – Results and Discussion: Structure-property relationships

**Figure 5.1.** Schematic representation of the work conducted on the study of the transport properties of ionic liquids 190

**Figure 5.2.** Schematic representation of the study on the effect of the cation's alkyl chain length on the transport properties of ionic liquids. 194

**Figure 5.3.** Structure of the studied $[^1C_n{}^3C_1im]BF_4$ ($n$ = 2 – 10, 12). 195

**Figure 5.4.** Density and derived properties of the $[^1C_n{}^3C_1im]BF_4$ ILs as functions of temperature and number of carbons on the alkyl chain of the cation. 197

**Figure 5.5.** Viscosity of the $[^1C_n{}^3C_1im]BF_4$ ILs as functions of temperature and number of carbons on the alkyl chain of the cation. 199

**Figure 5.6.** Impact of the alkyl chain length on the VFT coefficients for the viscosity of $[^1C_n{}^3C_1im]BF_4$ ILs. 199

**Figure 5.7.** Graphical representation of the energy barrier and strength parameter derived from the experimental viscosity data of the $[^1C_n{}^3C_1im]BF_4$. 201

**Figure 5.8.** Deviation of the available viscosity data to the experimental results for the $[^1C_n{}^3C_1im]BF_4$ series. 202

**Figure 5.9.** Typical resistance and reactance spectra for the $[^1C_n{}^3C_1im]BF_4$ series. 202

**Figure 5.10.** Deviation of the available electrical conductivity data to the experimental results for the $[^1C_n{}^3C_1im]BF_4$ series. 204

**Figure 5.11.** Molar conductivity of the $[^1C_n{}^3C_1im]BF_4$ ILs as functions of temperature and number of carbons on the alkyl chain of the cation. 205

**Figure 5.12.** Impact of the alkyl chain length on the VFT coefficients for the molar conductivity of $[^1C_n{}^3C_1im]BF_4$ ILs. 206

**Figure 5.13.** Graphical representation of the energy barrier and strength parameter derived from the experimental molar conductivity data of the $[^1C_n{}^3C_1im]BF_4$ ILs. 208

**Figure 5.14.** Structure of the studied $[^1C_n{}^3C_1im]PF_6$ ($n$ = 3 – 10) ionic liquids. 208

**Figure 5.15.** Density and derived properties of the $[^1C_n{}^3C_1im]PF_6$ ILs as functions of temperature and number of carbons on the alkyl chain of the cation. 210

**Figure 5.16.** Viscosity of the $[^1C_n{}^3C_1im]PF_6$ ILs as functions of temperature and number of carbons on the alkyl chain of the cation. 211

**Figure 5.17.** Impact of the alkyl chain length on the VFT coefficients for the viscosity of $[^1C_n{}^3C_1im]PF_6$ ILs. 212

**Figure 5.18.** Graphical representation of the energy barrier and strength parameter derived from the experimental viscosity data of the $[^1C_n{}^3C_1im]PF_6$. 213

**Figure 5.19.** Deviation of the available viscosity data to the experimental results for the $[^1C_n{}^3C_1im]PF_6$ series 214

**Figure 5.20.** Typical resistance and reactance spectra for the $[^1C_n{}^3C_1im]PF_6$ series. 215

**Figure 5.21.** Deviation of the available electrical conductivity data to the experimental results for the $[^1C_n{}^3C_1im]PF_6$ series. 216

**Figure 5.22.** Molar conductivity of the $[^1C_n{}^3C_1im]PF_6$ ILs as functions of temperature and number of carbons on the alkyl chain of the cation). 217

**Figure 5.23.** Impact of the alkyl chain length on the VFT coefficients for the molar conductivity of $[^1C_n{}^3C_1im]PF_6$ series**.** 218

**Figure 5.24.** Graphical representation of the energy barrier and strength parameter derived from the experimental molar conductivity data of the $[^1C_n{}^3C_1im]PF_6$ series. 220

**Figure 5.25.** Structure of the studied $[^1C_n{}^3C1im]OTf$ ($n$ = 2, 4, 6, 8, 10, 12) ionic liquids. 220

**Figure 5.26.** Density and derived properties of the $[^1C_n{}^3C_1im][OTf]$ ILs as functions of temperature and number of carbons on the alkyl chain of the cation. 222

**Figure 5.27.** Viscosity of the $[^1C_n{}^3C_1im][OTf]$ series as functions of temperature and number of carbons on the alkyl chain of the cation. 223

**Figure 5.28.** Impact of the alkyl chain length on the VFT coefficients for the viscosity of $[^1C_n{}^3C_1im][OTf]$ series. 224

**Figure 5.29.** Graphical representation of the energy barrier and strength parameter derived from the experimental viscosity data of the $[^1C_n{}^3C_1im][OTf]$ series. 225

**Figure 5.30.** Deviation of the available viscosity data to the experimental results for the $[^1C_n{}^3C_1im][OTf]$ series. 226

**Figure 5.31.** Typical resistance and reactance spectra for the [$^1C_n{}^3C_1$im][OTf] series. 227

**Figure 5.32.** Deviation of the available electrical conductivity data to the experimental results for the [$^1C_n{}^3C_1$im][OTf] series. 228

**Figure 5.33.** Molar conductivity of the [$^1C_n{}^3C_1$im][OTf] series as functions of temperature and number of carbons on the alkyl chain of the cation. 229

**Figure 5.34.** Impact of the alkyl chain length on the VFT coefficients for the molar conductivity of [$^1C_n{}^3C_1$im][OTf] series. 230

**Figure 5.35.** Graphical representation of the energy barrier and strength parameter derived from the experimental molar conductivity data of the [$^1C_n{}^3C_1$im][OTf] series. 231

**Figure 5.36.** Structure of the studied [$^1C_n{}^3C_1$im][$NTf_2$] ($n$ = 1 – 12) ionic liquids. 232

**Figure 5.37.** Typical resistance and reactance spectra for the [$^1C_n{}^3C_1$im][$NTf_2$] series. 232

**Figure 5.38.** Deviation of the available electrical conductivity data to the experimental results for the [$^1C_n{}^3C_1$im][$NTf_2$] series. 234

**Figure 5.39.** Molar conductivity of the [$^1C_n{}^3C_1$im][$NTf_2$] series as a function of temperature and number of carbons on the alkyl chain of the cation. 235

**Figure 5.40.** Impact of the alkyl chain length on the VFT coefficients for the molar conductivity of [$^1C_n{}^3C_1$im][$NTf_2$] series**.** 236

**Figure 5.41.** Graphical representation of the energy barrier and strength parameter derived from the experimental molar conductivity data of the [$^1C_n{}^3C_1$im][$NTf_2$] series. 238

**Figure 5.42.** Structure of the studied [$^1C_n{}^3C_1$im][FAP] ($n$ = 2, 4, 6) ionic liquids. 238

**Figure 5.43.** Density and derived properties of the [$^1C_n{}^3C_1$im][FAP] series as a function of temperature and number of carbons on the alkyl chain of the cation. 240

**Figure 5.44.** Viscosity of the [$^1C_n{}^3C_1$im][FAP] series as a function of temperature and number of carbons on the alkyl chain of the cation. 241

**Figure 5.45.** Impact of the alkyl chain length on the VFT coefficients for the viscosity of [$^1C_n{}^3C_1$im][FAP] series. 242

**Figure 5.46.** Graphical representation of the energy barrier and strength parameter derived from the experimental viscosity data of the [$^1C_n{}^3C_1$im][FAP] series. 243

**Figure 5.47.** Deviation of the available viscosity data to the experimental results for the [$^1C_n{}^3C_1$im][FAP] series. 244

**Figure 5.48.** Typical resistance and reactance spectra for the [$^1C_n{}^3C_1$im][FAP] series 245

**Figure 5.49.** Deviation of the available electrical conductivity data to the experimental results for the [$^1C_n{}^3C_1$im][FAP] series 246

**Figure 5.50.** Molar conductivity of the [$^1C_n{}^3C_1$im][FAP] series as a function of temperature and number of carbons on the alkyl chain of the cation. 247

**Figure 5.51.** Impact of the alkyl chain length on the VFT coefficients for the molar conductivity of [$^1C_n{}^3C_1$im][FAP] series. 248

**Figure 5.52.** Graphical representation of the energy barrier and strength parameter derived from the experimental molar conductivity data of the [$^1C_n{}^3C_1$im][FAP] series. 249

**Figure 5.53.** Structure of the studied [$^1C_n$py][$NTf_2$] ($n$ = 3 – 9) ionic liquids. 249

**Figure 5.54.** Density and derived properties of the [$^1C_n$py][$NTf_2$] series as a function of temperature and number of carbons on the alkyl chain of the cation. 251

**Figure. 5.55.** Viscosity of the [$^1C_n$py][$NTf_2$] series as a function of temperature and number of carbons on the alkyl chain of the cation. 252

**Figure 5.56.** Impact of the alkyl chain length on the VFT coefficients for the viscosity of [$^1C_n$py][$NTf_2$] series. 253

**Figure 5.57.** Graphical representation of the energy barrier and strength parameter derived from the experimental viscosity data of the [$^1C_n$py][$NTf_2$]. 254

**Figure 5.58.** Deviation of the available viscosity data to the experimental results the [$^1C_n$py][$NTf_2$]. 255

**Figure 5.59.** Typical resistance and reactance spectra for the [$^1C_n$py][$NTf_2$] ionic liquids. 256

**Figure 5.60.** Deviation of the available electrical conductivity data to the experimental results for the [$^1C_n$py][$NTf_2$]. 257

**Figure 5.61.** Molar conductivity of the [$^1C_n$py][$NTf_2$] series as a function of temperature and number of carbons on the alkyl chain of the cation.. 258

**Figure 5.62.** Impact of the alkyl chain length on the VFT coefficients for the molar conductivity of [$^1C_n$py][$NTf_2$] ILs. 259

**Figure 5.63.** Graphical representation of the energy barrier and strength parameter derived from the experimental molar conductivity data of the [$^1C_n$py][$NTf_2$] ILs. 260

**Figure 5.64.** Structure of the studied [$^1C_n{}^1C_1$pyr][$NTf_2$] ($n$ = 3, 4, 6, 8) ionic liquids. 261

**Figure 5.65.** Density and derived properties of the [$^1C_n{}^1C_1$pyr][$NTf_2$] ILs as a function of temperature and number of carbons on the alkyl chain of the cation. 262

**Figure 5.66.** Viscosity of the [$^1C_n{}^1C_1$pyr][$NTf_2$] series as a function of temperature and number of carbons on the alkyl chain of the cation. 263

**Figure 5.67.** Impact of the alkyl chain length on the VFT coefficients for the viscosity of [$^1C_n{}^1C_1$pyr][$NTf_2$] series. 264

**Figure 5.68.** Graphical representation of the energy barrier and strength parameter derived from the experimental viscosity data of the [$^1C_n{}^1C_1$pyr][$NTf_2$]. 265

**Figure 5.69.** Deviation of the available viscosity data to the experimental results for the [$^1C_n{}^1C_1$pyr][$NTf_2$] series. 266

**Figure 5.70.** Typical resistance and reactance spectra for the [$^1C_n{}^1C_1$pyr][$NTf_2$] ionic liquids. 267

**Figure 5.71.** Deviation of the available electrical conductivity data to the experimental results for the $[^1C_nC_1pyr][NTf_2]$ series. 268

**Figure 5.72.** Molar conductivity of the $[^1C_n{}^1C_1pyr][NTf_2]$ series as a function of temperature and number of carbons on the alkyl chain of the cation. 269

**Figure 5.73.** Impact of the alkyl chain length on the VFT coefficients for the molar conductivity of $[^1C_n{}^1C_1pyr][NTf_2]$ series. 270

**Figure 5.74.** Graphical representation of the energy barrier and strength parameter derived from the experimental molar conductivity data of the $[^1C_n{}^1C_1pyr][NTf_2]$ series. 271

**Figure 5.75.** Effect of the alkyl chain length on the volumetric properties of the studied homologue series. 272

**Figure 5.76.** Effect of the alkyl chain on the reactance spectra. 272

**Figure 5.77.** Effect of the alkyl chain of the transport properties of the studied homologue ionic liquids series. 274

**Figure 5.78.** Walden plot of the studied homologue series based on the experimental viscosity and molar conductivity results. 277

**Figure 5.79.** Viscosity – molar conductivity correlations for the studied homologue series. 278

**Figure 5.80.** Correlation between the enthalpy of vaporization and energy barrier for the studied IL homologue series. 279

**Figure 5.81.** Ratio between energy barrier and enthalpy of vaporization (cohesive energy) for the studied ionic liquid homologue series. 279

**Figure 5.82.** Ion structures of the $[^1C_4{}^3C_1im][X]$ ionic liquids involved in the study focused on the effect of the nature of the anion on the transport properties of ILs. 281

**Figure 5.83.** Density and derived properties of the $[^1C_4{}^3C_1im][X]$ ILs as functions of temperature and at the reference temperature $T$ = 298.15 K. 283

**Figure 5.84.** Effect of the anion on the VFT coefficients derived from the experimental molar viscosity-temperature data of the [$^{1}C_{4}{}^{3}C_{1}$im][X] ILs. 284

**Figure 5.85.** Temperature dependence of the viscosity and derived energy barrier of the studied [$^{1}C_{4}{}^{3}C_{1}$im][X] ILs. 285

**Figure 5.86.** Deviation of the available viscosity data to the experimental results for the [$^{1}C_{4}{}^{3}C_{1}$im][X] ionic liquids. 286

**Figure 5.87.** Deviation of the available electrical conductivity data to the experimental results for the [$^{1}C_{4}{}^{3}C_{1}$im][X] ionic liquids. 287

**Figure 5.88.** Effect of the anion on the VFT coefficients derived from the experimental molar conductivity-temperature data of the [$^{1}C_{4}{}^{3}C_{1}$im][X] ILs. 289

**Figure 5.89.** Temperature dependence of the molar conductivity and derived energy barrier of the studied [$^{1}C_{4}{}^{3}C_{1}$im][X] ILs. 290

**Figure 5.90.** Graphical summary of the results obtained for the measured transport properties and respective derived parameters of the [$^{1}C_{4}{}^{3}C_{1}$im][X] ILs. 291

**Figure 5.91.** Walden plot for the [$^{1}C_{4}{}^{3}C_{1}$im][X] ILs based on the experimental viscosity and molar conductivity results. 295

**Figure 5.92.** Relationship between viscosity and molar conductivity for the [$^{1}C_{4}{}^{3}C_{1}$im][X] ILs. 295

**Figure 5.93.** Schematic representation of the study strategy on the effect of the cation-anion pairing. 297

**Figure 5.94.** Density and derived properties of the selected imidazolium, pyridinium, and pyrrolidinium ILs as functions of temperature and at the reference temperature. 298

**Figure 5.95.** Temperature dependence of viscosity for the selected imidazolium, pyridinium, and pyrrolidinium. 300

**Figure 5.96.** Deviation of the available viscosity data to the experimental results for [$^{1}C_{4}$py][OTf], [$^{1}C_{4}{}^{1}C_{1}$pyr][OTf], and [$^{1}C_{4}{}^{1}C_{1}$pyr][FAP]. 301

**Figure 5.97.** Deviation of the available electrical conductivity data to the experimental results for [$^1C_4$py][OTf], [$^1C_4{}^1C_1$pyr][OTf], and [$^1C_4{}^1C_1$pyr][FAP]. 302

**Figure 5.98.** Temperature dependence of molar conductivity for the selected imidazolium, pyridinium, and pyrrolidinium. 304

**Figure 5.99.** Viscosity and derived properties for the selected imidazolium, pyridinium, and pyrrolidinium. 305

**Figure 5.100.** Molar conductivity and derived properties for the selected imidazolium, pyridinium, and pyrrolidinium. 306

**Figure 5.101.** Walden plot for the selected imidazolium, pyridinium, and pyrrolidinium ILs 308

**Figure 5.102.** Viscosity-molar conductivity correlations for the selected imidazolium, pyridinium, and pyrrolidinium. 308

**Figure 5.103.** Schematic representation of the study of the impact of C2-methylation on transport properties of ILs. 309

**Figure 5.104.** Density and derived properties of the [$^1C_n{}^2C_1{}^3C_1$im][$NTf_2$] ILs and their protonated analogues and isomers as functions of temperature and number of carbons on the alkyl chain of the cation. 311

**Figure 5.105.** Temperature dependence of viscosity and derived energy barrier for the [$^1C_n{}^2C_1{}^3C_1$im][$NTf_2$] ILs and their protonated analogues and isomers. 313

**Figure 5.106.** Deviation of the available viscosity data to the experimental results for the [$^1C_n{}^2C_1{}^3C_1$im][$NTf_2$] ILs. 314

**Figure 5.107.** Deviation of the available electrical conductivity data to the experimental results for the [$^1C_n{}^2C_1{}^3C_1$im][$NTf_2$] ILs. 315

**Figure 5.108.** Temperature dependence of molar conductivity and derived energy barrier for the [$^1C_n{}^2C_1{}^3C_1$im][$NTf_2$] ILs and their protonated analogues and isomers. 316

**Figure 5.109.** Transport properties and derived parameters of the $[^1C_n{}^2C_1{}^3C_1im][NTf_2]$ ILs and their protonated analogues and isomers as functions of the number of carbons on the alkyl side chain of the imidazolium cation. 317

**Figure 5.110.** Schematic diagram of the effect of C2-methylation on the transport properties and derived parameters. 318

**Figure 5.111.** Correlation between the transport properties energy barrier and the enthalpy of vaporization of $[^1C_n{}^2C_1{}^3C_1im][NTf_2]$ and $[^1C_n{}^3C_1im][NTf_2]$ ILs. 319

**Figure 5.112.** Ratio between energy barrier and enthalpy of vaporization (cohesive interaction) for the $[^1C_n{}^2C_1{}^3C_1im][NTf_2]$ and $[^1C_n{}^3C_1im][NTf_2]$ ILs. 319

**Figure 5.113.** Walden plot for the $[^1C_n{}^2C_1{}^3C_1im][NTf_2]$ ILs and their protonated analogues and isomers. 320

**Figure 5.114.** Viscosity – molar conductivity correlations for the $[^1C_n{}^2C_1{}^3C_1im][NTf_2]$ ILs and their protonated analogues and isomers. 321

**Figure 5.115.** Schematic representation of the study on the effect of the isomerization of the pyridinium ring on the transport properties of ILs. 322

**Figure 5.116.** Density and derived properties of the selected imidazolium, pyridinium, and pyrrolidinium ILs as functions of temperature and at the reference temperature ($T$ = 298.15 K). 323

**Figure 5.117.** Temperature dependence of viscosity for the pyridinium isomers. 325

**Figure 5.118.** Deviation of the available viscosity literature data to the experimental results for the pyridinium isomers. 326

**Figure 5.119.** Deviation of the available molar conductivity literature data to the experimental results for the pyridinium isomers 327

**Figure 5.120.** Temperature dependence of molar conductivity for the pyridinium isomers. 328

**Figure 5.121.** Graphical summary of the results obtained for the measured transport properties and respective derived parameters of the pyridinium isomers. 329

**Figure 5.122.** Schematic diagram of the effect of isomerization of the pyridinium ring on the transport properties and derived parameters. 330

**Figure 5.123.** Walden plot for the pyridinium isomers based on the experimental viscosity and molar conductivity data. 331

**Figure 5.124.** Correlation between the transport properties energy barrier and the enthalpy of vaporization for the pyridinium isomers. 331

**Figure 5.125.** Ratio between energy barrier and enthalpy of vaporization for the pyridinium isomers. 332

## Chapter 6 – Conclusions and Achievements

**Figure 6.1.** Summary of the characteristics of the ILDEM Apparatus. 350

**Figure 6.2.** Summary of the conclusions on the effect of structure on the transport properties of ionic liquids. 352

## Appendix

**Figure A.1.** Schematic representation and images of the Peltier wiring configuration. 357

**Figure A.2.** Representation Control Box – Thermal Chamber connection with highlight to the powered/connected devices. 358

**Figure A.3.** Installation of the wiring installation on the Data Logger board. 359

# List of Symbols and Abbreviations

## Symbols and Abbreviations of Physical Properties and Constants

| | |
|---|---|
| A | Effective electrode surface area |
| $A_\eta$ | Pre-exponential VFT coefficient (viscosity) |
| $A_\Lambda$ | Pre-exponential VFT coefficient (molar conductivity) |
| $A_\sigma$ | Pre-exponential VFT coefficient (electrical conductivity) |
| $A_\mathrm{w}$ | Warburg coefficient |
| $a_0$ | Zero order fitting coefficient for the temperature dependence of density |
| $a_1$ | First-order fitting coefficient for the temperature dependence of density |
| $a_2$ | Second-order fitting coefficient for the temperature dependence of density |
| $\alpha$ | Hydrogen bond donor ability/acidity |
| $\alpha_\rho$ | Thermal expansion coefficient |
| $\alpha_\mathrm{w}$ | Walden slope |
| $B$ | Susceptance |
| $B_\eta$ | Energy barrier VFT coefficient (viscosity) |
| $B_\Lambda$ | Energy barrier VFT coefficient (molar conductivity) |
| $B_\sigma$ | Energy barrier VFT coefficient (electrical conductivity) |
| $\beta$ | Hydrogen bond acceptor ability/basicity |
| $C$ | Capacitance |
| $c$ | Concentration |
| $c_\mathrm{i}$ | Ionic concentration |
| $c_\mathrm{o}$ | Concentration of oxidized species |
| $c_\mathrm{r}$ | Concentration of reduced species |
| $C_\eta$ | Vogel temperature VFT coefficient (viscosity) |
| $C_\Lambda$ | Vogel temperature VFT coefficient (molar conductivity) |
| $C_\sigma$ | Vogel temperature VFT coefficient (electrical conductivity) |
| $C^\mathrm{o}_{p,\mathrm{m}}$ | Standard molar isobaric heat capacity |
| $c^o_p$ | Standard molar specific heat capacity |
| $C^\mathrm{o}_p/V$ | Standard molar volumic heat capacity |

| | |
|---|---|
| $\gamma$ | Surface tension |
| $D$ | Self-diffusion coefficient |
| $D_\eta$ | Strength parameter (viscosity) |
| $D_\Lambda$ | Strength parameter (molar conductivity) |
| $D_\sigma$ | Strength parameter (electrical conductivity) |
| $D_o$ | Self-diffusion coefficients of oxidized species |
| $D_r$ | Self-diffusion coefficients of reduced species |
| $d$ | Distance between two ions |
| $\Delta C_p$ | Isobaric heat capacity change |
| $\Delta^l_{gl} C_p$ | Change in isobaric heat capacity associated with glass transition |
| $\Delta^g_l G^o_m$ | Standard molar free Gibbs energy of vaporization (volatility) |
| $\Delta G^\ddagger$ | Free Gibbs activation energy for the viscous flow |
| $\Delta^g_l H^o_m$ | Standard molar enthalpy of vaporization |
| $\Delta^l_s H^o_m$ | Standard molar enthalpy of fusion |
| $\Delta^g_l S^o_m$ | Molar entropy of vaporization |
| $\Delta^l_s S^o_m$ | Molar entropy of fusion |
| $\Delta_{NE}$ | Deviation to the Nernst-Einstein relation |
| $\Delta\mu$ | Activation energy per particle |
| $\Delta W$ | Deviation to Walden line |
| $\delta$ | random probability distribution of molecular hoping |
| E | Electric field |
| $E_\Lambda$ | Energy barrier associated with molar conductivity |
| $E_\eta$ | Energy barrier associated with viscosity |
| $\xi$ | Ionicity |
| $f$ | Frequency |
| $f_i$ | Velocity cross-correlation coefficients |
| $f_r$ | Resonance frequency |
| $G$ | Conductance |
| $G_c$ | Configurational free Gibbs energy |
| $H$ | Energy difference between the broken and intact states |
| $H_r$ | Haven ratio |

| | |
|---|---|
| $H^{\gamma}$ | Surface enthalpy |
| $I$ | Electrical current |
| $J$ | Current density |
| $K_s$ | System stiffness (U-tube densimeter) |
| $l$ | Distance between electrodes |
| $\Lambda$ | Molar conductivity |
| $\Lambda_{NMR}$ | Molar conductivity (derived from NMR self-diffusion coefficients) |
| $M$ | Molar mass |
| $m$ | Fragility index |
| $m_{min}$ | Minimum fragility index |
| $m_t$ | Mass of the transducer (U-tube densimeter) |
| $n$ | Molar quantity |
| $N$ | Number of atoms |
| $N_c$ | Number of possible configurations |
| $n_e$ | Number of electrons |
| $q$ | Ion charge |
| $R$ | Electrical resistance |
| $R_\infty$ | Electrical resistance at infinite frequence |
| $R_{ct}$ | Charge-transfer electrical resistance |
| $R_s$ | Solution electrical resistance |
| $\rho$ | Density |
| $S_c$ | Configurational entropy |
| $S^{\gamma}$ | Surface entropy |
| $s^*$ | Minimum energy required for rearrangement |
| $\sigma$ | Specific electrical conductivity |
| $T$ | Temperature |
| $T_g$ | Glass transition temperature |
| $T_K$ | Kauzmann temperature |
| $T_m$ | Melting temperature |
| $t$ | Time |
| $\tau$ | Shear force |

| | |
|---|---|
| $\tau_r$ | Relaxation time |
| $\theta$ | Phase angle |
| $u$ | Speed of sound |
| $U_{pot}$ | Potential of electrostatic interactions |
| $\mu$ | Chemical potential |
| $\mu_i$ | Ionic mobility |
| $\phi_a(r)$ | Attractive component of the potential pair |
| $\phi(r)$ | The mutual potential energy of the two adjacent molecules |
| $V$ | Voltage |
| $V_m$ | Molar volume |
| $W$ | Probability of a cooperative region to translate to a new arrangement |
| $\omega$ | Angular velocity |
| $\Omega$ | Number of degenerate configurations |
| $x$ | Molar fraction |
| $X$ | Reactance |
| $X_C$ | Capacitive reactance |
| $X_L$ | Capacitive inductance |
| $\dot{\gamma}$ | Shear rate |
| $z$ | Number of particles |
| $z_i$ | Effective ionic charge |

## Methodologies and Software

| | |
|---|---|
| EDS | Energy dispersive spectroscopy |
| ILDEM | Ionic liquid dynamics and electrical mobility |
| HPVEE | Visual programming language from Hewlett Packard |
| MD | Molecular dynamics simulation |
| MS-CG | Multiscale coarse-graining |
| NMR | Nuclear magnetic resonance |
| SEM | Scanning electronic microscopy |
| SVM | Stabinger viscometer |

# Ionic Liquids Abbreviation Nomenclature

| | |
|---|---|
| C2 | Carbon situated between the nitrogen atoms in imidazolium cation |
| CAS | Critical alkyl size |
| H(C2) | Pre-exponential VFT coefficient (viscosity) |
| IL | Ionic liquid |
| *n* | Number of carbon atoms on the alkyl side chain of the IL cation |
| *N* | Total number of carbon atoms on the alkyl side chain of the IL cation |

## Anions:

| | |
|---|---|
| Ac | Acetate |
| BETI | bis(pentafluoroethylsulfonyl)imide |
| $BF_4^-$ | Tetrafluoroborate |
| $Br^-$ | Bromide |
| $Cl^-$ | Chloride |
| $C_nSO_4$ | Alkylsulfate |
| DCA | Dicyanamide |
| $EtSO_4$ | Ethylsulfate |
| FAP | Tris(pentafluoroethyl)trifluorophosphate |
| FSI | Bis(fluorosulfonyl)imide |
| $I^-$ | Iodide |
| $MeSO_3$ | Methylsulfonate |
| $MePO_4$ | Methylphosphate |
| NCS | Thiocyanate |
| $NTf_2$ | Bis(trifluoromethylsulfonyl)imide |
| $NO_3^-$ | Nitrate |
| OTf | Trifluoromethanesulfonate |
| $PF_6^-$ | Hexafluorophosphate |
| $SbF_6^-$ | Hexafluoroantimonate |
| TFA | Trifluoroacetate |
| Ty | Tysolate |

Cations:

| | |
|---|---|
| $[^1C_n{}^3C_1im]^+$ | 1-alkyl-3-methylimidazolium |
| $[^1C_n{}^3C_nim]^+$ | 1,3-dialkylimidazolium |
| $[^1C_n{}^2C_1{}^3C_1im]^+$ | 1-alkyl-2,3-dimethylimidazolium |
| $[C_n\text{-im-}CH_2OMen]$ | 3-alkyl-1-[(1R,2S,5R)-(−)-menthoxymethyl]imidazolium |
| $[^1C_n{}^1C_1pyr]^+$ | 1-alkyl-1-methylpyrrolidinium |
| $[^1C_npy]^+$ | 1-alkylpyridinium |
| $[^1C_2{}^2C_npy]^+$ | 1-ethyl-2-alkylpyridinium |
| $[^1C_n{}^2C_1py]^+$ | 1-alkyl-2-methylpyridinium |
| $[^1C_n{}^3C_1py]^+$ | 1-alkyl-3-methylpyridinium |
| $[^1C_n{}^1C_1pip]^+$ | 1-alkyl-1-methylpiperidinium |
| $[^1C_n{}^4C_1tz]^+$ | 1-alkyl-4-methyl-1,2,4-triazolium |
| $[N_{n,n,n,n}]^+$ | tetraalkylammonium |
| $[P_{n,n,n,n}]^+$ | tetraalkylphosphonium |

## Other Materials

| | |
|---|---|
| FFKM | Perfluoroelastomer (Kalrez ®) |
| KCl | Potassium Chloride |
| $LiPF_6$ | Lithium hexafluorophosphate |
| $N_2$ | Gaseous nitrogen |
| Ni | Nickel |
| PEEK | Polyether ether ketone |
| Pt | Platinum |
| PTFE | Polytetrafluoroethylene (Teflon ®) |
| TiN | Titanium nitride |

# Units and Constants

This thesis follows the International System of Units (SI) defined for the base physical quantities, as follows:

| SI Unit | Physical Quantity |
|---|---|
| A | Electric current |
| K | Temperature |
| kg | Mass |
| m | Length |
| mol | Amount of substance |
| s | Time |

All other physical quantities are derived from these seven base quantities, either by multiplication or division. Some of the SI derived units have special symbols:

| Derived SI Unit | | Physical Quantity |
|---|---|---|
| J | $m^2 \cdot kg \cdot s^{-2}$ | Energy, Work, Heat |
| Pa | $kg \cdot m^{-1} \cdot s^{-2}$ | Pressure |
| S | $s \cdot A^2 \cdot J^{-1}$ | Electrical conductivity |
| V | $J \cdot s^{-1} \cdot A^{-1}$ | Electrical potential difference |
| W | $J \cdot s^{-1}$ | Power, Heat Flow |
| Ω | $J \cdot s^{-1} \cdot A^{-2}$ | Electrical resistance |

The relative atomic masses used in this work are those recommended by the IUPAC Commission in 2016 [1]. The fundamental constants used for the calculations are the recommended values from CODATA [2], which are now presented in its concise form.

| | **Fundamental Constants** | **Value** |
|---|---|---|
| $\varepsilon_0$ | Electric permittivity in vacuum | $8.8541878128 \times 10^{-12}$ $m^{-3}\cdot kg^{-1}\cdot s^4\cdot A^2$ |
| $k_B$ | Boltzmann Constant | $1.380649 \times 10^{-23}$ $J\cdot K^{-1}$ |
| $N_a$ | Avogadro constant | $6.02214076 \times 10^{23}$ $mol^{-1}$ |
| $R$ | Molar gas constant | $8.314462618$ $J\cdot mol^{-1}\cdot K^{-1}$ |

---

[1] Norman, J. Irrgeher, D. Loss Robert, T. Walczyk, T. Prohaska, Pure Appl. Chem. 88 (2016) 265. https://doi.org/10.1515/pac-2015-0305

[2] NIST. The NIST Reference on Constants, Units and Uncertainty. CODATA: https://physics.nist.gov/cuu/Constants/index.html

# Organization of the Thesis

This thesis is divided into 6 chapters, structured as follows:

### Chapter 1 – Introduction

A brief introduction is provided on the structure and organization of ionic liquids, particularly the impact of nanostructuration on their physicochemical properties. A state-of-the-art on the study of the transport properties of ionic liquids is presented, and the relevance of this field is discussed based on the use of ILs in battery application. The aim of this thesis and the strategy followed are briefly explained.

### Chapter 2 – Methods, Theory, and Fundamentals

This chapter presents fundamental concepts concerning the measurement of density, viscosity, and electrical conductivity of ionic liquids, as well as the experimental conducted experimental procedures. The dependence of transport properties with temperature is discussed, namely by introducing concepts and properties that can be derived from these relations.

### Chapter 3 – Materials and Sample Purification

This chapter presents a list of the ionic liquids studied. It also describes the purification process of the samples and some procedures regarding the handling of samples. Details on additional materials used as calibrants or test materials are also provided.

## Chapter 4 – Development of an Impedance Measuring Apparatus

This chapter is dedicated to the description of the work conducted on the development of the ILDEM apparatus. This includes the design and development of the conductivity cells, the air bath thermal chamber, and the data acquisition software, as well as the presentation of the applied data analysis methods and the performance and accuracy tests.

## Chapter 5 – Results and Discussion: Structure–Transport Properties Relationships

This chapter is dedicated to the presentation and discussion of the experimental results. The discussion will be based on the several concepts introduced in Chapter 2 and will focus on the effect of ionic structure on the transport properties of the studied ionic liquids. The conducted experimental work is based on the systematic study of density, viscosity, and electrical conductivity for ionic liquids with different anionic and cationic structures. The results are divided into three sub-thematics:

- Effect of the alkyl chain length;
- Effect of the nature of the anion;
- Effect of the nature of the cation.

## Chapter 6 – Conclusions and Achievements

The main accomplishments and conclusions of this work are outlined in this chapter. The relevance of the work performed and some future work is also included.

# Chapter 1

# Introduction

**1.1.** Ionic Liquids (ILs), a General Overview

**1.2.** Structuration and Organization of ILs

**1.3.** Impact of Nanostructuration on the Macroscopic Properties of ILs

**1.4.** ILs in Energy Storage Applications

**1.5.** Transport Properties of ILs

**1.6.** Aim, Strategy and Motivation

**References**

# 1. Introduction

Ionic liquids (ILs) are low-melting compounds fully composed of ions [1, 2]. In the literature, ILs are usually defined as ionic compounds with a melting point lower than the normal boiling point of water (100 ºC) [1, 3]. However, this arbitrary upper limit presents no physical meaning, and this definition can be somewhat reductive. The interest in ionic liquids is related to their unique and attractive set of properties, such as high thermal and electrochemical stability, ability to dissolve both polar and nonpolar species, broad liquid phase window (due to low melting point and high decomposition temperature, and very low volatility [4-6]. These properties make ILs promising candidates for synthesis, catalysis, heat transference processes, electrochemistry, and energy-related applications [1, 7, 8]. Furthermore, the physicochemical properties of ILs can be easily tuned/altered by changing their molecular structure, particularly by changing the nature of the anion or the cation, the length of the alkyl chain of the cation, or introducing functionalized groups. The high number of possible combinations offers great versatility to this class of compounds [1]. Based on these characteristics, ILs are often referred to as “designer solvents” [1, 3, 8].

The first report on ionic liquids is usually attributed to Walden in 1914 [9] with the synthesis of the ethylamnonium nitrate, $[EtNH_3][NO_3]$, an ionic compound with a melting point of around 287 K (14 ºC). In 1951, Hurley and Wier [10] found that the mixture of 1-ethypyridinium bromide with aluminum chloride, $[^1C_2py]Br{:}AlCl$ in a 2:1 proportion yielded a melting point of 233 K (40 ºC). Following that, chloroaluminate-based compounds played a key role in the early days of ionic liquids. In 1982, Wikes *et al.*[11] introduced the now very common 1-alkyl-3-methylimidazolium cation for the first time by studying the binary system $[^1C_2{}^3C_1im]Cl{:}AlCl_3$. While these systems presented attractive properties, such as great electrochemical stability, they are typically very unstable in contact with air or water [12]. In 1992, Wilkes and Zaworokto [13] achieved the synthesis of ionic liquids with superior air/water stability by combining the $[^1C_2{}^3C_1im]^+$ with nitrate ($NO3^-$), tetrafluoroborate ($BF4^-$), and acetate anions (Ac). As a consequence of their improved stability, these ILs were much easier to handle than the chloroaluminate-based compounds. This marked the start of a new generation of ionic liquids and promoted scientific research and development in this field.

The current-day ILs are usually composed of a large organic cation with a head-charged group and a hydrocarbonated chain combined with an inorganic or organic anion [12]. Consequently, similar to molten salts, ILs exhibit a degree of short-range organization in

order to fulfill the electroneutrality conditions [14]. The nature of the ions is the main difference between ionic liquids and molten salts. While the latter are usually composed of small and spherical ions, ILs are composed of larger and sometimes asymmetric/irregularly shaped ions with a high degree of charge dispersion. These characteristics reduce the potential of the anion-cation interactions, which hinders the crystalline packing and the formation of highly-ordered phases [14-16]. Furthermore, due to their more complex nature, the organization of ionic liquids is also influenced by other types of interactions, namely hydrogen bonding and dispersive forces, which can perturb the electrostatic network [14-16]. An illustrative comparison of the crystalline packing in conventional salts and ionic liquids is presented in Figure 1.1.

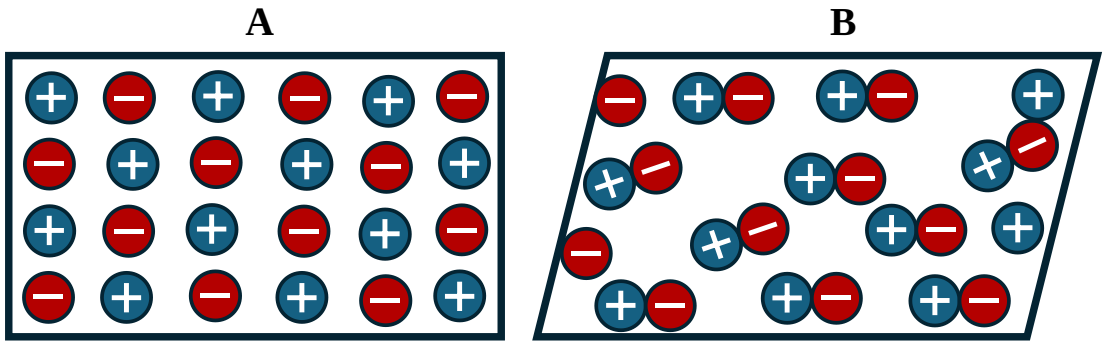



**Figure 1.1.** Schematic illustration comparing the structure and packing of conventional salts (**A**) and ionic liquids (**B**). The red and blue circles represent the anions and cations, respectively. Adapted from Gomes *et al*., 2009 [14].

Nowadays, the most common ionic liquids cations are based on positively charged heterocyclic rings, such as imidazolium (im), pyrrolidinium (pyr), and pyridinium (py) with alkyl side chains of variable length. These structures present a high degree of charge dispersion, contributing to the weakening of the electrostatic interactions. Additionally, quaternary aliphatic cations, namely ammonium and phosphonium based are also common. In the literature, there are studies with varied types of anions. While halides such as chloride, bromide, and iodide are somewhat common, larger and/or more asymmetric anions seem to be more popular nowadays. Fluorine-based anions are very attractive as the presence of fluorine contributes to charge delocalization, promoting lower melting points [17]. Tetrafluoroborate and hexafluorophosphate anions are very commonly used, although, just like the halide anions, these structures tend to be unstable in the presence of water due to the occurrence of hydrolysis, resulting in the

formation of hydrofluoric acid. Based on that, perfluorinated anions, such as $NTf_2$ and OTf, which present a superior water stability, gained increasing interest in the last decades [18, 19]. Additionally, the presence of these types of chains seems to be key in reducing the viscosity of the liquid, which can be very desirable for several applications, including electrochemistry and fluid engineering processes [17, 20]. The structures of the most commonly used and studied ionic liquids are presented in Fig 1.2.

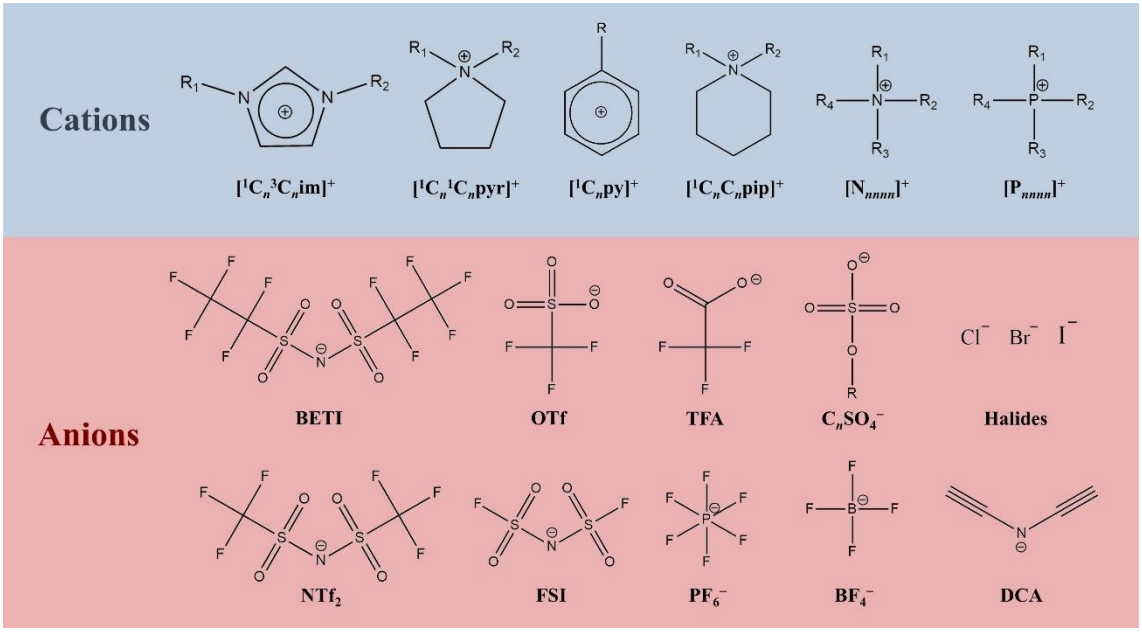



**Figure 1.2.** Molecular structures of the most common anions and cations of ion liquids. The "n" describes the size of the alkyl chains noted as "R". **Cations**: $[^1C_n{}^3C_n im]^+$ 1,3-dialkylimidazolium; $[^1C_n{}^3C_n pyr]^+$ 1,1-dialkylpyrrolidinium; $[^1C_n py]^+$ 1-alkylpyridinium; $[^1C_n{}^3C_n pyr]^+$ 1,3-dialkylpiperidinium; $[N_{nnnn}]^+$ tetraalkylammonium; $[P_{nnnn}]^+$ tetraalkylphosphonium. **Anions**: $C_nSO_4$ alkyl sulfate; BETI bis(pentafluoroethylsulfonyl)imide; OTf trifluoromethanesulfonate; TFA trifluoroacetate; $NTf_2$ bis(trifluoromethylsulfonyl)imide; FSI bis(fluorosulfonyl)imide; $PF_6^-$ hexafluorophosphate, $BF_4^-$ tetrafluoroborate and $[DCA]^-$ dicyanoamide.

## 1.1. Structuration and Organization of Ionic Liquids

Due to their nature, the structuration and organization of ILs at the molecular level are governed by different types of interactions. Electrostatic interactions, hydrogen bonding, and π-π stacking prevail in charged regions (anion and cation headgroup), while van der Waals interactions dominate the non-charged domain (hydrocarbonated chains) [7, 21]. Electrostatic and van der Waals interactions are the major factors, but the other two can

also present significant contributions to the structuration of the system. The dispersive interactions between the alkyl chains become more significant with the introduction of more methylene (-$CH_2$-) groups. The potential of electrostatic interactions between two oppositely charged ions is related to their charge ($q_i$ and $q_j$) and the distance between them ($r$), as described by Eq. 1.1.

$$U_{\text{pot}} = \frac{q_i q_j}{4\pi\varepsilon_0 r} \tag{1.1}$$

Where $\varepsilon_0$ is the permittivity in vacuum. However, as referred to earlier, ILs are composed of ions with a high degree of charge dispersion. Based on that, to properly calculate the electrostatic potential, Eq 1.1 should be applied to all interaction sites. Hydrogen bonding can occur in some ILs, although its potential is extremely dependent on the basicity of the anion and the availability of acidic interaction sites [22]. In the case of the imidazolium ring, the hydrogen in the C2 position, H(C2), is by far the preferred interaction site due to its high acidity, which is a consequence of being bonded to the positively charged C2 [23]. In fact, introducing a methyl group at this position (C2-methylation) was reported to lead to dramatic changes in the physicochemical properties, which in some cases might be associated with the blocking of hydrogen bonding [24-26]. In these systems, the anion tends to move around the cations to establish the preferred interaction. The presence of long or branched chains or other steric hindrances may restrict access to these preferred sites. Alternatively, in the case of the imidazolium ring, the anion might interact with the less acidic H(C4) and H(C5) [23]. In ionic liquids, there can be found different types of hydrogen bonding depending on the nature of the anion [7, 22, 27]. Halides can interact both as monoatomic ions ($Cl^-$ and $Br^-$) or bonded to halide atoms of molecular ions ($BF_4$ and $PF_6$). Hydrogen bonding can also be established with the oxygen atoms of acetate ($CO_2^-$), sulfate ($SO_4^{2-}$), sulfonate ($SO_3^-$), phosphate ($PO_4^{3-}$), and nitrate ($NO_3^-$) based anions. The third and less common type of hydrogen bonding would be with the central nitrogen atom of the “wing”-shaped anions, such as DCA, $NTf_2$, FSI, and BETI. The hydrogen bonding ability of an anion can be evaluated based on the Kamlet-Taft $\beta$ parameter, which can be experimentally determined by UV-Vis spectroscopy. Based on several literature sources, Hunt *et al.* [22], in a review on the hydrogen bonding in ionic liquids, presented the following trend:

$$\text{Ac} > \text{MePO}_4^- > \text{MeSO}_3^- > \text{Cl}^- > \text{NO}_3^- \approx \text{MeSO}_4^- > \text{DCA} >$$

> OTf > $BF_4^-$ > $NTf_2$ > $PF_6^-$ > $SbF_6^-$

While same-charge ions would normally repulse each other, cation-cation interaction might be stabilized by π-π stacking between two aromatic rings such as imidazolium [27]. However, these types of interaction are not usually very strong and can be hindered by the movement of the anion around the cation.

The interplay between these different types of interactions plays a key role in the organization of the liquid phase, which may lead to the segregation in two distinct domains (polar and nonpolar), resulting in a nanostructured liquid. A schematic representation of the type of interaction that can be found in an ionic liquid system is presented in Fig 1.3.

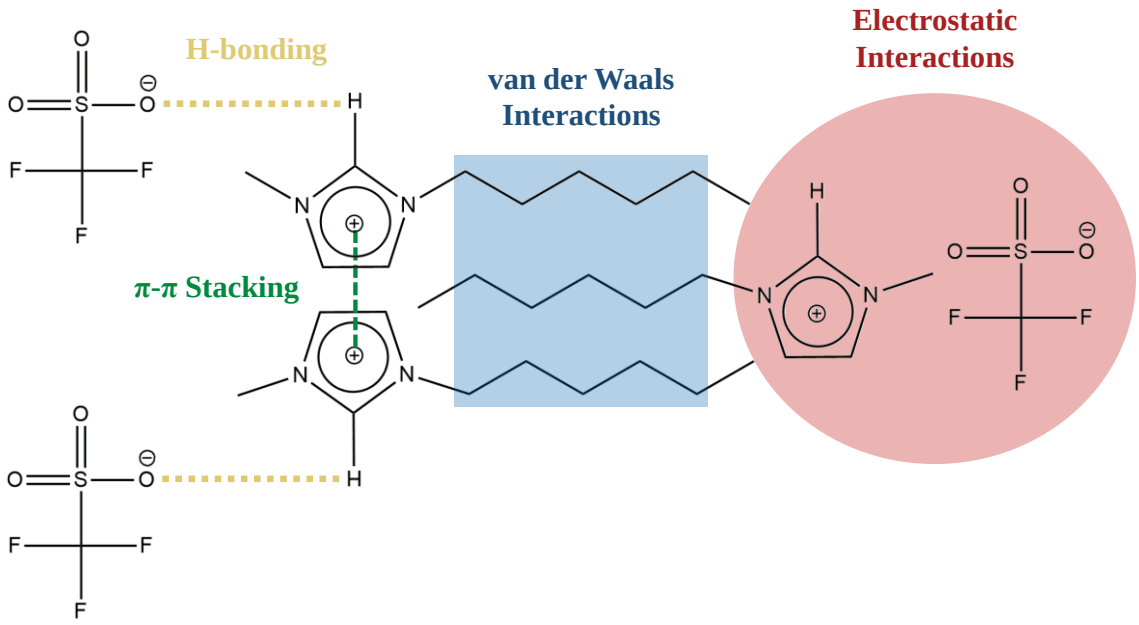



**Figure 1.3.** Schematic representation of the types of intermolecular interactions of an ionic liquid.

The present understanding and knowledge concerning the nanostructuration of ionic liquids is a result of several computational and experimental works developed in the last decades. Urahata and Ribeiro [28], using molecular dynamics simulation with atom force fields, studied the effect of the alkyl chain length for alkylimidazolium series, $[^1C_n{}^3C_1im]^+$, paired with different anions ($F^-$, $Cl^-$, $Br^-$ and $PF_6^-$). The authors found that the increase of the alkyl chain pushed the anions, resulting in a shift of the anion location to zones further from the nonpolar regions. In other work, Wang and Voth [29] based on a multiscale coarse-graining (MS-CG) method studied the effect of the alkyl chain for the

homologue series $[^1C_n{}^3C_1im]NO_3$. In this work, it was found that for ILs with longer alkyl chains, these nonpolar regions start to aggregate by establishing short-scale interactions, resulting in the formation of spatial heterogeneous domains. Meanwhile, the charged groups are somewhat homogeneously distributed due to the strong electrostatic interactions. Later on, Canongia Lopes and Pádua [15] further explored the concept of the existence of two domains by simulating the $[^1C_n{}^3C_1im]PF_6$ series using an all-atom force field. These findings were then complemented with a following work on $[^1C_n{}^3C_1im][NTf_2]$ series [30]. In these works, it was reported that polar regions behave as a tridimensional network of ionic channels permeated by the nonpolar region. The nature of the latter was found to be dependent on the size of the alkyl chain:

1. **Short chains ($n \leq 6$) –** a dispersed microphase described as small isolated "islands" inside the tridimensional polar network
2. **Long chains ($n \geq 6$) –** a bi-continuous mesoscopic phase formed by the aggregation of the "islands"

The snapshots of the simulation boxes of the $[C_nC_1im]PF_6$ ILs obtained by Canongia Lopes and Pádua [15] are presented in Fig. 1.4. These images further illustrate the organization and topology of the polar and nonpolar domains.

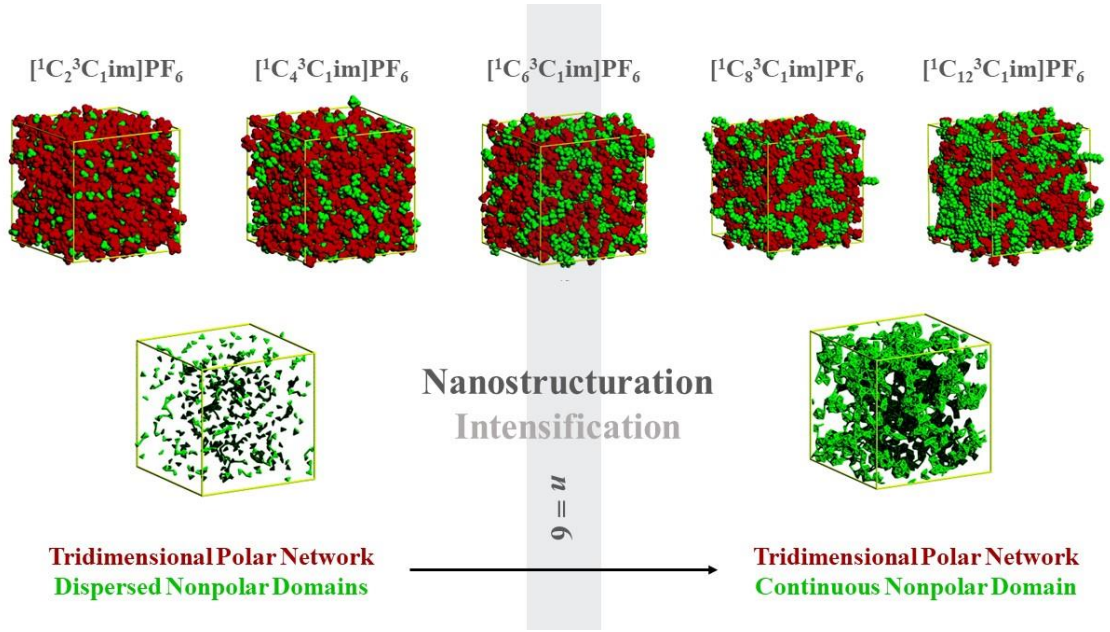



**Figure 1.4.** Schematic representation of the intensification of ionic liquid nanostructuration with the increases of the cation´s alkyl chain. Polar (red), nonpolar (green). The images correspond to snapshots of MD simulation of $[C_nC_1im]PF_6$ ILs and were adapted from Canongia Lopes and Pádua 2006 [15].

The enlargement of the nonpolar domain forces the polar network to expand without compromising its structure and continuity. Bernardes *et al.* [31] by analyzing the structure factors for the $[^1C_n{}^3C_1im][NTf_2]$ series obtained from MD simulations, found that the distance from the centroid of the imidazolium ring until the carbon 6 of the alkyl chain (0.7 – 0.8 nm), is comparable to characteristic length of the stretched polar network (0.77 nm). This observation suggests that the alkyl side chain must be longer than the sphere of influence of the polar network, causing separation of the polar network strands instead of just the sheath between them.

To summarize, the combination of these findings contributed to the characterization of ILs as complex fluids with a high degree of nanostructuration. Later on, experimental evidence of nanostructuration was reported based on x-ray diffraction [16] and dispersion studies [32].

The increase of the alkyl chains will change the potential of the interactions between the ions. A model has been proposed to rationalize these alterations [33] (Fig. 1.5). As the nonpolar domain becomes larger, it will further perturb and extend the polar network. This will increase the distance between the charged groups, which will result in a decrease in the potential of the anion-cation interactions. This trend continues until the network reaches its expansion limit ($n$ = 6) without compromising the electroneutrality condition [14]. After this point, the potential of the electrostatic interaction is maintained somewhat constant. Meanwhile, the potential of the dispersive interactions between these nonpolar regions will increase linearly with the introduction of new methylene (-$CH_2$-) groups. This model predicts that the overall interaction potential is maintained constant until the percolation limit ($n$ = 6) as a consequence of the balance between the weakening of the electrostatic interactions and the enhancement of dispersive forcers. After $n$ = 6, the overall potential is solely a reflection of the increase of the van der Waals interactions. The point of trendshift is usually referred to as the critical alkyl size (CAS) [33].

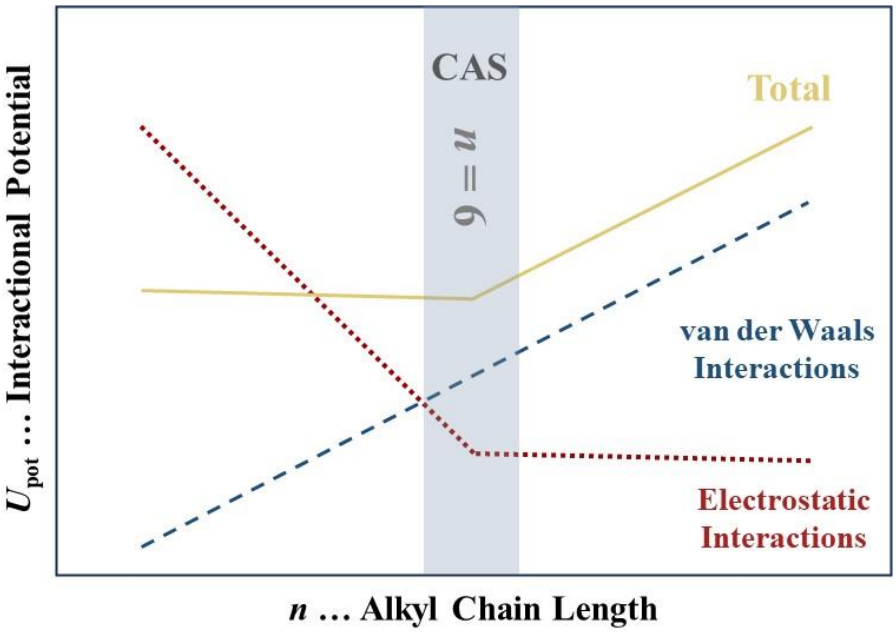



**Figure 1.5.** Schematic diagram of the interaction potentials present in the ionic liquids as a function of the cation alkyl chain size. Figure adapted from Vilas *et al.* 2011 [33].

## 1.2. Effect of Nanostructuration on the Physicochemical Properties of ILs

The nanostrucration of the liquid phase and the balance between the different types of interactions in ionic liquids have a major role in the macroscopic properties of these compounds, including solid-liquid equilibria, vaporization, heat capacity, and transport properties. In the last decade, several studies have been reported concerning the measurement of different physicochemical properties, revealing the occurrence of a trendshift (CAS). This is most likely a reflection of the changes in interactional potential described by the model of Fig. 1.5.

### 1.2.1. Solid-Liquid Equilibria

Holbrey *et al.*. [34] reported a study on the thermal behavior of the [$^1C_n{}^3C_1$im]BF4 ($n$ = 0 – 18) homolog series. Based on the experimental results, the authors classified the ILs into three groups depending on the size of the alkyl chain:

- **Short chains ($n$ < 3):** crystalline solids with strong interactions and relatively high melting points.
- **Intermediate chains (3 < $n$ < 10):** compounds with a broad liquid range and a tendency to form glasses on cooling.

- **Long chains (*n* > 10):** compounds with complex crystalline phases with the presence of mesomorphism associated with the presence of polar and nonpolar domains.

The tendency for the intermediate chains (*n* around CAS) to not form crystalline solids has also been verified for the $[^1C_n{}^3C_1im]PF_6$ [35] and $[^1C_n{}^3C_1im][NTf_2]$ [36] series. This can be a reflection of the complex IL structuration, which promotes the formation of a non-organized glass state. On the other hand, this absence of crystallization was not observed for the $[^1C_n{}^4C_npy][NTf_2]$ [36] and $[^1C_2{}^4C_npy][NTf_2]$ series [37]. This might suggest that the size ratio between the cation and anion plays a key role in the crystallization process.

Overall, in these works, it was found that the melting temperature does not change linearly with the increase of the alkyl chain, but instead, it tends to present a "V-shape" with an initial decrease (until around CAS) followed by an increase [34, 36-38]. This is likely evidence of the alterations in the liquid structure with the addition of methylene groups. The melting temperature is given by the ratio between the enthalpy and entropy of fusion, $T_m = \Delta^{\mathrm{l}}_{\mathrm{s}}H^{\mathrm{o}}_{\mathrm{m}}/\Delta^{\mathrm{l}}_{\mathrm{s}}S^{\mathrm{o}}_{\mathrm{m}}$. Based on that, this trend can be rationalized as follows [35-37]:

1. **Before CAS (n < 6):** the initial increase of the alkyl chain increases the distance between the counterions, reducing the potential of the electrostatic interactions, and therefore reducing $\Delta^{\mathrm{l}}_{\mathrm{s}}H^{\mathrm{o}}_{\mathrm{m}}$. Additionally, the addition of $-CH_2-$ groups leads to an increase in $\Delta^{\mathrm{l}}_{\mathrm{s}}S^{\mathrm{o}}_{\mathrm{m}}$ associated with the increase of the conformational entropy of the liquid. Both these effects are reflections of the perturbation of the packing mechanism and contribute to the decrease of $T_{\mathrm{m}}$.
2. **After CAS (n > 6):** in this region $\Delta^{\mathrm{l}}_{\mathrm{s}}H^{\mathrm{o}}_{\mathrm{m}}$ and $\Delta^{\mathrm{l}}_{\mathrm{s}}S^{\mathrm{o}}_{\mathrm{m}}$ increase regularly presenting a similar behavior to *n*-alkanes. This is a consequence of the similarity between *n*-alkanes and nonpolar domain of ILs. The increase of $\Delta^{\mathrm{l}}_{\mathrm{s}}H^{\mathrm{o}}_{\mathrm{m}}$ is a consequence of the enhancement of van der Waals interactions with the increase of the hydrocarbonated chains. This effect seems to overcompensate the increase in the conformational entropy of the liquid results in a steady increase of $T_{\mathrm{m}}$ after CAS.

A graphical representation of the variation of the thermodynamic melting properties with the increase of the alkyl chain is presented in Fig. 1.6.

Ionic liquids tend to form glasses upon rapid cooling. Since the glassy state is amorphous, it is not restricted by the packing requirements typical of the highly ordered crystalline phase. Therefore, glass stability is related to the strength of interactions and

the inability to generate both internal rotational degrees of freedom and external rotations and translations [36, 37]. From the published results, the trend of the glass transition temperature, $T_g$, seems to be different from the trend of $T_m$, as it increases with the addition of -$CH_2$- groups [35-37]. The [$^1C_n{}^3C_1$im][$NTf_2$] and [$^1C_n{}^3C_n$im][$NTf_2$] series [36] showed a remarkable decrease in slope after CAS (nearly reaching a plateau), although for pyridinium-based ILs, a slow and steady increase after $n$ > 6 was found (Fig. 1.6A) [37].

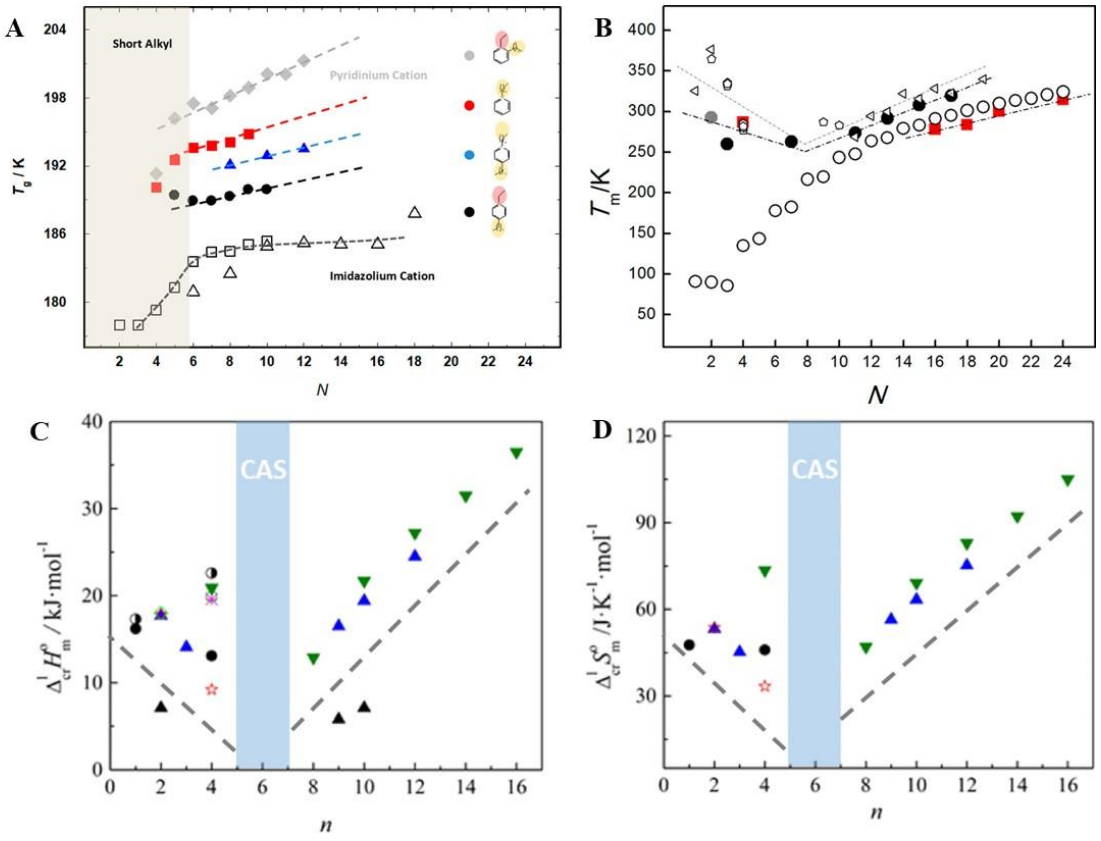



**Figure 1.6.** Effect of the cation's alkyl chain on the solid-liquid equilibrium of ionic liquids. **A**: glass transition temperature, image taken from Lobo Ferreira *et al.* [37]; **B**: melting temperature, image taken from Rodrigues *et al*. [36], ● [$^1C_n{}^3C_1$im][$NTf_2$], ■ [$^1C_n{}^3C_n$im][$NTf_2$], ● [$^1C_1{}^3C_1$im][$NTf_2$], □ [$^1C_n{}^3C_1$im][$PF_6$], ◁ [$^1C_n{}^3C_1$im][$BF_4$]; ○ alkanes; **C**: enthalpy of fusion of [$^1C_n{}^3C_1$im][$PF_6$] ILs, image taken from Serra *et al.* [35] **D**: entropy of fusion [$^1C_n{}^3C_1$im][$PF_6$] ILs, image taken from Serra *et al.* [35].

### 1.2.2. Heat Capacity

The molar heat capacity, $C_{p,\mathrm{m}}^{\mathrm{o}}$, is the amount of energy required to raise the temperature of one mole of a substance by one K. Therefore $C_{p,\mathrm{m}}^{\mathrm{o}}$ is expected to increase with the increase of the number of atoms as this corresponds to a larger amount of energy

storage modes (vibrational, rotational, and translational) [35, 39]. In 2010, Paulechka [40] published a review compiling the experiment heat capacity data for several ionic liquids. The author found that the molar heat capacity of a homologue series increases linearly with the number of carbons on the alkyl chain. The average value for the increment per -$CH_2$- group was reported to be 32.1 $J{\cdot}K^{-1}{\cdot}mol^{-1}$. This value is similar to the characteristic value for *n*-alkanes, 1-alkanols, and 1-chloro-*n*-alkanes. This is coherent with the $\Delta_s^l H_m^o$ and $\Delta_s^l S_m^o$ trends presented above. Later on, Rocha *et al*. [41] measured the heat capacities of the [$^1C_n{}^3C_1$im][$NTf_2$] (*n* = 2 – 8, 10, 12) using a high-precision drop calorimeter. The data showed an apparent linearity with *n* (Fig. 1.7A), consistent with what had been previously reported by Paulechka [40]. However, the representation of the residuals from the linear fitting based on the shorter chain ILs presented strong evidence of a trendshift after *n* = 6 [41] (Fig. 1.7B). The authors attributed the ability to detect these changes to the precision of the measurements and the fact of including both even and odd numbers of carbons in the alkyl chain. The odd-numbered ILs are usually less studied due to lower availability and higher costs. Furthermore, the authors found that the trendshift is much clearer for specific heat capacity, $c_p^o$, and particularly volumic heat capacity, $C_p^o/V$ (Fig. 1.7 C, D). The reported trend for $C_p^o/V$ is highlighted by a *plateau* (~ 1.92 $J{\cdot}K^{-1}{\cdot}cm^{-3}$) after *n* = 6. The authors interpreted this as a result of a balance between the decrease in density and the increase in volumic heat capacity per -$CH_2$- group [41]. Similar observations/trends were later found for other [$^1C_2{}^2C_n$py][$NTf_2$] [42] and [$^1C_n{}^3C_1$im]$PF_6$ [35] series. The fact that the trendshift is cleared from a volumetric basis is likely an indication that this effect is related to the cohesive energy of the liquid [41].

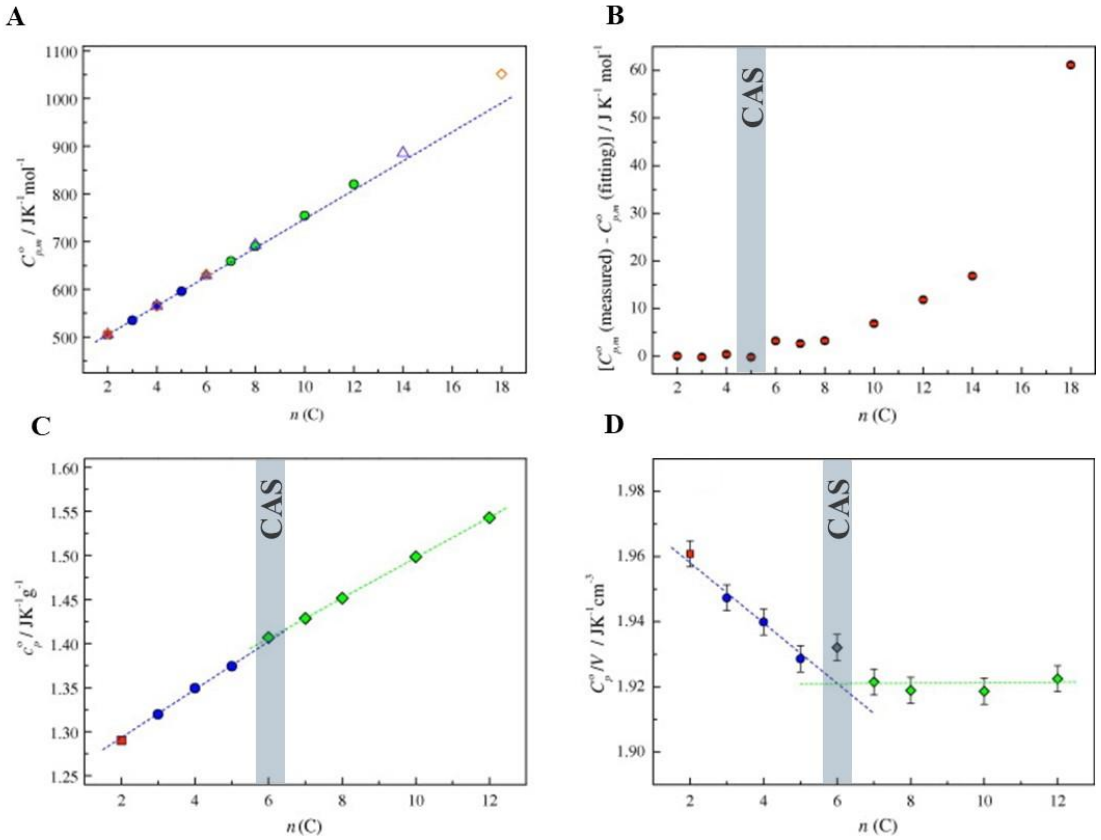



**Figure 1.7.** Effect of the cation's alkyl chain length on the isobaric heat capacity of [$^1C_n{}^3C_1$im][$NTf_2$] ionic liquids. **A:** Molar heat capacity; **B:** Fitting residuals of the molar heat capacity; **C:** Specific heat capacity; **D:** Volumic heat capacity. Figure adapted from Rocha *et al.* [41].

### 1.2.3. Volatility and Vaporization Thermodynamics

For a long time, ILs were thought to be non-volatile with unmeasurable vapor pressures. In 2005, Earle *et al.* [43] showed that it is possible to distillate ILs at reduced pressure without the occurrence of thermal decomposition. In 2007, Santos *et al.* [44] reported the first direct measurements of the cohesive energy (enthalpy of vaporization, $\Delta_l^g H_m^o$) of ionic liquids using a high-precision, vacuum-vaporization drop microcalorimetric method. In this work it was found that $\Delta_l^g H_m^o$ of [$^1C_n{}^3C_1$im][$NTf_2$] ($n$ = 2 – 8) increased linearly with $n$. Later on, the experimental results from this work were key on proving that ILs evaporate as ionic pairs, since the separation of the ionic species would yield much higher $\Delta_l^g H_m^o$ (experimental results: 130 – 180 kJ·mol$^{-1}$; estimated based on ionic pair separation: 300 kJ·mol$^{-1}$) [44-46]. More recently, Santos' group published a series of works concerning the measurement of vapor pressures of homologues ILs series ([$^1C_n{}^3C_1$im][$NTf_2$] [47, 48], [$^1C_n{}^3C_n$im][$NTf_2$] [49, 50], [$^1C_2{}^2C_n$py][$NTf_2$] [33]) using a Knudsen effusion method coupled with a quartz crystal microbalance. Overall, these

works demonstrated that the increase of the alkyl chain leads to an increase in $\Delta_l^g G_m^o$ (decrease in volatility), $\Delta_l^g H_m^o$, and $\Delta_l^g S_m^o$ (Fig. 1.8). The enthalpic increase reflects the increase in cohesive energy associated with the increase in van der Waals interactions. Both the $\Delta_l^g H_m^o$ and $\Delta_l^g S_m^o$ variation profiles present a trendshift around *n* = 6, reflected by a decrease in slope. This seems to be more highlighted for the symmetric [$^1$C$_n$$^3$C$_n$im][NTf$_2$] where $\Delta_l^g H_m^o$ and $\Delta_l^g S_m^o$ reached a *plateau*-like stage with a marked odd-even effect behavior (Fig. 1.8 C, D). From an enthalpic point of view, this represents a decrease in the contribution to the cohesive energy per -CH$_2$- group. On the other hand, considering that the standard molar entropy of the gas phases increases linearly, the decrease in the $\Delta_l^g S_m^o$ slope is likely related to an increase in the absolute entropy of the liquid phase. The free Gibbs energy of vaporization , $\Delta_l^g G_m^o$, has been found to typically show a "*plateau* – V-shape" behavior for the shorter alkyl chain *n* < 4 (Fig. 1.8B). This is most likely a consequence of the expansion of the electrostatic network and the balance between the electrostatic and non-electrostatic interactions, as presented in the model of Fig. 1.5 [33]. After the initial *plateau* $\Delta_l^g G_m^o$ tends to increase almost linearly, which might be a reflection of a mutual compensation between the enthalpic and entropic terms [33, 41, 49].

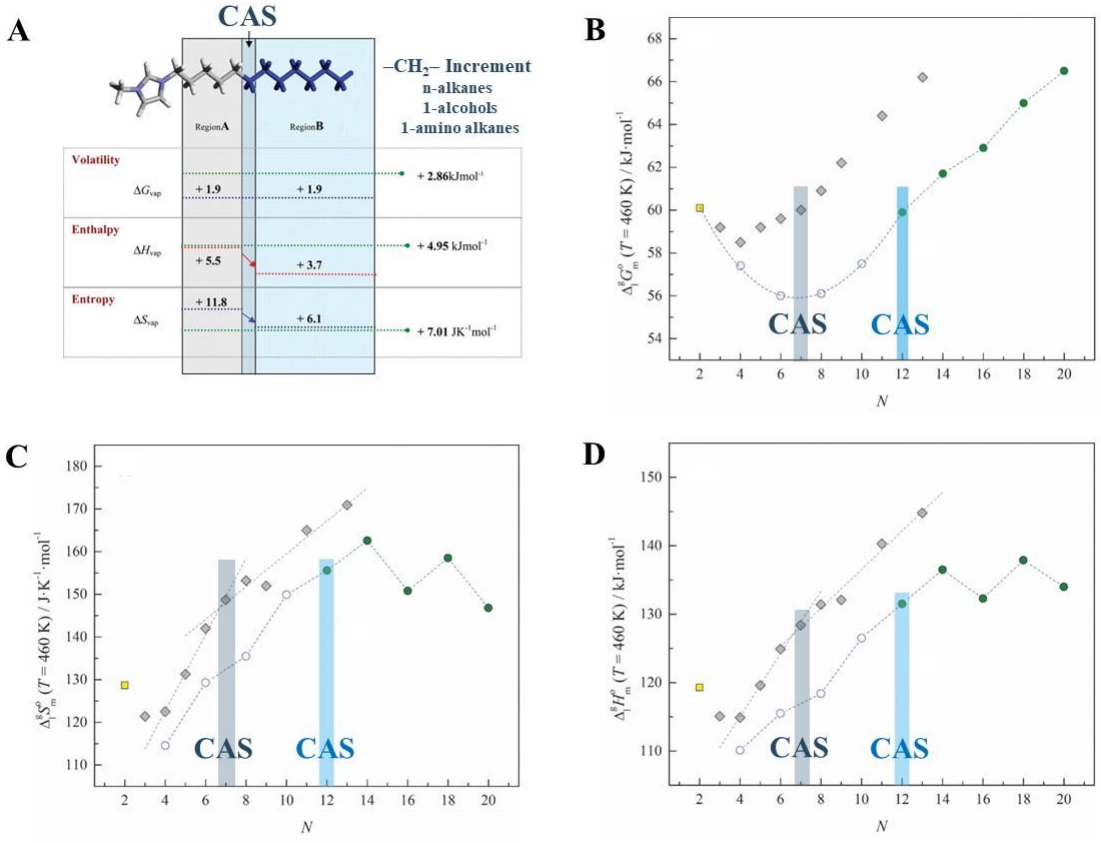



**Figure 1.8.** Effect of the cation's alkyl chain length on the vaporization properties of ionic liquids. **A:** Schematic diagram of the trendshift of the thermodynamic vaporization properties; **B:** Gibbs energy of vaporization (volatility); **C:** Entropy of vaporization; **D:** Enthalpy of vaporization. Image **A** was adapted from Rocha *et al.*. [47]. Images B, C, and D were adapted from Rocha *et al.*. [50]. ■ [$^1C_1{}^3C_1$im][$NTf_2$], ◆ [$^1C_n{}^3C_1$im][$NTf_2$], ●○ [$^1C_n{}^3C_n$im][$NTf_2$].

### 1.2.4. Transport Properties

Transport properties are related to the mobility of the system. Based on that, it is expected that the introduction of longer chains results in an increase in viscosity and a decrease in the electrical conductivity and self-diffusion coefficients associated with the enhancement of the van der Waals interaction and aggregation of the polar regions. In fact, previous to the publication of the work of Canongia Lopes and Pádua [15], Tokuda *et al.* [51] presented the formation of hydrocarbonated clusters as a reasoning behind the decrease of inicity $(\Lambda/\Lambda_{\mathrm{NMR}})$ with the increase of the cation's alkyl chain. Ionicity lower than the unit suggests that the measured molar conductivity, $\Lambda$, is lower than the one estimated from the self-diffusion coefficients, $\Lambda_{\mathrm{NMR}}$, suggesting a degree of ion association/aggregation [51]. Rocha *et al.* found a slight trendshift on dependence of viscosity with the alkyl chain length for the series (Fig. 1.9A) [$^1C_n{}^3C_1$im][$NTf_2$] [52],

[$^1C_n{}^3C_n$im][$NTf_2$] [52], [$^1C_2{}^2C_n$py][$NTf_2$] [42], and [$^1C_n{}^3C_1$im][$PF_6$] [53]. For the [$^1C_n{}^3C_1$im][$NTf_2$] and [$^1C_n{}^3C_n$im][$NTf_2$], the longer alkyl chains ($n$ > 12) seem to present a positive deviation to the linear behavior between 6 < $n$ < 12 [52]. A similar result was found for the [$^1C_n{}^3C_1$im][$PF_6$] series, but in this case, the acceleration in the increase of viscosity starts at $n$ = 7 [53]. This is identical to what is typically observed for long-chained alkanes and is likely associated with the increase of conformational entropy and chain folding [52]. An odd−even effect is observed in the electrostatic dominated region (before CAS). This is related to the predominant orientation of the terminal methyl group of the alkyl chain to the imidazolium ring [52]. A similar effect has also been observed for the thermodynamic properties of vaporization [47, 49]. Furthermore, the trendshift was found to be clearer for properties derived from the temperature dependence of viscosity, particularly the energy barrier, $E_\eta$, (associated with the cohesive energy of the liquid) and the VFT pre-exponential coefficient, $A_\eta$, (associated with the shape/size/flexibility of the ions) [42, 52, 53]. The slope of $E_\eta$ decreases after the trendshift similar to what has been reported for $\Delta_l^g H_m^o$ (Fig. 1.9C,D). The coefficient $A_\eta$ seems to suffer an accentuated slowdown after CAS even reaching a *plateau* for the [$^1C_n{}^3C_1$im][$NTf_2$] and [$^1C_n{}^3C_n$im][$NTf_2$] series (Fig. 1.9B, D). The authors interpreted this as a consequence of the decrease of the surface−volume ratio of the ion pair associated with the loss of the sphericity and increasing elongation [52]. The [$^1C_2{}^2C_n$py][$NTf_2$] presents a strange behavior as both viscosity and energy barrier exhibit a *plateau* right before CAS, 3 ≤ $n$ ≤ 5, (Fig. 1.9C) [42]. The difference between the variation profiles of [$^1C_n{}^3C_1$im][$NTf_2$] and [$^1C_2{}^2C_n$py][$NTf_2$] might be related to the difference in the nature of the cation and its impact on the structuration of the liquid phase.

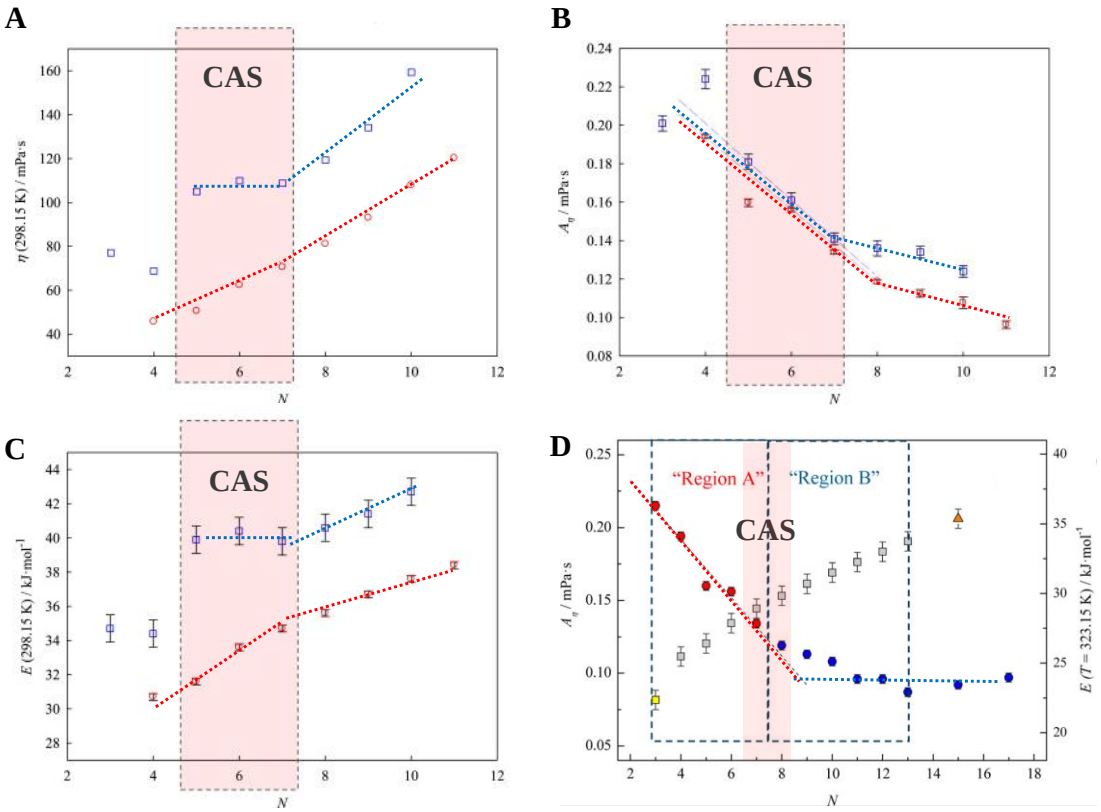



**Figure 1.9.** Effect of the cation's alkyl chain length on the viscosity of ionic liquids. **A:** Viscosity at the reference temperature $T$ = 298.15 K; **B:** VFT pre-exponential coefficient; **C:** Energy barrier at the reference temperature $T$ = 298.15 K; **D:** VFT pre-exponential coefficient and Energy barrier. Images **A**, **B**, and **C** are adapted from Rocha *et al.* [42], ○ [$^1C_2{}^2C_n$py][$NTf_2$], □ [$^1C_n{}^3C_1$im][$NTf_2$]; Image **D** is adapted from Rocha *et al.* [52], ■■▲ $E_\eta$ of [$^1C_n{}^3C_1$im][$NTf_2$], ●● $A_\eta$ of [$^1C_n{}^3C_1$im][$NTf_2$] ILs.

Zorębski's group found an interesting dependence of the speed of sound with the number of carbons on the alkyl chain for the [$^1C_n{}^3C_1$im][$NTf_2$] [54], [$^1C_n$py][$NTf_2$] [55], and [$^1C_n{}^1C_1$pyr][$NTf_2$] [56]. The authors reported the existence of a minimum at $n$ = 6 (Fig. 1.10), suggesting a relation between the speed of sound and the formation and segregation of the polar and nonpolar domains. However, this type of behavior was only found for the $NTf_2$ series [57].

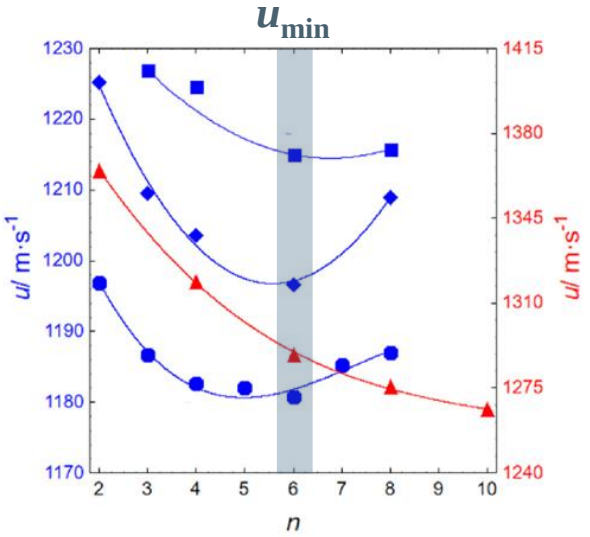



**Figure 1.10.** Effect of the cation's alkyl chain length on the speed of sound of ionic liquids. ● [$^1C_n{}^3C_1$im][$NTf_2$], ■ [$^1C_n{}^1C_1$pyr][$NTf_2$], ◆ [$^1C_n$py][$NTf_2$], ▲ [$^1C_n{}^3C_1$im][OTf].

### 1.2.5. Surface Properties

Surface tension, $\gamma$, and derived properties can provide meaningful information on the structuration and organization of the liquid. A clear trendshift on the surface tension behavior composed by an initial decrease followed by a *quasi-plateau* has been reported for several homologue series, [$^1C_n{}^3C_1$im][$NTf_2$] [58], [$^1C_n{}^3C_n$im][$NTf_2$] [59], [$^1C_n$py][$NTf_2$] [55], [$^1C_n{}^1C_1$pyr][$NTf_2$] [57], and [$C_n$-im-$CH_2$OMen][$NTf_2$] [60]. This is likely associated with the decrease of the electrostatic interactions due to the increase of the alkyl chain steric hindrance between the ion pairs. Almeida *et al.* found that the surface tension of [$^1C_n{}^3C_n$im][$NTf_2$] converges to the values presented by *n*-alkanes (Fig. 1.11A). This observation suggests that the surface is dominated by the hydrocarbonated chains. All these series also showed similar trends for the surface enthalpy, $H^\gamma$, and entropy, $S^\gamma$, derived for the temperature dependence of the surface tension (Fig. 11B, C). Surface enthalpy tends to present a "V-shape" with a minimum around $n$ = 5 or 6 and is probably a consequence of the balance between the electrostatic and dispersion interactions. The surface entropy seems rather irregular in the polar region (before CAS), but in all series, it appears to convert to a similar value. Based on the fact that this is observed for both symmetric and asymmetric series, Almeida *et al.* [59] presented this as a suggestion that the IL surface only involves one of the chains. Musial *et al.* [57] measured the surface tension of the [$^1C_n{}^3C_1$im][OTf] series and compiled data from other [$^1C_n{}^3C_1$im]+-based series paired with different anions [61-66]. While overall, it was possible to observe the presence of two regions, the behavior of $H^\gamma$ and $S^\gamma$ was irregular and different from what

was described for the $NTf_2$−based series. This once again highlights the impact of the anion on the IL structuration.

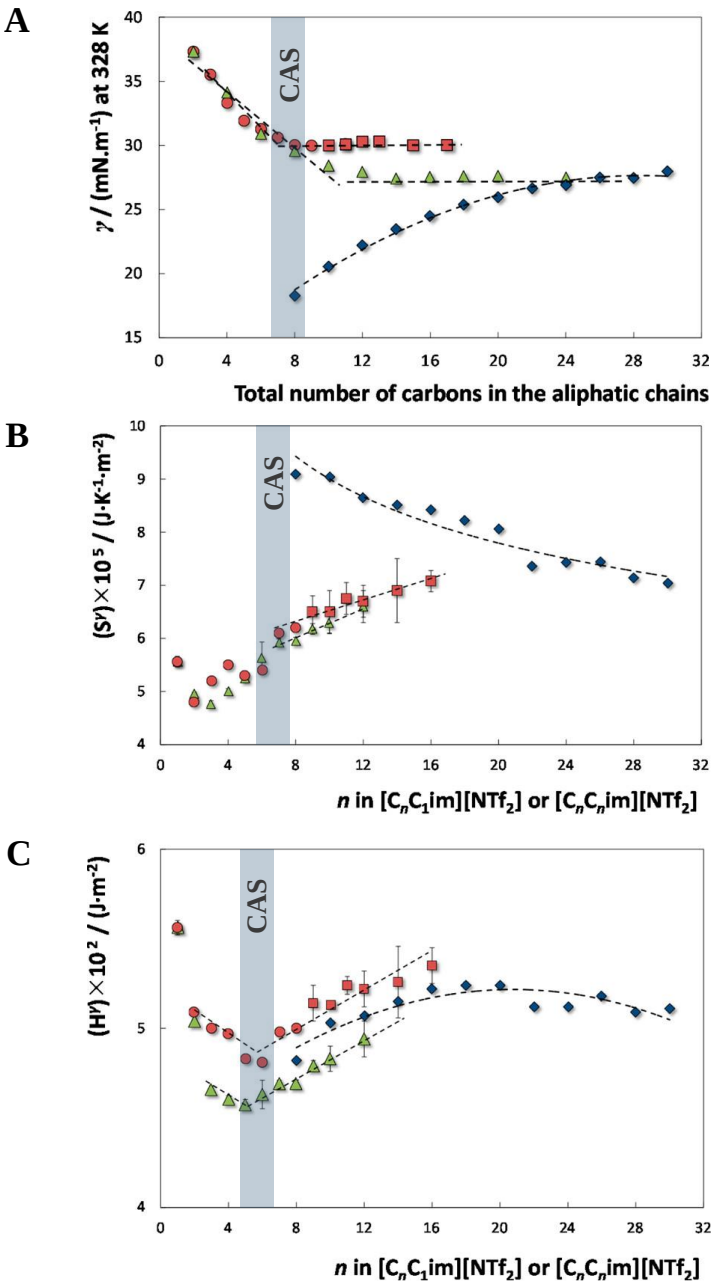



**Figure 1.11.** Effect of the cation's alkyl chain length on the surface properties of ionic liquids. **A:** Surface tension; **B:** Surface entropy; **C:** Surface enthalpy. Image adapted from Almeida et al. [59]. ● and ■ $[^1C_n{}^3C_1im][NTf_2]$, ▲ $[^1C_n{}^3C_nim][NTf_2]$, ◆ n-alkane.

### 1.2.6. Summary

In these sections, several studies concerning the impact of nanostrucration on different properties of ionic liquids where the existence of two variation profiles is usually observed. Overall, in these studies, the shorter−chain ($n$ = 1,2) ILs seem to behave as outliers compared to the rest of the homologue series. This is likely a consequence of their strong ionic character due to the short size of the aliphatic part [47, 52]. Besides this exception, a trendshift in the variation profile is typically observed around $n$ = 6. After CAS, the properties of ILs were found to often behave similarly to simpler compounds, such as *n*-alkanes and 1-alcohols, which is coherent with the enlargement of the alkyl chains and the formation of the bicontinuous nonpolar domain. An illustrative summary of the characteristics of these three regions (outlier, before CAS, and after CAS) is presented in Fig.1.12. While these results are reasonably described by the model presented in Fig. 1.5, this brief discussion also highlighted the existence of some different behaviors which make difficult the generalization of the impact of nanostructuration on the physicochemical properties of ionic liquids.

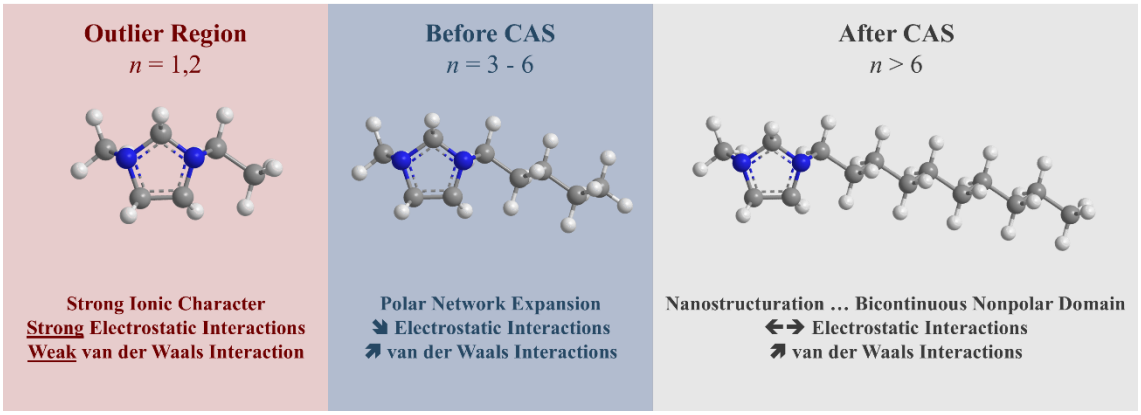



**Figure 1.12.** Summary of three regions/behaviors typically observed by increasing the length of the cation's alkyl chain.

## 1.3. Ionic Liquids in Energy Storage Applications

The current energy economy relies heavily on fossil fuels usage and therefore is inherently related to harsh future consequences due to the inevitable depletion of non-renewable resources, as well as the increasing climacteric risk concerning $CO_2$ emissions and global warming [67]. The urgency for an energy economy renewal requires the use of clean energy sources at a much higher level than the current state [68]. Lithium-ion batteries (LIBs) are one of the most popular energy storage

technologies nowadays and are at the forefront of energy storage development. LIBs display high energy densities (up to 250 Wh/kg or up to 800 Wh/L), relatively high power, good cyclic stability, and design versatility as they can be produced in different shapes and sizes [69]. Due to these characteristics, LIBs currently dominate the portable electronics market. However, the present Li-ion battery technology does not meet the requirements for the realization of efficient hybrid or electric vehicles [69, 70]. Furthermore, LIBs technology alone might not be sustainable enough for large-scale application due to its high production cost and the low lithium abundance [71]. In this regard, sodium-ion batteries (NIBs) and other "beyond lithium-ion batteries" have become major contenders for large-scale electrochemical energy storage [71, 72].

Innovation and development concerning electrical energy storage represent a multi-disciplinary challenge for both fundamental and applied research. In this sense, multiple research and development works have been/are being conducted to develop more advanced, efficient, and safer batteries components, namely, electrodes and electrolytes [70, 72-75]. The advance of the ion-battery technology is then intrinsically associated with the development of high-capacity anodes and high-voltage cathodes and electrolytes [70, 74, 75]. Currently, one of the main challenges in ion-battery research is the development of safe and stable high-voltage electrolytes. The standard electrolyte for LIBs is a binary mixture of $LiPF_6$ (lithium source) and an organic solvent, typically dimethyl carbonate [76]. Some of the conventional and currently used multicomponent electrolyte systems are presented in Figure 1.13. However, the utilization of these systems poses safety issues associated with their flammability, volatility, and poor thermal stability. These safety hazards are mainly related to $O_2$ release at the anode or the runaway reaction from graphite exfoliation at the cathode, which may cause fires, explosions, and the release of toxic chemicals [76, 77]. Thus, the interest and research targeting the development of new/alternative electrolytes for ion-batteries is a hot topic due to the need for a more efficient and safer "ion-based" type batteries. An adequate ion-battery electrolyte should fulfill the following requisites [77]:

1. wide liquid range (low melting point and high boiling point);
2. high thermal stability;
3. good alkaline salt solubility (high dielectric constant);
4. low enough viscosity to allow the realization of desirable electrical conductivities and fast ion transport;
5. High chemical stability (inert to the cell electrodes).
6. Good wettability to enhance electrolyte-electrode interfacial contact.

Ionic liquids (ILs) are low-melting ionic compounds (often below or near room temperature) composed of large ions with a high degree of charge delocalization. ILs have been gaining increasing attraction and interest in the last decade as possible candidates for new ion-battery electrolytes due to their excellent characteristics as low vapor pressure, non-flammability, and high thermal and electrochemical stability [69, 73, 78]. Despite the great potential of ILs for energy storage applications, the utilization of ILs as electrolytes for ion batteries also presents some drawbacks and challenges, namely due to their inferior transport properties in comparison to the conventional electrolytes [73, 79, 80]. Similar to the conventional organic solvents, for application in ion batteries, ILs are doped with a suitable alkaline cation, such as lithium and sodium, by the addition of the appropriate salt. The addition of charged species to the already charged IL leads to the realization of transport properties inferior to the conventional electrolytes associated with the stability of the IL−alkaline salts mixture. More precisely, the addition of the alkaline cation results in an increase in the IL viscosity and a decrease in electrical conductivity, as the presence of salts promotes the aggregation of anions around the small Li-ion, forming a more rigid structure [79, 81, 82]. Furthermore, the presence of different ionic species leads to a low $Li^+$ transference number [83]. A comparative summary of IL-based electrolytes and conventional electrolytes (organic solvent-based) is presented in Fig. 1.13.

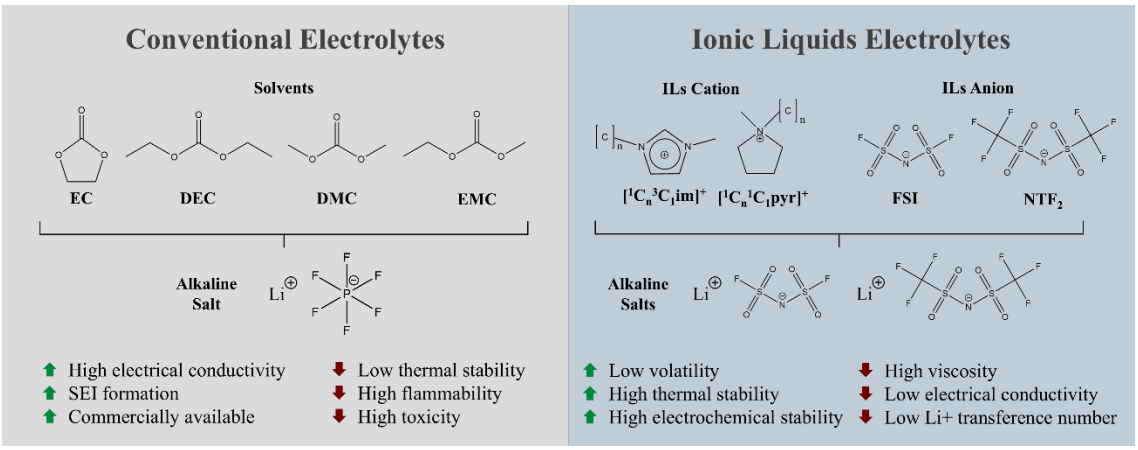



**Figure 1.13.** Summarized comparison between conventional electrolytes and ionic liquids electrolytes.

### 1.3.1. Ionic Liquids as Electrolytes

Several ILs/alkaline salts have been explored as potential electrolytes. The most common and more promising ILs for this application are constituted by imidazolium, $[^1C_n{}^3C_1im]^+$, or pyrrolidinium cations, $[^1C_n{}^1C_1pyr]^+$, with short alkyl chains and perfluorinated anions, namely, bis(trifluoromethanesulfonyl)imide, $NTf_2$, and bis(fluorosulfonyl)imide, FSI. The utilization of asymmetric and flexible ions is usually more desirable as it promotes the realization of ILs with lower melting points, which extends the liquid range. The use of imidazolium-based cations and FSI is associated with higher electrical conductivities, while pyrrolidinium-based cations and $NTf_2$ appear to have a positive influence on the thermal stability of the electrolyte. Additionally, pyrrolidinium-based ILs present a wider electrochemical window than their imidazolium analogues [69, 84, 85]. In the literature, FSI is typically preferred over $NTf_2$ as the former anion favors the formation of an effective solid electrolyte interface (SEI) that prevents undesirable electrolyte–electrode reactions, leading to a positive effect on the battery cyclability [69, 86, 87]. This highlights the advantage of the use of ILs for practical applications due to their tuning ability, allowing the design of systems with the optimal properties by changing the ions structure and the anion-cation pairing. Furthermore, the diverse characteristics of each ion encourage the mixing of different cations or anions in one electrolyte in order to optimize a specific set of properties. For instance, studies concerning systems composed of both $NTf_2$ and FSI have been previously reported in the literature [88, 89]. The molecular structures of the most common cations and anions in the study of the application of ILs as electrolytes are presented in Fig. 1.14.

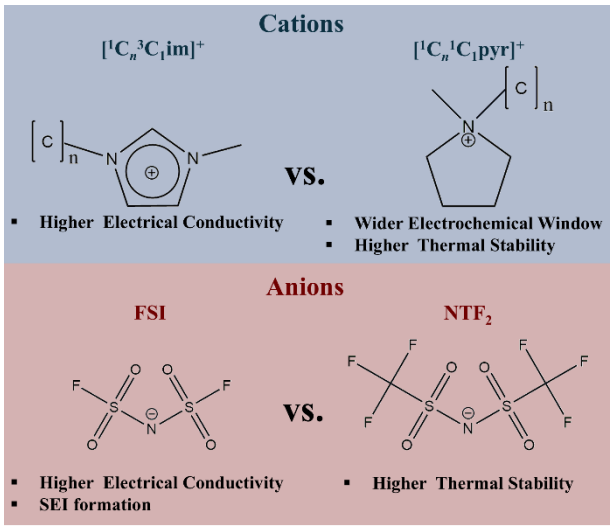



**Figure 1.14.** Commonly used ions in ionic liquid electrolytes.

### 1.3.2. Effect of the Addition of Alkaline Cations

To this date several studies concerning the effect of the addition of alkaline salts to the transport properties of ionic liquids, namely electrical conductivity, viscosity, and diffusivity have been reported, mainly concerning systems of pyrrolidinium and imidazolium cations combined with perfluoroalkyl anions, such as $NTF_2$ and FSI [80, 89-102]. Furthermore, although to a lesser extent, works focusing on sodium electrolytes were also reported [103-105]. The addition of lithium salt is now known to increase the viscosity and decrease ion diffusion and mobility, which consequently leads to a decrease in electrical conductivity associated with the reduction of the species mobility [79, 80, 96, 99, 105, 106]. The decrease in species mobility is reflected in the decrease in self-diffusion coefficients for each involved species [106]. This is interesting as it demonstrates that the introduction of an alkaline cation slows the mobility of every species. Generally, in these IL-LiX systems, the following trend is observed for the self-diffusion coefficients of the present species: D(IL-cation) > D(IL-anion) > D($Li^+$) [98, 99, 106-108]. The lower self-diffusion values for the alkaline cation are due to the strong interactions with the anion and its higher hydrodynamic radius associated with its solvation ability [99, 106]. The same effect has also been reported for sodium-based electrolytes [103]. As expected, the reduced mobility upon the addition of alkaline salt is reflected in the increase of dynamic viscosity. The introduction of the small and highly charged-localized alkaline cations enhances the electrostatic interactions, resulting in a more hindered system due to the formation of anionic clusters and aggregates [79, 108]. Raman [79, 81, 82] and XRD [97] studies focusing on $NTf_2$-based electrolytes have shown the formation of $[Li(NTF2)_2]^-$ clusters with preferential cisoid conformation for the coordinated anions. The formation of $[Li(X)_3]^{2-}$ ($X$ = FSI, $NTf_2$) clusters was also reported based on MD [99] and NMR studies [109]. Even more complex structures, referred to as lithium crosslinking bridges, were reported for $NTf_2$ systems, $Li\cdots NTf_2\cdots Li$ [79, 89, 108], and also $BF_4$-based electrolytes [101]. Lesch *et al.* [89] reported that lithium ions involved in crosslinking bridges move as fast as single $Li^+$ but present slower anion exchange rates. Pitawala *et al.* [79], based on a Raman spectroscopy study of $[C_4C_1pyr][NTf_2]$ + $Li[NTf_2]$, $0.01 \leq x(Li) \leq 0.4$, reported the existence of three coordinating regimes depending on the lithium content (Fig. 1.15)

- Low salt concentrations, $x(Li) < 0.05$: multiple $NTf_2$ anions coordinated with one Lithium-ion
- Intermediate salt concentrations, $0.1 \leq x(Li) \leq 0.2$: two $NTf_2$ anions coordinate one Lithium-ion, formation of $[Li(NTf_2)_2]^{-1}$ anionic clusters

- Higher salt concentrations, x(Li) > 0.2: Formation of complex structures with lithium dimers bridging $[NTf_2]$ anions, $[Li_x(NTf_2)_y]^{(-y-x)}$. The formation of these types of structures had been previously reported by Zhou *et al.* [110] for $[C_4C_1pyr][NTf_2]$ + $Li[NTf_2]$ and $[C_5C_1pyr][NTf_2]$ + $Li[NTf_2]$ mixtures based on XRD and Raman studies. The authors characterized these structures as “polymeric-like networks”.

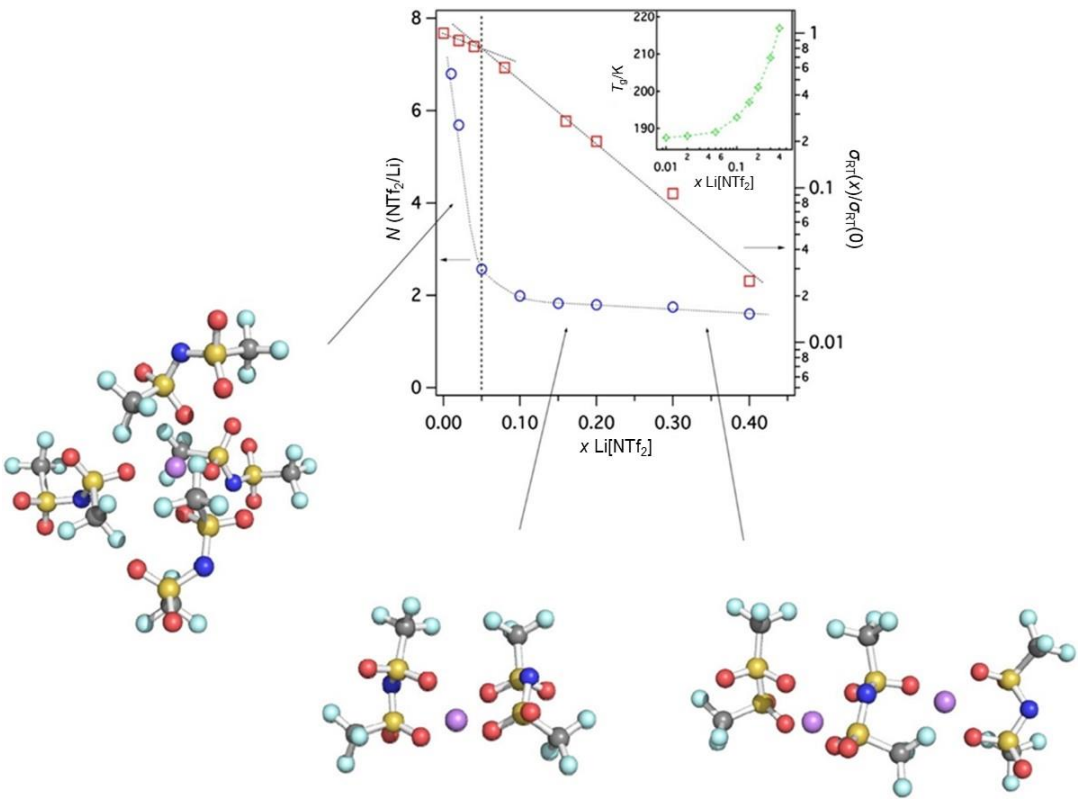



**Figure 1.15.** Correlation between the Lithium coordination and electrical conductivity on an ionic liquid - lithium salt mixture. ○ number of $NTf_2$ anions coordinating a lithium cation, $N(NTf_2/Li)$, □ electrical conductivity (room temperature electrical conductivity of the mixture is normalized based on room temperature electrical conductivity of the pure IL, $\sigma_{RT}(x)/\sigma_{RT}(0)$) and ◇ glass transition temperature profiles as a function of $Li[NTf_2]$ concentration for the $[C_4C_1pyr]$ $[NTf_2]$ + $Li[NTf_2]$ mixtures. Correlation between the coordination regimes and the macroscopic properties, Adapted from Pitawala *et al.* [79].

Besides electrical conductivity, viscosity, and species mobility, a high Li-ion transport number is also a key requirement for the design of efficient electrolytes for ion-battery applications [99]. However, the transport number of IL-LiX systems is frequently low and inferior to their conventional electrolyte counterparts. In this sense, systems with higher salt concentration (usually referred in the literature as IL-in-salt or solvent-in-salt mixtures) are gaining increasing attention [111-113], as the higher concentrations of the alkali cation tend to lead to an increase in the fraction of charge carried by the target ion [114, 115]. However, the use of highly concentrated electrolytes is generally associated with an increase in viscosity, which is usually reflected in a decrease in electrical conductivity. Fig. 1.16 highlights the opposing effect of the increase in

lithium transference number to the decrease of mobility (viscosity and diffusion) upon the addition of lithium. Furthermore, the addition of salt content often leads to the formation of crystalline phases and therefore reduces the liquid range or even promotes the crystallization at room temperature [116]. To overcome these disadvantages, the applicability of these IL-in-salt systems at high-temperature applications has been explored and proposed [111]. On the other hand, the utilization of asymmetric ions to decrease the melting point or suppress the crystallization has also been highlighted in the literature as a promising approach [107].

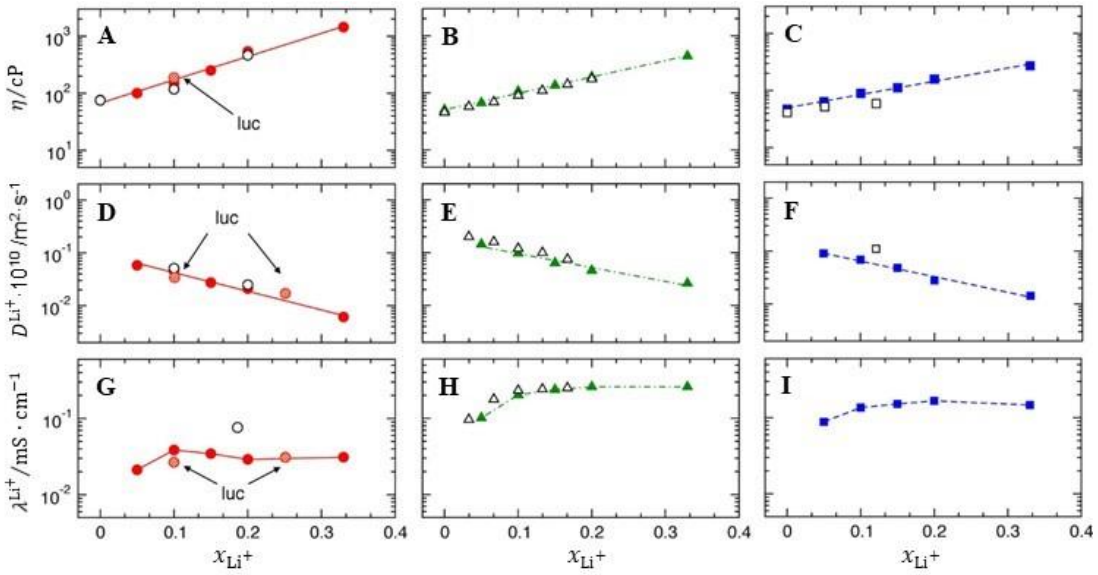



**Figure 1.16.** Variation profiles for dynamic viscosity **(a-c)**, lithium self-diffusion coefficients **(d-f)**, and lithium transport number with lithium-ion content **(g-i)**. Filled symbols: computational data, outlined symbols: represent experimental data. Left column **(a,d,g)** [$C_4C_1$pyr][$NTF_2$] + Li[$NTf_2$] [98, 106, 117-119]; middle column **(b,e,h)** [$C_2C_1$im][$BF_4$] + $LiBF_4$ [98, 120]; right column **(c,f,i)** [$C_3C_1$pyr][FSI] + Li[FSI] [21, 98]. Luc stands for the utilization of Lucretius, a simulation package specifically tailored to perform MD simulation using the APPLE&P. Adapted from Haskins *et al.* 2014 [98].

## 1.4. Transport Properties of Ionic Liquids

Electrical conductivity and viscosity studies combined with other transport properties, such as diffusion coefficients, may provide important insights concerning the type of interactions, ion dynamics, and the degree of ion dissociation or aggregation [121].

Currently, there are numerous electrical conductivity and viscosity data on neat ionic liquids in the literature. The most commonly studied ionic liquids are based on imidazolium, ammonium, pyrrolidinium, and pyridinium cations, while dicyanamide, bis(trifluoromethylsulfonyl)imide, tetrafluoroborate, hexafluorophosphate, and trifluoromethanesulfonate are the most common anions [122]. Although a significant contribution of these data comes from studies focusing on one or a few ILs or focusing

on the study of mixtures between ILs and other solvents or materials. Therefore, these studies do not directly contribute to the interpretation of the effect of the molecular structure on electrical conductivity. Still, there are several works focused on structural effects, mainly the anion nature [20, 123-137] but also on the cation nature [119, 134, 138-143] and the length of the alkyl chain of the cation [51, 134-136, 142-149].

### 1.4.1. Anion Effect

Generally, for the most common anions, the following trend is observed for the electrical conductivity of ionic liquids [122]:

$$DCA > NTf_2 > BF_4 > OTf > PF_6$$

A similar trend of reverse order is usually found for viscosity [150].

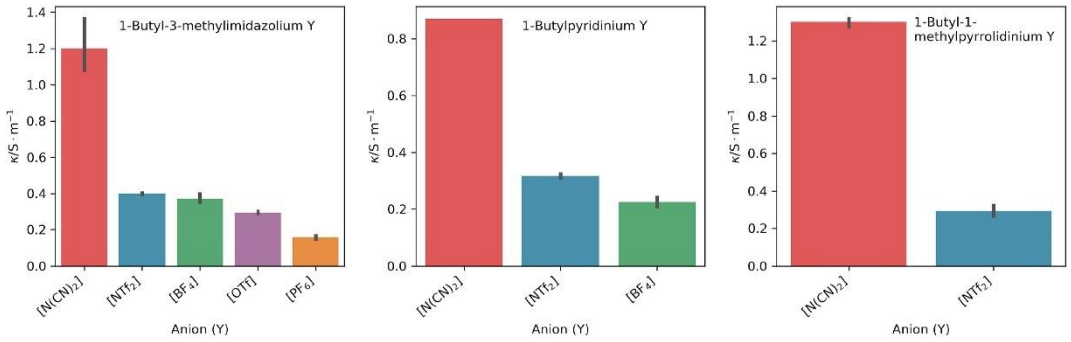



**Figure 1.17.** Effect of the nature of the anion on the electrical conductivity of ionic liquids based on common cationic groups. Image taken from Nancarrow *et al.* [122].

Yu *et al.* [124, 129] studied the electrical conductivity of $[C_2C_1im]^+$ and $[C_4C_1im]^+$ based on ILs paired with different anions. The authors stated that overall electrical conductivity would decrease with the increase in the size of the anion. On the other hand, in similar studies, Jin *et al.* [134] and Zech *et al*. [125] stated that no correlation was observed between the size of the anion and the electrical conductivity of the IL. Vila *et al.* [128] suggested that the effect of the anion size on the IL electrical conductivity can be described by two opposing factors: the superficial electrical charge density and the level of dynamics. Based on their results, $\Lambda_{298.15K}$(Ty < $Cl^-$ < $Br^-$ < EtSO4 < $PF_6^-$ < $BF_4^-$), the authors identified the $BF_4^-$ anion as the optimal size for electrical conductivity enhancement. Tokuda *et al.* [123] used the ratio between the molar conductivity measured by impedance measurements and the molar conductivity derived from NMR-diffusion experiments to evaluate the ionicity of six imidazolium ILs with different anions.

The lowest ionicity values were found for $[C_4C_1im][OTf]$ and $[C_4C_1im][TFA]$, which highlights the impact of the presence of pronounced negatively charged sites such as $S(=O)_2O^-$ and $C=OO^-$ groups. Leys *et al.* [20] further explained this effect by alerting for the impact of anion basicity and charge localization on the potential of hydrogen bonds and Coulombic interactions. The presence of strong cohesive interactions should decrease the mobility of the ions, resulting in a decrease in electrical conductivity. This would explain the trend obtained from this work $\Lambda_{298.15K}$(Cl < Br < I < $BF_4^-$< NCS < DCA). Similar conclusions were presented in other works. Ning *et al.* [130] justified the lower conductivity and higher viscosity of $[C_6C_1im][Cl]$ compared to $[C_6C_1im][BF_4]$ and $[C_6C_1im][PF_6]$ based on the stronger interaction between $Cl^-$ and the hydrogen at the C2 position of the imidazolium ring. Calado *et al.* [133] suggested that the strong charge localization and hydrogen bond basicity of $[C_2C_1im][EtSO_4]$ due to the presence of the sulfate group was the reasoning behind its lower conductivity compared to $[C_2C_1im][OTf]$ and $[C_2C_1im][NTf_2]$. Pandit *et al..* [126] measured the conductivity and viscosity of an imidazolium-based IL combined with salicylate, an aromatic anion. The authors attributed its low conductivity and high viscosity to the presence of π-π interactions between the benzene and the imidazolium rings. On the other hand, Sun *et al.* [127] published a study focused on ILs composed of aprotic heterocyclic anions. The authors stated that these systems yielded high electrical conductivities related to their viscosity and ionicities much higher than the values typically reported for the common $[C_2C_1im][NTf_2]$ ionic liquid. Xu and co-workers studied a series of 1-butyl-3-methylimidazolium [151] and 1-allyl-3-methylimidazolium [152] carboxylate ionic liquids. The results revealed that the introduction of hydroxyl (-OH), amino ($-NH_2$), and phenyl ($-C_6H_5$) groups leads to a decrease in electrical conductivity and an increase in the deviation to the ideal Walden line, associated with stronger ion association and reduced mobility as a consequence of the introduction of hydrogen bonding (-OH, $-NH_2$) and π-π stacking interactions ($-C_6H_5$).

### 1.4.2. Effect of the Cation

When analyzing the effect of the cation on the physicochemical properties of ILs, two features are highlighted: the nature of the charge head group/core structure of the cation and the length of the alkyl side chains. Relative to the cation nature, the general trend for electrical conductivity of the most common families is the following [122]:

imidazolium > pyridinium > pyrrolidinium > ammonium > piperidinium

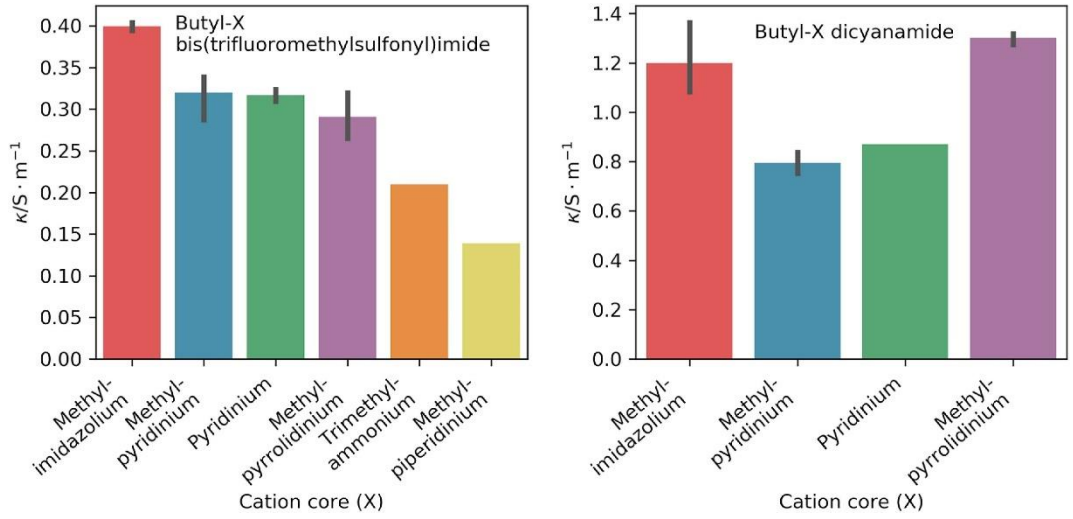



**Figure 1.18.** Effect of the nature of the cation head charge group on the electrical conductivity of bistriflimide and dicyanamide ionic liquids. Image taken from Nancarrow *et al.* [122].

However, in the same work and based on the available literature data for DCA and NTf2-based ILs combined with different cationic families, the authors demonstrated that the general trend for the cation nature also depends on the paired anion. Analogous to the anion effect, structural changes of the cation may affect the interactions and thus may impact the electrical conductivity of the ionic liquids. Sánchez-Ramírez *et al.* [139] found by means of DFT calculations, that the higher experimental electrical conductivity and lower viscosity of a pyrrolidinium-based IL, $[^1C_4{}^1C_1pyr][NTf_2]$, compared to its piperidinium-based analogue, $[^1C_4{}^1C_1pip][NTf_2]$, is supported by the higher ability of the latter to establish hydrogen bond interactions. On a similar note, Ibrahim et al. [140] and Tokuda, Ishii *et al.* [119] found a dependence of the cation structure on the electrical conductivity and ionicity of ILs. Ibrahim et al. [140] studied a series of $[NTf_2]$-based ILS with piperidinium, pyrrolidinium, ammonium, and morpholinium cations. The pyrrolidinium was found to yield higher conductivities and ionicities, while the morpholinium IL presented the lowest conductivity and the larger deviation to the ideal Walden plot, which might be related to the presence of an oxygen atom in the ring. Tokuda, Ishii, *et al.* [119] found different trends for the electrical conductivity: $[^1C_4{}^3C_1im][NTf_2] > [^1C_4py][NTf_2] > [^1C_4{}^1C_1pyr][NTf_2] > [N_{4,1,1,1}][NTf_2]$ and ionicity ($\Lambda/\Lambda_{NE}$): $[^1C_4{}^1C_1pyr][NTf_2] > [N_{4,1,1,1}][NTf_2] > [^1C_4py][NTf_2] > [^1C_4{}^3C_1im][NTf_2]$. Interestingly, the aromatic ILs were found to yield higher electrical conductivities, while the aliphatic ILs presented higher ionicities, which highlights the role of π-π interactions, planarity, and charge distribution on the cation-anion interaction potential. De La Hoz *et al.* [142] reported that 1-alkyl-4-methyl-1,2,4-triazolium bis(trifluoromethylsulfonyl)imide ILs

presented inferior transport properties when compared with the common 1-alkyl-3-methylimidazolium analogues. This is likely associated with the stronger anion-cation interactions due to the more acidic triazolium cation. Furthermore, structural changes in the common cationic rings, particularly the methylation at the position 2 of the imidazolium ring, have been found to drastically increase viscosity and decrease electrical conductivity [19, 146, 150, 153]

### 1.4.3. Effect of the Alkyl Chain Length

Concerning the effect of the alkyl chain length, the trend is usually more straightforward as the viscosity increases and the electrical conductivity decreases with the increase of the alkyl chain. This effect is associated with the increase of the potential of van der Waals interactions, which greatly decrease the ion mobility [134, 135, 142-144, 146, 154-156]. Umecky et al. presented the increase in the ratio between the hydrodynamic volume and molar volume with the increase of the alkyl chain for the $[^1C_n{}^3C_1im][PF_6]$ series as evidence of the enhancement of the overall interaction of liquid. This effect seems to persist independent of the anion and cation structure, as it was reported for $[^1C_n{}^3C_1im][NTf_2]$ [19, 51, 146], $[^1C_n{}^3C_1im]BF_4$ [130, 144, 157], $[^1C_n{}^3C_1im]Cl$ chloride [130], $[^1C_n{}^3C_1im][DCA]$ [143], $[^1C_n{}^3C_1im][OTf]$ [19], $[^1C_n{}^3C_1im][TFA]$ [19], $[^1C_n{}^3C_nim][NTf_2]$ [146], phosphonium [145], $[^1C_n{}^4C_1tz][NTf_2]$ [142], $[^1C_n{}^1C_1pyr][NTf_2]$ [134], dimethyl(isopropyl)alkylammonium bis(trifluoromethylsulfonyl)imide [134], protic ammonium carboxylates [155], protic alkylammonium trifluoromethanesulfonate [156], protic allylammonium trifluoromethanesulfonate [156]. However, the results reported by Jin *et al.* [134] indicate that the way that the electrical conductivity decreases with the increase of the alkyl chain along a homologous IL family depends on the nature of the cation. For instance, while the electrical conductivity of $[^1C_n{}^1C_1pyr][NTf_2]$ is around two times the conductivity of $[N_{i3,n,1,1}][NTf_2]$ for $n$ = 3, this difference becomes gradually smaller with the increase of $n$ until it is almost negligible for $n$ = 10. The authors suggested that this might be related to packing and interaction differentiation in the liquid state. Tokuda *et al.* [51] studied the electrical conductivity and ion diffusivity of $[^1C_n{}^3C_1im][NTf_2]$ ($n$ = 1,2,4,6,8). Molar conductivity and ionicity exhibited similar plots with the increase of the alkyl chain, with similar values between $n$ = 1 and 2, a pronounced decrease from $n$ = 2 to 4, and a gradual and slow decrease afterward $n$ = 4. The authors explained these variation profiles based on the interplay between electrostatic and van der Waals interactions and the formation of aggregates with the increase of the alkyl chain. However, apart from the observation of Tokuda *et al.* [51] and the viscosity studies

previously reported by the group where this thesis was conducted, the effect of nanostructuration on the transport properties is usually not explored. Leys *et al.* [158] reported a non-monotonic dependence of viscosity and electrical conductivity with the alkyl chain length for nitrile-functionalized pyrrolidinium bis(trifluoromethylsulfonyl)imide. The others found that the presence of the strongly polar nitrile group at the end of the chain plays a major impact on the coulombic interactions from the charge spreading effects and steric effects resulting in a pronounced odd-even effect on the dependence of the transport properties with the number of carbons on the alkyl chain of the cation [158].

## 1.5. Motivation, Aim and Strategy

As presented previously ionic liquids have desirable properties that present them as good candidates for battery applications. Nevertheless, there are some challenges associated with their typically high viscosity. The main objective of this work is to provide high-accuracy viscosity and electrical conductivity data for ILs with varied ionic structures. For this a systematic study involving around 60 ionic liquids was conducted, focusing on the effect of the alkyl chain length, the nature of the anion, and the nature of the cation on the transport properties of these compounds. Additionally, the temperature dependencies have been studied in order to derive insightful properties, including energy barrier and fragility. This information will be used to understand the nanostructuration, liquid dynamics, and viscous flow/ionic conduction mechanisms.

For the measurement of electrical conductivity, an impedance measuring methodology, ILDEM, was developed and tested during this PhD project. Electrical conductivity measurements at a fixed frequency are intrinsically affected by polarization effects. Although high frequencies diminish the impact of the polarization effect, it raises other problems associated with parasitic effects. Therefore, measuring impedance across a wide range of frequencies is a state-of-the-art procedure. For this a Precision LCR meter (20 Hz - 500 kHz) from Keysight (model E4980AL) was used in order to evaluate the effect of frequency in the resistivity of ILs and conversely the impact of ion structure on the impedance spectra. The main focus for this was to create a measuring system based which allowed a high-precision temperature control, the degassing/atmospheric isolation of the sample, the mitigation of polarization/electric field effects, and the use of a small amount of sample.

# References

[1] N.V. Plechkova, K.R. Seddon, Chem. Soc. Rev. 37 (2008) 123. https://doi.org/10.1039/B006677J

[2] Y.-L. Wang, B. Li, S. Sarman, F. Mocci, Z.-Y. Lu, J. Yuan, A. Laaksonen, M.D. Fayer, Chem. Rev. (2020). https://doi.org/10.1021/acs.chemrev.9b00693

[3] H. Weingärtner, Angew. Chem. Int. Ed. 47 (2008) 654. https://doi.org/10.1002/anie.200604951

[4] J. Holbrey, R. Rogers, R. A. Mantz, P. Trulove, V. Cocalia, A. E. Visser, J. L. Anderson, J. L. Anthony, J. F. Brennecke, E. Maginn, T. Welton, R. Mantz, 2008, p. 57-174. https://doi.org/10.1002/9783527621194.ch3

[5] T. Welton, Chem. Rev. 99 (1999) 2071. https://doi.org/10.1021/cr980032t

[6] J.F. Brennecke, E.J. Maginn, AIChE J. 47 (2001) 2384. https://doi.org/10.1002/aic.690471102

[7] R. Hayes, G.G. Warr, R. Atkin, Chem. Rev. 115 (2015) 6357. https://doi.org/10.1021/cr500411q

[8] Z. Lei, B. Chen, Y.-M. Koo, D.R. MacFarlane, Chem. Rev. 117 (2017) 6633. https://doi.org/10.1021/acs.chemrev.7b00246

[9] P. Walden, Bull. Acad. Imper. Sci. (St. Petersburg) 1800 (1914).

[10] F.H. Hurley, T.P. WIer, J. Electrochem. Soc. 98 (1951) 207. https://doi.org/10.1149/1.2778133

[11] J.S. Wilkes, J.A. Levisky, R.A. Wilson, C.L. Hussey, Inorg. Chem. 21 (1982) 1263. https://doi.org/10.1021/ic00133a078

[12] J.S. Wilkes, Green Chem. 4 (2002) 73. https://doi.org/10.1039/B110838G

[13] J.S. Wilkes, M.J. Zaworotko, J. Chem. Soc., Chem. Commun. (1992) 965. https://doi.org/10.1039/C39920000965

[14] M.F. Gomes, J.N. Lopes, A.A. Padua, Top. Curr. Chem. 290 (2010) 161. https://doi.org/10.1007/128_2009_2

[15] J.N.A. Canongia Lopes, A.A.H. Pádua, J. Phys. Chem. B 110 (2006) 3330. https://doi.org/10.1021/jp056006y

[16] A. Triolo, O. Russina, H.-J. Bleif, E. Di Cola, J. Phys. Chem. B 111 (2007) 4641. https://doi.org/10.1021/jp067705t

[17] H. Ohno, Bull. Chem. Soc. Jpn. 79 (2006) 1665. https://doi.org/10.1246/bcsj.79.1665

[18] M. Grätzel, Journal of Photochemistry and Photobiology C: Photochemistry Reviews 4 (2003) 145. https://doi.org/10.1016/S1389-5567(03)00026-1

[19] P. Bonhôte, A.-P. Dias, N. Papageorgiou, K. Kalyanasundaram, M. Grätzel, Inorg. Chem. 35 (1996) 1168. https://doi.org/10.1021/ic951325x

[20] J. Leys, R.N. Rajesh, P.C. Menon, C. Glorieux, S. Longuemart, P. Nockemann, M. Pellens, K. Binnemans, J. Chem. Phys. 133 (2010). https://doi.org/10.1063/1.3455892

[21] Y. Wang, K. Zaghib, A. Guerfi, F. Camilo, R. Torresi, J.R. Dahn, Electrochim. Acta 52 (2007) 6346. https://doi.org/10.1016/j.electacta.2007.04.067

[22] P.A. Hunt, C.R. Ashworth, R.P. Matthews, Chem. Soc. Rev. 44 (2015) 1257. https://doi.org/10.1039/C4CS00278D

[23] P.A. Hunt, B. Kirchner, T. Welton, Chem. Eur. J. 12 (2006) 6762. https://doi.org/10.1002/chem.200600103

[24] P.A. Hunt, J. Phys. Chem. B 111 (2007) 4844. https://doi.org/10.1021/jp067182p

[25] K. Fumino, A. Wulf, R. Ludwig, Angew. Chem. Int. Ed. 47 (2008) 8731. https://doi.org/10.1002/anie.200803446

[26] C.F.P. Miranda, A.I.M.C. Lobo Ferreira, L.M.N.B.F. Santos, J. Mol. Liq. 353 (2022) 118772. https://doi.org/10.1016/j.molliq.2022.118772

[27] Y.-L. Wang, B. Li, S. Sarman, F. Mocci, Z.-Y. Lu, J. Yuan, A. Laaksonen, M.D. Fayer, Chem. Rev. 120 (2020) 5798. https://doi.org/10.1021/acs.chemrev.9b00693

[28] S.M. Urahata, M.C.C. Ribeiro, J. Chem. Phys. 120 (2004) 1855. https://doi.org/10.1063/1.1635356

[29] Y. Wang, G.A. Voth, Journal of the American Chemical Society 127 (2005) 12192. https://doi.org/10.1021/ja053796g

[30] K. Shimizu, M.F. Costa Gomes, A.A.H. Pádua, L.P.N. Rebelo, J.N. Canongia Lopes, Journal of Molecular Structure: THEOCHEM 946 (2010) 70. https://doi.org/10.1016/j.theochem.2009.11.034

[31] C.E.S. Bernardes, K. Shimizu, A.I.M.C. Lobo Ferreira, L.M.N.B.F. Santos, J.N. Canongia Lopes, J. Phys. Chem. B 118 (2014) 6885. https://doi.org/10.1021/jp502968u

[32] O. Russina, A. Triolo, L. Gontrani, R. Caminiti, D. Xiao, L. G. Hines, R. A Bartsch, E. Quitevis, N. Plechkova, K. Seddon, Morphology and intermolecular dynamics of 1-Alkyl-3-methylimidazolium bis{(trifluoromethane)sulfonyl}amide ionic liquids: Structural and dynamic evidence of nanoscale segregation. 2009. https://doi.org/10.1088/0953-8984/21/42/424121

[33] M. Vilas, M.A.A. Rocha, A.M. Fernandes, E. Tojo, L.M.N.B.F. Santos, Phys. Chem. Chem. Phys. 17 (2015) 2560. https://doi.org/10.1039/C4CP05191B

[34] J. D. Holbrey, K. R. Seddon, J. Chem. Soc., Dalton Trans. (1999) 2133. https://doi.org/10.1039/A902818H

[35] P.B.P. Serra, F.M.S. Ribeiro, M.A.A. Rocha, M. Fulem, K. Růžička, J.A.P. Coutinho, L.M.N.B.F. Santos, J. Mol. Liq. 248 (2017) 678. https://doi.org/10.1016/j.molliq.2017.10.042

[36] A.S.M.C. Rodrigues, L.M.N.B.F. Santos, ChemPhysChem 17 (2016) 1512. https://doi.org/10.1002/cphc.201501128

[37] A.I.M.C. Lobo Ferreira, A.S.M.C. Rodrigues, M. Villas, E. Tojo, L.P.N. Rebelo, L.M.N.B.F. Santos, ACS Sustainable Chemistry & Engineering 7 (2019) 2989. https://doi.org/10.1021/acssuschemeng.8b04343

[38] P.B.P. Serra, F.M.S. Ribeiro, M.A.A. Rocha, M. Fulem, K. Růžička, L.M.N.B.F. Santos, J. Chem. Thermodyn. 100 (2016) 124. https://doi.org/10.1016/j.jct.2016.04.009

[39] J.M. Crosthwaite, M.J. Muldoon, J.K. Dixon, J.L. Anderson, J.F. Brennecke, J. Chem. Thermodyn. 37 (2005) 559. https://doi.org/10.1016/j.jct.2005.03.013

[40] Y.U. Paulechka, J. Phys. Chem. Ref. Data 39 (2010) 033108. https://doi.org/10.1063/1.3463478

[41] M.A.A. Rocha, M. Bastos, J.A.P. Coutinho, L.M.N.B.F. Santos, J. Chem. Thermodyn. 53 (2012) 140. https://doi.org/10.1016/j.jct.2012.04.025

[42] M.A.A. Rocha, M. Vilas, A.S.M.C. Rodrigues, E. Tojo, L.M.N.B.F. Santos, Fluid Phase Equilib. 428 (2016) 112. https://doi.org/10.1016/j.fluid.2016.05.030

[43] M.J. Earle, J.M.S.S. Esperança, M.A. Gilea, J.N. Canongia Lopes, L.P.N. Rebelo, J.W. Magee, K.R. Seddon, J.A. Widegren, Nature 439 (2006) 831. https://doi.org/10.1038/nature04451

[44] L.M.N.B.F. Santos, J.N. Canongia Lopes, J.A.P. Coutinho, J.M.S.S. Esperança, L.R. Gomes, I.M. Marrucho, L.P.N. Rebelo, Journal of the American Chemical Society 129 (2007) 284. https://doi.org/10.1021/ja067427b

[45] J. M. S. S. Esperança, J.N. Canongia Lopes, M. Tariq, L.M.N.B.F. Santos, J.W. Magee, L.P.N. Rebelo, J. Chem. Eng. Data 55 (2010) 3. https://doi.org/10.1021/je900458w

[46] J.P. Leal, J.M.S.S. Esperança, M.E. Minas da Piedade, J.N. Canongia Lopes, L.P.N. Rebelo, K.R. Seddon, J. Phys. Chem. A 111 (2007) 6176. https://doi.org/10.1021/jp073006k

[47] M.A.A. Rocha, C.F.R.A.C. Lima, L.R. Gomes, B. Schröder, J.A.P. Coutinho, I.M. Marrucho, J.M.S.S. Esperança, L.P.N. Rebelo, K. Shimizu, J.N.C. Lopes, L.M.N.B.F. Santos, J. Phys. Chem. B 115 (2011) 10919. https://doi.org/10.1021/jp2049316

[48] E. Paulechka, A.V. Blokhin, A.S.M.C. Rodrigues, M.A.A. Rocha, L.M.N.B.F. Santos, J. Chem. Thermodyn. 97 (2016) 331. https://doi.org/10.1016/j.jct.2016.02.009

[49] M.A.A. Rocha, J.A.P. Coutinho, L.M.N.B.F. Santos, J. Phys. Chem. B 116 (2012) 10922. https://doi.org/10.1021/jp306937f

[50] M.A.A. Rocha, J.A.P. Coutinho, L.M.N.B.F. Santos, J. Chem. Phys. 141 (2014) 134502. https://doi.org/10.1063/1.4896704

[51] H. Tokuda, K. Hayamizu, K. Ishii, M.A.B.H. Susan, M. Watanabe, J. Phys. Chem. B 109 (2005) 6103. https://doi.org/10.1021/jp044626d

[52] M.A.A. Rocha, C.M.S.S. Neves, M.G. Freire, O. Russina, A. Triolo, J.A.P. Coutinho, L.M.N.B.F. Santos, J. Phys. Chem. B 117 (2013) 10889. https://doi.org/10.1021/jp406374a

[53] M.A.A. Rocha, F.M.S. Ribeiro, A.I.M.C.L. Ferreira, J.A.P. Coutinho, L.M.N.B.F. Santos, J. Mol. Liq. 188 (2013) 196. https://doi.org/10.1016/j.molliq.2013.09.031

[54] M. Zorębski, E. Zorębski, M. Dzida, J. Skowronek, S. Jężak, P. Goodrich, J. Jacquemin, J. Phys. Chem. B 120 (2016) 3569. https://doi.org/10.1021/acs.jpcb.5b12635

[55] M. Dzida, M. Musiał, E. Zorębski, M. Zorębski, J. Jacquemin, P. Goodrich, Z. Wojnarowska, M. Paluch, J. Mol. Liq. 278 (2019) 401. https://doi.org/10.1016/j.molliq.2019.01.022

[56] M. Musiał, E. Zorębski, M. Zorębski, M. Dzida, J. Mol. Liq. 293 (2019) 111511. https://doi.org/10.1016/j.molliq.2019.111511

[57] M. Musiał, E. Zorębski, M. Zorębski, M. Dzida, J. Mol. Liq. 293 (2019) 111511. https://doi.org/10.1016/j.molliq.2019.111511

[58] P.J. Carvalho, M.G. Freire, I.M. Marrucho, A.J. Queimada, J.A.P. Coutinho, J. Chem. Eng. Data 53 (2008) 1346. https://doi.org/10.1021/je800069z

[59] H.F.D. Almeida, M.G. Freire, A.M. Fernandes, J.A. Lopes-da-Silva, P. Morgado, K. Shimizu, E.J.M. Filipe, J.N. Canongia Lopes, L.M.N.B.F. Santos, J.A.P. Coutinho, Langmuir 30 (2014) 6408. https://doi.org/10.1021/la501308q

[60] J. Feder-Kubis, M. Geppert-Rybczyńska, M. Musiał, E. Talik, A. Guzik, Colloids and Surfaces A: Physicochemical and Engineering Aspects 529 (2017) 725. https://doi.org/10.1016/j.colsurfa.2017.06.040

[61] H.F.D. Almeida, A.R.R. Teles, J.A. Lopes-da-Silva, M.G. Freire, J.A.P. Coutinho, J. Chem. Thermodyn. 54 (2012) 49. https://doi.org/10.1016/j.jct.2012.03.008

[62] H.F.D. Almeida, P.J. Carvalho, K.A. Kurnia, J.A. Lopes-da-Silva, J.A.P. Coutinho, M.G. Freire, Fluid Phase Equilib. 409 (2016) 458. https://doi.org/10.1016/j.fluid.2015.10.044

[63] M. Součková, J. Klomfar, J. Pátek, Fluid Phase Equilib. 303 (2011) 184. https://doi.org/10.1016/j.fluid.2011.01.027

[64] M. Součková, J. Klomfar, J. Pátek, J. Chem. Thermodyn. 100 (2016) 79. https://doi.org/10.1016/j.jct.2016.04.008

[65] J. Klomfar, M. Součková, J. Pátek, J. Chem. Eng. Data 54 (2009) 1389. https://doi.org/10.1021/je800895q

[66] J. Klomfar, M. Součková, J. Pátek, Fluid Phase Equilib. 385 (2015) 62. https://doi.org/10.1016/j.fluid.2014.10.029

[67] N. Abas, A. Kalair, N. Khan, Futures 69 (2015) 31. https://doi.org/10.1016/j.futures.2015.03.003

[68] J.B. Goodenough, K.-S. Park, Journal of the American Chemical Society 135 (2013) 1167. https://doi.org/10.1021/ja3091438

[69] A. Balducci, Top. Curr. Chem. 375 (2017) 20. https://doi.org/10.1007/s41061-017-0109-8

[70] S. Chen, K. Wen, J. Fan, Y. Bando, D. Golberg, Journal of Materials Chemistry A 6 (2018) 11631. https://doi.org/10.1039/C8TA03358G

[71] K. Vignarooban, R. Kushagra, A. Elango, P. Badami, B.E. Mellander, X. Xu, T.G. Tucker, C. Nam, A.M. Kannan, Int. J. Hydrogen Energy 41 (2016) 2829. https://doi.org/10.1016/j.ijhydene.2015.12.090

[72] Y. Tian, G. Zeng, A. Rutt, T. Shi, H. Kim, J. Wang, J. Koettgen, Y. Sun, B. Ouyang, T. Chen, Z. Lun, Z. Rong, K. Persson, G. Ceder, Chem. Rev. 121 (2021) 1623. https://doi.org/10.1021/acs.chemrev.0c00767

[73] E. Jónsson, Energy Storage Materials 25 (2020) 827. https://doi.org/10.1016/j.ensm.2019.08.030

[74] N. Nitta, F. Wu, J.T. Lee, G. Yushin, Mater. Today 18 (2015) 252. https://doi.org/10.1016/j.mattod.2014.10.040

[75] C. Li, Z.-y. Wang, Z.-j. He, Y.-j. Li, J. Mao, K.-h. Dai, C. Yan, J.-c. Zheng, Sustainable Materials and Technologies 29 (2021) e00297. https://doi.org/10.1016/j.susmat.2021.e00297

[76] S. Wilken, S. Xiong, J. Scheers, P. Jacobsson, P. Johansson, Journal of Power Sources 275 (2015) 935. https://doi.org/10.1016/j.jpowsour.2014.11.071

[77] M. Marcinek, J. Syzdek, M. Marczewski, M. Piszcz, L. Niedzicki, M. Kalita, A. Plewa-Marczewska, A. Bitner, P. Wieczorek, T. Trzeciak, M. Kasprzyk, P.Łężak, Z. Zukowska, A. Zalewska, W. Wieczorek, Solid State Ionics 276 (2015) 107. https://doi.org/10.1016/j.ssi.2015.02.006

[78] M. Armand, F. Endres, D.R. MacFarlane, H. Ohno, B. Scrosati, Nature Materials 8 (2009) 621. https://doi.org/10.1038/nmat2448

[79] J. Pitawala, A. Martinelli, P. Johansson, P. Jacobsson, A. Matic, J. Non-Cryst. Solids 407 (2015) 318. https://doi.org/10.1016/j.jnoncrysol.2014.08.043

[80] A. Martinelli, A. Matic, P. Jacobsson, L. Börjesson, A. Fernicola, B. Scrosati, J. Phys. Chem. B 113 (2009) 11247. https://doi.org/10.1021/jp905783t

[81] S. Duluard, J. Grondin, J.-L. Bruneel, I. Pianet, A. Grélard, G. Campet, M.-H. Delville, J.-C. Lassègues, Journal of Raman Spectroscopy 39 (2008) 627. https://doi.org/10.1002/jrs.1896

[82] Y. Umebayashi, T. Mitsugi, S. Fukuda, T. Fujimori, K. Fujii, R. Kanzaki, M. Takeuchi, S.-I. Ishiguro, J. Phys. Chem. B 111 (2007) 13028. https://doi.org/10.1021/jp076869m

[83] T.-Y. Wu, L. Hao, P.R. Chen, J.W. Liao, International Journal of Electrochemical Science 8 (2013) 2606.

[84] G. Appetecchi, M. Montanino, S. Passerini, 1117 (2013) 57. https://doi.org/10.1021/bk-2012-1117.ch004

[85] K. Matsumoto, J. Hwang, S. Kaushik, C.-Y. Chen, R. Hagiwara, Energy & Environmental Science 12 (2019) 3247. https://doi.org/10.1039/C9EE02041A

[86] I.A. Shkrob, T.W. Marin, Y. Zhu, D.P. Abraham, The Journal of Physical Chemistry C 118 (2014) 19661. https://doi.org/10.1021/jp506567p

[87] A. Eftekhari, Y. Liu, P. Chen, J. Power Sources 334 (2016) 221. https://doi.org/10.1016/j.jpowsour.2016.10.025

[88] M. Kerner, N. Plylahan, J. Scheers, P. Johansson, Physical Chemistry Chemical Physics 17 (2015) 19569. https://doi.org/10.1039/C5CP01891A

[89] V. Lesch, S. Jeremias, A. Moretti, S. Passerini, A. Heuer, O. Borodin, J. Phys. Chem. B 118 (2014) 7367. https://doi.org/10.1021/jp501075g

[90] E. Paillard, Q. Zhou, W.A. Henderson, G.B. Appetecchi, M. Montanino, S. Passerini, J. Electrochem. Soc. 156 (2009) A891. https://doi.org/10.1149/1.3208048

[91] M. Ikeda, M. Aniya, Solid State Ionics 262 (2014) 476. https://doi.org/10.1016/j.ssi.2013.10.023

[92] J.-K. Kim, A. Matic, J.-H. Ahn, P. Jacobsson, J. Power Sources 195 (2010) 7639. https://doi.org/10.1016/j.jpowsour.2010.06.005

[93] Y. Deguchi, J. Serra Moreno, S. Panero, B. Scrosati, H. Ohno, G.B. Appetecchi, Electrochem. Commun. 43 (2014) 5. https://doi.org/10.1016/j.elecom.2014.02.017

[94] G.B. Appetecchi, M. Carewska, M. Montanino, F. Alessandrini, S. Passerini, ECS Transactions 25 (2010) 49. https://doi.org/10.1149/1.3393839

[95] P.M. Bayley, A.S. Best, D.R. MacFarlane, M. Forsyth, ChemPhysChem 12 (2011) 823. https://doi.org/10.1002/cphc.201000909

[96] J. Pitawala, J.-K. Kim, P. Jacobsson, V. Koch, F. Croce, A. Matic, Faraday Discuss. 154 (2012) 71. https://doi.org/10.1039/C1FD00056J

[97] Q. Zhou, K. Fitzgerald, P.D. Boyle, W.A. Henderson, Chem. Mater. 22 (2010) 1203. https://doi.org/10.1021/cm902691v

[98] J.B. Haskins, W.R. Bennett, J.J. Wu, D.M. Hernández, O. Borodin, J.D. Monk, C.W. Bauschlicher, J.W. Lawson, J. Phys. Chem. B 118 (2014) 11295. https://doi.org/10.1021/jp5061705

[99] J. Tong, S. Wu, N. von Solms, X. Liang, F. Huo, Q. Zhou, H. He, S. Zhang, Frontiers in Chemistry 7 (2020). https://doi.org/10.3389/fchem.2019.00945

[100] P. Jankowski, M. Dranka, G.Z. Żukowska, The Journal of Physical Chemistry C 119 (2015) 10247. https://doi.org/10.1021/acs.jpcc.5b01826

[101] P. Judeinstein, M. Zeghal, D. Constantin, C. Iojoiu, B. Coasne, J. Phys. Chem. B 125 (2021) 1618. https://doi.org/10.1021/acs.jpcb.0c09597

[102] M. Egashira, S. Okada, J.-i. Yamaki, N. Yoshimoto, M. Morita, Electrochim. Acta 50 (2005) 3708. https://doi.org/10.1016/j.electacta.2005.01.016

[103] S. Brutti, M.A. Navarra, G. Maresca, S. Panero, J. Manzi, E. Simonetti, G.B. Appetecchi, Electrochim. Acta 306 (2019) 317. https://doi.org/10.1016/j.electacta.2019.03.139

[104] S.A. Mohd Noor, P.C. Howlett, D.R. MacFarlane, M. Forsyth, Electrochim. Acta 114 (2013) 766. https://doi.org/10.1016/j.electacta.2013.09.115

[105] D. Monti, E. Jónsson, M.R. Palacín, P. Johansson, J. Power Sources 245 (2014) 630. https://doi.org/10.1016/j.jpowsour.2013.06.153

[106] F. Castiglione, A. Famulari, G. Raos, S.V. Meille, A. Mele, G.B. Appetecchi, S. Passerini, J. Phys. Chem. B 118 (2014) 13679. https://doi.org/10.1021/jp509387r

[107] P. Nürnberg, E.I. Lozinskaya, A.S. Shaplov, M. Schönhoff, The Journal of Physical Chemistry B 124 (2020) 861. https://doi.org/10.1021/acs.jpcb.9b11051

[108] O. Borodin, G.D. Smith, W. Henderson, J. Phys. Chem. B 110 (2006) 16879. https://doi.org/10.1021/jp061930t

[109] Y. Saito, T. Umecky, J. Niwa, T. Sakai, S. Maeda, J. Phys. Chem. B 111 (2007) 11794. https://doi.org/10.1021/jp072998r

[110] Q. Zhou, P.D. Boyle, L. Malpezzi, A. Mele, J.-H. Shin, S. Passerini, W.A. Henderson, Chem. Mater. 23 (2011) 4331. https://doi.org/10.1021/cm201427k

[111] M.J. Marczewski, B. Stanje, I. Hanzu, M. Wilkening, P. Johansson, Physical Chemistry Chemical Physics 16 (2014) 12341. https://doi.org/10.1039/C4CP01133C

[112] L. Suo, Y.-S. Hu, H. Li, M. Armand, L. Chen, Nature Communications 4 (2013) 1481. https://doi.org/10.1038/ncomms2513

[113] H. Yoon, A.S. Best, M. Forsyth, D.R. MacFarlane, P.C. Howlett, Physical Chemistry Chemical Physics 17 (2015) 4656. https://doi.org/10.1039/C4CP05333H

[114] D. Al-Masri, R. Yunis, A.F. Hollenkamp, J.M. Pringle, Chemical Communications 54 (2018) 3660. https://doi.org/10.1039/C8CC00531A

[115] M. Forsyth, G.M.A. Girard, A. Basile, M. Hilder, D.R. MacFarlane, F. Chen, P.C. Howlett, Electrochimica Acta 220 (2016) 609. https://doi.org/10.1016/j.electacta.2016.10.134

[116] M. Brinkkötter, G.A. Giffin, A. Moretti, S. Jeong, S. Passerini, M. Schönhoff, Chemical Communications 54 (2018) 4278. https://doi.org/10.1039/C8CC01416G

[117] H. Matsumoto, H. Sakaebe, K. Tatsumi, M. Kikuta, E. Ishiko, M. Kono, J. Power Sources 160 (2006) 1308. https://doi.org/10.1016/j.jpowsour.2006.02.018

[118] A.I. Bhatt, A.S. Best, J. Huang, A.F. Hollenkamp, J. Electrochem. Soc. 157 (2010) A66. https://doi.org/10.1149/1.3257978

[119] H. Tokuda, K. Ishii, M.A.B.H. Susan, S. Tsuzuki, K. Hayamizu, M. Watanabe, J. Phys. Chem. B 110 (2006) 2833. https://doi.org/10.1021/jp053396f

[120] K. Hayamizu, S. Tsuzuki, S. Seki, J. Chem. Eng. Data 59 (2014) 1944. https://doi.org/10.1021/je500065k

[121] O. Nordness, J.F. Brennecke, Chem. Rev. 120 (2020) 12873. https://doi.org/10.1021/acs.chemrev.0c00373

[122] P. Nancarrow, A. Al-Othman, D.K. Mital, S. Döpking, Energy 220 (2021) 119761. https://doi.org/10.1016/j.energy.2021.119761

[123] H. Tokuda, K. Hayamizu, K. Ishii, M.A.B.H. Susan, M. Watanabe, J. Phys. Chem. B 108 (2004) 16593. https://doi.org/10.1021/jp047480r

[124] Y.-H. Yu, A.N. Soriano, M.-H. Li, Thermochim. Acta 482 (2009) 42. https://doi.org/10.1016/j.tca.2008.10.015

[125] O. Zech, A. Stoppa, R. Buchner, W. Kunz, J. Chem. Eng. Data 55 (2010) 1774. https://doi.org/10.1021/je900793r

[126] S.A. Pandit, M.A. Rather, S.A. Bhat, G.M. Rather, M.A. Bhat, J. Solution Chem. 45 (2016) 1641. https://doi.org/10.1007/s10953-016-0514-6

[127] L. Sun, O. Morales-Collazo, H. Xia, J.F. Brennecke, J. Phys. Chem. B 119 (2015) 15030. https://doi.org/10.1021/acs.jpcb.5b09175

[128] J. Vila, L.M. Varela, O. Cabeza, Electrochim. Acta 52 (2007) 7413. https://doi.org/10.1016/j.electacta.2007.06.044

[129] Y.-H. Yu, A.N. Soriano, M.-H. Li, J. Chem. Thermodyn. 41 (2009) 103. https://doi.org/10.1016/j.jct.2008.07.013

[130] H. Ning, M. Hou, Q. Mei, Y. Liu, D. Yang, B. Han, Science China Chemistry 55 (2012) 1509. https://doi.org/10.1007/s11426-012-4655-1

[131] A. Nazet, S. Sokolov, T. Sonnleitner, T. Makino, M. Kanakubo, R. Buchner, J. Chem. Eng. Data 60 (2015) 2400. https://doi.org/10.1021/acs.jced.5b00285

[132] C. Schreiner, S. Zugmann, R. Hartl, H.J. Gores, J. Chem. Eng. Data 55 (2010) 1784. https://doi.org/10.1021/je900878j

[133] M.S. Calado, J.C.F. Diogo, J.L. Correia da Mata, F.J.P. Caetano, Z.P. Visak, J.M.N.A. Fareleira, Int. J. Thermophys. 34 (2013) 1265. https://doi.org/10.1007/s10765-013-1491-2

[134] H. Jin, B. O'Hare, J. Dong, S. Arzhantsev, G.A. Baker, J.F. Wishart, A.J. Benesi, M. Maroncelli, The Journal of Physical Chemistry B 112 (2008) 81. https://doi.org/10.1021/jp076462h

[135] Z.-B. Zhou, H. Matsumoto, K. Tatsumi, Chem. Eur. J. 11 (2005) 752. https://doi.org/10.1002/chem.200400817

[136] J.A. Widegren, E.M. Saurer, K.N. Marsh, J.W. Magee, J. Chem. Thermodyn. 37 (2005) 569. https://doi.org/10.1016/j.jct.2005.04.009

[137] S. Aparicio, R. Alcalde, B. García, J.M. Leal, J. Phys. Chem. B 113 (2009) 5593. https://doi.org/10.1021/jp9003467

[138] T. Vogl, P. Goodrich, J. Jacquemin, S. Passerini, A. Balducci, The Journal of Physical Chemistry C 120 (2016) 8525. https://doi.org/10.1021/acs.jpcc.6b01945

[139] N. Sánchez-Ramírez, B.D. Assresahegn, D. Bélanger, R.M. Torresi, Journal of Chemical & Engineering Data 62 (2017) 3437. https://doi.org/10.1021/acs.jced.7b00458

[140] M.H. Ibrahim, M. Hayyan, M.A. Hashim, A. Hayyan, M.K. Hadj-Kali, Fluid Phase Equilib. 427 (2016) 18. https://doi.org/10.1016/j.fluid.2016.06.028

[141] E.P. Grishina, N.O. Kudryakova, L.M. Ramenskaya, Y.A. Fadeeva, Russ. J. Electrochem. 55 (2019) 970. https://doi.org/10.1134/S1023193519100057

[142] A.T. De La Hoz, U.G. Brauer, K.M. Miller, J. Phys. Chem. B 118 (2014) 9944. https://doi.org/10.1021/jp505592t

[143] Y. Yoshida, O. Baba, G. Saito, J. Phys. Chem. B 111 (2007) 4742. https://doi.org/10.1021/jp067055t

[144] A. Stoppa, O. Zech, W. Kunz, R. Buchner, J. Chem. Eng. Data 55 (2010) 1768. https://doi.org/10.1021/je900789j

[145] L. Sun, O. Morales-Collazo, H. Xia, J.F. Brennecke, J. Phys. Chem. B 120 (2016) 5767. https://doi.org/10.1021/acs.jpcb.6b03934

[146] S. Papović, S. Gadžurić, M. Bešter-Rogač, M. Vraneš, J. Chem. Thermodyn. 102 (2016) 367. https://doi.org/10.1016/j.jct.2016.07.039

[147] M. Vraneš, S. Rackov, S. Papović, R. Tomaš, B. Pilić, J. Chem. Eng. Data 67 (2022) 3329. https://doi.org/10.1021/acs.jced.2c00377

[148] J. Leys, M. Wübbenhorst, C. Preethy Menon, R. Rajesh, J. Thoen, C. Glorieux, P. Nockemann, B. Thijs, K. Binnemans, S. Longuemart, J. Chem. Phys. 128 (2008). https://doi.org/10.1063/1.2827462

[149] E.P. Grishina, N.O. Kudryakova, L.M. Ramenskaya, Y.A. Fadeeva, Russian Journal of Physical Chemistry A 92 (2018) 724. https://doi.org/10.1134/S0036024418040040

[150] S. Jiang, Y. Hu, Y. Wang, X. Wang, J. Phys. Chem. Ref. Data 48 (2019). https://doi.org/10.1063/1.5090486

[151] A. Xu, Y. Zhang, W. Lu, K. Yao, J. Wang, J. Chem. Eng. Data 60 (2015) 580. https://doi.org/10.1021/je500710v

[152] A. Xu, Y. Zhang, Z. Li, J. Wang, Journal of Molecular Liquids 214 (2016) 192. https://doi.org/10.1016/j.molliq.2015.12.091

[153] M. Musiał, M. Kuczak, A. Mrozek-Wilczkiewicz, R. Musiol, E. Zorębski, M. Dzida, ACS Sustainable Chemistry & Engineering 6 (2018) 7960. https://doi.org/10.1021/acssuschemeng.8b01317

[154] Q. Zhang, Y. Lan, H. Liu, X. Zhang, X. Zhang, Y. Wei, J. Chem. Eng. Data 61 (2016) 2002. https://doi.org/10.1021/acs.jced.5b00860

[155] T.L. Greaves, A. Weerawardena, C. Fong, I. Krodkiewska, C.J. Drummond, J. Phys. Chem. B 110 (2006) 22479. https://doi.org/10.1021/jp0634048

[156] T. Yasuda, H. Kinoshita, M.S. Miran, S. Tsuzuki, M. Watanabe, Journal of Chemical & Engineering Data 58 (2013) 2724. https://doi.org/10.1021/je301284x

[157] T. Nishida, Y. Tashiro, M. Yamamoto, J. Fluorine Chem. 120 (2003) 135. https://doi.org/10.1016/S0022-1139(02)00322-6

[158] J. Leys, C.S.P. Tripathi, C. Glorieux, S. Zahn, B. Kirchner, S. Longuemart, K.C. Lethesh, P. Nockemann, W. Dehaen, K. Binnemans, Phys. Chem. Chem. Phys. 16 (2014) 10548. https://doi.org/10.1039/C4CP00259H

# Chapter 2

## Methods, Theory and Fundamentals

**2.1.** Density of Liquids

**2.2.** Viscosity of Liquids

**2.3.** Electrical Conductivities of Liquids

**2.4.** Effect of Temperature on the Transport Properties

**2.5.** Relation Between Viscosity and Electrical Conductivity

**2.6.** Experimental Measurements

**References**

# 2. Methods, Theory and Fundamentals

This chapter presents the theoretical fundamentals behind the experimental methodologies used in this work. Additionally, the dependence of the transport properties of ionic liquids is described, the concept of liquid fragility is introduced and the approaches used to derive important thermodynamic information from the experimental data are presented. The relation between viscosity and electrical conductivity is explored and its validity to be correlated to the degree of ion association or ionicity is discussed. Finally the used experimental methodologies, the Antor Paar SVM 3001 densimeter-viscometer and the developed electrical conductivity measuring apparatus ILDEM, are presented and described together with the respective experimental procedures.

## 2.1. Density of Liquids

The density, $\rho$, of a substance is defined as its mass per volume unit (Eq. 2.1). Since density is related to the volume of a substance it is expected to be significantly affected by the temperature and pressure of the system. This physicochemical property has both fundamental and applied interest, as it is key in process/engineering design, but it is also very important for the development of equations of state and to derive relevant information when combined with other properties (e.g. electrical conductivity, heat capacity).

$$\rho = \frac{m}{V} \tag{2.1}$$

By knowing the molar mass of a compound, it is possible to relate its density with the molar volume (Eq. 2.2)

$$V_m = \frac{M}{\rho} \tag{2.2}$$

### 2.1.1. Measuring Principle

Through the years various methods have been designed and developed to measure density of liquids. These methods are based on different approaches and physical phenomena, ranging from simple apparatus to complex digital devices [1].

1. Pycnometer, Hydrostatic weighing, Balance-type: Fixed volume vessels. The density is measured by weighing the vessel with and without sample.
2. Buoyancy-type, Hydrometer: Based on the Archimedes principle of buoyancy.
3. Column-type: Based on differential pressure measurements between the sample column and the reference (water) column
4. Radioactive: Consists of the emission of γ-rays through the sample. The density is calculated from the intensity of radiation before and after passing through the sample.
5. Refractometer: Based on the relation between the angle of refraction of the laser beam and the density of the sample.
6. Absorption: Consists of irradiating the sample with x-rays / visible light / UV light / sonic waves. The wave attenuation and phase shift upon contact with the sample is related to its density.
7. Vibrating/Resonating element, Coriolis: Based on the relation between the resonance frequency and density.

In this work, a resonating element densimeter based on a vibrating U-tube was used to measure the density of the ionic liquids. In this approach a piezoelectric/magnetic transducer is used to oscillate the metal U-tube. When empty the tube as a characteristic resonance frequency which is defined, by its material, size and shape. Filling the tube with a fixed volume of sample will lead to decrease of the resonance frequency depending on the mass of the liquid. The oscillation process only occurs in a specific part of the tube and the amount of volume subject to it is always the same. A schematic representation of the measuring principle of a vibrating U-tube densimeter is presented in Fig. 2.1.

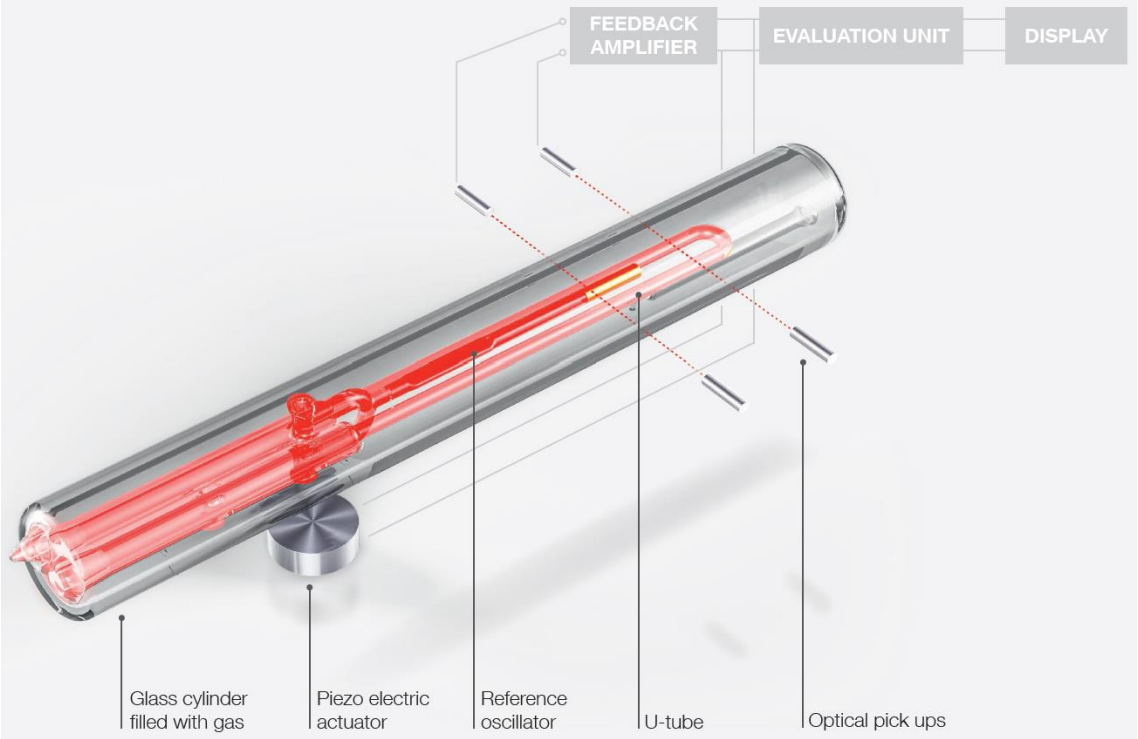



**Figure 2.1.** Schematic representation of the measuring principle of a vibrating U-tube densimeter. Figure adapted from Anton Paar GmbH [2].

The relation between the resonance frequency, $f_r$, and the density of the sample is given by Eq. 2.3.

$$f_r = \frac{K_s}{m_t + k_s \rho} \tag{2.3}$$

Where, $K_s$ is the system stiffness, $m_t$ is the mass of the transducer, and $k_s$ is a system constant which is associated with the mass and characteristics of the U-tube. A schematic representation of the measuring principle of a vibrating U-tube densimeter is presented in Fig. 2.1.

### 2.1.2. Dependency of Density with Temperature

Usually, the density of ionic liquids shows a weak temperature dependence reflected by an almost linear decrease in density as the temperature increases. In literature, linear and quadratic functions are often applied to describe the density-temperature

dependency. In this work, the experimental data was fitted using a second-order polynomial equation as presented in Eq. 2.4, where $a_2$, $a_1$, and $a_0$ are fitting coefficients.

$$\ln \rho = a_2 T^2 + a_1 T + a_0 \tag{2.4}$$

The isobaric thermal expansion coefficient, $\alpha_p$, is related to the change in the volume of the system with temperature (Eq. 2.5).

$$\alpha_p = \frac{1}{V}\left(\frac{\partial V}{\partial T}\right)_p \tag{2.5}$$

Since mass is independent of temperature and density is inversely proportional to volume (Eq. 2.1), the relation between the isobaric thermal expansion coefficient and density is given by Eq. 2.6.

$$\alpha_p = -\frac{1}{\rho}\left(\frac{\partial \rho}{\partial T}\right)_p \tag{2.6}$$

By combing the equations 2.4 and 2.6, the following relation is obtained.

$$\alpha_p = -\left(\frac{\partial \ln \rho}{\partial T}\right)_p = -(2a_2 T + a_1) \tag{2.7}$$

## 2.2. Viscosity of Liquids

Viscosity is an essential physicochemical property of a liquid or fluid. It is related to the resistance of a fluid to movement and therefore it is classified as a transport property. Given that this property can be interpreted as a measure of the internal friction between the neighbour molecules, it is highly dependent on the chemical structure of the fluid, namely, molecular shape, size, and interactions. Therefore, from a fundamental perspective, this macroscopic property can provide important insights into the dynamic and structuration of a liquid at the molecular level. On the other hand, knowledge concerning the viscous properties of a fluid is essential on the design and optimization

of several industrial and engineering systems, such as mixing, injection, and pipeline operations [3].

Dynamic viscosity is a common way to describe the viscosity, $\eta$, of a liquid and it is related to the shear stress, $\tau$, and shear rate, $\gamma$. The former is the tangential force, $F$, that is applied per unit area, $A$, in order to cause motion (Eq. 2.8), while the latter is related to the difference in velocity between the adjacent liquid layers as a consequence of the deformation due to the applied shear force.

$$\tau = \frac{F}{A} \tag{2.8}$$

Considering the classic example where a fluid is placed between two parallel plates (Fig. 2.2), one in motion and the other stationary, the shear rate would be given by the ratio between the velocity of the moving plate, $v$, and distance between the two plates, $x$, as presented in Eq. 2.9:

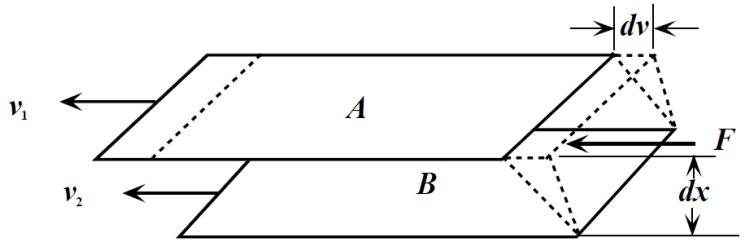



**Figure 2.2.** Schematic representation of the simple shear of a liquid film. Adapted from Viscosity of Liquids, Springer 2007[4].

$$\Upsilon = \frac{1}{x} \cdot \frac{dx}{dt} = \frac{v}{x} \tag{2.9}$$

In a Newtonian fluid, which is the case of all the systems studied and described in this work, the viscosity is independent of the applied shear rate, as described by Eq. 2.10:

$$\tau = \eta\Upsilon \tag{2.10}$$

Non-Newtonian are compounds whose viscosity depends on the shear rate. The two main types of non-Newtonian fluids are the pseudoplastics which are characterized by

an initially fast increase in $\tau$ with the increase of $\gamma$, and the dilatants which present an initially slow variation. Other example is the Bingham plastic, these types of compounds behave like a rigid body at low $\tau$ and become fluid with the increase of shear stress. The behavior of each type of liquid can be summarized in a shear stress – shear rate graphical representation (Fig. 2.3). Interestingly, the two axes of this graph represent the ideal solid and fluid behavior, as the former is characterized by the absence of fluidity/movement ($\dot{\gamma} = 0$) while the latter is defined by the absence of viscosity ($\tau = 0$).

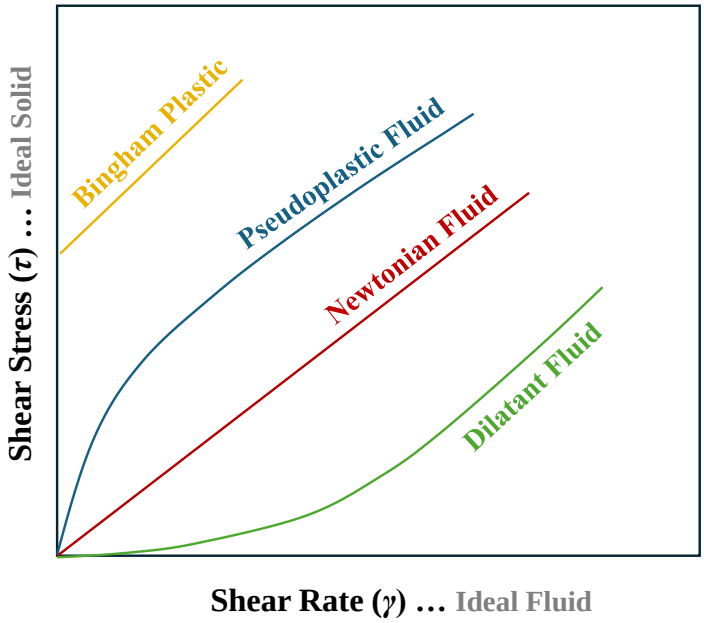



**Figure. 2.3.** Schematic representation of the different fluid behaviors.

In some fields, the viscosity of a fluid is represented by the kinematic viscosity, $k$, which is given by the ratio between the dynamic viscosity and the density of the liquid, $\rho$, as presented in Eq. 2.11.

$$k = \frac{\eta}{\rho} \tag{2.11}$$

### 2.2.1. Theory

Through the years several models have been developed to describe the viscosity of liquids. As the liquid state is an intermediate state of order compared to the low-density state of the gases and the regular lattice structure of the solids, the accurate

mathematical description of its viscous behavior is a rather complex operation [5]. Therefore, the models for the viscosity of liquids are usually based on approximations of solid or gaseous states. As referred to earlier the viscosity is deeply related to the structure and interactions at a molecular level. Based on that, Born and Green developed an equation that relates the liquid dynamic viscosity with the distance and interaction potential between neighbour molecules (Eq. 2.12).

$$\eta = 0.48\frac{r}{V}[m\phi_a(r)]^{1/2}\exp\left[-\frac{1}{kT}\phi(r)\right] \quad (2.12)$$

This relation is based on a short-range pair distribution assuming the approximation of the disordered liquid to a gas, where $r$ is the distance between the center of two adjacent molecules, $V$ is the molecular volume, $m$ is the molecular mass, $\phi_a(r)$ is the attractive component of the potential pair, $\phi(r)$ is the mutual potential energy of the two adjacent molecules and $k_B$ is the Boltzmann constant. In models where the liquid is approximated to a solid structure, the viscous flow is usually explained by the transference of momentum in the lattice due to the vibration of the molecules or by the dislocation of a molecule to an unoccupied hole on the lattice. The latter approach is the basis for the Eyring theory. In this model the viscous flow is considered as an analogue to a chemical reaction, as in this case the molecules must overcome a potential barrier in order to jump to a hole. Based on this approach the dynamic viscosity of the liquid is described by Eq. 2.13:

$$\eta = \frac{hN_A}{V_m}exp\left(\frac{\Delta G^{\ddagger}}{RT}\right) \quad (2.13)$$

Where $N_a$ is the Avogadro number, $V_m$ is the molar volume, $R$ is the ideal gas constant and $\Delta G^{\ddagger}$ is the free activation energy for the viscous flow. The viscosity of the liquid can also be mathematically related to the mobility of the involved species by assuming that they move as spheres. Stokes' law (Eq. 2.14) relates the necessary force (drag force) applied to move a spheric object of radium, $r$, with velocity, $v$, through a viscous medium.

$$F = 6\pi\eta r v \quad (2.14)$$

The mobility of a particle, $\mu$ is given by the ratio between the velocity and the applied shear force $\mu = v/F$. The relation between the self-diffusion coefficient of a species, *D*, and mobility is described by the Einstein relation on the kinetic theory (Eq. 2.15).

$$D = \mu k_{\mathrm{B}} T \tag{2.15}$$

The combination of equations 2.14 and 2.15 results in the Stokes-Einstein equation (Eq. 2.16), which relates the self-diffusion coefficient of the involved species with the viscosity of the fluid.

$$D = \frac{k_{\mathrm{B}} T}{6\pi\eta r} \tag{2.16}$$

### 2.2.2. Measuring Principle

Through the years various methods have been designed and developed to measure the viscosity of liquids. Even in ionic liquids literature, there is a diverse range of methodologies, namely falling body, capillary, and rotational viscometers. These methods are based on different approaches to measure viscosity and ensure the replenishment of the sample in the measuring site.

1. Capillary: Based on measuring the time necessary to pass between a fixed distance in a glass capillary tube by action of gravity or a controlled pressure. The two most common versions of this type of apparatus are the Ostwald and the Ubbelohde viscometer.

2. Falling body: A body of known size and density is placed in a vertical vessel filled with the sample. By measuring the time it takes to travel through a well-defined distance and by knowing the density of the sample is possible to calculate the viscosity of the liquid based on Stokes' law. The most common methodologies of this type are the falling/rolling sphere and moving piston.

3. Rotational: A known body is made to rotate in the liquid sample. The shear rate is associated with the rotational speed which is controlled by the apparatus. The shear stress is derived from the torque required for the rotation. The viscosity of the sample is then calculated from the shear stress and shear rate. The most

common methodologies are the “cup and bob”, “cone and plate”, and concentrical cylinders viscosimeter.

4. Vibrational: An oscillating electromechanical resonator is immersed on the liquid. The viscosity of the sample is proportional to the damping of the vibration (amplitude change).

In this work a Stabinger rotational viscometer was used to measure the viscosity of the ionic liquids. The Stabinger viscometer is based on the Couette’s measuring principle. In this approach the liquid sample is introduced on a cylindrical vessel. A smaller solid cylinder is suspended coaxially to the larger cylinder. The outer cylinder rotates at a defined speed causing a torque on the internal cylinder which is dependent of the viscosity of the liquid (Fig. 2.4).

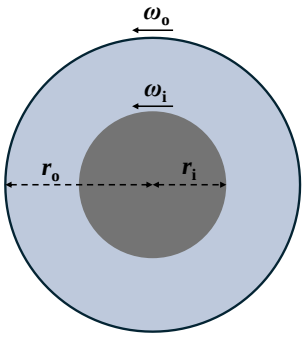



**Fig. 2.4.** Schematic representation of the Couette measuring principle for the viscosity of liquids. Solid line: outer cylinder; **sample**; **inner cylinder**. $\omega_o$ and $\omega_i$ are the angular velocities of the outer and inner cylinder. $r_o$ and $r_i$ are the radius of the outer and inner cylinder.

A Stabinger is a miniature Couette viscometer designed to reduce the sample size and eliminate friction effects. This approach uses an outer hollow tube and a cylindrical inner rotor which has an incorporated magnet. The rotation is magnetically induced by a rotating magnet and the outer tube rotates at a constant velocity. The inner rotor is made to be of low density, so it is kept centered due to the centrifugal forces. The rotor is freely floating on the sample, so no bearings are used which eliminates the friction effects. The rotation velocity of the rotor is slower than the outer tube, as it is a reflection of the balance between the impulsion shear forces of the sample and the eddy current brake. The equilibrium between these driving and retarding forces is used to derive the viscosity of the sample. A schematic illustration of the working principle of a Stabinger viscometer is presented in Fig. 2.5.

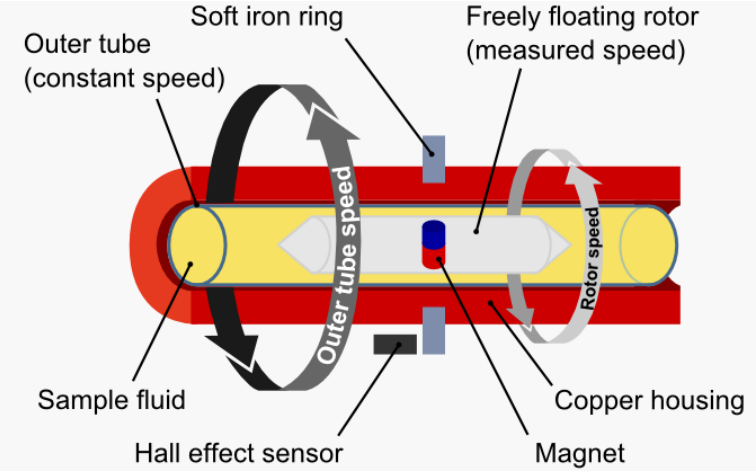



**Fig. 2.5.** Schematic representation of a Stabinger viscometer. Image adapted from Anton Paar GmbH [6].

## 2.3. Electrical Conductivity of Liquids

Electrical conductivity, $\sigma$, is a measure of charge conduction associated with the movement of ions or electrons. The conduction occurs as a consequence of applying an electric field, $E$, to a conductor material. The velocity of flow of electric charge, $q$, is known as electrical current, I, and is given by Eq. 2.17:

$$I = \frac{dq}{dt} \tag{2.17}$$

The electrical conductivity is then a measure of the resulting electric current relative to the applied electric field, as described in Eq. 2.18, where $A$ is the cross-sectional area of the conductor and $J$ is the current density.

$$\sigma = \frac{I}{AE} = \frac{J}{E} \tag{2.18}$$

When an electric field is applied to a solution or fluid composed by ions, the conduction mechanism is given by the migration of ions. Based on that, in this case the resulting current density is described by Eq. 2.19:

$$J = \sum [z_i] c_i v_i F \tag{2.19}$$

Where $F$ is the faradaic constant and $J_i$, $z_i$, $c_i$, and $v_i$ are respectively the current density, effective charge, concentration, and velocity corresponding to each ionic species on the electrolyte. By combining Eq. 2.18 and 2.19, the following definition for the electrical conductivity of electrolytes is reached (Eq. 2.20)

$$\sigma = \frac{\sum [z_i] c_i v_i F}{E} \tag{2.20}$$

Often in literature, the conductivity of an electrolyte is often presented as the molar conductivity, $\Lambda$, which is the electrical conductivity per mol of conducting species (Eq. 2.21).

$$\Lambda = \frac{\sigma}{c} \tag{2.21}$$

Therefore, for a pure liquid composed of ions, such as ionic liquids, the previous equations becomes:

$$\Lambda = \frac{\sigma \cdot M}{\rho} \tag{2.22}$$

To compare and rationalize trends between a series of compounds, especially considering the impact of molecular structure, molar conductivity is usually more insightful than electrical conductivity, as it is a measure of the ability to conduct electricity per mole unit. Therefore, the discussion presented in Chapter 5 will be based on the molar conductivity data.

### 2.3.1. Theory

As a transport property, it is expected that the electrical conductivity of a fluid is strongly dependent on the fluidity of the system. Similar to viscosity, the electrical conductivity of the system is also deeply related to the structuration and interaction of a fluid at the molecular level. Analogous to what was presented earlier for viscosity, it is also possible to relate the mobility and diffusion of a species with the molar conductivity of the electrolyte. In this case, the mobility of a species, $\mu$, is given by the ratio between the

velocity and the applied electric field $\mu = v/E$. Equation 2.23 presents a variation of the Einstein relation on the kinetic theory presented in equation 2.15 for the diffusion of charged particles. This equation is known as the Einstein-Smoluchowski relation.

$$D = \frac{\mu_q k_B T}{q} \tag{2.23}$$

Taking into consideration equations 2.20 and 2.23, it is possible to obtain the Nernst-Einstein relation (Eq. 2.24), which relates the self-diffusion coefficient of the involved charged species with the total electrical conductivity of the fluid.

$$\Lambda = \frac{F^2(z_+^2 D_+^2 + z_-^2 D_-^2)}{k_B T} \tag{2.24}$$

This version of the Nernst-Einstein relation is valid for electrolytes composed of a single anionic species and a single cationic species. In this equation $z_+^2$, $D_+^2$, $z_-^2$, and $D_-^2$ are respectively the charge number of cation, self-diffusion coefficient of the cation, charge number of the anion and self-diffusion coefficient of the anion.

## 2.3.2. Measurement of Electrical Conductivity

### 2.3.2.1. Measuring Principle

To measure electrical conductivity, a voltage is applied through the electrodes, generating a current in the medium. The resistance of the solution, *R*, is then calculated by applying Ohm's Law (Eq. 2.25) and taking into account the applied voltage, *V*, and the measured current, *I*.

$$R = \frac{V}{I} \tag{2.25}$$

Contrary to conductivity, which is specific to the material in study, resistance is dependent on the geometry of the measuring cell. Conductivity is related to the reciprocal of resistance, known as conductance, *G,* by Eq. 2.26, where *l* is the effective length of the current path, *A* is the effective cross-sectional area of the current, and *c* is the cell

constant. The ratio between the length and cross-sectional area of the current path is known as the cell constant.

$$R = \frac{1}{G} = \frac{c}{\sigma} = \frac{l}{A \cdot \sigma} \tag{2.26}$$

In a simple cell with two electrodes, one acts as the positive pole and the other as the negative pole. Ideally, the electrodes are inside a protector tube, which helps the reproducibility of the generated electric field, minimizing measuring errors associated with perturbation on the distribution of the electric field across the sample. As the input voltage is applied, the cations in solution migrate to the negative pole while the anions migrate to the positive pole. If the input signal is direct current (DC), the ions start to accumulate on the surface of the electrodes, creating an electric double layer (EDL). The presence of an EDL leads to some undesirable effects, such as the occurrence of electrolysis, secondary chemical reactions, and solution polarization, leading to erroneous measurements. The accumulation of ions at the electrode surface hinders the overall ionic movement, leading to an additional increase of the measured resistance (polarization resistance, $R_{pol}$). The utilization of alternate current (AC) means that the orientation of ion migration keeps changing periodically, depending on the frequency of the input signal. This prevents the ions from migrating solely in one direction, avoiding the formation of the double layer on the surface of the electrodes (Fig. 2.6).

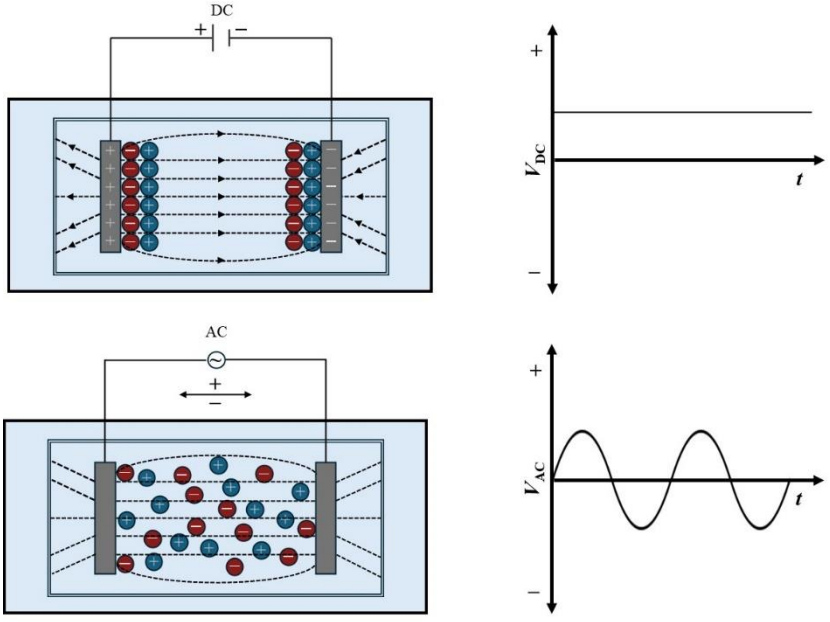



**Figure 2.6.** Schematic representation of ion conduction when DC and AC are applied to an electrolyte.

However, the use of AC does not completely nullify the polarization effect. Thus, strategies focused on cell design are frequently implemented to minimize the impact of polarization.

Frequency: Higher frequencies reduce polarization resistance, as the rapid field alternation prevents the accumulation of ions on the electrode surface. However, the operation at high frequencies promotes undesired effects related to stray capacitance contributions from the measuring circuit or with adjustments in the ionic environment associated with the rapid alternation of the electric field (Debye-Falkenhagen effect) [7, 8].

Electrode Surface: The utilization of a porous surface is recommended, as the higher surface area results in a decrease in the interfacial resistance and current density [9]. This is the reason why platinized platinum (black platinum) electrodes are preferred over bright platinum electrodes.

Number of Poles: Four-pole conductivity cells are cells containing four electrodes (two pairs). This approach is analogous to the 4-wire methodology applied in various signal measurements, including temperature and resistance. The current passes through the outer electrodes while the inner electrodes measure the voltage. This minimizes the current passing through the measuring pair, which reduces the impact of resistance polarization. Based on that, 4-pole cells are recommended for the measurement of electrical conductivity of highly conductive concentrated ionic solutions. Unfortunately, these cells are usually more expensive and require a larger sample volume.

#### 2.3.2.2. Impedance

The opposition to the flow of AC is known as impedance, *Z*. Impedance is a complex quantity composed of a real part, resistance, and an imaginary part known as reactance, *X*, as described in Eq. 2.27.

$$Z = R + jX \tag{2.27}$$

In terms of physical meaning, resistance corresponds to the loss of energy, while reactance corresponds to the storage of energy. Ideally, in pure resistive elements, such as resistors, the power absorbed is instantaneously dissipated. Furthermore, the reactance of these components is equal to zero ($X$ = 0), and their resistance is independent of frequency. On the other hand, pure reactive components have a null resistive contribution ($R$ = 0). There are two types of reactance: capacitive reactance, $X_C$, and inductive reactance, $X_C$, which are respectively related to two other electric properties, capacitance, $X$, and inductance, $L$, as described by equations 2.28 and 2.29.

$$X_C = -\frac{1}{2\pi f C} \tag{2.28}$$

$$X_L = 2\pi f L \tag{2.29}$$

An ideal capacitor and an ideal inductor are differentiated by how the absorbed power is stored. In the former, the power is absorbed as electrostatic energy, while in the latter, it is absorbed as magnetic energy. Furthermore, as presented in Fig. 2.7, $X_C$ decreases with the increase of frequency while $X_L$ increases with the increase in frequency.

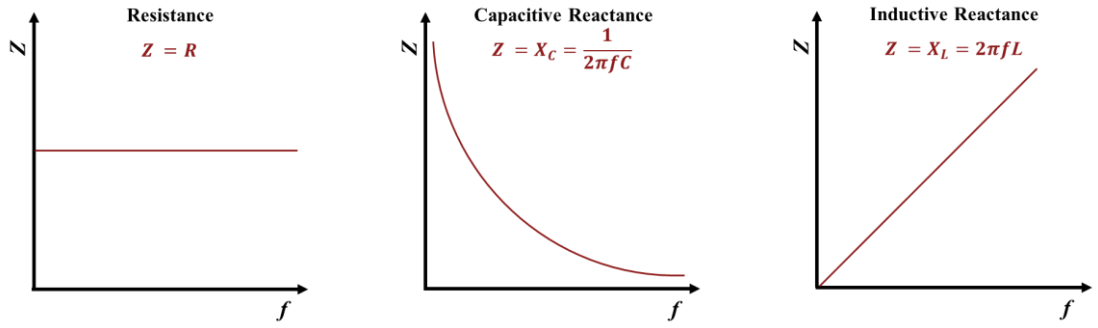



**Figure 2.7.** Ideal frequency dependency for resistive, capacitive, and inductive elements.

In an ideal resistive process, the peaks of the sinusoidal waves of voltage and current in a given period are synchronized. In these conditions, voltage and current are in phase. However, the presence of reactive processes causes the $I$(t) and $V$(t) to become out of phase. The measure of voltage-current desynchronization is known as the phase angle, $\theta$. In capacitive systems, voltage lags relative to current, while in inductive elements, the reverse is observed. Fig. 2.8 presents the current and voltage functions for ideal resistive, capacitive, and inductive systems.

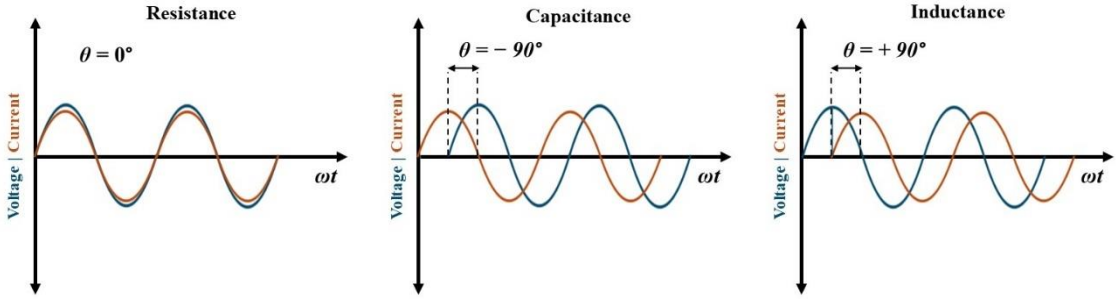



**Figure 2.8.** Typical representation of current and voltage as a function of the angular frequency time product ($\omega t$ , $\omega = 2\pi f$) for ideal resistive, capacitive, and inductive systems.

Considering Ohm's Law (Eq. 2.25), the description of impedance as a complex quantity (Eq. 2.27), and the concept of phase (Fig. 2.8) it is possible to represent impedance in a complex plane (Fig. 2.9). The magnitude of reactance, $|Z|$ is determined by the ratio between amplitudes of $V(t)$ and $I(t)$ functions. The phase angle is given by the displacement between the voltage and current curves on the x-axis.

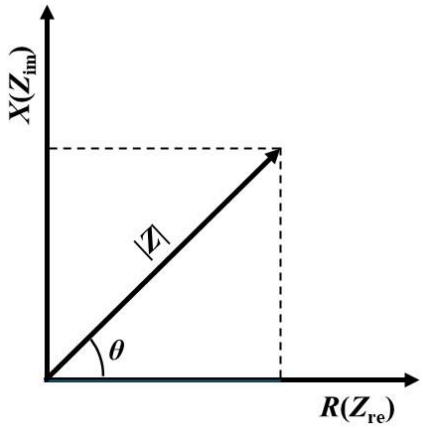



**Figure 2.9.** Graphical representation of the impedance complex plane.

Based on that, resistance and reactance can be described by the trigonometric relations presented in equations 2.30 and 2.31:

$$R = |Z| + \cos\theta \tag{2.30}$$

$$X = |Z| + \sin\theta \tag{2.31}$$

On the other hand, the magnitude and phase angle of impedance can also be described in terms of resistance and reactance. The phase angle is associated with the tangent of the ratio between reactance and resistance (Eq. 2.32):

$$\theta = \tan^{-1}\left(\frac{X}{R}\right) \tag{2.32}$$

By applying the Pythagorean theorem, the magnitude of impedance can also be described as terms of resistance and reactance, as follows:

$$Z = \sqrt{R^2 + X^2} \tag{2.33}$$

#### 2.3.2.3. Determination of Solution Resistance

As presented earlier, the impact of polarization is weakened with the increase of frequency. Therefore, usually in frequency sweep from slower to faster field alternations, the measured resistance decreases until it reaches a *plateau*. This region corresponds to a frequency interval where the measured resistance is purely described by ohmic conduction, and undesired effects, such as solution polarization and interfacial (solution-electrode) processes, are minimized/non-existent. A graphical representation of the typical resistance-frequency dependence can be found in Fig 2.10.

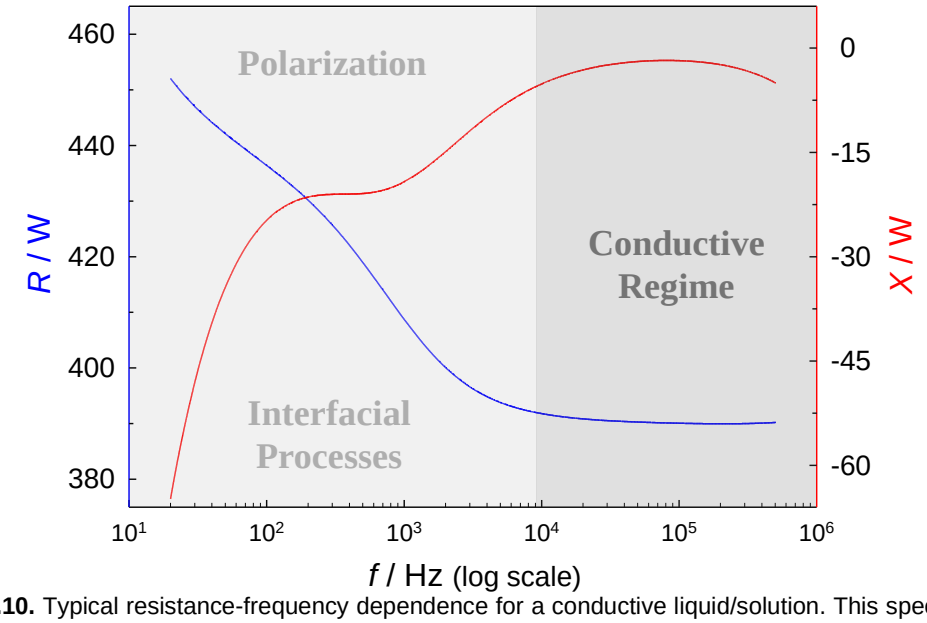



**Figure 2.10.** Typical resistance-frequency dependence for a conductive liquid/solution. This spectrum was obtained using the ILDEM measuring system.

The weakening of the impact of polarization with the increase in frequency is reflected in the resistance drop. However, the operation at high frequencies would generate other undesired effects related to stray capacitance contributions from the measuring circuit or with adjustments on the ionic environment associated with the electric field's rapid alternation (Debye-Falkenhagen effect) [7, 8]. Based on this, the current state-of-the-art procedure to correctly measure the electrical resistance of a liquid/solution is to select an appropriate frequency range and extrapolate the resistance to infinite frequency. In the literature, different mathematical functions have been utilized to calculate the $R_\infty$ of ionic liquids. The most common approach is the use of Eq. 2.34:

$$R(1/f^a) = \frac{A}{f^a} + R_\infty \tag{2.34}$$

Where the exponent is usually $a$ = 1 [10-18] or $a = 1/2$ [11, 14, 19-23], and $A$ is a fitting parameter. An example of the extrapolation using Eq. 2.34 with $a$ = 1 is presented in Fig. 2.11.

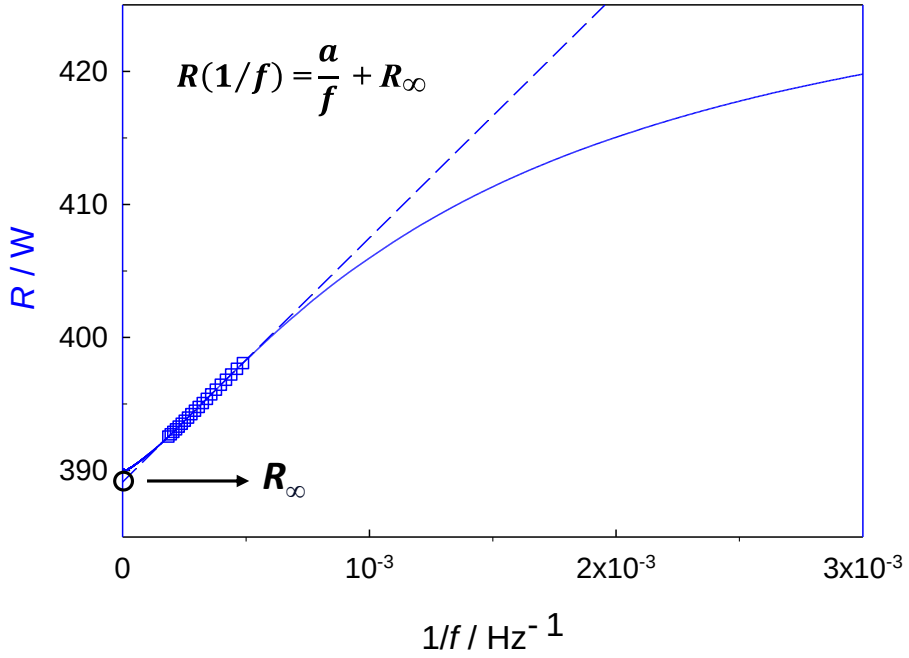



**Figure 2.11.** Example of the extrapolation of resistance to infinite frequency using Eq. 2.34 with $a$ = 1.

Alternatively, Buchner and his coworkers have been using Eq. 2.34, where the variable $a$ is usually found to be between 1/2 and 1 [24-26]. These functions have been widely tested for aqueous electrolyte solutions [27, 28], organic electrolyte solutions [29-31], and molten salts [32]. Jones and Christian [27] used $a = 1/2$ when they first proposed

the implementation of the extrapolation procedure. Nichol and Fuoss [30] found that $a = 1$ resulted in a better fitting of their experimental data. Other works also showed that the utilization of $a = 1/2$ may lead to erroneous results [33, 34]. On the other hand, Calado *et al.*. found a better fit with $\alpha = 1/2$ than with $a = 1$ for imidazolium ionic liquid [23]. Later, Hoover first proposed the use of the non-fixed exponent approach now used by Buchner and his coworkers [29]. The author reported that while this method usually leads to an excellent fitting of the experimental data, it can also lead to extrapolation errors [28]. In this work, Hoover also proposed the utilization of the function presented in Eq. 2.35:

$$R = \frac{b}{1+cf^2} + R_\infty \tag{2.35}$$

Kanakubo *et al.* [35] found comparable extrapolation results between Eq. 2.35 and $R(1/f^2)$. Additionally, the authors reported that these equations yield a better fitting to their experimental results compared to the more commonly used functions described by Eq. 2.27 [35, 36]. Overall, several studies concluded that the application of the appropriate function is affected by the frequency dependence behavior, which seems to be dependent on the apparatus and the measured systems [28]. As referred to earlier in the resistance *plateau* region, the measured resistance is well related to the conduction process. Therefore, a common practice is to take the value of this region as the resistance of the solution [37, 38]. Previously, Hoover [28] commented that if the extrapolation to infinite frequency is not appropriately done, it may lead to too low resistance results, and in these cases, the value at the plateau might be a more accurate option. Apart from the extrapolation to infinite frequency method, other approaches to calculate the resistance of ILs can also be found in the literature. Methods based on the Nyquist Plot, such as the extrapolation to intercept the real axis [25, 36, 39-44], are commonly used. This approach is based on finding the resistance point where the imaginary part of impedance, reactance, is equal to zero ($X = 0$). In measurements performed with impedance analyzers, the Nyquist plot analysis is usually combined with the fitting of the raw impedance data to an equivalent circuit [45-51]. An equivalent circuit is a theoretical circuit that adequately describes the electrical characteristics of the system under measurement, allowing a more practical interpretation of the Nyquist Plot. The Randel circuit is a simple electrical circuit composed of two resistances, a capacitor, and a Warburg element. This type of circuit is widely used in electrochemistry and the study of electrical properties. An example of the use of a Randel circuit to interpret a typical Nyquist plot is presented in Fig. 2.12. The two ohmic resistances represent the

solution and change transfer resistance; a capacitor is used to module the capacitive properties of the double layer formed in the electrode-electrolyte interface; a virtual electronic component (Warburg impedance) is applied to module the diffusion of ionic species. The presented example (Fig. 2.12) also highlights a change in the reactance sign (Lp), corresponding to an inductive effect associated with parasitic contributions from the wires and connects, which becomes more significant at high frequencies.

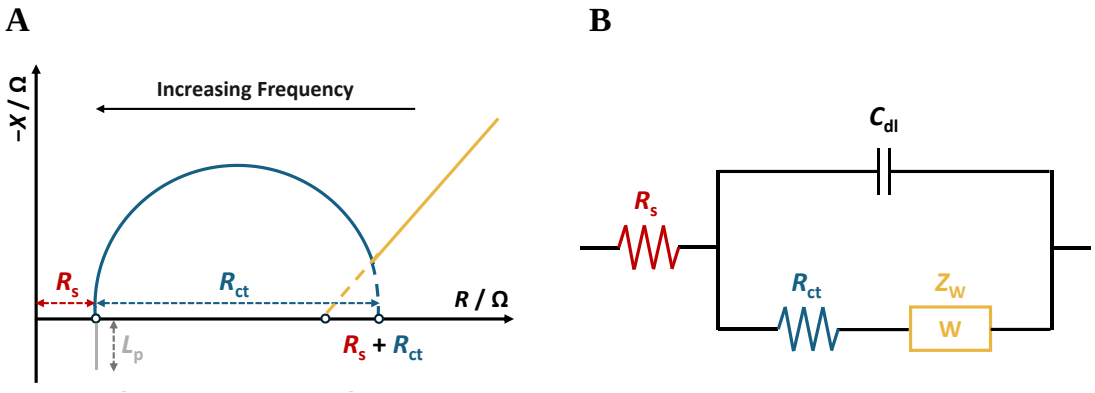



**Figure 2.12.** Typical Nyquist Plot (**A**) and Randel circuit (**B**). $R_s$: solution resistance; $R_{ct}$: charge-transference resistance; $Z_w$: Warburg Impedance; Lp: Parasitic inductive contributions (wires and connections).

As can be seen, a typical Nyquist Plot is mainly divided into three key points:

- Solution resistance, $R_s$**:** *x*-access ($X = 0$) intercept at the high-frequency region;
- Charge-transfer resistance, $R_{ct}$**:** transference of electrons at the double layer / electrode-electrolyte interface (Fig 2.13). In the Nyquist plot, this contribution is represented by the semi-circle.

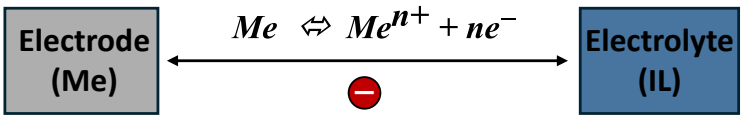



**Figure 2.13.** Schematic representation of the charge-transfer process (Nyquist Plot semi-circle).

- Warburg impedance, $Z_w$**:** Low frequency (low field alternation rate) allows for ionic species to diffuse into the electrode surface, leading to an ion depletion in front of the electrode surface. This leads to a drop in current and, therefore, an increase in resistance as is described by the Cottrell equation (Eq. 2.36) and observed in Fig. 2.7 A.

$$I = n_e FAc\sqrt{\frac{D}{\pi t}} \tag{2.36}$$

Where *c* is the bulk concentration and *n* is the number of electrons involved. The Warburg impedance can be calculated by Eq. 2.37:

$$Z_W = \frac{A_W}{\sqrt{2\pi f}} - j\frac{A_W}{\sqrt{2\pi f}} \tag{2.37}$$

Where $A_w$, is the Warburg coefficient, which is described by Eq. 2.38,

$$A_W = \frac{RT}{An^2F^2\sqrt{2}}\left(\frac{1}{c_o\sqrt{D_o}} + \frac{1}{c_R\sqrt{D_R}}\right) \tag{2.38}$$

Where, *n* is the number of electrons involved in the diffusion process, A is the active electrode surface, $c_o$ is the concentration of the oxidized species, $c_r$ is the concentration of the reduced species, and $D_o$ is the diffusion coefficients of the oxidized species, and $D_r$ is the diffusion coefficients of the reduced species.

A summary of the commonly used methods of resistance extrapolation (correction of polarization effects) is presented in Table 2.1.

**Table 2.1.** Summary of analytical methods commonly applied to determine polarization-corrected resistance.

| Method | *R* Calculation | Literature |
|---|---|---|
| Extrapolation to Infinite Frequency, $R_\infty$ | $R\left(1/f^{1/2}\right) = \frac{a}{f^{1/2}} + R_\infty$ | [11, 14, 19-23] |
| | $R(1/f) = \frac{a}{f} + R_\infty$ | [10-18] |
| | $R(1/f^2) = \frac{A}{f^2} + R_\infty$ | |
| | $R(1/f^2) = \frac{b}{f^2} + \frac{b}{f} + R_\infty$ | [35, 36] |
| | $R(1/f^2) = \frac{b}{1 + cf^2} + R_\infty$ | [35, 36] |
| Nyquist Plot, $R(-X)$ | $R(X = 0)$, Abscess intercept | [25, 36, 39-51] |
| *Plateau* | Average *R*(*plateau*) | [37, 38] |

The parameters *a*, *b*, and *c* are fitting coefficients for each functional.

## 2.4. Effect of Temperature on the Transport Properties

Viscosity and electrical conductivity are deeply associated with the mobility and dynamics of the molecules/ions. Therefore, these transport properties are highly dependent on the temperature of the system, as higher temperatures are associated with higher levels of molecular motion. As in most systems, for ILs, the viscosity decreases, and electrical conductivity increases with temperature. The study of temperature dependence is a major aspect in the field of transport properties, as it can be used to derive important thermodynamic properties and characteristics of the system under study. Based on this, over the years, multiple fitting methods have been developed and applied to modulate the effect of temperature on the viscosity and electrical conductivities of ionic liquids. In this section, some of the most common methods will be presented. For the purpose of clarity and simplification, a generalized notation, $\Psi$, will be used in the presented equations to represent viscosity and electrical conductivity. However it is important to remember that for these two cases the signal of the function is different, as viscosity decreases and electrical conductivity increases with the increase in temperature.

### 2.4.1. Arrhenius Relation

The Arrhenius equation is an empirical relation derived from the previously introduced van't Hoff equation [52, 53]. This relation is typically associated with the temperature dependence of reaction rates. However, it is also widely used to describe the temperature dependence of transport properties, such as viscosity, electrical conductivity, and diffusion coefficients (Eq. 2.39).

$$\Psi = A_\Psi \exp\left(\frac{E_\Psi}{RT}\right) \tag{2.39}$$

$A_\psi$ is a fitting coefficient, known as the pre-exponential coefficient, and $E_\psi$ is the energy barrier associated with the conduction process (viscous flow in the case of viscosity). By linearization of Eq. 2.39 the following equation is obtained:

$$\ln(\Psi/\Psi_0) = A_\Psi + \frac{E_\Psi}{RT} \tag{2.40}$$

A system that obeys the Arrhenius behavior shows a linear dependence of ln $\Psi$ vs 1/$T$, where the energy barrier can be derived from the slope of the line. A schematic representation of the Arrhenius temperature dependence on electrical conductivity is presented in Fig. 2.14.

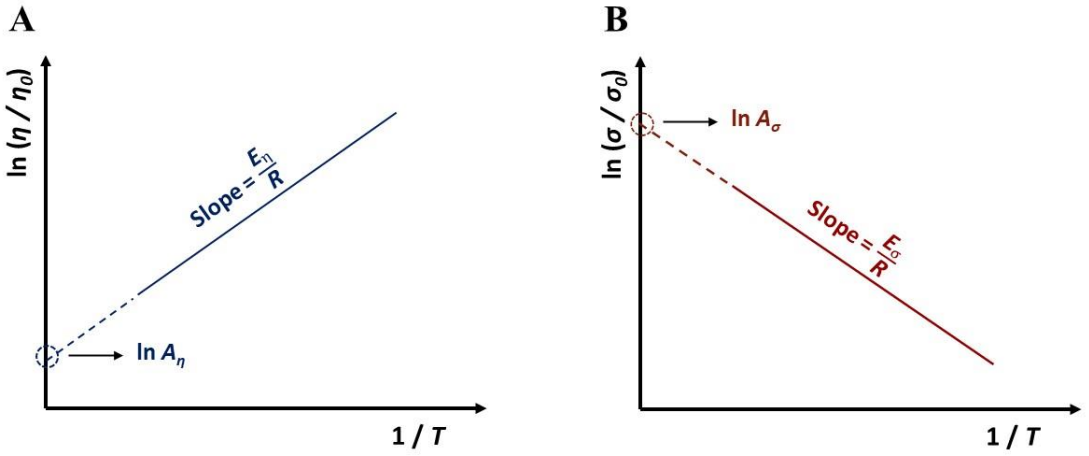



**Figure 2.14.** Schematic representation of the Arrhenius temperature dependence on the viscosity (**A**) and electrical conductivity (**B**).

### 2.4.2. Non-Arrhenius Behavior in Glassformers: VFT Equation

Ionic liquids are glass-forming compounds, meaning that it is possible to achieve a glassy state upon cooling of the liquid. A glass is an intermediate between the crystalline and liquid phases, characterized as an amorphous and low-ordered solid. The change from liquid to glass is known as glass transition. This is usually classified as a second-order transition, as no latent heat is involved. Therefore, when studying a glass transition by differential scanning calorimetry (DSC), the phase change is not reflected by a peak as in the case of fusion or crystallization, but by a change in heat capacity over a Material-characteristic temperature range. The glass transition has been previously defined as the temperature interval where the liquid in equilibrium with the glass reaches a viscosity in the order of $10^{12}$ Pa·s and an average relaxation time, $\tau$ of 100 s [54-56]. Based on this, a glass can be thought of as an extremely low-fluidity liquid. The relaxation time is the period necessary to allow a system to achieve structural equilibrium after a perturbation. Angell introduced the concept of fragility to classify different glassformers in terms of the degree of deviation to the Arrhenius behavior [55-58]. The fragility, *m*, is defined as the rate of change of the conductivity, viscosity, and relaxation time with temperature at the range of glass transition, as described by Eq. 2.41:

$$m = \left.\frac{\delta \log(\Psi/\Psi_0)}{\delta\left(T_g/T\right)}\right|_{T = T_g} \tag{2.41}$$

Liquids that deviate significantly from the Arrhenius behavior exhibit large changes in viscosity and relaxation time in a narrow temperature range close to the glass transition temperature, $T_g$. These compounds are classified as fragile liquids and present large *m* values. On the other hand, glassformers whose properties are less affected by temperature changes are known as strong liquids. The former are usually compounds with non-directional bonds, such as van der Waals, and often present ionic/aromatic character (e.g., ionic liquids and molten salts), while the latter are usually tetrahedral covalent network structures (e.g., $SiO_2$ and $GeO_2$) [55, 56, 59, 60]. Since fragility is a reflection of the intermolecular interactions, it is also related to the heat capacity change at the glass transition temperature, $\Delta^{l}_{gl}C_p$. Strong glassformers present small heat capacity changes while fragile glassformers exhibit larger $\Delta^{l}_{gl}C_p$ values [55, 61] (Fig. 2.15).

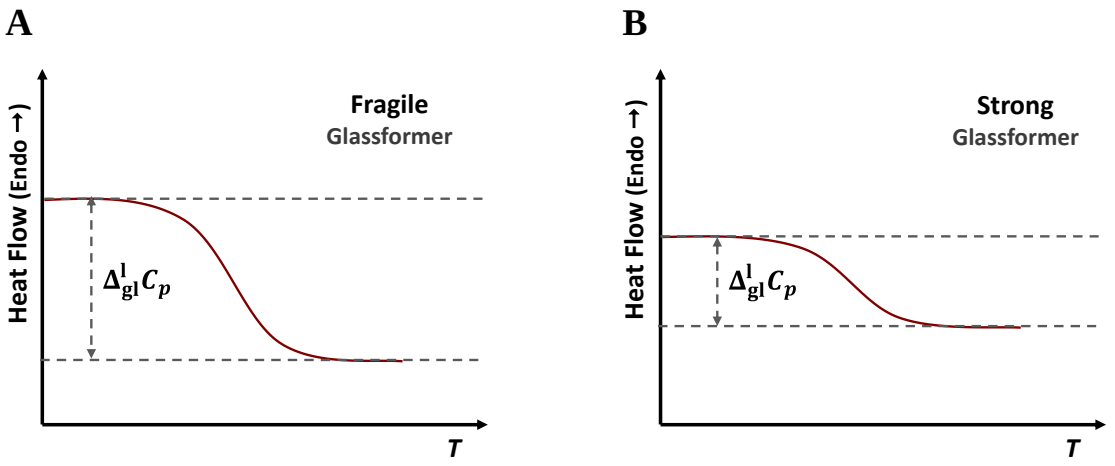



**Figure 2.15.** Schematic representation of the heat capacity change at the glass transition temperature for fragile (**A**) and strong (**B**) glassformers.

Adam and Gibbs [62] have explained molecular rearrangement in terms of energy fluctuations. The theory's basis is that viscous flow is due to the increasingly cooperative rearrangement of groups of particles. The probability of occurrence of an energy fluctuation relevant to the cooperative rearrangement is given by the following partition function:

$$\Delta_c(z,P,T) = \sum_{E,V} w(z,E,V)\exp(-E/k_BT)\exp(-PV/k_BT) \tag{2.42}$$

The Gibbs free energy of the process is given by Eq. 2.43,

$$G = z\,\mu = -k_BT\ln\Delta(z,P,T) \tag{2.43}$$

Where $z$ is the number of molecules involved and $\mu$ is the chemical potential. The probability of a cooperative region to translate to a new arrangement, $W$, is dependent on temperature and number of particles in an Arrhenius-like model:

$$W(T) = A_W \exp\left(\frac{-z\Delta\mu}{k_BT}\right) \tag{2.44}$$

Where $\Delta\mu$ is the activation energy per rearranging particle, or in other words, it is the energy potential hindering the cooperative rearrangement. Angell correlated the fragility of the liquid with the number of minima at the potential energy surface [57] (Fig. 2.16).

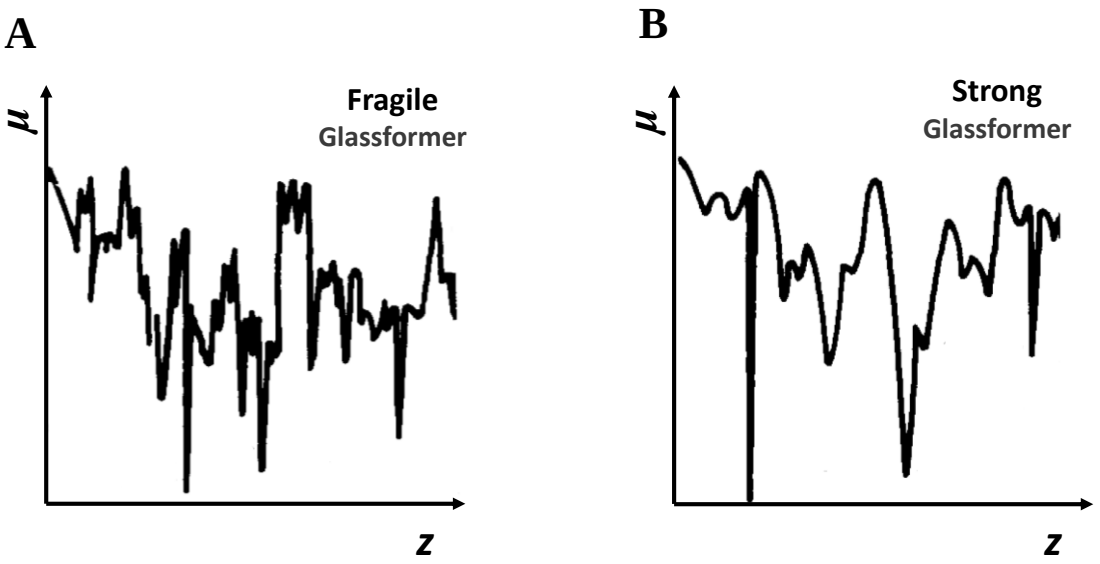



**Figure 2.16.** Characteristic energy potential surfaces (chemical potential as a function of the number of cooperative particles) for fragile (**A**) and strong (**B**) glassformers. Adapted from Angell 1988 [57].

The lower number of minima for the strong liquids might indicate the higher difficulty of rearranging (moving particles) in the highly ordered and strongly connected structure characteristic of the tetrahedral covalent networks in comparison to the weakly coordinated structures of the fragile liquids [57]. Based on that, $\Delta\mu$ is a measure of the intermolecular interactions of the system. The configurational entropy, $S_c$ of a system is defined as [62]:

$$S_c = -\left(\frac{G_c}{T}\right)_{p,z} \tag{2.45}$$

Where $G_c$ is the configurational free Gibbs energy. Alternatively, $S_{c\ can}$ be expressed based on the number of possible configurations, $N_c$ as is described in Eq. 2.46:

$$S_c = k_B \ln\left(N_c^{\,z/N_A}\right) \tag{2.46}$$

The effect of temperature on the configurational entropy is given by:

$$S_{c,2} - S_{c,1} = \int_{T_1}^{T_2} \left( \frac{\partial \Delta C_p}{\partial T} \right) dT \tag{2.47}$$

Considering that the heat capacity of the liquid is not significantly affected by the change in temperature, Eq. 2.47 can be written as:

$$S_{c,2} - S_{c,1} = \Delta C_p \ln \frac{T_2}{T_1} \tag{2.48}$$

The entropy of a liquid decreases upon cooling towards the glass transition temperature. The extrapolated temperature corresponding to the point where the entropy of the liquid equals the entropy of the crystal ($S_c = 0$) is known as the Kauzmann temperature, $T_K$. Considering $T_1 = T_K$, Eq. 2.48 becomes:

$$S_c(T) = \Delta C_p \ln \frac{T}{T_K} \tag{2.49}$$

The configurational entropy at the glass transition temperature is given by:

$$S_c(T_g) = \Delta^{l}_{gl} C_p \ln \frac{T_g}{T_K} \tag{2.50}$$

The temperature dependency of the transport properties of fragile liquids, like ionic liquids, is not well described by the Arrhenius relation, as for these compounds the representation of ln *P* vs 1/*T* leads to a pronounced curvature [55, 56] (Fig. 2.17).

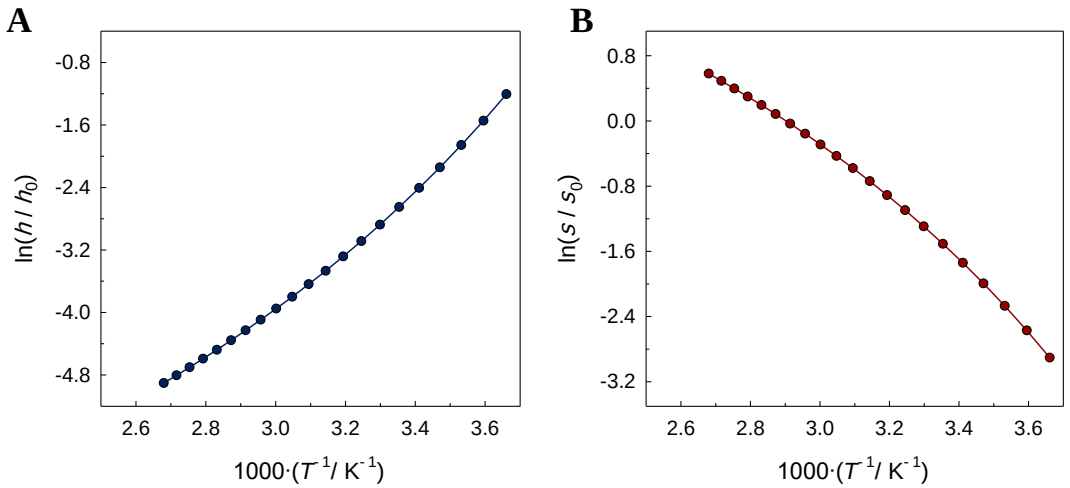



**Figure 2.17.** Representation of the Arrhenius relation for the temperature dependence of viscosity (**A**) and electrical conductivity (**B**) for the $[^1C_6{}^3C_1im][NTf_2]$ ionic liquid. $\eta_0$ = 1 Pa·s, $\sigma_0$ = 1 S·m$^{-1}$.

Since the Arrhenius relation fails to describe the temperature dependence of the transport properties of most glassformers, the Vogel-Fulcher-Tammann (VFT) equation (2.51) is widely used [63-66].

$$\Psi = A_\Psi \exp\left(\frac{B_\Psi}{T - C_\Psi}\right) \tag{2.51}$$

$A_\Psi$, $B_\Psi$, and $C_\Psi$ are the VFT fitting coefficients. By linearization, Eq. 2.51 becomes

$$\ln(\Psi/\Psi_0) = \ln A_\Psi + \frac{B_\Psi}{T - C_\Psi} \tag{2.52}$$

A schematic representation of the typical VFT fitting is presented in Fig. 2.18.

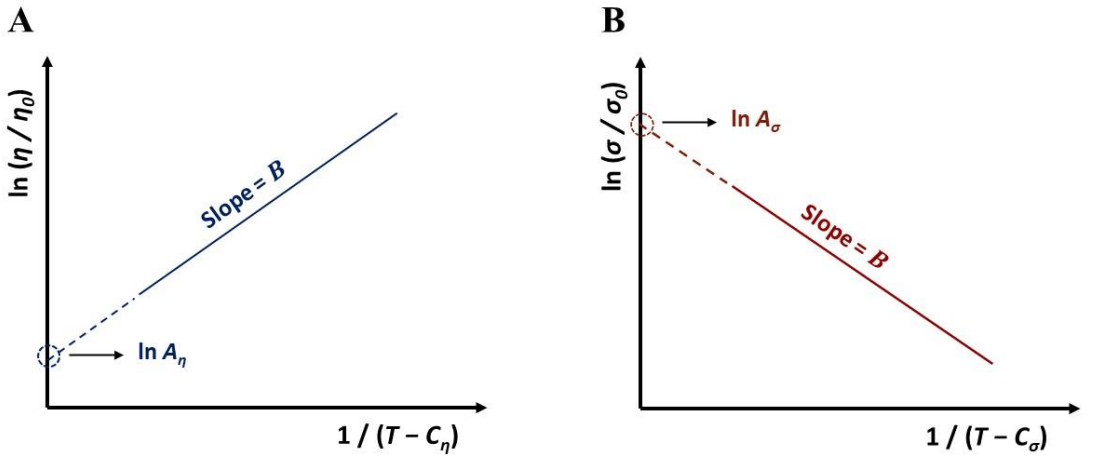



**Figure 2.18.** Schematic representation of the VFT temperature dependence on the viscosity (**A**) and electrical conductivity (**B**).

The VFT equation (Eq. 2.51 and 2.52) may seem similar to the Arrhenius relation. (Eq. 2.32 and 2.33), but the introduction of the third parameter, $C_{\Psi,}$ presents a key difference. This parameter is related to the $T_g$ of the compound and is usually found to be around 20 K lower than the glass transition temperature [57]. It is possible to observe that in a case where $C_\Psi \rightarrow 0$, the VFT relation obeys the Arrhenius law [60]. Therefore, $C_\Psi$ can also be seen as a measure of deviation to Arrhenius, with larger $C_\Psi$ being associated with higher fragilities. Similarly, in the extreme region of very high temperatures, where $T \rightarrow \infty$ and therefore $T - C_\Psi \rightarrow T$, the Arrhenius behavior would also be verified. A summary focused on the meaning of the application of the VFT equation at different temperatures and the balance between $T$ and $C_\Psi$ is presented in Fig. 2.19.

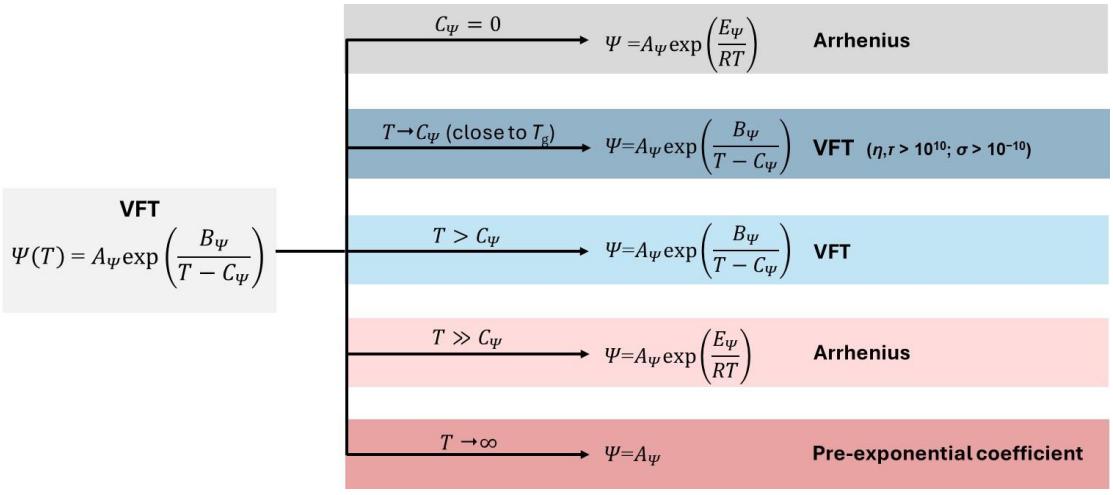



**Figure 2.19.** Summary of the application of the VFT equation at different temperatures.

The slope of the VFT representation is given by $B_\Psi$. However, since the temperature dependence is presented as a function of $1/(T - C_\Psi)$ and not of $1/T$ (as in the case of Arrhenius), $B_\Psi$ should not be confused with the energy barrier associated with the process. The relation between a property's temperature dependence and the energy barrier is described by the van't Hoff equation (Eq. 2.53) [67].

$$\frac{\partial(\ln[\Psi(T)/\Psi_0])}{\partial(T)} = \frac{E_\Psi}{RT^2} \tag{2.53}$$

Based on that, to properly derive the energy barrier from a VFT fitting, it is necessary to combine the equations 2.52 and 2.53. With this, Eq. 2.47 is obtained [68, 69]:

$$E_\Psi(T) = -R\frac{\partial(\ln[\Psi(T)/\Psi_0])}{\partial(1/T)} = -R\left(\frac{B_\Psi}{\frac{C_\Psi^2}{T^2} - \frac{2C_\Psi}{T} + 1}\right) \tag{2.54}$$

As can be seen from the previous equation, a temperature-dependent energy barrier is derived from the VFT relation. This is a consequence of fragility and a key aspect of a system that deviates from the regular Arrhenius behavior [57, 70]. The Eq. 2.54 also provides some important insight into the role of the $B_\Psi$ and $C_\Psi$ coefficients. The $B_\sigma$ acts solely as a magnitude multiplier with higher coefficients leading to higher energy barriers. As referred to earlier, strong liquids present stronger and directional bonds, which should result in higher cohesive energies and, therefore, larger $B_\Psi$ values. On the other hand, $C_\sigma$ is also responsible for the shape of the curvature. A higher $C_\Psi$ leads to a higher energy barrier, as well as a more pronounced curvature (energy-temperature dependence). A graphical representation of the impact of the $B_\Psi$ and $C_\Psi$ coefficients on the energy barrier is presented in Fig. 2.20.

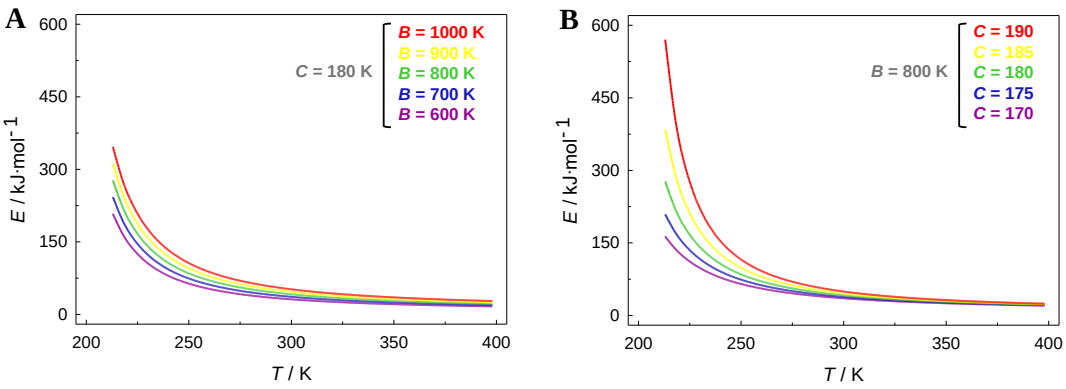



**Figure 2.20.** Graphical representation of the impact of the $B_\Psi$ and $C_\Psi$ coefficients on the energy barrier. **A:** Constant $C_\Psi$ and variable $B_\Psi$. **B:** Constant $B_\Psi$ and variable $C_\Psi$.

As can be seen from Fig 2.19 and Eq. 2.54 at $T \rightarrow \infty$ , the energy-related parameters, $B_\Psi$ and $C_\Psi$, are not relevant for the conductivity value, and therefore, the pre-exponential coefficient is often referred to as the conductivity at infinite temperature. This means that at this point, the system is fully thermal-activated, and the energy potential/cohesive energy restraining the transport mechanism is not relevant. Therefore, $A_\Psi$ is mainly related to the characteristics associated with the structure and mobility of the molecule, such as size, shape, flexibility, and dynamics. In the literature, the fragility has also been discussed in terms of VFT coefficients [56, 60]. The combination of VFT with the previously presented fragility and configurational-related concepts might clarify the meaning behind each of the VFT coefficients. $C_\Psi$ is often known as the Vogel divergence temperature and has been verified to coincide closely with the Kauzmann temperature estimated from calorimetric data ($C_\Psi \approx T_K$) [56, 60]. Based on that, the Eq. 2.50 can be now written as:

$$S_c(T_g) = \Delta^{l}_{gl}C_p \ln\frac{T_g}{C_\Psi} \tag{2.55}$$

From this equation $\Delta^{l}_{gl}C_p$ is expected to increase with increasing $C_\Psi/T_g$. Therefore, the gap between the Vogel temperature and the glass transition temperature seems to be a viable indication of the fragility of a liquid. The combination of the VFT (Eq. 2.51) and Adam-Gibbs (Eq. 2.44) and configurational entropy (Eq. 2.50) equations, highlight a clearer definition of $B_\Psi$ [60]:

$$B_\Psi = \frac{N_A \cdot s^* \cdot \Delta\mu}{k_B \cdot \Delta C_p(C_\Psi)} = \frac{N_A \cdot s^* \cdot \Delta\mu \cdot C_\Psi}{k_B \cdot T_g \cdot \Delta^{\mathrm{l}}_{\mathrm{gl}} C_p} \tag{2.56}$$

se of $\Delta\mu$ and the decrease of $\Delta^{\mathrm{l}}_{\mathrm{gl}} C_p$.The ratio between the $B_\Psi$ and $C_\Psi$ coefficients is known as the strength parameter $D_\Psi$.

$$D_\Psi = \frac{B_\Psi}{C_\Psi} = \frac{N_A \cdot s^* \cdot \Delta\mu}{C_\Psi \cdot k_B \cdot \Delta C_p(C_\Psi)} = \frac{N_A \cdot s^* \cdot \Delta\mu}{k_B \cdot T_g \cdot \Delta^{\mathrm{l}}_{\mathrm{gl}} C_p} \tag{2.57}$$

Taking that into account, the VFT equation is often presented as follows:

$$\ln \Psi = \ln A_\Psi + \frac{C_\Psi \cdot D_\Psi}{T - C_\Psi} \tag{2.58}$$

By combining the fragility definition (Eq. 2.41) with Eq. 2.57, the following relation between the fragility index, $m$, and the strength parameter, $D_\Psi$, is achieved.

$$m = \frac{D_\Psi \left(C_\Psi / T_{\mathrm{g}}\right)}{\ln 10 \left(1 - C_\Psi / T_{\mathrm{g}}\right)^2} \tag{2.59}$$

The minimum value for the fragility index, $m_{\mathrm{min}}$, can be calculated based on the ratio between the values of the property (relaxation, conductivity, or viscosity) at the two extreme temperature points: glass transition temperature and infinite temperature [60]. As can be seen from the VFT equation, the latter value at infinite temperature corresponds to the pre-exponential coefficient ($\Psi(T \to \infty) = A_\Psi$). Based on that the calculation of $m_{\mathrm{min}}$ is as follows:

$$m_{\mathrm{min}} = \log\left(\frac{\Psi\left(T_{\mathrm{g}}\right)}{A_\Psi}\right) \tag{2.60}$$

Considering that at infinite temperature the structural relaxation time would be comparable with the vibrational lifetime, $A_\tau$ can be estimated to be around $10^{-14}$ s. By combining this with the characteristic relation time at the glass transition of 100 s, $m_{\min}$ can be estimated to be around 16 ($m_{\min} \approx 16$) [56, 60]. By applying the VFT relation to the definition of $m_{\min}$, Eq 2.61 is achieved.

$$m_{\min} = \frac{D_\Psi \left(C_\Psi / T_g\right)}{\ln 10 \left(1 - C_\Psi / T_g\right)} \tag{2.61}$$

Based on the equations 2.59 and 2.61 and the concept of minimum fragility, a more practical relationship between the fragility index $m$, and the strength parameter $D$ is obtained:

$$m = m_{\min} + \frac{m_{\min}^2 (\ln 10)}{D_\Psi} = 16 + \frac{590}{D_\Psi} \tag{2.62}$$

A useful tool to compare the fragilities of different compounds is the Angell plot [57], a $T_g$-scaled graphical representation of the property ($\Psi$) temperature dependence (log $P$ vs $T_g/T$). Fig. 2.21 presents a simulated Angell plot (relaxation time, viscosity, and electrical conductivity) for compounds with varying fragilities. The plot is scaled between $T_g/T$ = 0 and 1, where 0 corresponds to a point in temperature tending to infinite ($T \rightarrow \infty$) and 1 corresponds to the glass transition temperature. As observed, the more fragile liquids present curves with more pronounced concavities, reflecting larger deviations to the Arrhenius behavior. By dividing the plot into two regions, high and low temperatures, it is possible to conclude that the more fragile liquids present a more drastic behavioral differentiation between the two areas. At low temperatures (close to $T_g$), the rate of property change is more drastic for the more fragile liquids, which is coherent with the definition of fragility that has been presented. However, interestingly, at high temperatures ($T \rightarrow \infty$), the rate of property change is milder for fragile liquids and more accentuated for strong liquids. This is a reflection of the typical higher $B_\Psi$ values of the latter [56, 70].

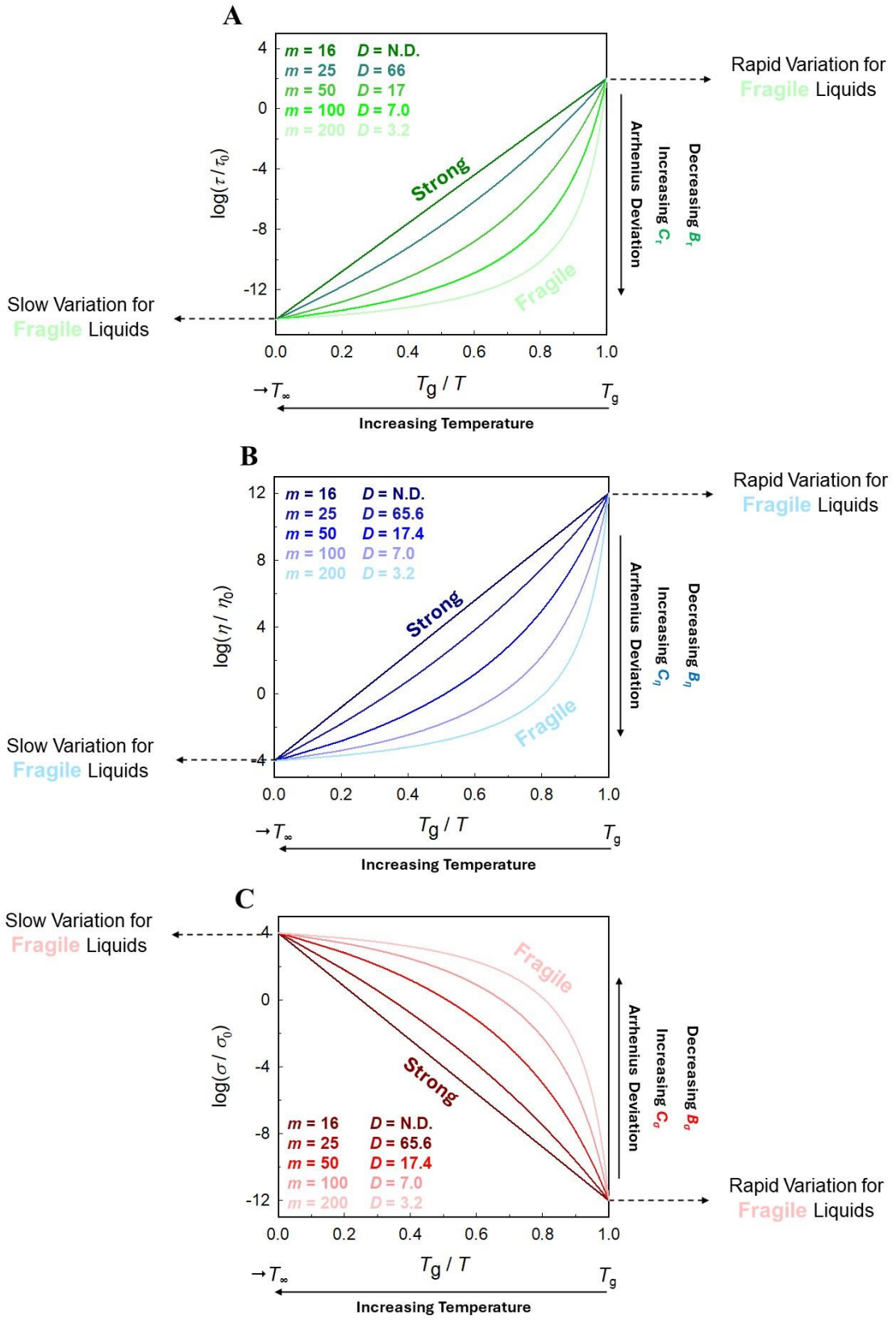



**Figure 2.21.** Simulated Angell plots for compounds with varying fragilities. **A**: Relaxation time; **B**: Viscosity, **C**: Electrical conductivity. The Angell curves were calculated by $\log(\Psi) = \log\left(\Psi(T_g)\right) - m_{min} + m^2(T_g/T)/m - (m - m_{min})(T_g/T)$, using a fixed $T_g$ = 190 K and varying fragilities ($m$ = 16, 25, 50, 100, and 200). $\tau_0$ = 1 s, $\eta_0$ = 1 Pa·s, $\sigma_0$ = 1 S·m$^{-1}$.

### 2.4.3. Non-Arrhenius Behavior in Glassformers: Other Models

While the VFT equation is the most common model to fit the temperature dependence of transport properties, other approaches have also been developed and applied. Based on that, the viscosity, electrical conductivity, and relaxation time at a given temperature can be described akin to the expression presented earlier for the probability of cooperative rearrangement, *W* (Eq. 2.44).

#### 2.4.3.1. Adam-Gibbs' Configurational Entropy Model

The Adam-Gibbs model [62] to describe the temperature dependence of transport properties of glassformers is based on the concept of configurational entropy discussed in the previous section.

$$\Psi(T) = A_W \exp\left(\frac{-z\Delta\mu}{k_B T}\right) \tag{2.63}$$

The relation between the number of rearranging particles, *z*, and the configurational entropy of the system is given by Eq. 2.64.

$$\frac{z}{s*} = \frac{N_A}{S_c(T)} \tag{2.64}$$

The combination of Eq. 2.63 and Eq. 2.64 results in the typical form of the Adam-Gibbs model (Eq. 2.65).

$$\Psi = \Psi_\infty \exp\left(\frac{B_\Psi}{S_c(T)T}\right) \tag{2.65}$$

Where $\Psi_\infty$ is the pre-exponential coefficient, $B_\Psi$ is related to the energy barrier, and $S_c(T)$ is the temperature-dependent configurational entropy [71].

In the typical VFT equation, the limits of the model are defined by the values of the parameter $C_\Psi$ and its comparison with the temperature of the system, *T*. Similarly, the limitations of this model are given by the value of $S_c(T)$, which is equal to zero at the Kauzmann temperature, yielding a non-defined result [72, 73]. On the other hand, at the point of maximum thermal activation ($T$, $S_c(T) \rightarrow \infty$), the electrical conductivity of the system is given by the pre-exponential coefficient (analog to the VFT model).

#### 2.4.3.2. Mauro's Configurational Entropy Model

The Mauro model [74, 75] is a variation of the Adam-Gibbs Configurational Entropy Theory combined with the concepts of topological degrees of freedom introduced by Thorpe' group [76-78]. In this approach the configurational entropy of a system is defined by Eq. 2.66,

$$S_c(T) = d_f N k_B \ln \Omega \tag{2.66}$$

Where *N* is the number of atoms and $\Omega$ is the number of degenerate configurations per floppy mode. Thorpe [76-78] defined sloppy as an atomic network where the number of degrees of freedom is larger than the number of constraints (related to bond length and angle). A floppy mode represents a channel-like pathway in the energy landscape along which a system can explore microstates without increasing its energy significantly. Therefore, $\Omega$ can be thought of as a measure of the volume in the energy landscape explored by a floppy mode.

The authors modulated the temperature dependence of the degrees of freedom by assuming a binary model where the network constraints are either intact or broken. This approach is described by Eq. 2.67.

$$d_f = 3\exp\left(-\frac{H}{k_B T}\right) \tag{2.67}$$

Where *H* is the energy difference between the broken and intact states. By applying Eq. 2.66 and Eq. 2.67 to the Adam-Gibbs model (Eq. 2.65) the Mauro´s model is obtained:

$$\Psi = \Psi_{\infty} \exp\left[\frac{K}{T}\exp\left(\frac{C_{\mathrm{M}}}{T}\right)\right], \tag{2.68}$$

where $K = B/3Nk_B \ln \Omega$ and $C_M = H/k_B$. By looking at the equations it is possible to observe that *K* is a quantity related to the energy barrier and $C_{\mathrm{M}}$ is the model limiting coefficient given its relation to the topological degrees of freedom and therefore the configurational temperature.

#### 2.4.3.3. Avramov-Milchev's (AM) Atomic Hoppin Model

The basis of the Avramov-Milchev's model [79] is that the amorphous disorder of the glassformers yields a random probability distribution of energy barriers, $\boldsymbol{\beta}$, corresponding to molecular hoping [80]. The relation between the entropy of the system is related to the dispersion as described in Eq. 2.69:

$$S - S_0 = \frac{R}{2Z}\ln\left(\frac{\boldsymbol{\beta}}{\boldsymbol{\beta}_0}\right) \tag{2.69}$$

Where *Z* is related to the molecular network as it corresponds to the number of directions the molecule can move along. In this model, the conductivity is described in terms of the distribution $\boldsymbol{\beta}$ as follows:

$$\Psi = \Psi_{\infty} \exp\left(\frac{B_{\mathrm{AM}}}{T}\right)^{\alpha_{\mathrm{AM}}} \tag{2.70}$$

Where $B_{\mathrm{AM}}$ is a fitting parameter related to the distribution $\boldsymbol{\beta}$ and the estimated maximum energy barrier (energy barrier related to the molecular jump in a crystal), and α is a fitting parameter associated with the heat capacity, $\alpha_{\mathrm{AM}} = 2C_p/RZ$.

#### 2.4.3.4. Litovitz's Empirical Model

Litovitz's model [81] consists of a simple empirical equation anchored on the concept of the temperature dependence of the energy barrier of fragile glassformers. The energy

barrier decreases with increasing temperature due to the decrease in the potential of the intermolecular interactions. In this approach, the author assumed a temperature dependence of:

$$E_\Psi = \frac{a_L}{T^2} \tag{2.71}$$

Where $a_L$ is a fitting parameter associated with the energy barrier, similar to what was seen in the previous models. Taking into account that the energy barrier associated with a process is given by $\partial(\ln[\Psi(T)/\Psi_0])/\partial(1/T)$ (Eq. 2.54), the Litovitz's model to describe the temperature dependency of the electrical conductivity is presented as follows:

$$\Psi = A_L \exp\left(\frac{a_L}{RT^3}\right) \tag{2.72}$$

However, as can be seen, contrary to the previous models, this fitting does not offer a temperature limitation associated with the characteristic of the glass. Therefore, this model should be expected to yield significant deviations closer to the glass transition temperature.

#### 2.4.3.5. Elmatad's Quadratic Model

Elmatad's model takes a similar approach to Litovitz's model in the sense that it is based on the temperature dependence of the energy barrier, which in this case is combined with the molecular hopping concept akin to the AM model. In this approach, the authors derived the energy barrier – temperature dependence based on kinetically constrained models used to describe the energy barrier necessary to relax a domain of length $\lambda = c^{-1/d}$. The authors found a Boltzmann distribution of $\log c \propto 1/T$ where $c$ is the concentration of localized excitations and $d$ is related to dimensionality. Based on this, the energy barrier was assumed to increase along $1/T$, and therefore, the temperature dependency of electrical conductivity takes the form of a quadratic:

$$\Psi = \Psi_0 exp\left[\left(\frac{J}{T_r}\right)^2 \cdot \left(\frac{T_r}{T-1}\right)^2\right], T_r > T > T_x \tag{2.73}$$

Where $T_r$ is a reference state temperature where excitations yielding molecular motion are present throughout the whole system, and $J$ is a parameter used to set the energy scale for excitations of correlated dynamics. This temperature is the upper limit of application of Eq. 2.73 and corresponds to a region of weaker conductivity-temperature dependency. On the other hand, $T_x$ is a lower temperature limit and corresponds to a region of Arrhenius behavior. The proximity of $T_x$ and $T_r$ can be interpreted as a characteristic of a strong glassformer.

## 2.5. Viscosity - Electrical Conductivity Relation

The process of electrical conduction in a liquid involves the movement of the charged species; therefore, a system's electrical conductivity is intricately related to its viscosity, as the former increases as the latter decreases. In 1906, Walden published an empirical relation known as the Walden rule (Eq. 2.74), which states that the product of the molar conductivity, $\Lambda$, of a solution and its viscosity, $\eta$, is always constant.

$$\Lambda\eta^{\alpha_w} = \text{constant} \tag{2.74}$$

This rule implies that the electrical conductivity of an ionic liquid/solution is solely dictated by the viscosity. However, this is only true for fully dissociated systems where no aggregation occurs, such as a potassium chloride solution. Ion association/aggregation would yield neutral charged pairs/aggregates, therefore resulting in a net decrease of charges in motion, which is reflected in a decrease in the electrical conductivity. The larger the degree of association, the larger the deviation from the Walden rule. The ion dissociation or ionicity, $\xi$, is given by the ratio between the number of free ions and the number of total ions (Eq. 2.75)

$$\xi = \frac{n(Free\ Ions)}{n(Total\ Ions)} \tag{2.75}$$

A schematic representation of the free aggregates equilibria and its effect on the ionicity is presented in Fig. 2.23.

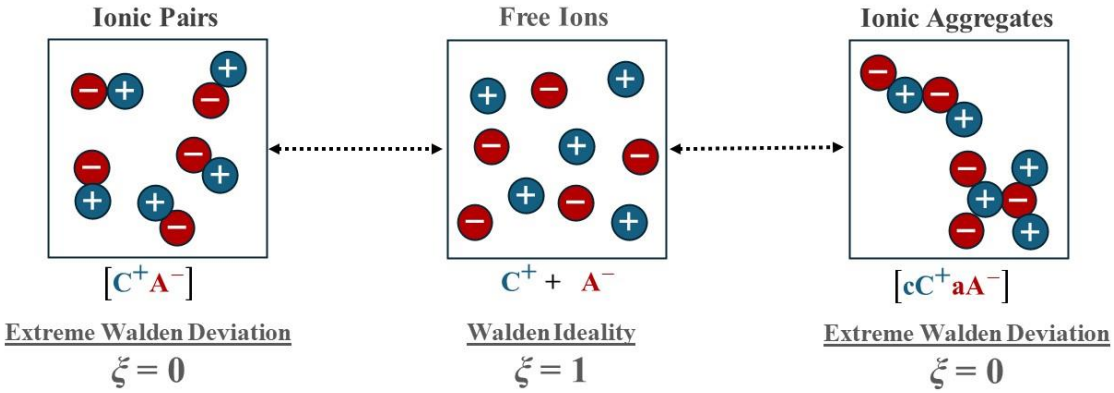



**Figure 2.22.** Schematic representation of types of ion distribution in the liquid phase/solution: free ions, ionic pairs, and ionic aggregates.

Ionic liquids are interesting compounds because while they are liquids solely composed of ions, these compounds are ruled by different types of interactions apart from electrostatic, such as van der Waals, hydrogen bonding, and π-π interactions, which contribute to ion association/aggregation. Thus, ionic liquids often present an ionicity lower than the unit (ξ = 1). As discussed in the previous chapter, the properties and characteristics of ILs are highly dependent on structural features (e.g., anion, cation, and alkyl chain length). These factors play a major role in the ionicity of each IL. While it represents the common ionic distribution, Fig. 2.22 paints an unrealistic case for ionic liquids, as a more realistic presentation would combine all three types (Fig. 2.23), with the proportions depending on the interaction characteristics of the IL.

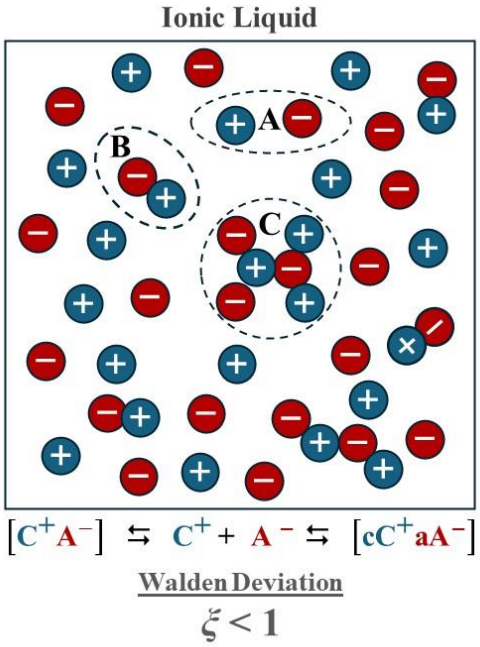



**Figure 2.23.** Schematic representation of types of ion distribution in a typical ionic liquid. **A**: Free ions; **B**: Ionic pair; **C**: Ionic aggregate.

By linearization of Eq. 2.74, the Eq. 2.76 is obtained:

$$\log[\Lambda(T)/\Lambda_0] = \log[\Psi] + \alpha_w \cdot \log\left[\eta^{-1}(T)/\eta_0^{-1}\right] \tag{2.76}$$

Where Ψ is a constant and $\alpha_w$ is the slope of the Walden line. The graphical representation of Eq. 2.76 is known as the Walden Plot, and it is a useful tool to evaluate the ionicity of an ionic liquid. In this approach, the relation between the molar conductivity and viscosity of a liquid is represented as log Λ = *f*(log$\eta^{-1}$) and is compared to the ideal Walden line. A schematic example of the Walden Plot is presented in Fig. 2.24.

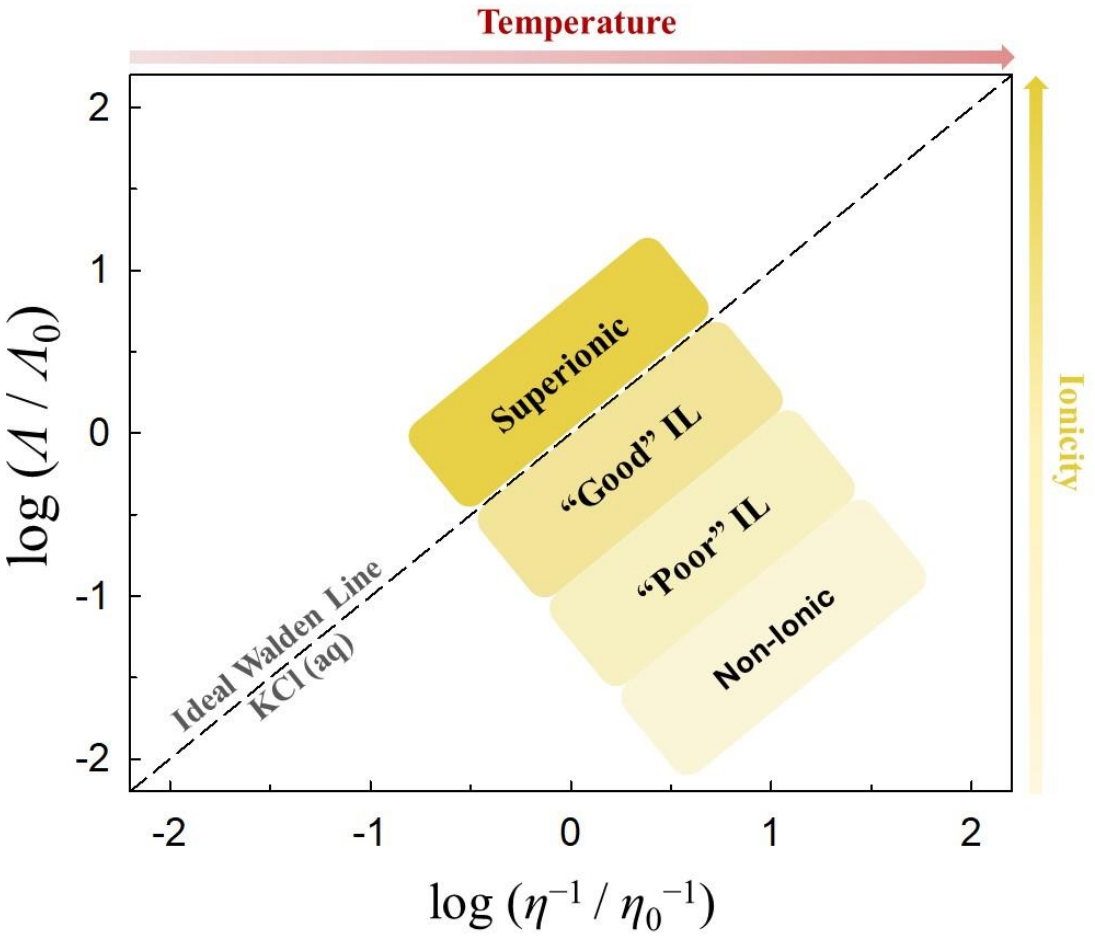



**Figure 2.24.** Schematic representation of the Walden plot as a tool to evaluate the ionicity of ionic liquids. $\eta_0$ = 1 Poise, $\Lambda_0$ = 1 S·cm$^2$·mol$^{-1}$.

The negative deviation from the ideal line indicates that the molar conductivity is lower than what was expected from the viscosity data, and therefore, it is an indication of ion association/aggregation and a decrease in ionicity [82-84]. Ionic liquids with Walden plots close to ideality are classified as "good ILs" while ILs with greater deviations are classified as "poor ILs" [85]. Even larger deviations to the Walden line would be regions for non-ionic molecular liquids, as they present lower electrical conductivities due to not being composed of ions. The superionic regions yield a positive deviation from the ideal line, meaning that the real conductivity is higher than the one estimated from the fluidity of the system. This usually means that in these cases, there is an additional mechanism other than the regular charge carrier diffusion (vehicular mechanism) that contributes to the charge conduction in the system. This is often observed in protic ILs where the

charge is also transferred by proton exchange through the hydrogen-bond network (proton-hoping mechanism). An approach to quantify the deviation to the Walden rule, Δ*w*, is to determine the vertical distance between the IL line and the ideal Walden line as illustrated in Fig. 2.24. Thus, Δ*w* is given by:

$$\Delta w = \log \Lambda(\mathrm{IL}) - \log \Lambda(\mathrm{W}) \tag{2.77}$$

Since in the ideal Walden line $\log \Lambda(\mathrm{W}) = \log \eta^{-1}(\mathrm{W})$, Eq. 2.77 can be rewritten as:

$$\Delta w = \log \Lambda(\mathrm{IL}) - \log \eta^{-1}(\mathrm{IL}) \tag{2.78}$$

Applying the VFT equation (Eq. 2.51) to the Walden rule (Eq. 2.76) makes it possible to relate the viscosity and conductivity fitting coefficients.

$$\Lambda\eta^{\alpha_\mathrm{w}} = \frac{M}{\rho}\sigma\eta^{\alpha_\mathrm{w}} = \frac{M}{\rho}\cdot A_\sigma \exp\left(\frac{B_\sigma}{T - C_\sigma}\right)\cdot A_\eta \exp\left(\frac{B_\eta}{T - C_\eta}\right)^{\alpha_\mathrm{w}} \tag{2.79}$$

By considering that the Vogel temperature obtained from the conductivity and viscosity fittings are equal $C_\sigma = C_\eta = C$, Eq. 2.79 becomes:

$$\Lambda\eta^{\alpha_\mathrm{w}} = \frac{M A_\sigma {A_\eta}^{\alpha_\mathrm{w}} T^{(k-1)/2}}{\rho} \exp\left(\frac{\alpha_\mathrm{w} B_\eta - B_\sigma}{T - C}\right) \tag{2.80}$$

Assuming that the pre-exponential parts are constants:

$$Constant \cdot \alpha_\mathrm{w} = {\alpha_\mathrm{w}}' = \frac{B_\sigma}{B_\eta} \tag{2.81}$$

Taking into consideration the derived equation for energy barrier and $C_\sigma = C_\eta = C$, the Eq. 2.82 is obtained.

$$\alpha_{\mathrm{w}}{}' = \frac{RE_\sigma\left(\frac{C_\sigma^2}{T^2} - \frac{2C_\sigma}{T} + 1\right)}{RE_\eta\left(\frac{C_\eta^2}{T^2} - \frac{2C_\eta}{T} + 1\right)} = \frac{E_\sigma}{E_\eta} \tag{2.82}$$

These two equations relate the Walden slope with the ratio between the conductivity energy barrier and viscosity energy barrier. Since ILs usually present a negative deviation from the ideal Walden line, $\eta^{-1}(\mathrm{IL}) > \sigma(\mathrm{IL})$, the slope *k* is lower than the unit. Therefore, based on Eq. 2.81 and 2.82, the following relations are usually observed or ILs: $B_\sigma < B_\eta$ and $E_\sigma < E_\eta$.

Another way of studying the ionicity of an ionic liquid is by complementing the electrical conductivity measurements with species diffusion data derived from nuclear magnetic resonance (NMR) spectroscopy. The Nernst-Einstein equation allows the calculation of electrical conductivity from the self-diffusion coefficients of the involved species.

$$\Lambda_{NE} = \frac{N_A e^2}{k_B T}(Z_+^2 D_+ + Z_-^2 D_-) \tag{2.83}$$

*e* is the electric charge of an electron, $k_B$ is the Boltzmann constant, $Z_+$ and $Z_-$ are respectively the charge of the cation and the anion, and $D_+$ and $D_-$ are respectively the self-diffusion of the cation and the anion. Contrary to the experimental measurements, where only the charged species contribute to the electrical conductivity, this approach takes into account the diffusion of the species in all forms, even the possible neutral aggregates/pairs formed in solution [84, 86, 87]. Based on that, ionicity ($\xi$), which was previously defined as the fraction of free ions, can also be quantified by the ratio between measured molar conductivity and the molar conductivity derived from the Nernst-Einstein equation, as described in Eq. 2.84 [87].

$$\xi = \frac{\Lambda}{\Lambda_{NE}} = \frac{1}{H_r} \tag{2.84}$$

In the literature, the utilization of the term Haven ratio ($H_r$), which corresponds to the reciprocal of ionicity, is also used [87]. Similar to what is observed for the Walden rule, $\Lambda/\Lambda_{NE}$ values for ionic liquids are usually less than unity, indicating the formation of noncharged ion aggregates/clusters that do not contribute to electrical conduction [84, 87]. Even though the relation between the Walden plot and ionicity has been applied

multiple times across the literature, some critiques about its validation and adequacy have been raised. Schreiner *et al.* [88] criticized the assumption of $k$ = 1 for a 1 mol·dm$^3$, as literature data indicates that the Walden slope for this system would be lower than the unit. The author also questions the validity of using a diluted electrolyte solution composed of ions with similar mobilities as a reference to understand the dynamic and aggregation behavior of a liquid composed solely of ions, which are usually large and complex. However, the author still recognizes the utility of the Walden plot as a tool for comparing the transport properties of ILs and suggests that more attention should be given to the derived Walden slopes ($\alpha_w$) than to the distance to the arbitrary ideal line ($\Delta W$). Harris [89, 90] proposed that the difference between $\Lambda$ and $\Lambda_{NE}$ for ILs is not a consequence of ion association/aggregation but instead is related to the correlation characteristics of the ions' motion. Ion correlation means that the ionic species may move together in a correlated motion due to strong interactions without involving the formation of longer-term pairs or aggregates. Due to being oppositely charged, anion-cation correlations are expected to be the strongest and most predominant type of interaction. However, correlations between like-charged ions (anion-anion and cation-cation) are also possible due to non-ionic interactions, such as dispersive, π-π stacking, and hydrogen bonding. A schematic representation of the possible ion cross-correlations in an IL is presented in Fig. 2.25.

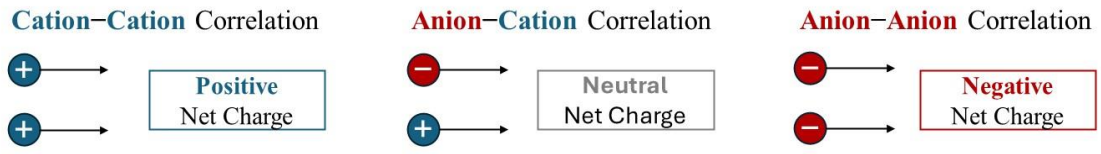



**Figure 2.25.** Schematic representation of the ion cross-correlations in an IL.

Velocity cross-correlation coefficients (VCC) are statistical mechanical quantities calculated based on the experimentally measured transport properties to describe ion correlation, as presented in equations 2.85, 2.86, and 2.87 [89-91]. The VCCs are represented as $f_{++}$, $f_{--}$, and $f_{+-}$ depending on the ions involved and correspond to time integrals of the ensemble average of the velocity correlations of two particles (denoted as α and β).

$$f_{++} = \frac{N_A V}{3}\int_0^\infty \langle v_{+\alpha}(0) v_{+\beta}(t)\rangle dt = \frac{RT\Lambda}{c}\left(\frac{M_-}{FMz_-}\right)^2 - \frac{D_+}{cv_+} \qquad (2.85)$$

$$f_{--} = \frac{N_A V}{3}\int_0^\infty \langle v_{-\alpha}(0) v_{-\beta}(t)\rangle dt = \frac{RT\Lambda}{c}\left(\frac{M_+}{FM+}\right)^2 - \frac{D_-}{cv_-} \quad (2.86)$$

$$f_{+-} = \frac{N_A V}{3}\int_0^\infty \langle v_{+\alpha}(0) v_{-\beta}(t)\rangle dt = \frac{RT\Lambda}{c}\frac{M_+ M_-}{z_+ z_- (FM)^2} \quad (2.87)$$

Where *v* is a stoichiometric number, z is the ion charge. The deviation to the Nernst-Einstein relation, $\Delta_{NE}$, can be described based on the difference between the velocity cross-correlation coefficients of the oppositely charged ions (anion-cation) and the mean of the coefficients for the like-charged ions (anion-anion and cation-cation) (Eq. 2.88):

$$\Delta_{NE} = 1 - \xi = -\frac{c(2v_+ v_- z_+ z_- f_{+-} + v_+^2 z_+^2 f_{++} + v_-^2 z_-^2 f_{--})}{(v_+ z_+^2 D_{s+} + v_- z_-^2 D_{s-})} \quad (2.88)$$

Considering the electroneutrality condition, $v_+ z_+ = -v_- z_-$, Eq. 2.89 becomes:

$$\Delta_{NE} = 1 - \xi = -\frac{c(2f_{+-} - f_{++} - f_{--})}{(D_{s+}/v_+ + D_{s-}/v_-)} \quad (2.89)$$

The VCCs in an IL are usually negative, with values closer to zero being associated with stronger correlations. Therefore, based on Eq. 2.89, the following cases might be observed:

1. Anion-Cation correlation is <u>stronger</u> than Anion-Anion and Cation-Cation correlations: $2f_{+-} < f_{--} + f_{++}$ ➡ $\Delta_{NE} > 0$ ➡ $\xi < 1$
2. Anion-Cation correlation is <u>weaker</u> than Anion-Anion and Cation-Cation correlations: $2f_{+-} > f_{--} + f_{++}$ ➡ $\Delta_{NE} < 0$ ➡ $\xi > 1$
3. Anion-Cation correlation is <u>equal</u> to Anion-Anion and Cation-Cation correlations: $2f_{+-} = f_{--} + f_{++}$ ➡ $\Delta_{NE} = 0$ ➡ $\xi = 1$
4. Ion correlations are <u>non-existent</u>: $f_{+-}, f_{--}, f_{++} = 0$ ➡ $\Delta_{NE} = 0$ ➡ $\xi = 1$

## 2.6. Experimental Methodologies

This section will present the methodologies and apparatus used in this work.

### 2.6.1. Density and Viscosity Measurements

In this work, the density and viscosity of the ionic liquids were measured simultaneously using an automated Anton Paar SVM 3001 rotational Stabinger viscometer–vibrating U-tube densimeter (Fig. 2.26). The SVM 3001 operates in a broad range of temperatures (253 to 373 K), and it uses integrated Peltier elements for fast and efficient thermostability. The system software features the customization of temperature programs.




**Figure 2.26**. Anton Paar SVM 3001 viscometer-densimeter, used for simultaneous viscosity and density measurements.

The viscosity and density cells are installed in-line, as presented in Fig. 2.27. The injected liquids enter first into the viscosity cell and then go into the density cell. After that, the liquid exits the apparatus and can be recovered if appropriate. The cells should be completely filled (1.5 mL) and without air bubbles for accurate measurements. The small sample volume allows extremely quick temperature changes and very short equilibration times.

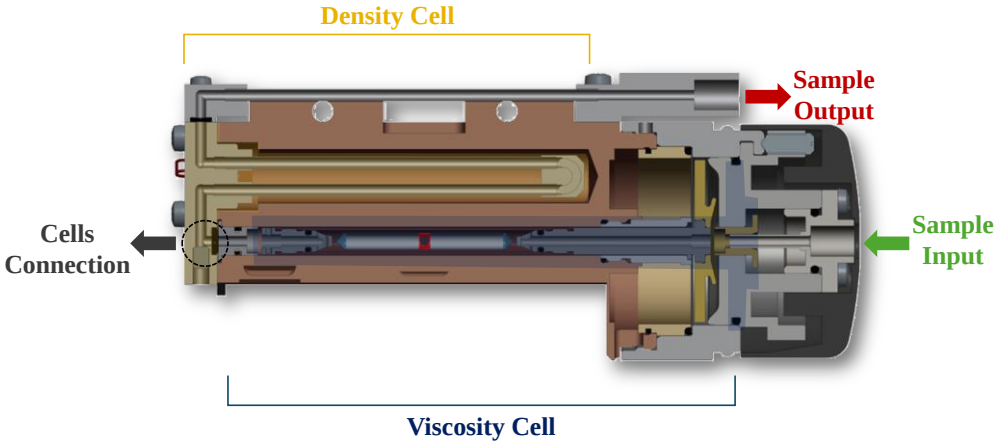



**Fig. 2.27.** Schematic representation of the density and viscosity cells inside the Anton Paar SVM 3001 apparatus. Adapted from Anton Paar GmbH [6].

The vibrating U-tube is incorporated into the apparatus and cannot be removed. On the other hand, the viscosity cell is easily removed and unassembled, facilitating the cleaning process. The viscosity cell is composed of four individual parts: Hastelloy® sample tube, titanium rotor, short tube PEEK bearing, and long tube PEEK bearing with copper drive disc. The bearing threads have KALREZ® (FFKM) O-rings to seal the cell. Images of the fully assembled cell and the individual parts are presented in Figure 2.28.

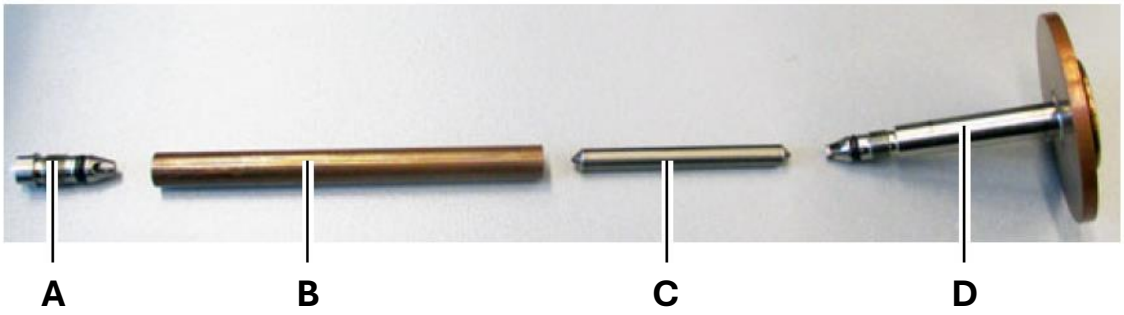



**Fig. 2.28.** Images of the viscosity cell of the Anton Paar SVM 3001 apparatus. **A:** Short tube PEEK bearing, B: stainless steel sample tube; **C:** titanium rotor; **D:** Long tube PEEK bearing.

After an experiment, the liquid is pushed out of the system first using the sample syringe and then the apparatus' pump mechanism. Both measuring cells are then cleaned by injecting an adequate solvent (usually ethanol for ionic liquids and toluene for the oil calibrants). The viscosity cell is then removed from the apparatus and is carefully cleaned on the exterior. After placing the cleaned viscosity cell on the apparatus, the measuring line is dried with dry nitrogen gas. The SVM 3001 has a cleaning check system based

on the measurement of the air density. This feature is used to check if the measuring cells are properly clean and dry.

The SVM 3001 viscometer-densimeter was calibrated using four Anton Paar standard calibration samples, APS3, APN7.5, APN26, and APN415. The calibration was performed at 253, 273, 293, 298, 313, 323, 333, 353, and 373 K (except APN415, where the two lowest temperatures were excluded). The deviations of the experimental results to the density and viscosity values recommended by the brand are presented in Fig. 2.29 and Fig. 2.30, respectively.

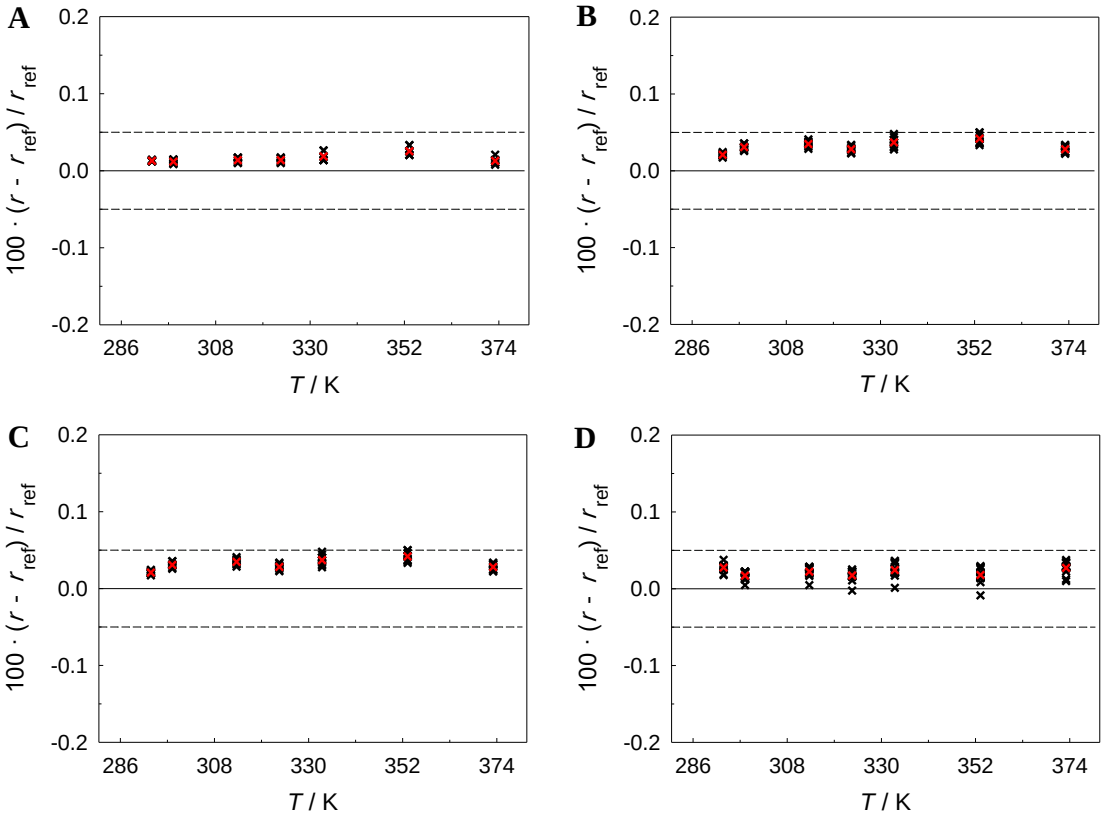



**Figure 2.29.** Deviation of the experimental results to the density values recommended by Anton Paar. **A:** APS3; **B:** APN7.5; **C:** APN26; **D:** APN415. ✖ Experimental results; ✖ Average values.

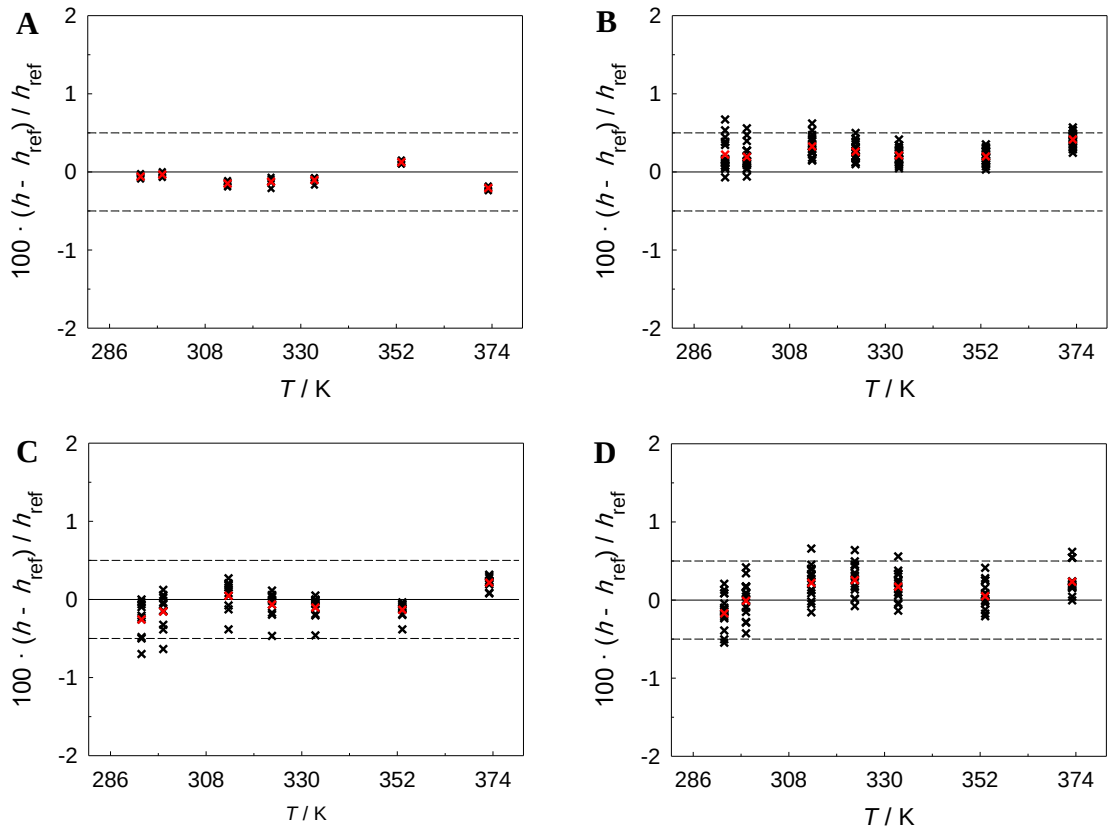



**Figure 2.30.** Deviation of the experimental results to the viscosity values recommended by Anton Paar. **A:** APS3; **B:** APN7.5; **C:** APN26; **D:** APN415. ✖ Experimental results; ✖ Average values.

The density results were found to lie within ± 0.05% and the viscosity results within ± 0.5% compared to the reference value. Before the measurements of the studied ionic liquids, the consistency of the apparatus calibration was evaluated by measuring the density and viscosity of the reference ionic liquid [$^1C_6{}^3C_1$im][$NTf_2$]. The deviation of the available density and viscosity literature data to the experimental results are presented in Fig. 2.31 and Fig. 2.32.

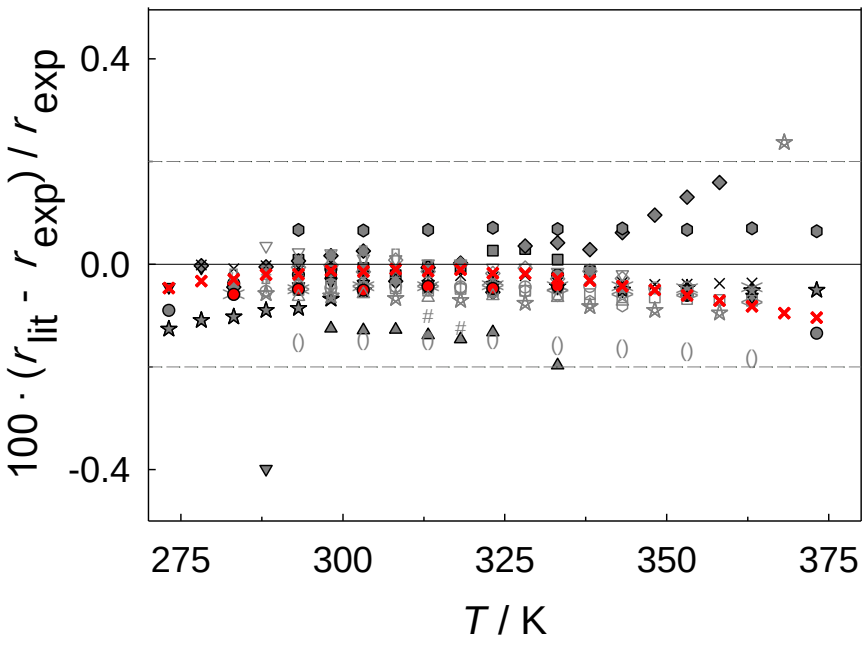



**Figure 2.31.** Deviation of the available density literature data to the experimental results of [$^1C_6{}^3C_1$im][$NTf_2$]. ●[92], ■ [93], ▲ [94], ▼ [95], ◆ [96], ⬢ [97], ★ [14], ✖[25], | [98], ○[99], □ [100], △[101], ▽[102], ◇[103], ⬡ [104], ☆ [105], >< [106], # [107], () [108], <> [109], [][110], ● [111] (IUPAC), ✖ [112] (NIST).

The experimental results are in good agreement with most of the literature data. (< ± 0.2%).

The uncertainty associated with the experimental results of density was attributed based on Eq. (2.90):

$$u_\rho = \sqrt{u_s{}^2 + u_m{}^2} \qquad (2.90)$$

$\boldsymbol{u_\rho}$: uncertainty associated with the experimental density data;

$\boldsymbol{u_s}$: uncertainty associated with the calibration with the standards;

$\boldsymbol{u_m}$: uncertainty associated with the ILs measurements.

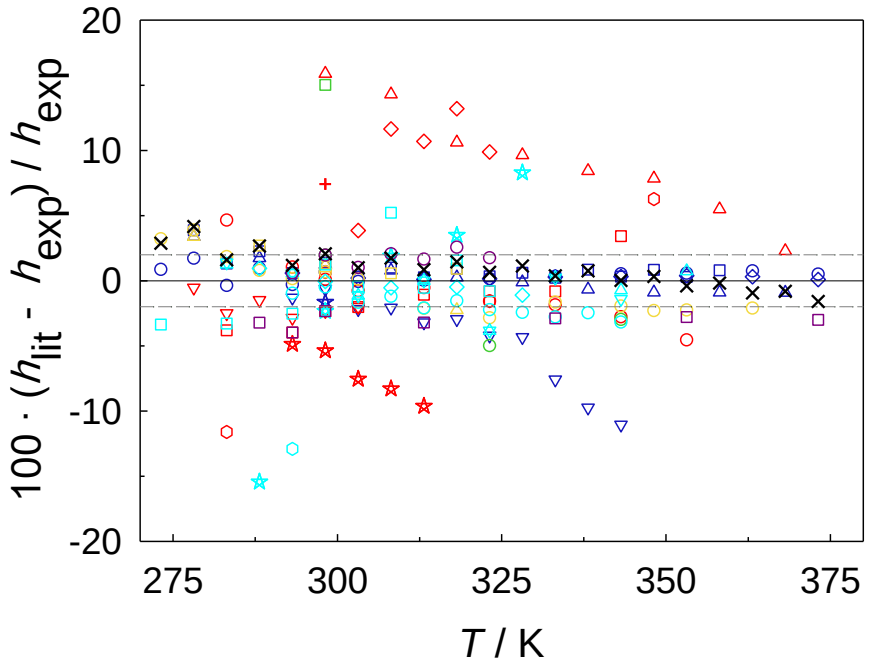



**Figure 2.32.** Deviation of the available viscosity literature data to the experimental results of [$^1C_6{}^3C_1$im][$NTf_2$]. Concentric cylinders: ○ [14], □ [113], △ [25], ▽ [114], ◇ [115], ☆ [116]; Cone and plate: ○ [117], □ [118], △ [111], ▽ [119], ◇ [120], ☆ [121], ⬡ [122], + [123]; Moving Piston: ○ [124], □ [125]; Falling/rolling sphere: ○ [126], □ [127], △ [128], Capillary tube: ○ [104], □ [129], △ [130], ▽ [131], ◇ [132], ☆ **[133],** ⬡ [134]; Vibrating wire: ○ [98], □ [135]; NIST recommended data (data compilation) ×.

Overall, the experimental results are in good agreement with most of the literature data (< ± 2%), particularly the ones measured using the same methodology that was used in this work (concentric cylinders). Some data present significant deviations from the present results. This is likely associated with the utilization of different measuring methods, high water content, as well as flaws in the temperature control, as can be seen by the clear temperature dependence of some data [111, 114, 121].

The uncertainty associated with the experimental results of viscosity was attributed based on Eq. (2.91):

$$u_\eta = \sqrt{u_s{}^2 + u_m{}^2} \qquad (2.91)$$

$\boldsymbol{u_\eta}$: uncertainty associated with the experimental viscosity data;

$\boldsymbol{u_s}$: uncertainty associated with the calibration with the standards;

$\boldsymbol{u_m}$: uncertainty associated with the ILs measurements;

### 2.6.2. Electrical Conductivity Measurements

The electrical conductivity measurements were performed using an apparatus designed and developed in the laboratory during this thesis. The measuring system was named ILDEM (Ionic Liquid Dynamics and Electrical Mobility). The applied measuring approach is an AC complex impedance methodology. The core of the system is a commercial high-precision LCR meter Keysight E4980AL (20 Hz – 500 kHz, 0.05% basic accuracy). The experimental approach is to measure the resistance and reactance of the ionic liquid sample in a broad frequency range, with the aim of not only determining the electrical conductivity but also gaining insight into the impedance-frequency dependence and other non-conductive processes, such as electrode-electrolyte interfacial behavior.

In this work, two different types of conductivity cells were developed: I) an adapted/customized commercial black platinum conductivity cell from Metrohm (model MTO-6.0908110) and II) a coin-type cell with switchable electrode discs, which was fully designed and developed in our laboratory. The first one is our reference cell, and therefore, the main focus was to obtain very high-precision measurements with *in situ* temperature measurement, degasification by reduced pressure, and atmospheric control with flowing dry $N_2$(g). The drawback of the dip-in cell is that it used a decent amount of IL sample (≈ 7.5 mL). While this typically is not a problem for pure ILs as this is a non-destructive methodology, it becomes a complication when studying IL mixtures where it is usually not possible to recover the pure ionic liquid. Furthermore, a small-volume cell is also useful to measure uncommon ionic liquids where the available amount is usually limited. The coin cell was developed as a solution to this problem. The volume of the measuring cell is ≈ 140 µL, corresponding to approximately a 50x reduction when compared to the dip-in cell. Additionally, this cell is easier to clean as it is completely demountable, and the use of the different electrode materials allows a deeper study of the IL-electrode interfacial behavior. Another advantage of this cell is that due to its lower mass and smaller sample size, the required temperature equilibration time is shorter. On the other hand, the main drawback of the coin cell is that it is harder to remove air bubbles inside the chamber as the measuring site is not visible from the exterior. Additionally, due to the measuring site being a much more confined space when compared to the dip-in cell, it may also be more susceptible to electrical field effects.

For thermal stabilization, the cells are placed inside a specially developed Peltier-controlled air bath thermal chamber designed for the high-precision temperature control of the electrical conductivity cells. The temperature readings are performed using an Agilent 34970A Data Logger (6½ digit). A customized software application package based on the VEE platform (Agilent) was developed for the Data acquisition, measurement automatization, and data analysis. The installation of the measuring system in our laboratory is presented in Fig. 2.33

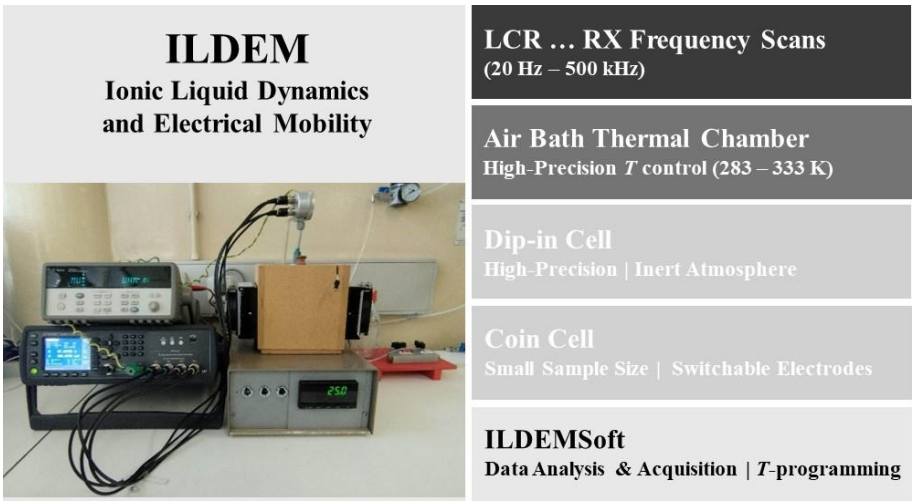



**Figure 2.33.** Ionic Liquid Dynamics and Electrical Mobility (ILDEM) measuring system: in laboratory image and features.

The experimental procedures are slightly different for measurements with the dip-in cell and the coil cell. The cells are initially cleaned with ethanol, Millipore water (resistivity of 18.2 MΩ·cm), and acetone. Then the cells are dried in reduced pressure (1 h) and with flowing dry $N_2$ (g) (1 h) at 333 K. In a typical ILDEM experiment, the ionic liquid samples were dried (to reduce water or other volatile impurity contents) in vacuum ($p$ < 10 Pa) under magnetic agitation at 333 K for at least 72 h prior to the measurements.

Dip-in Cell: For a dip-in cell experiment, the drying process is conducted with the IL sample already in the glass tube that will act as the sample vessel for the conductivity measurements. After attaching the sample vessel to the conductivity cell, the sample is once again placed under a vacuum for degassing and to remove air bubbles if necessary. Once the *in-situ* degassing process is completed, the measuring cell is filled with gaseous dry nitrogen, and the flowing gas is maintained for the entirety of the experiment.

Coin Cell: For a coin cell experiment, the necessary amount of sample is pulled from the Schlenk with a syringe, which is then used to inject the sample into the coin cell. The sample is pushed from the bottom to the top of a cell, and a pull-push motion is often applied to remove air bubbles if necessary. After filling the cell, the sample is once again placed under vacuum for a short period to ensure the absence of air bubbles inside the measuring chamber. Once the *in-situ* degassing process is completed, the measuring cell is filled with gaseous dry nitrogen. The measuring cell is then placed inside the thermostatic chamber, and then the Data Acquisition, Signal Monitoring, and Air Bath Regulation modules are started simultaneously. The experiments are usually done in 5 K steps (either heating or cooling), with a period of thermal stabilization in each step (60 min for the dip-in cell and 30 min for the coin cell). The smaller stabilization period for the coin cell is related to the much smaller sample volume and also with the overall smaller dimensions and total mass of this cell. For each temperature, five measuring scans (200 points logarithmic spaced between the selected frequency range) are conducted in order to evaluate the repeatability and stability of the measurements. At the end of the run, the initial point is repeated to evaluate if the resistance of the sample is maintained. Finally, the raw data is treated and analyzed using the Data Analysis Module. A schematic representation of the complete experimental procedure for an ILDEM experiment is presented in Fig. 2.34.

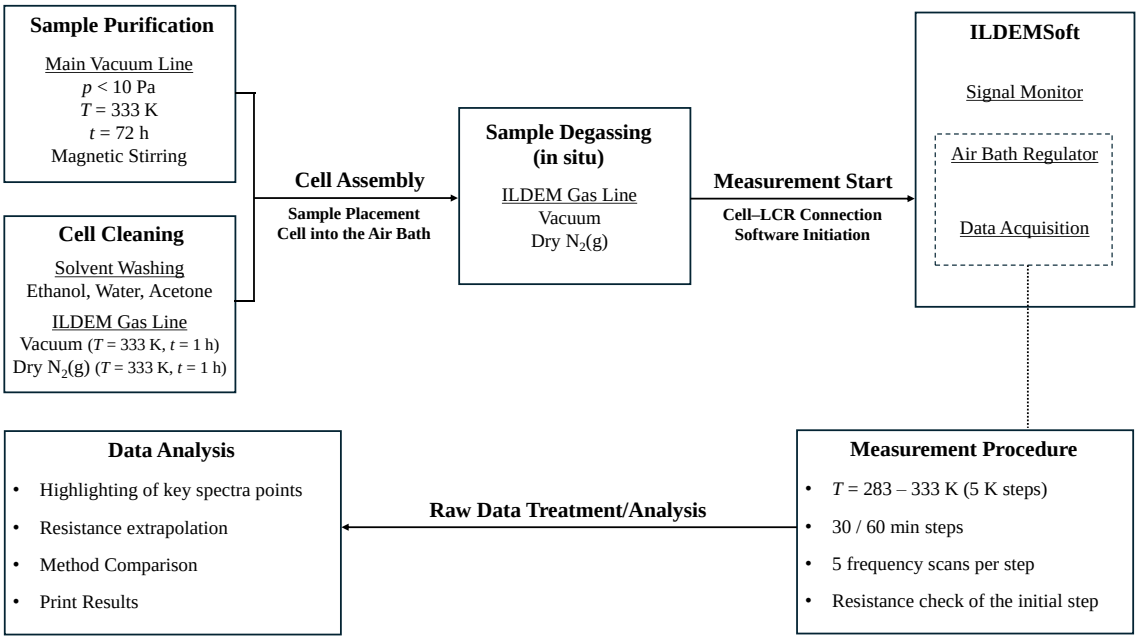



**Figure 2.34.** Schematic representation of the complete experimental procedure of an ILDEM experiment.

The cell constant of both conductivity cells was experimentally determined by measuring the resistance of standard aqueous 0.1000 mol·kg$^{-1}$ potassium chloride solutions as recommended by Barthel *et al.* [136].

The performance and accuracy of the ILDEM system for the measurement of the electrical conductivity were evaluated by measuring the 1-hexyl-3-methylimidazolium bis(trifluoromethylsulfonyl)imide, [$C_6C_1$im][$NTf_2$]. The obtained experimental data was compared with the reference data recommended by NIST [112].

The extensive description of the accuracy and performance tests for both cells is presented in the chapter dedicated to the ILDEM apparatus (Chapter 4).

# References

[1] H. Eren, in: H.E. John G Webster (Ed.) The Measurement, Instrumentation, and Sensors Handbook – Spatial, Mechanical, Thermal, and Radiation Measurement, CRC Press, 2014.

[2] A.P. GmbH, (2024) Density and Density Measurement. https://wiki.anton-paar.com/en/density-and-density-measurement/.

[3] N.V. Plechkova, K.R. Seddon, Chem. Soc. Rev. 37 (2008) 123. https://doi.org/10.1039/B006677J

[4] T. Ghosh, D. Prasad, N. Dutt, K.Y. Rani, Viscosity of Liquids: Theory, Estimation, Experiment, and Data. 2007. https://doi.org/10.1007/978-1-4020-5482-2

[5] M.A.X. Born, H.S. Green, Nature 159 (1947) 251. https://doi.org/10.1038/159251a0

[6] (2024) SVM Kinematic Viscometer Series. https://www.anton-paar.com/corp-en/products/details/svm-series/?sku=105003.

[7] J. Braunstein, G.D. Robbing, J. Chem. Educ. 48 (1971) 52. https://doi.org/10.1021/ed048p52

[8] G. Jones, G.M. Bollinger, Journal of the American Chemical Society 53 (1931) 411. https://doi.org/10.1021/ja01353a005

[9] G. Jones, D.M. Bollinger, Journal of the American Chemical Society 57 (1935) 280. https://doi.org/10.1021/ja01305a016

[10] S. Papović, S. Gadžurić, M. Bešter-Rogač, M. Vraneš, J. Chem. Thermodyn. 102 (2016) 367. https://doi.org/10.1016/j.jct.2016.07.039

[11] J.A. Widegren, E.M. Saurer, K.N. Marsh, J.W. Magee, J. Chem. Thermodyn. 37 (2005) 569. https://doi.org/10.1016/j.jct.2005.04.009

[12] A. Pinkert, K.L. Ang, K.N. Marsh, S. Pang, Phys. Chem. Chem. Phys. 13 (2011) 5136. https://doi.org/10.1039/C0CP02222E

[13] N. Zec, M. Bešter-Rogač, G. Marolt, M. Vraneš, S. Gadžurić, J. Chem. Thermodyn. 101 (2016) 293. https://doi.org/10.1016/j.jct.2016.06.017

[14] J.A. Widegren, J.W. Magee, Journal of Chemical & Engineering Data 52 (2007) 2331. https://doi.org/10.1021/je700329a

[15] E.P. Grishina, L.M. Ramenskaya, M.S. Gruzdev, O.V. Kraeva, Journal of Molecular Liquids 177 (2013) 267. https://doi.org/10.1016/j.molliq.2012.10.023

[16] A. Nazet, S. Sokolov, T. Sonnleitner, S. Friesen, R. Buchner, J. Chem. Eng. Data 62 (2017) 2549. https://doi.org/10.1021/acs.jced.7b00060

[17] J.M. Andanson, M. Traïkia, P. Husson, The Journal of Chemical Thermodynamics 77 (2014) 214. https://doi.org/10.1016/j.jct.2014.01.031

[18] A. Andresova, J. Storch, M. Traïkia, Z. Wagner, M. Bendova, P. Husson, Fluid Phase Equilibria 371 (2014) 41. https://doi.org/10.1016/j.fluid.2014.03.004

[19] A. Stoppa, R. Buchner, G. Hefter, Journal of Molecular Liquids 153 (2010) 46. https://doi.org/10.1016/j.molliq.2009.05.001

[20] A. Stoppa, J. Hunger, R. Buchner, J. Chem. Eng. Data 54 (2009) 472. https://doi.org/10.1021/je800468h

[21] Y. Pan, L.E. Boyd, J.F. Kruplak, W.E. Cleland, J.S. Wilkes, C.L. Hussey, Journal of The Electrochemical Society 158 (2011) F1. https://doi.org/10.1149/1.3505006

[22] F. Santos, C. Nieto de Castro, P. Mota, International Journal of Thermophysics - INT J THERMOPHYS 31 (2010) 1869. https://doi.org/10.1007/s10765-009-0584-4

[23] M.S. Calado, J.C.F. Diogo, J.L. Correia da Mata, F.J.P. Caetano, Z.P. Visak, J.M.N.A. Fareleira, Int. J. Thermophys. 34 (2013) 1265. https://doi.org/10.1007/s10765-013-1491-2

[24] A. Stoppa, O. Zech, W. Kunz, R. Buchner, J. Chem. Eng. Data 55 (2010) 1768. https://doi.org/10.1021/je900789j

[25] A. Nazet, S. Sokolov, T. Sonnleitner, T. Makino, M. Kanakubo, R. Buchner, J. Chem. Eng. Data 60 (2015) 2400. https://doi.org/10.1021/acs.jced.5b00285

[26] O. Zech, A. Stoppa, R. Buchner, W. Kunz, J. Chem. Eng. Data 55 (2010) 1774. https://doi.org/10.1021/je900793r

[27] G. Jones, S.M. Christian, Journal of the American Chemical Society 57 (1935) 272. https://doi.org/10.1021/ja01305a015

[28] T.B. Hoover, The Journal of Physical Chemistry 74 (1970) 2667. https://doi.org/10.1021/j100707a013

[29] T.B. Hoover, The Journal of Physical Chemistry 68 (1964) 876. https://doi.org/10.1021/j100786a030

[30] J.C. Nichol, R.M. Fuoss, Journal of the American Chemical Society 77 (1955) 198. https://doi.org/10.1021/ja01606a075

[31] J.C. Nichol, R.M. Fuoss, The Journal of Physical Chemistry 58 (1954) 696. https://doi.org/10.1021/j150519a005

[32] G.D. Robbins, J. Electrochem. Soc. 116 (1969) 813. https://doi.org/10.1149/1.2412059

[33] G.J. Hills, S. Djordjević, Electrochim. Acta 13 (1968) 1721. https://doi.org/10.1016/0013-4686(68)80156-2

[34] E.R. Buckle, P.E. Tsaoussoglou, Journal of the Chemical Society (Resumed) (1964) 658. https://doi.org/10.1039/jr9640000667

[35] M. Kanakubo, K.R. Harris, N. Tsuchihashi, K. Ibuki, M. Ueno, J. Phys. Chem. B 111 (2007) 2062. https://doi.org/10.1021/jp067328k

[36] M. Kanakubo, K.R. Harris, N. Tsuchihashi, K. Ibuki, M. Ueno, J. Chem. Eng. Data 60 (2015) 1495. https://doi.org/10.1021/acs.jced.5b00071

[37] P. Vallet, J.J. Parajó, F. Sotuela, A. Morcillo, M. Villanueva, O. Cabeza, L.M. Varela, J. Salgado, Chemistry Proceedings 3 (2021) 119. https://doi.org/10.3390/ecsoc-24-08369

[38] S. Vavra, E. Ahlberg, A. Martinelli, Phys. Chem. Chem. Phys. 24 (2022) 24469. https://doi.org/10.1039/D2CP01634F

[39] N. Sánchez-Ramírez, B.D. Assresahegn, D. Bélanger, R.M. Torresi, Journal of Chemical & Engineering Data 62 (2017) 3437. https://doi.org/10.1021/acs.jced.7b00458

[40] D.R. MacFarlane, P. Meakin, J. Sun, N. Amini, M. Forsyth, The Journal of Physical Chemistry B 103 (1999) 4164. https://doi.org/10.1021/jp984145s

[41] J. Sun, M. Forsyth, D.R. MacFarlane, The Journal of Physical Chemistry B 102 (1998) 8858. https://doi.org/10.1021/jp981159p

[42] A. Hofmann, M. Migeot, T. Hanemann, J. Chem. Eng. Data 61 (2016) 114. https://doi.org/10.1021/acs.jced.5b00338

[43] D.R. MacFarlane, M. Forsyth, E.I. Izgorodina, A.P. Abbott, G. Annat, K. Fraser, Phys. Chem. Chem. Phys. 11 (2009) 4962. https://doi.org/10.1039/B900201D

[44] K.-S. Kim, B.-K. Shin, H. Lee, Korean J. Chem. Eng. 21 (2004) 1010. https://doi.org/10.1007/BF02705586

[45] T. Makino, M. Kanakubo, T. Umecky, A. Suzuki, Journal of Chemical & Engineering Data 58 (2013) 370. https://doi.org/10.1021/je3010062

[46] T. Makino, M. Kanakubo, T. Umecky, A. Suzuki, T. Nishida, J. Takano, Journal of Chemical & Engineering Data 57 (2012) 751. https://doi.org/10.1021/je200864h

[47] T. Makino, M. Kanakubo, T. Umecky, A. Suzuki, Fluid Phase Equilibria 357 (2013) 64. https://doi.org/10.1016/j.fluid.2013.01.003

[48] T. Makino, M. Kanakubo, Y. Masuda, H. Mukaiyama, Journal of Solution Chemistry 43 (2014) 1601. https://doi.org/10.1007/s10953-014-0232-x

[49] M. Watanabe, D. Kodama, T. Makino, M. Kanakubo, J. Chem. Eng. Data 61 (2016) 4215. https://doi.org/10.1021/acs.jced.6b00575

[50] K.R. Harris, L.A. Woolf, M. Kanakubo, T. Rüther, J. Chem. Eng. Data 56 (2011) 4672. https://doi.org/10.1021/je2006049

[51] T. Makino, M. Kanakubo, T. Matsuki, E. Kamio, H. Takaba, H. Matsuyama, Fluid Phase Equilibria 420 (2016) 89. https://doi.org/10.1016/j.fluid.2016.02.013

[52] K.J. Laidler, J. Chem. Educ. 61 (1984) 494. https://doi.org/10.1021/ed061p494

[53] S. Arrhenius, Z. Phys. Chem. 4U (1889) 96. https://doi.org/doi:10.1515/zpch-1889-0408

[54] W.T. Laughlin, D.R. Uhlmann, The Journal of Physical Chemistry 76 (1972) 2317. https://doi.org/10.1021/j100660a023

[55] C.A. Angell, J. Non-Cryst. Solids 131-133 (1991) 13. https://doi.org/10.1016/0022-3093(91)90266-9

[56] R. Böhmer, K.L. Ngai, C.A. Angell, D.J. Plazek, J. Chem. Phys. 99 (1993) 4201. https://doi.org/10.1063/1.466117

[57] C.A. Angell, J. Phys. Chem. Solids 49 (1988) 863. https://doi.org/10.1016/0022-3697(88)90002-9

[58] W. Xu, E.I. Cooper, C.A. Angell, J. Phys. Chem. B 107 (2003) 6170. https://doi.org/10.1021/jp0275894

[59] S. Sastry, Nature 409 (2001) 164. https://doi.org/10.1038/35051524

[60] I.M. Hodge, J. Non-Cryst. Solids 202 (1996) 164. https://doi.org/10.1016/0022-3093(96)00151-2

[61] K.F. Kelton, J. Phys. Condens. Matter 29 (2017) 023002. https://doi.org/10.1088/0953-8984/29/2/023002

[62] G. Adam, J.H. Gibbs, J. Chem. Phys. 43 (1965) 139. https://doi.org/10.1063/1.1696442

[63] G.S. Fulcher, J. Am. Ceram. Soc. 8 (1925) 339. https://doi.org/10.1111/j.1151-2916.1925.tb16731.x

[64] H. Vogel, Phys. Z. 22 (1921) 645.

[65] G. Tammann, W. Hesse, Z. Anorg. Allg. Chem. 156 (1926) 245. https://doi.org/10.1002/zaac.19261560121

[66] L.S. Garca-Coln, L.F. del Castillo, P. Goldstein, Physical Review B 40 (1989) 7040. https://doi.org/10.1103/PhysRevB.40.7040

[67] S.I. Smedley, in: S.I. Smedley (Ed.) The Interpretation of Ionic Conductivity in Liquids, Springer US, Boston, MA, 1980, p. 101-132. https://doi.org/10.1007/978-1-4684-3818-5_4

[68] M.A.A. Rocha, C.M.S.S. Neves, M.G. Freire, O. Russina, A. Triolo, J.A.P. Coutinho, L.M.N.B.F. Santos, J. Phys. Chem. B 117 (2013) 10889. https://doi.org/10.1021/jp406374a

[69] M.A.A. Rocha, F.M.S. Ribeiro, A.I.M.C.L. Ferreira, J.A.P. Coutinho, L.M.N.B.F. Santos, J. Mol. Liq. 188 (2013) 196. https://doi.org/10.1016/j.molliq.2013.09.031

[70] P.G. Debenedetti, F.H. Stillinger, Nature 410 (2001) 259. https://doi.org/10.1038/35065704

[71] J. Leys, R.N. Rajesh, P.C. Menon, C. Glorieux, S. Longuemart, P. Nockemann, M. Pellens, K. Binnemans, J. Chem. Phys. 133 (2010). https://doi.org/10.1063/1.3455892

[72] W. Kauzmann, Chem. Rev. 43 (1948) 219. https://doi.org/10.1021/cr60135a002

[73] R.J. Speedy, Biophys. Chem. 105 (2003) 411. https://doi.org/10.1016/S0301-4622(03)00105-4

[74] P.K. Gupta, J.C. Mauro, J. Chem. Phys. 130 (2009). https://doi.org/10.1063/1.3077168

[75] J.C. Mauro, P.K. Gupta, R.J. Loucks, J. Chem. Phys. 130 (2009). https://doi.org/10.1063/1.3152432

[76] J.C. Phillips, M.F. Thorpe, Solid State Commun. 53 (1985) 699. https://doi.org/10.1016/0038-1098(85)90381-3

[77] M.F. Thorpe, J. Non-Cryst. Solids 182 (1995) 135. https://doi.org/10.1016/0022-3093(94)00545-1

[78] H. He, M.F. Thorpe, Phys. Rev. Lett. 54 (1985) 2107. https://doi.org/10.1103/PhysRevLett.54.2107

[79] I. Avramov, A. Milchev, J. Non-Cryst. Solids 104 (1988) 253. https://doi.org/10.1016/0022-3093(88)90396-1

[80] M.P. Longinotti, J.A. Trejo González, H.R. Corti, Cryobiology 69 (2014) 84. https://doi.org/10.1016/j.cryobiol.2014.05.008

[81] T.A. Litovitz, J. Chem. Phys. 20 (1952) 1088. https://doi.org/10.1063/1.1700671

[82] H. Ning, M. Hou, Q. Mei, Y. Liu, D. Yang, B. Han, Science China Chemistry 55 (2012) 1509. https://doi.org/10.1007/s11426-012-4655-1

[83] S.A. Pandit, M.A. Rather, S.A. Bhat, G.M. Rather, M.A. Bhat, J. Solution Chem. 45 (2016) 1641. https://doi.org/10.1007/s10953-016-0514-6

[84] K. Ueno, H. Tokuda, M. Watanabe, Phys. Chem. Chem. Phys. 12 (2010) 1649. https://doi.org/10.1039/B921462N

[85] C.A. Angell, Proceedings of the National Academy of Sciences 92 (1995) 6675. https://doi.org/10.1073/pnas.92.15.6675

[86] H. Tokuda, S. Tsuzuki, M.A.B.H. Susan, K. Hayamizu, M. Watanabe, J. Phys. Chem. B 110 (2006) 19593. https://doi.org/10.1021/jp064159v

[87] O. Nordness, J.F. Brennecke, Chem. Rev. 120 (2020) 12873. https://doi.org/10.1021/acs.chemrev.0c00373

[88] C. Schreiner, S. Zugmann, R. Hartl, H.J. Gores, J. Chem. Eng. Data 55 (2010) 1784. https://doi.org/10.1021/je900878j

[89] K.R. Harris, J. Phys. Chem. B 120 (2016) 12135. https://doi.org/10.1021/acs.jpcb.6b08381

[90] K.R. Harris, J. Phys. Chem. B 123 (2019) 7014. https://doi.org/10.1021/acs.jpcb.9b04443

[91] K.R. Harris, M. Kanakubo, J. Phys. Chem. B 120 (2016) 12937. https://doi.org/10.1021/acs.jpcb.6b10341

[92] J. Safarov, R. Hamidova, S. Zepik, H. Schmidt, I. Kul, A. Shahverdiyev, E. Hassel, J. Mol. Liq. 187 (2013) 137. https://doi.org/10.1016/j.molliq.2013.05.032

[93] J.M.S.S. Esperança, H.J.R. Guedes, J.N.C. Lopes, L.P.N. Rebelo, J. Chem. Eng. Data 53 (2008) 867. https://doi.org/10.1021/je700628w

[94] R. Gomes de Azevedo, J.M.S.S. Esperança, J. Szydlowski, Z.P. Visak, P.F. Pires, H.J.R. Guedes, L.P.N. Rebelo, J. Chem. Thermodyn. 37 (2005) 888. https://doi.org/10.1016/j.jct.2005.04.018

[95] M. Kanakubo, K.R. Harris, J. Chem. Eng. Data 60 (2015) 1408. https://doi.org/10.1021/je501118w

[96] M. Součková, J. Klomfar, J. Pátek, J. Chem. Thermodyn. 77 (2014) 31. https://doi.org/10.1016/j.jct.2014.04.017

[97] M. Tariq, A.P. Serro, J.L. Mata, B. Saramago, J.M.S.S. Esperança, J.N. Canongia Lopes, L.P.N. Rebelo, Fluid Phase Equilib. 294 (2010) 131. https://doi.org/10.1016/j.fluid.2010.02.020

[98] J.C.F. Diogo, F.J.P. Caetano, J.M.N.A. Fareleira, W.A. Wakeham, Fluid Phase Equilib. 353 (2013) 76. https://doi.org/10.1016/j.fluid.2013.05.012

[99] J.J. Fillion, J.F. Brennecke, J. Chem. Eng. Data 62 (2017) 1884. https://doi.org/10.1021/acs.jced.7b00221

[100] M. Zorębski, E. Zorębski, M. Dzida, J. Skowronek, S. Jężak, P. Goodrich, J. Jacquemin, J. Phys. Chem. B 120 (2016) 3569. https://doi.org/10.1021/acs.jpcb.5b12635

[101] M.G. Montalbán, C.L. Bolívar, F.G. Díaz Baños, G. Víllora, J. Chem. Eng. Data 60 (2015) 1986. https://doi.org/10.1021/je501091q

[102] A. Andresová, M. Bendová, J. Schwarz, Z. Wagner, J. Feder-Kubis, J. Mol. Liq. 242 (2017) 336. https://doi.org/10.1016/j.molliq.2017.07.012

[103] J. Rotrekl, J. Storch, J. Kloužek, P. Vrbka, P. Husson, A. Andresová, M. Bendová, Z. Wagner, Fluid Phase Equilib. 443 (2017) 32. https://doi.org/10.1016/j.fluid.2017.03.021

[104] R.G. Seoane, S. Corderí, E. Gómez, N. Calvar, E.J. González, E.A. Macedo, Á. Domínguez, Industrial & Engineering Chemistry Research 51 (2012) 2492. https://doi.org/10.1021/ie2029255

[105] J. Skowronek, M. Dzida, E. Zorebski, M. Chorążewski, S. Jezak, M. Żarska, M. Zorębski, P. Goodrich, J. Jacquemin, J. Chem. Eng. Data 61 (2016) 3794. https://doi.org/10.1021/acs.jced.6b00413

[106] C.M. Tenney, M. Massel, J.M. Mayes, M. Sen, J.F. Brennecke, E.J. Maginn, J. Chem. Eng. Data 59 (2014) 391. https://doi.org/10.1021/je400858t

[107] M. Vraneš, S. Papović, S. Rackov, K. Alenezi, S. Gadžurić, A. Tot, B. Pilić, J. Chem. Thermodyn. 139 (2019) 105871. https://doi.org/10.1016/j.jct.2019.07.013

[108] J. Jacquemin, R. Ge, P. Nancarrow, D.W. Rooney, M.F. Costa Gomes, A.A.H. Pádua, C. Hardacre, J. Chem. Eng. Data 53 (2008) 716. https://doi.org/10.1021/je700707y

[109] T. Song, M.J. Lubben, J.F. Brennecke, Fluid Phase Equilib. 504 (2020) 112334. https://doi.org/10.1016/j.fluid.2019.112334

[110] L. Xue, E. Gurung, G. Tamas, Y.P. Koh, M. Shadeck, S.L. Simon, M. Maroncelli, E.L. Quitevis, J. Chem. Eng. Data 61 (2016) 1078. https://doi.org/10.1021/acs.jced.5b00658

[111] K.N. Marsh, J.F. Brennecke, R.D. Chirico, M. Frenkel, A. Heintz, J.W. Magee, C.J. Peters, L.P.N. Rebelo, K.R. Seddon, Pure Appl. Chem. 81 (2009) 781. https://doi.org/doi:10.1351/PAC-REP-08-09-21

[112] X. Paredes, C.S.G.P. Queirós, F.J.V. Santos, A.F. Santos, M.S.C.S. Santos, M.J.V. Lourenço, C.A.N.d. Castro, J. Phys. Chem. Ref. Data 49 (2020) 043101. https://doi.org/10.1063/5.0023160

[113] M. Tariq, P.J. Carvalho, J.A.P. Coutinho, I.M. Marrucho, J.N.C. Lopes, L.P.N. Rebelo, Fluid Phase Equilib. 301 (2011) 22. https://doi.org/10.1016/j.fluid.2010.10.018

[114] A. Aljasmi, A.S. AlJimaz, K.H.A.E. AlKhaldi, M.S. AlTuwaim, J. Chem. Eng. Data 67 (2022) 858. https://doi.org/10.1021/acs.jced.1c00919

[115] M. Iguchi, Y. Hiraga, Y. Sato, T.M. Aida, M. Watanabe, R.L. Smith, Jr., J. Chem. Eng. Data 59 (2014) 709. https://doi.org/10.1021/je4007844

[116] N.M. Yunus, M.I. Abdul Mutalib, Z. Man, M.A. Bustam, T. Murugesan, J. Chem. Thermodyn. 42 (2010) 491. https://doi.org/10.1016/j.jct.2009.11.004

[117] H. Tokuda, K. Hayamizu, K. Ishii, M.A.B.H. Susan, M. Watanabe, J. Phys. Chem. B 109 (2005) 6103. https://doi.org/10.1021/jp044626d

[118] J.M. Crosthwaite, M.J. Muldoon, J.K. Dixon, J.L. Anderson, J.F. Brennecke, J. Chem. Thermodyn. 37 (2005) 559. https://doi.org/10.1016/j.jct.2005.03.013

[119] J.J. Fillion, H. Xia, M.A. Desilva, M. Quiroz-Guzman, J.F. Brennecke, J. Chem. Eng. Data 61 (2016) 2897. https://doi.org/10.1021/acs.jced.6b00269

[120] M.M. Akbar, T. Murugesan, J. Mol. Liq. 169 (2012) 95. https://doi.org/10.1016/j.molliq.2012.02.014

[121] D. Warmińska, I. Cichowska-Kopczyńska, J. Chem. Thermodyn. 171 (2022) 106789. https://doi.org/10.1016/j.jct.2022.106789

[122] A. Ahosseini, L.R. Weatherley, A.M. Scurto, J. Chem. Eng. Data 56 (2011) 3715. https://doi.org/10.1021/je1009224

[123] K. Nakamura, T. Shikata, Chemphyschem 11 (2010) 285. https://doi.org/10.1002/cphc.200900642

[124] A. Ahosseini, A.M. Scurto, Int. J. Thermophys. 29 (2008) 1222. https://doi.org/10.1007/s10765-008-0497-7

[125] G. McHale, C. Hardacre, R. Ge, N. Doy, R.W.K. Allen, J.M. MacInnes, M.R. Bown, M.I. Newton, Anal. Chem. 80 (2008) 5806. https://doi.org/10.1021/ac800490q

[126] K.R. Harris, M. Kanakubo, J. Chem. Eng. Data 66 (2021) 4618. https://doi.org/10.1021/acs.jced.1c00628

[127] A. Haghani, D.R. Saeva, H. Iloukhani, M.M. Hoffmann, J. Chem. Eng. Data 60 (2015) 3272. https://doi.org/10.1021/acs.jced.5b00503

[128] R. Salinas, J. Pla-Franco, E. Lladosa, J.B. Montón, J. Chem. Eng. Data 60 (2015) 525. https://doi.org/10.1021/je500594z

[129] S. Papović, M. Bešter-Rogač, M. Vraneš, S. Gadžurić, J. Chem. Thermodyn. 99 (2016) 1. https://doi.org/10.1016/j.jct.2016.03.034

[130] Y. Sun, X. Wang, Q. Wei, X. Wang, J. Chem. Eng. Data 67 (2022) 3557. https://doi.org/10.1021/acs.jced.2c00363

[131] Y. Zhang, X. Wang, J. Yin, J. Chem. Thermodyn. 141 (2020) 105970. https://doi.org/10.1016/j.jct.2019.105970

[132] M.S. Calado, A.S.H. Branco, J.C.F. Diogo, J.M.N.A. Fareleira, Z.P. Visak, J. Chem. Thermodyn. 80 (2015) 79. https://doi.org/10.1016/j.jct.2014.08.018

[133] A. Muhammad, M.I. Abdul Mutalib, C.D. Wilfred, T. Murugesan, A. Shafeeq, J. Chem. Thermodyn. 40 (2008) 1433. https://doi.org/10.1016/j.jct.2008.04.016

[134] B.D. Fitchett, T.N. Knepp, J.C. Conboy, J. Electrochem. Soc. 151 (2004) E219. https://doi.org/10.1149/1.1751197

[135] M.E. Kandil, K.N. Marsh, A.R.H. Goodwin, J. Chem. Eng. Data 52 (2007) 2382. https://doi.org/10.1021/je7003484

[136] J. Barthel, R. Wachter, H.-J. Gores, Temperature Dependence of Conductance of Electrolytes in Nonaqueous Solutions. Springer US, Boston, MA, 1979. https://doi.org/10.1007/978-1-4615-7455-2_1

# Chapter 3

## Materials and Sample Preparation

**3.1.** Ionic Liquids

**3.2.** Purification of Ionic Liquids

**3.3.** Other Materials

**3.4.** Preparation of Potassium Chloride Solutions

**References**

# 3. Materials and Sample Preparation

This section presents the list of compounds used in this work, including the studied ionic liquids and other materials used for calibration and testing purposes. Additionally, the applied methods for sample purification are also described.

## 3.1. Ionic Liquids

In this work, the electrical conductivity and viscosity of several ionic liquids from various cationic and anionic families were studied. The list of the studied ILs with the respective sample specifications and molecular structures are presented in Tables 3.1 and 3.2.

**Table 3.1.** Summary of the ionic liquids studied in this work.

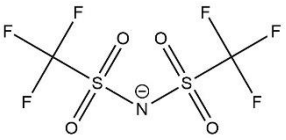
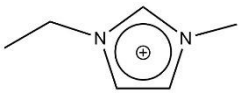
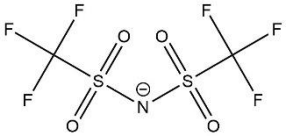
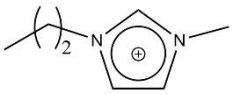
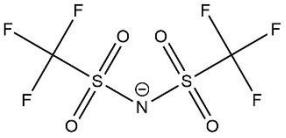
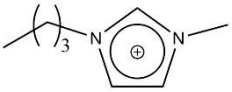
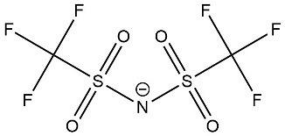
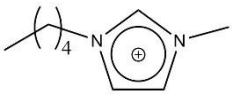
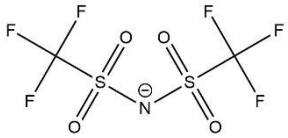
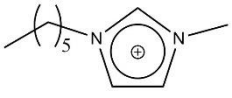
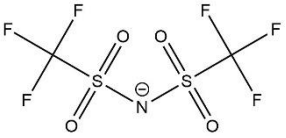
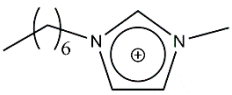
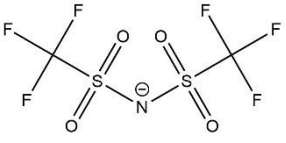
| Ionic Liquid | Abbreviation | CAS | Supplier (Purity) |
|---|---|---|---|
| 1,3-dimethylimidazolium bis(trifluoromethylsulfonyl)imide | $[^1C_1{}^3C_1im][NTf_2]$ | 174899-81-1 | IoLiTec (99%) |
| 1-ethyl-3-methylimidazolium bis(trifluoromethylsulfonyl)imide | $[^1C_2{}^3C_1im][NTf_2]$ | 174899-82-2 | IoLiTec (99.5%) |
| 1-methyl-3-propylimidazolium bis(trifluoromethylsulfonyl)imide | $[^1C_1{}^3C_3im][NTf_2]$ | 216299-72-8 | IoLiTec (99%) |
| 1-butyl-3-methylimidazolium bis(trifluoromethylsulfonyl)imide | $[^1C_4{}^3C_1im][NTf_2]$ | 174899-83-3 | IoLiTec (99.5%) |
| 1-Methyl-3-pentylimidazolium bis(trifluoromethylsulfonyl)imide | $[^1C_1{}^3C_5im][NTf_2]$ | 280779-53-5 | IoLiTec (>99%) |
| 1-Hexyl-3-methylimidazolium bis(trifluoromethylsulfonyl)imide | $[^1C_6{}^3C_1im][NTf_2]$ | 382150-50-7 | IoLiTec (99.5%) |
| 1-Heptyl-3-methylimidazolium bis(trifluoromethylsulfonyl)imide | $[^1C_7{}^3C_1im][NTf_2]$ | 425382-14-5 | IoLiTec (>99%) |
| 1-Methyl-3-octylimidazolium bis(trifluoromethylsulfonyl)imide | $[^1C_1{}^3C_8im][NTf_2]$ | 178631-04-4 | IoLiTec (99%) |
| 1-Methyl-3-nonylimidazolium bis(trifluoromethylsulfonyl)imide | $[^1C_1{}^3C_9im][NTf_2]$ | 433337-21-4 | IoLiTec (>99%) |
| 1-Decyl-3-methylimidazolium bis(trifluoromethylsulfonyl)imide | $[^1C_{10}{}^3C_1im][NTf_2]$ | 433337-23-6 | IoLiTec (>98%) |
| 1-Methyl-3-undecylimidazolium bis(trifluoromethylsulfonyl)imide | $[^1C_1{}^3C_{11}im][NTf_2]$ | ---------- | IoLiTec (97%) |
| 1-Dodecyl-3-methylimidazolium bis(trifluoromethylsulfonyl)imide | $[^1C_{12}{}^3C_1im][NTf_2]$ | 404001-48-5 | IoLiTec (>98%) |
| 1-ethyl-2,3-dimethylimidazolium bis(trifluoromethylsulfonyl)imide | $[^1C_2{}^2C_1{}^3C_1im][NTf_2]$ | 174899-90-2 | IoLiTec (99%) |
| 1,2-dimethyl-3-propylimidazolium bis(trifluoromethylsulfonyl)imide | $[^1C_1{}^2C_1{}^3C_3im][NTf_2]$ | 169051-76-7 | IoLiTec (99%) |

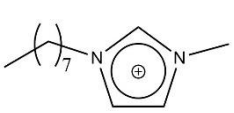
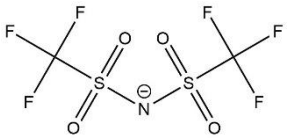
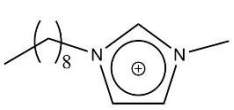
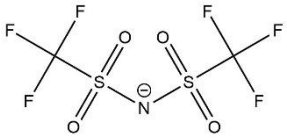
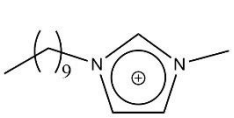
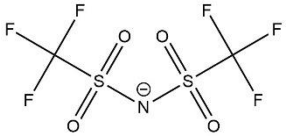
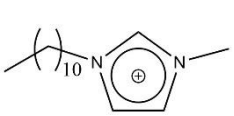
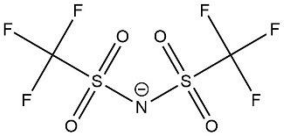
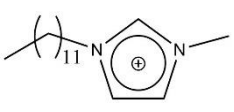
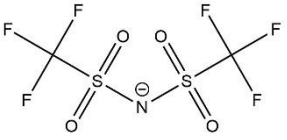
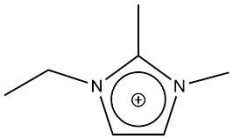
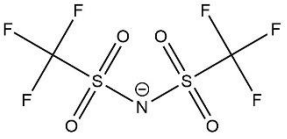
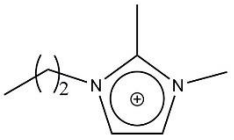
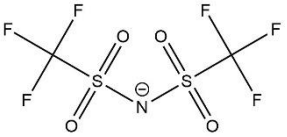
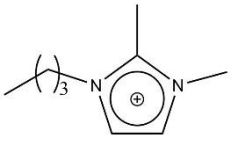
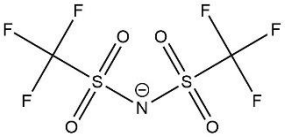
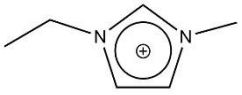
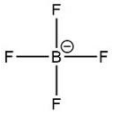
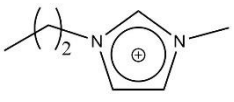
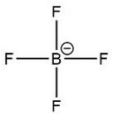
| | | | |
|---|---|---|---|
| 1-butyl-2,3-dimethylimidazolium bis(trifluoromethylsulfonyl)imide | $[^1C_4{}^2C_1{}^3C_1im][NTf_2]$ | 350493-08-2 | IoLiTec (99%) |
| 1-Ethyl-3-methylimidazolium tetrafluoroborate | $[^1C_2{}^3C_1im][BF_4]$ | 143314-16-3 | IoLiTec (99%) |
| 1-Methyl-3-propylimidazolium tetrafluoroborate | $[^1C_1{}^3C_3im][BF_4]$ | 244193-48-4 | IoLiTec (>98%) |
| 1-Butyl-3-methylimidazolium tetrafluoroborate | $[^1C_4{}^3C_1im][BF_4]$ | 174501-65-6 | IoLiTec (99%) |
| 1-Methyl-3-pentylimidazolium tetrafluoroborate | $[^1C_1{}^3C_5im][BF_4]$ | 244193-49-5 | IoLiTec (>99%) |
| 1-Hexyl-3-methylimidazolium tetrafluoroborate | $[^1C_6{}^3C_1im][BF_4]$ | 244193-50-8 | IoLiTec (99%) |
| 1-Heptyl-3-methylimidazolium tetrafluoroborate | $[^1C_7{}^3C_1im][BF_4]$ | 244193-51-9 | IoLiTec (>99%) |
| 1-Methyl-3-octylimidazolium tetrafluoroborate | $[^1C_1{}^3C_8im][BF_4]$ | 244193-52-0 | IoLiTec (99%) |
| 1-Methyl-3-nonylimidazolium tetrafluoroborate | $[^1C_1{}^3C_9im][BF_4]$ | 244193-55-3 | IoLiTec (>99%) |
| 1-Decyl-3-methylimidazolium tetrafluoroborate | $[^1C_{10}{}^3C_1im][BF_4]$ | 244193-56-4 | IoLiTec (>98%) |
| 1-Dodecyl-3 methylimidazolium tetrafluoroborate | $[^1C_{12}{}^3C_1im][BF_4]$ | 244193-59-7 | IoLiTec (>98%) |
| 1-Methyl-3-propylimidazolium hexafluorophosphate | $[^1C_1{}^3C_3im][PF_6]$ | 216300-12-8 | IoLiTec (99%) |
| 1-Butyl-3-methylimidazolium hexafluorophosphate | $[^1C_4{}^3C_1im][PF_6]$ | 174501-64-5 | IoLiTec (99.5%) |
| 1-Methyl-3-pentylimidazolium hexafluorophosphate | $[^1C_1{}^3C_5im][PF_6]$ | 280779-52-4 | IoLiTec (>99%) |
| 1-Hexyl-3-methylimidazolium hexafluorophosphate | $[^1C_6{}^3C_1im][PF_6]$ | 304680-35-1 | IoLiTec (99%) |
| 1-Heptyl-3-methylimidazolium hexafluorophosphate | $[^1C_7{}^3C_1im][PF_6]$ | 357915-04-9 | IoLiTec (>99%) |
| 1-Methyl-3-octylimidazolium hexafluorophosphate | $[^1C_1{}^3C_8im][PF_6]$ | 304680-36-2 | IoLiTec (99%) |
| 1-Methyl-3-nonylimidazolium hexafluorophosphate | $[^1C_1{}^3C_9im][PF_6]$ | 343952-29-4 | IoLiTec (>99%) |
| 1-Decyl-3-methylimidazolium hexafluorophosphate | $[^1C_{10}{}^3C_1im][PF_6]$ | 362043-46-7 | IoLiTec (>98%) |
| 1-Ethyl-3-methylimidazolium trifluoromethanesulfonate | $[^1C_2{}^3C_1im][OTf]$ | 145022-44-2 | IoLiTec (99%) |
| 1-Butyl-3-methylimidazolium trifluoromethanesulfonate | $[^1C_4{}^3C_1im][OTf]$ | 174899-66-2 | IoLiTec (99%) |
| 1-Hexyl-3-methylimidazolium trifluoromethanesulfonate | $[^1C_6{}^3C_1im][OTf]$ | 460345-16-8 | IoLiTec (99%) |
| 1-Octyl-3-methylimidazolium trifluoromethanesulfonate | $[^1C_8{}^3C_1im][OTf]$ | 900797-94-6 | IoLiTec (99%) |
| 1-Decyl-3-methylimidazolium trifluoromethanesulfonate | $[^1C_{10}{}^3C_1im][OTf]$ | 412009-62-2 | IoLiTec (99%) |
| 1-Dodecyl-3-methylimidazolium trifluoromethanesulfonate | $[^1C_{12}{}^3C_1im][OTf]$ | 404001-52-1 | IoLiTec (99%) |

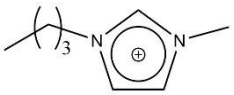
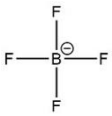
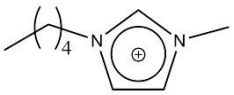
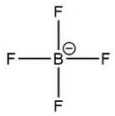
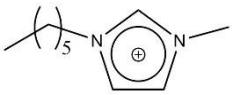
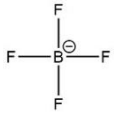
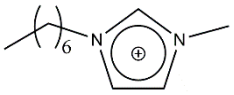
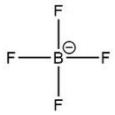
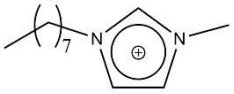
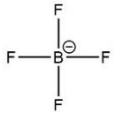
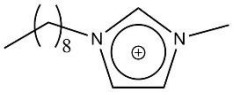
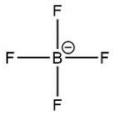
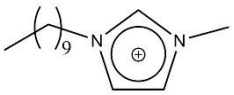
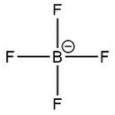
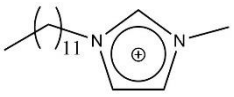
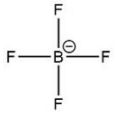
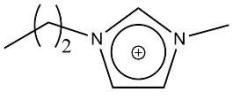
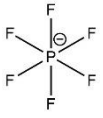
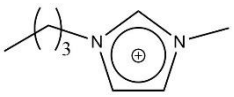
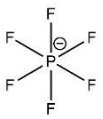
| | | | |
|---|---|---|---|
| 1-Ethyl-3-methylimidazolium tris(pentafluoroethyl)trifluorophosphate | $[^1C_2{}^3C_1im][FAP]$ | 377739-43-0 | Merck ( ≥99%) |
| 1-Butyl-3-methylimidazolium tris(pentafluoroethyl)trifluorophosphate | $[^1C_4{}^3C_1im][FAP]$ | 917762-91-5 | Merck (>99%) |
| 1-Hexyl-3-methylimidazolium tris(pentafluoroethyl)trifluorophosphate | $[^1C_6{}^3C_1im][FAP]$ | 713512-19-7 | Merck (>99%) |
| 1-Ethyl-3-methylimidazolium bis(fluorosulfonyl)imide | $[^1C_2{}^3C_1im][FSI]$ | 235789-75-0 | IoLiTec (>98%) |
| 1-Butyl-3-methylimidazolium bis(fluorosulfonyl)imide | $[^1C_4{}^3C_1im][FSI]$ | 1235234-58-8 | IoLiTec (>98%) |
| 1-Ethyl-3-methylimidazolium bis(pentafluoroethylsulfonyl)imide | $[^1C_2{}^3C_1im][BETI]$ | 216299-76-2 | IoLiTec (>98%) |
| 1-Butyl-3-methylimidazolium bis(pentafluoroethylsulfonyl)imide | $[^1C_4{}^3C_1im][BETI]$ | 254731-29-8 | IoLiTec (>98%) |
| 1-Butyl-3-methylimidazolium acetate | $[^1C_4{}^3C_1im][Ac]$ | 284049-75-8 | Fluka (>95%) |
| 1-Butyl-3-methylimidazolium trifluoroacetate | $[^1C_4{}^3C_1im][TFA]$ | 174899-94-6 | IoLiTec (99%) |
| 1-Butyl-3-methylimidazolium dicyanamide | $[^1C_4{}^3C_1im][DCA]$ | 448245-52-1 | IoLiTec (>98%) |
| 1-Propylpyridinium bis(trifluoromethylsulfonyl)imide | $[^1C_3py][NTf_2]$ | 1104525-90-7 | IoLiTec (99%) |
| 1-Butylpyridinium bis(trifluoromethylsulfonyl)imide | $[^1C_4py][NTf_2]$ | 187863-42-9 | IoLiTec (99%) |
| 1-Pentylpyridinium bis(trifluoromethylsulfonyl)imide | $[^1C_5py][NTf_2]$ | ---------- | IoLiTec (98%) |
| 1-Hexylpyridinium bis(trifluoromethylsulfonyl)imide | $[^1C_6py][NTf_2]$ | ---------- | IoLiTec (98%) |
| 1-Heptylpyridinium bis(trifluoromethylsulfonyl)imide | $[^1C_7py][NTf_2]$ | ---------- | IoLiTec (98%) |
| 1-Octylpyridinium bis(trifluoromethylsulfonyl)imide | $[^1C_8py][NTf_2]$ | ---------- | IoLiTec (98%) |
| 1-Nonylpyridinium bis(trifluoromethylsulfonyl)imide | $[^1C_9py][NTf_2]$ | ---------- | IoLiTec (98%) |
| 1-Propyl-2-methylpyridinium bis(trifluoromethylsulfonyl)imide | $[^1C_3{}^2C_1py][NTf_2]$ | 1456877-99-8 | IoLiTec (99%) |
| 1-Propyl-3-methylpyridinium bis(trifluoromethylsulfonyl)imide | $[^1C_3{}^3C_1py][NTf_2]$ | 817575-06-7 | IoLiTec (99%) |
| 1-Butylpyridinium trifluoromethanesulfonate | $[^1C_4py][OTf]$ | 390423-43-5 | IoLiTec (99%) |
| 1-Methyl-1-propylpyrrolidinium bis(trifluoromethylsulfonyl)imide | $[^1C_3{}^1C_1pyr][NTf_2]$ | 223437-05-6 | IoLiTec (99%) |
| 1-Butyl-1-methylpyrrolidinium bis(trifluoromethylsulfonyl)imide | $[^1C_4{}^1C_1pyr][NTf_2]$ | 223437-11-4 | IoLiTec (99%) |
| 1-Hexyl-1-methylpyrrolidinium bis(trifluoromethylsulfonyl)imide | $[^1C_6{}^1C_1pyr][NTf_2]$ | 380497-19-8 | IoLiTec (99%) |
| 1-Hexyl-1-methylpyrrolidinium bis(trifluoromethylsulfonyl)imide | $[^1C_6{}^1C_1pyr][NTf_2]$ | 380497-19-8 | IoLiTec (99%) |
| 1-Methyl-1-octylpyrrolidinium bis(trifluoromethylsulfonyl)imide | $[^1C_8{}^1C_1pyr][NTf_2]$ | 927021-43-0 | IoLiTec (99%) |

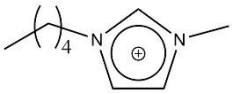
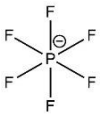
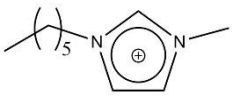
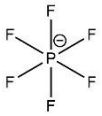
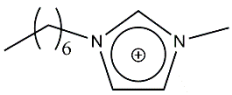
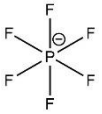
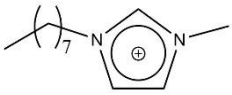
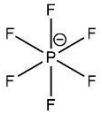
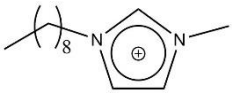
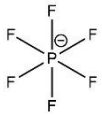
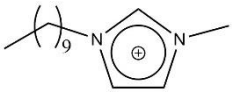
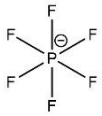
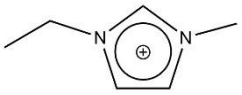
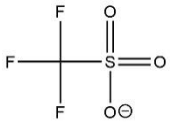
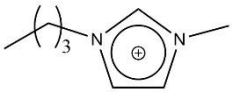
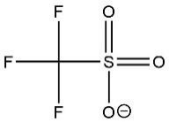
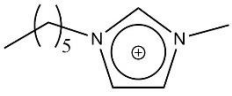
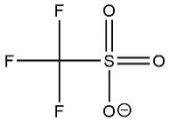
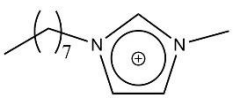
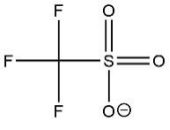
| | | | |
|---|---|---|---|
| 1-Butyl-1-methylpyrrolidinium trifluoromethanesulfonate | [$^1$C$_4$$^1$C$_1$pyr][OTf] | 367522-96-1 | IoLiTec (99%) |
| 1-Butyl-1-methylpyrrolidinium tris(pentafluoroethyl)trifluorophosphate | [$^1$C$_4$$^1$C$_1$pyr][FAP] | 851856-47-8 | Merck (>99%) |

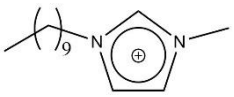
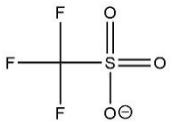
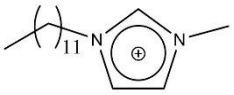
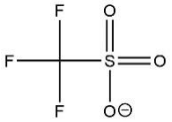
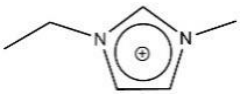
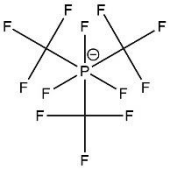
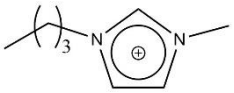
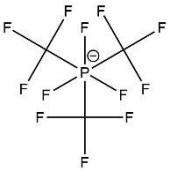
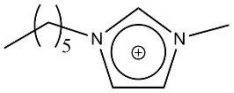
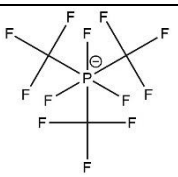
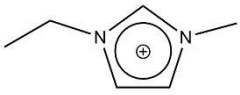
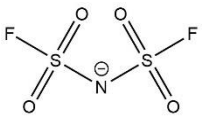
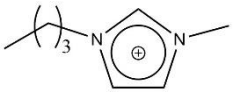
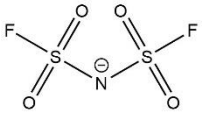
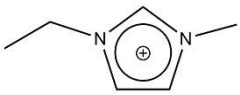
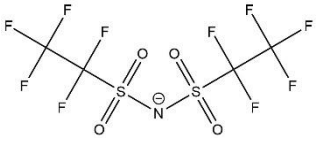
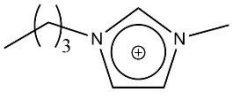
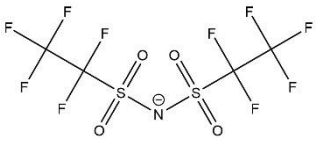
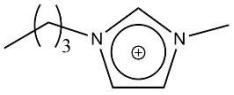
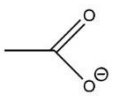
**Table 3.2.** Molecular structures of the ionic liquids studied in this work.

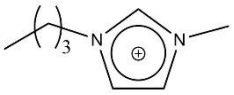
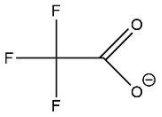
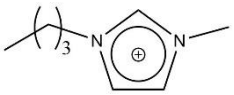
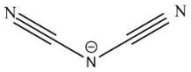
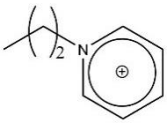
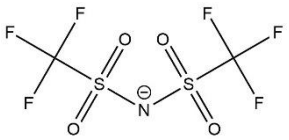
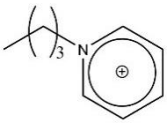
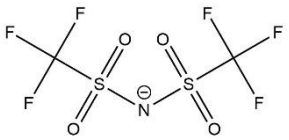
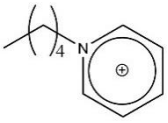
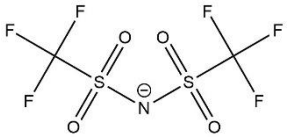
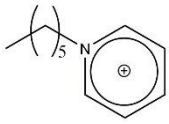
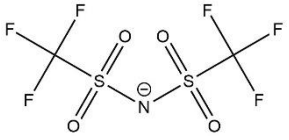
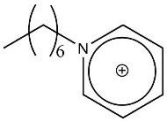
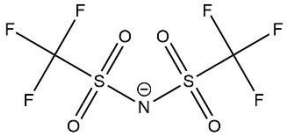
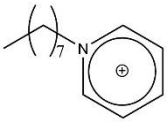
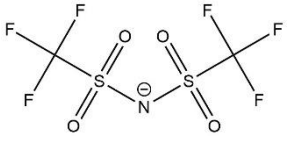
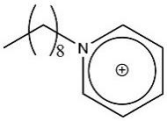
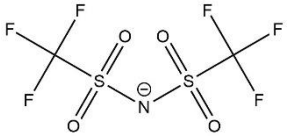
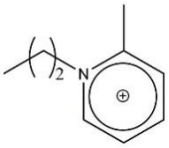
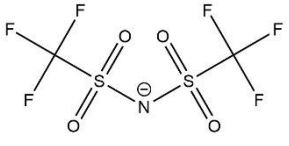
| Abbreviation | $M$ / g·mol$^{-1}$ | Molecular Structure | |
|---|---|---|---|
| | | Cation | Anion |
| [$^1$C$_1$$^3$C$_1$im][NTf$_2$] | 377.29 |  |  |
| [$^1$C$_2$$^3$C$_1$im][NTf$_2$] | 391.32 |  |  |
| [$^1$C$_1$$^3$C$_3$im][NTf$_2$] | 405.34 |  |  |
| [$^1$C$_4$$^3$C$_1$im][NTf$_2$] | 419.37 |  |  |
| [$^1$C$_1$$^3$C$_5$im][NTf$_2$] | 433.40 |  |  |
| [$^1$C$_6$$^3$C$_1$im][NTf$_2$] | 447.42 |  |  |
| [$^1$C$_7$$^3$C$_1$im][NTf$_2$] | 461.45 |  |  |

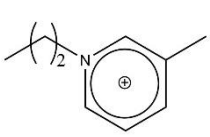
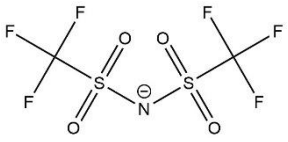
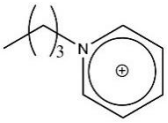
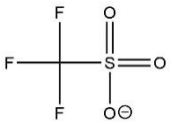
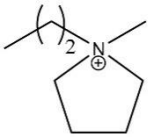
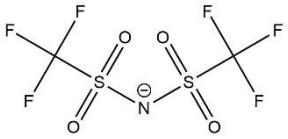
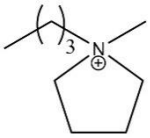
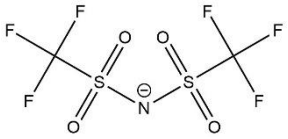
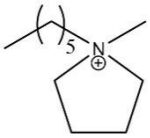
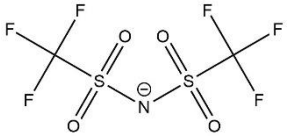
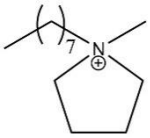
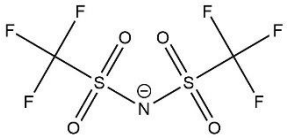
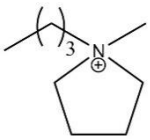
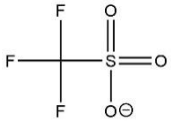
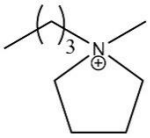
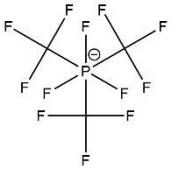
| | | | |
|---|---|---|---|
| $[^1C_1{}^3C_8im][NTf_2]$ | 475.48 |  |  |
| $[^1C_1{}^3C_9im][NTf_2]$ | 489.50 |  |  |
| $[^1C_{10}{}^3C_1im][NTf_2]$ | 503.53 |  |  |
| $[^1C_1{}^3C_{11}im][NTf_2]$ | 517.56 |  |  |
| $[^1C_{12}{}^3C_1im][NTf_2]$ | 531.58 |  |  |
| $[^1C_2{}^2C_1{}^3C_1im][NTf_2]$ | 405.34 |  |  |
| $[^1C_1{}^2C_1{}^3C_3im][NTf_2]$ | 419.37 |  |  |
| $[^1C_4{}^2C_1{}^3C_1im][NTf_2]$ | 433.40 |  |  |
| $[^1C_2{}^3C_1im][BF_4]$ | 197.97 |  |  |
| $[^1C_1{}^3C_3im][BF_4]$ | 212.00 |  |  |

| | | | |
|---|---|---|---|
| $[^1C_4{}^3C_1im][BF_4]$ | 226.02 |  |  |
| $[^1C_1{}^3C_5im][BF_4]$ | 240.05 |  |  |
| $[^1C_6{}^3C_1im][BF_4]$ | 254.08 |  |  |
| $[^1C_7{}^3C_1im][BF_4]$ | 268.10 |  |  |
| $[^1C_1{}^3C_8im][BF_4]$ | 282.13 |  |  |
| $[^1C_1{}^3C_9im][BF_4]$ | 296.16 |  |  |
| $[^1C_{10}{}^3C_1im][BF_4]$ | 310.18 |  |  |
| $[^1C_{12}{}^3C_1im][BF_4]$ | 338.24 |  |  |
| $[^1C_1{}^3C_3im][PF_6]$ | 270.16 |  |  |
| $[^1C_4{}^3C_1im][PF_6]$ | 284.18 |  |  |

| | | | |
|---|---|---|---|
| $[^1C_1{}^3C_5im][PF_6]$ | 298.21 |  |  |
| $[^1C_6{}^3C_1im][PF_6]$ | 312.24 |  |  |
| $[^1C_7{}^3C_1im][PF_6]$ | 326.26 |  |  |
| $[^1C_1{}^3C_8im][PF_6]$ | 340.29 |  |  |
| $[^1C_1{}^3C_9im][PF_6]$ | 354.32 |  |  |
| $[^1C_{10}{}^3C_1im][PF_6]$ | 368.34 |  |  |
| $[^1C_2{}^3C_1im][OTf]$ | 260.24 |  |  |
| $[^1C_4{}^3C_1im][OTf]$ | 288.29 |  |  |
| $[^1C_6{}^3C_1im][OTf]$ | 316.34 |  |  |
| $[^1C_8{}^3C_1im][OTf]$ | 344.40 |  |  |

| | | | |
|---|---|---|---|
| $[^1C_{10}{}^3C_1im][OTf]$ | 372.45 |  |  |
| $[^1C_{12}{}^3C_1im][OTf]$ | 400.50 |  |  |
| $[^1C_2{}^3C_1im][FAP]$ | 556.17 |  |  |
| $[^1C_4{}^3C_1im][FAP]$ | 584.23 |  |  |
| $[^1C_6{}^3C_1im][FAP]$ | 612.28 |  |  |
| $[^1C_2{}^3C_1im][FSI]$ | 291.30 |  |  |
| $[^1C_4{}^3C_1im][FSI]$ | 319.36 |  |  |
| $[^1C_2{}^3C_1im][BETI]$ | 491.33 |  |  |
| $[^1C_4{}^3C_1im][BETI]$ | 519.39 |  |  |
| $[^1C_4{}^3C_1im][Ac]$ | 198.26 |  |  |

| | | | |
|---|---|---|---|
| $[^1C_4{}^3C_1im][TFA]$ | 252.23 |  |  |
| $[^1C_4{}^3C_1im][DCA]$ | 205.26 |  |  |
| $[^1C_3py][NTf_2]$ | 402.34 |  |  |
| $[^1C_4py][NTf_2]$ | 416.37 |  |  |
| $[^1C_5py][NTf_2]$ | 430.39 |  |  |
| $[^1C_6py][NTf_2]$ | 444.42 |  |  |
| $[^1C_7py][NTf_2]$ | 458.45 |  |  |
| $[^1C_8py][NTf_2]$ | 472.47 |  |  |
| $[^1C_9py][NTf_2]$ | 486.50 |  |  |
| $[^1C_3{}^2C_1py][NTf_2]$ | 416.37 |  |  |

| | | | |
|---|---|---|---|
| $[^1C_3{}^3C_1py][NTf_2]$ | 416.37 |  |  |
| $[^1C_4py][OTf]$ | 285.29 |  |  |
| $[^1C_3{}^1C_1pyr][NTf_2]$ | 408.39 |  |  |
| $[^1C_4{}^1C_1pyr][NTf_2]$ | 422.41 |  |  |
| $[^1C_6{}^1C_1pyr][NTf_2]$ | 450.47 |  |  |
| $[^1C_8{}^1C_1pyr][NTf_2]$ | 481.54 |  |  |
| $[^1C_4{}^1C_1pyr][OTf]$ | 291.33 |  |  |
| $[^1C_4{}^1C_1pyr][FAP]$ | 587.27 |  |  |

The molecular masses of the studied ionic liquids were calculated based on the atomic weights published by IUPAC [1].

## 3.2. Purification of Ionic Liquids

Before all measurements, the ionic liquid samples were dried and stored under reduced pressure ($p$ < 10 Pa) at 330 K for at least 72 h in order to minimize the content of water, gases, and other volatile impurities. The drying system consists of a rotatory vacuum pump (Edwards RV5) connected to the main vacuum line, which is attached to multiple outputs. The samples are dried/degassed in customized *Schlenks* to facilitate sample handling and avoid contamination with grease. For thermostatization, the *Schlenks* were placed in machined aluminum blocks (cylinders, diameter = 10.0 cm and height = 10.0 cm) connected to a temperature controller (LAE X5 AC1-JS1RW). To improve the efficiency of the drying/degassing, the aluminum block is placed on a magnetic stirring plate. A schematic representation of the purification system is presented in Fig. 3.1. After the drying process and before the experiments, the water content was evaluated by Karl Fischer coulometric titration using a Metrohm Coulometer (737 KF Coulometer using HYDRANAL™ - Coulomat AG from Riedel-de Haën). Overall, the water content was found to be always lower than 100 ppm.

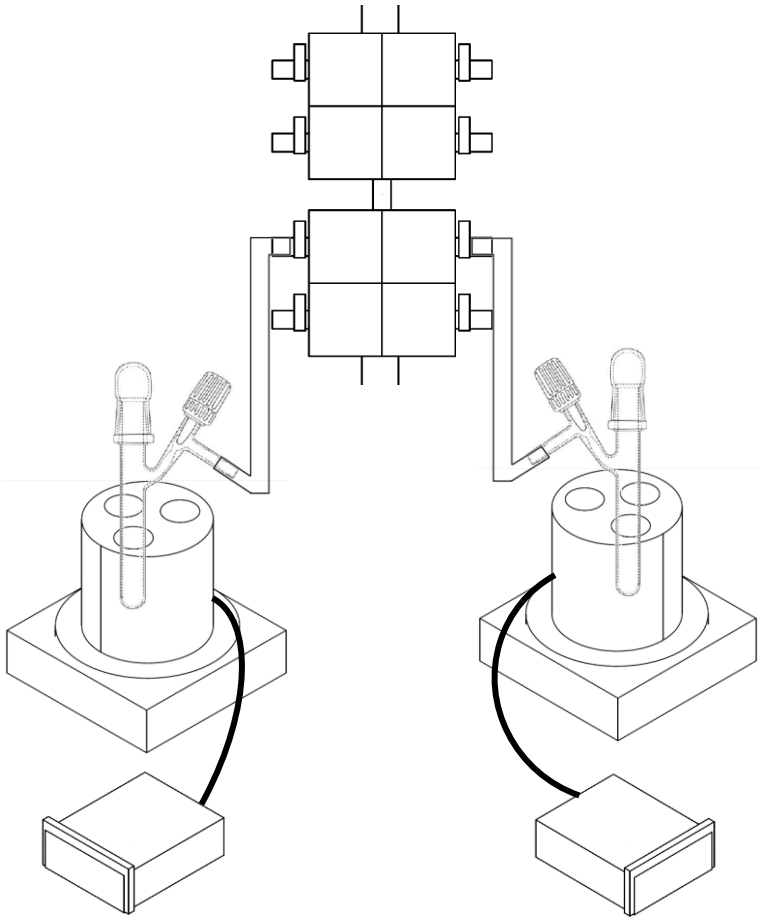


**Figure 3.1** Schematic representation of the drying/degassing system used for the purification of ionic liquids.

## 3.3. Other Materials

In this work, other materials were used, especially for the testing and calibration of the electrical conductivity (ILDEM) and viscosity/density (SVM 3001) measuring apparatus. The list of these materials is presented in Table 3.3.

**Table 3.3.** List of compounds used in the testing and calibration of ILDEM and SVM 3001.

| Compound | Supplier | Reference | Purpose |
|---|---|---|---|
| KCl Suprapur 99.999% | Merck | CAS No. 7447-40-7 | Cell Constant Determination ILDEM |
| APS3 | Anton Paar | Lot No. 4212007 | Testing and Calibration SVM 3001 |
| APN7.5 | Anton Paar | Lot No. 2210704 | Testing and Calibration SVM 3001 |
| APN26 | Anton Paar | Lot No. 1221103 | Testing and Calibration SVM 3001 |
| APN415 | Anton Paar | Lot No. 1210410 | Testing and Calibration SVM 3001 |

### 3.3.1. Preparation of Potassium Chloride Solutions

Aqueous 0.1000 mol·kg$^{-1}$ potassium chloride solutions were prepared to determine experimentally the cell constant of the conductivity cells of the ILDEM measuring system as recommended by Barthel *et al.* [2]. The solutions were prepared with potassium chloride Suprapur® 99.999% from Merck KGaA (CAS-No. 7447-40-7) and Millipore water (resistivity of 18.2 MΩ·cm). Prior to the preparation of the solutions, the potassium chloride was dried on a stove at 473 K for 72 hours. The water was first deionized and then purified using a Millipore Milli-Q® Gradient Water Purification System. Additionally, the ultrapure water was degassed under a vacuum immediately before the preparation of the solutions. For the degassing process, the water was placed in laboratory bottles of 1000 cm$^3$ attached to GL25 DURAN® caps, which were specially modified in the laboratory in order to fit and seal in PE tubing (diameter = 4 mm). The degassing system can be found in Fig. 3.1.

The potassium chloride solutions were gravimetrically prepared using a standard procedure applying the buoyancy correction in the mass measurements (using Mettler Toledo PM11N and AT201 balances). Buoyancy errors are originated by the difference between the densities of the calibration material and the objects that are being weighted. The correction of the effect of buoyancy is given by Eq. 2.1 [3]:

$$m_{\mathrm{V}} = 0.0012 m_{\mathrm{a}} \cdot \left[1 + \left(\frac{1}{\rho_{\mathrm{o}}} - \frac{1}{\rho_{\mathrm{c}}}\right)\right] \qquad (2.1)$$

Where $m_{\mathrm{v}}$ is the mass of the object in vacuum, $m_{\mathrm{a}}$ is the mass of the object in air, $\rho_{\mathrm{o}}$ is the density of the object, and $\rho_{\mathrm{c}}$ is the density of the calibration material.

# References

[1] J. Meija, B. Coplen Tyler, M. Berglund, A. Brand Willi, P. De Bièvre, M. Gröning, E. Holden Norman, J. Irrgeher, D. Loss Robert, T. Walczyk, T. Prohaska, Pure Appl. Chem. 88 (2016) 265.https://doi.org/10.1515/pac-2015-0305

[2] J. Barthel, R. Wachter, H.-J. Gores, in: B.E. Conway, J.O.M. Bockris (Eds.), Modern Aspects of Electrochemistry: No. 13, Springer US, Boston, MA, 1979, p. 1-79.

[3] R. Battino, A.G. Williamson, J. Chem. Educ. 61 (1984) 51.https://doi.org/10.1021/ed061p51

# Chapter 4

## Development of a Impedance Measuring Apparatus

**2.1.** LCR Meter

**2.2.** Cell Design

**2.3.** Vacuum/Gas Line

**2.4.** Air Bath Thermal Chamber

**2.5.** ILDEM Software

**References**

# 4. Ionic Liquid Dynamics and Electrical Mobility Measuring System

This section presents the design and development of a system to measure the electrical conductivity of ionic liquids and fluids. The core of the Ionic Liquid Dynamics and Electrical Mobility (ILDEM) measuring system is a high-precision LCR meter Keysight E4980AL (20 Hz – 500 kHz, 0.05% basic accuracy), which is connected to the conductivity cells in a four-wire configuration. In this work, two different types of conductivity cells were developed: I) an adapted/customized commercial black platinum conductivity cell from Metrohm (model MTO-6.0908110) and II) a coin-type cell with switchable electrode discs, which was fully designed and developed in our laboratory. The measuring system is also composed of a specially designed thermal chamber (air bath) designed for high-precision temperature control of the electrical conductivity cell. A customized software application based on the VEE platform (Agilent) was developed for Data acquisition, measurement automatization, and data analysis. The installation of the measuring system in our laboratory is presented in Fig. 4.1. A schematic representation of the complete ILDEM measuring system is presented in Fig. 4.2



**Figure 4.1.** In laboratory image of the Ionic Liquid Dynamics and Electrical Mobility (ILDEM) measuring system.

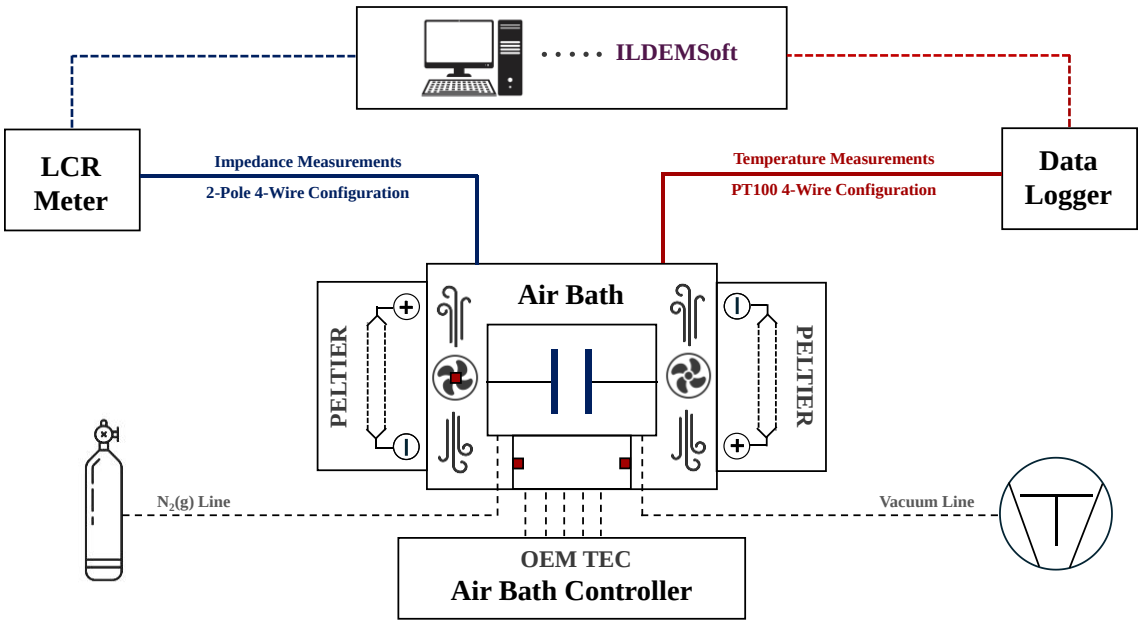



**Figure 4.2.** Schematic representation of the Ionic Liquid Dynamics and Electrical Mobility (ILDEM) measuring system.

## 4.1. LCR Meter

The LCR meter measures the complex impedance vector of the device under test, DUT, and automatically converts it in the desired displayed properties: impedance magnitude ($|Z|$), admittance magnitude ($|Y|$), phase angle ($\theta$), resistance ($R$), reactance ($X$), conductance ($G$), sustenance ($B$), capacitance ($C$), and inductance ($L$). The LCR meter offers diverse measuring systems depending on the type of electric circuit/configuration and measuring objective. For this work, the R-X function was found to be the most appropriate measuring approach.
In order to enhance the quality of the measurement, a 4-wire configuration is applied, as described in Fig. 4.3. In this methodology, the current is driven into the DUT through the outer leads (HC and LC) while the potential is directly measured by the inner terminals (HP and LP). This removes the impact of the voltage drop in the source leads on the measurement of the voltage of the DUT. The impedance of the DUT is determined by the ratio of voltage of the high potential port and current measured at the low current port, respectively, as described in Equation 4.1.

$$Z = \frac{V_{\mathrm{HP}}}{I_{\mathrm{LC}}} \tag{4.1}$$

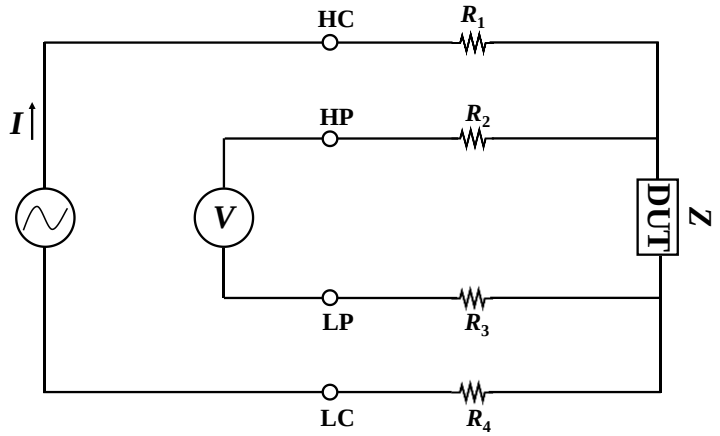



**Figure 4.3.** Schematic representation of the 4-wire configuration for the measurement of the impedance of a DUT.

### 4.1.1. Auto-balance Bridge

The measurement of impedance using an auto-balancing bridge is similar to the simplest case discussed above, where it is based on the measurement of voltage and current using a voltmeter and ammeter, respectively. However, in this case, the ammeter is substituted by an I-V converter feedback loop, where the current passing through it, $I_2$, is equal to the current passing through the DUT, $I$. A schematic representation of the auto-balancing bridge method is presented in Fig. 4.4.

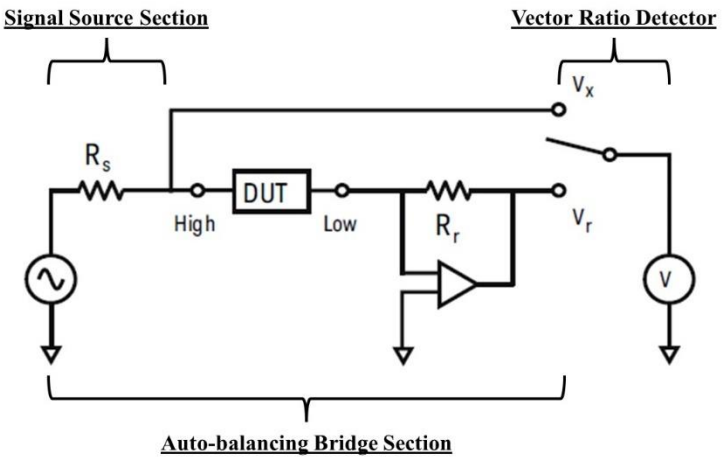



**Figure 4.4.** Schematic representation of the measuring principle of the auto-balance bridge method.

Since $I_x$ and $I_r$ are equal the potential at the low terminal is consequently equal to zero, and thus it becomes a reference point known as a virtual ground. Based on that the output voltage of the I-V converter, $V_r$, is described by Eq. 4.2:

$$V_r = I_r \cdot R_r = I_x \cdot R_r \tag{4.2}$$

Where $R_r$ is the resistor of the I-V converter. The current passing through the DUT is represented by the Equation 4.3:

$$I_x = \frac{V_x}{Z_x} \tag{4.3}$$

By combining Equations 4.2 and 4.3, the impedance of a DUT, $Z_r$, measured using an auto-balancing method is described as Eq. 4.4:

$$Z_x = \frac{V_x}{I_r} = R_r \frac{V_x}{V_r} \tag{4.4}$$

In practical terms, $R_r$ is a constant value intrinsic to the measuring system, known as a range resistor. Therefore, the determination of the impedance of a DUT is based on the measurement of the potential of $V_x$ and $V_r$. Usually, to avoid measuring errors associated with the usage of two different voltmeters, a single voltmeter is alternatively used to measure $V_x$ and $V_r$.

A measuring instrument based on the auto-balancing approach can be thought to be composed of three main sections: signal source section, auto-balancing section, and vector ratio detector section (Fig. 4.4).

Signal source section

As its nomination suggests, the signal source section is the point of generation of the test signal. The signal with the selected frequency and input level is generated on a power source, passes through a resistor, and is then applied to the DUT at the high current terminal.

Auto-balancing section

As referred to previously, the balance condition is established when the current flowing through the DUT is equal to the current flowing through the I-V converter. The key component for maintaining this equality state is a null detector. A null detector is a type of instrument that measures a certain quantity in comparison to its opposition. In this

application, when the null detector indicates an unbalancing of the current, it applies an adjustment to the magnitude and phase of the I-V converter current to reestablish the balancing condition. For instruments that operate at frequencies higher than 100 kHz, other components, such as phase detectors and vector modulators, are needed.

Vector ratio section

This section is responsible for the measurement of $V_x$ and $V_r$ quantities that are then used to calculate the impedance of the DUT as described by Equation 4.5. These voltages are measured as vectors being consisted by a real and an imaginary component (Fig. 4.5). A phase detector is used to determine the real and imaginary component which are then digitally outputted via an A-D converter. The ratio between the voltages across the DUT and the range resistor can be described by Eq. 4.5:

$$\frac{V_x}{V_r} = \frac{a+jb}{c+jd} = \frac{ac+bd}{c^2+d^2} + j\frac{bc-ad}{c^2+d^2} \tag{4.5}$$

Where *a* is the real component of the DUT voltage vector, *b* is the imaginary component of the DUT voltage vector, *c* is the real component of the range resistor voltage vector, and *d* is the imaginary component of the range resistor voltage vector.

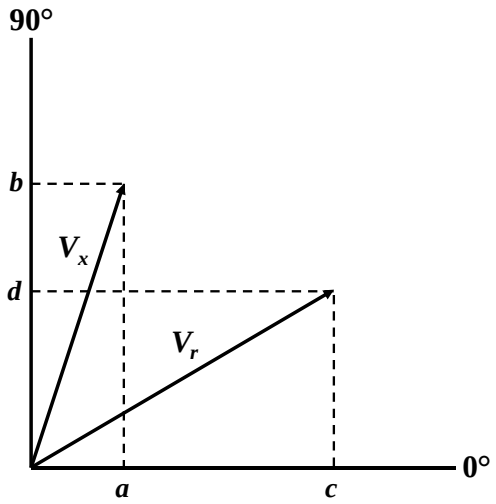



**Figure 4.5.** Representation of the voltage complex quantities measured in the vector ratio section of the auto-balance bridge.

By combining equations 4.4 and 4.5, the impedance of a DUT measuring using an auto-balancing bridge is given by the following equation:

$$Z_x = R_r \left[\frac{ac + bd}{c^2 + d^2} + j\frac{bc - ad}{c^2 + d^2}\right] \quad (4.6)$$

Finally, taking into account the definition of impedance presented at the beginning of this chapter, the real (resistance) and imaginary (reactance) components of the DUT can be described by Eqs. 4.7 and 4.8, respectively.

$$R_x = R_r \left[\frac{ac + bd}{c^2 + d^2}\right] \quad (4.7)$$

$$X_x = R_r \left[j\frac{bc - ad}{c^2 + d^2}\right] \quad (4.8)$$

### 4.1.2. Compensation and Correction

Calibration and compensation are essential to ensure the quality and accuracy of the measurements. The calibration process defines a reference plane where the measurement accuracy is specified. The calibration of the LCR meter used in this work was performed by the manufacturer. This process is based on the measurement of multiple impedance standards (standards with a precisely known impedance) in order to evaluate and quantify measuring errors associated with imperfections of the internal circuit of the instrument. These are known as error terms, and their contributions are compiled in a model used to relate the measured impedance with the real impedance value. These models are frequently described by a linear fractional transformation, known as the Möbius transformation (Eq. 4.9):

$$Z_m = f(Z) = \frac{AZ + B}{CZ + D} \quad (4.9)$$

Where A, B, C, and D are the calibration coefficients and $Z_m$ is the corrected impedance value.

However, the presence of test fixtures/cables between the apparatus and the measuring device leads to the manifestation of parasitic contributions, which affect the quality of the measurements. To minimize the impact of these effects, compensation techniques are used by including compensation algorithms in the firmware of the instrument. In this work, a type of signal correction known as open/short compensation is used. The open/short compensation allows the removal of both residual impedance ($Z_r$) and stray admittance ($Y_s$) contributions of the test fixture. By measuring the open circuit, it is possible to quantify the $Y_s$, while $Z_r$ is evaluated with the shorted circuit. The open compensation consists of measuring the parasitic contributions in parallel to the impedance of the DUT, while the short compensation measures the parasitic contributions in series to the impedance of the DUT. For the open circuit, the parasitic contributions are mainly related to the capacitance of the cables and the sample holder, while in the case of the short circuit, the evaluated contributions are mainly associated with the resistance and inductance of the cables. These contributions are then automatically applied to compensate the measurement value in order to obtain the correct value for the device under measurement. The compensation is mathematically described by Equation 4.10.

$$Z_{\mathrm{DUT}} = \frac{Z_m - Z_r}{1 - (Z_m - Z_r)/Y_s} \tag{4.10}$$

A schematic representation of the open and short corrections on a representative LCR circuit is presented in Fig. 4.6 together with a practical example executed in the laboratory. In this figure, a Tonghui TH26022AS text fixture was used to perform the open/short compensation. This device was used in the initial part of the project to test the LCR meter with standard circuit components, such as resistances, capacitors, and inductors. For the conductivity measurements, the open/short corrections were performed for the real circuits corresponding to the electric installation of each cell, as will be described in further detail in the following sections.

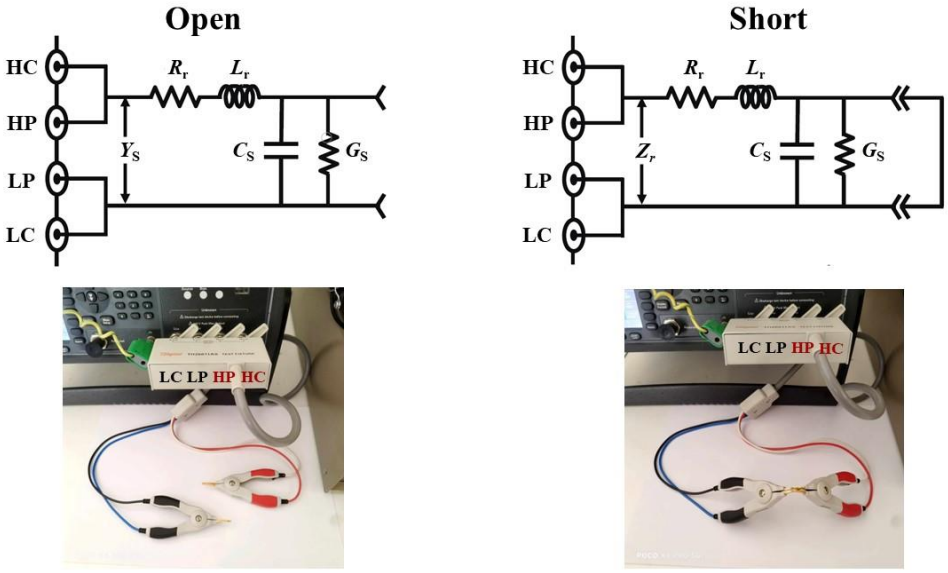



**Figure 4.6.** Schematic representation and in-laboratory images of the open and short compensation on an LCR circuit.

## 4.2. Cell Design

This section will be dedicated to the description of the two developed electrical conductivity cells.

### 4.2.1. Dip-in Cell

This measuring device is an adapted/customized commercial black platinum conductivity cell from Metrohm (model MTO-6.0908110). This is the first cell that was developed during this work, and it is the one that was used for the majority of the conductivity measurements that will be presented in this thesis. The major modifications/adaptations were performed to minimize the size of the ionic liquid sample, fixate the position and immersion level of the electrodes, and allow the *in situ* degassing of the sample. For that, the conductivity cell is installed in a soda-lime glass tube (Ø 19 mm x 70 mm, 7.5 mL of sample) via the adaptation of a customized polyether ether ketone (KETRON PEEK) holder (Fig. 4.7). This part was designed to ensure the vacuum and gastightness of the sample container, and it is composed of three main parts. The bottom part fixes the glass tube, while the top part fixes the position and immersion depth of the conductivity cell on the sample. The connection between the top and bottom parts of the holder and its main body is realized with perfluoroelastomer FFKM O-rings and pressing discs to ensure the sealing of the cell. The middle part acts as the main body

of the holder and is equipped with two PTFE tubes on opposite sides. The input is connected to vacuum and nitrogen lines, allowing the in-situ degassing of the sample and the control of the atmosphere during the measurements. The conductivity cell contains an incorporated Pt100 temperature sensor, which was calibrated using a 100 Ω secondary platinum resistance thermometer, Fluke SPRT 5626. The cell is connected in a four-wire configuration to a Precision LCR meter (20 Hz - 500 kHz), Keysight E4980AL, and an Agilent 34970A Data Logger for the measurement of impedance and temperature, respectively. The accuracy of the temperature readings was found to be ± 0.02 K.

Images of the conductivity cell and the individual parts of the cell holder are presented in Fig. 4.7 together with a detailed schematic representation. Additionally, for a better representation of the assembly process, the exploded view of the dip-in cell is presented in Fig. 4.8.

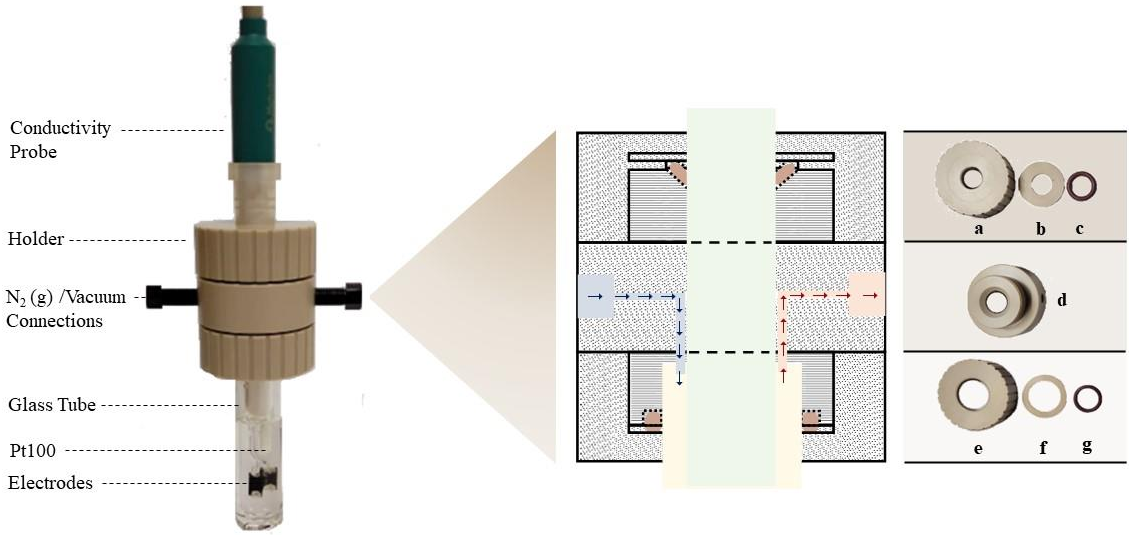



**Figure 4.7.** Images of the conductivity cell with specific detail on a schematic representation of the specially designed PEEK holder. Parts of the Cell Holder: Cross Pattern: PEEK; Line Pattern: PEEK Screw; **Red** and **blue** channels: vacuum and $N_2$(g) lines (blue represents $N_2$(g) input and red represents $N_2$(g) output); **Green**: Metrohm conductivity cell; **Yellow**: glass tube (sample vessel); **Brown**: Kalrez® O-rings; **a** - Top/electrode lock; **b** - Top clamping disk; **c** - Top FFKM O-ring; **d** - Core/main part; **e** - Bottom/ tube lock; **f** - Bottom clamping disk; **g** - Bottom FFKM O-ring.

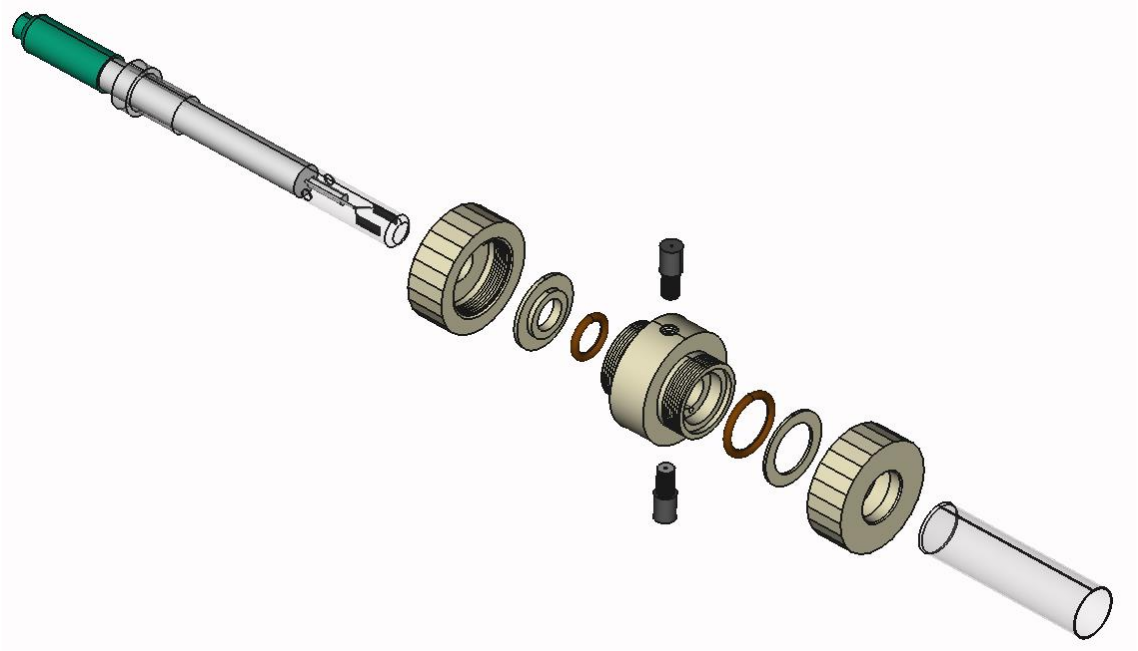


**Figure 4.8.** Exploded view of the dip-in conductivity cell, including the Metrohm conductivity probe, the PEEK holder, the PTFE connections to the vacuum/gas lines, and the glass tube sample vessel.

The detailed dimensions of the customized conductivity cell and the developed holder are presented in Fig. 4.9.

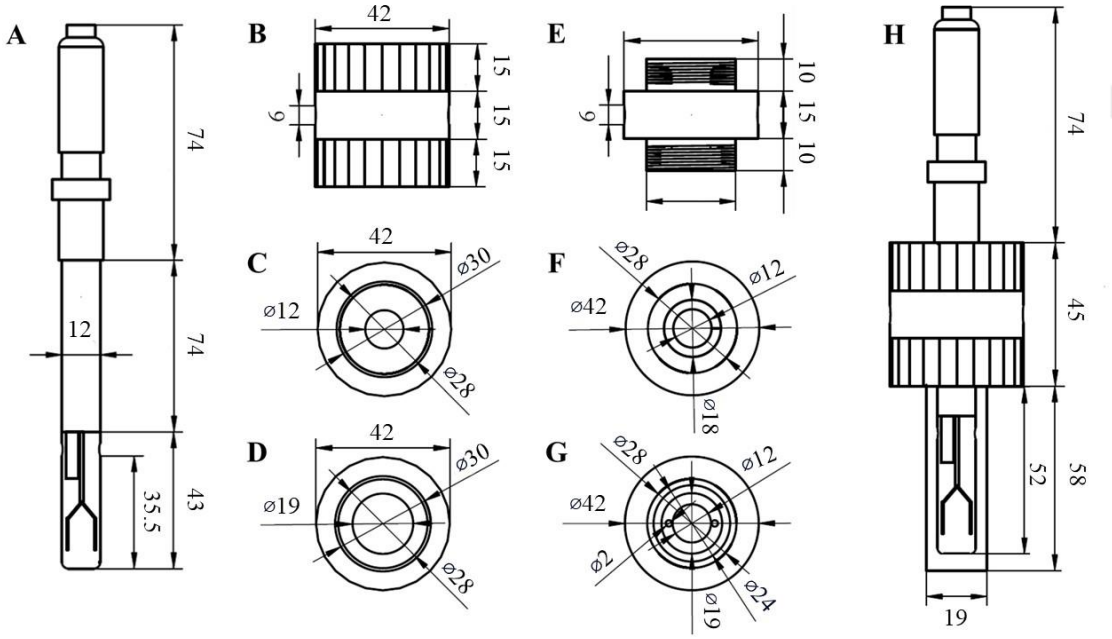



**Figure 4.9.** Drawings of the customized conductivity cell and the cell holder. **A**: Commercial Metrohm conductivity cell; **B**: Assembled cell holder; **C**: Top part of the cell holder; **D**: Bottom part of the cell holder; **E**: Middle/Core part of the cell holder; **F**: Middle/Core part of the cell holder (top section); **G**: Middle/Core part of the cell holder (bottom section); **H**: Fully assembled customized conductivity cell. The dimensions are in mm.

In the first setup, the dip-in cell was connected to the LCR using the standard 2-wire cable of the commercial electrode (Fig. 4.10 A). The 2-wire configuration was then converted into a 4-wire configuration using a connection box built in the laboratory (Fig. 4.109 B), where four ML--SYV-2-41 cables were connected to the LCR. This box is also used to connect the Pt100 incorporated on the conductivity cell to the Data Logger to allow the measurement of the temperature of the sample.

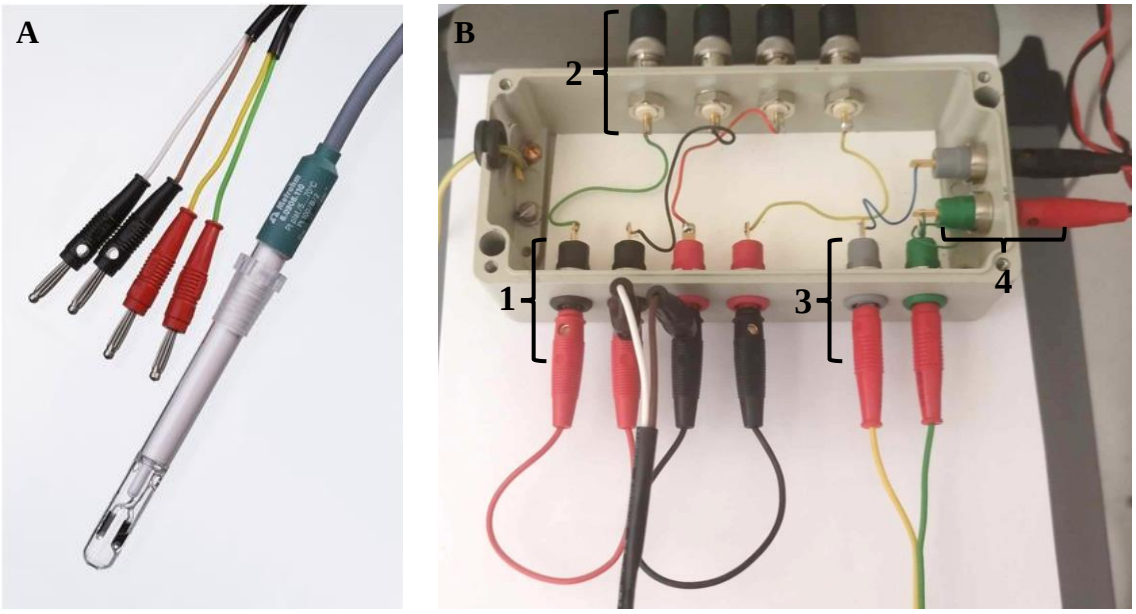



**Figure 4.10.** Images of the first setup of the dip-in cell – LCR cable connection. **A:** Commercial Dip-in Metrohm cell (black connectors are connected to the electrodes, red connectors are connected to the Pt100); **B:** Connection box (**1:** input of electrode connectors, conversion of 2-wire to 4-wire, **2:** electrode connectors output and connection to the ML--SYV-2-41 cables that go into the LCR; **3:** input of the Pt100 connectors; **4:** output of the Pt100 connectors into the Data Logger.

An example of the typical impedance spectra for both an aqueous 0.1000 mol/kg KCl solution and an ionic liquid, $[C_4C_1im]BF_4$, is presented in Figure 4.11. As can be observed, initially, the resistance decreases with the increase in frequency until it reaches a *plateau*. This behavior is associated with the effect of solution polarization, which is more impactful for low frequencies. However, the resistance *plateau* is followed by a significant increase in the measured resistance in the range of higher frequencies ($f$ > 100 kHz). This effect is likely due to parasitic contributions from the cables and electrical connections.

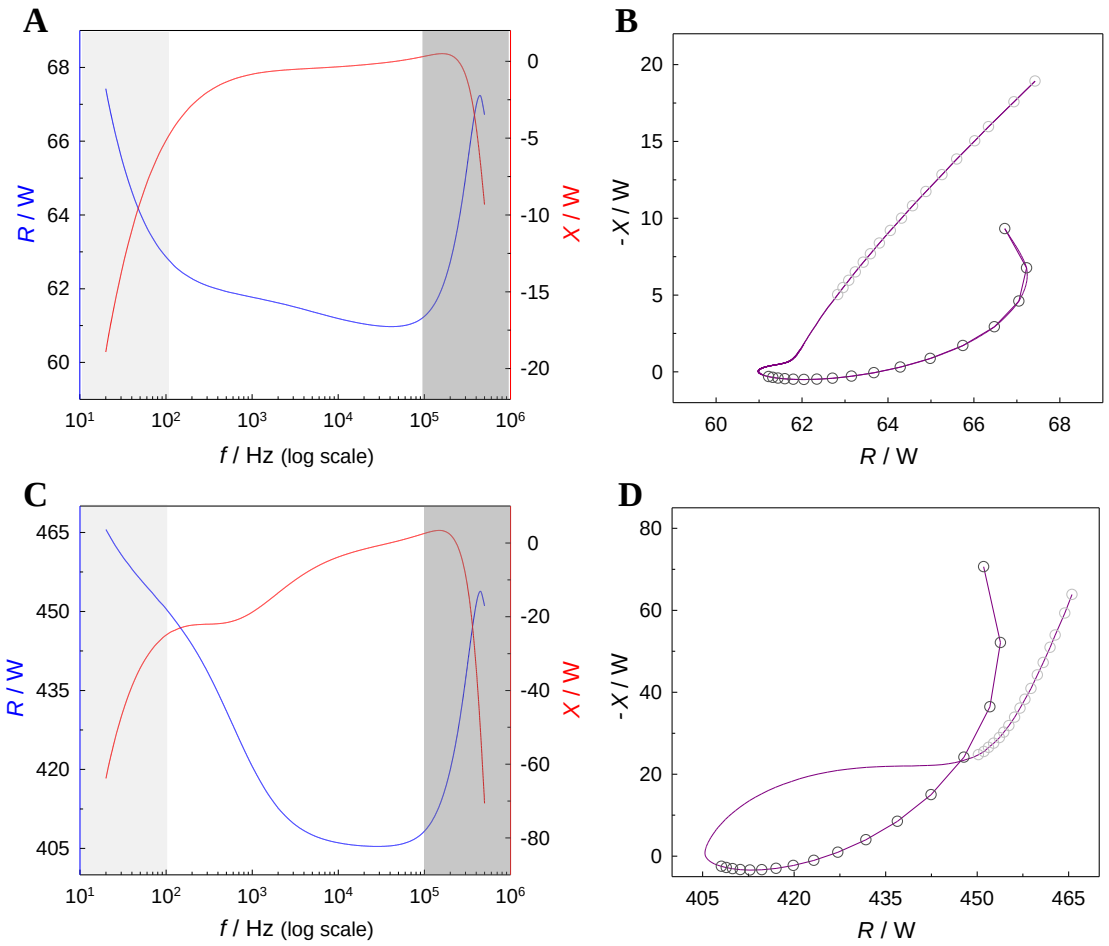



**Figure 4.11.** Spectra obtained using the wiring configuration based on the commercial dip-in cell cable setup. **A:** RX spectra aqueous 0.1000 mol/kg KCl solution; **B:** Nyquist plot aqueous 0.1000 mol/kg KCl solution; **C:** RX spectra Ionic liquid, $[C_4C_1im]BF_4$; **D:** Nyquist plot Ionic liquid, $[C_4C_1im]BF_4$.

In order to minimize the impact of these parasitic contributions, two adaptations to the connection setup presented above were made:

**A:** The standard cable of the Metrohm cell was cut as it was found to not be suitable for high frequencies ($f$ > 100 kHz), and a new connection box was constructed directly on top of the conductivity cell.

**B:** A *shunt* was applied between the 4-wire terminals in the new connection box (Fig. 4.12).

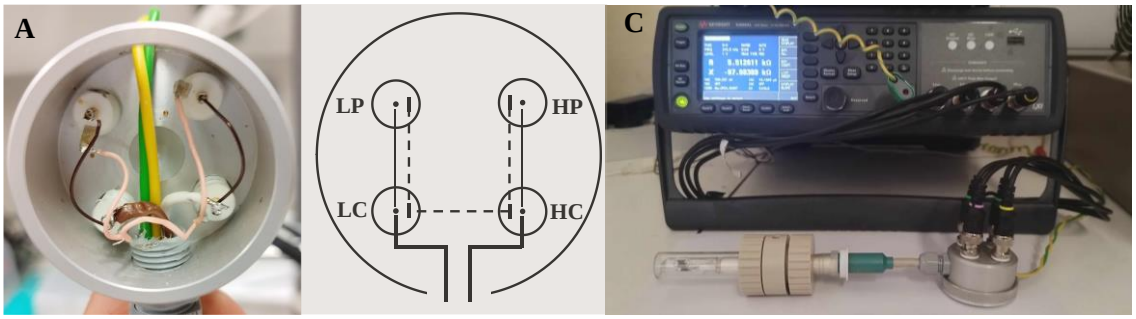



**Figure 4.12.** Second and definitive setup for the Dip-in cell – LCR 4-wire connection. **A**: Images of the 4-wire configuration; **B**: schematic representation the straight lines represent the LP-LC and HP-HC pairs while the dashed lines represent the *shunt*). **C**: Overall image of the Dip-in cell and the LCR meter.

The typical impedance spectra obtained from experiments using the configurational setup presented in Figure 4.12 are presented in Figure 4.13.

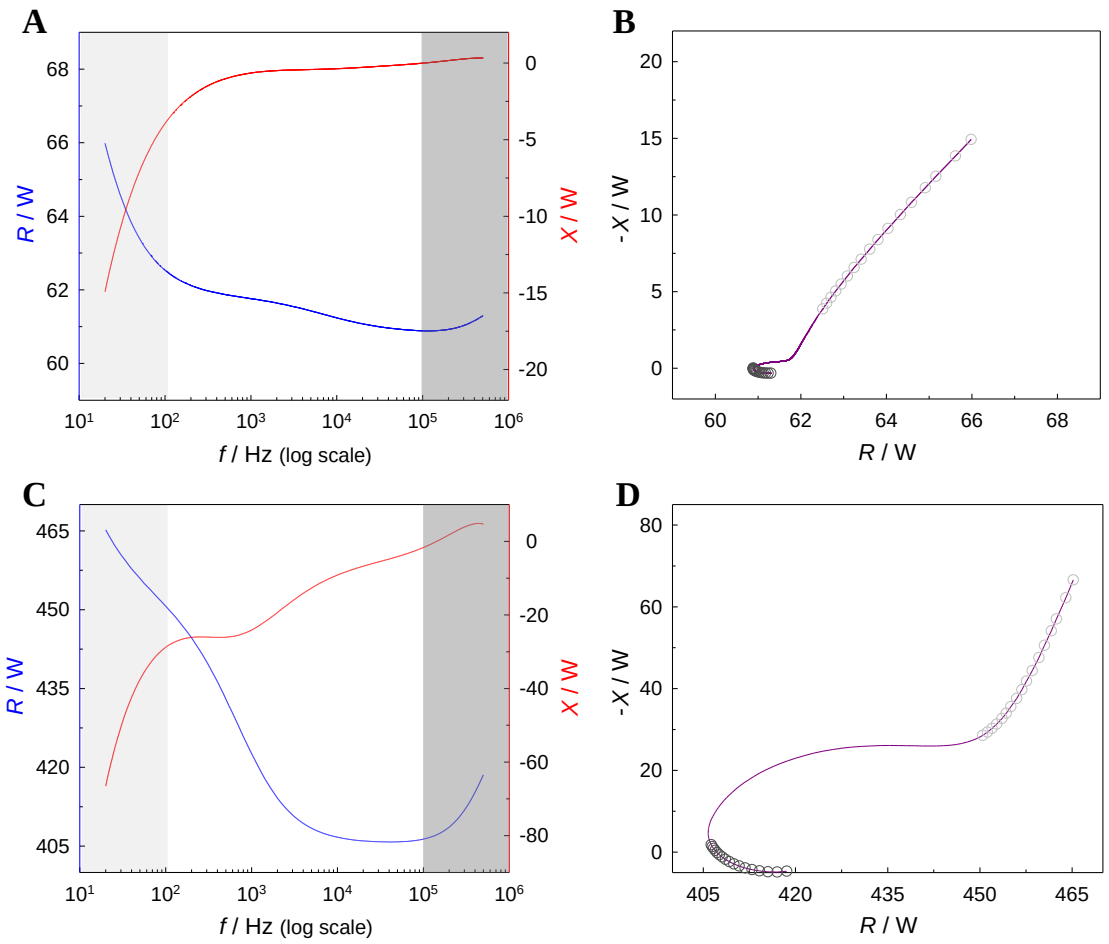



**Figure 4.13.** Spectra obtained using the wiring configuration based on the customized cable/connection system. **A:** RX spectra aqueous 0.1000 mol/kg KCl solution; **B:** Nyquist plot aqueous 0.1000 mol/kg KCl solution; **C:** RX spectra Ionic liquid, $[C_4C_1im]BF_4$; **D:** Nyquist plot Ionic liquid, $[C_4C_1im]BF_4$.

### 4.2.2. Coin Cell

The coin cell is a two-electrode conductivity cell with a sandwich-like configuration. The main motivations for the development of this cell were:

**A**: To minimize the amount of sample necessary in order to increase the sustainability/viability of experiments with expensive samples (e.g., mixtures of ionic liquids);

**B**: Allow the testing and evaluation of different electrode materials.

#### 4.2.2.1. Cell Design

The main part of the cell is a PEEK core, which acts as the sample vessel and the spacer between the two electrode discs. The discs are symmetrically pressed into the main core by squared plates composed of aluminum and PEEK. A FFKM o-ring is placed in between the disc and the PEEK core to ensure the tightness of the sample vessel and thus prevent sample leakage as well as water absorption. The PEEK block is in the center of the plate, and it is the part that is actually in contact with the electrode. The remainder of the plate is in aluminum to improve the thermal conductivity of the cell. The PEEK parts of the plates are embedded with a spring-loaded contact pin to perform the electric contact with the electrodes. To finish the assembly process, the two pressing plates are clamped together using four threaded bars placed near each of the plates' vertices. In the interior of the sample vessel, there are two opposed orifices that act as the sample injection and withdrawal system. The bottom one is the input (⌀ = 1 mm), and the top one is the output (⌀ = 2 mm). This configuration allows a smoother filling of the sample vessel and minimizes the formation of air bubbles. The orifices are connected to the exterior by two flangeless tubing connectors, 1/4 inch-28 tube end fittings with collapsible PTFE ferrules, which are attached to the PTFE tube ($\varnothing_{int}$ = 1, $\varnothing_{ext}$ = 2 ). The output line is connected to the $N_2$(g)/vacuum lines that are part of the ILDEM system by a flangeless 1/4 inch tubing connector and the adequate female counterpart. This allows the drying of the cell and degassing of the sample *in situ.* To perform the injection of the sample, a syringe is connected to the input line by a flangeless 1/4 inch tubing connector and an adequate syringe adaptor. Fig. 4.14 presents images of the coin cell and each of the individual parts, as well as a schematic representation of the assembly process.

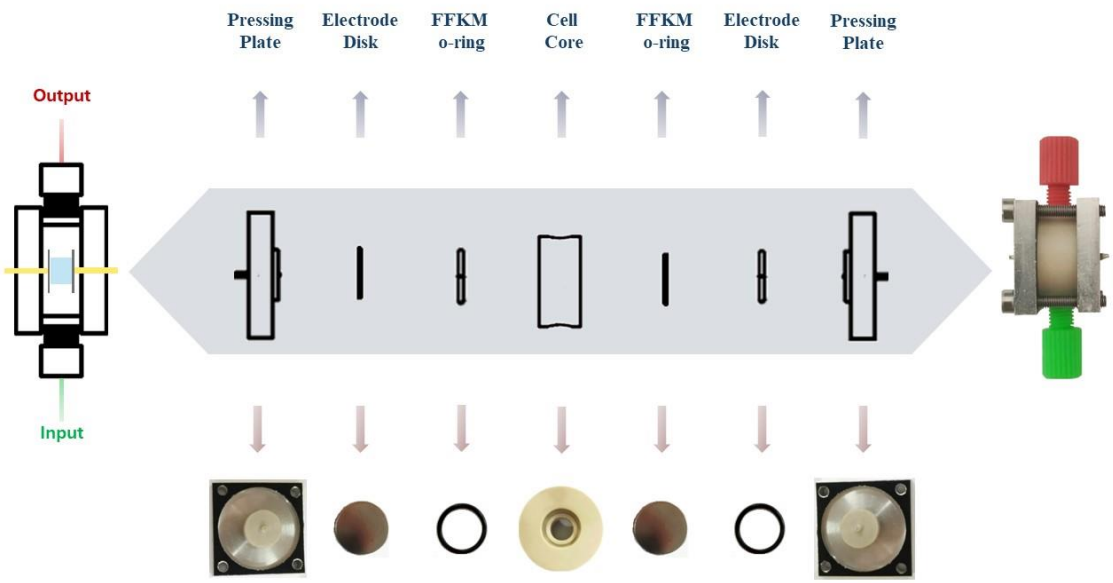



**Figure 4.14.** Images and schematic representation of the complete coin cell and the individual components.

The exploded view of the dip-in cell is presented in Fig. 4.15 and illustrates the assembly process of the coin cell.

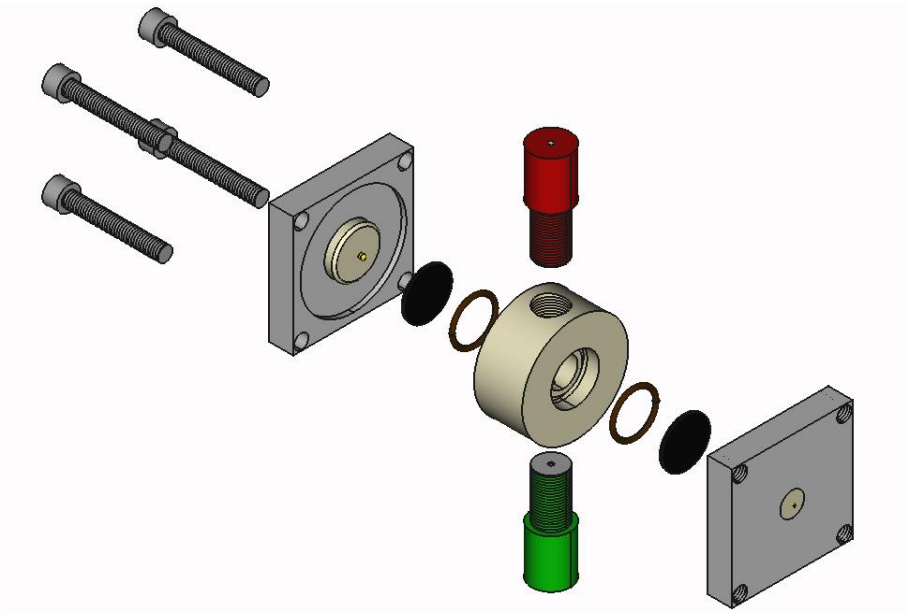


**Figure 4.15.** Exploded view of the coin conductivity cell. PEEK, aluminum, brass alloy with gold over nickel plated finish, input tubing connector, output tubing connector, FFKM o-ring, **electrode discs** (stainless steel 316, stainless steel 316 coated with titanium nitride, nickel, platinum).

Upon assembly, the coin cell has an external dimension of 25 mm x 25 mm x 18 mm. The detailed drawings of the coin cell and the individual components are presented in Fig. 4.16.

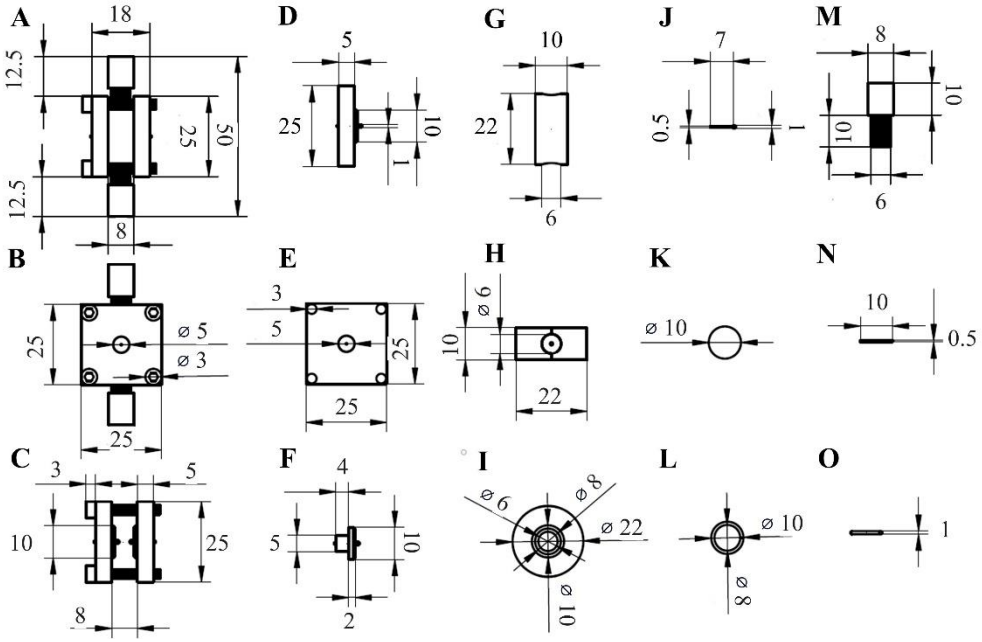



**Figure 4.16.** Drawings of the coin cell and the individual components. **A:** overall (front view); **B**: overall (side view); **C**: pressing plate and threaded bars (cage); **D**: pressing plate (side view); **E**: pressing plate (rear view); **F**: PEEK block of the pressing plate; **G**: core PEEK part (front view), **H**: core PEEK part (top view); **I**: core PEEJ part (side view); **J**: electric contract spring-loaded pin; **K**: electrode disc ( top view); **L**: FFKM o-ring (top view); **M**: connecting tube with the PTFE ferrule; **N**: electrode disc (front view); **O**: FFKM o-ring (front view). All dimensions are in mm.

To better present the cell design and the applied measuring technique, a 2D cut drawing of the interior of the coin cell, as well as a schematic representation of the sample vessel, can be found in Fig. 4.17. The sample vessel/measuring chamber corresponds to the compartment where the sample is in contact with the electrodes. This chamber is delimited by the electrode discs and the tube-like PEEK compartment that acts as the electrode spacer. Therefore, the effective measuring cell can be described as a cylinder with a base diameter of 6 mm and a height of 5 mm (Figure 4.17). As referred earlier, the cell constant of a conductivity cell is related to its dimensions, particularly the area of the electrode in contact with the sample and the distance between the electrodes. Based on the dimensions of the sample vessel and cell constant relation (Equation 4.11), the cell constant for the coin cell is given by Eq. 4.11 and was estimated to be ≈ 1.8| $cm^{-1}$,

$$C_{\text{cell}} = \frac{l}{A} = \frac{l}{\pi r^2} = \frac{5}{9\pi} \tag{4.11}$$

Similarly, the capacity of the measuring chamber can be determined based on the volume of a cylinder as described in Eq. 4.12, and it was estimated to be ≈ 141.3 µL.

$$V_{\text{cell}} = l \cdot A = l \cdot \pi r^2 = 45\pi \tag{4.12}$$

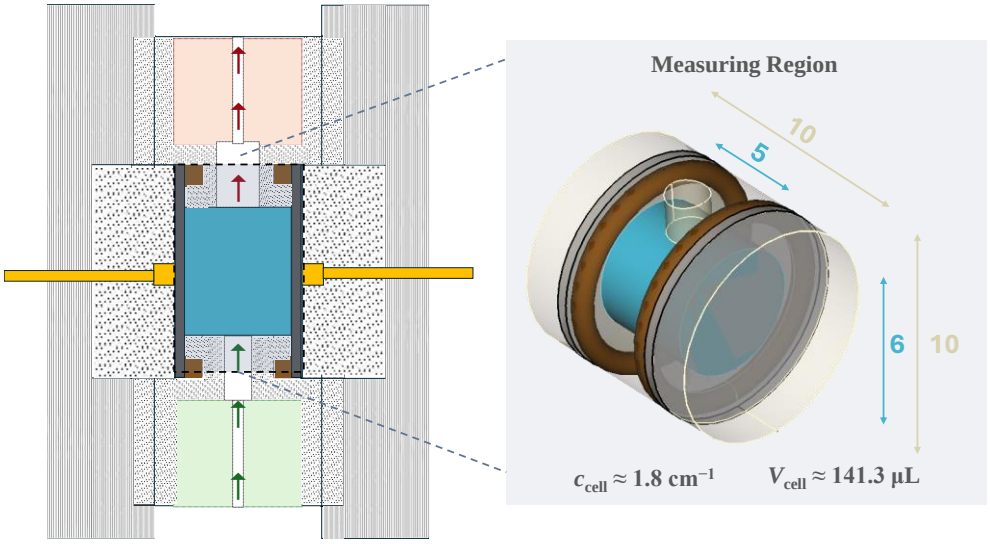



**Figure 4.17**. Schematic representation of the coin cell (2D cut and geometry) and the measuring chamber (3D perspective). All dimensions are in mm.

In order to facilitate the handling of the cell, as well as its placement and fixation inside the Air Bath Thermal Chamber, a dedicated cell holder was designed (Fig. 4.18).

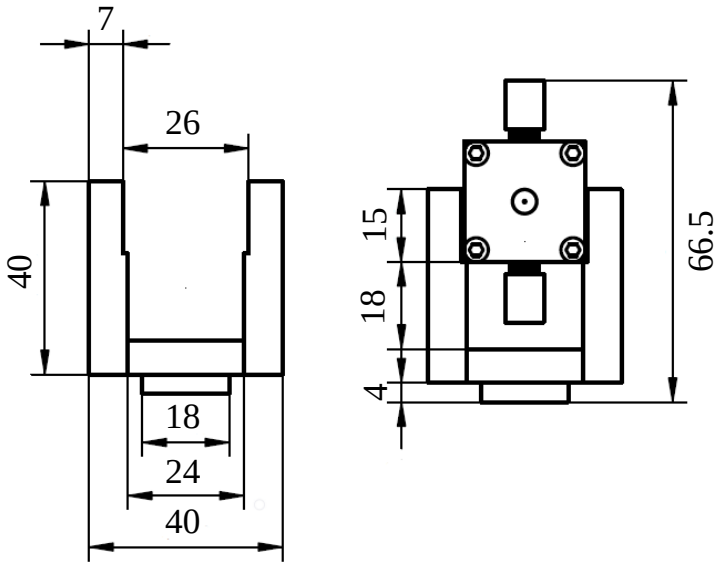



**Figure 4.18**. Drawings of the dedicated support for the coin cell. All dimensions are in mm.

In-laboratory images of the complete setup of the Coin Cell (cell, support, injection/gas/vacuum lines) are presented in Fig. 4.19.

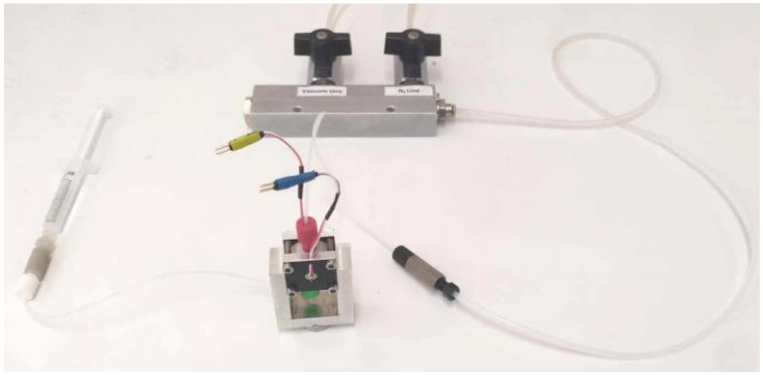


**Figure 4.19.** Image of the in-laboratory setup of the Coin Cell.

#### 4.2.2.2. Characterization of the Electrode Discs

In this work, four different types of electrodes were studied and tested: stainless steel 316 (SS), stainless steel 316 coated with titanium nitride (SSTiN), platinum (Pt), and nickel (Ni). All discs have a diameter of 10 mm and a thickness of 0.5 mm and were commercially obtained from Goodfellow. The specifications of each material are presented in Table 4.1. The images of the electrode discs are presented in Fig. 4.20.

**Table 4.1.** Specifications of the coin cell electrode discs.

| Material | CAS No. | Reference | Composition | Process |
|---|---|---|---|---|
| Stainless Steel 316 (SS) | ---------- | 875-099-53 | Fe/Cr18/Ni10/Mo3 | Temper: Annealed |
| Stainless Steel 316 w/ Titanium Nitride coating (SSTiN) | ---------- | 118-342-65 | Fe/Cr18/Ni10/Mo3 2-3 μm TiN coating | Ion Implanted |
| Platinum (Pt) | 7440-06-4 | 438-912-82 | Purity (99.95%) | Temper: as rolled |
| Nickel (Ni) | 7440-02-0 | 907-642-20 | Purity (99.999%) | Temper: as rolled |

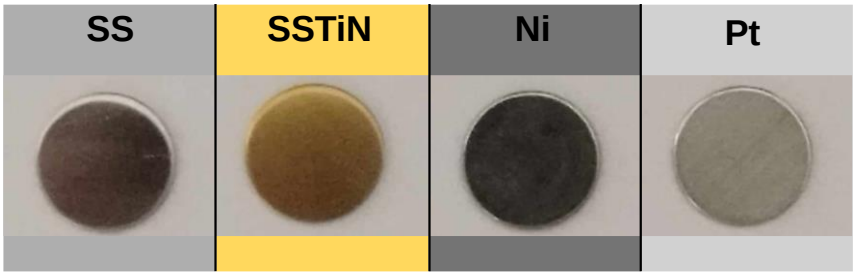



**Figure 4.20.** Images of the coin cell electrode discs: stainless steel 316 (SS), stainless steel 316 coated with titanium nitride (SSTiN), nickel (Ni), platinum (Pt).

The surfaces of the electrode discs were characterized by scanning electronic microscopy (SEM), and the composition of materials was verified by energy dispersive spectroscopy (EDS). The obtained results are presented in the following figures: Fig. 4.21 (SS), Fig. 4.22 (SSTiN), Fig. 4.23 (Ni), and Fig. 4.24 (Pt).

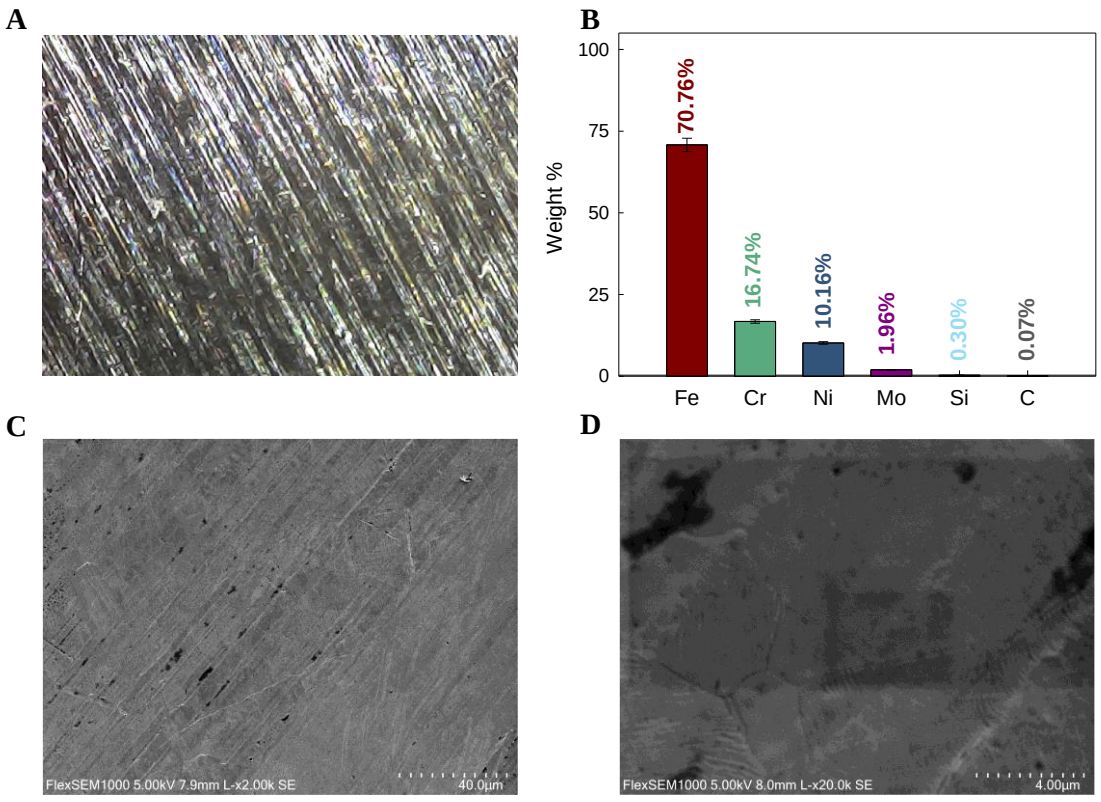



**Figure 4.21.** Characterization of the stainless steel discs. **A**: Optic microscopy 500x; **B**: EDS; **C**: SEM 2000x; **D**: SEM 20000x.

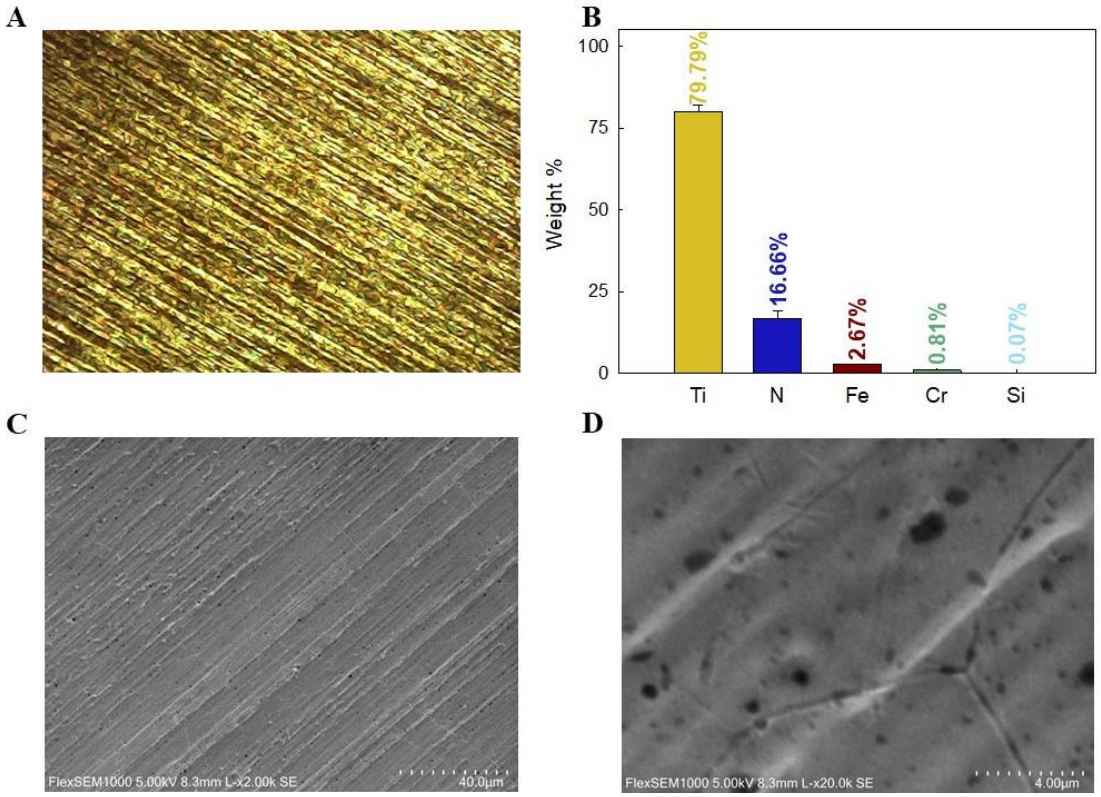



**Figure 4.22.** Characterization of discs of stainless steel coated with titanium nitride. **A**: Optic microscopy 500x; **B**: EDS; **C**: SEM 2000x; **D**: SEM 20000x.

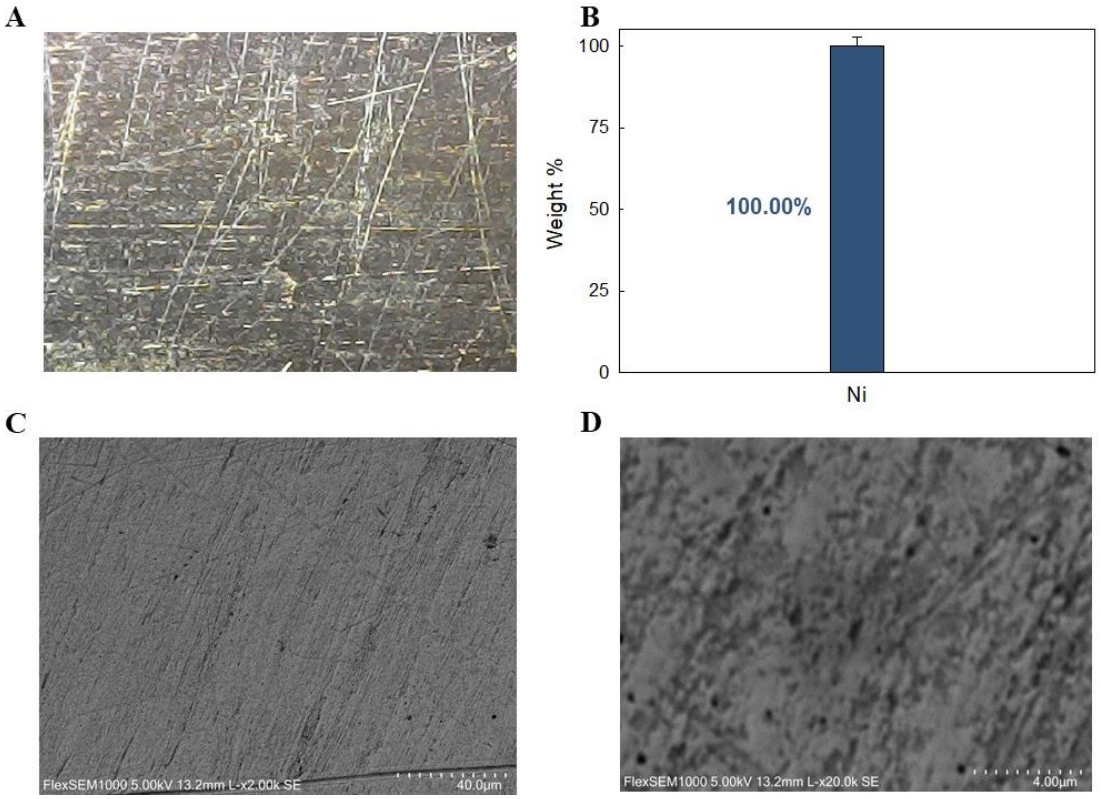



**Figure 4.23.** Characterization of the nickel discs. **A**: Optic microscopy 500x; **B**: EDS; **C**: SEM 2000x; **D**: SEM 20000x.

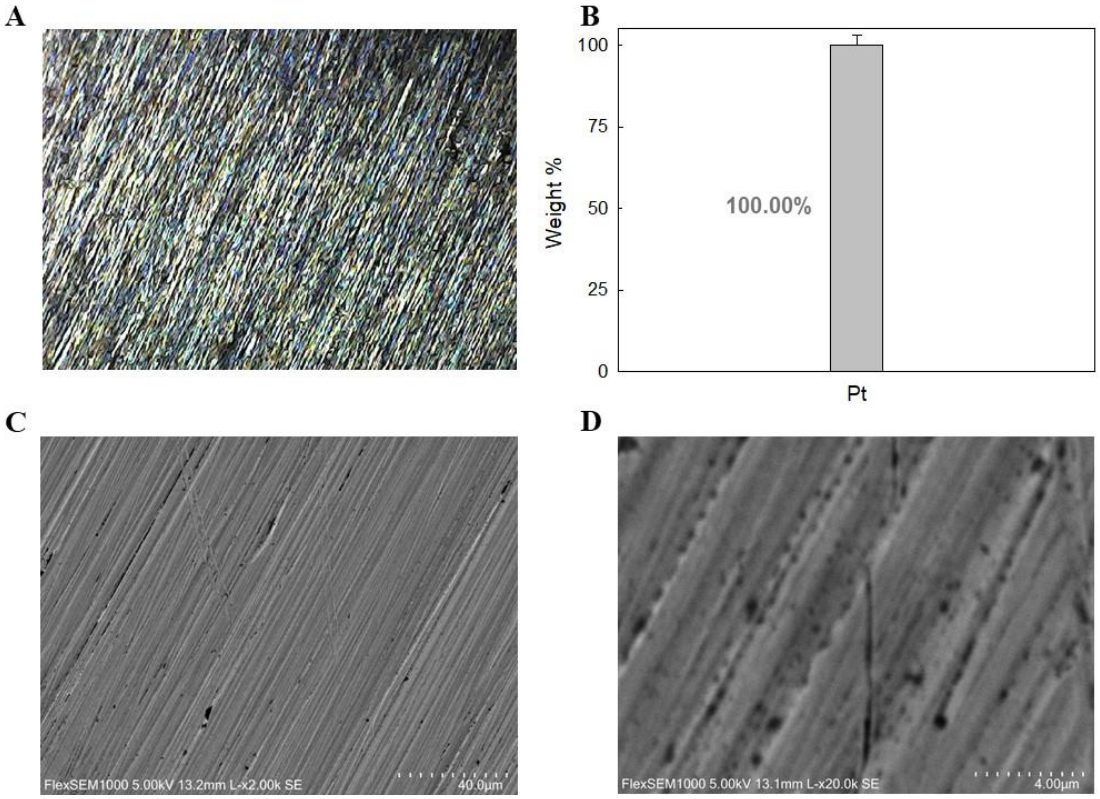



**Figure 4.24.** Characterization of the platinum discs. **A**: Optic microscopy 500x; **B**: EDS; **C**: SEM 2000x; **D**: SEM 20000x.

#### 4.2.2.3. Electric Configuration

The coin cell is connected to the LCR meter in a 4-wire configuration. Contrary to the previous cell that was attached with a connection box, for this cell, the connections are made through a panel installed in the air bath chamber. For this, the contact pins on each pressing plate were welded to two electric cables. On the other end of the cable, the wires were welded to one contact pin each. The contact pins of each pair are kept together with electrical insulation tape and sleeves, as presented in Fig. 4.25.

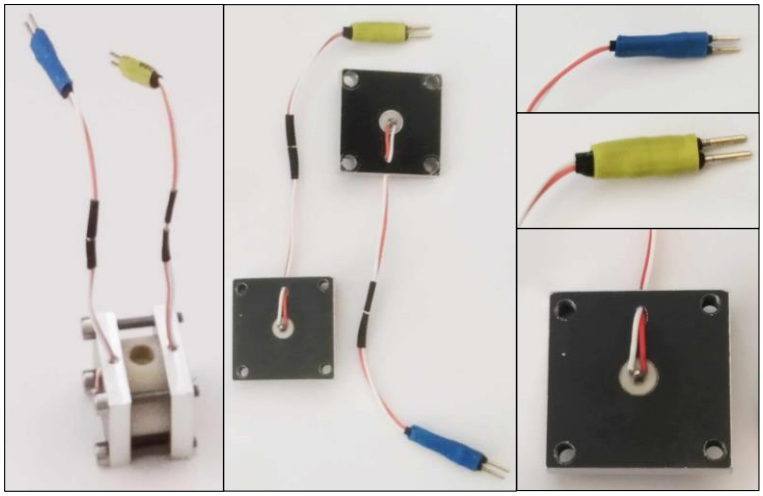


**Figure 4.25.** Images of the coin cell's electric connections.

Each pair is connected to a female connector pair that is welded to 2 BNCs connectors that are embedded on one of the thermal chamber plates. The BNCs are used to connect the four ML--SYV-2-41 cables to the LCR meter. This configuration allows the conversion from 2-wire to 4-wire. Images of the electrical installation and the corresponding schematic representation are presented in Fig. 4.26.

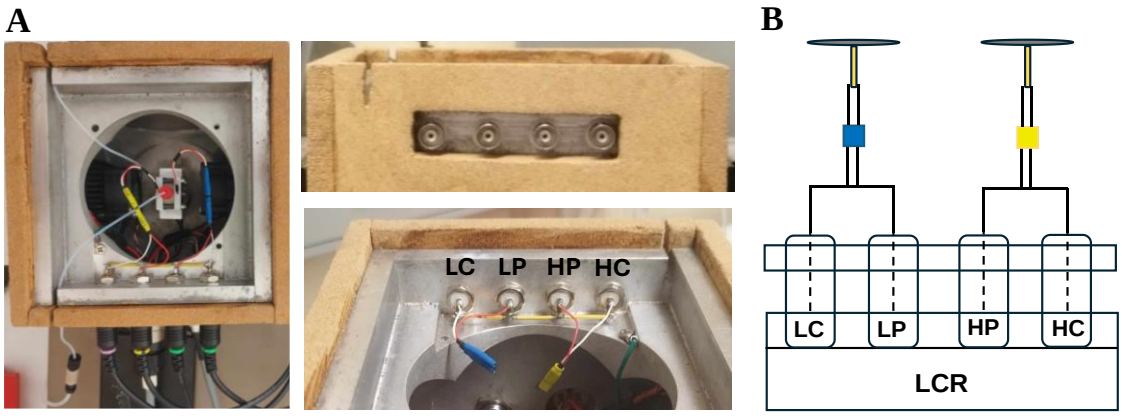



**Figure 4.26.** Coin cell – LCR connection. **A**: Images of the installation in the laboratory; **B**: Schematic representation.

## 4.3. Vacuum/Gas line

As referred to previously, both cells are prepared to be attached to gas and vacuum lines. A two-valve machined aluminum block was designed to connect a diaphragm to an oil-free vacuum pump (Boeco model R400) and the dry Nitrogen gas cylinder to the electrical conductivity cells. The gas line contains a flow regulator, while the vacuum line has a glass container between the aluminum block and the rotary pump acting as a trap. The block is connected to the cells by a PTFE tube, which connects to the cells using a flangeless 1/4 inch tubing connector and the adequate female counterpart (as exemplified in Fig. 4.19). The schematic representation of the ILDEM vacuum/gas line is presented in Fig. 4.27.

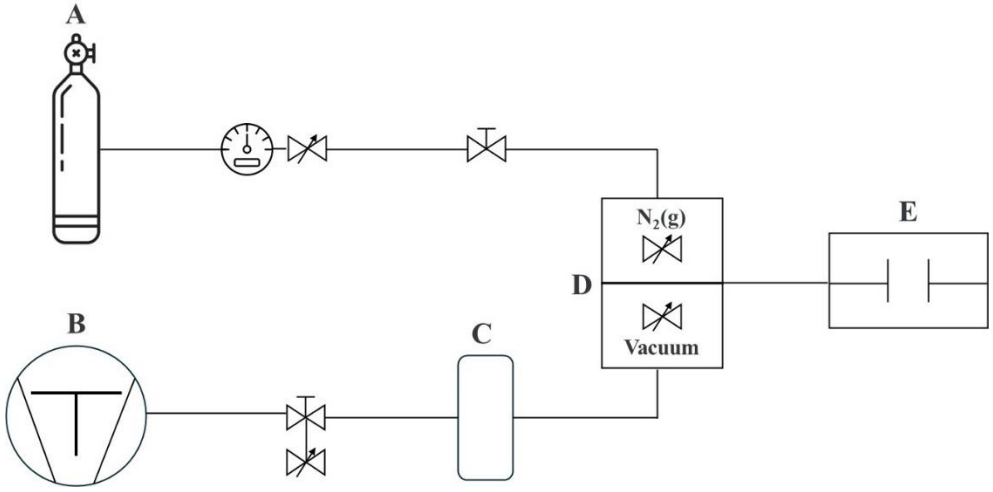



**Figure 4.27.** Schematic representation of the ILDEM vacuum/gas line. **A:** Dry Nitrogen gas cylinder; **B:** diaphragm vacuum pump (Boeco R-400); **C:** glass vessel trap; **D:** machined aluminum block; **E:** Electrical conductivity cell.

## 4.4. Air Bath Thermal Chamber

For the temperature control in the measuring cell, a customized Air Bath Thermal Chamber was designed and developed. When designing the thermal box, special care was taken to ensure that it would be appropriate to accommodate both the dip-in cell and the coin cell.

### 4.4.1. Description

For the temperature control in the measuring cell, a customized Air Bath Thermal Chamber was designed and developed. When designing the thermal box, special care was taken to ensure that it would be appropriate to accommodate both the dip-in cell and the coin cell. The core of the chamber is a cubic-shaped structure in aluminum connected to aluminum plates (AW7075-T6/T651, 10 mm thickness). The exterior of the chamber was covered with cork board (5 mm thickness) to improve its thermal isolation and stability. Images of the exterior of the thermal chamber are presented in Fig. 4.28.




**Figure 4.28.** Images of the air bath thermal chamber. **A**: Aluminum core structure; **B**: Assembled aluminum thermal chamber; **C**: Assembled aluminum thermal chamber covered with corkboard.

The cooling and heating of the system are based on the two Peltier assemblies (Laird PowerCool DA-044-12-02) mounted symmetrically, which are controlled using an OEM precision thermoelectric controller (Meerstetter Engineering TEC-1089). To further improve the temperature homogeneity inside the chamber, two interior ventilators were installed as opposed to the Peltier assemblies. The Air Bath Thermal Chamber is powered and controlled by a specially designed electronic box made in the laboratory electronic box (Air Bath Control Box). The connections of the Thermal Chamber to the Control Box, Data Logger, LCR, and computer are established from the back panel. An image of the fully connected Thermal Chamber is presented in Fig. 4.29. Images of each plate can be found in Fig. 4.30, and an illustration of the exploded view is presented in Fig. 4.31.

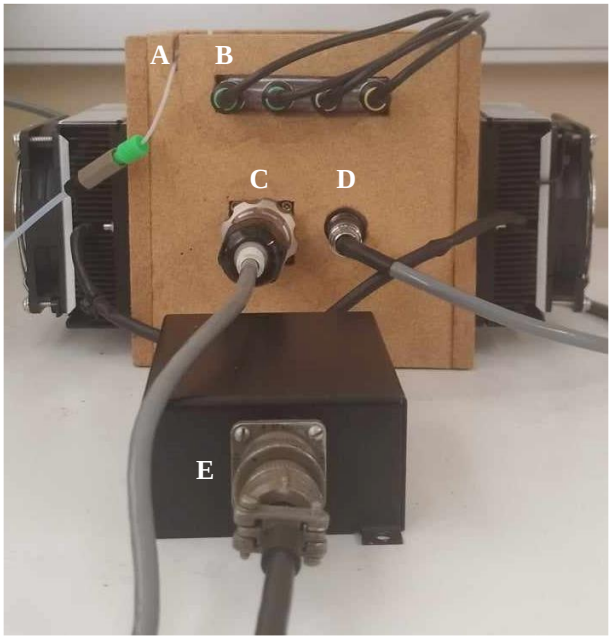



**Figure 4.29.** Image of the fully connected Air Bath Thermal Chamber. **A:** Vacuum/gas line; **B:** LCR connection (BNC); **C:** Control Box connection (7-pin plug); **D:** Data Logger connection (4-pin plug); **E:** Peltier Connection (4-pin military plug).

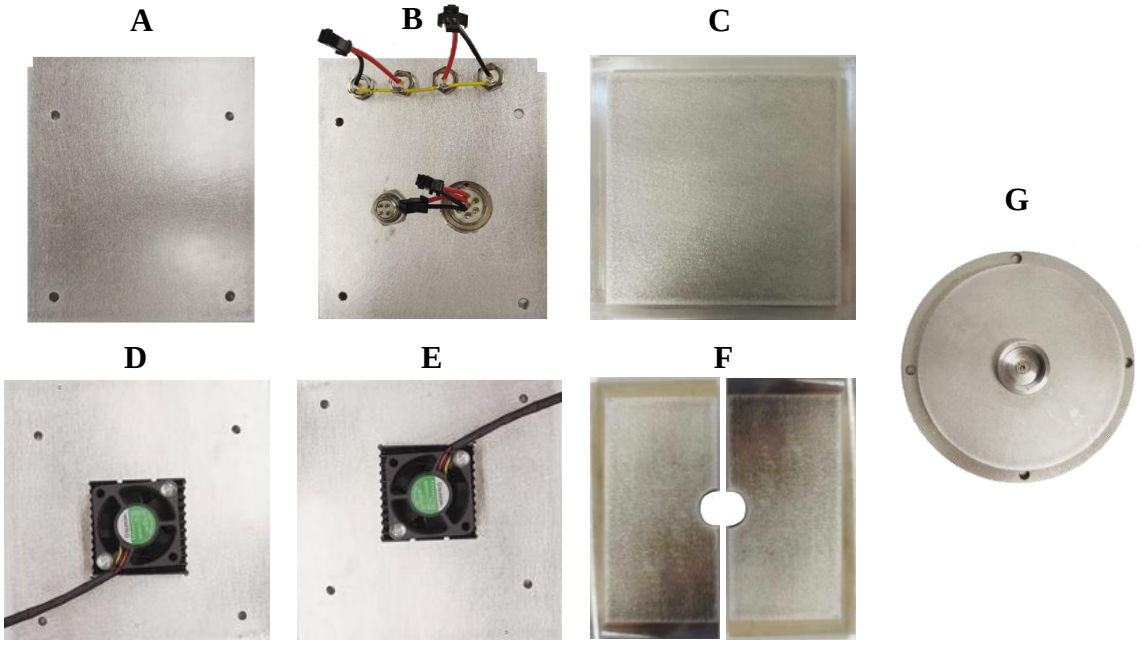



**Figure 4.30. A**: Front panel with a slit for the N2(g)/vacuum lines; **B**: Connection panel with a slit for the N2(g)/vacuum lines; **C**: lid compatible with the coin cell; **D**: left ventilation plate; **E**: right ventilation plate; **F**: lid compatible with the dip-in cell; **G**: base.

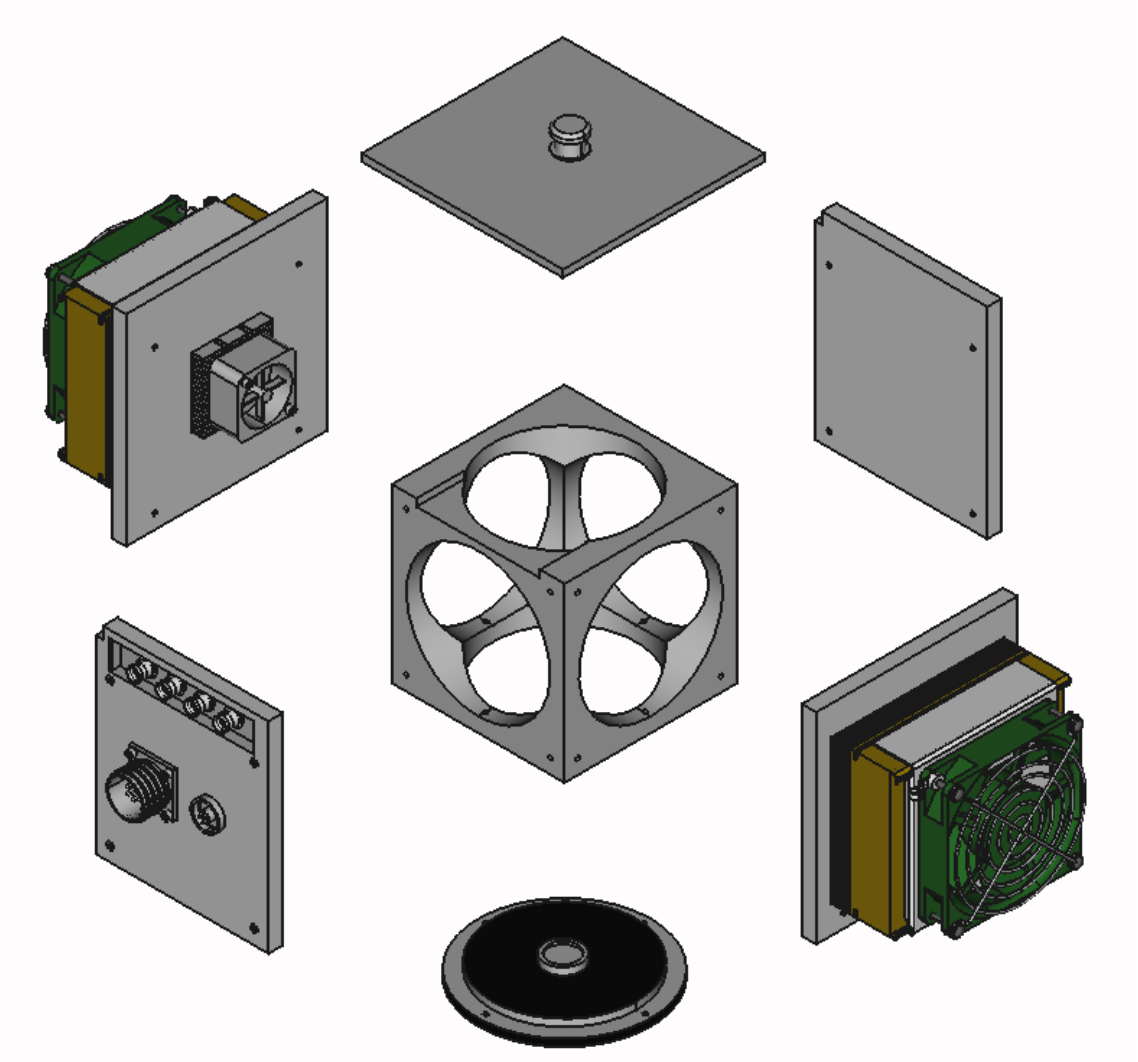


**Figure 4.31.** Exploded view of the air bath thermal chamber.

The detailed drawings with the dimensions of the air bath temperature chamber are presented in Fig. 4.32. The detailed drawings of each of the individual parts are presented in the following figures (from Fig. 4.33 to Fig. 4.39). Fig 4.33 illustrates the structure that functions as the core of the chamber (Fig. 4.28 A). Fig 4.34 presents the front panel, and Fig 4.35 presents the back panel. The front panel is plain, while the back panel has the outlets to connect to the LCR and the electronic box. Both of these panels have a worked conner to allow the vacuum/gas tubing in and out of the chamber. Fig. 4.36 is related to both lateral sides attached to the internal ventilators and the Peltier assemblies. Fig. 4.37 presents the circular bottom part (base) drawing. This part contains an incorporated circular part that acts as the cell site. Figures 4.38 and 4.39 correspond to the lid for the dip-in and coin cell setups, respectively. The dip-in setup uses a two-part lid with a centered circular opening (Fig. 4.30 F), allowing the upper body of the

conductivity cell and connection box to be outside of the box, while the coin cell setup uses a completely closed lid (Fig. 4.30 C). Both types of lids have a handles to facilitate their placement and removal.

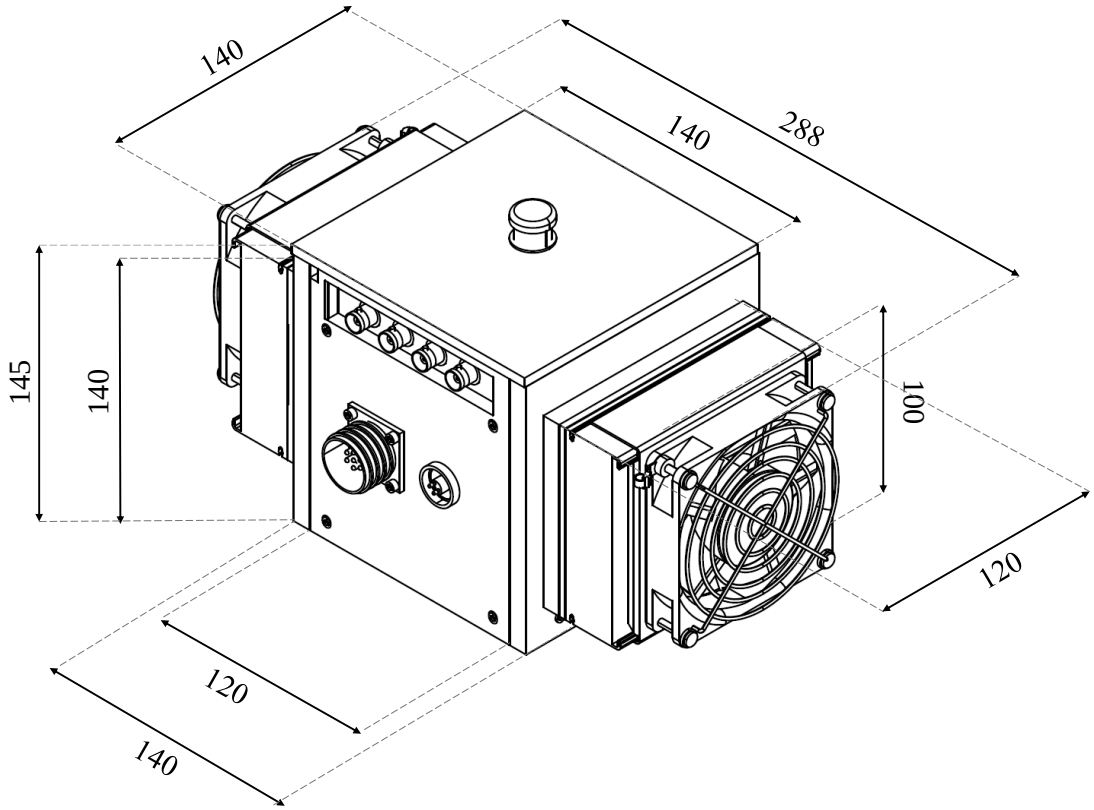



**Figure 4.32.** Detailed drawing of the air bath thermal chamber. Dimensions are in mm.

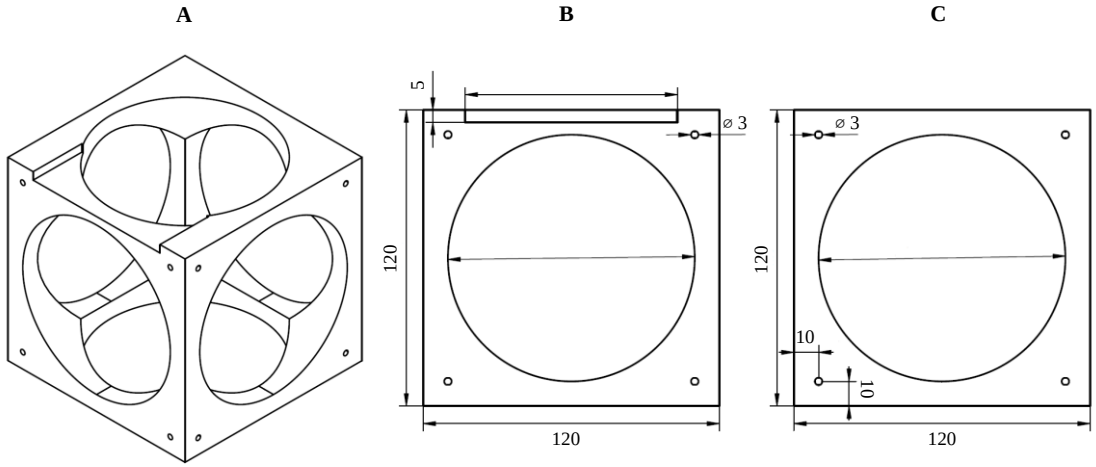



**Figure 4.33.** Detailed drawings of the core structure of the air bath thermal chamber. **A**: Overall perspective; **B**: The face that is attached to the back/connection panel; **C**: Representation of all other faces. Dimensions are in mm.

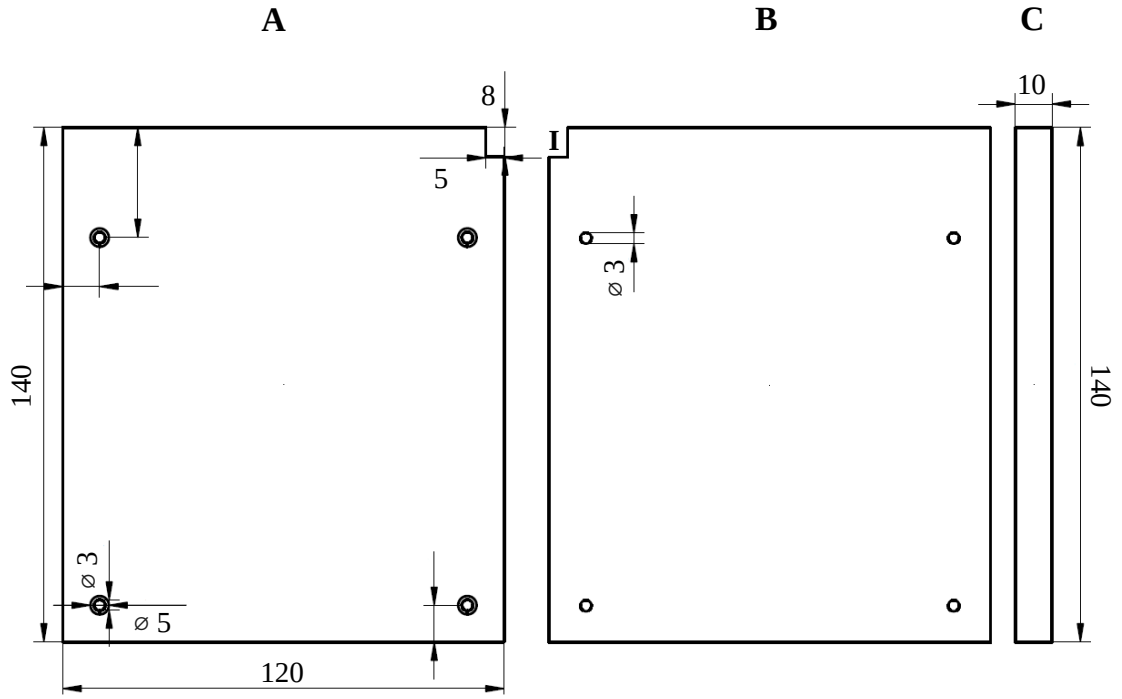



**Figure 4.34.** Detailed drawings of the front panel of the air bath thermal chamber. **A**: Outside view; **B**: Inside view; **C**: lateral view. Dimensions are in mm.

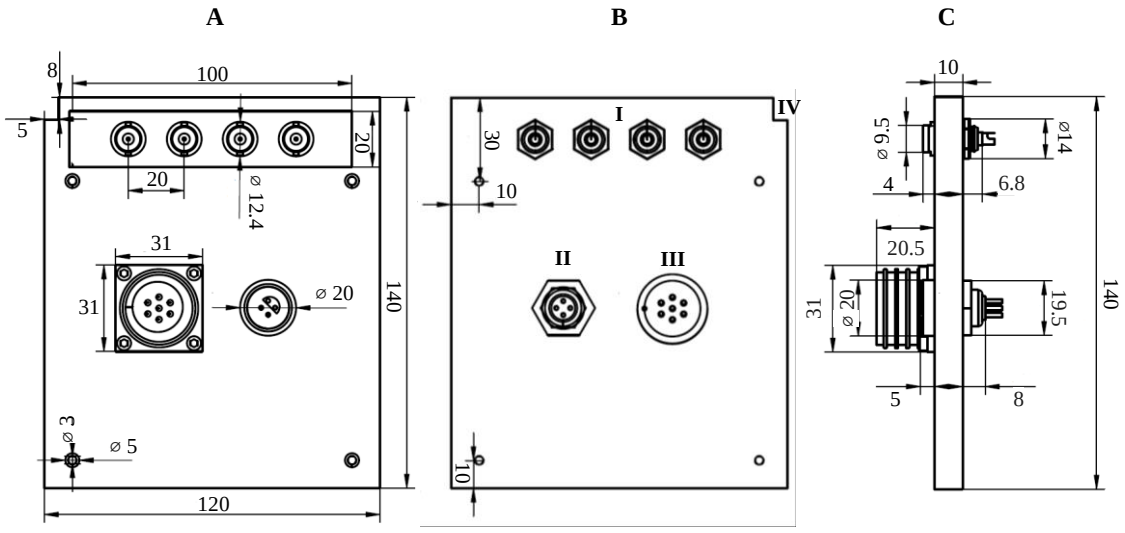



**Figure 4.35.** Detailed drawings of the back panel of the air bath thermal chamber. **A**: Outside view; **B**: Inside view; **C**: lateral view. **I**: BNC connections (chamber – LCR … impedance measurements); **II**: 4-pin plug (chamber – Data Logger … temperature readings); **III**: (chamber – electronic box … internal ventilators and temperature sensors ); **IV**: worked corner for vacuum/gas tubing. Dimensions are in mm.

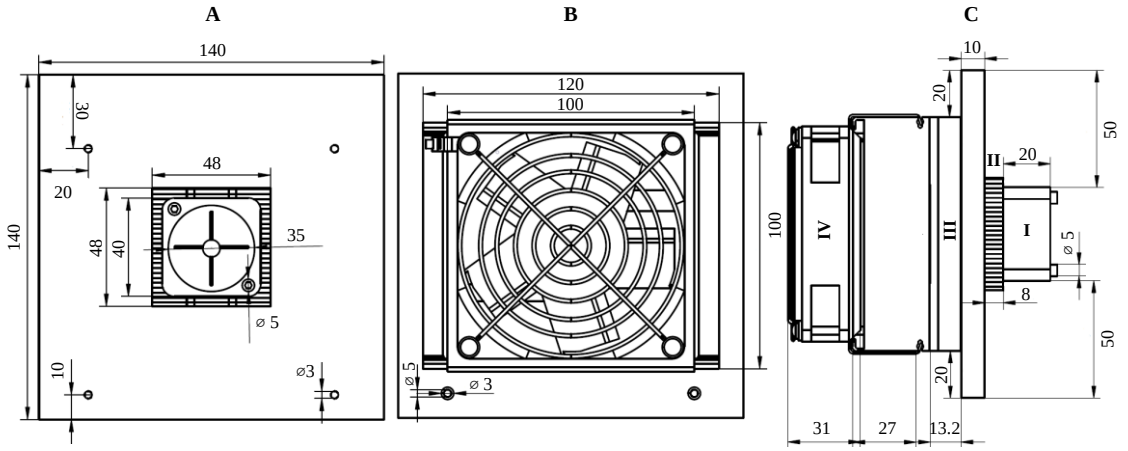



**Figure 4.36.** Detailed drawings of the lateral panels of the air bath thermal chamber. **A**: Outside view; **B**: Inside view; **C**: lateral view. **I**: Internal ventilator; **II**: Internal heat sink; **III**: Peltier module; **IV**: Peltier cooler. Dimensions are in mm.

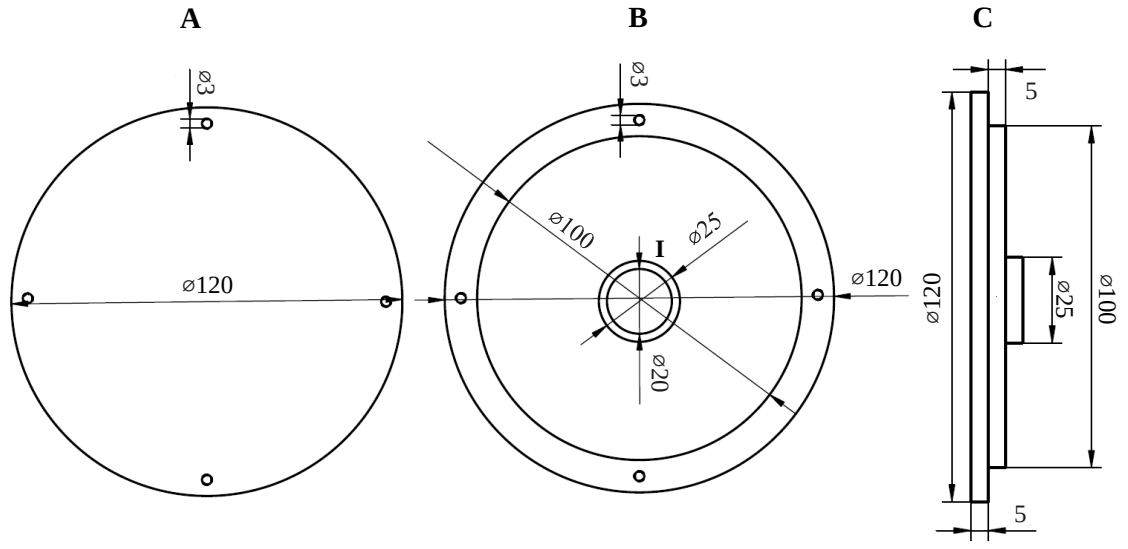



**Figure 4.37.** Detailed drawings of the circular bottom/base of the air bath thermal chamber. **A**: Outside view; **B**: Inside view; **C**: lateral view. **I**: conductivity cell site; Dimensions are in mm.

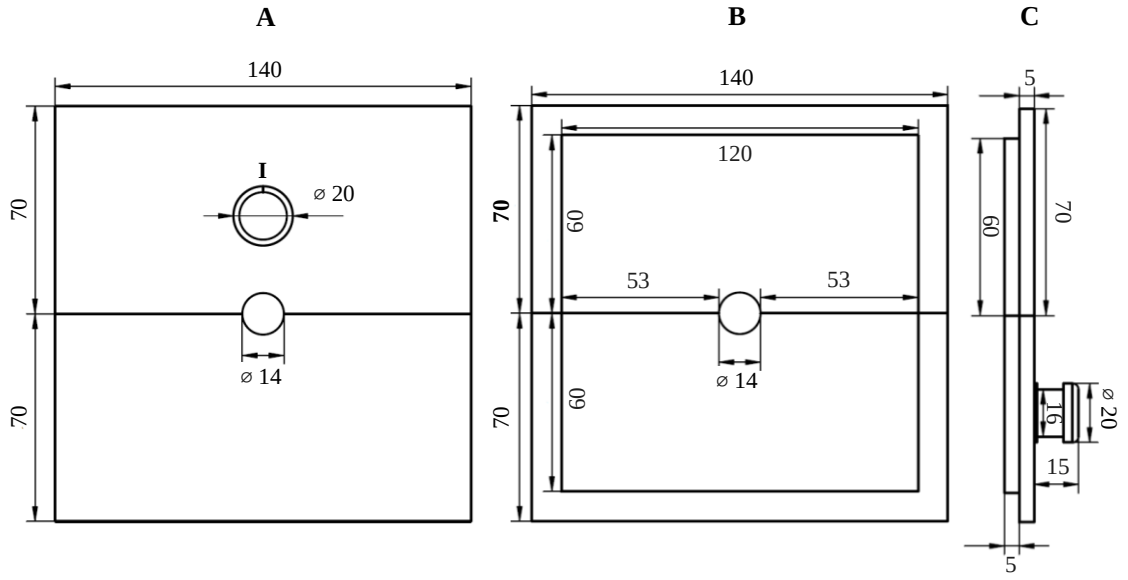



**Figure 4.38.** Detailed drawings of the lid of the air bath thermal chamber (Dip-in Cell setup). **A**: Outside view; **B**: Inside view; **C**: Lateral view. **I**: Lid´s handle; Dimensions are in mm.

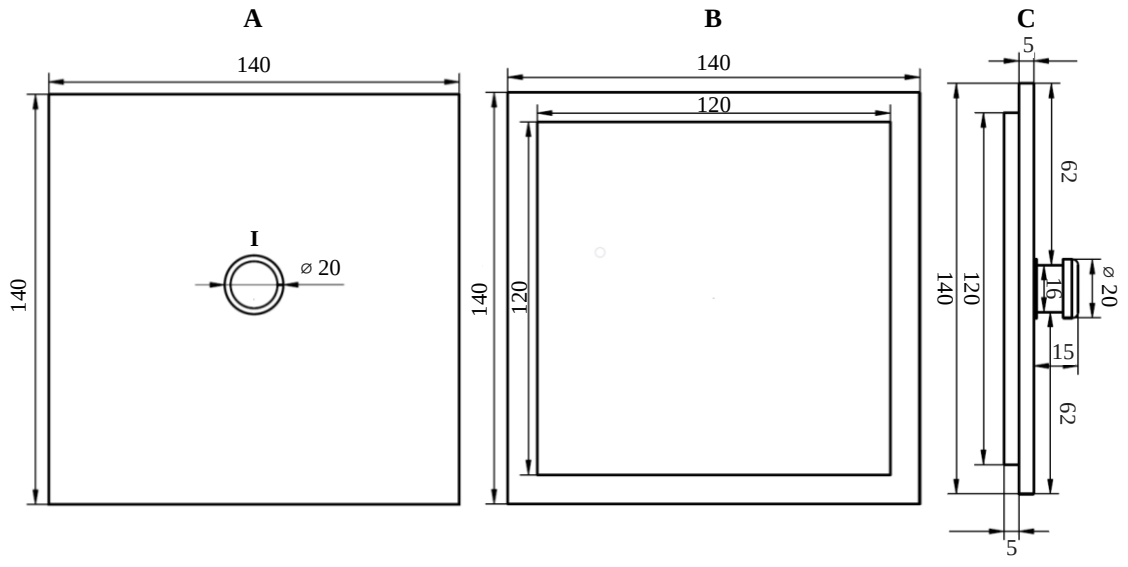



**Figure 4.39.** Detailed drawings of the lid of the air bath thermal chamber (Coin Cell setup). **A**: Outside view; **B**: Inside view; **C**: Lateral view. **I**: Lid´s handle; Dimensions are in mm.

### 4.4.2. Air Bath Control Box

A customized electronic box was built to incorporate the OEM TEC device and to power the Peltier and ventilation systems. The core of the system is an OEM Thermoelectric Controller (TEC-1089-SV 105 W), which controls/regulates the Peltier assemblies of the air bath thermal chamber. The electronic box has an incorporated temperature digital meter (OMRON K3MA-L 4-digits). These devices are powered by a DC power supply OMRON S8FS-C15024 (24 V). The front panel of the electronic box is equipped with three toggle switches:

- Main: This switch is connected to the DC Power supply and automatically turns on the Peltier ventilators (outside of the chamber).
- Heating/Cooling: This switch is connected to the OEM TEC device and automatically turns on/off the Peltier assembly and internal ventilators.
- Digital Meter: This switch is connected to the Digital Temperature Meter

Images of the front (switches and screen) and rear (connection plugs) panels of the Control Box can be found in Fig. 4.40.

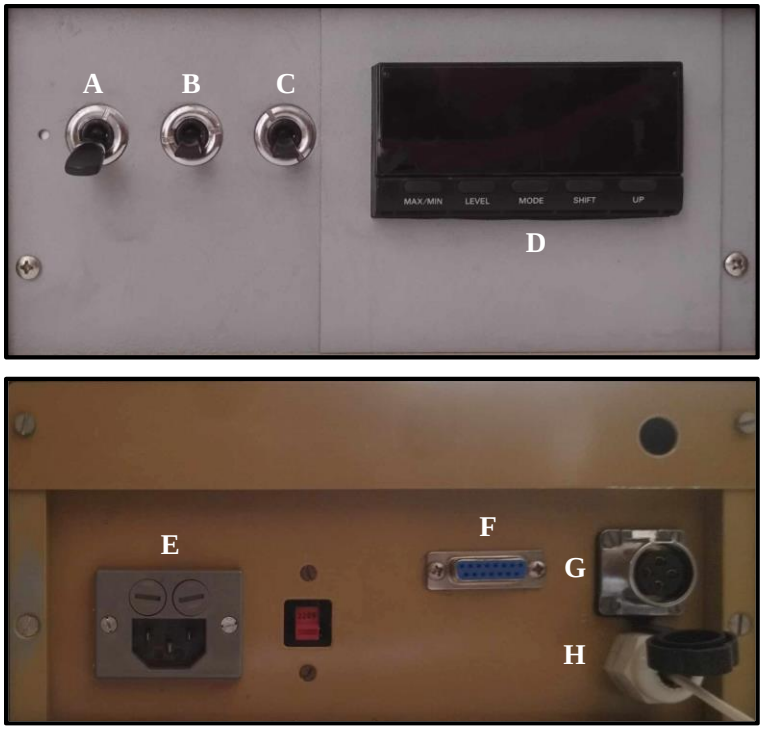



**Figure 4.40.** Images of the front (above) and rear (below) panels of the air bath control box. **A:** Main switch; **B:** Heating/cooling switch; **C:** Digital temperature meter switch; **D:** Digital temperature meter; **E:** Power source plug; **F:** Thermal Chamber connection plug (DB-15); **G:** Peltier assembly connection plug (4-pin); **H:** Computer connection (USB).

The schematic representation of the Air Bath Control Box is in Fig. 4.41.

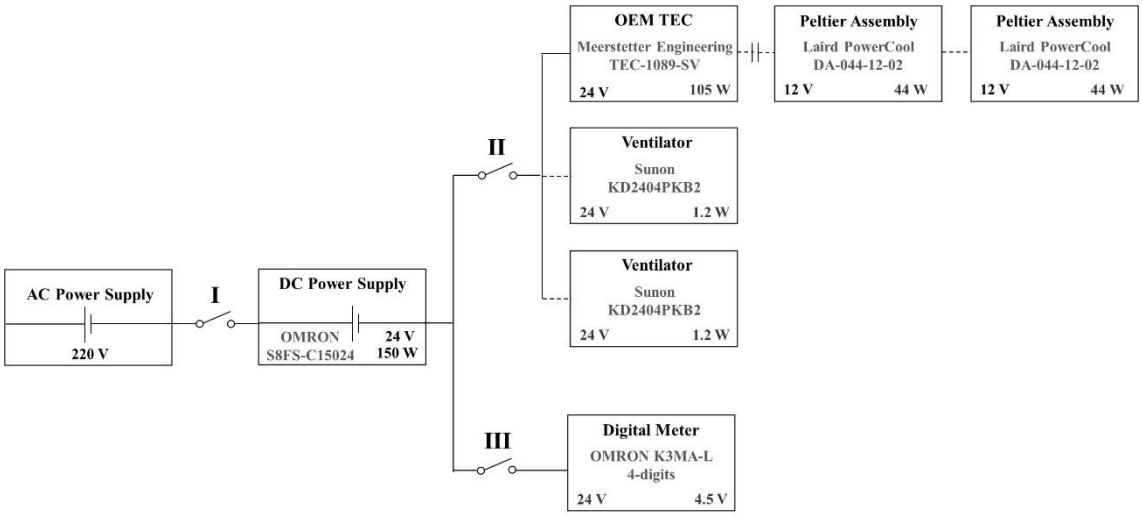



**Figure 4.41.** Schematic representation of the electrical configuration of the air bath control box. Straight lines: connections inside the Air Bath Control Box. Dashed Lines: connection from the Air Bath Control Box to the Air Bath Thermal Chamber. **I**: Main switch; **II**: Heating/cooling switch; **III**: Digital meter.

Fig. 4.42 presents an image of the Air Bath Control Box setup with identification of the main components.

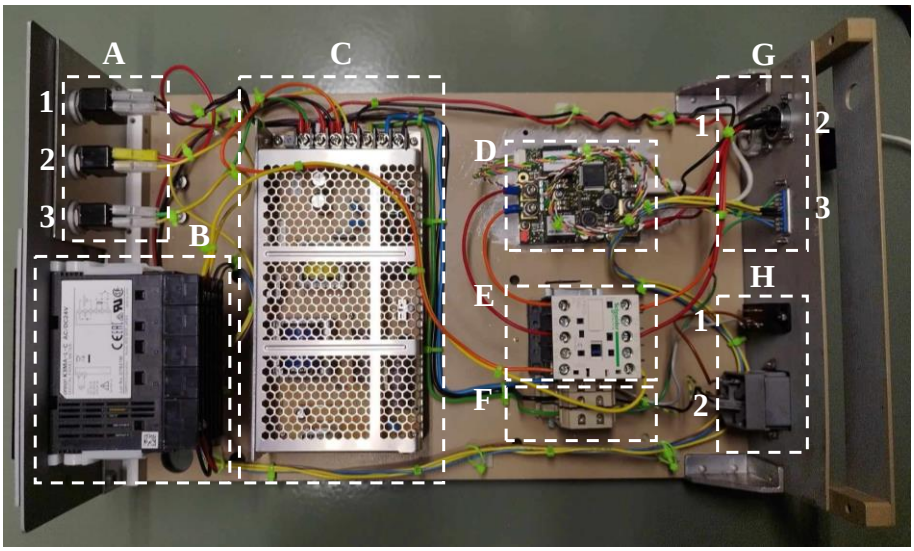



**Figure 4.42.** Image of the inside of the air bath control box. **A:** Switches, **a1** - Main, **a2** - Heating/Cooling, **a3** - Digital meter; **B:** Digital temperature meter; **C:** Power supply; **D:** OEM thermoelectric controller (TEC); **E:** Contactor; **F:** Connectors; **G:** Wiring outlets, **g1** - USB connection to the computer, **g2** - 4 pin plug connection to the Air Box Thermal Chamber), **g3** - DB15 plug connection to the Air Box Thermal Chamber; **H:** power inlet, **h1 -** voltage selector, **h2 -** connection to power source.

A more detailed image and description of the OEM thermoelectric controller is presented in Fig. 4.43.




**Figure 4.43.** Image of the TEC controller (TEC-1089-SV). **A:** Power supply 24 V; **B:** Power supply ground; **C:** USB connection with the computer; **D:** Microcontroller; **E:** Connectors to the Peltier element; **F:** Connector to object temperature sensor.

The temperature sensor connector CAB-6154 (Fig. 4.29 I) is prepared for two types of sensors: Pt-100, 4-wire configuration (pink, green, yellow, gray) and NTC, 2-wire configuration (brown, white). The Air Bath Thermal Chamber used Pt-100 sensors, so the 4-wire configuration was applied. A schematic representation of the wiring configuration of the temperature sensor connected is presented in Fig. 4.44.

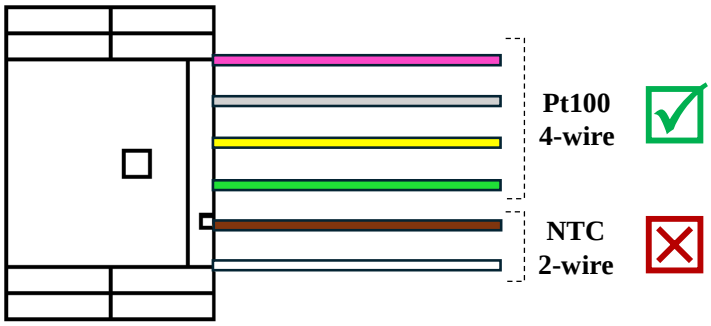



**Figure 4.44.** Schematic representation of the wiring configuration of the temperature sensor connector (CAB-6154).

Two cables were prepared to connect the Control Box to the Thermal Chamber. The first is a 4-wire cable that connects the 4-pin plug in the box (Fig. 4.42 G1) to the 4-pin military plug that connects to the Peltier assemblies. Since the used Peltier assemblies operate

at a voltage of 12 V and the used power source applies a voltage of 24 V, these modules were wired in series. The second cable connects the DB-15 plug in the box (Fig. 4.43 G3) to the 7-pin plug (Fig. 4.29 C) in the thermal chamber. This connection has three functions:

1. Power the internal ventilators;
2. Connect the OEM TEC to a temperature sensor (Pt100) inside the chamber;
3. Connect the Digital Meter to a temperature sensor (Pt100) inside the chamber;

The pinout and images of the inside of thermal chamber with highlights to the devices powered/connect via this cable are presented in the Appendix A.

### 4.4.3. Temperature Measurements and Thermal Stability

In the case of the Dip-in Cell setup, the glass vessel of the cell is inserted on the cell holder (Fig. 4.45 A). In the Coin Cell setup, the cell is first placed on a specially designed cell holder, which is then inserted into the chamber's cell site (Fig. 4.45 B). The Dip-in Cell setup carries three temperature sensors (Pt100):

1. Control Point: Pt100 located on the surface of one of the internal ventilators (Fig. 45 I). This sensor is connected to the OEM TEC and allows a fast response to temperature changes.
2. Measuring Point (Chamber): Pt100 is located on the surface of the chamber's cell site (Fig. 45 II). This sensor is connected to the OMRON LCD temperature reader on the electronic box and the Data Logger. The measured values are recorded by the dedicated ILDEM software (ILDEMSoft). This Pt100 is connected to the Data Logger in a 4-wire configuration by an 8-wire cable that connects to the 4-pin plug of the Thermal Chamber (Fig. 4.29 D).
3. Measuring Point (Cell): Pt100 is incorporated in the Metrohm conductivity cell (Fig. 45 III). This sensor is connected to the Data Logger and the measured values are recorded by the dedicated ILDEM software (ILDEMSoft). These are the values taken as the experimental temperature. The 2-wire cable of the commercial electrode configuration was then converted into a 4-wire configuration using a connection box built in the laboratory (Fig. 4.10 B).

The Coin Cell setup only carries the “control point” and “measuring point (chamber)” sensors. Therefore for this case, the values of experimental temperature are taken from the “measuring point (chamber)” sensor. The schematic representation of both the Dip-

in Cell and Coin Cell setups with the highlight to the location of each of the temperature sensors can be found in Fig. 4.45.

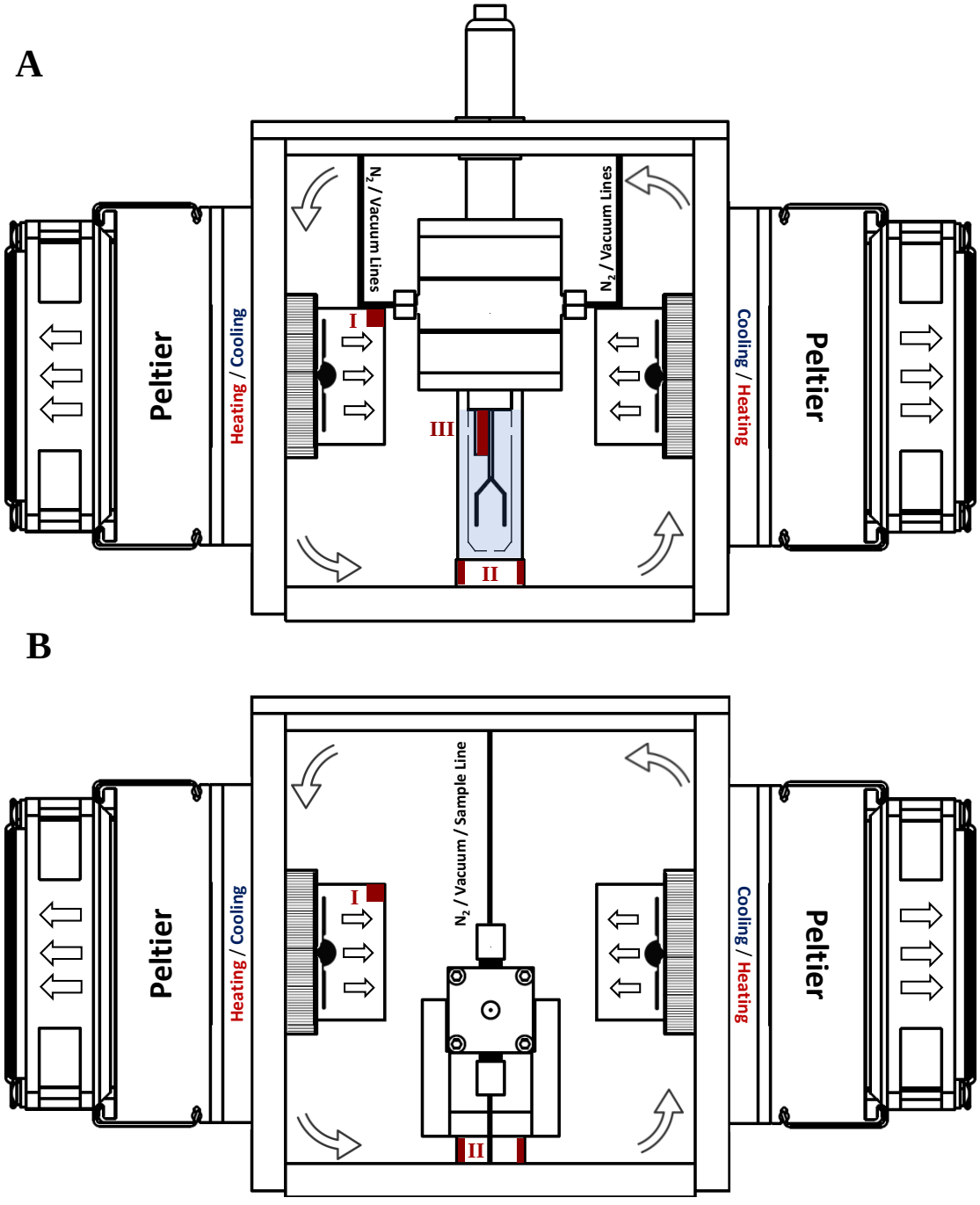



**Figure 4.45**. Schematic representation of the conductivity cells on the air bath thermal box. **A**: Dip-in cell; **B**: Coin cell. The red marks represent the Pt100 sensors, **I**: Pt100 placed on one of the internal ventilators (connected to the TEC OEM); **II**: Pt100 placed on the chamber's cell site (connected to the LCD temperature reader and the Data Logger); **III**: Dedicated Pt100 of the Metrohm conductivity cell (connected to the Data Logger). The arrows represent the air flow.

Images of the temperature sensors and the respective placements on the air bath thermal chamber are presented in Fig. 4.46.

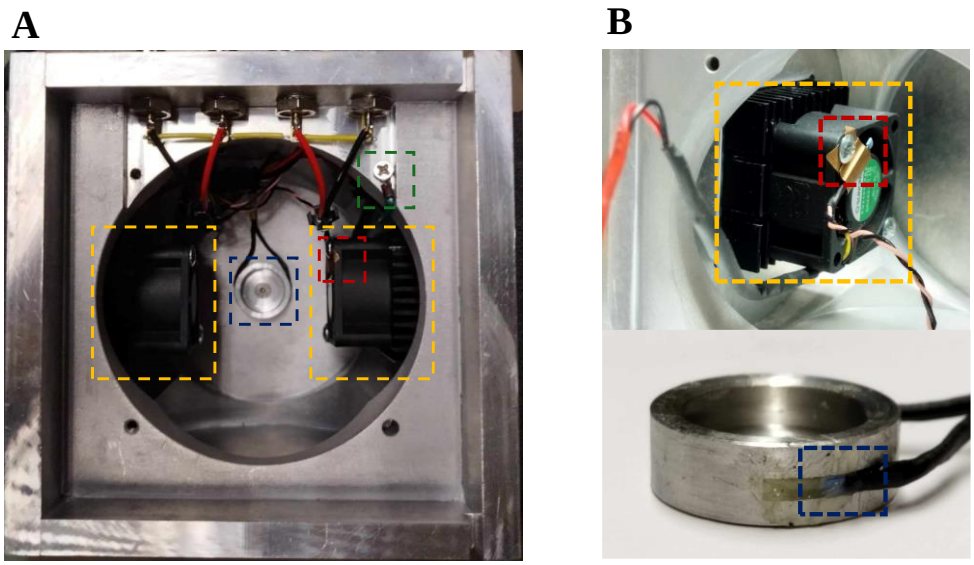



**Figure 4.46.** Images of the temperature sensors and the respective placement on the air bath thermal chamber. **A:** Wiring pinout; **B:** Interior of the Thermal Chamber; **C:** Images focused on the Pt100 temperature sensors. Ground; Internal ventilators; OEM TEC – Pt100; Digital Meter – Pt100. + and – represent the positive and negative terminals, respectively. The colored links between the pins represent the electrical pairings.

The Pt100 temperature sensors were calibrated using a 100 Ω secondary platinum resistance thermometer, Fluke SPRT 5626. The calibrations were performed by immersing the Fluke SPRT 5626 and Pt100 temperature sensors to be calibrated in a precision refrigerated/heating circulator (Julabo F25-MP) using an ethylene glycol solution bath. The calibration was performed by measuring the resistance of the Pt100 under calibration from 283 to 333 K (10 K steps) and correlating it with the real temperature measured by the secondary platinum resistance thermometer. The procedure was done in various sets (at least 3) and consisted of both cooling and heating ramps. The 273 K point was measured by preparing an ice bath in an aluminum dewar flask. The obtained calibration polynomial is presented in Table 4.2. The resulting coefficients were introduced on the ILDEM dedicated software to convert the resistance values recorded by the Data Logger into temperature data. The graphical representation of the residuals associated with the performed calibration is presented in Fig. 4.47.

**Table 4.2.** Coefficients of the Pt100 calibration curve.

| Function | $\frac{a \cdot 10^5}{K^{-3}}$ | $\frac{b \cdot 10^2}{K^{-2}}$ | $\frac{c}{K^{-1}}$ | $d$ |
|---|---|---|---|---|
| $T = aR^3 + bR^2 + cR + d$ | 6.01315 | 2.10086 | 0.164003 | 106.089 |

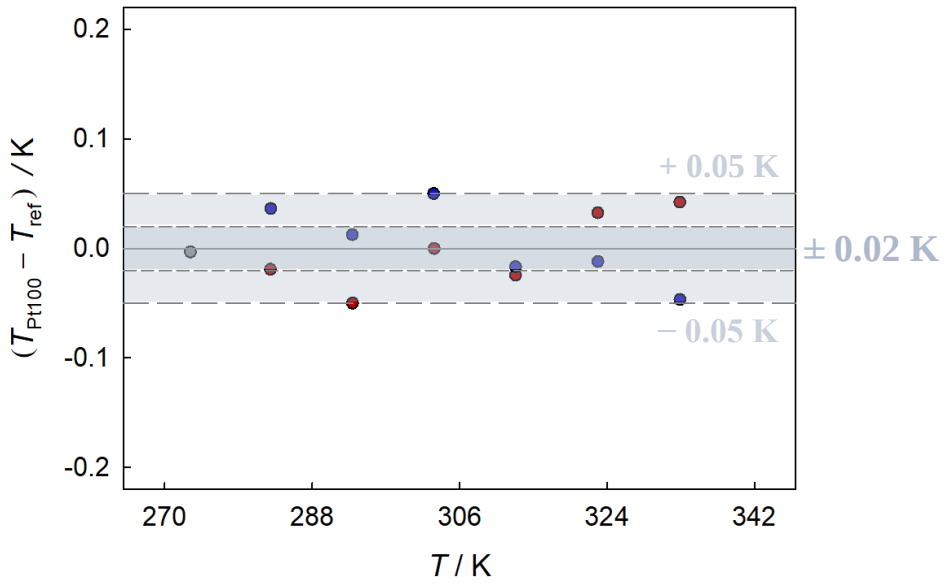



**Figure 4.47.** Residuals associated with the Pt100 calibration. • data recorded in cooling scans, • data recorded in heating scans, • 273 K point (ice bath).

The thermal stability of the air bath and the resolution of the temperature measurements were found to be ± 0.005 K with an accuracy of ± 0.02 K. The graphical representation of the long-term (5 h) thermal stability can be found in Fig. 4.48. The applied air bath methodology results in an excellent temperature control comparable to oil baths. This is mainly due to the high thermal inertia of the chamber due to its robustness and cork coating. The placement of the temperature sensors and inner ventilators also have positive effect on the homogeneous heat distribution and response to temperature changes, which ultimately enhances the thermal stability. However, the high thermal inertia of the chamber and the cell (PEEK block) leads to long thermal stabilization periods. Still this is a tolerable drawback since a high precision temperature control is essential to achieve high-accuracy electrical conductivity measurements.

Additionally, the utilization of a dry air bath offers a cleaner and more practical alternative to the oil baths while also preventing the stray capacitance effects typically associated with water baths.

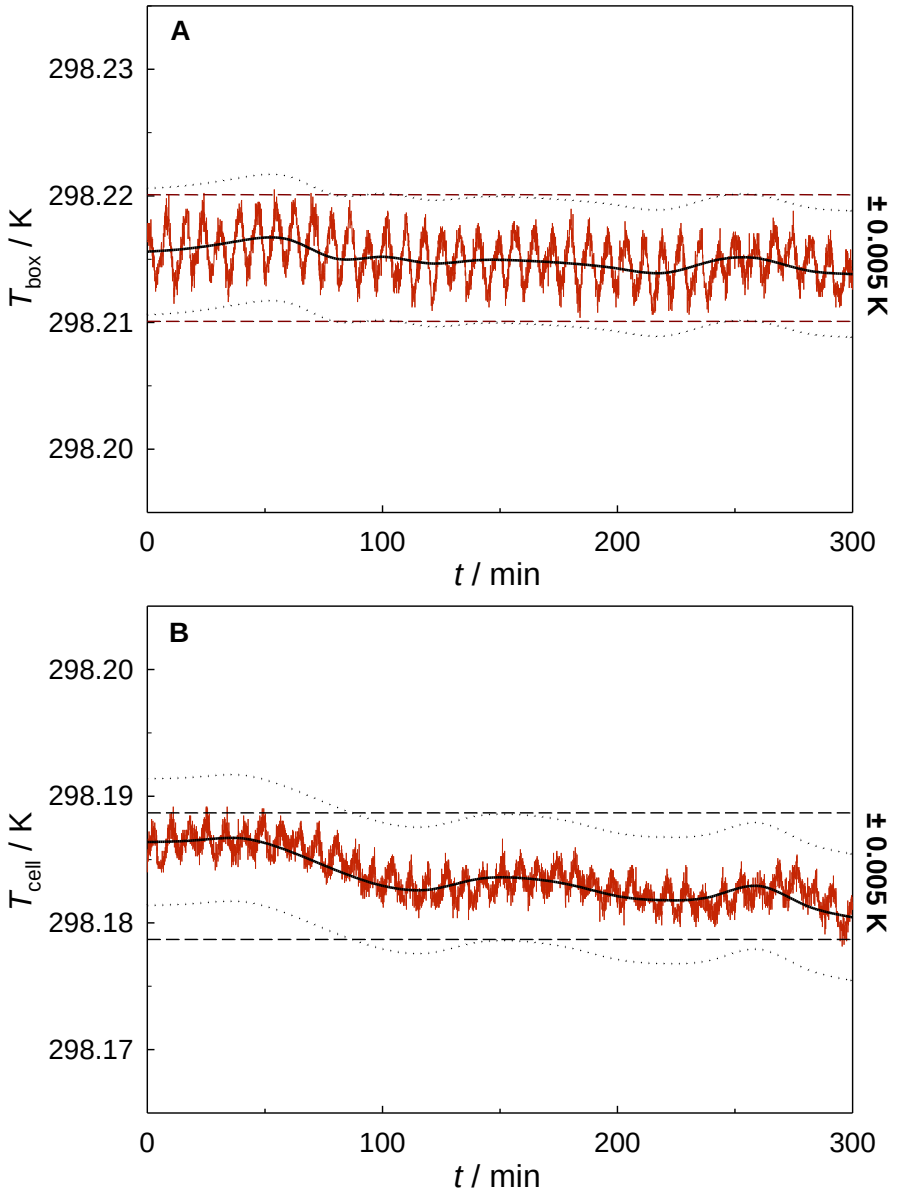



**Figure 4.48.** Long-term thermal stability on the air bath thermal chamber. **A:** temperature control inside the chamber (Pt100 on the cell site - measuring point chamber). **B:** temperature control inside the measuring cell (Pt 100 in contact with the sample - measuring point cell). Straight line: moving average considering a period of 20 min; Upper and lower deviation limits (0.005 K) to the average (dashed lines), moving average (dot lines).

## 4.5. ILDEM Software (ILDEMSoft)

A dedicated software application was developed for the automation, configuration, monitorization, and data acquisition of the ILDEM measurements, as well as for the treatment and analysis of the obtained raw data. The software application was developed in the VEE platform (Agilent, VEE Pro v. 9.0), and it consists of a package composed of four different modules:

1. Data Acquisition Module: main application used for measurement configuration and data acquisition.
2. Signal Monitoring Module: support application that runs simultaneously with the main application and it is used to check resistance and temperature stability.
3. Air Bath Regulator Module: application dedicated to the programming of the air bath thermal chamber. Runs simultaneously with the main application.
4. Data Analysis Module: application dedicated to the data treatment and analysis of the raw data. It is used to highlight key points on the impedance spectra, as well as apply and compare various resistance extrapolation procedures.

A schematic summary of the ILDEMSoft application and the respective modules is presented in Fig. 4.49.

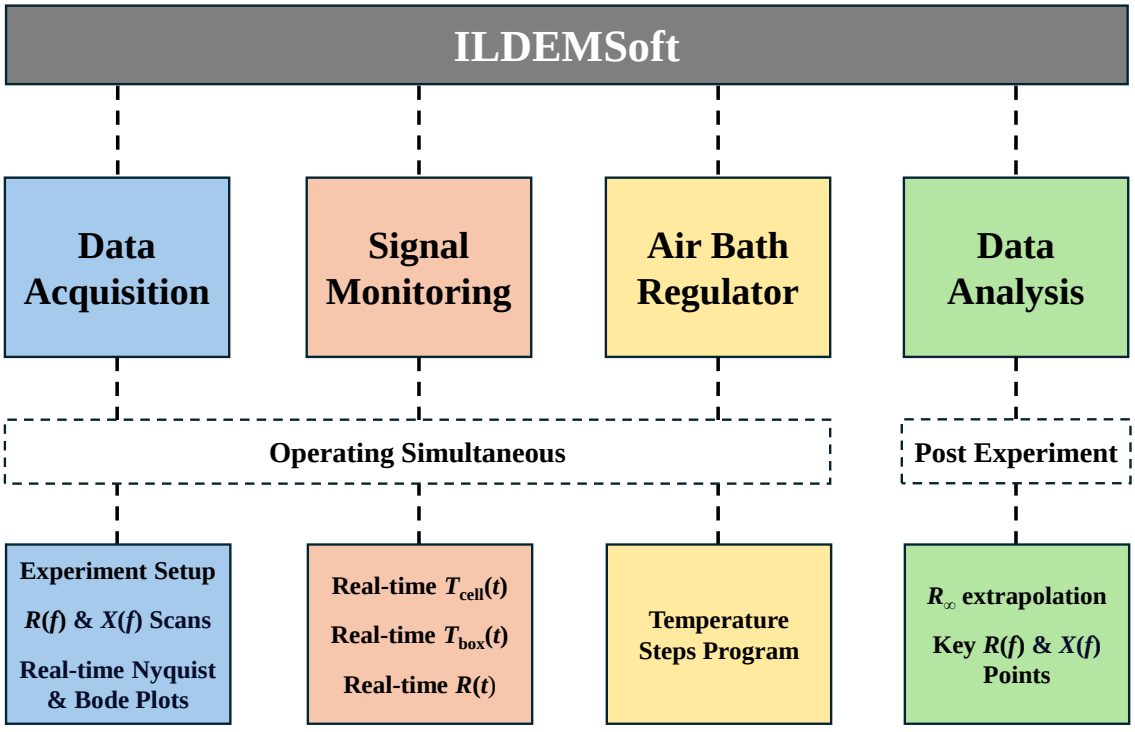



**Figure 4.49.** Schematic summary of the ILDEMSoft application.

### 4.5.1. Data Acquisition Module

The data acquisition module has two main functions: I) configuration of the measurement conditions and II) real-time data acquisition of the impedance spectra. In each measurement, the ILDEM apparatus measures the resistance and reactance of the sample through a pre-selected frequency range. A screenshot of the Data Acquisition Module interface is presented in Fig. 4.50.

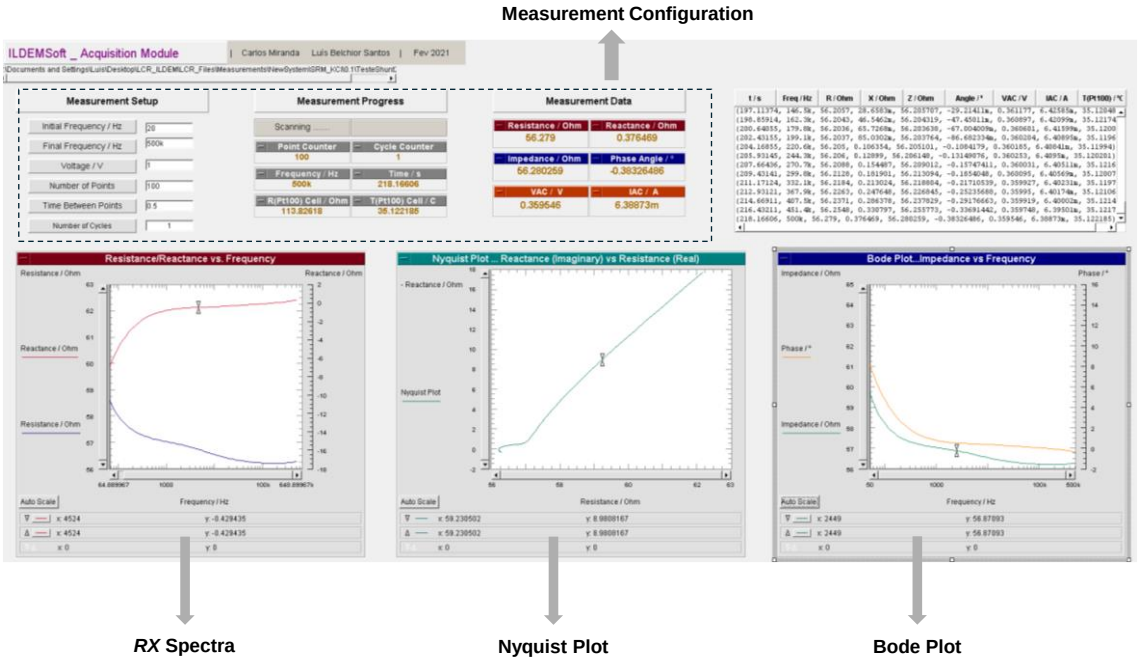



**Figure 4.50** Screenshot of the Data Acquisition Module interface.

Upon the initiation of this software application, the LCR meter Keysight E4980AL (impedance measurements) and the Agilent 34970A Data Logger (temperature measurements) are appropriately configured.

The Data Logger is connected to the computer via RS232, and two channels are active (channel 1: temperate inside the dip-in cell, channel 2: temperature inside the thermal chamber). When initiated, the software starts a timer and programs the device to remote mode (“SYSTEM: REMOTE”) so it can be controlled by the software and resets the device to the factory preset state (“*RST”). Then, the software configures the number of power line cycles performed (NPLC) of each channel successively with a wait interval of 1 s in between. Higher NPLC values decrease the instrumental noise and increase the time of the readings. Based on some practical tests, an NPLC equal to 20 was found to strike a good balance between accuracy and reading time.

The LCR meter is connected to the computer via USB. Similar to the Data Logger, upon initiation, the software starts a timer and programs the device to remote mode

("SYSTEM: REMOTE"), so it can be controlled by the software and reset the device to the factory preset state ("*RST"). The LCR can operate under different functions, with each measuring/displaying two main electrical properties. For the ILDEM apparatus, the "*RX*" function, which presents the resistance and reactance of the DUI, was found to be the most appropriate. However, the software is prepared to automatically calculate the impedance and phase of the angle based on the *R* and *X* data. Furthermore, using this module, it is possible to select the desired measurement conditions, particularly:

1. Initial frequency, $f_i$
2. Final frequency, $f_f$
3. Number of frequency points
4. Interval between each point
5. Number of cycles (frequency scans from $f_i$ to $f_f$)
6. Applied voltage level
7. Stabilization time

Upon the selection of the frequency range and the number of frequency points, the software application determines the frequency points to be measured based on logarithmical increments. In a typical experiment, the full operating frequency range of the LCR is used (20 Hz – 500 kHz) to derive a complete insight into the processes/phenomena/effects occurring across the whole interval (low frequency, conductive regime, and high frequency). A number of frequency points of 200 was found to be a good compromise between acquisition time and spectra definition. Usually, five frequency scans are performed for each temperature step to evaluate the stability and reproducibility of the measurements. During the process of condition optimization, different voltage levels were tested (10 mV, 100 mV, and 1 V). The voltage of 1 V was found to be preferred due to presenting a significant improvement in sign quality compared to 10 mV and 100 mV. The stabilization time corresponds to the period of thermal stabilization in between temperature steps. During this period, this application is in standby, and the data acquisition of frequency scans starts automatically once the designated stabilization time is up. Upon termination of the selected number of frequency cycles, the Data Acquisition Module enters once again on standby for the thermal stabilization of the next temperature step.

For each scan, the program continuously records the time, frequency, resistance, reactance, impedance, phase angle, AC voltage, AC current, and temperature. This information is simultaneously presented on the software interface (text log form and graphical representation) and stored in a .txt file for posterior treatment and analysis. In the software interface, it is possible to observe the real-time generation of the RX-spectra: $R(f)$ and $X(f)$, Nyquist Plot: $R(X)$, and Bode Plot: $Z(f)$ and $\theta(f)$. The name of the .txt file is automatically generated based on some pre-written specifications, such as sample name, date, and temperature. For clarity purposes, in experiments where multiple temperatures are studied, a different .txt file is generated for each temperature. The summary of the features and operational procedures of the Data Acquisition Module is schematically represented in Fig. 4.51.

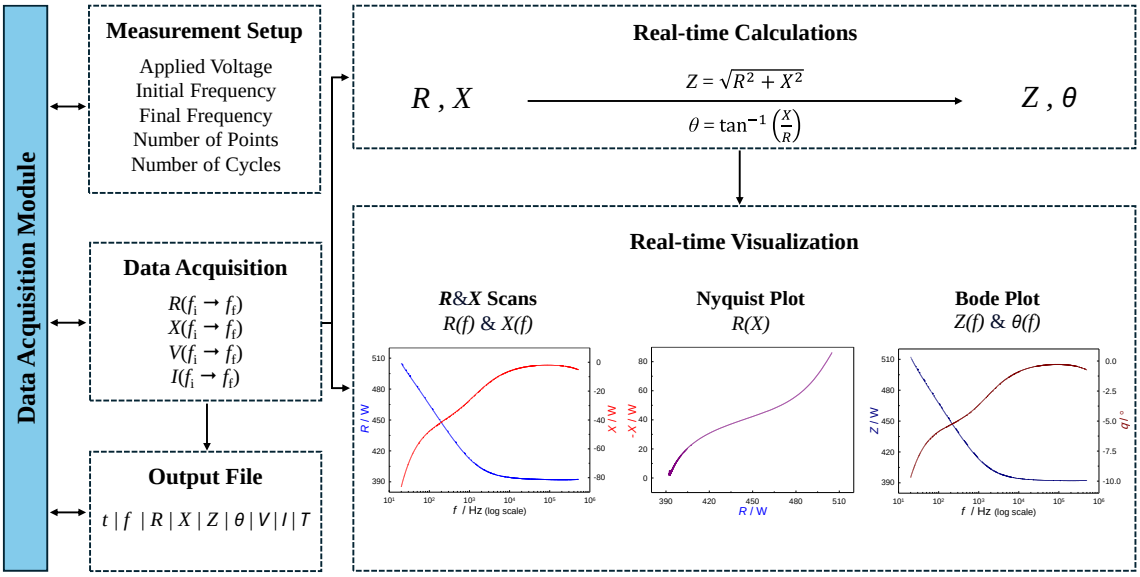



**Figure 4.51** Schematic representation of the features and operational procedure of the Data Acquisition Module.

### 4.5.2. Signal Monitoring Module

The Signal Monitoring Module is a support application for the Data Acquisition Module. A screenshot of the Signal Monitoring Module interface is presented in Fig. 4.52.

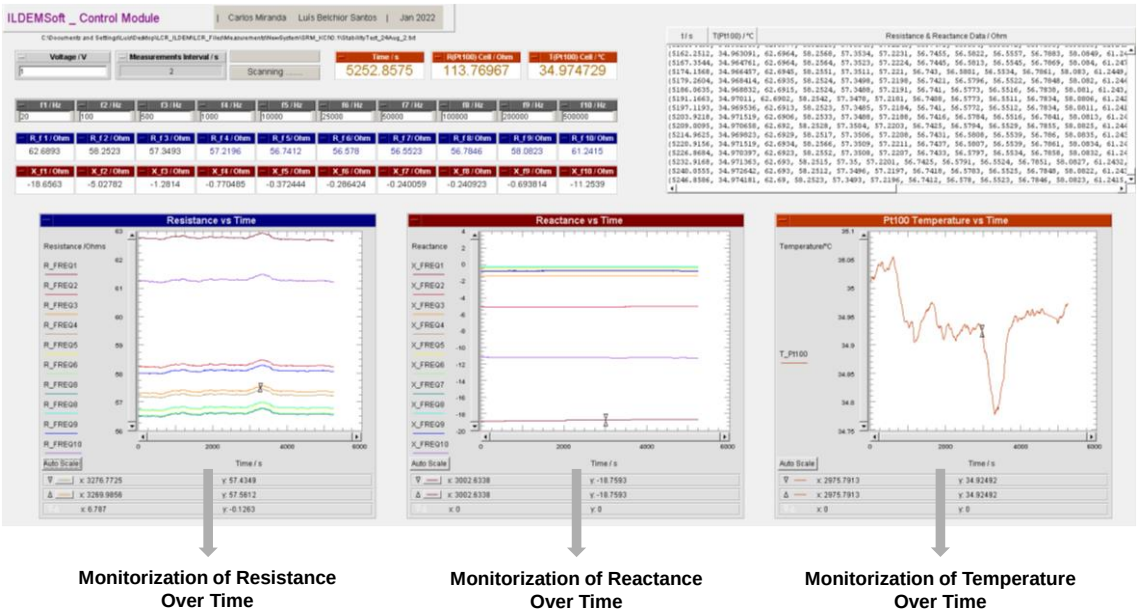



**Figure 4.52.** Screenshot of the Signal Monitoring Module interface.

It is configured in a very similar way to the main application. However, in this case, instead of performing *RX* cycles, the resistance and reactance at ten pre-selected frequencies, as well as the cell/box temperature, are measured over time to evaluate the stabilization of the signal. Contrary to the main application, the Signal Monitoring Module records for the entirety of the experiment, allowing the verification of the occurrence of any anomaly during the measurements. The time, temperature, resistance, and reaction for each of the ten selected frequencies are simultaneously presented on the software interface (text log form and graphical representation) and stored in a .txt file. The instance shows the real-time generation of the overtime stability of resistance, reactance, and temperature. The summary of the features and operational procedures of the data acquisition module is schematically represented in Fig. 4.53.

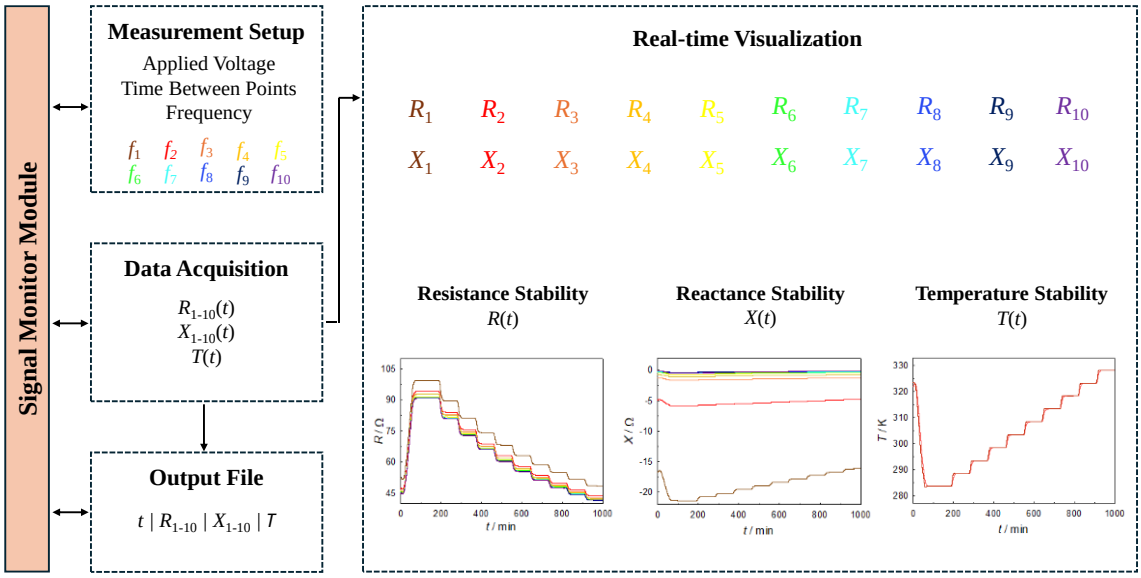



**Figure 4.53.** Schematic representation of the features and operational procedure of the Signal Monitoring Module.

### 4.5.3. Air Bath Regulation Module

The Air Bath Regulator Module is an application dedicated to the control of the air bath thermal chamber. A screenshot of the Air Bath Regulation Module interface is presented in Fig. 4.54.

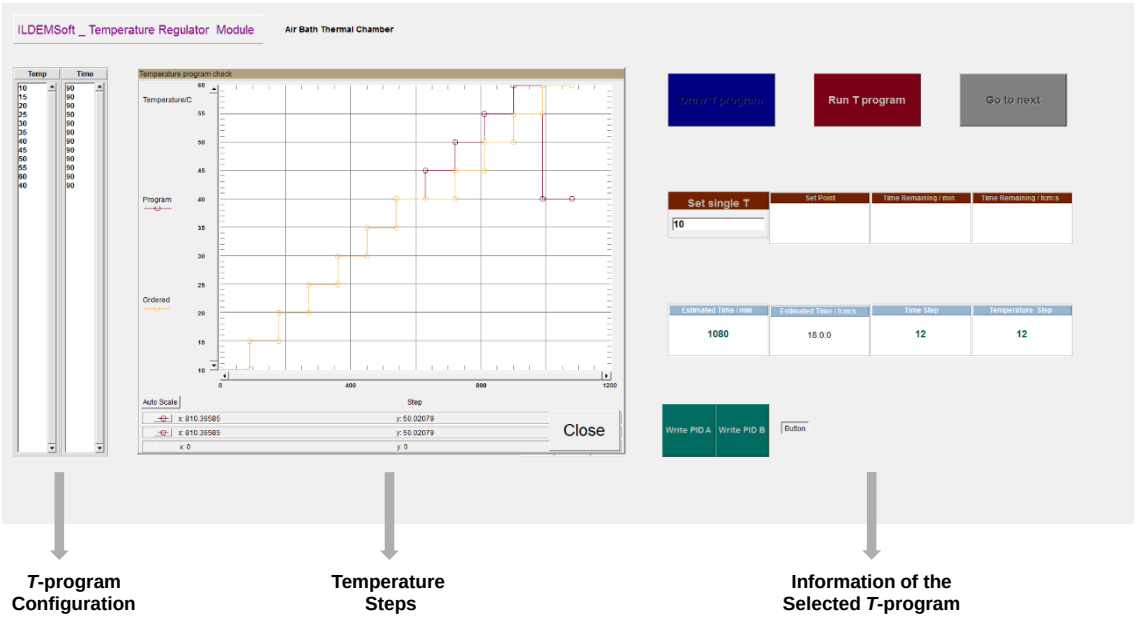



**Figure 4.54.** Screenshot of the Air Bath Regulation Module interface.

The OEM TEC located on the electronic box (as described above) is connected to the computer via USB. The dedicated communication protocol of OEM TEC (MeCom, written in hexadecimal format) was incorporated into the software application to allow the writing of PID parameters and the introduction of a customized temperature program. The optimal PID parameters were first found using the "PID Auto-tuning" feature of the official TEC Service Software from Meerstetter Engineering. In the software interface, it is possible to generate customizable temperature programs (with graphical visualization) by introducing the desired temperature and the time for each temperature step. Additionally, the interface also presents information relative to the experiment's progress, such as total time, lapsed time, and current step. The summary of the features and operational procedures of the Air Bath Regulation Module is schematically represented in Fig. 4.55.

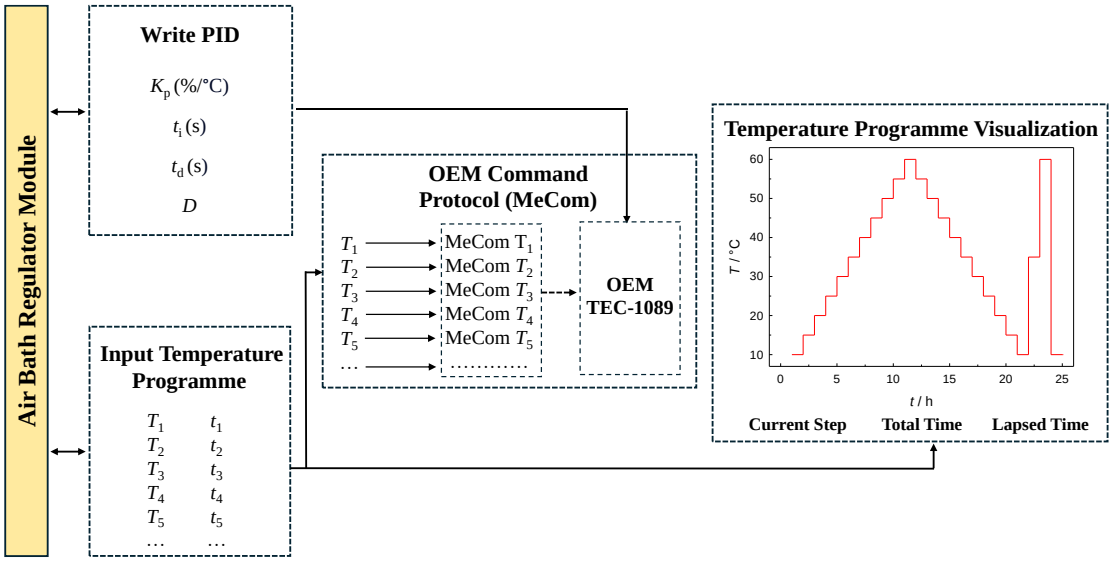



**Figure 4.55.** Schematic representation of the features and operational procedure of the Air Bath Regulation Module.

### 4.5.4. Data Analysis Module

The Data Analysis Module is a software application dedicated to the treatment and analysis of the ILDEM raw data. A screenshot of the Data Analysis Module interface is presented in Fig. 4.56.

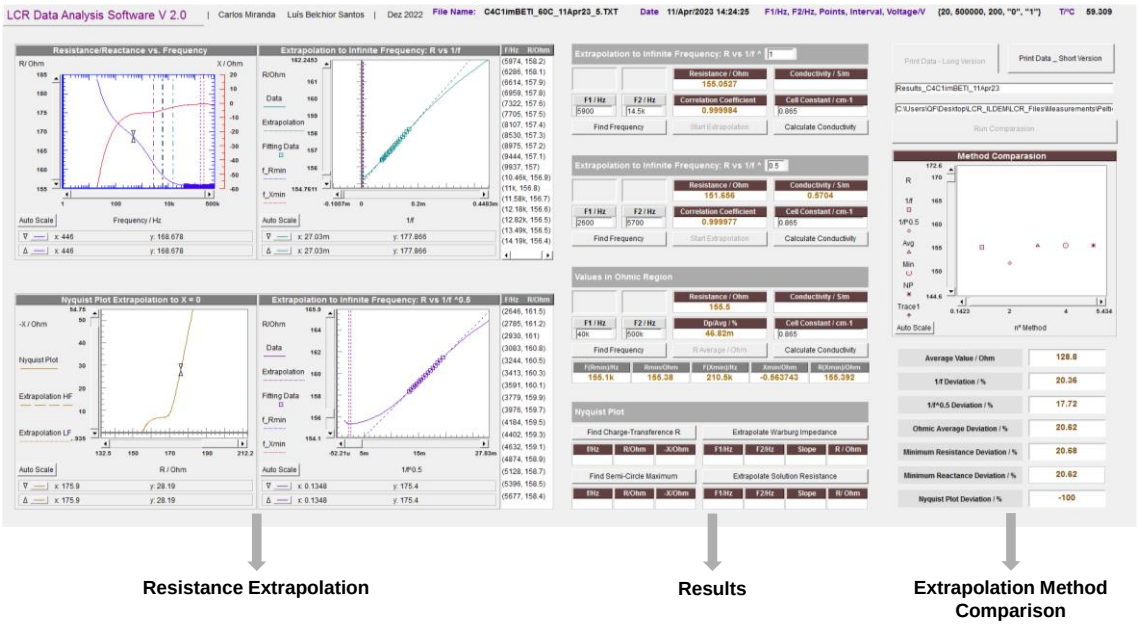



**Figure 4.56.** Screenshot of the Data Analysis Module interface.

This program reads the .txt file generated by the Data Acquisition Module and presents the raw data in various appropriate representations, such as RX-spectra and Nyquist Plot. The application automatically highlights key points of the spectra, particularly, resistance minimum ($R_{min}$) and reactance minimum ($X_{min}$). The application also allows the calculation of the resistance average in a selected frequency range, which is particularly useful to determine the resistance in the ohmic region (region of resistance *plateau*). The main feature of the Data Analysis Module is the incorporation of different analytical methods to calculate the corrected (no polarization effect) resistance of the solution. The resistance is extrapolated to infinite frequency by selecting the appropriate frequency range and applying the following fitting equation (Eq. 4.13)

$$R(1/f^{\alpha}) = \frac{A}{f^{a}} + R_{\infty} \qquad (4.13)$$

where *a* can be equal to 0.5, 1, or 2 depending on which yields the best fitting. The current setup of the Data Analysis Module offers two graphs for the representation of $R(1/f^{a})$. This module also has a feature to extrapolate the Nyquist Plot the x-axis interception (reactance, *X*, equals 0). The frequency ranges for each of these extrapolations are automatically highlighted on the RX-spectra for clarity purposes.

Furthermore, a comparison function is also incorporated to compare the resistance values obtained from each method and evaluate their validity relative to the key points: resistance minimum ($R_{min}$), resistance at minimum reactance ($R(X_{min})$), and average resistance at the ohmic region ($R_{ohm}$). The final extrapolation results are printed into a new .txt file. The summary of the features and operational procedures of the Data Analysis module is schematically represented in Fig. 4.57.

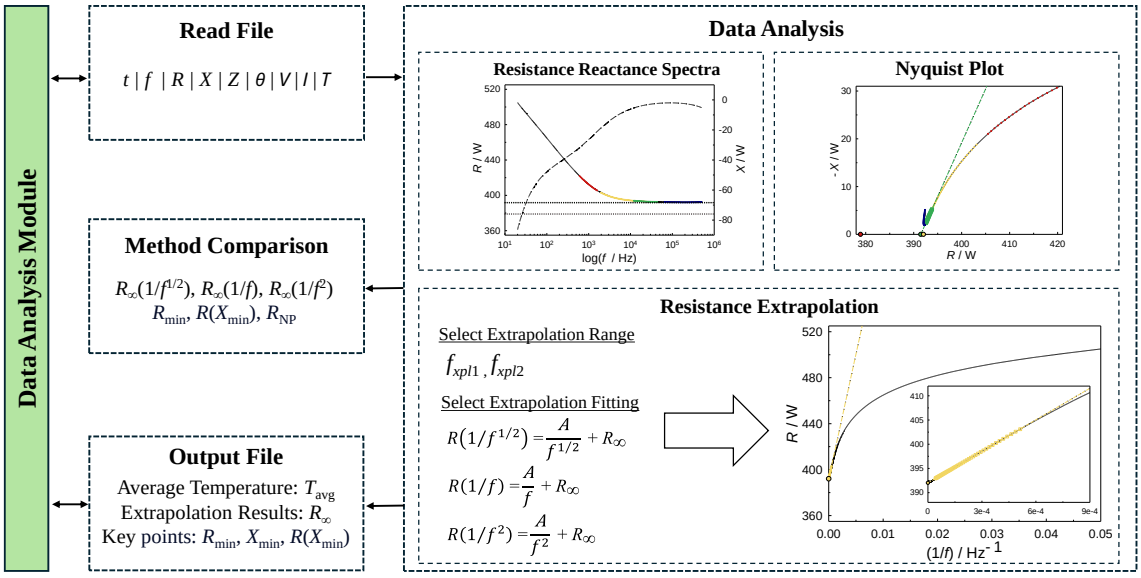



**Figure 4.57.** Schematic representation of the features and operational procedure of the Data Analysis Module.

## 4.6. Accuracy and Performance

The cell constants of the Dip-in and Coin conductivity cells were experimentally determined by measuring the electrical resistance of a standard aqueous potassium chloride solution 0.1000 mol/kg, as recommended by Barthel *et al.* [1]. The solutions used in this work were gravimetrically prepared with potassium chloride Suprapur® 99.999% from Merck KGaA (CAS-No. 7447-40-7) and Milli-Q® ultrapure water (resistivity of 18.2 MΩ·cm). The cell constants, $c$, were then calculated based on the reference values of electrical conductivity, $\sigma_{ref}$, for the solution recommended by IUPAC [2], and the experimentally measured resistance of the KCl solutions, as described by Eq. 4.14.

$$c = R \cdot \sigma_{ref} \qquad (4.14)$$

The performance and accuracy of both cells for the measurement of electrical conductivity were evaluated by measuring the 1-hexyl-3-methylimidazolium bis(trifluoromethylsulfonyl)imide, $[^1C_6{}^3C_1im][NTf_2]$. This IL is recommended by NIST as a reference for the measurement of various physicochemical properties of ionic liquids [45]. The sample used in this work was commercially obtained through IoLiTec with a mass fraction purity higher than 99%. The detailed description of the preparation of the potassium chloride solution and the purification of the IL sample can be found in Chapter 2 – Materials sections 2.4 and 2.2, respectively. In the case of the Coin Cell, the experimental verification of the cell constant and the performance test with $[^1C_6{}^3C_1im][NTf_2]$ were performed for all four types of electrodes (SS, SSTiN, Ni, and Pt). The uncertainty associated with the experimental results of electrical conductivity was attributed based on Eq. (4.15):

$$u_\sigma = \sqrt{u_c{}^2 + u_m{}^2 + u_e{}^2} \tag{4.15}$$

$\boldsymbol{u_\sigma}$: uncertainty associated with the experimental electrical conductivity data;
$\boldsymbol{u_c}$: uncertainty associated with the determination of the cell constant;
$\boldsymbol{u_m}$: uncertainty associated with the ILs measurements;
$\boldsymbol{u_e}$: uncertainty associated with the extrapolation of the infinite frequency resistance, $R_\infty$.

### 4.6.1. Dip-in Cell

The representation of the typical impedance spectra, as well as the procedure followed for the determination of the corrected ionic liquid resistance, can be found in Fig. 4.58. This figure presents the typical functions and frequency regions used for the extrapolation of $R_\infty$ based on Eq. 2.34. A method based on the extrapolation of *x*-axis interception on the Nyquist Plot (resistance when reactance equals zero) was also added to serve as a base of comparison with the $R_\infty$ results. Overall, the $1/f$ functional yields extrapolation results closer to the selected reference(*plateau* values) as the $1/f^{1/2}$functional tends to present a slight negative deviation (around −1%).

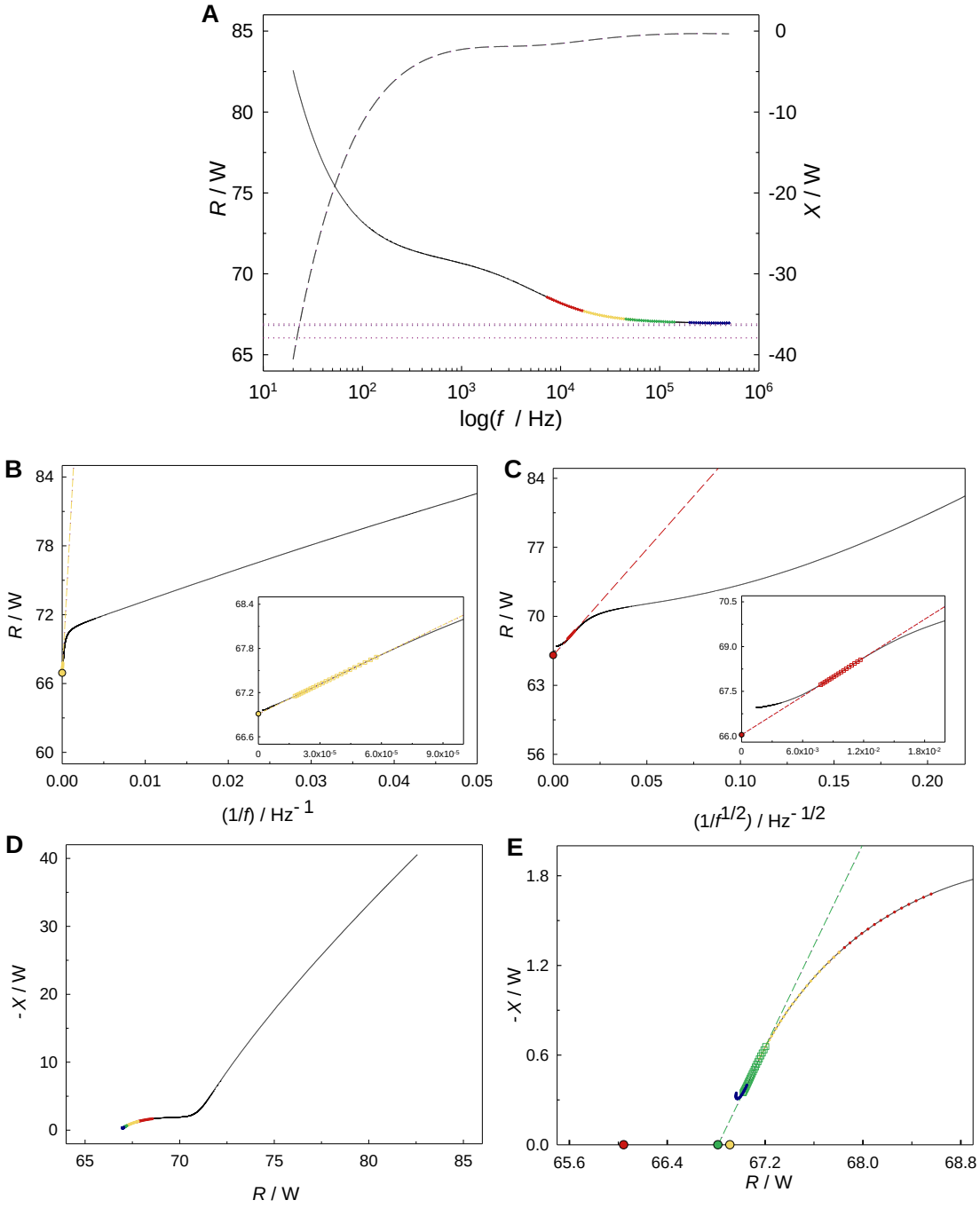



**Figure 4.58.** Representation of the typical resistance/reactance spectra and procedure for the extrapolation of $R_\infty$ for the standard aqueous 0.1000 mol·kg$^{-1}$ KCl solution. **A** - Resistance (straight line) and reactance (dashed line) as function of frequency; **B** - Extrapolation of $R_\infty$ based on equation $R(1/f) = a/f + R_\infty$ ; **C** - Extrapolation of $R_\infty$ based on equation $R\left(1/f^{1/2}\right) = a/f^{1/2} + R_\infty$; **D** - Nyquist plot; **E** - Estimation of solution resistance by Nyquist plot, $R(X = 0)$, comparison with $R_\infty$ derived from $1/f$ and $1/f^{1/2}$.

The experimental results obtained from the experiments of cell constant determination are graphically presented in Fig. 4.59. The average cell constant value was found to be

$c_{avg}$ = 0.865 $cm^{-1}$ (~8% deviation to the nominal 0.8 $cm^{-1}$ value indicated by the brand), and the experimental results were found to be within an uncertainty range of ± 0.5%.

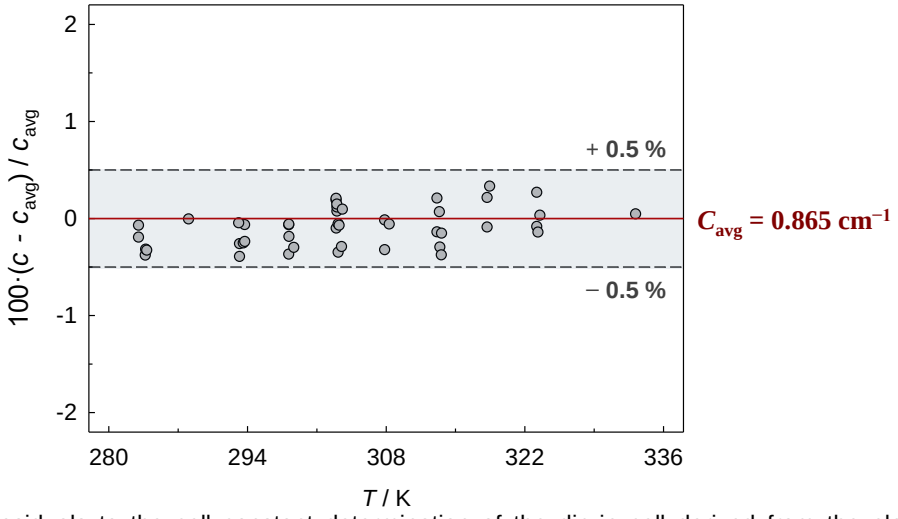



**Figure 4.59.** Residuals to the cell constant determination of the dip-in cell derived from the electrical resistance measurement of a standard aqueous 0.1000 mol·$kg^{-1}$ KCl solution.

Figure 4.60 presents the typical resistance and reactance spectra obtained for $[^1C_6{}^3C_1im][NTf_2]$ at different experimental temperatures. As observed, the reactance spectra presents two peaks: the one at higher frequencies corresponds to the ohmic conduction region where the value of imaginary impedance approaches zero ( X → 0) and the real impedance reaches a *plateau*; the low-frequency peak is likely related to the interfacial processes between the ionic liquid and the electrode surface. This peak becomes less clear with the increase in temperature (decrease in resistivity). Additionally, the resistance and reactance spectra tend to shift to higher frequencies with the increase in temperature, which impacts the appropriate frequency range for resistance extrapolation. Similar observations have been reported in literature and are usually attributed to the effect of temperature on the relaxation times of the electrochemical processes (higher temperatures → lower relaxation times) [3, 4].

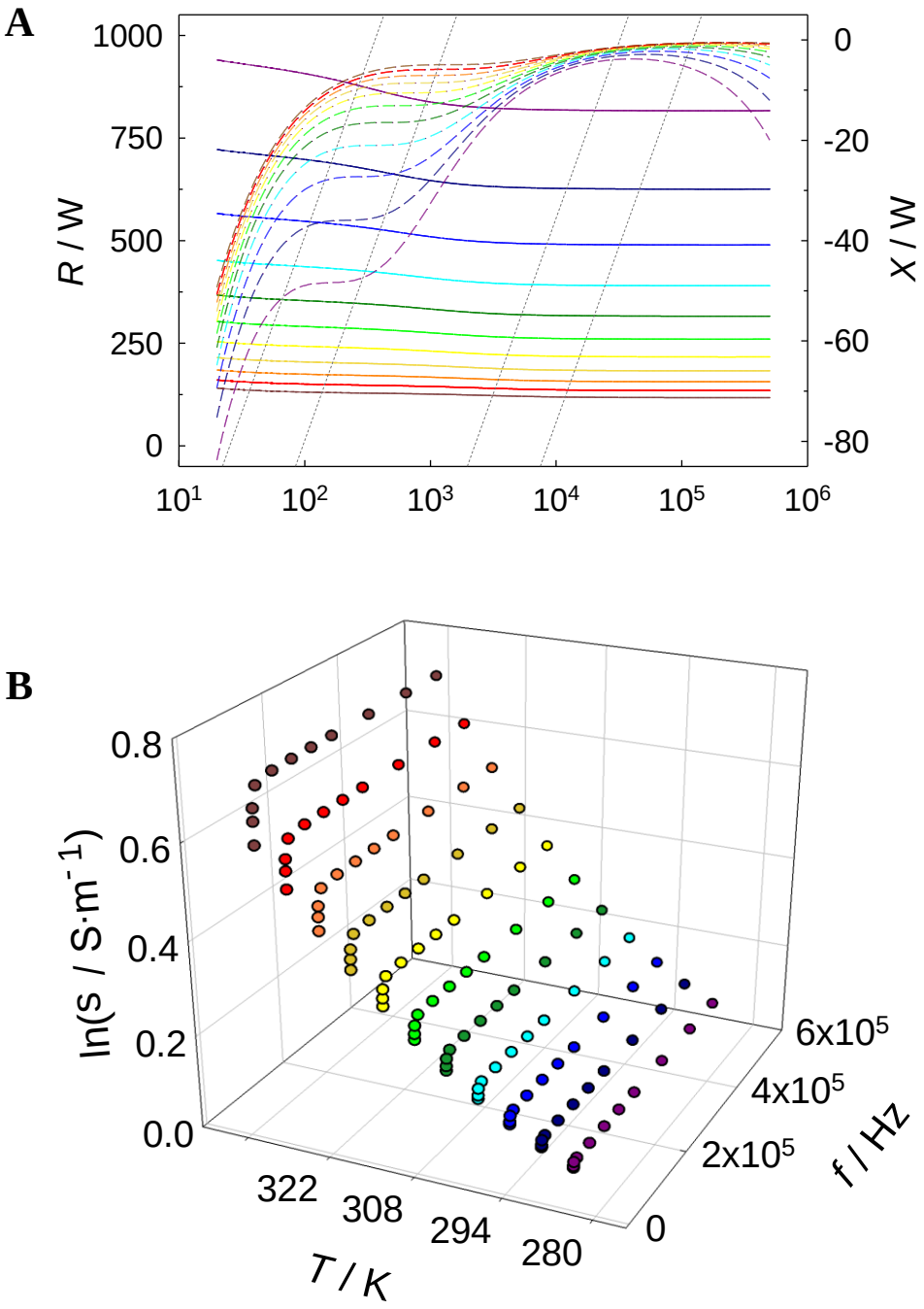



**Figure 4.60.** Typical impedance spectra for [$^{1}C_{6}{}^{3}C_{1}$im][$NTf_2$] at different experimental temperatures (283 – 333 K). **A:** Resistance (straight lines) and reactance (dashed lines) as functions of frequency (log scale). **B:** Electrical conductivity-frequency-temperature 3D plot. *T* / K = 283, 288, 293, 298. 303. 308, 313, 318, 323, 328, 333.

The representation of the typical impedance spectra, as well as the procedure followed for the determination of the corrected ionic liquid resistance, can be found in Fig. 4.61. The utilization of the functional with $1/f$ seems to yield a better fit of the obtained experimental data compared to the approach using $1/f^{1/2}$, as the former allows an extrapolation in a larger range of frequencies. Additionally, the slight discrepancy between the extrapolation presented in the previous section seems to be more significant and consistent in this case. The results obtained based on the $1/f$ functional are in good agreement with the resistance estimated by the Nyquist plot and the resistance *plateau* in $R(f)$ (deviation of 0.1%). Meanwhile, the functional $1/f^{1/2}$yields significant negative deviations from the plateau values (around −3%). Further analysis showed that this is consistent for all the ionic liquids studied in this work, and the negative deviation yielded by the $1/f^{1/2}$functional seems to be larger for more resistive systems. This is coherent with the smaller differentiation seen for the KCl 0.1000 mol·kg$^{-1}$ solutions. Procedures based on either linear or quadratic regression using the $1/f^2$ functional were also assessed, but it was found that these functions do not accurately describe the obtained experimental results.

The graphical comparison of the experimental results with the recommended literature data in the studied temperature range can be found in Fig. 4.61. Additionally, the values of the coefficients of the fitting obtained through each method are presented in Table 4.3, together with the recommended fitting parameters [5].

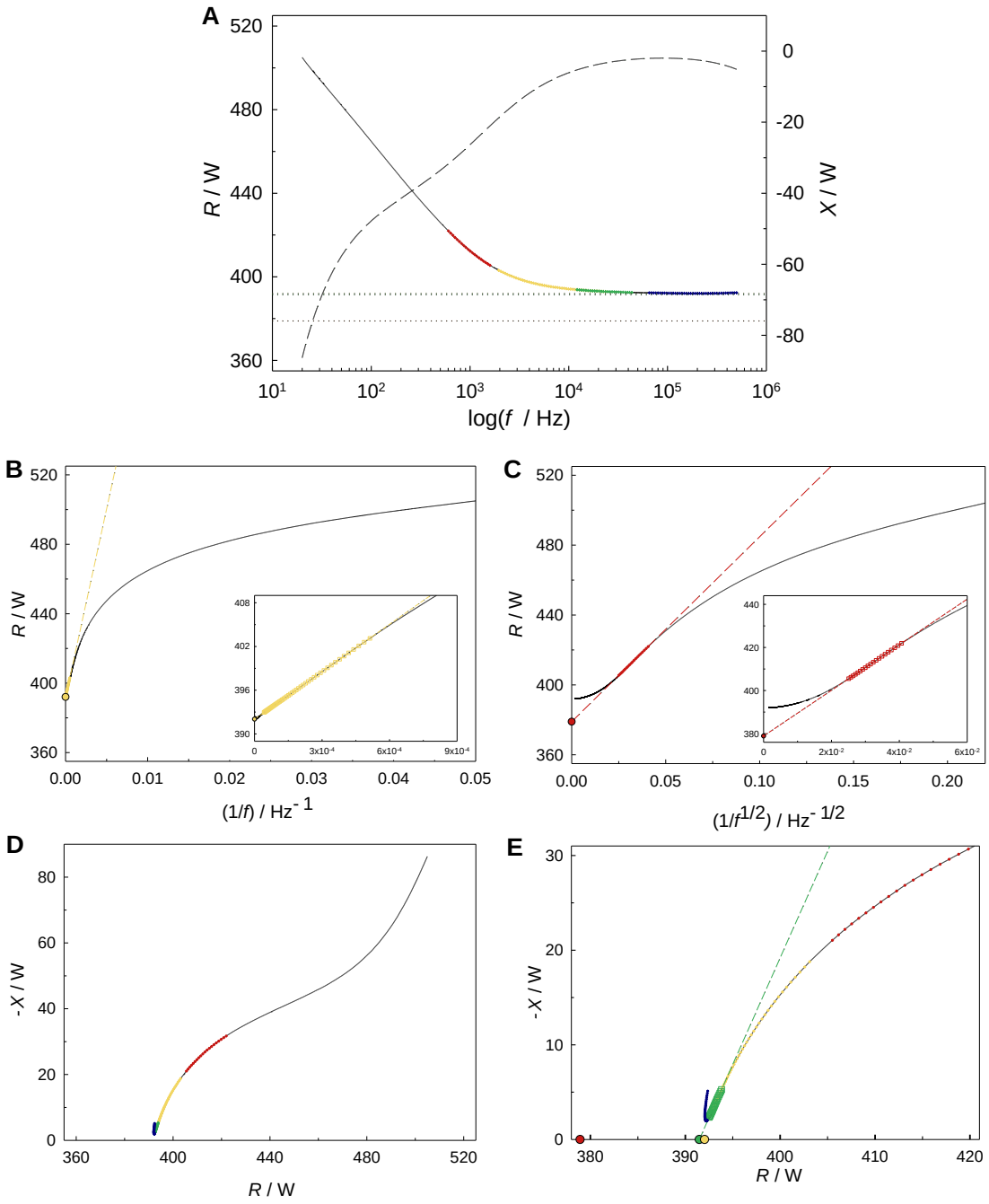



**Figure 4.61.** Representation of the typical resistance/reactance spectra and procedure for the extrapolation of $R_\infty$ for the $[^1C_6{}^3C_1im][NTf_2]$. **A** - Resistance (straight line) and reactance (dashed line) as function of frequency; **B** - Extrapolation of $R_\infty$ based on equation $R(1/f) = a/f + R_\infty$ ; **C** - Extrapolation of $R_\infty$ based on equation $R\left(1/f^{1/2}\right) = a/f^{1/2} + R_\infty$; **D** - Nyquist plot; **E** - Estimation of solution resistance by Nyquist plot, $R(X = 0)$, comparison with $R_\infty$ derived from $1/f$ and $1/f^{1/2}$.

Fig. 4.62 presents the comparison between the applied resistance correction methods and the values recommended by NIST [5]. The results using the $1/f$ functional are in excellent agreement with the resistance *plateau* and are within the uncertainty recommended by NIST [5], while the conductivity results obtained from the $1/f^{1/2}$ functional present a positive deviation. This suggests that the latter method leads to an overestimation of the electrical conductivity. Fig. 4.62B presents the residual representation of each individual experiment to the overall experimental fitting, showing a deviation lower than 1%. Fig. 4.62C and 4.62D present a graphical comparison of the experimental results to the available literature data. Apart from Leys *et al.* [6], who used dielectric spectrometry, and Calado *et al.* [7], who used a customized conductance bridge, the presented literature data corresponds to measurements using commercial LCR meters [8-11] or commercial impedance analyzers [12-15]. In the majority of cases, the resistance was stated to have been corrected or polarization effects by extrapolation to infinite frequency [8-12, 7]. The results obtained from the $R(1/f) = a/f + R_\infty$ are slightly more in agreement with the literature, with most of the data points being contained within the ± 5% uncertainty range. The data from Leys *et al.* [16] present significant positive deviations from our data and the rest of the presented literature, which is likely due to the usage of a distinct measurement method. Based on previous analysis, the following presented electrical conductivity results concerning the other studied ILs correspond to calculations based on the extrapolation of $R_\infty$ using the $R(1/f) = a/f + R_\infty$ functional.

**Table 4.3.** Derived VFT coefficients, using different polarization correction models, applied experimental electrical conductivity data for $[^1C_6{}^3C_1im][NTf_2]$.

| Method | $\frac{A_\sigma}{S\cdot m^{-1}}$ | $\frac{B_\sigma}{K}$ | $\frac{C_\sigma}{K}$ | $\frac{\sigma(T=298.15\ K)}{S\cdot m^{-1}}$ |
|---|---|---|---|---|
| $R = 1/f^{1/2} + R_\infty$ | 55.39 ± 0.68 | 675.9 ± 3.4 | 173.1 ± 0.3 | 0.2485 ± 0.0037 |
| $R = 1/f + R_\infty$ | 56.97 ± 0.88 | 690.6 ± 4.3 | 173.7 ± 0.4 | 0.2217 ± 0.0033 |
| $R_{min}$ [a] | 57.84 ± 0.75 | 692.7 ± 3.6 | 173.7 ± 0.4 | 0.2209 ± 0.0033 |
| $R(X_{min})$ [a] | 57.68 ± 0.76 | 690.7 ± 3.7 | 173.7 ± 0.4 | 0.2208 ± 0.0033 |
| NIST [b] | 54.427 ± 0.419 | 691.07 ± 3.21 | 173.11 ± 0.45 | 0.21655 ± 0.00866 |

**a** - Corresponds to the resistance on the region of *plateau* $R(f)$ dependence (ohmic behavior). $R_{min}$: minimum resistance value in the *plateau* region; $R(X_{min})$: value of resistance at the frequency of minimum reactance.
**b** – Data recommended by NIST, Paredes *et al.* 2020 [5]. The values of $\sigma(T=298.15\ K)$ were calculated from the VFT fitting (Eq. 6) based on the experimental data. The standard uncertainties related to the VFT coefficients and $\sigma$ were calculated to the confidence level 0.95 ($k \approx 2$), $u(\sigma) = 1.5\%$.

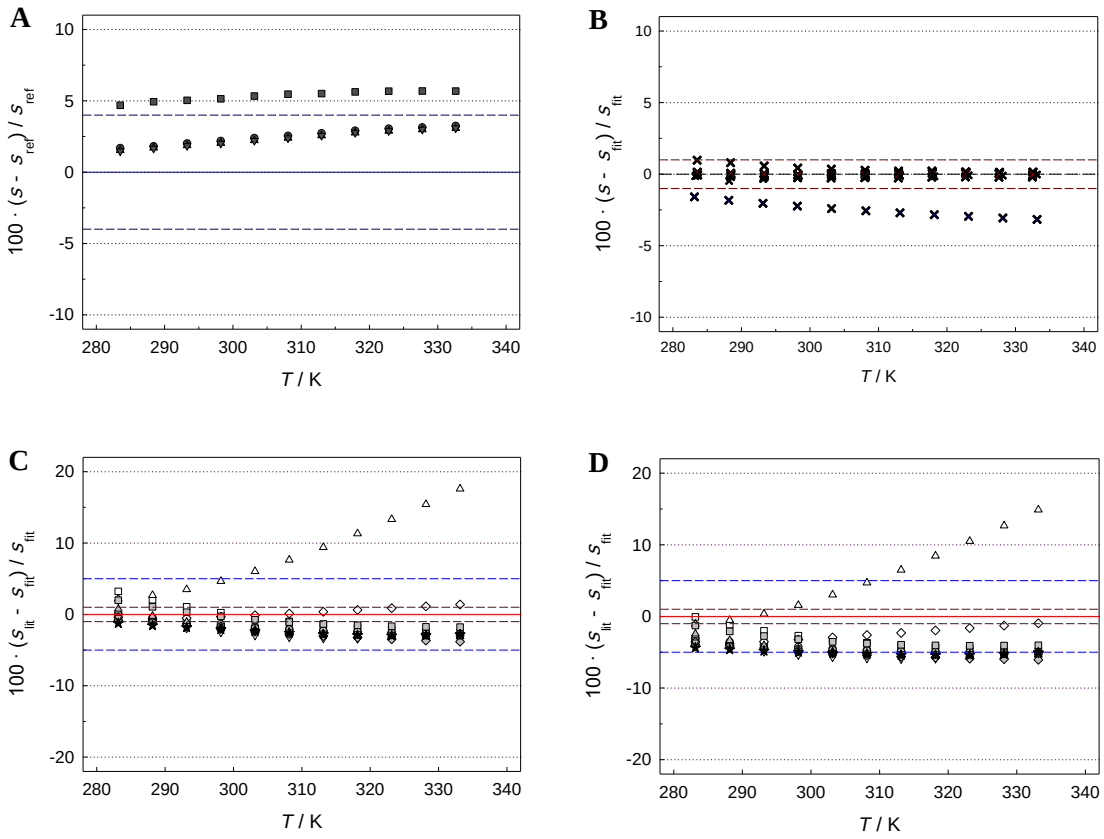



**Figure 4.62.** Evaluation of the precision and accuracy evaluation of the dip-in cell with the reference ionic liquid [$C_6C_1$im][$NTf_2$]. **A** - Deviation of each resistance determination method to the recommended data by NIST [5] (The recommended values are based on the literature data obtained through alternated current methods and using corrections for the effect of polarization); ----- error associated with the recommended data ($u(\sigma)$ = ± 4%); ● Infinite frequency extrapolation $R(1/f) = a/f + R_\infty$; ■ Infinity frequency extrapolation $R\left(1/f^{1/2}\right) = a/f^{1/2} + R_\infty$; ▲ Minimum resistance value; ▼ Resistance at the point of minimum reactance; **B** - Deviation of each independent experiment and reference data to the obtained average experimental fitting; ----- Maximum error between the experimental measurements ($u$ = ± 1.5%); × independent experiments; × overall experimental fitting; × Data recommended by NIST [5]; **C** - Comparison of the experimental results based on $R(1/f) = a/f + R_\infty$ to the literature data; **D** - Comparison of the experimental results based on $R\left(1/f^{1/2}\right) = a/f^{1/2} + R_\infty$ with the literature data. ----- overall deviation to literature ($u$ = ± 5%). Literature data: ○ Nazet *et al.* [11]; □ Tokuda *et al.* [13]; ◇ Moralez-Ugarte *et al.* [14]; △ Leys *et al.* [16]; ▽ Harris *et al.* [15]; ● Widegren *et al.* [9]; ■ Papović *et al.* [8]; ◆ Kandil *et al.* [10]; ▲ Santos *et al.* [12]; ▼ Calado *et al.* [7], ★ Chirico *et al*. IUPAC data [17].

### 4.6.2. Coin Cell

Comparatively to the Dip-in Cell, the Coin Cell has a key advantage as it uses a much smaller quantity of sample. However, its confined space and lack of visibility present a significant disadvantage associated with the state of the sample in the measuring zone. Throughout the experiments and testing, it became clear that the presence of air bubbles has a major impact on the measurements. Therefore, extra care is needed during the injection process. As expected, the presence of the air bubbles results in an increase in resistance due to a decrease in the effective volume of the liquid medium. The impact of this effect is illustrated in Fig. 4.63.

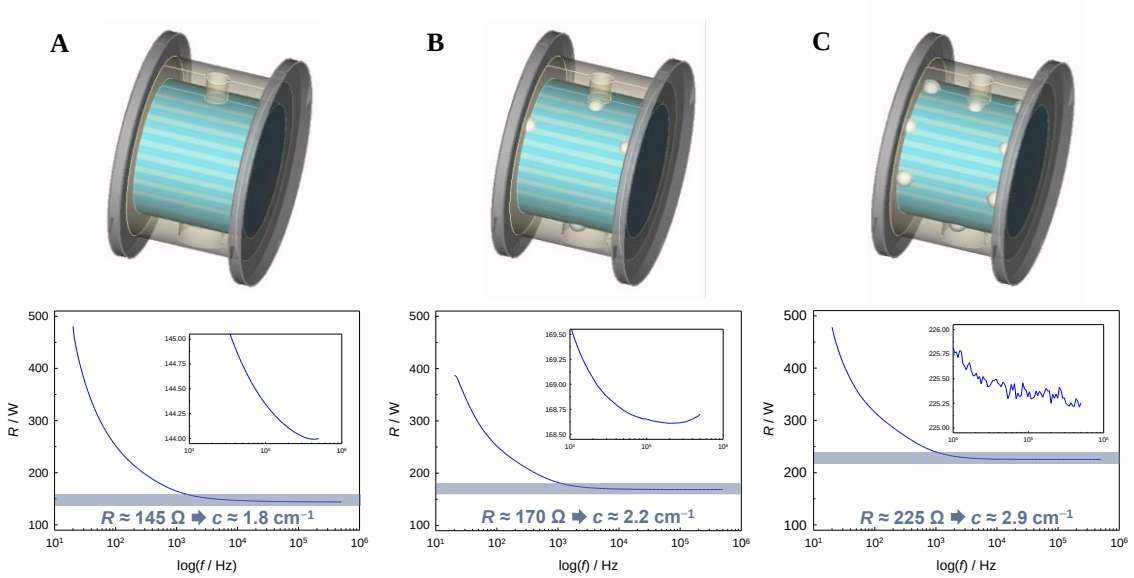



**Figure 4.63.** Representation of the impact of air bubbles inside the measuring region on the electrical resistance. The spectra shown are from experiments with an aqueous KCl 0.1000 mol·kg$^{-1}$ solution.

The example presented in Fig. 4.63 is from experiments with an aqueous KCl 0.1000 mol·kg$^{-1}$ solution. The situation in Fig. 4.63A illustrates a proper fill of the measuring chamber without the presence of air bubbles. The cell constant derived from these measurements is in agreement with the value theoretically predicted based on the dimensions of the cell. On the other hand, the other two situations lead to an unrealistic experimental cell constant. Additionally, the presence of bubbles seems to also increase the noise of the resistance signal. Fortunately, this can be useful as a qualitative tool to evaluate the presence of air bubbles inside the measuring cell.

The experimental determination of constant cell and resistance extrapolation for the coin cell were performed as described for the dip-in cell. The experimental results obtained

from the experiments of cell constant determination are graphically presented in Fig. 4.64. The average cell constant value was found to be $c_{avg}$ = 1.86 $cm^{-1}$ (~3.5 % deviation to the theoretical 1.8 $cm^{-1}$ value calculated based on the dimensions of the cell) and the experimental results were found to be within an uncertainty range of ± 1%.

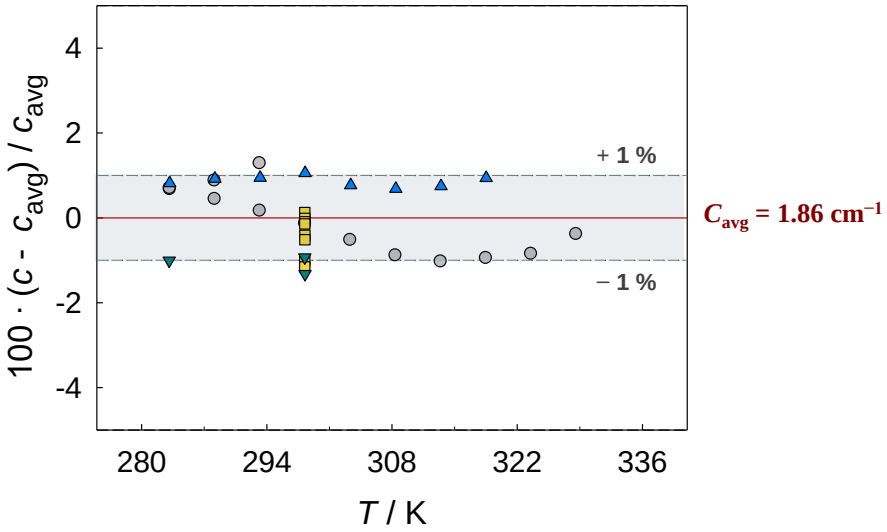



**Figure 4.64.** Residuals associated with the cell constant determination of the coin cell derived from the electrical resistance measurement of a standard aqueous 0.1000 mol·kg$^{-1}$ KCl solution. ● stainless steel 316; ■ stainless steel 316 coated with titanium nitride; ▲ nickel; ▼platinum.

The coin cell's performance was evaluated by measuring the electrical conductivity of [$^1C_6{}^3C_1$im][$NTf_2$] and by comparing the obtained results with the data from the experiments with the dip-in and the recommended values from IUPAC Fig. 4.65.

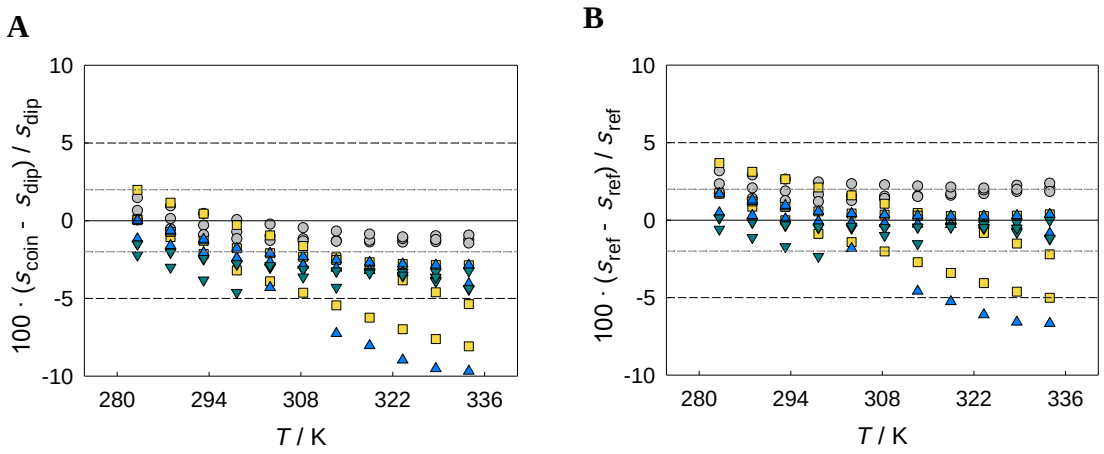



**Figure 4.65.** Evaluation of the precision and accuracy evaluation of the coin cell with the reference ionic liquid [$^1C_6{}^3C_1$im][$NTf_2$]. **A:** Comparison with the dip-in cell; **B:** Comparison with the data recommended by IUPAC [2]. ● stainless steel 316; ■ stainless steel 316 coated with titanium nitride; ▲ nickel; ▼platinum.

### 4.6.3. Comparison between the Dip-in and Coin Cell

The two cells were found to perform well in the measurement of the electrical conductivity of ionic liquids. While the coin cell allows the utilization of a much smaller sample volume, the reduced dimensions raise problems associated with the filling of the cell, particularly the presence of air bubbles, which can affect the precision and reproducibility of the measurements. Additionally, the filling by injection method is obviously more difficult for samples with a melting point close to room temperature. These two problems are easier to overcome using the assembly method of the dip-in cell. On the other hand, the smaller dimensions of the coin cell lead to shorter periods of thermal stabilization. This is facilitated by the utilization of aluminum plates and the minimization of PEEK. Furthermore, the good performance of the coin cell with stainless steel electrodes demonstrates the possibility of the development of viable and affordable conductivity cells, compared to the more expensive and difficult-to-maintain black platinum electrode cells. A comparative summary of the main features of the two cells is presented in Fig. 4.66.

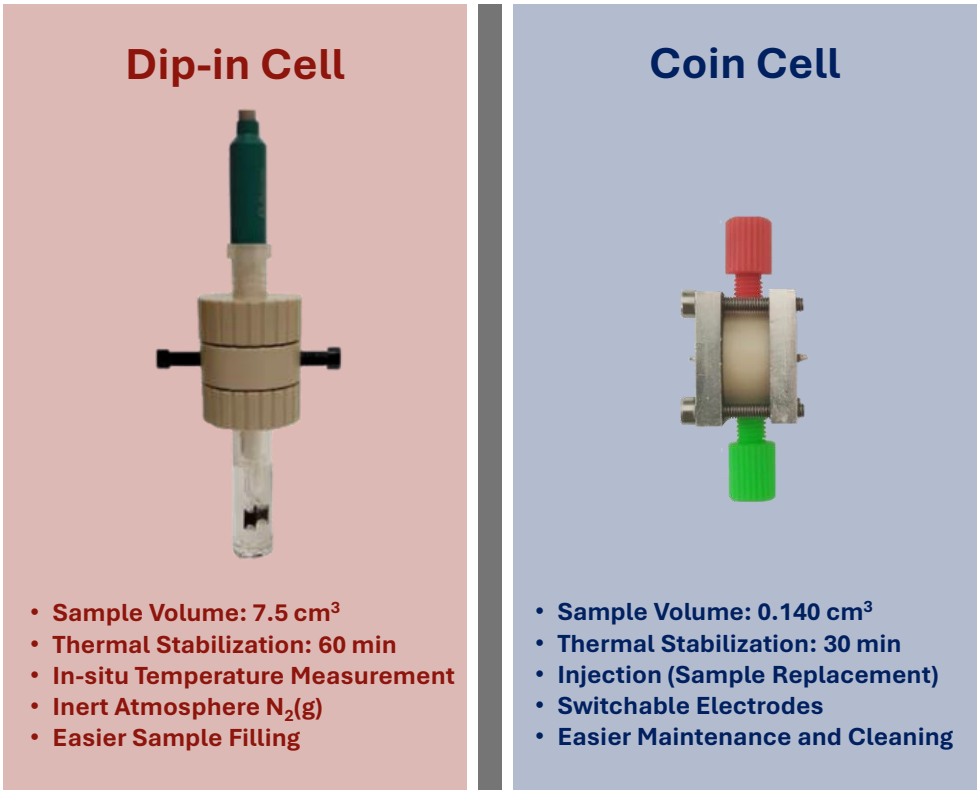



**Figure 4.66.** Comparative summary of the main features of the dip-in and coin electrical conductivity cells.

# References

[1] J. Barthel, R. Wachter, H.J. Gores, Modern Aspects of Electrochemistry: No. 13 (1979) 1. https://doi.org/10.1007/978-1-4615-7455-2_1

[2] K.W. Pratt, W.F. Koch, Y.C. Wu, P.A. Berezansky, Pure Appl. Chem. 73 (2001) 1783. https://doi.org/doi:10.1351/pac200173111783

[3] M. Drüschler, N. Borisenko, J. Wallauer, C. Winter, B. Huber, F. Endres, B. Roling, Phys. Chem. Chem. Phys. 14 (2012) 5090. https://doi.org/10.1039/C2CP40288B

[4] R. Atkin, N. Borisenko, M. Drüschler, F. Endres, R. Hayes, B. Huber, B. Roling, J. Mol. Liq. 192 (2014) 44. https://doi.org/10.1016/j.molliq.2013.08.006

[5] X. Paredes, C.S.G.P. Queirós, F.J.V. Santos, A.F. Santos, M.S.C.S. Santos, M.J.V. Lourenço, C.A.N.d. Castro, J. Phys. Chem. Ref. Data 49 (2020) 043101. https://doi.org/10.1063/5.0023160

[6] J. Leys, R.N. Rajesh, P.C. Menon, C. Glorieux, S. Longuemart, P. Nockemann, M. Pellens, K. Binnemans, J. Chem. Phys. 133 (2010). https://doi.org/10.1063/1.3455892

[7] M.S. Calado, J.C.F. Diogo, J.L. Correia da Mata, F.J.P. Caetano, Z.P. Visak, J.M.N.A. Fareleira, Int. J. Thermophys. 34 (2013) 1265. https://doi.org/10.1007/s10765-013-1491-2

[8] S. Papović, S. Gadžurić, M. Bešter-Rogač, M. Vraneš, J. Chem. Thermodyn. 102 (2016) 367. https://doi.org/10.1016/j.jct.2016.07.039

[9] J.A. Widegren, E.M. Saurer, K.N. Marsh, J.W. Magee, J. Chem. Thermodyn. 37 (2005) 569. https://doi.org/10.1016/j.jct.2005.04.009

[10] M.E. Kandil, K.N. Marsh, A.R.H. Goodwin, J. Chem. Eng. Data 52 (2007) 2382. https://doi.org/10.1021/je7003484

[11] A. Nazet, S. Sokolov, T. Sonnleitner, T. Makino, M. Kanakubo, R. Buchner, J. Chem. Eng. Data 60 (2015) 2400. https://doi.org/10.1021/acs.jced.5b00285

[12] F. Santos, C. Nieto de Castro, P. Mota, International Journal of Thermophysics - INT J THERMOPHYS 31 (2010) 1869. https://doi.org/10.1007/s10765-009-0584-4

[13] H. Tokuda, K. Hayamizu, K. Ishii, M.A.B.H. Susan, M. Watanabe, J. Phys. Chem. B 109 (2005) 6103. https://doi.org/10.1021/jp044626d

[14] J.E. Morales-Ugarte, C.C. Santini, R. Bouchet, A. Benayad, J. Phys. Chem. B 124 (2020) 7625. https://doi.org/10.1021/acs.jpcb.0c04090

[15] K.R. Harris, M. Kanakubo, Phys. Chem. Chem. Phys. 17 (2015) 23977. https://doi.org/10.1039/C5CP04277A

[16] J. Leys, M. Wübbenhorst, C. Preethy Menon, R. Rajesh, J. Thoen, C. Glorieux, P. Nockemann, B. Thijs, K. Binnemans, S. Longuemart, J. Chem. Phys. 128 (2008). https://doi.org/10.1063/1.2827462

[17] R.D. Chirico, V. Diky, J.W. Magee, M. Frenkel, K.N. Marsh, Pure Appl. Chem. 81 (2009) 791. https://doi.org/doi:10.1351/PAC-REP-08-09-22

# Chapter 5

## Results and Discussion

### Structure-Property Relationships

**5.1.** Effect of the cation's alkyl chain length

**5.2.** Effect of the anion's nature

**5.3.** Effect of the cation's nature

**References**

# 5. Results and Discussion: Structure-Property Relationship

Density, viscosity, and electrical conductivity of several ionic liquids were measured, and the discussion will be focused on the correlation between the experimental results and the concepts introduced in Chapter 2 – Methods and Theory. Physicochemical properties and the derived thermodynamic quantities will be correlated with the ILs structure to establish property-structure relationships and provide insight concerning the structuration and dynamics of the ionic liquids. A set of systematic studies will be presented and discussed individually, which were organized into three lines according to their systematic structural differentiation (Fig. 5.1):

1. Effect of the cation alkyl chain length: The focus of this work was to explore the effect of nanostructuration on the transport properties of ionic liquids. This section can be divided into two sub-thematics: **a)** increase of the alkyl chain length on four 1-alkyl-3-methylimidazolium series with varying anions; **b)** increase of the alkyl chain length in different cationic series (1-alkyl-3-methylimidazolium, 1-alkyl-1-methylpyrolidinium; 1-alkylpyridinum) combined with the bis(trifluoromethylsulfonyl)imide. The study of different anionic and cationic series allows a deeper understanding of the effect of the change of the polar domains in the alkyl chain interaction potential.

2. Effect of the anion: Study involving a group of ILs with different anions and the same short chain imidazolium cation, $[^{1}C_{4}{}^{3}C_{1}im]^{+}$. The aim of this work was to evaluate the impact of different characteristics of the anion, such as size, shape, dynamics, flexibility, charge localization, and basicity on the viscosity and electrical conductivity of ILs.

3. Effect of the cation: This part is focused on the effect of the structure and nature of the cationic group on the viscosity and electrical conductivity of ILs. With this aim, cations with different charged head groups and ring substitution are explored. This study is divided into three different sub-groups: **a)** effect of the cationic ring ($[^{1}C_{4}{}^{3}C_{1}im]^{+}$, $[^{1}C_{4}{}^{1}C_{1}pyr]^{+}$, $[^{1}C_{4}py]^{+}$) with is evaluated by pairing different anions with three different cationic structures; **b)** effect of methylation at the C2 position of the imidazolium ring; **c)** effect of isomerization of the pyridinium ring.

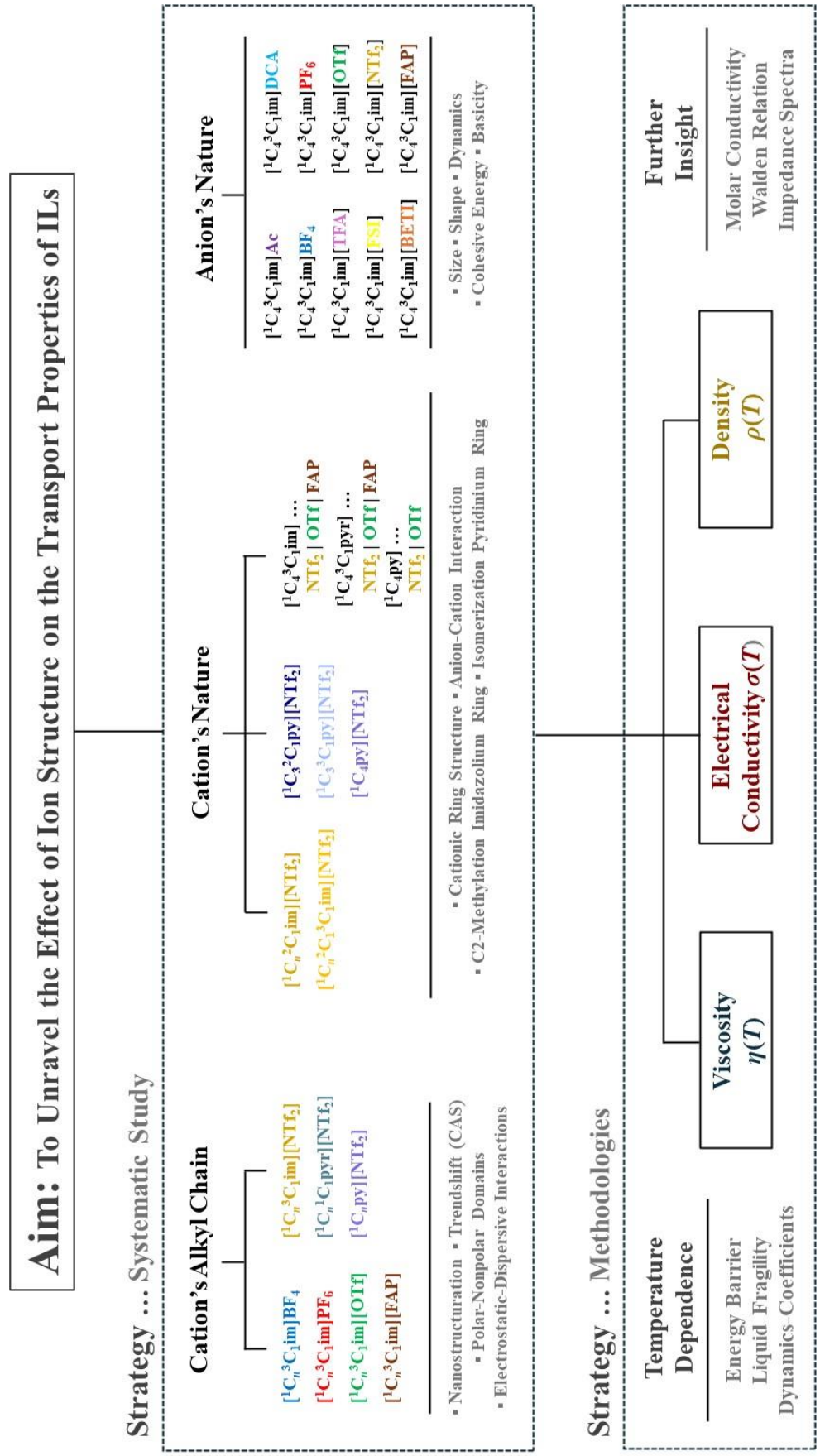



**Figure 5.1.** Schematic representation of the work conducted on the study of the transport properties of ionic liquids.

For clarity, only the coefficients of the temperature dependence fittings and the values at the reference temperature, $T$ = 298.15 K, are included in the main text of this thesis, as the average experimental results are presented in the appendix. A summary of the properties measured for each IL and the indication of the localization of the respective experimental results in the appendix are presented in Table 5.1.

**Table 5.1.** Summary of ionic liquids measurements performed in this work.

| Ionic Liquid | Density | Viscosity | Electrical Conductivity |
|---|---|---|---|
| $[^1C_1{}^3C_1im][NTf_2]$ | a | a | ✓ Table B.1 |
| $[^1C_2{}^3C_1im][NTf_2]$ | a | a | ✓ Table B.2 |
| $[^1C_1{}^3C_3im][NTf_2]$ | a | a | ✓ Table B.3 |
| $[^1C_4{}^3C_1im][NTf_2]$ | a | a | ✓ Table B.4. |
| $[^1C_1{}^3C_5im][NTf_2]$ | a | a | ✓ Table B.5 |
| $[^1C_6{}^3C_1im][NTf_2]$ | ✓ a | ✓ a | ✓ Table B.6 |
| $[^1C_7{}^3C_1im][NTf_2]$ | a | a | ✓ Table B.7 |
| $[^1C_1{}^3C_8im][NTf_2]$ | a | a | ✓ Table B.8 |
| $[^1C_1{}^3C_9im][NTf_2]$ | a | a | ✓ Table B.9 |
| $[^1C_{10}{}^3C_1im][NTf_2]$ | a | a | ✓ Table B.10 |
| $[^1C_1{}^3C_{11}im][NTf_2]$ | a | a | ✓ Table B.11 |
| $[^1C_{12}{}^3C_1im][NTf_2]$ | a | a | ✓ Table B.12 |
| $[^1C_2{}^2C_1{}^3C_1im][NTf_2]$ | ✓ Table B.13 | ✓ Table B.13 | ✓ Table B.13. |
| $[^1C_1{}^2C_1{}^3C_3im][NTf_2]$ | ✓ Table B.14 | ✓ Table B.14 | ✓ Table B.14 |
| $[^1C_4{}^2C_1{}^3C_1im][NTf_2]$ | ✓ Table B.15 | ✓ Table B.15 | ✓ Table B.15 |
| $[^1C_2{}^3C_1im][BF_4]$ | ✓ Table B.16 | ✓ Table B.16 | ✓ Table B.16 |
| $[^1C_1{}^3C_3im][BF_4]$ | ✓ Table B.17 | ✓ Table B.17 | ✓ Table B.17 |
| $[^1C_4{}^3C_1im][BF_4]$ | ✓ Table B.18 | ✓ Table B.18 | ✓ Table B.18 |
| $[^1C_1{}^3C_5im][BF_4]$ | ✓ Table B.19 | ✓ Table B.19 | ✓ Table B.19 |

| | | | |
|---|---|---|---|
| $[^1C_6{}^3C_1im][BF_4]$ | ✓ Table B.20 | ✓ Table B.20 | ✓ Table B.20 |
| $[^1C_7{}^3C_1im][BF_4]$ | ✓ Table B.21 | ✓ Table B.21 | ✓ Table B.21 |
| $[^1C_1{}^3C_8im][BF_4]$ | ✓ Table B.22 | ✓ Table B.22 | ✓ Table B.22 |
| $[^1C_1{}^3C_9im][BF_4]$ | ✓ Table B.23 | ✓ Table B.23 | ✓ Table B.23 |
| $[^1C_{10}{}^3C_1im][BF_4]$ | ✓ Table B.24 | ✓ Table B.24 | ✓ Table B.24 |
| $[^1C_{12}{}^3C_1im][BF_4]$ | × | ✓ Table B.25 | ✓ Table B.25 |
| $[^1C_1{}^3C_3im][PF_6]$ | ✓ Table B.26 | ✓ Table B.26 | ✓ Table B.26. |
| $[^1C_4{}^3C_1im][PF_6]$ | b | b | ✓ Table B.27 |
| $[^1C_1{}^3C_5im][PF_6]$ | b | b | ✓ Table B.28 |
| $[^1C_6{}^3C_1im][PF_6]$ | b | b | ✓ Table B.29 |
| $[^1C_7{}^3C_1im][PF_6]$ | b | b | ✓ Table B.30 |
| $[^1C_1{}^3C_8im][PF_6]$ | b | b | ✓ Table B.31 |
| $[^1C_1{}^3C_9im][PF_6]$ | b | b | ✓ Table B.32 |
| $[^1C_{10}{}^3C_1im][PF_6]$ | ✓ Table B.33 | ✓ Table B.33. | ✓ Table B.33 |
| $[^1C_2{}^3C_1im][OTf]$ | ✓ Table B.34 | ✓ Table B.34 | ✓ Table B.34 |
| $[^1C_4{}^3C_1im][OTf]$ | ✓ Table B.35 | ✓ Table B.35 | ✓ Table B.35 |
| $[^1C_6{}^3C_1im][OTf]$ | ✓ Table B.36 | ✓ Table B.36 | ✓ Table B.36 |
| $[^1C_8{}^3C_1im][OTf]$ | ✓ Table B.37 | ✓ Table B.37 | ✓ Table B.37 |
| $[^1C_{10}{}^3C_1im][OTf]$ | ✓ Table B.38 | ✓ Table B.38 | ✓ Table B.38 |
| $[^1C_{12}{}^3C_1im][OTf]$ | ✓ Table B.39 | ✓ Table B.39 | ✓ Table B.39 |
| $[^1C_2{}^3C_1im][FAP]$ | ✓ Table B.40 | ✓ Table B.40 | ✓ Table B.40 |
| $[^1C_4{}^3C_1im][FAP]$ | ✓ Table B.41 | ✓ Table B.41 | ✓ Table B.41 |
| $[^1C_6{}^3C_1im][FAP]$ | ✓ Table B.42 | ✓ Table B.42 | ✓ Table B.42 |
| $[^1C_4{}^3C_1im][FSI]$ | ✓ Table B.43 | ✓ Table B.43 | ✓ Table B.43 |

| | | | |
|---|---|---|---|
| $[^1C_4{}^3C_1im][BETI]$ | ✓ Table B.44 | ✓ Table B.44 | ✓ Table B.44 |
| $[^1C_4{}^3C_1im][Ac]$ | ✓ Table B.45 | ✓ Table B.45 | ✓ Table B.45 |
| $[^1C_4{}^3C_1im][TFA]$ | ✓ Table B.46 | ✓ Table B.46 | ✓ Table B.46 |
| $[^1C_4{}^3C_1im][DCA]$ | ✓ Table B.47 | ✓ Table B.47 | ✓ Table B.47 |
| $[^1C_3py][NTf_2]$ | ✓ Table B.48 | ✓ Table B.48 | ✓ Table B.48 |
| $[^1C_4py][NTf_2]$ | ✓ Table B.49 | ✓ Table B.49 | ✓ Table B.49 |
| $[^1C_5py][NTf_2]$ | ✓ Table B.50 | ✓ Table B.50 | ✓ Table B.50 |
| $[^1C_6py][NTf_2]$ | ✓ Table B.51 | ✓ Table B.51 | ✓ Table B.51 |
| $[^1C_7py][NTf_2]$ | ✓ Table B.52 | ✓ Table B.52 | ✓ Table B.52 |
| $[^1C_8py][NTf_2]$ | ✓ Table B.53 | ✓ Table B.53 | ✓ Table B.53 |
| $[^1C_9py][NTf_2]$ | ✓ Table B.54 | ✓ Table B.54 | ✓ Table B.54 |
| $[^1C_4py][OTf]$ | ✓ Table B.55 | ✓ Table B.55 | ✓ Table B.55 |
| $[^1C_3{}^2C_1py][NTf_2]$ | ✓ Table B.56 | ✓ Table B.56 | ✓ Table B.56 |
| $[^1C_3{}^3C_1py][NTf_2]$ | ✓ Table B.57 | ✓ Table B.57 | ✓ Table B.57 |
| $[^1C_3{}^1C_1pyr][NTf_2]$ | ✓ Table B.58 | ✓ Table B.58 | ✓ Table B.58 |
| $[^1C_4{}^1C_1pyr][NTf_2]$ | ✓ Table B.59 | ✓ Table B.59 | ✓ Table B.59 |
| $[^1C_6{}^1C_1pyr][NTf_2]$ | ✓ Table B.60 | ✓ Table B.60 | ✓ Table B.60 |
| $[^1C_8{}^1C_1pyr][NTf_2]$ | ✓ Table B.61 | ✓ Table B.61 | ✓ Table B.61 |
| $[^1C_4{}^1C_1pyr][OTf]$ | ✓ Table B.62 | ✓ Table B.62 | ✓ Table B.62 |
| $[^1C_4{}^1C_1pyr][FAP]$ | ✓ Table B.63 | ✓ Table B.63 | ✓ Table B.63 |

The symbol ✓ indicates measurements performed in this work. The density and viscosity data of some $[^1C_n{}^3C_1im][NTf_2]$ and $[^1C_n{}^3C_1im]PF_6$ ILs were taken from previous works of this research group. a Rocha *et al.* [1]; b Rocha *et al.* [2]. The symbol ✕ indicates that valid measurements could not be performed due to the high melting point of the $[^1C_{12}{}^3C_1im]BF_4$.

## 5.1. Effect of the Cation's Alkyl Chain Length

A summary of the homologue series involved in the study of the effect of the alkyl chain length on the transport properties of ionic liquids is presented in Fig. 5.2.

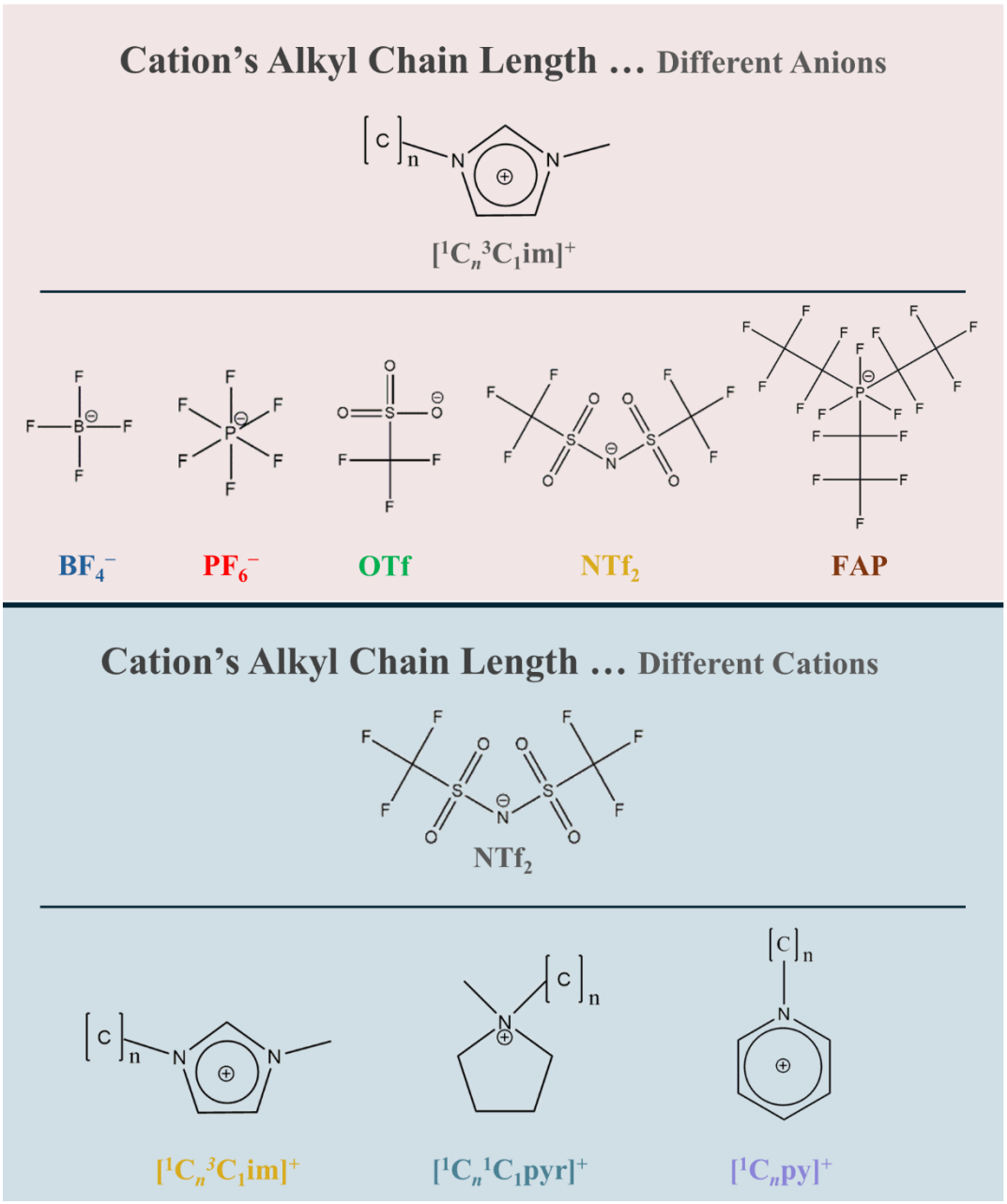



**Figure 5.2.** Schematic representation of the study on the effect of the cation's alkyl chain length on the transport properties of ionic liquids.

### 5.1.1. $[^1C_n{}^3C_1im]BF_4$ Series

In this work, the density, viscosity, and electrical conductivity of the 1-alkyl-3-methylimidazolium tetrafluoroborate series, $[^1C_n{}^3C_1im]BF_4$ $n$ = 2 – 10, 12 (Fig. 5.3) were measured for different temperatures.

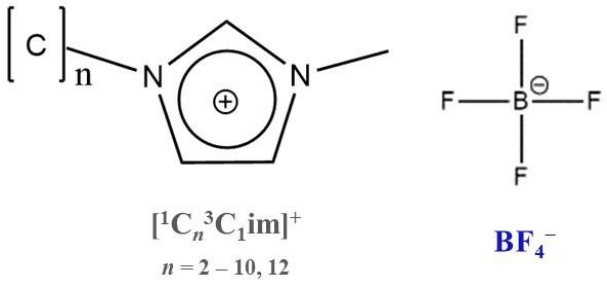



**Figure 5.3.** Structure of the studied $[^1C_n{}^3C_1im]BF_4$ ($n$ = 2 – 10, 12).

#### 5.1.1.1. Density

The resulting fitting coefficients from the temperature dependence of density of the $[^1C_n{}^3C_1im]BF_4$, ILs (Eq. 2.4) are presented in Table 5.2. The densities at the reference temperature ($T$ = 298.15 K) are presented in Table 5.3 together with the molar volume and thermal expansion coefficient derived from Eq. 2.2 and Eq. 2.7 respectively. The graphical representation of density, thermal expansion coefficient, and molar volume as functions of temperature and number of carbons on the cations alkyl chain are presented in Fig 5.4.

**Table 5.2.** Fitting coefficients of the temperature dependence of density of the studied $[^1C_n{}^3C_1im]BF_4$ homologue series.

| Ionic Liquid | $\frac{T_{interval}}{K}$ | $\frac{10^7 \cdot a_2}{K^{-2}}$ | $\frac{10^4 \cdot a_1}{K^{-1}}$ | $\frac{a_0}{K}$ |
|---|---|---|---|---|
| $[^1C_2{}^3C_1im]BF_4$ | 283 − 373 | 1.128 ± 0.078 | −6.609 ± 0.051 | 7.3424 ± 0.0008 |
| $[^1C_3{}^3C_1im]BF_4$ | 283 − 373 | 1.022 ± 0.076 | −6.565 ± 0.052 | 7.3077 ± 0.0008 |
| $[^1C_4{}^3C_1im]BF_4$ | 283 − 373 | 0.971 ± 0.078 | −6.518 ± 0.051 | 7.2806 ± 0.0008 |
| $[^1C_5{}^3C_1im]BF_4$ | 283 – 373 | 0.558 ± 0.085 | −6.293 ± 0.056 | 7.2487 ± 0.0009 |
| $[^1C_6{}^3C_1im]BF_4$ | 283 – 373 | 0.543 ± 0.055 | −6.348 ± 0.042 | 7.2281 ± 0.0007 |
| $[^1C_7{}^3C_1im]BF_4$ | 283 – 373 | 0.360 ± 0.073 | −6.275 ± 0.048 | 7.2073 ± 0.0008 |
| $[^1C_8{}^3C_1im]BF_4$ | 283 – 373 | 0.405 ± 0.086 | −6.361 ± 0.056 | 7.1926 ± 0.0009 |
| $[^1C_9{}^3C_1im]BF_4$ | 283 – 373 | 0.453 ± 0.077 | −6.465 ± 0.051 | 7.1805 ± 0.0008 |
| $[^1C_{10}{}^3C_1im]BF_4$ | 283 – 373 | 0.83 ± 0.14 | −6.798 ± 0.093 | 7.1733 ± 0.0015 |
| $[^1C_{12}{}^3C_1im]BF_4$ | 323 – 373 | −0.55 ± 0.14 | −5.995 ± 0.096 | 7.1390 ± 0.0017 |

The presented fitting coefficients were derived from the experimental $\rho(T)$ data (appendix) by applying a polynomial fitting function, $\ln[\rho(T)] = a_2T^2 + a_1T + a_0$ (Eq. 2.4). The standard uncertainties related to the fitting coefficients were calculated to the confidence level of 0.95 ($k \approx 2$).

**Table 5.3.** Density, thermal expansion coefficient, and molar volume at the reference temperature, $T$ = 298.15 K for the studied $[^1C_n{}^3C_1im]BF_4$ homologue series.

| Ionic Liquid | $\frac{\rho(298.15\ K)}{kg \cdot m^{-3}}$ | $\frac{10^4 \cdot \alpha_\rho(298.15\ K)}{K^{-1}}$ | $\frac{10^6 \cdot V_m(298.15\ K)}{m^3 \cdot mol^{-1}}$ |
|---|---|---|---|
| $[^1C_2{}^3C_1im]BF_4$ | 1280.9 ± 0.5 | 5.94 ± 0.05 | 154.6 ± 0.4 |
| $[^1C_3{}^3C_1im]BF_4$ | 1237.7 ± 0.5 | 5.96 ± 0.05 | 171.3 ± 0.4 |
| $[^1C_4{}^3C_1im]BF_4$ | 1205.8 ± 0.5 | 5.94 ± 0.05 | 187.4 ± 0.5 |
| $[^1C_5{}^3C_1im]BF_4$ | 1171.5 ± 0.5 | 5.96 ± 0.06 | 204.9 ± 0.5 |
| $[^1C_6{}^3C_1im]BF_4$ | 1145.6 ± 0.5 | 6.02 ± 0.04 | 221.8 ± 0.5 |
| $[^1C_7{}^3C_1im]BF_4$ | 1122.6 ±0.5 | 6.06 ± 0.05 | 238.8 ± 0.5 |
| $[^1C_8{}^3C_1im]BF_4$ | 1103.9 ± 0.5 | 6.12 ± 0.06 | 255.6 ± 0.6 |
| $[^1C_9{}^3C_1im]BF_4$ | 1087.6 ± 0.5 | 6.19 ± 0.05 | 272.3 ± 0.6 |
| $[^1C_{10}{}^3C_1im]BF_4$ | 1072.7 ± 0.5 | 6.30 ± 0.09 | 298.2 ± 0.6 |
| $[^1C_{12}{}^3C_1im]BF_4$ | 1048.8 ± 0.5 | 6.32 ± 0.10 | 322.5 ± 0.7 |

$\rho(T = 298.15\ K)$ and $\alpha_\rho(T = 298.15\ K)$ were calculated from the fitting coefficients presented in Table 5.2 and by applying Eq. 2.4 and Eq. .7 respectively. $V_m(298.15\ K) = M/\rho(298.15\ K)$. The standard uncertainty associated with $\alpha_\rho$ and $V_m$ were calculated by applying the propagation of uncertainty to Eq. 2.7 and 2.2, respectively.

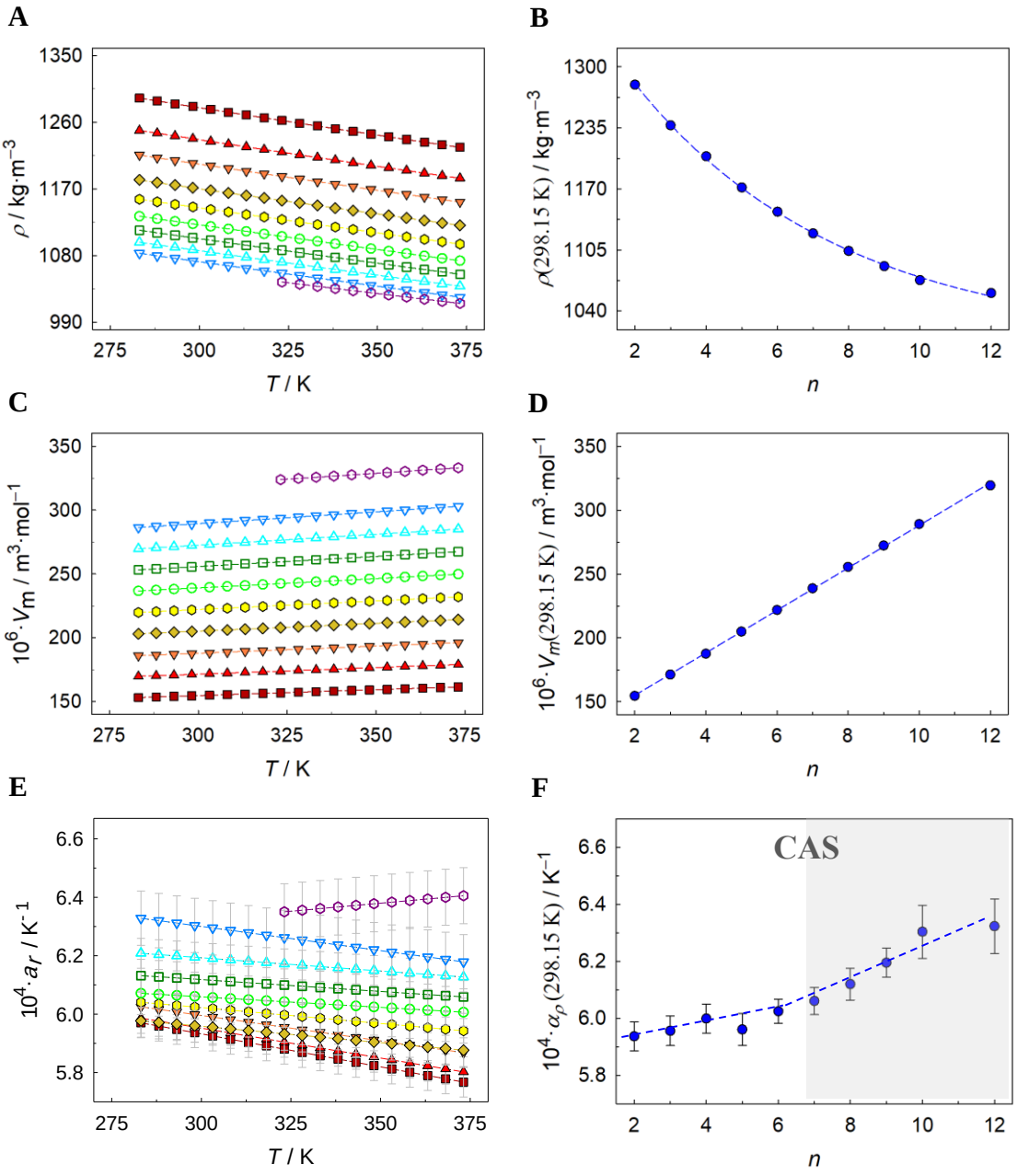



**Figure 5.4.** Density and derived properties of the $[^1C_n{}^3C_1im]BF_4$ ILs as functions of temperature (A, C, E) and number of carbons on the alkyl chain of the cation (B, D, F). **A**, **B**: Density; **C**, **D**: Molar volume; **E**, **F**: Thermal expansion coefficient. $n$ = 2 ■, 3 ▲, 4 ▼, 5 ◆, 6 ⬢, 7 ○, 8 □, 9 △, 10 ▽, 12 ⬡.

### 5.1.1.2. Viscosity

The obtained viscosity data for the $[^1C_n{}^3C_1im]BF_4$ ILs is presented as a function of temperature and the number of carbons of the cation's alkyl chain in Fig. 5.5. It was not possible to measure the viscosity of $[^1C_{12}{}^3C_1im]BF_4$ due to the occurrence of solidification during the injection procedure.

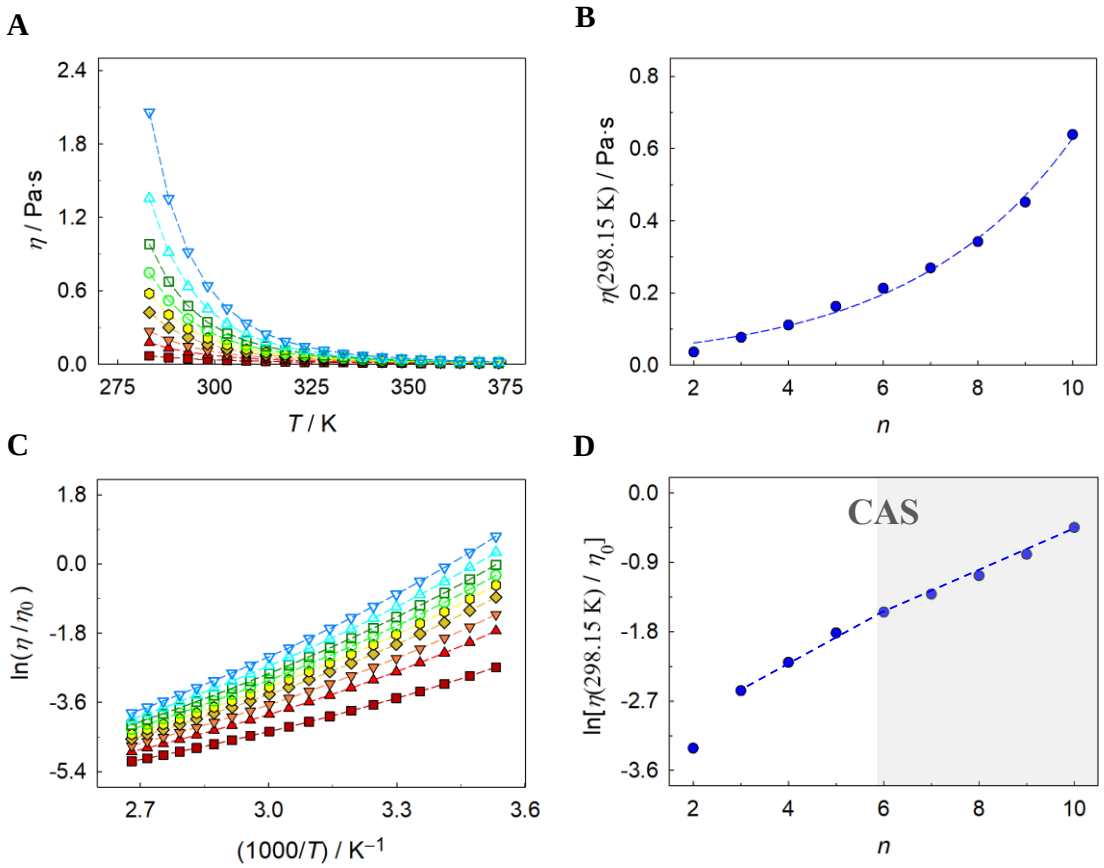



**Figure 5.5.** Viscosity of the $[^1C_n{}^3C_1im]BF_4$ ILs as functions of temperature (A, C) and number of carbons on the alkyl chain of the cation (B, D). **A**: Temperature dependence of viscosity; **B**: Dependence of viscosity with the alkyl chain length; **C**: Temperature dependence of viscosity (Arrhenius representation); **D**: Dependence of viscosity with the alkyl chain length (logarithmic form). $n$ = 2 ■, 3 ▲, 4 ▼, 5 ◆, 6 ⬢, 7 ○, 8 □, 9 △, 10 ▽, 12 ⬡. $\eta_0$ = 1 Pa·s.

The VFT coefficients (Eq. 2.51) obtained from the experimental viscosity-temperature data, $\eta(T)$, are presented in Table 5.4. The effect of the alkyl chain length on the obtained VFT coefficients is presented in Fig. 5.6 together with the graphical representation of the linearized VFT equation (Eq. 2.52).

**Table 5.4** Fitting coefficients used to describe the temperature dependence of viscosity of the studied $[^1C_n{}^3C_1im]BF_4$ homologue series.

| Ionic Liquid | $\frac{T_{interval}}{K}$ | $\frac{10^3 \cdot A_\eta}{Pa \cdot s}$ | $\frac{B_\eta}{K}$ | $\frac{C_\eta}{K}$ |
|---|---|---|---|---|
| $[^1C_2{}^3C_1im]BF_4$ | 283 − 373 | 0.1965 ± 0.0013 | 731.5 ± 1.9 | 158.1 ± 0.2 |
| $[^1C_3{}^3C_1im]BF_4$ | 283 − 373 | 0.1440 ± 0.0031 | 806.6 ± 5.7 | 169.7 ± 0.5 |
| $[^1C_4{}^3C_1im]BF_4$ | 283 − 373 | 0.0978 ± 0.0033 | 940.1 ± 8.7 | 164.5 ± 0.6 |
| $[^1C_5{}^3C_1im]BF_4$ | 283 – 373 | 0.0740 ± 0.0028 | 1047 ± 10 | 162.1 ± 0.7 |
| $[^1C_6{}^3C_1im]BF_4$ | 283 – 373 | 0.0587 ± 0.0027 | 1134 ± 13 | 159.8 ± 0.8 |
| $[^1C_7{}^3C_1im]BF_4$ | 283 – 373 | 0.0478 ± 0.0023 | 1225 ± 14 | 156.3 ± 0.8 |
| $[^1C_8{}^3C_1im]BF_4$ | 283 – 373 | 0.0395 ± 0.0002 | 1306 ± 16 | 154.1 ± 0.9 |
| $[^1C_9{}^3C_1im]BF_4$ | 283 – 373 | 0.0341 ± 0.0019 | 1372 ± 16 | 153.6 ± 0.8 |
| $[^1C_{10}{}^3C_1im]BF_4$ | 283 – 373 | 0.0310 ± 0.0010 | 1413 ± 12 | 155.9 ± 0.6 |

The presented fitting coefficients were derived from the experimental $\eta(T)$ data (appendix) by applying the VFT fitting function, Eq. 2.44. The standard uncertainties related to the VFT coefficients were calculated to the confidence level of 0.95 ($k \approx 2$).

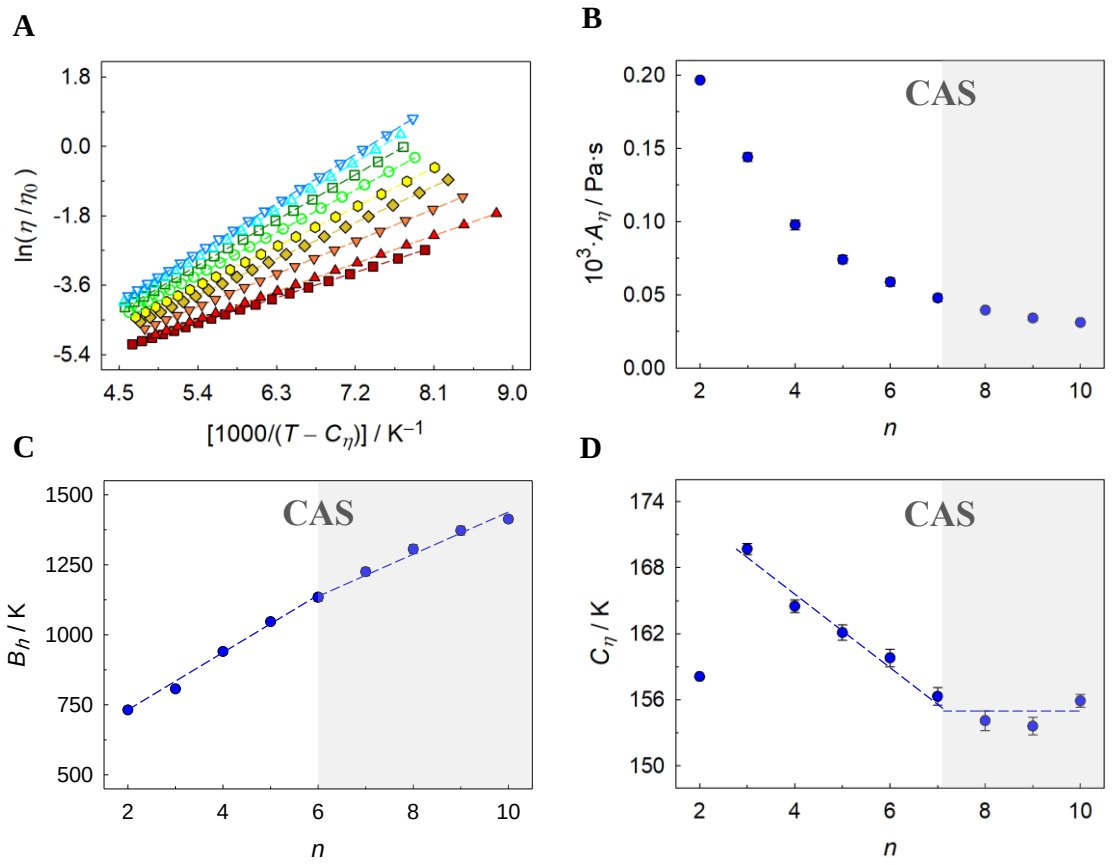



**Fig. 5.6.** Impact of the alkyl chain length on the VFT coefficients for the viscosity of $[^1C_n{}^3C_1im]BF_4$ ILs. **A**: Linearized VFT representation $n$ = 2 ■, 3 ▲, 4 ▼, 5 ◆, 6 ⬢, 7 ○, 8 □, 9 △, 10 ▽, 12 ⬡; **B**: Pre-exponential coefficient, $A_\eta$; **C**: energy barrier-related coefficient, $B_\eta$; **D**: Vogel temperature, $C_\eta$.

The viscosities at the reference temperature ($T$ = 298.15 K) are presented in Table 5.5, together with the energy barrier and strength parameter derived from Eq. 2.47 and Eq. 2.49 respectively. The temperature dependence of the viscosity-related energy barrier, $E_\eta$, and the effect of the alkyl chain length on $E_\eta$ and on the liquid fragility (strength parameter, $D_\eta$) are represented in Fig. 5.7.

**Table 5.5.** Viscosity and derived energy barrier of the studied $[^1C_n{}^3C_1im]BF_4$ homologue series at the reference temperature ($T$ = 298.15 K), together with the strength parameter.

| Ionic Liquid | $\eta(T$=298.15 K) / Pa·s | $E_\eta(T$=298.15 K) / kJ·mol$^{-1}$ | $D_\eta$ |
|---|---|---|---|
| $[^1C_2{}^3C_1im]BF_4$ | 0.03645 ± 0.00036 | 27.56 ± 0.11 | 4.627 ± 0.013 |
| $[^1C_3{}^3C_1im]BF_4$ | 0.07683 ± 0.00077 | 36.13 ± 0.38 | 4.753 ± 0.036 |
| $[^1C_4{}^3C_1im]BF_4$ | 0.1453 ± 0.0011 | 38.90 ± 0.50 | 5.715 ± 0.057 |
| $[^1C_5{}^3C_1im]BF_4$ | 0.1627 ± 0.0016 | 41.81 ± 0.59 | 6.459 ± 0.068 |
| $[^1C_6{}^3C_1im]BF_4$ | 0.2130 ± 0.0021 | 43.79 ± 0.71 | 7.096 ± 0.089 |
| $[^1C_7{}^3C_1im]BF_4$ | 0.2691 ± 0.0027 | 45.00 ± 0.72 | 7.837 ± 0.098 |
| $[^1C_8{}^3C_1im]BF_4$ | 0.3420 ± 0.0034 | 46.52 ± 0.81 | 8.48 ± 0.12 |
| $[^1C_9{}^3C_1im]BF_4$ | 0.4517 ± 0.0045 | 48.53 ± 0.78 | 8.93 ± 0.11 |
| $[^1C_{10}{}^3C_1im]BF_4$ | 0.6387 ± 0.0064 | 51.61 ± 0.62 | 9.064 ± 0.085 |

$\eta(T$ = 298.15 K) and $E_\eta(T$ = 298.15 K) were calculated from the fitting coefficients presented in Table 5.4 and by applying Eq. 2.44 and Eq. 2.47, respectively. The strength parameter was calculated by Eq. 2.49, $D_\eta = B_\eta/C_\eta$. The relative standard uncertainty associated with the viscosity measurements was estimated as $u(\eta)$ = 1.0% (Eq. 2.72); The standard uncertainty associated with the derived energy barrier, $u(E_\eta)$, and strength parameter, $u(D_\eta)$, was calculated by applying the propagation of uncertainty to Eq. 2.47 and Eq. 2.49, respectively.

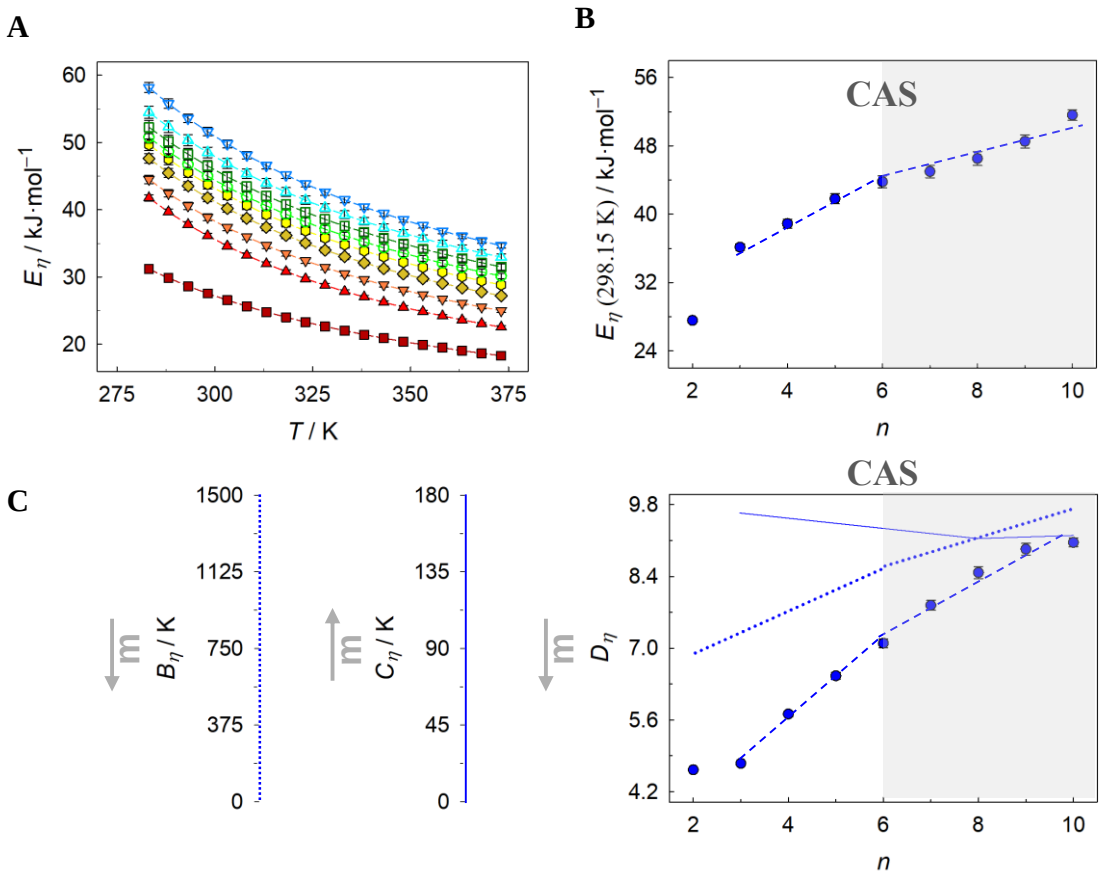



**Figure 5.7.** Graphical representation of the energy barrier and strength parameter derived from the experimental viscosity data of the [$^1$C$_n$$^3$C$_1$im]BF$_4$. **A**: Temperature dependence of the derived energy barrier $n$ = 2 ■, 3 ▲, 4 ▼, 5 ◆, 6 ⬢, 7 ○, 8 □, 9 △, 10 ▽, 12 ⬡; **B**: Effect of the alkyl chain length on the energy barrier; C: Effect of the alkyl chain length on the liquid fragility ($B_\eta$ and $C_\eta$ scales are included as guide lines).

The deviation of the available viscosity data to the experimental results for the [$^1$C$_n$$^3$C$_1$im]BF$_4$ series is presented in Fig. 5.8. There are a lot of literature sources for $n$ = 2, 4, 6, and 8, and only data with deviations lower than 25% were included in this analysis. While the majority of the data is in good agreement with the present work (<5%), there is still a lot of dispersity overall. The tetrafluoroborate is an anion that readily reacts with water, leading to the formation of hydrogen fluoride, which might affect the results. Additionally, the utilization of different methods may also affect the coherence between the data. The data reported by Schreiner *et al.* ($n$ = 2) [3], Neves *et al.* ($n$ = 2) [4], Almeida *et al.* ($n$ = 4) [5], Wu *et al.* ($n$ = 4) [6], Harris *et al*. ($n$ = 8) [7] and Tomida *et al.* ($n$ = 8) [8], were in excellent agreement with the results obtained in this work (<2%). No literature data was found for $n$ = 7, 9, and 10.

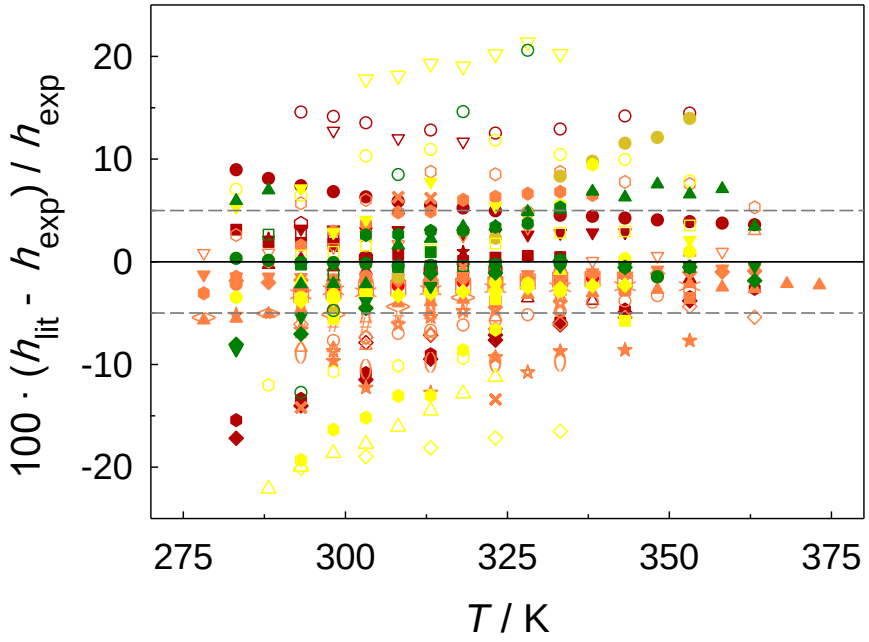



**Figure. 5.8.** Deviation of the available viscosity data to the experimental results for the $[^1C_n{}^3C_1im]BF_4$ series. ***n* = 2:** ● [4], ■ [9], ▲ [3], ▼ [10], ◆ [11], ⬢ [12], ○ [13], □ [14], △ [15], ▽ [16], ◇ [17], ⬡ [18]; ★ [19]; ***n* = 3:** ● [10]; ***n* = 4:** ● [20], ■ [21], ▲ [22], ▼ [4], ◆ [5], ⬢ [23] , ○ [24], □ [10] , △ [25], ▽ [26], ◇ [27], ⬡ [28], ★ [29], ☆ [30], >< [3], # [31], () [32], <> [16], /\ [33], [] [34], ✖ [35], ✚ [6]; ***n* = 5:** ● [36]; ***n* = 6:** ● [37], ■ [38], ▲ [8], ▼ [39], ◆ [10], ⬢ [40], ○ [28], □ [13], △ [31], ▽ [41], ◇ [42], ⬡ [19]; ***n* = 8:** ● [7], ■ [8], ▲ [43], ▼ [44], ◆ [28], ⬢ [41], ○ [45], □ [19].

### 5.1.1.3. Electrical Conductivity

The resistance and reactance spectra obtained for the $[^1C_n{}^3C_1im]BF_4$ ionic liquids through the ILDEM experiments are presented in Fig. 5.9.

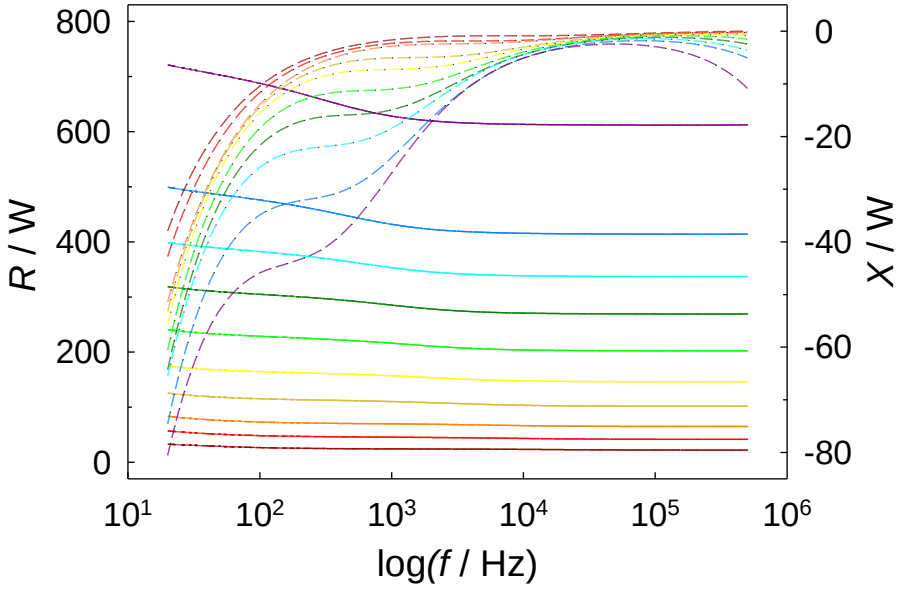



**Figure. 5.9.** Typical resistance (straight line) and reactance (dashed line) spectra for the $[^1C_n{}^3C_1im]BF_4$ series. *n* = 2, 3, 4, 5, 6, 7, 8, 9, 10, 12.

The VFT coefficients (Eq. 2.44) obtained from the experimental electrical conductivity-temperature data, $\sigma(T)$, are presented in Table 5.6.

**Table 5.6.** Fitting coefficients used to describe the temperature dependence of electrical conductivity of the studied $[^1C_n{}^3C_1im]BF_4$ homologue series.

| Ionic Liquid | $\frac{A_\sigma}{S\cdot m^{-1}}$ | $\frac{B_\sigma}{K}$ | $\frac{C_\sigma}{K}$ | $\frac{\sigma(T=298.15\ K)}{S\cdot m^{-1}}$ |
|---|---|---|---|---|
| $[^1C_2{}^3C_1im]BF_4$ | 131.9 ± 1.6 | 587.4 ± 3.6 | 165.8 ± 0.4 | 1.559 ± 0.023 |
| $[^1C_3{}^3C_1im]BF_4$ | 152.2 ± 1.1 | 669.2 ± 1.9 | 176.5 ± 0.2 | 0.6214 ± 0.0093 |
| $[^1C_4{}^3C_1im]BF_4$ | 164.0 ± 0.9 | 765.1 ± 1.6 | 173.7 ± 0.1 | 0.3506 ± 0.0053 |
| $[^1C_5{}^3C_1im]BF_4$ | 204.6 ± 8.3 | 899 ± 12 | 168.7 ± 1.0 | 0.1975 ± 0.0030 |
| $[^1C_6{}^3C_1im]BF_4$ | 230.7 ± 4.4 | 998.0 ± 5.7 | 165.5 ± 0.4 | 0.1246 ± 0.0019 |
| $[^1C_7{}^3C_1im]BF_4$ | 261 ± 20 | 1099 ± 23 | 161.1 ± 1.6 | 0.0858 ± 0.0013 |
| $[^1C_8{}^3C_1im]BF_4$ | 231.6 ± 9.6 | 1131 ± 13 | 160.7 ± 0.9 | 0.0618 ± 0.0009 |
| $[^1C_9{}^3C_1im]BF_4$ | 279 ± 11 | 1244 ± 13 | 155.3 ± 0.8 | 0.0460 ± 0.0007 |
| $[^1C_{10}{}^3C_1im]BF_4$ | 277 ± 16 | 1306 ± 19 | 151.9 ± 1.2 | 0.0367 ± 0.0006 |
| $[^1C_{12}{}^3C_1im]BF_4$ | 287 ± 17 | 1426 ± 21 | 145.3 ± 1.1 | 0.0255 ± 0.0004 |

The presented fitting coefficients were derived from the experimental $\sigma(T)$ data (appendix) by applying the VFT fitting function, Eq. 2.44. The standard uncertainties related to the VFT coefficients were calculated to the confidence level of 0.95 ($k \approx 2$). The relative standard uncertainty associated with the viscosity measurements was estimated as $u(\sigma) = 1.5\%$ (Eq. 4.15).

The deviation of the available electrical conductivity data to the experimental results for the $[^1C_n{}^3C_1im]BF_4$ series is presented in Fig. 5.10. Most of the data is in relatively good agreement with the experimental results ( deviation <5%). Once again the observed discrepancies might arise from the difficulties of handling tetrafluoroborate ILs. Some cases also seem to present a dependence with temperature suggesting the presence of problems associated with temperature control [46, 47].

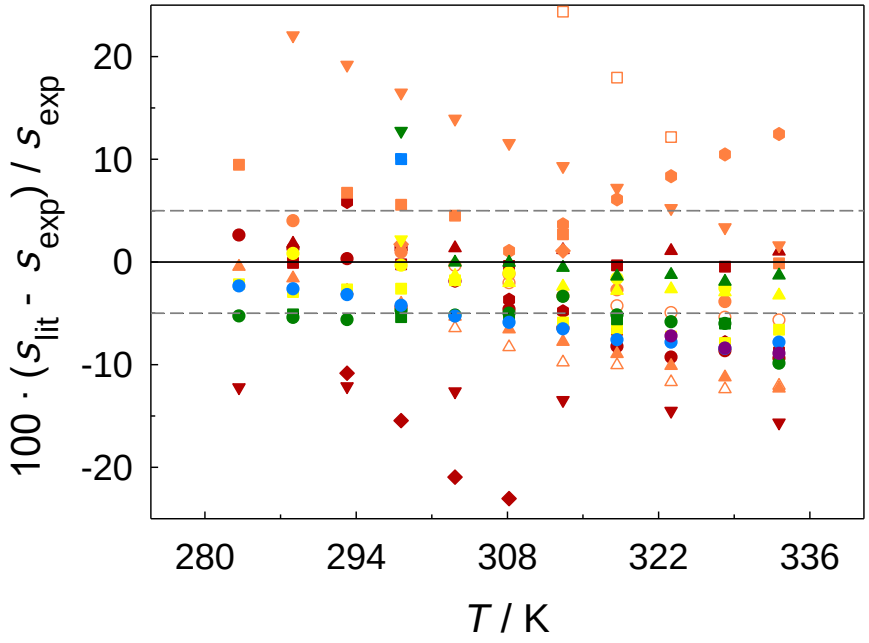



**Figure 5.10.** Deviation of the available electrical conductivity data to the experimental results for the $[^1C_n{}^3C_1im]BF_4$ series. ***n* = 2:** ● [48], ■ [49], ▲ [3], ▼ [11], ◆ [46], ⬢ [50]; ***n* = 3:** ● [51], ***n* = 4:** ● [49], ■ [29], ▲ [52], ▼ [47], ◆ [53], ⬢ [26], ○ [54], □ [55], △[24]; ***n* = 6:** ● [49], ■ [56], ▲ [41], ▼ [19]; ***n* = 8:** ● [57], ■ [49], ▲ [41], ▼ [19]; ***n* = 10:** ● [58], ■ [59]; ***n* = 12:** ● [58].

#### 5.1.1.4. Molar Conductivity

The molar conductivity of the $[^1C_n{}^3C_1im]BF_4$ ILs was calculated from the experimentally measured electrical conductivity and density data ILs. The molar conductivity is presented as a function of temperature and the number of carbons of the cation's alkyl chain in Fig. 5.11.

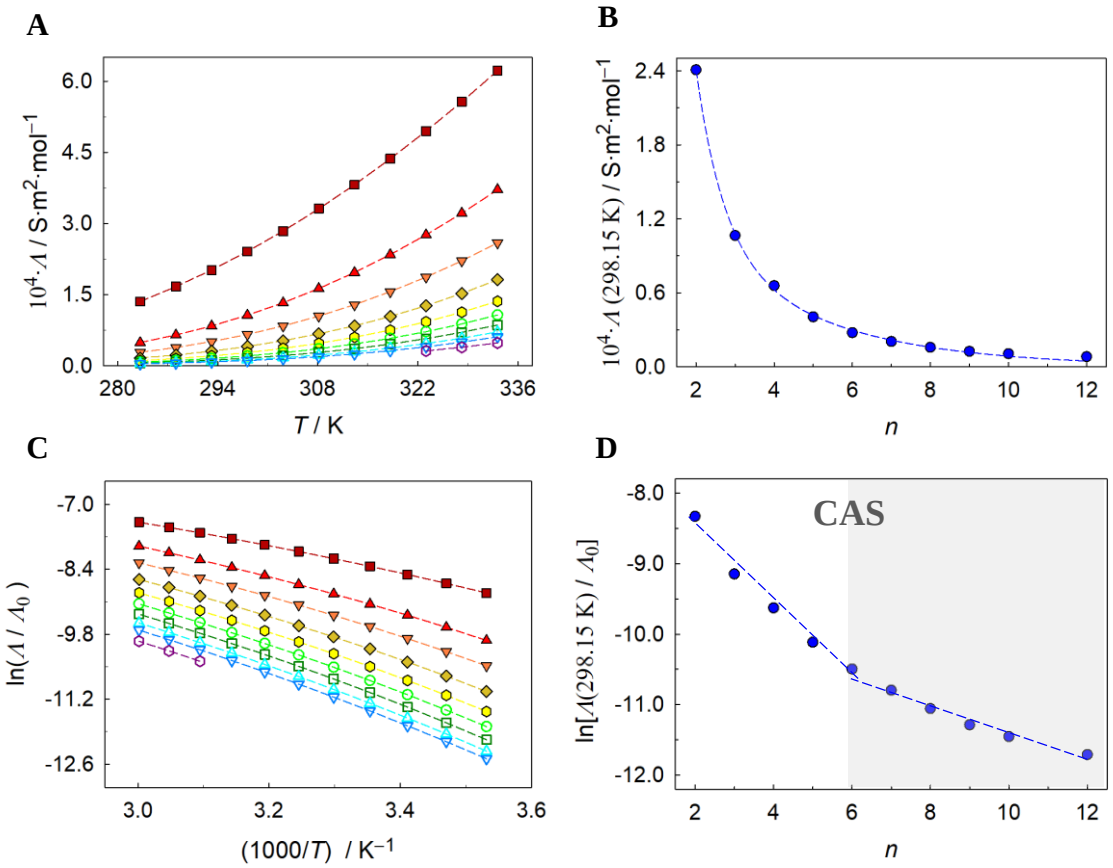



**Figure 5.11.** Molar conductivity of the $[^1C_n{}^3C_1im]BF_4$ ILs as functions of temperature (A, C) and number of carbons on the alkyl chain of the cation (B, D). **A**: Temperature dependence of molar conductivity; **B**: Dependence of molar conductivity with the alkyl chain length; **C**: Temperature dependence of molar conductivity (Arrhenius representation); **D**: Dependence of molar conductivity with the alkyl chain length (logarithmic form). $n$ = 2 ■, 3 ▲, 4 ▼, 5 ◆, 6 ⬢, 7 ○, 8 □, 9 △, 10 ▽, 12 ⬡. $\Lambda_0$ = 1 S·m$^2$·mol$^{-1}$.

The VFT coefficients (Eq. 2.44) obtained from the experimental molar conductivity-temperature data, $\Lambda(T)$, are presented in Table 5.7. The effect of the alkyl chain length on the obtained VFT coefficients is presented in Fig. 5.12 together with the graphical representation of the linearized VFT equation (Eq. 2.45).

**Table. 5.7.** Fitting coefficients used to describe the temperature dependence of molar conductivity of the studied $[^1C_n{}^3C_1im]BF_4$ homologue series.

| Ionic Liquid | $\frac{T_{interval}}{K}$ | $\frac{10^4 \cdot A_\Lambda}{S \cdot m^2 \cdot mol^{-1}}$ | $\frac{B_\Lambda}{K}$ | $\frac{C_\Lambda}{K}$ |
|---|---|---|---|---|
| $[^1C_2{}^3C_1im]BF_4$ | 283 − 333 | 243.5 ± 3.7 | 624.3 ± 4.5 | 162.9 ± 0.5 |
| $[^1C_3{}^3C_1im]BF_4$ | 283 − 333 | 308.8 ± 2.9 | 702.0 ± 2.7 | 174.3 ± 0.3 |
| $[^1C_4{}^3C_1im]BF_4$ | 283 − 333 | 366.1 ± 2.5 | 799.4 ± 1.9 | 171.7 ± 0.2 |
| $[^1C_5{}^3C_1im]BF_4$ | 283 – 333 | 501 ± 20 | 935 ± 12 | 166.8 ± 0.9 |
| $[^1C_6{}^3C_1im]BF_4$ | 283 – 333 | 615 ± 11 | 1036.6 ± 5.3 | 163.7 ± 0.4 |
| $[^1C_7{}^3C_1im]BF_4$ | 283 – 333 | 753 ± 58 | 1140 ± 24 | 159.3 ± 1.6 |
| $[^1C_8{}^3C_1im]BF_4$ | 283 – 333 | 719 ± 26 | 1173 ± 13 | 158.9 ± 0.9 |
| $[^1C_9{}^3C_1im]BF_4$ | 283 – 333 | 931 ± 39 | 1291 ± 14 | 153.4 ± 0.9 |
| $[^1C_{10}{}^3C_1im]BF_4$ | 283 – 333 | 994 ± 62 | 1355 ± 21 | 149.9 ± 1.3 |
| $[^1C_{12}{}^3C_1im]BF_4$ | 323 – 333 | 846 ± 53 | 1513 ± 23 | 141.3 ± 1.2 |

The presented fitting coefficients were derived from the experimental $\eta(T)$ data (appendix) by applying the VFT fitting function, Eq. 2.44. The standard uncertainties related to the VFT coefficients were calculated to the confidence level of 0.95 ($k \approx 2$).

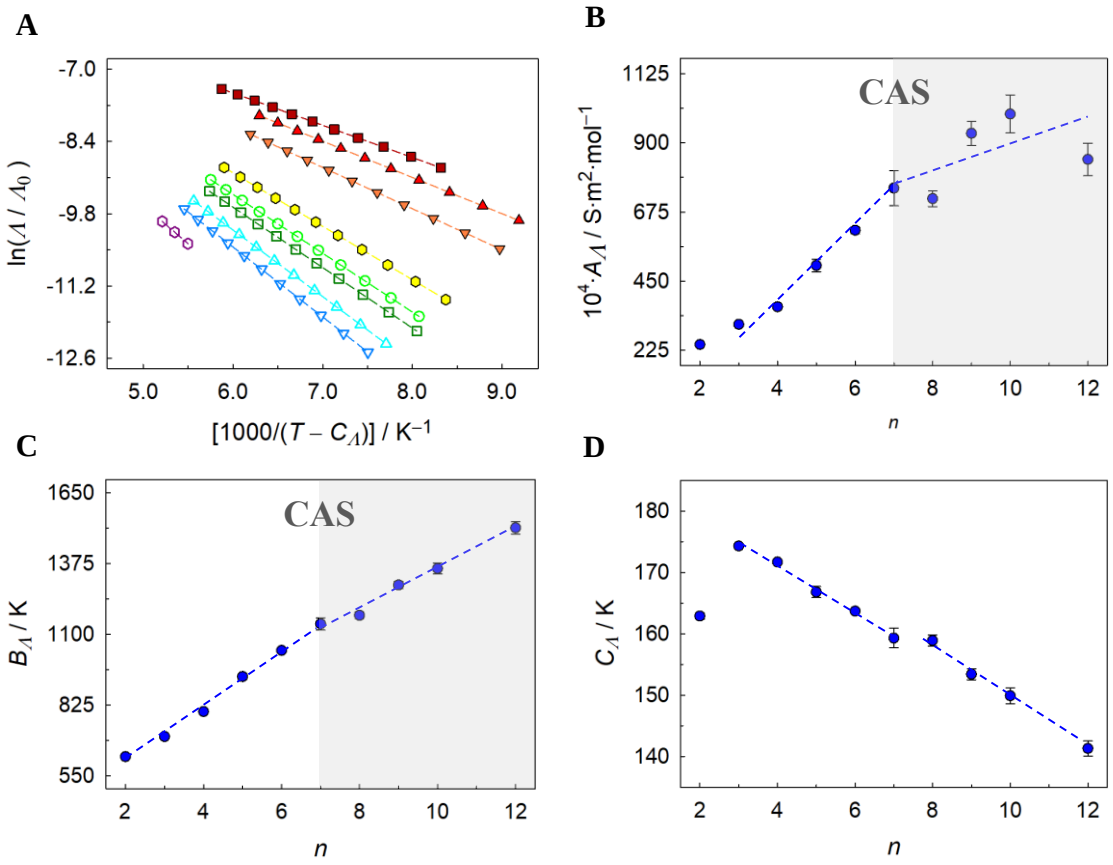



**Figure 5.12.** Impact of the alkyl chain length on the VFT coefficients for the molar conductivity of $[^1C_n{}^3C_1im]BF_4$ ILs. **A**: Linearized VFT representation $n$ = 2 ■, 3 ▲, 4 ▼, 5 ◆, 6 ⬢, 7 ○, 8 □, 9 △, 10 ▽, 12 ⬡; **B**: Pre-exponential coefficient, $A_\eta$; **C**: energy barrier-related coefficient, $B_\eta$; **D**: Vogel temperature, $C_\eta$. $\Lambda_0$ = 1 S·m²·mol⁻¹.

The molar conductivities at the reference temperature ($T$ = 298.15 K) are presented in Table 5.8, together with the energy barrier and strength parameter derived from Eq. 2.47 and Eq. 2.49, respectively. The temperature dependence of the conductivity-related energy barrier, $E_\Lambda$, and the effect of the alkyl chain length on $E_\Lambda$ and on the liquid fragility (strength parameter, $D_\Lambda$) are represented in Fig. 5.13.

**Table 5.8.** Molar conductivity and derived energy barrier of the studied $[^1C_n{}^3C_1im]BF_4$ homologue series at the reference temperature ($T$ = 298.15 K), together with the strength parameter.

| Ionic Liquid | $\frac{10^4 \cdot \Lambda(T=298.15\ K)}{S \cdot m^2 \cdot mol^{-1}}$ | $\frac{E_\Lambda(T=298.15\ K)}{kJ \cdot mol^{-1}}$ | $D_\Lambda$ |
|---|---|---|---|
| $[^1C_2{}^3C_1im]BF_4$ | 2.409 ± 0.036 | 25.22 ± 0.26 | 3.832 ± 0.030 |
| $[^1C_3{}^3C_1im]BF_4$ | 1.067 ± 0.016 | 33.83 ± 0.21 | 4.028 ± 0.017 |
| $[^1C_4{}^3C_1im]BF_4$ | 0.6577 ± 0.0099 | 36.95 ± 0.15 | 4.656 ± 0.012 |
| $[^1C_5{}^3C_1im]BF_4$ | 0.4058 ± 0.0061 | 40.05 ± 0.74 | 5.605 ± 0.076 |
| $[^1C_6{}^3C_1im]BF_4$ | 0.2758 ± 0.0041 | 42.38 ± 0.33 | 6.332 ± 0.036 |
| $[^1C_7{}^3C_1im]BF_4$ | 0.2046 ± 0.0031 | 43.7 ± 1.4 | 7.16 ± 0.17 |
| $[^1C_8{}^3C_1im]BF_4$ | 0.1578 ± 0.0024 | 44.71 ± 0.76 | 7.382 ± 0.092 |
| $[^1C_9{}^3C_1im]BF_4$ | 0.1246 ± 0.0019 | 45.54 ± 0.75 | 8.42 ± 0.10 |
| $[^1C_{10}{}^3C_1im]BF_4$ | 0.1066 ± 0.0016 | 45.6 ± 1.1 | 9.04 ± 0.16 |
| $[^1C_{12}{}^3C_1im]BF_4$ | 0.05478 ± 0.00082 | 45.5 ± 1.0 | 10.71 ± 0.19 |

$\Lambda$($T$ = 298.15 K) and $E_\Lambda$($T$ = 298.15 K) were calculated from the fitting coefficients presented in Table 5.7 and by applying Eq. 2.44 and Eq. 2.47, respectively. The strength parameter was calculated by Eq. 2.49, $D_\Lambda = B_\Lambda / C_\Lambda$. The relative standard uncertainty associated with the viscosity measurements was estimated as $u(\Lambda)$ = 1.5% (Eq. 4.15); The standard uncertainty associated with the derived energy barrier, $u(E_\Lambda)$, and strength parameter, $u(D_\Lambda)$, was calculated by applying the propagation of uncertainty to Eq. 2.47 and Eq. 2.49, respectively.

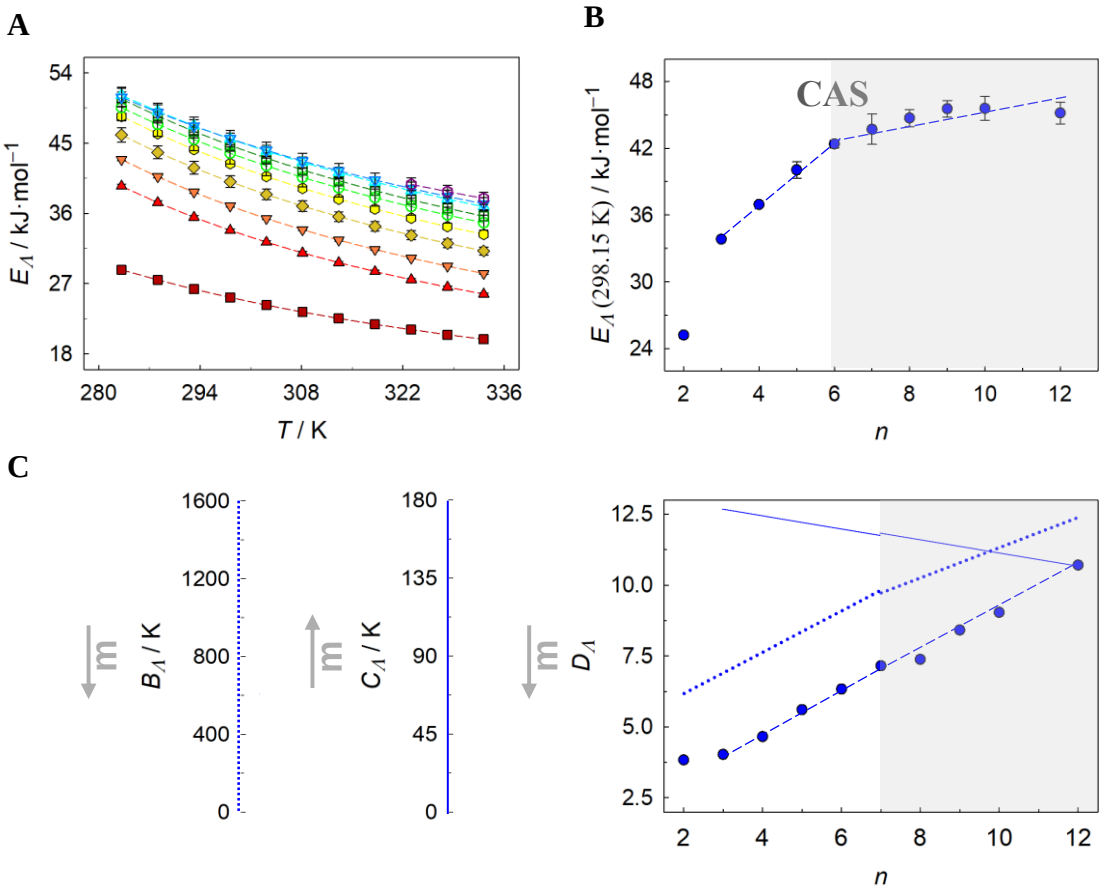



**Figure 5.13.** Graphical representation of the energy barrier and strength parameter derived from the experimental molar conductivity data of the $[^1C_n{}^3C_1im]BF_4$ ILs. **A**: Temperature dependence of the derived energy barrier $n$ = 2 ■, 3 ▲, 4 ▼, 5 ◆, 6 ⬢, 7 ○, 8 □, 9 △, 10 ▽, 12 ⬡; **B**: Effect of the alkyl chain length on the energy barrier; **C**: Effect of the alkyl chain length on the liquid fragility ($B_\Lambda$ and $C_\Lambda$ scales are included as guide lines).

### 5.1.2. $[^1C_n{}^3C_1im]PF_6$ Series

In this work, the density, viscosity, and electrical conductivity of the 1-alkyl-3-methylimidazolium hexafluorophosphate series, $[^1C_n{}^3C_1im]PF_6$ $n$ = 3 – 10 (Fig. 5.14) were measured for different temperatures.

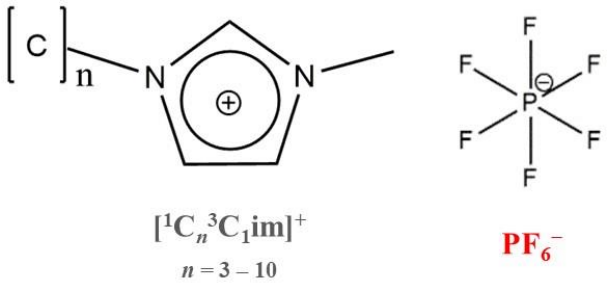



**Figure 5.14.** Structure of the studied $[^1C_n{}^3C_1im]PF_6$ ($n$ = 3 – 10).

#### 5.1.2.1. Density

The resulting fitting coefficients from the temperature dependence of density of the $[^1C_n{}^3C_1im]PF_6$ ILs (Eq. 2.4) are presented in Table 5.9. The densities at the reference temperature ($T$ = 298.15 K) are presented in Table 5.10, together with the molar volume and thermal expansion coefficient derived from Eq. 2.2 and Eq. 2.7 respectively. The graphical representation of density, thermal expansion coefficient, and molar volume as functions of temperature and number of carbons on the cations alkyl chain are presented in Fig 5.15.

**Table 5.9.** Fitting coefficients used to describe the temperature dependence of density of the studied $[^1C_n{}^3C_1im]PF_6$ homologue series.

| Ionic Liquid | $\frac{T_{\text{interval}}}{\text{K}}$ | $\frac{10^7 \cdot a_1}{\text{K}^{-2}}$ | $\frac{10^4 \cdot a_2}{\text{K}^{-1}}$ | $\frac{a_0}{\text{K}}$ |
|---|---|---|---|---|
| $[^1C_3{}^3C_1im]PF_6$ | 308 – 373 | −0.088 ± 0.167 | −6.033 ± 0.116 | 7.4316 ± 0.0020 |
| $[^1C_{10}{}^3C_1im]PF_6$ | 318 – 373 | 6.711 ± 1.512 | −5.834 ± 0.105 | 7.2475 ± 0.0018 |

The presented fitting coefficients were derived from the experimental $\rho(T)$ data (appendix) by applying a polynomial fitting function, $\ln[\rho(T)] = a_2T^2 + a_1T + a_0$ (Eq. 2.4). The standard uncertainties related to the fitting coefficients were calculated to the confidence level of 0.95 ($k \approx 2$).

**Table 5.10.** Density, thermal expansion coefficient, and molar volume at the reference temperature ($T$ = 298.15 K) for the studied $[^1C_n{}^3C_1im]PF_6$ homologue series.

| Ionic Liquid | $\frac{\rho(298.15\ \text{K})}{\text{kg·m}^{-3}}$ | $\frac{10^4 \cdot \alpha_p(298.15\ \text{K})}{\text{K}^{-1}}$ | $\frac{10^6 \cdot V_m(298.15\ \text{K})}{\text{m}^3\text{·mol}^{-1}}$ |
|---|---|---|---|
| $[^1C_3{}^3C_1im]PF_6$ | 1409.6 ± 0.5 | 6.08 ± 0.12 | 191.7 ± 0.5 |
| $[^1C_{10}{}^3C_1im]PF_6$ | 1252.9 ± 0.5 | 6.23 ± 0.11 | 313.9 ± 0.7 |

$\rho(T$ = 298.15 K) and $\alpha_p(T$ = 298.15 K) were calculated from the fitting coefficients presented in Table 5.9 and by applying Eq. 2.4. and Eq. 2.7 respectively. $V_m(298.15\ \text{K}) = M/\rho(298.15\ \text{K})$. The standard uncertainty associated with $\alpha_p$ and $V_m$ were calculated by applying the propagation of uncertainty to Eq. 2.7 and 2.2, respectively.

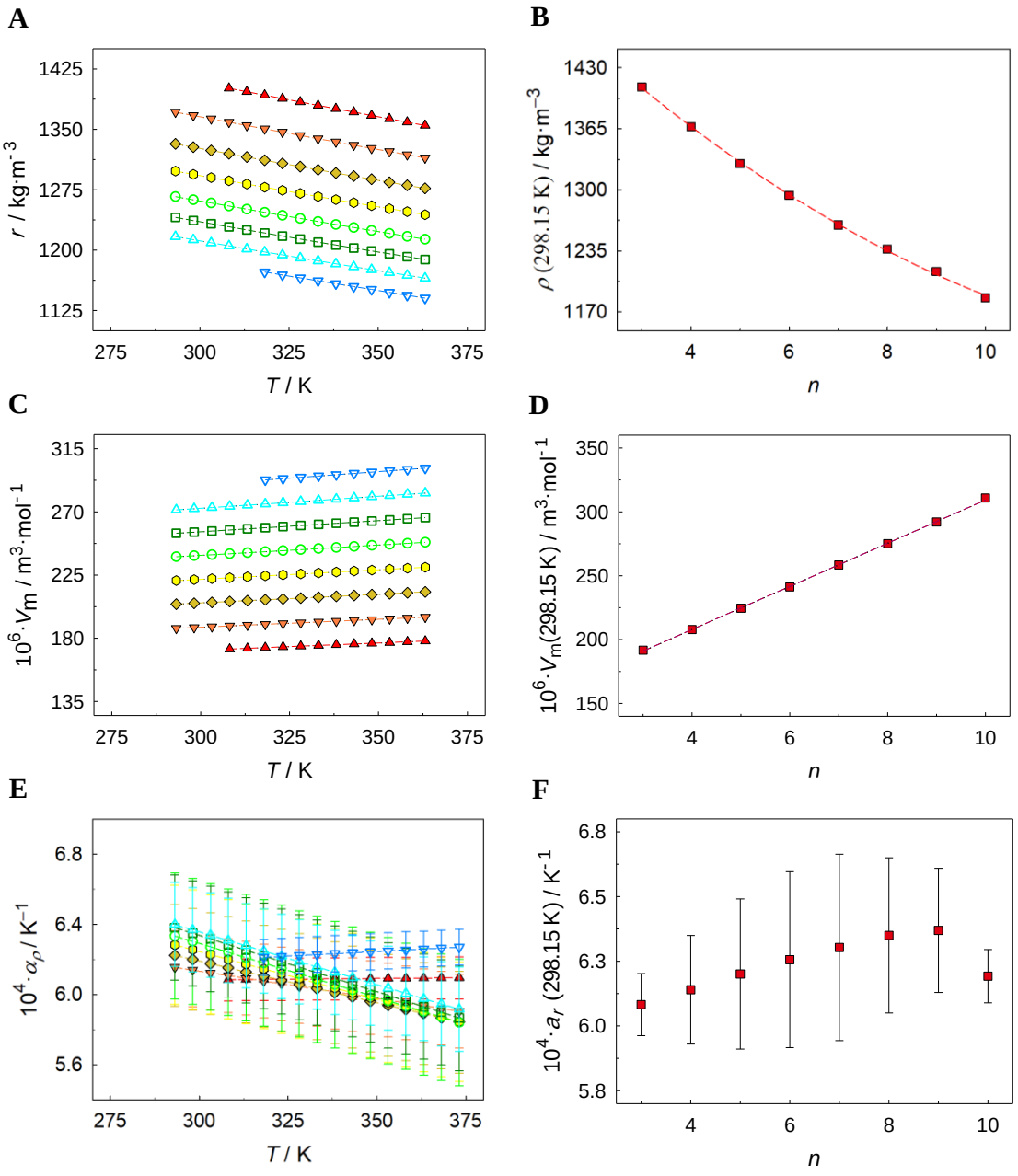



**Figure 5.15.** Density and derived properties of the [$^1C_n{}^3C_1$im]$PF_6$ ILs as functions of temperature (A, C, E) and number of carbons on the alkyl chain of the cation (B, D, F). **A**, **B**: Density; **C**, **D**: Molar volume; **E**, **F**: Thermal expansion coefficient. $n$ = 3 ▲, 4 ▼, 5 ◆, 6 ⬢, 7 ○, 8 □, 9 △, 10 ▽.

#### 5.1.2.2. Viscosity

The obtained viscosity data for the $[^1C_n{}^3C_1im]PF_6$ ILs is presented as a function of temperature and the number of carbons of the cation's alkyl chain in Fig. 5.16.

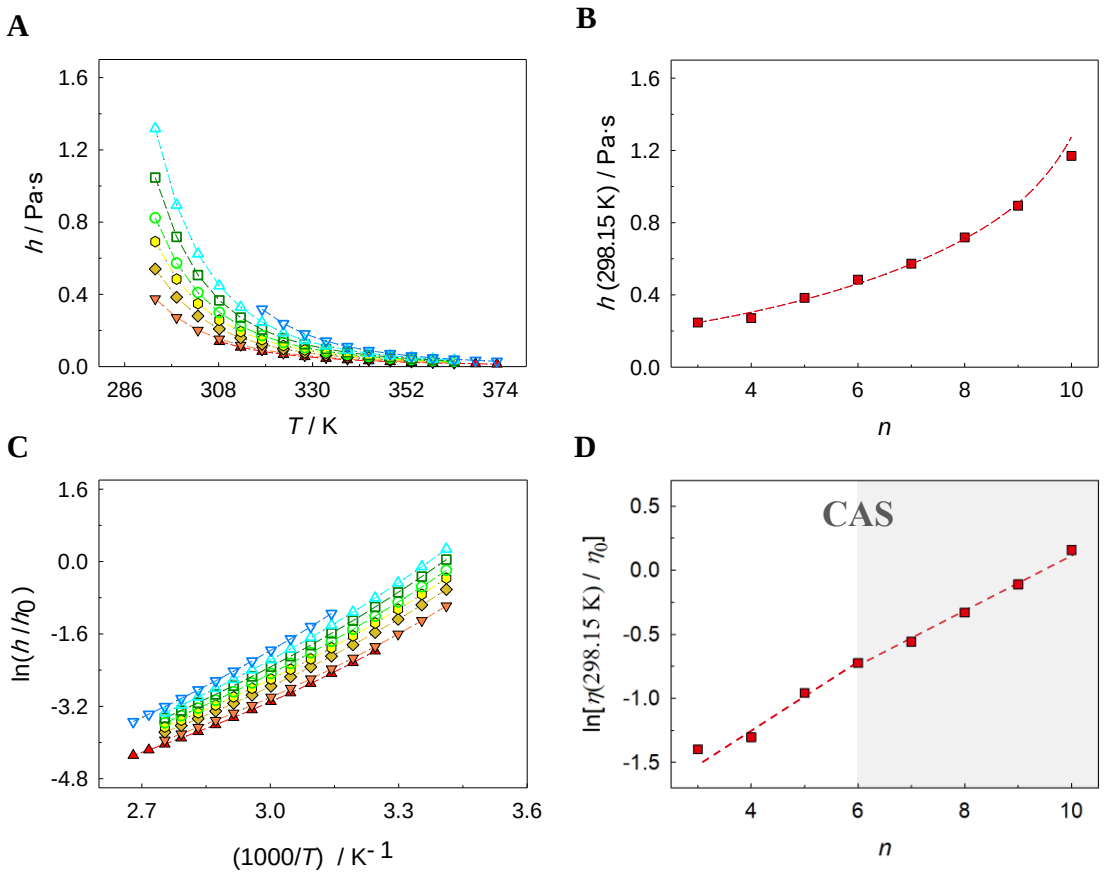



**Figure 5.16.** Viscosity of the $[^1C_n{}^3C_1im]PF_6$ ILs as functions of temperature (A, C) and number of carbons on the alkyl chain of the cation (B, D). **A**: Temperature dependence of viscosity; **B**: Dependence of viscosity with the alkyl chain length; **C**: Temperature dependence of viscosity (Arrhenius representation); **D**: Dependence of viscosity with the alkyl chain length (logarithmic form). $n$ = 3 ▲, 4 ▼, 5 ◆, 6 ⬢, 7 ○, 8 □, 9 △, 10 ▽. $\eta_0$ = 1 Pa·s.

The VFT coefficients (Eq 2.44) obtained from the experimental viscosity-temperature data, $\eta(T)$, are presented in Table 5.11. The effect of the alkyl chain length on the obtained VFT coefficients is presented in Fig. 5.17 together with the graphical representation of the linearized VFT equation (Eq. 2.45).

**Table 5.11.** Fitting coefficients used to describe the temperature dependence of viscosity of the studied $[^1C_n{}^3C_1im]PF_6$ homologue series.

| Ionic Liquid | $\frac{T_{interval}}{K}$ | $\frac{10^3 \cdot A_\eta}{Pa{\cdot}s}$ | $\frac{B_\eta}{K}$ | $\frac{C_\eta}{K}$ |
|---|---|---|---|---|
| $[^1C_3{}^3C_1im]PF_6$ | 308 – 373 | 0.1434 ± 0.0031 | 884.5 ± 6.8 | 179.5 ± 0.6 |
| $[^1C_{10}{}^3C_1im]PF_6$ | 318 – 373 | 0.0516 ± 0.0022 | 1270 ± 14 | 172.6 ± 0.9 |

The presented fitting coefficients were derived from the experimental $\eta(T)$ data (appendix) by applying the VFT fitting function, Eq. 2.44. The standard uncertainties related to the VFT coefficients were calculated to the confidence level of 0.95 ($k \approx 2$).

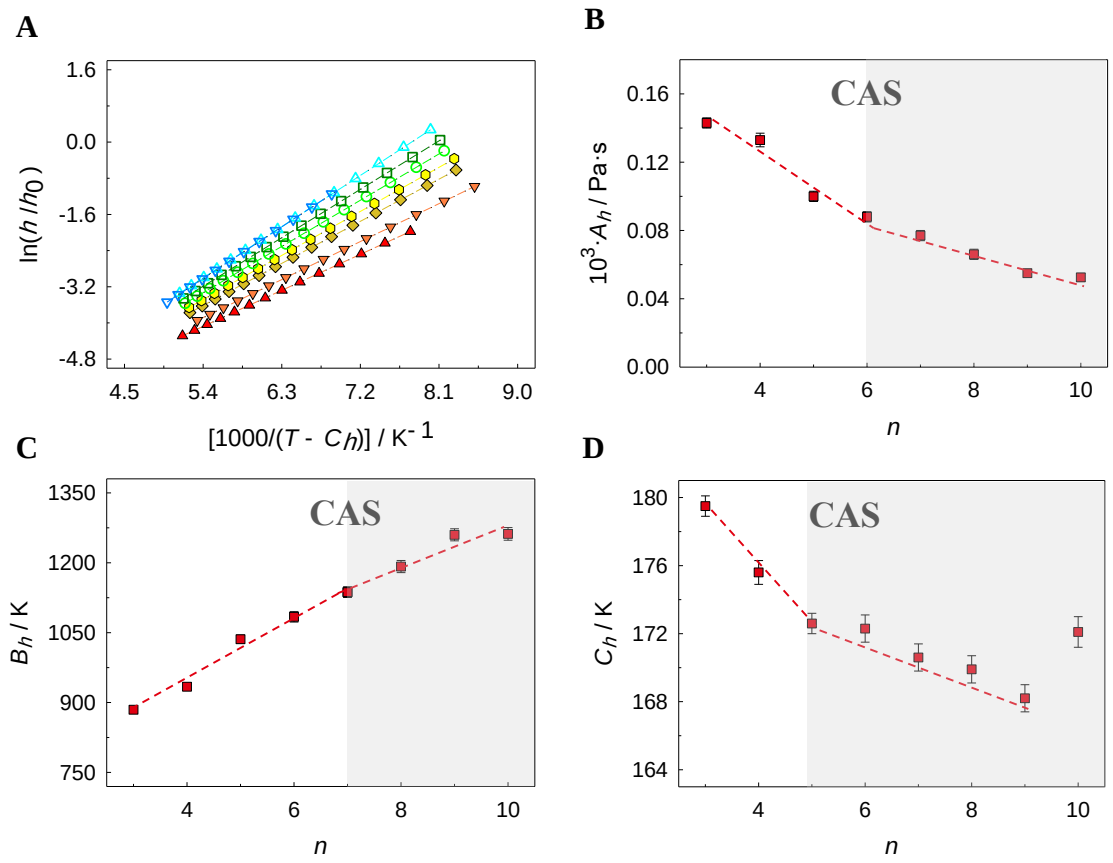



**Figure 5.17.** Impact of the alkyl chain length on the VFT coefficients for the viscosity of $[^1C_n{}^3C_1im]PF_6$ ILs. **A**: Linearized VFT representation $n$ = 3 ▲, 4 ▼, 5 ◆, 6 ⬢, 7 ○, 8 □, 9 △, 10 ▽; **B**: Pre-exponential coefficient, $A_\eta$; **C**: energy barrier-related coefficient, $B_\eta$; **D**: Vogel temperature, $C_\eta$.

The viscosities at the reference temperature ($T$ = 298.15 K) are presented in Table 5.12, together with the energy barrier and strength parameter derived from Eq. 2.47 and Eq. 2.49 respectively. The temperature dependence of the viscosity-related energy barrier, $E_\eta$, and the effect of the alkyl chain length on $E_\eta$ and on the liquid fragility (strength parameter, $D_\eta$) are represented in Fig. 5.18.

**Table 5.12.** Viscosity and derived energy barrier of the studied $[^1C_n{}^3C_1im]PF_6$ homologue series at the reference temperature ($T$ = 298.15 K), together with the strength parameter.

| Ionic Liquid | $\eta(T=298.15\ K)$ / Pa·s | $E_\eta(T=298.15\ K)$ / kJ·mol$^{-1}$ | $D_\eta$ |
|---|---|---|---|
| $[^1C_3{}^3C_1im]PF_6$ | 0.2471 ± 0.0025 | 46.44 ± 0.12 | 4.928 ± 0.041 |
| $[^1C_{10}{}^3C_1im]PF_6$ | 1.2768 ± 0.0128 | 59.57 ± 0.12 | 7.355 ± 0.087 |

$\eta(T = 298.15\ K)$ and $E_\eta(T = 298.15\ K)$ were calculated from the fitting coefficients presented in Table 5.11 and by applying Eq. 2.44 and Eq. 2.47, respectively. The strength parameter was calculated by Eq. 2.49, $D_\eta = B_\eta / C_\eta$. The relative standard uncertainty associated with the viscosity measurements was estimated as $u(\eta)$ = 1.0% (Eq. 2.72); The standard uncertainty associated with the derived energy barrier, $u(E_\eta)$, and strength parameter, $u(D_\eta)$, was calculated by applying the propagation of uncertainty to Eq. 2.47 and Eq. 2.49, respectively.

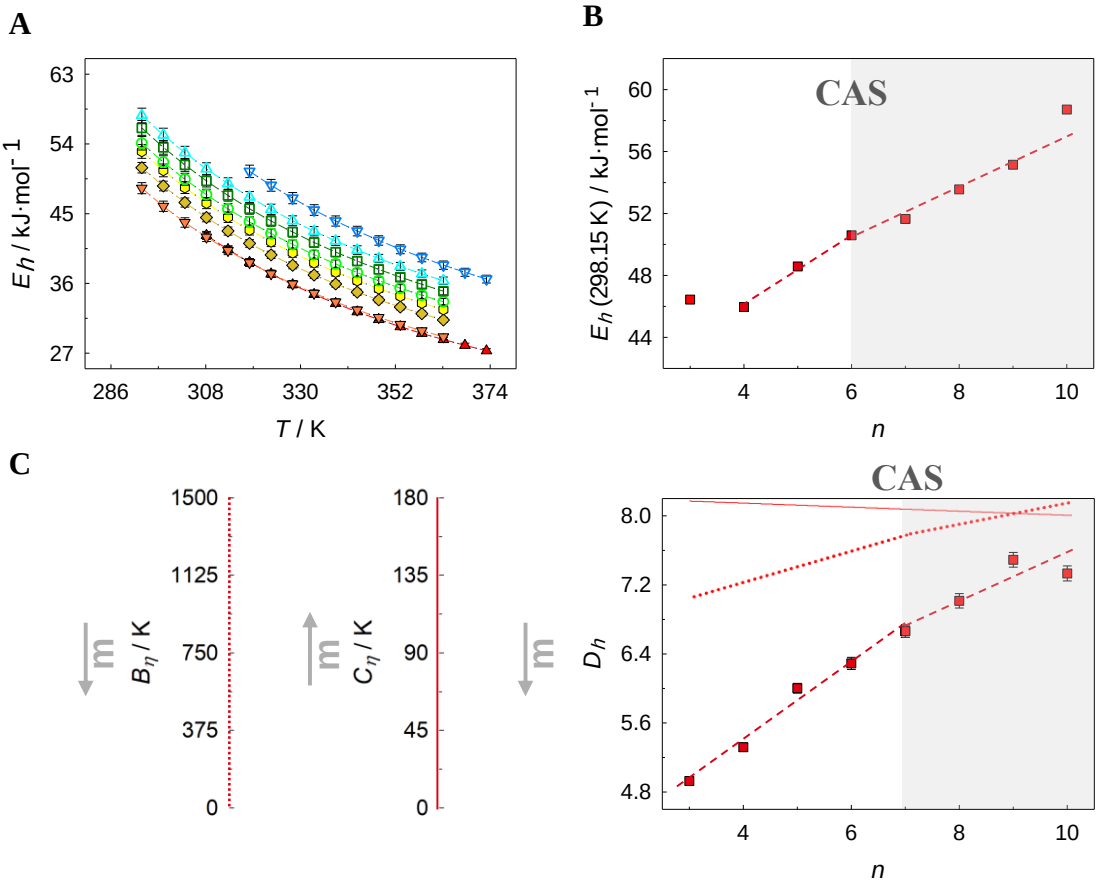



**Figure 5.18.** Graphical representation of the energy barrier and strength parameter derived from the experimental viscosity data of the $[^1C_n{}^3C_1im]PF_6$. **A**: Temperature dependence of the derived energy barrier $n$ = 3 ▲, 4 ▼, 5 ◆, 6 ⬢, 7 ○, 8 □, 9 △, 10 ▽; **B**: Effect of the alkyl chain length on the energy barrier; C: Effect of the alkyl chain length on the liquid fragility ($B_\eta$ and $C_\eta$ scales are included as guide lines).

The deviation of the available viscosity data to the experimental results for the $[^1C_n{}^3C_1im]PF_6$ series is presented in Fig. 5.19.

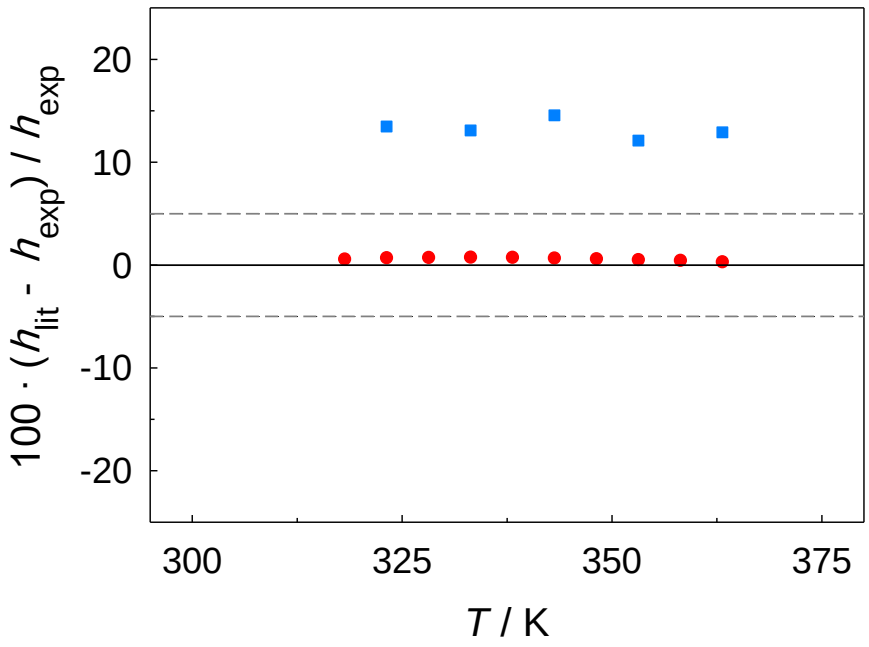



**Figure 5.19.** Deviation of the available viscosity data to the experimental results for the $[^1C_n{}^3C_1im]PF_6$ series. ***n* = 3** ● [60]; ***n* = 10** ■ [28].

Only one source was found for each ionic liquid. The literature data for $[^1C_3{}^3C_1im]PF_6$ reported by Neves *et al.*. is in excellent agreement with the present results. However, the results reported by Seddon *et al.* [28] for $[^1C_3{}^3C_1im]PF_6$ deviate significantly (>10%) from the results obtained in this work. Still, the experimental values for $[^1C_3{}^3C_1im]PF_6$ fit well with the trend of the remaining ILs of the series.

#### 5.1.2.3. Electrical Conductivity

The resistance and reactance spectra obtained for the $[^1C_n{}^3C_1im]PF_6$ ionic liquids through the ILDEM experiments are presented in Fig. 5.20.

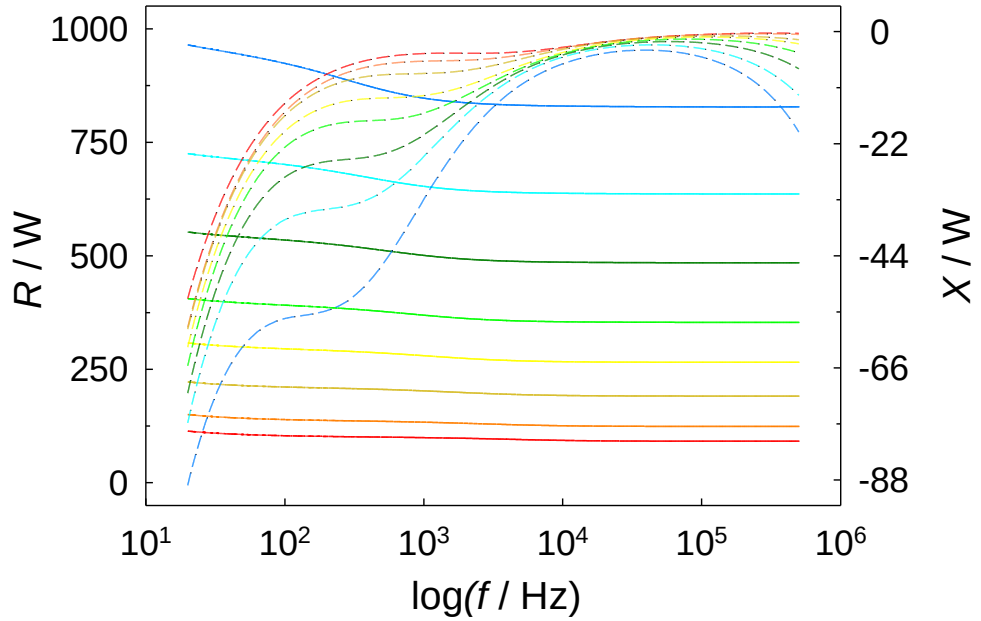



**Figure 5.20.** Typical resistance (straight line) and reactance (dashed line) spectra for the $[^1C_n{}^3C_1im]PF_6$ series. 3, 4, 5, 6, 7, 8, 9, 10.

The VFT coefficients (Eq 2.24) obtained from the experimental electrical conductivity-temperature data, $\sigma(T)$, are presented in Table 5.13.

**Table 5.13.** Fitting coefficients used to describe the temperature dependence of electrical conductivity of the studied $[^1C_n{}^3C_1im]PF_6$ homologue series.

| Ionic Liquid | $\frac{A_\sigma}{S\cdot m^{-1}}$ | $\frac{B_\sigma}{K}$ | $\frac{C_\sigma}{K}$ | $\frac{\sigma(T=298.15\ K)}{S\cdot m^{-1}}$ |
|---|---|---|---|---|
| $[^1C_3{}^3C_1im]PF_6$ | 171 ± 12 | 792 ± 20 | 180.3 ± 1.8 | 0.2062 ± 0.0031 |
| $[^1C_4{}^3C_1im]PF_6$ | 182.0 ± 7.0 | 880 ± 11 | 174.5 ± 0.9 | 0.1474 ± 0.0022 |
| $[^1C_5{}^3C_1im]PF_6$ | 204.4 ± 3.9 | 976.3 ± 5.5 | 172.5 ± 0.4 | 0.0863 ± 0.0013 |
| $[^1C_6{}^3C_1im]PF_6$ | 235 ± 17 | 1074 ± 22 | 169.6 ± 1.5 | 0.0555 ± 0.0008 |
| $[^1C_7{}^3C_1im]PF_6$ | 341.5 ± 9.2 | 1245.1 ± 8.4 | 161.4 ± 0.5 | 0.0380 ± 0.0006 |
| $[^1C_8{}^3C_1im]PF_6$ | 304 ± 26 | 1263 ± 26 | 163.0 ± 1.6 | 0.0266 ± 0.0004 |
| $[^1C_9{}^3C_1im]PF_6$ | 362 ± 28 | 1366 ± 25 | 159.6 ± 1.4 | 0.0198 ± 0.0003 |
| $[^1C_{10}{}^3C_1im]PF_6$ | 336 ± 19 | 1402 ± 18 | 159.0 ± 1.0 | 0.0142 ± 0.0002 |

The presented fitting coefficients were derived from the experimental $\sigma(T)$ data (appendix) by applying the VFT fitting function, Eq. 2.44. The standard uncertainties related to the VFT coefficients were calculated to the confidence level of 0.95 ($k \approx 2$). The relative standard uncertainty associated with the viscosity measurements was estimated as $u(\sigma)$ = 1.5% (Eq. 4.15).

The deviation of the available electrical conductivity data to the experimental results for the $[^1C_n{}^3C_1im]PF_6$ series is presented in Fig. 5.21.

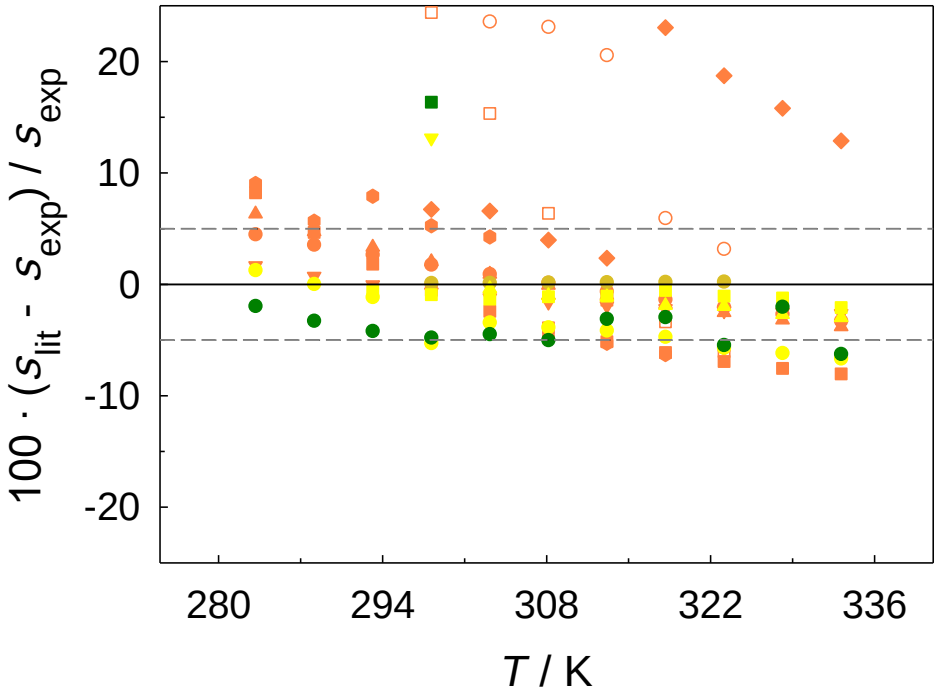



**Figure 5.21.** Deviation of the available electrical conductivity data to the experimental results for the [$^1C_n{}^3C_1$im]$PF_6$ series. ***n* = 4** ● [61], ■ [55], ▲ [29], ▼ [62], ◆ [63], ⬢ [64], ○ [65], □ ; ***n* = 5** ● [36]; ***n* = 6** ● [52], ■ [66], ▲ [41], ▼ [67]; ***n* = 8** ● [57], ■ [67].

As observed, the majority of the data is in good agreement with the results obtained in this work, particularly the results published by Wu *et al.* (*n* = 5) [36] and Li *et al.* (*n* = 6) [66] (deviation <2%). There are some sources with significant positive deviations that might be due to high water content in the sample or the formation of conductive species from the reaction of water with the hexafluorophosphate anion. No data was found for *n* = 3, 7, 9, and 10.

#### 5.1.2.4. Molar Conductivity

The molar conductivity of the [$^1C_n{}^3C_1$im]$PF_6$ ILs was calculated from the experimentally measured electrical conductivity and density data of the ILs. The molar conductivity is presented as a function of temperature and the number of carbons of the cation's alkyl chain in Fig. 5.22.

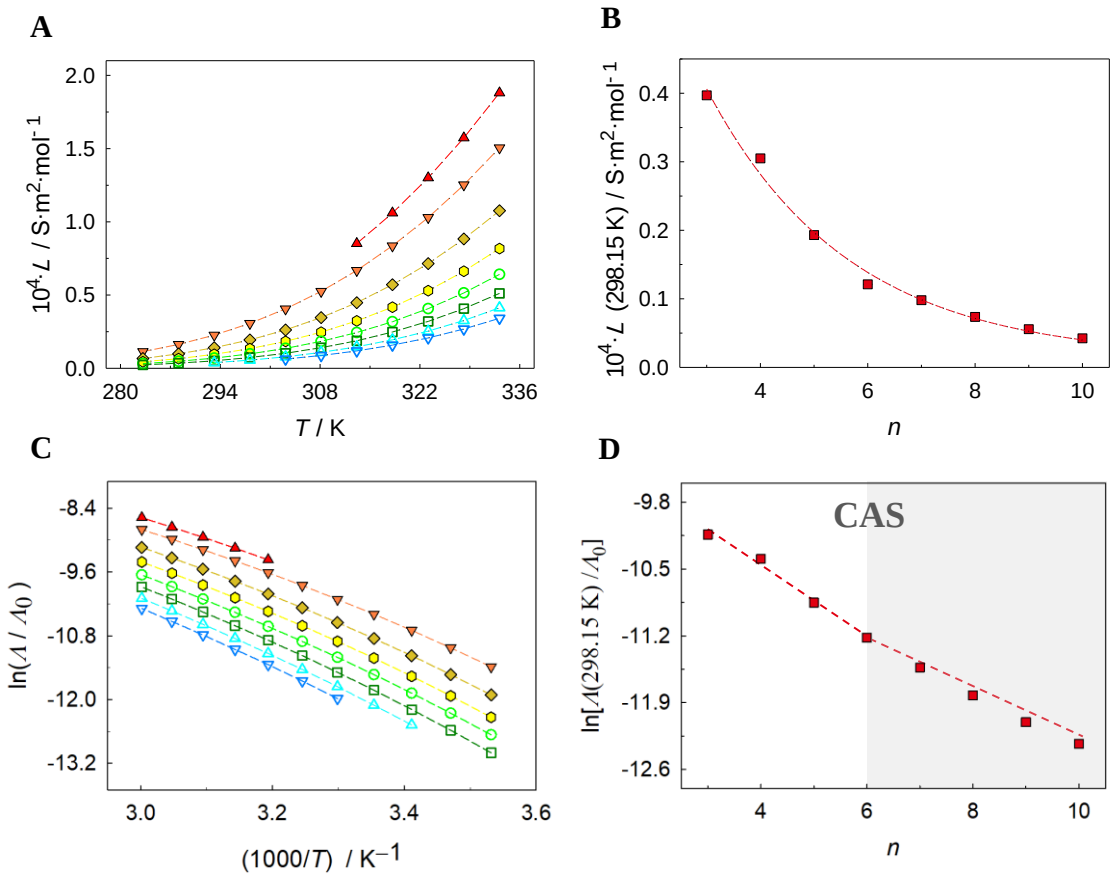



**Figure 5.22.** Molar conductivity of the [$^1$C$_n$$^3$C$_1$im]PF$_6$ ILs as functions of temperature (A, C) and number of carbons on the alkyl chain of the cation (B, D). **A**: Temperature dependence of molar conductivity; **B**: Dependence of molar conductivity with the alkyl chain length; **C**: Temperature dependence of molar conductivity (Arrhenius representation); **D**: Dependence of molar conductivity with the alkyl chain length (logarithmic form). $n$ = 3 ▲, 4 ▼, 5 ◆, 6 ●, 7 ○, 8 □, 9 △, 10 ▽. $\Lambda_0$ = 1 S·m$^2$·mol$^{-1}$.

The VFT coefficients (Eq 2.44) obtained from the experimental molar conductivity-temperature data, $\Lambda(T)$, are presented in Table 5.14. The effect of the alkyl chain length on the obtained VFT coefficients is presented in Fig. 5.23 together with the graphical representation of the linearized VFT equation (Eq. 2.45).

**Table. 5.14.** Fitting coefficients used to describe the temperature dependence of molar conductivity of the studied $[^1C_n{}^3C_1im]PF_6$ homologue series.

| Ionic Liquid | $\frac{T_{interval}}{K}$ | $\frac{10^4 \cdot A_\Lambda}{S \cdot m^2 \cdot mol^{-1}}$ | $\frac{B_\Lambda}{K}$ | $\frac{C_\Lambda}{K}$ |
|---|---|---|---|---|
| $[^1C_3{}^3C_1im]PF_6$ | 313 – 333 | 396 ± 28 | 830 ± 21 | 178.0 ± 1.8 |
| $[^1C_4{}^3C_1im]PF_6$ | 283 – 333 | 450 ± 17 | 914 ± 11 | 172.9 ± 0.8 |
| $[^1C_5{}^3C_1im]PF_6$ | 283 – 333 | 546.7 ± 9.0 | 1010.7 ± 4.8 | 171.0 ± 0.3 |
| $[^1C_6{}^3C_1im]PF_6$ | 283 – 333 | 678 ± 50 | 1109 ± 22 | 169.6 ± 1.5 |
| $[^1C_7{}^3C_1im]PF_6$ | 283 – 333 | 862 ± 24 | 1219.3 ± 8.2 | 163.9 ± 0.5 |
| $[^1C_8{}^3C_1im]PF_6$ | 283 – 333 | 1011 ± 87 | 1302 ± 27 | 161.5 ± 1.6 |
| $[^1C_9{}^3C_1im]PF_6$ | 293 – 333 | 1291 ± 99 | 1409 ± 25 | 158.0 ± 1.4 |
| $[^1C_{10}{}^3C_1im]PF_6$ | 303 – 333 | 1244 ± 69 | 1451 ± 18 | 157.1 ± 1.0 |

The presented fitting coefficients were derived from the experimental $\eta(T)$ data (appendix) by applying the VFT fitting function, Eq. 2.44. The standard uncertainties related to the VFT coefficients were calculated to the confidence level of 0.95 ($k \approx 2$).

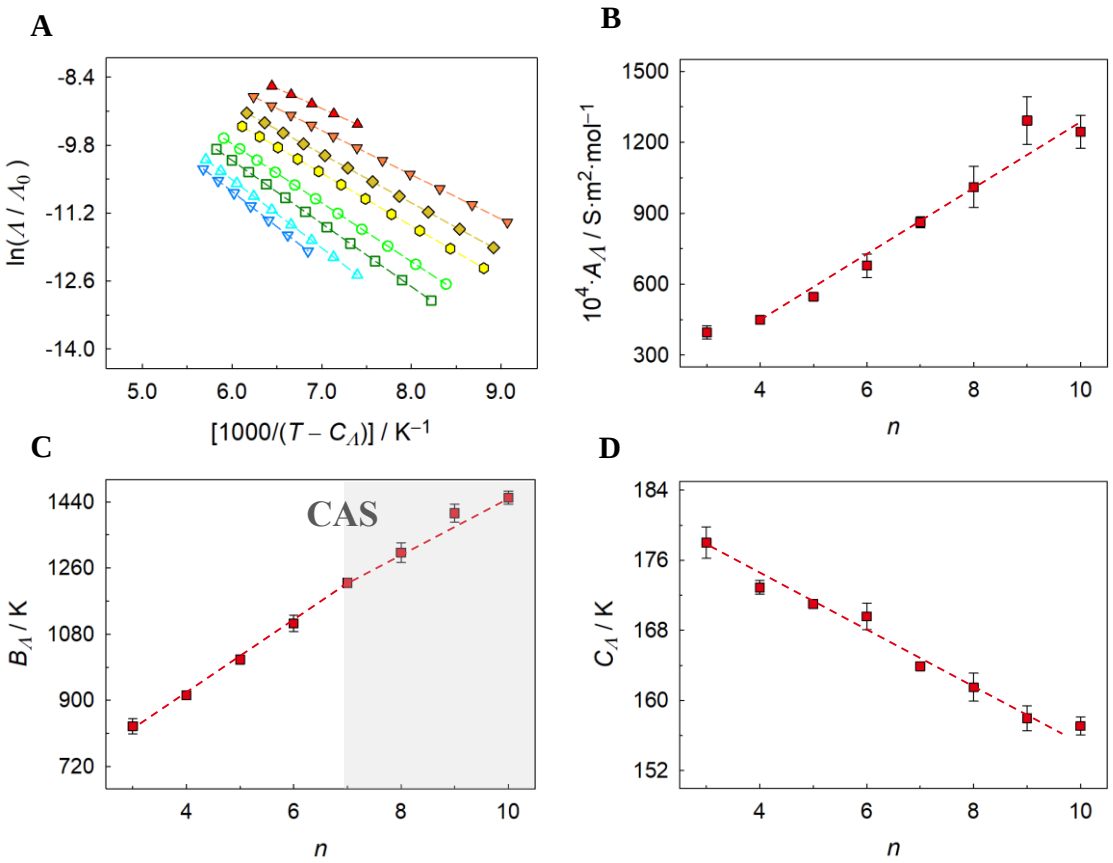



**Figure 5.23.** Impact of the alkyl chain length on the VFT coefficients for the molar conductivity of $[^1C_n{}^3C_1im]PF_6$ series**. A**: Linearized VFT representation $n$ = 3 ▲, 4 ▼, 5 ◆, 6 ⬢, 7 ○, 8 □, 9 △, 10 ▽; **B**: Pre-exponential coefficient, $A_\Lambda$; **C**: energy barrier-related coefficient, $B_\Lambda$; **D**: Vogel temperature, $C_\Lambda$. $\Lambda_0$ = 1 S·m$^2$·mol$^{-1}$.

The molar conductivities at the reference temperature ($T$ = 298.15 K) are presented in Table 5.15, together with the energy barrier and strength parameter derived from Eq. 2.47 and Eq. 2.49, respectively. The temperature dependence of the conductivity-related energy barrier, $E_\Lambda$, and the effect of the alkyl chain length on $E_\Lambda$ and on the liquid fragility (strength parameter, $D_\Lambda$) are represented in Fig. 5.24.

**Table 5.15**. Molar conductivity and derived energy barrier of the studied $[^1C_n{}^3C_1im]PF_6$ homologue series at the reference temperature ($T$ = 298.15 K), together with the strength parameter.

| Ionic Liquid | $10^4 \cdot \Lambda(T$=298.15 K) / S·m²·mol$^{-1}$ | $E_\Lambda(T$=298.15 K) / kJ·mol$^{-1}$ | $D_\Lambda$ |
|---|---|---|---|
| $[^1C_3{}^3C_1im]PF_6$ | 0.3969 ± 0.0060 | 42.5 ± 1.7 | 4.661 ± 0.124 |
| $[^1C_4{}^3C_1im]PF_6$ | 0.3050 ± 0.0046 | 43.05 ± 0.74 | 5.285 ± 0.066 |
| $[^1C_5{}^3C_1im]PF_6$ | 0.1930 ± 0.0029 | 46.21 ± 0.31 | 5.911 ± 0.030 |
| $[^1C_6{}^3C_1im]PF_6$ | 0.1211 ± 0.0018 | 49.6 ± 1.5 | 6.541 ± 0.142 |
| $[^1C_7{}^3C_1im]PF_6$ | 0.0980 ± 0.0015 | 50.00 ± 0.50 | 7.439 ± 0.055 |
| $[^1C_8{}^3C_1im]PF_6$ | 0.0736 ± 0.0011 | 51.5 ± 1.6 | 8.062 ± 0.185 |
| $[^1C_9{}^3C_1im]PF_6$ | 0.05568 ± 0.00084 | 53.0 ± 1.4 | 8.919 ± 0.177 |
| $[^1C_{10}{}^3C_1im]PF_6$ | 0.04238 ± 0.00064 | 53.9 ± 1.0 | 9.236 ± 0.129 |

$\Lambda$($T$ = 298.15 K) and $E_\Lambda$($T$ = 298.15 K) were calculated from the fitting coefficients presented in Table 5.14 and by applying Eq. 2.44 and Eq. 2.47, respectively. The strength parameter was calculated by Eq. 2.49, $D_\Lambda = B_\Lambda / C_\Lambda$. The relative standard uncertainty associated with the viscosity measurements was estimated as $u(\Lambda)$ = 1.5% (Eq. 4.15); The standard uncertainty associated with the derived energy barrier, $u(E_\Lambda)$, and strength parameter, $u(D_\Lambda)$, was calculated by applying the propagation of uncertainty to Eq. 2.47 and Eq. 2.49, respectively.

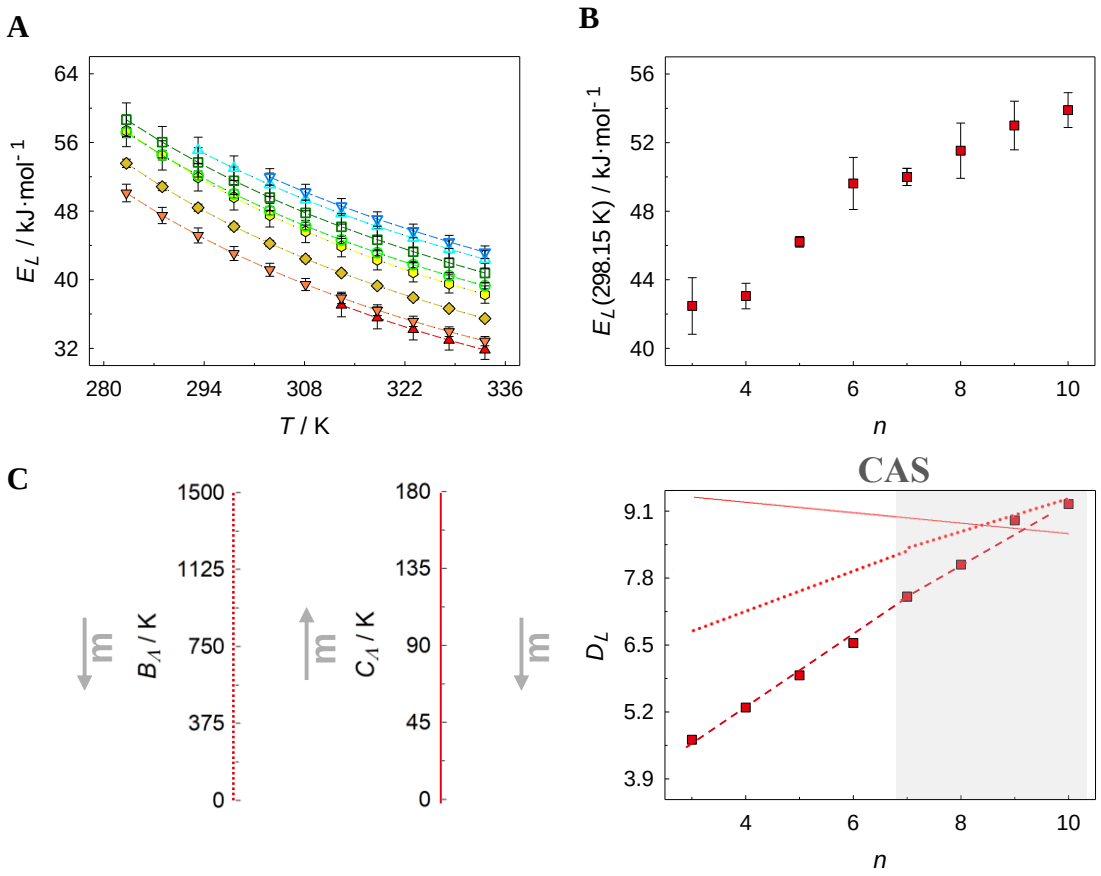



**Figure 5.24.** Graphical representation of the energy barrier and strength parameter derived from the experimental molar conductivity data of the $[^1C_n{}^3C_1im]PF_6$ series. **A**: Temperature dependence of the derived energy barrier $n$ = 2 ■, 3 ▲, 4 ▼, 5 ◆, 6 ⬢, 7 ○, 8 □, 9 △, 10 ▽, 12 ⬡; **B**: Effect of the alkyl chain length on the energy barrier; **C**: Effect of the alkyl chain length on the liquid fragility ($B_\Lambda$ and $C_\Lambda$ scales are included as guide lines).

### 5.1.3. $[^1C_n{}^3C_1im][OTf]$ Series

In this work, the density, viscosity, and electrical conductivity of the 1-alkyl-3-methylimidazolium trifluoromethanesulfonate series, $[^1C_n{}^3C_1im][OTf]$ $n$ = 2, 4, 6, 8, 10, 12 (Fig. 5.25) were measured for different temperatures.

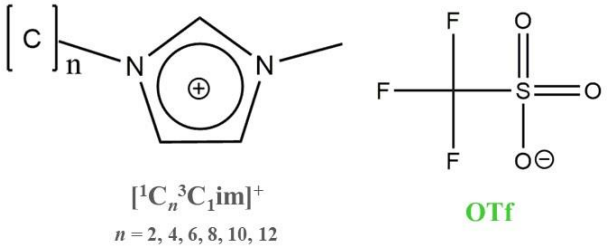



**Fig. 5.25.** Structure of the studied $[^1C_n{}^3C1im][OTf]$ ($n$ = 2, 4, 6, 8, 10, 12) ionic liquids.

#### 5.1.3.1. Density

The resulting fitting coefficients from the temperature dependence of density of the $[^1C_n{}^3C_1im][OTf]$ ILs (Eq. 2.4) are presented in Table 5.16. The densities at the reference temperature ($T$ = 298.15 K) are presented in Table 5.17, together with the molar volume and thermal expansion coefficient derived from Eq. 2.2 and Eq. 2.7 respectively. The graphical representation of density, thermal expansion coefficient, and molar volume as functions of temperature and number of carbons on the cation's alkyl chain are presented in Fig 5.26.

**Table 5.16.** Fitting coefficients used to describe the temperature dependence of density of the studied $[^1C_n{}^3C_1im][OTf]$ homologue series.

| Ionic Liquid | $\frac{T_{\text{interval}}}{\text{K}}$ | $\frac{10^7 \cdot a_2}{\text{K}^{-2}}$ | $\frac{10^4 \cdot a_1}{\text{K}^{-1}}$ | $\frac{a_0}{\text{K}}$ |
|---|---|---|---|---|
| $[^1C_2{}^3C_1im][OTf]$ | 273 – 373 | 0.475 ± 0.056 | −6.344 ± 0.037 | 7.4178 ± 0.0006 |
| $[^1C_4{}^3C_1im][OTf]$ | 273 – 373 | 0.417 ± 0.052 | −6.348 ± 0.034 | 7.3536 ± 0.0005 |
| $[^1C_6{}^3C_1im][OTf]$ | 293 – 373 | 0.088 ± 0.055 | −6.244 ± 0.037 | 7.3049 ± 0.0006 |
| $[^1C_8{}^3C_1im][OTf]$ | 283 – 373 | 0.007 ± 0.067 | −6.249 ± 0.044 | 7.2671 ± 0.0007 |
| $[^1C_{10}{}^3C_1im][OTf]$ | 293 – 373 | 0.077 ± 0.074 | −6.422 ± 0.048 | 7.2431 ± 0.0008 |
| $[^1C_{12}{}^3C_1im][OTf]$ | 318 – 373 | 0.172 ± 0.128 | −6.355 ± 0.089 | 7.2178 ± 0.0015 |

The presented fitting coefficients were derived from the experimental $\rho(T)$ data (appendix) by applying a polynomial fitting function, $\ln[\rho(T)] = a_2T^2 + a_1T + a_0$ (Eq. 2.4). The standard uncertainties related to the fitting coefficients were calculated to the confidence level of 0.95 ($k \approx 2$).

**Table 5.17.** Density, thermal expansion coefficient, and molar volume at the reference temperature ($T$ = 298.15 K) for the studied $[^1C_n{}^3C_1im][OTf]$ homologue series.

| Ionic Liquid | $\frac{\rho(298.15\ \text{K})}{\text{kg}\cdot\text{m}^{-3}}$ | $\frac{10^4 \cdot \alpha_p(298.15\ \text{K})}{\text{K}^{-1}}$ | $\frac{10^6 \cdot V_m(298.15\ \text{K})}{\text{m}^3\cdot\text{mol}^{-1}}$ |
|---|---|---|---|
| $[^1C_2{}^3C_1im][OTf]$ | 1384.2 ± 0.5 | 6.06 ± 0.04 | 188.0 ± 0.5 |
| $[^1C_4{}^3C_1im][OTf]$ | 1297.3 ± 0.5 | 6.10 ± 0.03 | 222.2 ± 0.6 |
| $[^1C_6{}^3C_1im][OTf]$ | 1220.6 ± 0.5 | 6.19 ± 0.04 | 259.2 ± 0.6 |
| $[^1C_8{}^3C_1im][OTf]$ | 1189.0 ± 0.5 | 6.25 ± 0.04 | 289.7 ± 0.7 |
| $[^1C_{10}{}^3C_1im][OTf]$ | 1155.6 ± 0.5 | 6.38 ± 0.05 | 322.3 ± 0.7 |
| $[^1C_{12}{}^3C_1im][OTf]$ | 1126.5 ± 0.5 | 6.46 ± 0.09 | 355.5 ± 0.8 |

$\rho(T = 298.15\ \text{K})$ and $\alpha_p(T = 298.15\ \text{K})$ were calculated from the fitting coefficients presented in Table 5.17 and by applying Eq. 2.4 and Eq. 2.7 respectively. $V_m(298.15\ \text{K}) = M/\rho(298.15\ \text{K})$. The standard uncertainty associated with $\alpha_p$ and $V_m$ were calculated by applying the propagation of uncertainty to Eq. 2.7 and 2.2, respectively.

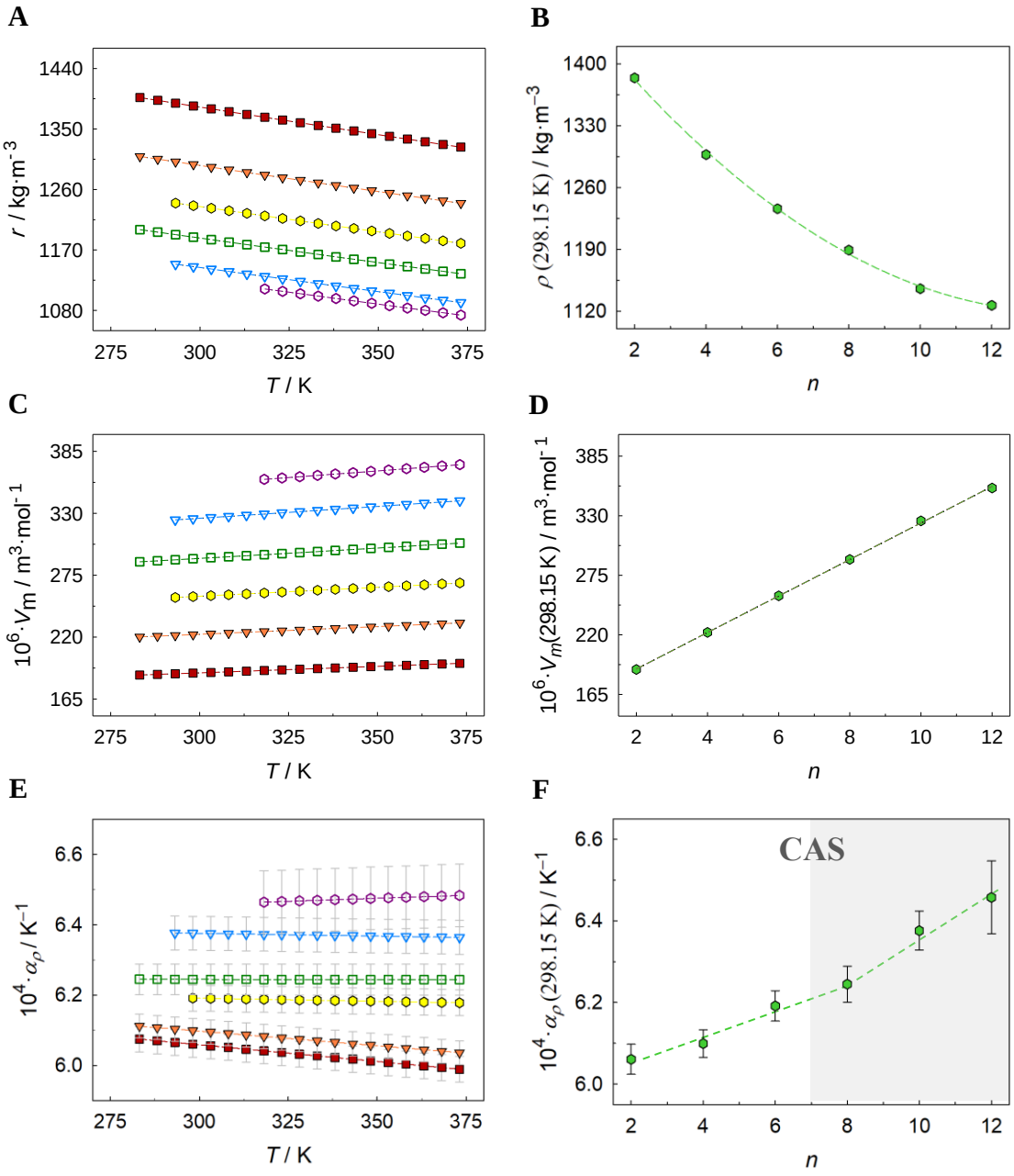



**Figure 5.26.** Density and derived properties of the [$^1$C$_n$$^3$C$_1$im][OTf] ILs as functions of temperature (A, C, E) and number of carbons on the alkyl chain of the cation (B, D, F). **A**, **B**: Density; **C**, **D**: Molar volume; **E**, **F**: Thermal expansion coefficient. $n$ = 2 ■, 4 ▼, 6 ⬢, 8 □, 10 ▽, 12 ⬡.

### 5.1.3.2. Viscosity

The obtained viscosity data for the [$^1C_n{}^3C_1$im][OTf] ILs is presented as a function of temperature and the number of carbons of the cation's alkyl chain in Fig. 5.27.

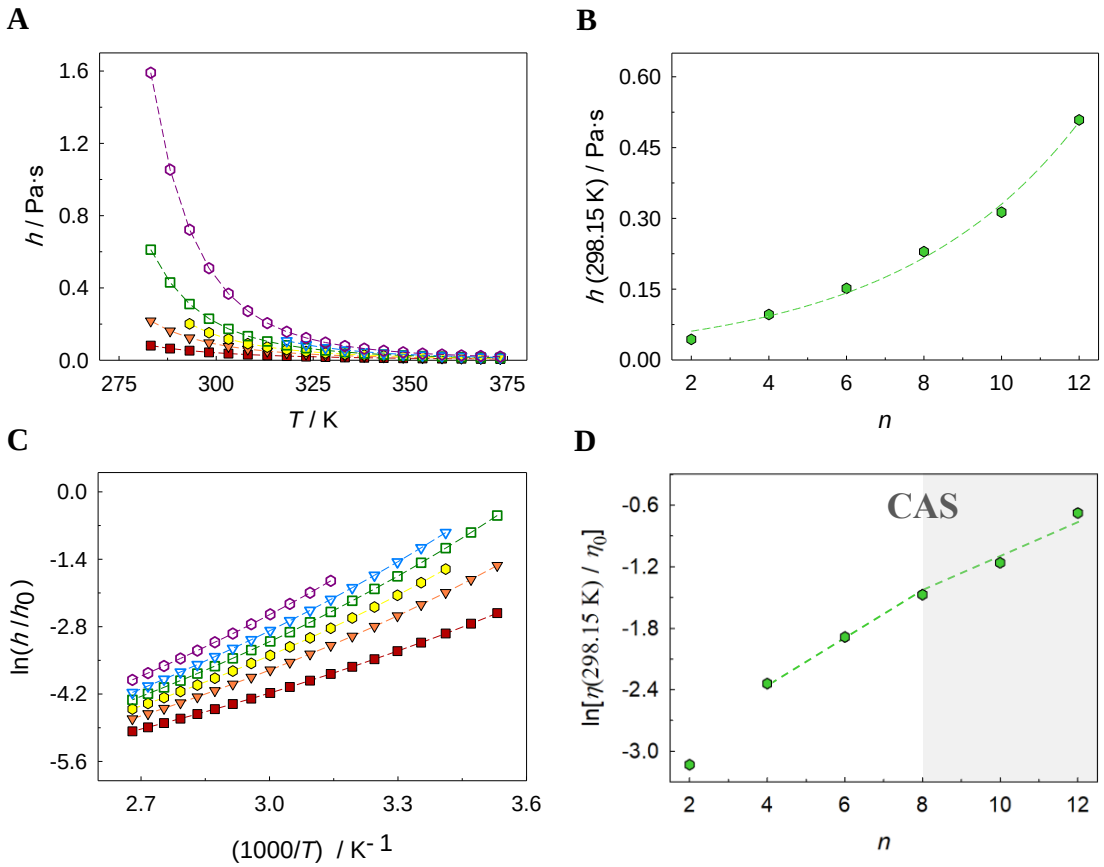



**Figure 5.27.** Viscosity of the [$^1C_n{}^3C_1$im][OTf] series as functions of temperature (A, C) and number of carbons on the alkyl chain of the cation (B, D). **A**: Temperature dependence of viscosity; **B**: Dependence of viscosity with the alkyl chain length; **C**: Temperature dependence of viscosity (Arrhenius representation); **D**: Dependence of viscosity with the alkyl chain length (logarithmic form). $n$ = 2 ■, 4 ▼, 6 ●, 8 □, 10 ▽, 12 ⬡. $\eta_0$ = 1 Pa·s.

The VFT coefficients (Eq 2.44) obtained from the experimental viscosity-temperature data, $\eta(T)$, are presented in Table 5.18. The effect of the alkyl chain length on the obtained VFT coefficients is presented in Fig. 5.28 together with the graphical representation of the linearized VFT equation (Eq. 2.45).

**Table 5.18.** Fitting coefficients used to describe the temperature dependence of viscosity of the studied [$^1C_n{}^3C_1$im][OTf] homologue series.

| Ionic Liquid | $\frac{T_{interval}}{K}$ | $\frac{10^3 \cdot A_\eta}{Pa{\cdot}s}$ | $\frac{B_\eta}{K}$ | $\frac{C_\eta}{K}$ |
|---|---|---|---|---|
| [$^1C_2{}^3C_1$im][OTf] | 273 – 373 | 0.1710 ± 0.0036 | 833.8 ± 6.2 | 147.7 ± 0.6 |
| [$^1C_4{}^3C_1$im][OTf] | 273 – 373 | 0.1021 ± 0.0032 | 968.1 ± 5.7 | 156.8 ± 0.4 |
| [$^1C_6{}^3C_1$im][OTf] | 293 – 373 | 0.0919 ± 0.0023 | 1012 ± 7 | 161.6 ± 0.5 |
| [$^1C_8{}^3C_1$im][OTf] | 283 – 373 | 0.0649 ± 0.0013 | 1144 ± 5 | 158.1 ± 0.3 |
| [$^1C_{10}{}^3C_1$im][OTf] | 293 – 373 | 0.0487 ± 0.0016 | 1260 ± 9 | 154.5 ± 0.5 |
| [$^1C_{12}{}^3C_1$im][OTf] | 318 – 373 | 0.0655 ± 0.0021 | 1190 ± 11 | 165.3 ± 0.7 |

The presented fitting coefficients were derived from the experimental $\eta(T)$ data (appendix) by applying the VFT fitting function, Eq. 2.44. The standard uncertainties related to the VFT coefficients were calculated to the confidence level of 0.95 ($k \approx 2$).

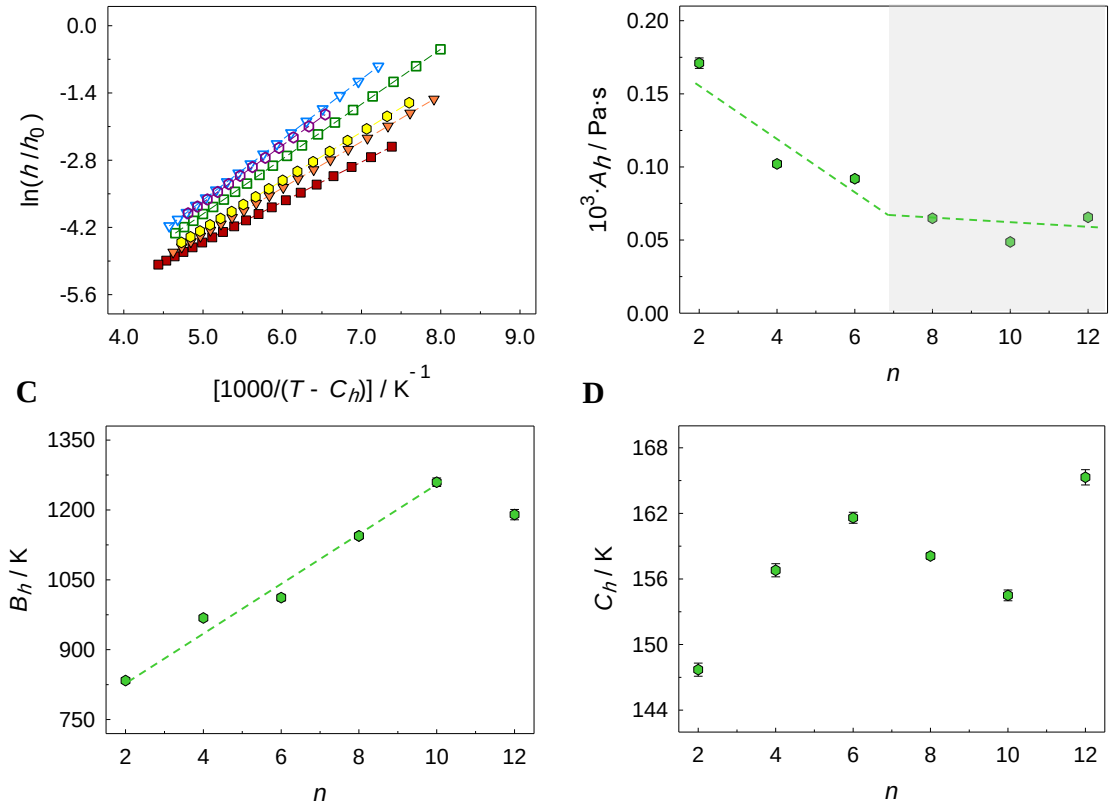



**Figure 5.28.** Impact of the alkyl chain length on the VFT coefficients for the viscosity of [$^1C_n{}^3C_1$im][OTf] series. **A**: Linearized VFT representation $n$ = 2 ■, 4 ▼, 6 ⬢, 8 □, 10 ▽, 12 ⬡; **B**: Pre-exponential coefficient, $A_\eta$; **C**: energy barrier-related coefficient, $B_\eta$; **D**: Vogel temperature, $C_\eta$. $\eta_0$ = 1 Pa·s.

The viscosities of the studied [$^1C_n{}^3C_1$im][OTf] ILs at the reference temperature ($T$ = 298.15 K) are presented in Table 5.19 together with the energy barrier and strength parameter derived from Eq. 2.47 and Eq. 2.49, respectively. The temperature dependence of the viscosity-related energy barrier, $E_\eta$, and the effect of the alkyl chain

length on $E_\eta$ and on the liquid fragility (strength parameter, $D_\eta$) are represented in Fig. 5.29.

**Table 5.19.** Viscosity and derived energy barrier of the studied [$^1C_n{}^3C_1$im][OTf] homologue series at the reference temperature ($T$ = 298.15 K), together with the strength parameter.

| Ionic Liquid | $\eta(T=298.15\ K)$ / Pa·s | $E_\eta(T=298.15\ K)$ / kJ·mol$^{-1}$ | $D_\eta$ |
|---|---|---|---|
| [$^1C_2{}^3C_1$im][OTf] | 0.04364 ± 0.00044 | 27.23 ± 0.30 | 5.645 ± 0.048 |
| [$^1C_4{}^3C_1$im][OTf] | 0.09627 ± 0.0096 | 35.81 ± 0.37 | 5.554 ± 0.043 |
| [$^1C_6{}^3C_1$im][OTf] | 0.1517 ± 0.0015 | 40.10 ± 0.41 | 6.261 ± 0.049 |
| [$^1C_8{}^3C_1$im][OTf] | 0.2295 ± 0.0023 | 43.12 ± 0.27 | 7.238 ± 0.037 |
| [$^1C_{10}{}^3C_1$im][OTf] | 0.3131 ± 0.0031 | 45.12 ± 0.45 | 8.153 ± 0.065 |
| [$^1C_{12}{}^3C_1$im][OTf] | 0.5087 ± 0.0051 | 49.83 ± 0.70 | 7.199 ± 0.073 |

$\eta(T$ = 298.15 K) and $E_\eta(T$ = 298.15 K) were calculated from the fitting coefficients presented in Table 5.18 and by applying Eq. 2.44 and Eq. 2.47, respectively. The strength parameter was calculated by Eq. 2.49, $D_\eta = B_\eta / C_\eta$. The relative standard uncertainty associated with the viscosity measurements was estimated as $u(\eta)$ = 1.0% (Eq. 4.15); The standard uncertainty associated with the derived energy barrier, $u(E_\eta)$, and strength parameter, $u(D_\eta)$, was calculated by applying the propagation of uncertainty to Eq. 2.47 and Eq. 2.49, respectively.

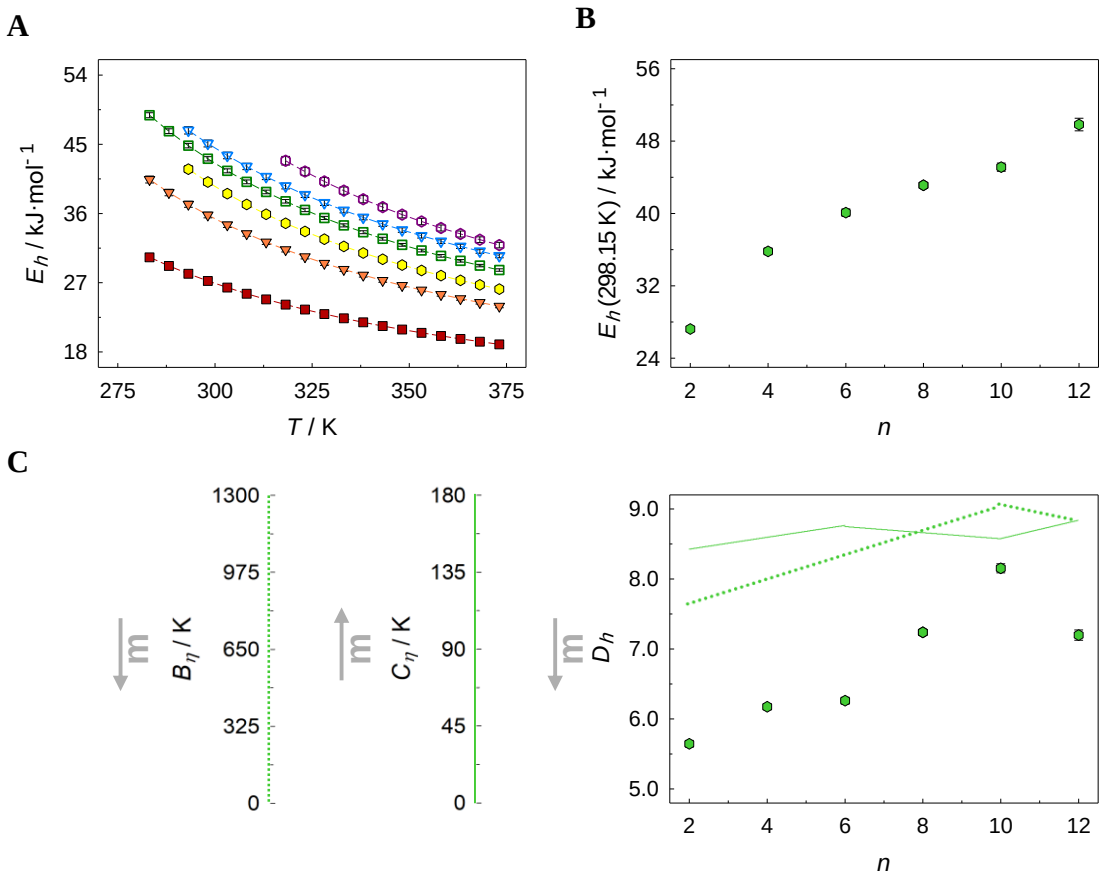



**Figure 5.29.** Graphical representation of the energy barrier and strength parameter derived from the experimental viscosity data of the [$^1C_n{}^3C_1$im][OTf] series. **A**: Temperature dependence of the derived energy barrier $n$ = 2 ■, 4 ▼, 6 ⬢, 8 □, 10 ▽, 12 ⬡; **B**: Effect of the alkyl chain length on the energy barrier; **C**: Effect of the alkyl chain length on the liquid fragility ($B_\eta$ and $C_\eta$ scales are included as guide lines).

Deviation of the available viscosity data to the experimental results for the $[^1C_n{}^3C_1im][OTf]$ series is presented in Fig. 5.30.

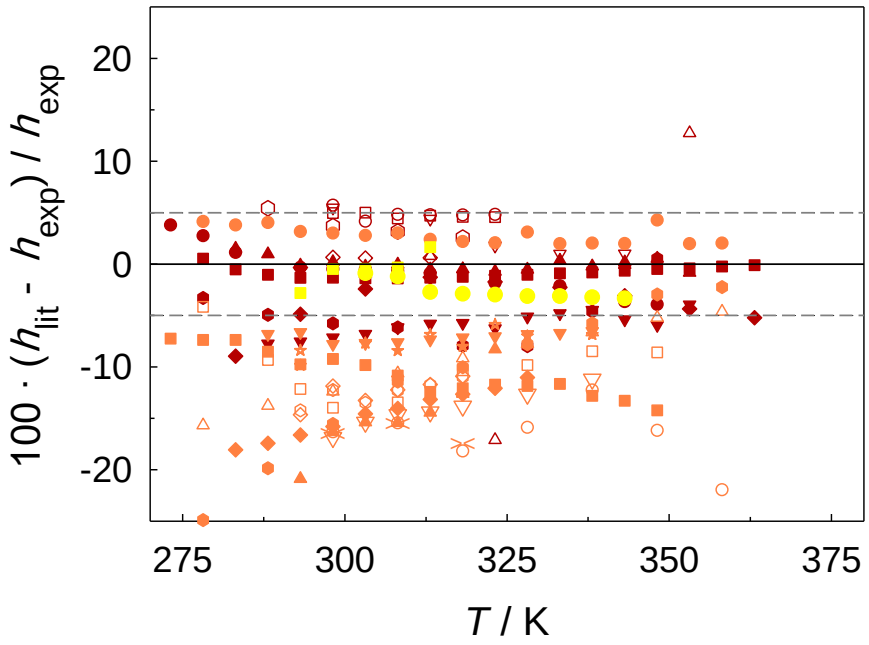



**Figure 5.30.** Deviation of the available viscosity data to the experimental results for the $[^1C_n{}^3C_1im][OTf]$ series. ***n* = 2** ● [68], ■ [69], ▲ [9], ▼ [70], ◆ [28], ⬢ [71], ○ [72], □ [73], △ [74], ▽ [75], ◇ [76], ⬡ [77], ***n* = 4** ● [5], ■ [78], ▲ [79], ▼[80], ◆ [81], ⬢ [28], ○ [12], □ [29], △ [82], ▽ [83], ◇ [84], ⬡ [85], ★ [74], ☆ [86], >< [87]. ***n* = 6** ● [80], ■ [88].

Overall, the literature data is in good agreement with the experimental results. However, there seem to be significant negative deviations for $[^1C_4{}^3C_1im][OTf]$. This means that these literature data represent lower viscosity values that might be associated with the presence of water. Still, the data reported by Almeida *et al.* [5] are in good agreement with the results obtained in this work. No data was found for $n$ = 8, 10, and 12.

#### 5.1.3.3. Electrical Conductivity

The resistance and reactance spectra obtained for the $[^1C_n{}^3C_1im][OTf]$ ionic liquids through the ILDEM experiments are presented in Fig. 5.31.

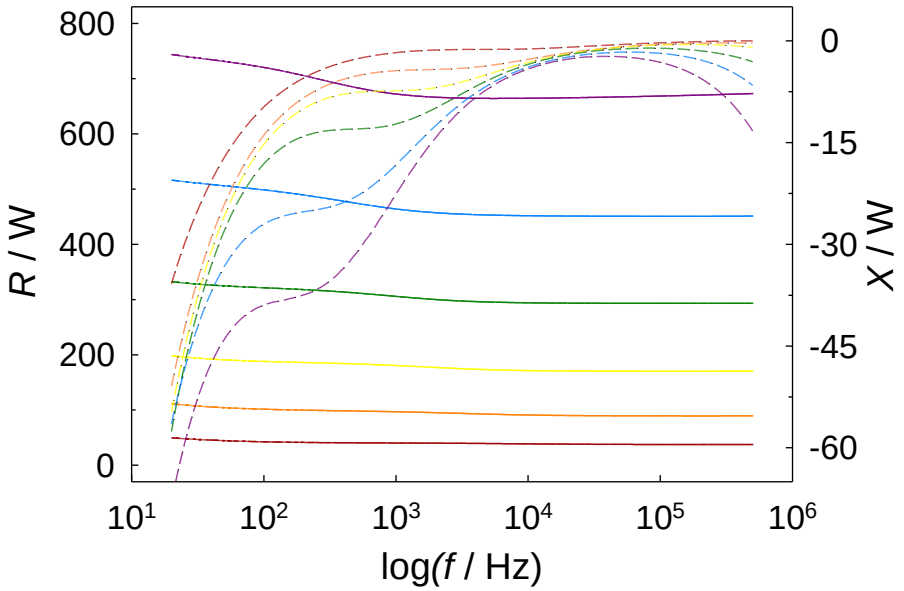



**Figure 5.31.** Typical resistance (straight line) and reactance (dashed line) spectra for the $[^1C_n{}^3C_1im][OTf]$ series. $n$ = **2**, **4**, **6**, **8**, **10**, **12**.

The VFT coefficients (Eq 2.24) obtained from the experimental electrical conductivity-temperature data, $\eta(T)$, are presented in Table 5.20.

**Table 5.20** Fitting coefficients used to describe the temperature dependence of electrical conductivity of the studied $[^1C_n{}^3C_1im][OTf]$ homologue series.

| Ionic Liquid | $A_\sigma$ / S·m$^{-1}$ | $B_\sigma$ / K | $C_\sigma$ / K | $\sigma(T$=298.15 K) / S·m$^{-1}$ |
|---|---|---|---|---|
| $[^1C_2{}^3C_1im][OTf]$ | 110.4 ± 2.1 | 695.1 ± 5.9 | 152.7 ± 0.7 | 0.9279 ± 0.0139 |
| $[^1C_4{}^3C_1im][OTf]$ | 105.5 ± 0.6 | 781.3 ± 1.5 | 166.1 ± 0.1 | 0.2842 ± 0.0043 |
| $[^1C_6{}^3C_1im][OTf]$ | 115.0 ± 1.1 | 909.2 ± 3.0 | 165.0 ± 0.3 | 0.1245 ± 0.0019 |
| $[^1C_8{}^3C_1im][OTf]$ | 134.4 ± 3.0 | 1051.1 ± 6.8 | 160.9 ± 0.5 | 0.06345 ± 0.00095 |
| $[^1C_{10}{}^3C_1im][OTf]$ | 130.5 ± 8.7 | 1144 ± 21 | 157.2 ± 1.5 | 0.03897 ± 0.00058 |
| $[^1C_{12}{}^3C_1im][OTf]$ | 139.1 ± 9.3 | 1246 ± 23 | 153.7 ± 1.5 | 0.02496 ± 0.00037 |

The presented fitting coefficients were derived from the experimental $\sigma(T)$ data (appendix) by applying the VFT fitting function, Eq. 2.44. The standard uncertainties related to the VFT coefficients were calculated to the confidence level of 0.95 ($k \approx 2$). The relative standard uncertainty associated with the viscosity measurements was estimated as $u(\sigma)$ = 1.5% (Eq. 4.15).

The deviations of the available electrical conductivity data to the experimental results for the [$^1C_n{}^3C_1$im][OTf] series are presented in Fig. 5.32. The majority of data is in good agreement with the experimental results (deviation <5%). The data for n = 6, 8, and 10 present significant deviations from the present work. Still, the experimental data for these ILs are in good agreement with the remaining ionic liquids of the series. No data was found for *n* = 12.

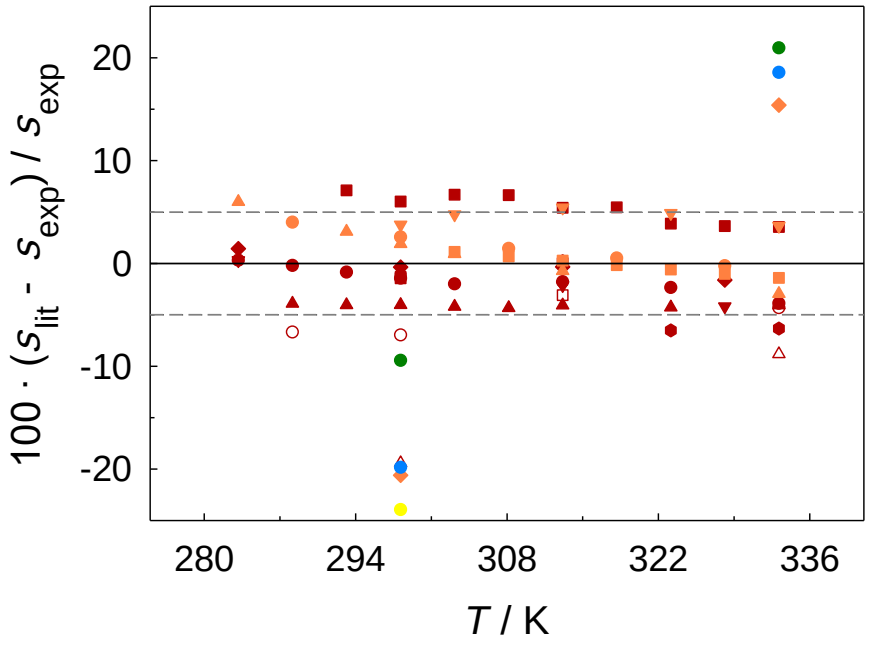



**Figure 5.32.** Deviation of the available electrical conductivity data to the experimental results for the [$^1C_n{}^3C_1$im][OTf] series. ***n* = 2:** ● [89], ■ [50], ▲ [90], ▼ [91], ◆ [92], ⬢ [74], ○ [93], □ [76], △ [94]; ***n* = 4:** ● [61], ■ [55], ▲ [29], ▼ [74], ◆ [94]; ***n* = 6:** ● [94]; ***n* = 8:** ● [94]; ***n* = 10:** ● [94].

### 5.1.3.4. Molar Conductivity

The molar conductivity of the [$^1C_n{}^3C_1$im][OTf] ILs was calculated from the experimentally measured electrical conductivity and density data of the ILs. The molar conductivity is presented as a function of temperature and the number of carbons of the cation's alkyl chain in Fig. 5.33.

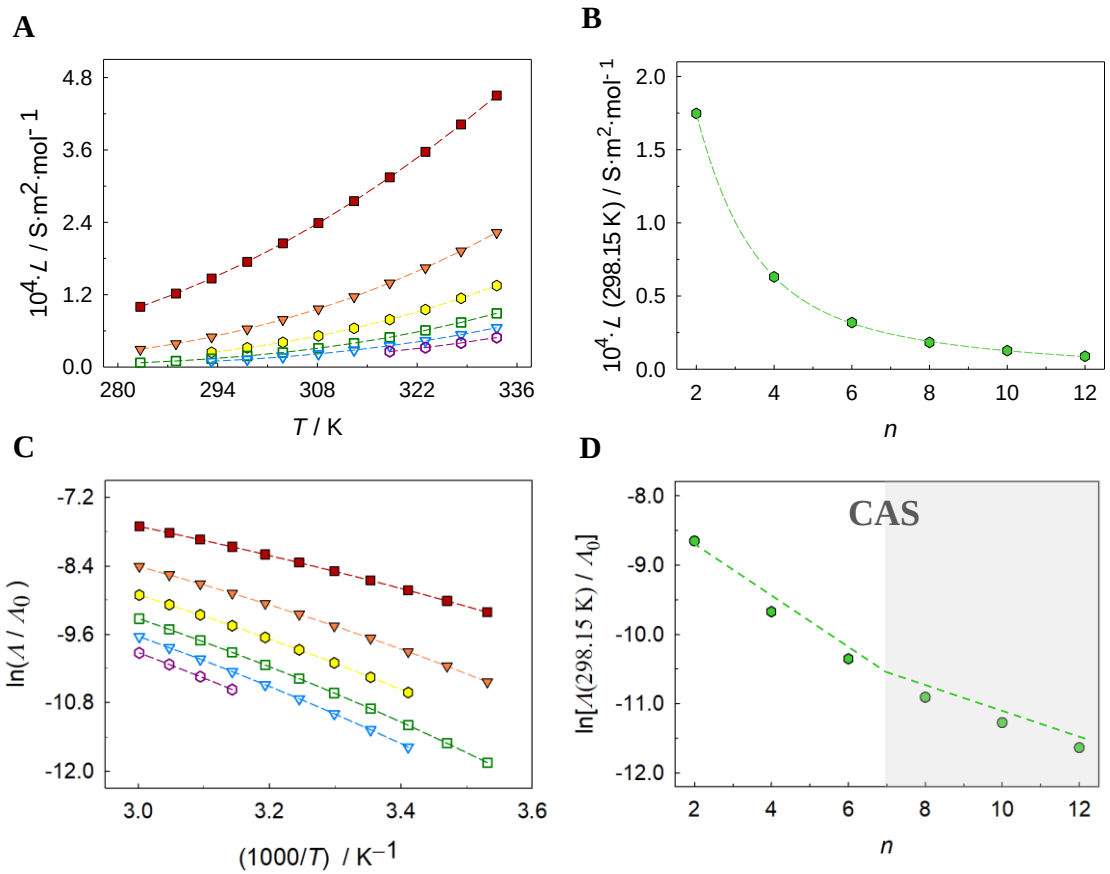



**Figure 5.33.** Molar conductivity of the [$^1C_n{}^3C_1$im][OTf] series as functions of temperature (A, C) and number of carbons on the alkyl chain of the cation (B, D). **A**: Temperature dependence of molar conductivity; **B**: Dependence of molar conductivity with the alkyl chain length; **C**: Temperature dependence of molar conductivity (Arrhenius representation); **D**: Dependence of molar conductivity with the alkyl chain length (logarithmic form). $n$ = 2 ■, 4 ▼, 6 ⬢, 8 □, 10 ▽, 12 ⬡. $\Lambda_0$ = 1 S·m$^2$·mol$^{-1}$

The VFT coefficients (Eq 2.44) obtained from the experimental molar conductivity-temperature data, $\Lambda(T)$, are presented in Table 5.21. The effect of the alkyl chain length on the obtained VFT coefficients is presented in Fig. 5.34, together with the graphical representation of the linearized VFT equation (Eq. 2.45).

**Table 5.21.** Fitting coefficients used to describe the temperature dependence of molar conductivity of the studied [$^1C_n{}^3C_1$im][OTf] homologue series.

| Ionic Liquid | $\frac{T_{interval}}{K}$ | $\frac{10^4 \cdot A_\Lambda}{S \cdot m^2 \cdot mol^{-1}}$ | $\frac{B_\Lambda}{K}$ | $\frac{C_\Lambda}{K}$ |
|---|---|---|---|---|
| [$^1C_2{}^3C_1$im][OTf] | 283 – 333 | 253.4 ± 5.6 | 740.8 ± 7.2 | 149.3 ± 0.8 |
| [$^1C_4{}^3C_1$im][OTf] | 283 – 333 | 282.6 ± 1.8 | 820.3 ± 1.9 | 163.8 ± 0.2 |
| [$^1C_6{}^3C_1$im][OTf] | 293 – 333 | 358.9 ± 5.3 | 951.8 ± 4.6 | 162.7 ± 0.4 |
| [$^1C_8{}^3C_1$im][OTf] | 283 – 333 | 476 ± 12 | 1095 ± 8 | 158.9 ± 0.6 |
| [$^1C_{10}{}^3C_1$im][OTf] | 293 – 333 | 528 ± 38 | 1194 ± 23 | 154.9 ± 1.6 |
| [$^1C_{12}{}^3C_1$im][OTf] | 318 – 333 | 589 ± 42 | 1281 ± 25 | 152.7 ± 1.6 |

The presented fitting coefficients were derived from the experimental $\eta(T)$ data (appendix) by applying the VFT fitting function, Eq. 2.44. The standard uncertainties related to the VFT coefficients were calculated to the confidence level of 0.95 ($k \approx 2$).

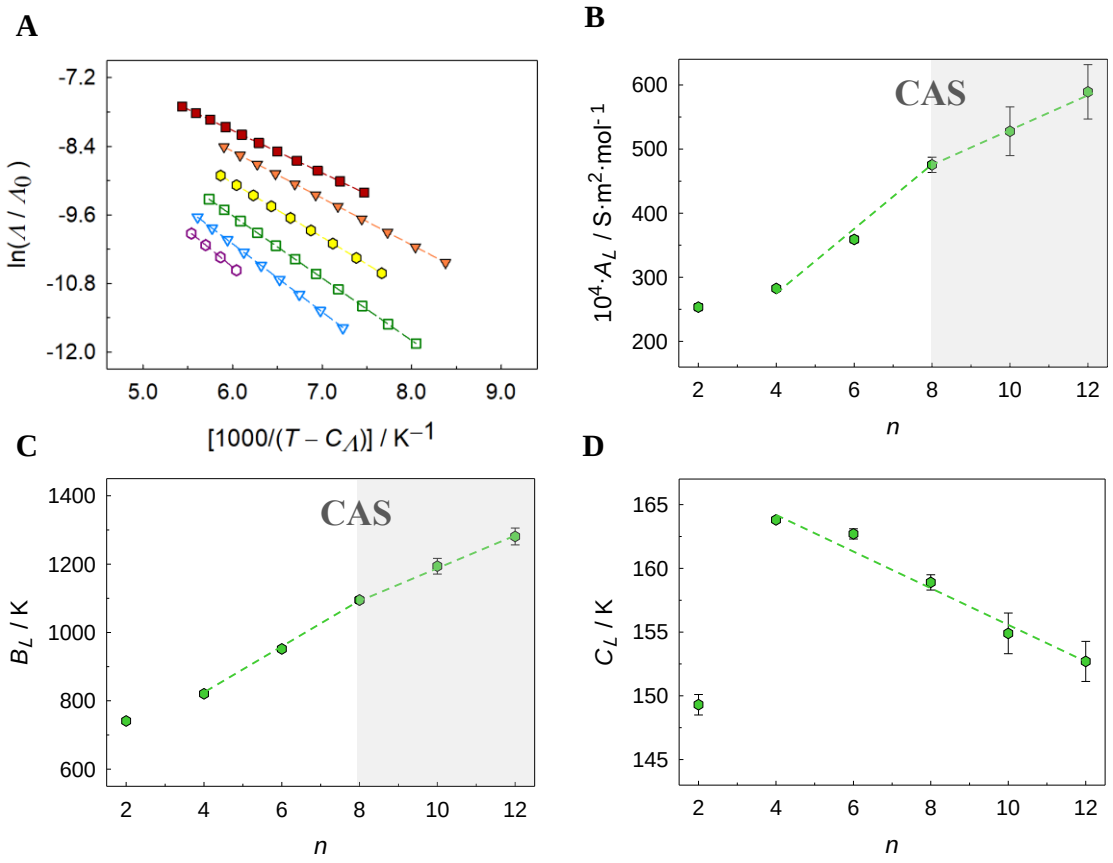



**Figure 5.34.** Impact of the alkyl chain length on the VFT coefficients for the molar conductivity of [$^1C_n{}^3C_1$im][OTf] series. **A**: Linearized VFT representation $n$ = 2 ■, 4 ▼, 6 ⬢, 8 □, 10 ▽, 12 ⬡; **B**: Pre-exponential coefficient, $A_\Lambda$; **C**: energy barrier-related coefficient, $B_\Lambda$; **D**: Vogel temperature, $C_\Lambda$. $\Lambda_0$ = 1 S·m$^2$·mol$^{-1}$.

The molar conductivities at the reference temperature ($T$ = 298.15 K) are presented in Table 5.22, together with the energy barrier and strength parameter derived from Eq. 2.47 and Eq. 2.49, respectively. The temperature dependence of the conductivity-related energy barrier, $E_\Lambda$, and the effect of the alkyl chain length on $E_\Lambda$ and on the liquid fragility (strength parameter, $D_\Lambda$) are represented in Fig. 5.35.

**Table 5.22.** Molar conductivity and derived energy barrier of the [$^1C_n{}^3C_1$im][OTf] homologue series at the reference temperature ($T$ = 298.15 K), together with the strength parameter.

| Ionic Liquid | $10^4 \cdot \Lambda(T{=}298.15\ \mathrm{K})$ / S·m²·mol$^{-1}$ | $E_\Lambda(T{=}298.15\ \mathrm{K})$ / kJ·mol$^{-1}$ | $D_\Lambda$ |
|---|---|---|---|
| [$^1C_2{}^3C_1$im][OTf] | 1.747 ± 0.026 | 24.71 ± 0.36 | 4.962 ± 0.055 |
| [$^1C_4{}^3C_1$im][OTf] | 0.6302 ± 0.0095 | 33.59 ± 0.13 | 5.008 ± 0.013 |
| [$^1C_6{}^3C_1$im][OTf] | 0.3186 ± 0.0048 | 38.34 ± 0.29 | 5.850 ± 0.032 |
| [$^1C_8{}^3C_1$im][OTf] | 0.1828 ± 0.0027 | 41.74 ± 0.47 | 6.891 ± 0.057 |
| [$^1C_{10}{}^3C_1$im][OTf] | 0.1267 ± 0.0019 | 43.0 ± 1.3 | 7.708 ± 0.168 |
| [$^1C_{12}{}^3C_1$im][OTf] | 0.0882 ± 0.0013 | 44.8 ± 1.3 | 8.389 ± 0.183 |

$\Lambda(T = 298.15\ \mathrm{K})$ and $E_\Lambda(T = 298.15\ \mathrm{K})$ were calculated from the fitting coefficients presented in Table 5.21 and by applying Eq. 2.44 and Eq. 2.47, respectively. The strength parameter was calculated by Eq. 2.49, $D_\Lambda = B_\Lambda / C_\Lambda$. The relative standard uncertainty associated with the viscosity measurements was estimated as $u(\Lambda)$ = 1.5% (Eq. 4.15); The standard uncertainty associated with the derived energy barrier, $u(E_\Lambda)$, and strength parameter , $u(D_\Lambda)$, was calculated by applying the propagation of uncertainty to Eq. 2.47 and Eq. 2.49, respectively.

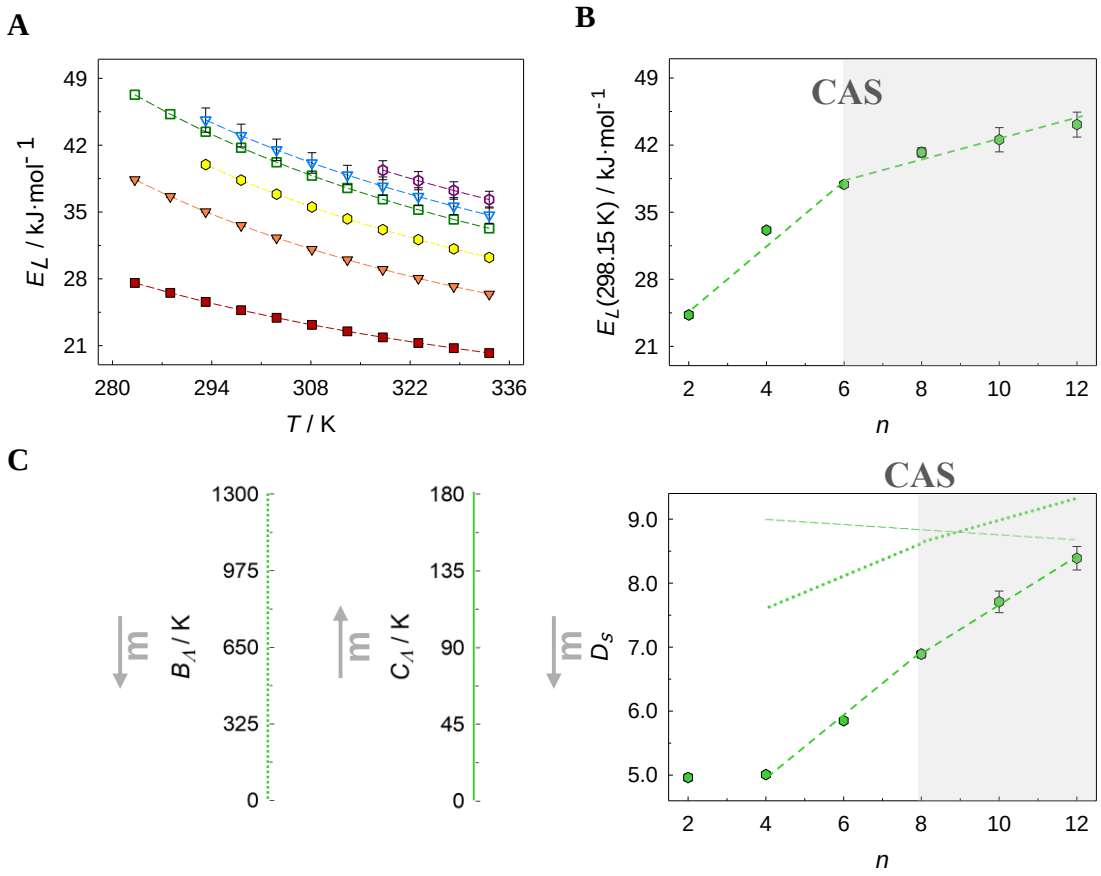



**Figure 5.35.** Graphical representation of the energy barrier and strength parameter derived from the experimental molar conductivity data of the [$^1C_n{}^3C_1$im][OTf] series. **A**: Temperature dependence of the derived energy barrier $n$ = 2 ■, 3 ▲, 4 ▼, 5 ◆, 6 ⬢, 7 ○, 8 □, 9 △, 10 ▽, 12 ⬡; **B**: Effect of the alkyl chain length on the energy barrier; **C**: Effect of the alkyl chain length on the liquid fragility ($B_\Lambda$ and $C_\Lambda$ scales are included as guide lines).

### 5.1.4. $[^1C_n{}^3C_1im][NTf_2]$ Series

In this work it was measured the electrical conductivity of the 1-alkyl-3-methylimidazolium bis(trifluoromethylsulfonyl)imide series, $[^1C_n{}^3C_1im][NTf_2]$ $n$ = 1 – 12 (Fig. 5.36). The obtained results were combined with the density and viscosity data from a previous work from the group where this thesis was elaborated.

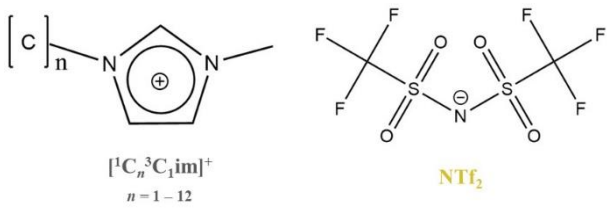



**Figure 5.36.** Structure of the studied $[^1C_n{}^3C_1im][NTf_2]$ ($n$ = 1 – 12) ionic liquids.

#### 5.1.4.1. Electrical Conductivity

The resistance and reactance spectra obtained for the $[^1C_n{}^3C_1im][NTf_2]$ ionic liquids though the ILDEM experiments are presented in Fig. 5.37.

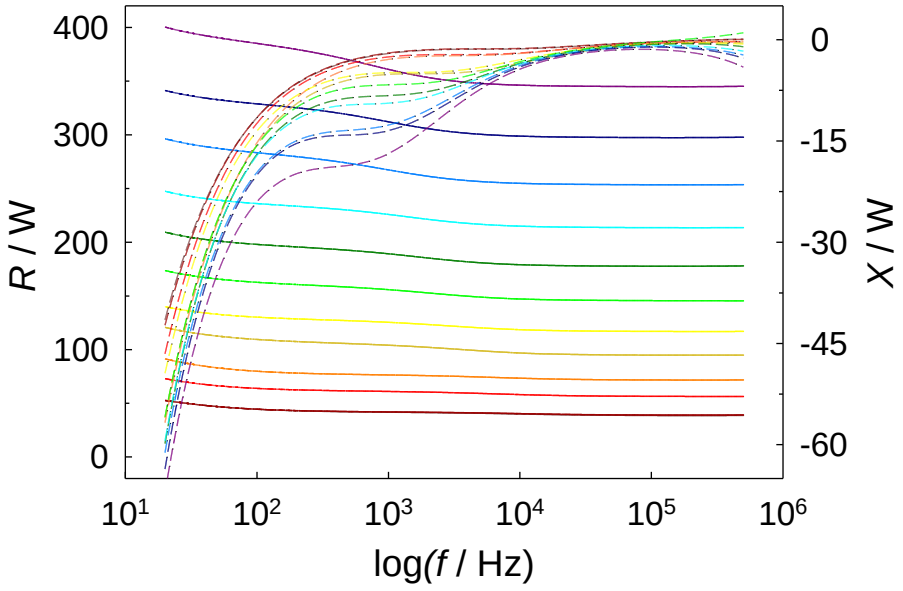



**Figure 5.37.** Typical resistance (straight line) and reactance (dashed line) spectra for the $[^1C_n{}^3C_1im][NTf_2]$ series. $n$ = **1**, **2**, **3**, **4**, **5**, **6**, **7**, **8**, **9**, **10**, **11**, **12**.

The VFT coefficients (Eq 2.24) obtained from the experimental electrical conductivity-temperature data, $\sigma(T)$, are presented in Table 5.23.

**Table 5.23.** Fitting coefficients used to describe the temperature dependence of electrical conductivity of the studied $[^1C_n{}^3C_1im][NTf_2]$ homologue series.

| Ionic Liquid | $\frac{A_\sigma}{S\cdot m^{-1}}$ | $\frac{B_\sigma}{K}$ | $\frac{C_\sigma}{K}$ | $\frac{\sigma(T=298.15\ K)}{S\cdot m^{-1}}$ |
|---|---|---|---|---|
| $[^1C_1{}^3C_1im][NTf_2]$ | 68.2 ± 1.3 | 556.3 ± 5.4 | 169.8 ± 0.7 | 0.895 ± 0.013 |
| $[^1C_2{}^3C_1im][NTf_2]$ | 68.6 ± 2.3 | 576 ± 10 | 164.6 ± 0.3 | 0.917 ± 0.014 |
| $[^1C_3{}^3C_1im][NTf_2]$ | 61.28 ± 0.70 | 581.0 ± 3.1 | 174.9 ± 0.4 | 0.5496 ± 0.0082 |
| $[^1C_4{}^3C_1im][NTf_2]$ | 58.77 ± 0.47 | 615.5 ± 2.2 | 174.1 ± 0.3 | 0.4114 ± 0.0062 |
| $[^1C_5{}^3C_1im][NTf_2]$ | 59.47 ± 0.38 | 662.8 ± 1.8 | 173.6 ± 0.2 | 0.2905 ± 0.0040 |
| $[^1C_6{}^3C_1im][NTf_2]$ | 56.97 ± 0.88 | 690.6 ± 4.3 | 173.7 ± 0.4 | 0.2216 ± 0.0033 |
| $[^1C_7{}^3C_1im][NTf_2]$ | 60.31 ± 0.69 | 744.3 ± 3.3 | 171.5 ± 0.3 | 0.1691 ± 0.0025 |
| $[^1C_8{}^3C_1im][NTf_2]$ | 62.56 ± 0.49 | 791.3 ± 2.3 | 169.6 ± 0.2 | 0.1327 ± 0.0020 |
| $[^1C_9{}^3C_1im][NTf_2]$ | 58.0 ± 1.5 | 805.5 ± 7.3 | 170.3 ± 0.6 | 0.1064 ± 0.0016 |
| $[^1C_{10}{}^3C_1im][NTf_2]$ | 58.7 ± 1.2 | 845.6 ± 6.1 | 168.3 ± 0.5 | 0.0872 ± 0.0013 |
| $[^1C_{11}{}^3C_1im][NTf_2]$ | 59.41 ± 0.62 | 879.8 ± 3.1 | 167.2 ± 0.3 | 0.0718 ± 0.0011 |
| $[^1C_{12}{}^3C_1im][NTf_2]$ | 55.8 ± 2.2 | 891 ± 12 | 167.6 ± 1.0 | 0.06057 ± 0.00091 |

The presented fitting coefficients were derived from the experimental $\sigma(T)$ data (appendix) by applying the VFT fitting function, Eq. 2.44. The standard uncertainties related to the VFT coefficients were calculated to the confidence level of 0.95 ($k \approx 2$). The relative standard uncertainty associated with the viscosity measurements was estimated as $u(\sigma) = 1.5\%$ (Eq. 4.15).

The deviation of the available electrical conductivity data to the experimental results for the $[^1C_n{}^3C_1im][NTf_2]$ series is presented in Fig. 5.38. As observed there is a lot of data for the even number ILs. While most data is included within ± 5% deviation, there are some cases of both negative and positive deviations. Too high electrical conductivity data might be associated with the presence of water while low values could be a consequence of polarization effects. No data was found for $n$ = 5, 7, 9, and 10.

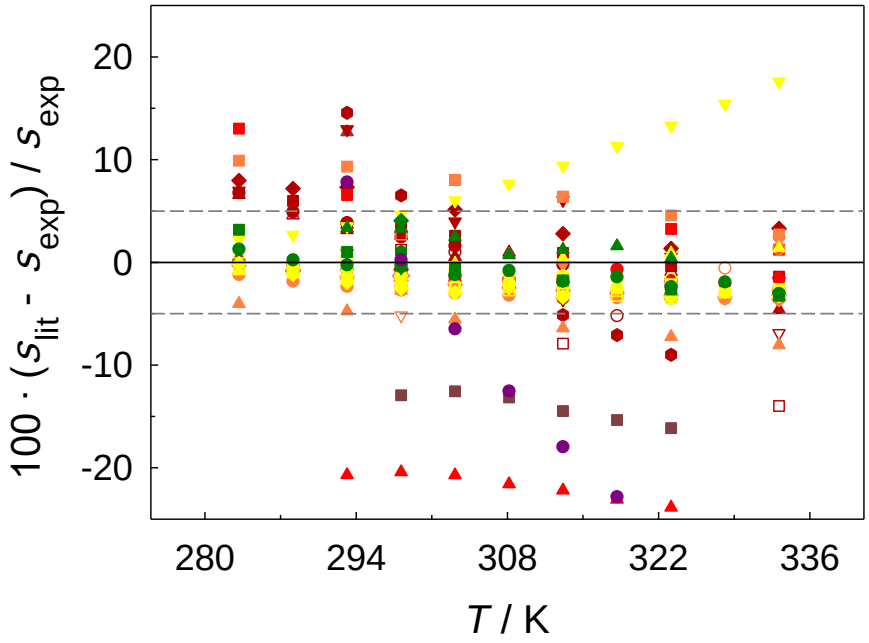



**Figure 5.38.** Deviation of the available electrical conductivity data to the experimental results for the [$^1C_n{}^3C_1$im][$NTf_2$] series. ***n* = 1:** ●[95], ■ [96], ▲ [91]; ***n* = 2:** ● [97], ■ [3], ▲ [95], ▼[98], ◆ [91], ⬢[99], ○ [100], □ [101], △ [62], ▽ [102], ◇ [93]; ***n* = 3:** ● [48], ■ [98], ▲[103]; ***n* = 4:** ●[104], ■ [98], ▲ [29], ▼ [105], ◆ [106], ⬢ [62], ○ [107], □ [67], △ [108], ▽ [109], ◇ [110]; ***n* = 6:** ● [111], ■ [95], ▲ [112], ▼ [47], ◆ [113], ⬢ [62], ○ [100], □ [114], △ [115], ▽ [90]; ***n* = 8:** ● [111], ■ [95], ▲ [100], ▼ [109], ◆ [67], ⬢ [108];***n* = 12:** ● [116].

### 5.1.4.2. Molar Conductivity

The molar conductivity of the [$^1C_n{}^3C_1$im][$NTf_2$] ILs was calculated from the experimentally measured electrical conductivity and density data. The molar conductivity is presented as a function of temperature and the number of carbons of the cation's alkyl chain in Fig. 5.39.

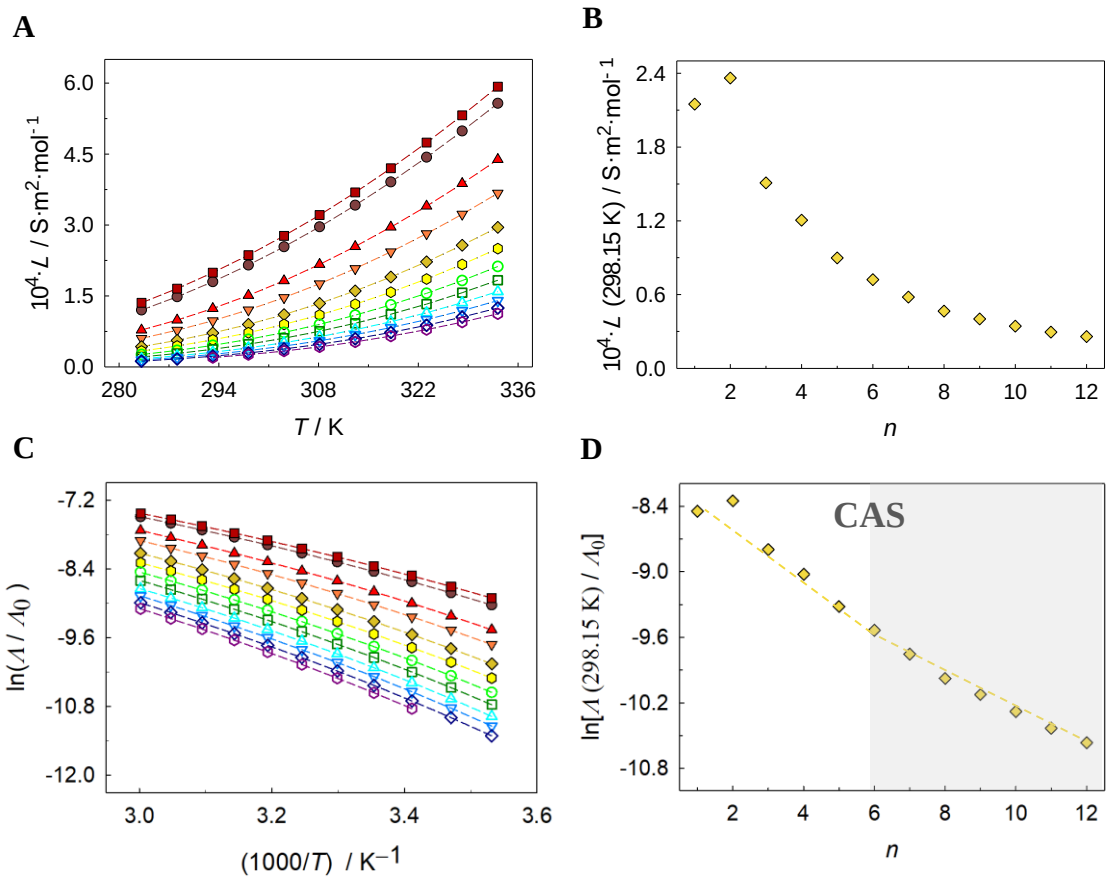



**Figure 5.39.** Molar conductivity of the [$^1C_n{}^3C_1$im][$NTf_2$] series as a function of temperature (A, C) and number of carbons on the alkyl chain of the cation (B, D). **A**: Temperature dependence of molar conductivity; **B**: Dependence of molar conductivity with the alkyl chain length; **C**: Temperature dependence of molar conductivity (Arrhenius representation); **D**: Dependence of molar conductivity with the alkyl chain length (logarithmic form). $n$ = 1 ●, 2 ■, 3 ▲, 4 ▼, 5 ◆, 6 ●, 7 ○, 8 □, 9 △, 10 ▽, 11 ◇, 12 ⬡. $\Lambda_0$ = 1 S·m$^2$·mol$^{-1}$

The VFT coefficients (Eq 2.44) obtained from the experimental molar conductivity-temperature data, $\Lambda(T)$, are presented in Table 5.24. The effect of the alkyl chain length on the obtained VFT coefficients is presented in Fig. 5.40 together with the graphical representation of the linearized VFT equation (Eq. 2.45).

**Table 5.24.** Fitting coefficients used to describe the temperature dependence of molar conductivity of the studied [$^1C_n{}^3C_1$im][$NTf_2$] homologue series.

| Ionic Liquid | $\frac{T_{interval}}{K}$ | $\frac{10^4 \cdot A_\Lambda}{S \cdot m^2 \cdot mol^{-1}}$ | $\frac{B_\Lambda}{K}$ | $\frac{C_\Lambda}{K}$ |
|---|---|---|---|---|
| [$^1C_1{}^3C_1$im][$NTf_2$] | 283 – 333 | 201.2 ± 4.5 | 598.5 ± 6.6 | 166.3 ± 0.8 |
| [$^1C_2{}^3C_1$im][$NTf_2$] | 283 – 333 | 217.1 ± 8.2 | 620 ± 11 | 161.1 ± 1.3 |
| [$^1C_3{}^3C_1$im][$NTf_2$] | 283 – 333 | 203.9 ± 3.0 | 618.4 ± 4.1 | 172.1 ± 0.5 |
| [$^1C_4{}^3C_1$im][$NTf_2$] | 283 – 333 | 208.3 ± 2.4 | 653.0 ± 3.2 | 171.4 ± 0.3 |
| [$^1C_5{}^3C_1$im][$NTf_2$] | 283 – 333 | 222.5 ± 1.1 | 700.4 ± 1.4 | 171.1 ± 0.1 |
| [$^1C_6{}^3C_1$im][$NTf_2$] | 283 – 333 | 225.1 ± 3.0 | 728.5 ± 3.8 | 171.3 ± 0.4 |
| [$^1C_7{}^3C_1$im][$NTf_2$] | 283 – 333 | 252.4 ± 2.2 | 784.1 ± 2.6 | 169.1 ± 0.2 |
| [$^1C_8{}^3C_1$im][$NTf_2$] | 283 – 333 | 268.6 ± 2.6 | 832.7 ± 2.8 | 167.2 ± 0.2 |
| [$^1C_9{}^3C_1$im][$NTf_2$] | 283 – 333 | 266.9 ± 6.2 | 845.9 ± 6.8 | 168.0 ± 0.6 |
| [$^1C_{10}{}^3C_1$im][$NTf_2$] | 283 – 333 | 283.9 ± 5.2 | 887.9 ± 5.4 | 166.0 ± 0.5 |
| [$^1C_{11}{}^3C_1$im][$NTf_2$] | 283 – 333 | 299.6 ± 2.6 | 922.6 ± 2.6 | 164.9 ± 0.2 |
| [$^1C_{12}{}^3C_1$im][$NTf_2$] | 293 – 333 | 295 ± 10 | 936 ± 11 | 165.2 ± 0.9 |

The presented fitting coefficients were derived from the experimental $\eta(T)$ data (appendix) by applying the VFT fitting function, Eq. 2.44. The standard uncertainties related to the VFT coefficients were calculated to the confidence level of 0.95 ($k \approx 2$).

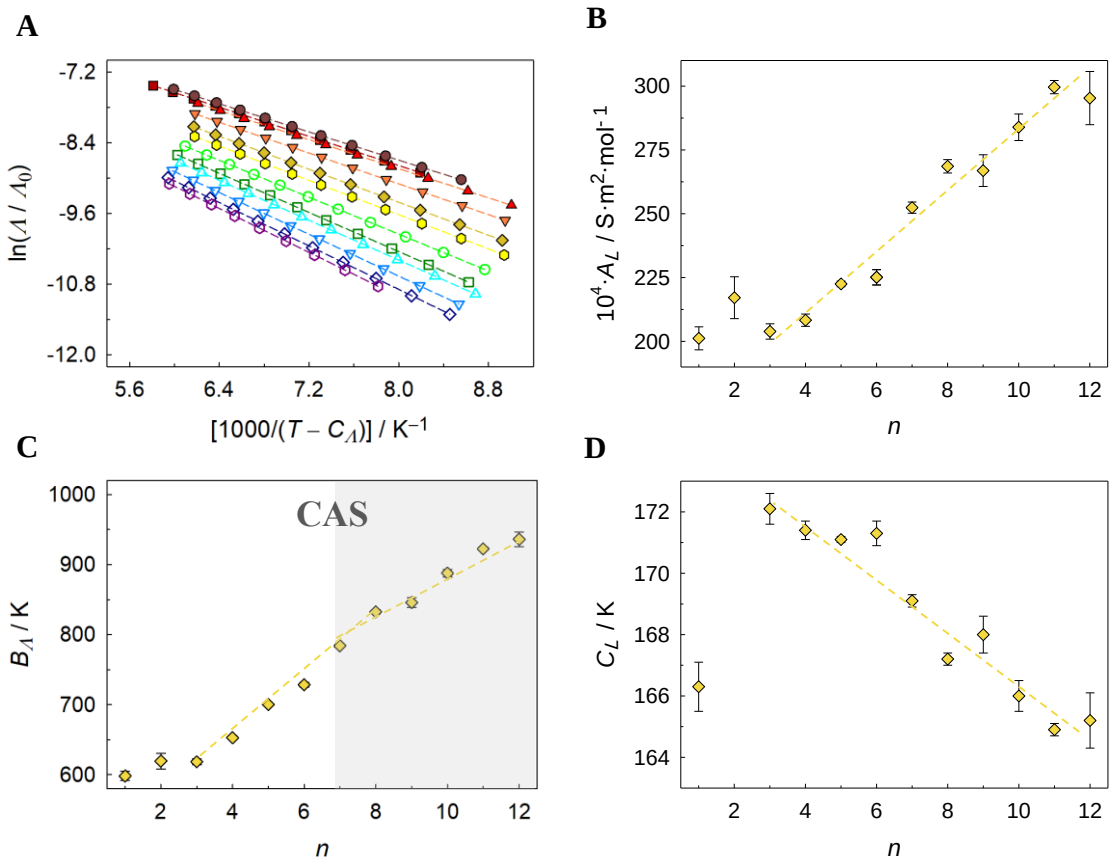



**Figure 5.40.** Impact of the alkyl chain length on the VFT coefficients for the molar conductivity of [$^1C_n{}^3C_1$im][$NTf_2$] series**.** **A**: Linearized VFT representation $n$ = 1 ●, 2 ■, 3 ▲, 4 ▼, 5 ◆, 6 ●, 7 ○, 8 □, 9 △, 10 ▽, 11 ◇, 12 ⬡; **B**: Pre-exponential coefficient, $A_\Lambda$; **C**: energy barrier-related coefficient, $B_\Lambda$; **D**: Vogel temperature, $C_\Lambda$. $\Lambda_0$ = 1 S·m$^2$·mol$^{-1}$

The molar conductivities at the reference temperature ($T$ = 298.15 K) are presented in Table 5.25 together with the energy barrier and strength parameter derived from Eq. 2.47 and Eq. 2.49 respectively. The temperature dependence of the conductivity-related energy barrier, $E_\Lambda$, and the effect of the alkyl chain length on $E_\Lambda$ and on the liquid fragility (strength parameter, $D_\Lambda$) are represented in Fig. 5.41.

**Table 5.25.** Molar conductivity and derived energy barrier of the studied $[^1C_n{}^3C_1im][NTf_2]$ homologue series at the reference temperature ($T$ = 298.15 K), together with the strength parameter.

| Ionic Liquid | $\frac{10^4 \cdot \Lambda(T=298.15\ K)}{S \cdot m^2 \cdot mol^{-1}}$ | $\frac{E_\Lambda(T=298.15\ K)}{kJ \cdot mol^{-1}}$ | $D_\Lambda$ |
|---|---|---|---|
| $[^1C_1{}^3C_1im][NTf_2]$ | 2.149 ± 0.032 | 25.45 ± 0.42 | 3.599 ± 0.043 |
| $[^1C_2{}^3C_1im][NTf_2]$ | 2.362 ± 0.035 | 24.38 ± 0.64 | 3.846 ± 0.077 |
| $[^1C_3{}^3C_1im][NTf_2]$ | 1.509 ± 0.023 | 28.77 ± 0.30 | 3.593 ± 0.026 |
| $[^1C_4{}^3C_1im][NTf_2]$ | 1.206 ± 0.018 | 30.04 ± 0.20 | 3.810 ± 0.020 |
| $[^1C_5{}^3C_1im][NTf_2]$ | 0.898 ± 0.014 | 32.07 ± 0.08 | 4.094 ± 0.009 |
| $[^1C_6{}^3C_1im][NTf_2]$ | 0.721 ± 0.011 | 33.46 ± 0.27 | 4.253 ± 0.024 |
| $[^1C_7{}^3C_1im][NTf_2]$ | 0.5798 ± 0.0087 | 34.80 ± 0.16 | 4.637 ± 0.016 |
| $[^1C_8{}^3C_1im][NTf_2]$ | 0.4650 ± 0.0070 | 35.89 ± 0.16 | 4.980 ± 0.018 |
| $[^1C_9{}^3C_1im][NTf_2]$ | 0.4015 ± 0.0060 | 36.91 ± 0.45 | 5.035 ± 0.044 |
| $[^1C_{10}{}^3C_1im][NTf_2]$ | 0.3432 ± 0.0051 | 37.57 ± 0.37 | 5.348 ± 0.036 |
| $[^1C_{11}{}^3C_1im][NTf_2]$ | 0.2948 ± 0.0044 | 38.40 ± 0.16 | 5.595 ± 0.017 |
| $[^1C_{12}{}^3C_1im][NTf_2]$ | 0.2585 ± 0.0039 | 39.14 ± 0.69 | 5.666 ± 0.072 |

$\Lambda(T$ = 298.15 K) and $E_\Lambda(T$ = 298.15 K) were calculated from the fitting coefficients presented in Table 5.24 and by applying Eq. 2.44 and Eq. 2.47, respectively. The strength parameter was calculated by Eq. 2.49, $D_\Lambda = B_\Lambda / C_\Lambda$. The relative standard uncertainty associated with the viscosity measurements was estimated as $u(\Lambda)$ = 1.5% (Eq. 4.15); The standard uncertainty associated with the derived energy barrier, $u(E_\Lambda)$, and strength parameter , $u(D_\Lambda)$, was calculated by applying the propagation of uncertainty to Eq. 2.47 and Eq. 2.49, respectively.

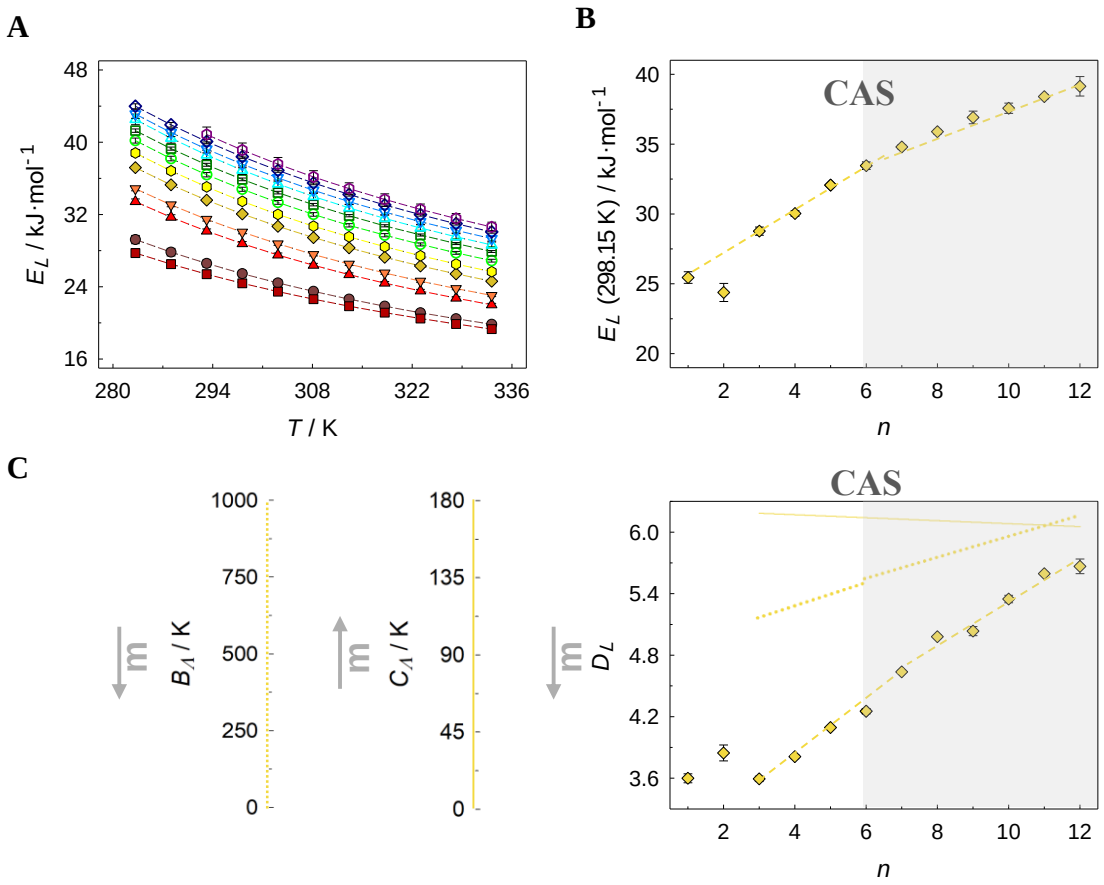



**Figure 5.41.** Graphical representation of the energy barrier and strength parameter derived from the experimental molar conductivity data of the [$^1C_n{}^3C_1$im][$NTf_2$] series. **A**: Temperature dependence of the derived energy barrier $n$ = 1 ●, 2 ■, 3 ▲, 4 ▼, 5 ◆, 6 ⬢, 7 ○, 8 □, 9 △, 10 ▽, 11 ◇, 12 ⬡; **B**: Effect of the alkyl chain length on the energy barrier; **C**: Effect of the alkyl chain length on the liquid fragility ($B_\Lambda$ and $C_\Lambda$ scales are included as guide lines).

### 5.1.5. [$^1C_n{}^3C_1$im][FAP] Series

In this work, the density, viscosity, and electrical conductivity of the of the 1-alkyl-3-methylimidazolium tris(pentafluoroethyl)trifluorophosphate series, [$^1C_n{}^3C_1$im][FAP] $n$ = 2 – 10, 12 (Fig. 5.42) were measured for different temperatures.

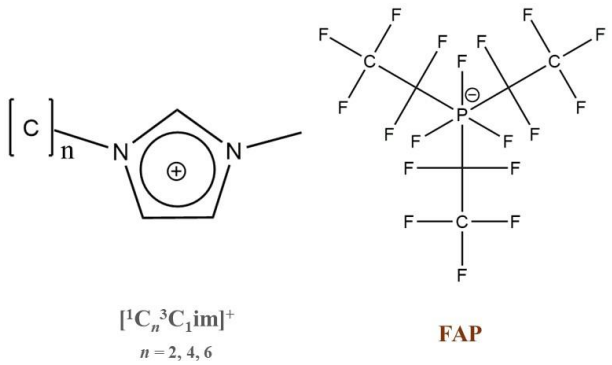



**Figure 5.42.** Structure of the studied [$^1C_n{}^3C_1$im][FAP] ($n$ = 2, 4, 6) ionic liquids.

#### 5.1.5.1. Density

The resulting fitting coefficients from the temperature dependence of density of the $[^1C_n{}^3C_1im][FAP]$ ILs (Eq. 2.4) are presented in Table 5.26. The densities at the reference temperature ($T$ = 298.15 K) are presented in Table 5.27 together with the molar volume and thermal expansion coefficient derived from Eq. 2.2 and Eq. 2.7 respectively. The graphical representation of density, thermal expansion coefficient, and molar volume as functions of temperature and number of carbons on the cations alkyl chain are presented in Fig 5.43.

**Table 5.26.** Fitting coefficients used to describe the temperature dependence of density of the studied $[^1C_n{}^3C_1im][FAP]$ homologue series.

| Ionic Liquid | $\frac{T_{\text{interval}}}{\text{K}}$ | $\frac{10^7 \cdot a_2}{\text{K}^{-2}}$ | $\frac{10^4 \cdot a_1}{\text{K}^{-1}}$ | $\frac{a_0}{\text{K}}$ |
|---|---|---|---|---|
| $[^1C_2{}^3C_1im][FAP]$ | 273 – 373 | 0.605 ± 0.054 | −6.559 ± 0.035 | 7.6443 ± 0.0006 |
| $[^1C_4{}^3C_1im][FAP]$ | 278 – 373 | 0.588 ± 0.034 | −6.592 ± 0.022 | 7.5921 ± 0.0004 |
| $[^1C_6{}^3C_1im][FAP]$ | 283 – 373 | 0.603 ± 0.040 | −6.617 ± 0.026 | 7.5497 ± 0.0004 |

The presented fitting coefficients were derived from the experimental $\rho(T)$ data (appendix) by applying a polynomial fitting function, $\ln[\rho(T)] = a_2T^2 + a_1T + a_0$ (Eq. 2.4). The standard uncertainties related to the fitting coefficients were calculated to the confidence level of 0.95 ($k \approx 2$).

**Table 5.27.** Density, thermal expansion coefficient, and molar volume at the reference temperature ($T$ = 298.15 K) for the studied $[^1C_n{}^3C_1im][FAP]$ homologue series.

| Ionic Liquid | $\frac{\rho(298.15\ \text{K})}{\text{kg}\cdot\text{m}^{-3}}$ | $\frac{10^4 \cdot \alpha_\rho(298.15\ \text{K})}{\text{K}^{-1}}$ | $\frac{10^6 \cdot V_\text{m}(298.15\ \text{K})}{\text{m}^3\cdot\text{mol}^{-1}}$ |
|---|---|---|---|
| $[^1C_2{}^3C_1im][FAP]$ | 1727.0 ± 0.5 | 6.20 ± 0.04 | 322.1 ± 1.1 |
| $[^1C_4{}^3C_1im][FAP]$ | 1637.0 ± 0.5 | 6.24 ± 0.02 | 356.8 ± 1.2 |
| $[^1C_6{}^3C_1im][FAP]$ | 1568.3 ± 0.5 | 6.26 ± 0.03 | 390.4 ± 1.2 |

$\rho(T$ = 298.15 K) and $\alpha_\rho(T$ = 298.15 K) were calculated from the fitting coefficients presented in Table 5.26 and by applying Eq. 2.4 and Eq. 2.7 respectively. $V_\text{m}(298.15\ \text{K}) = M/\rho(298.15\ \text{K})$. The standard uncertainty associated with $\alpha_\rho$ and $V_\text{m}$ were calculated by applying the propagation of uncertainty to Eq. 2.7 and 2.2 respectively.

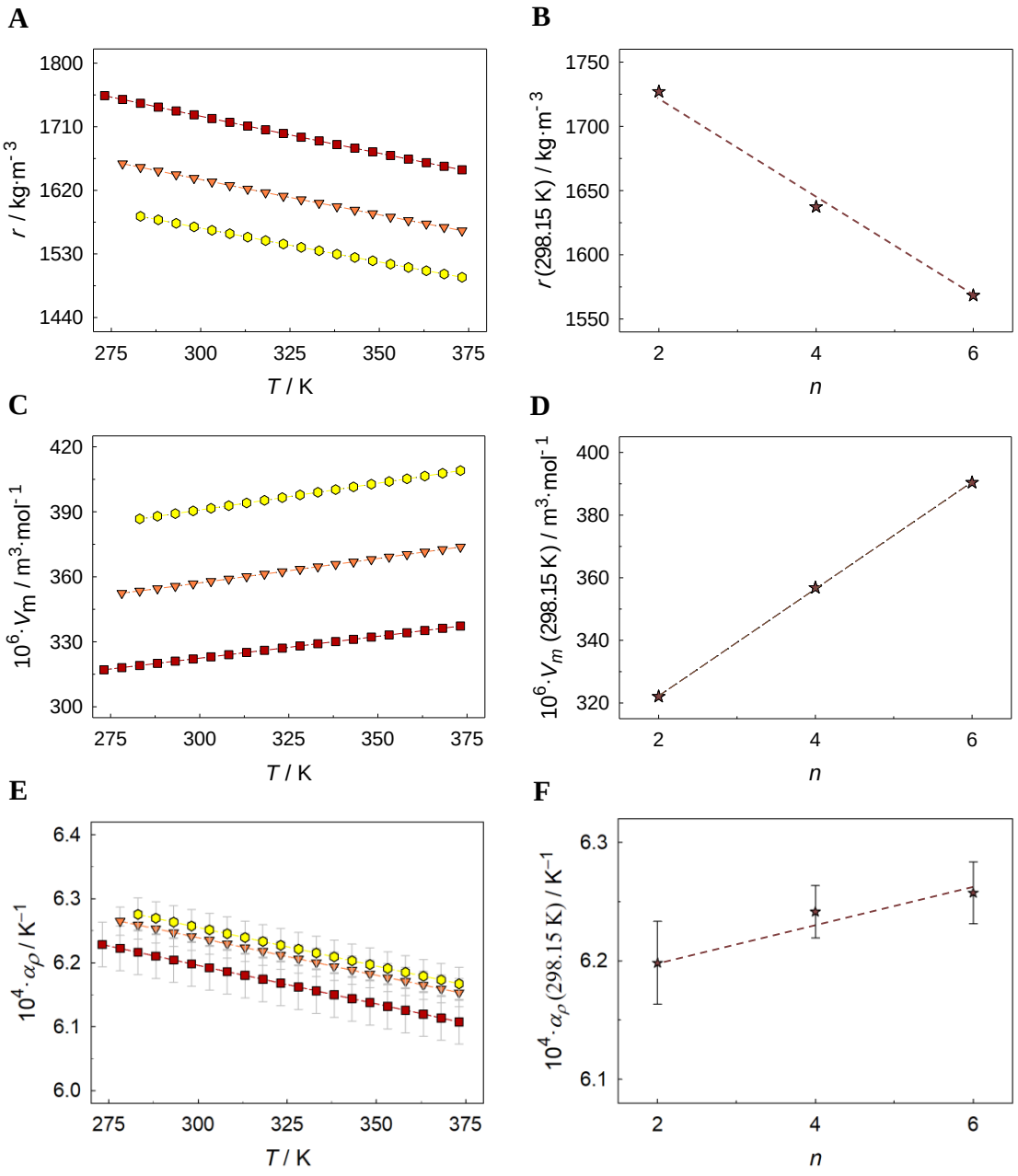



**Figure 5.43.** Density and derived properties of the [$^{1}C_{n}{}^{3}C_{1}$im][FAP] series as a function of temperature (A, C, E) and number of carbons on the alkyl chain of the cation (B, D, F). **A**, **B**: Density; **C**, **D**: Molar volume; **E**, **F**: Thermal expansion coefficient. $n$ = 2 ■, 4 ▼, 6 ⬢

#### 5.1.5.2. Viscosity

The obtained viscosity data for the [$^1C_n{}^3C_1$im][FAP] ILs is presented as a function of temperature and the number of carbons of the cation's alkyl chain in Fig. 5.44.

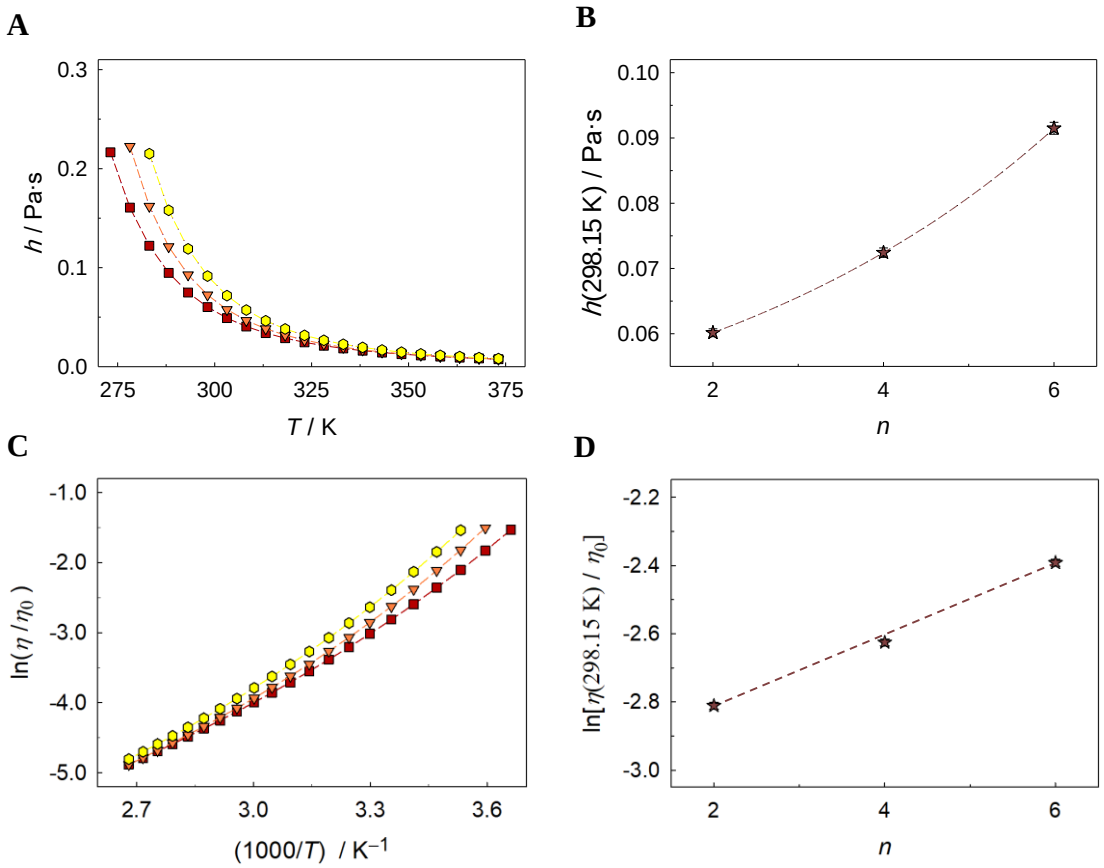



**Figure 5.44.** Viscosity of the [$^1C_n{}^3C_1$im][FAP] series as a function of temperature (A, C) and number of carbons on the alkyl chain of the cation (B, D). **A**: Temperature dependence of viscosity; **B**: Dependence of viscosity with the alkyl chain length; **C**: Temperature dependence of viscosity (Arrhenius representation); **D**: Dependence of viscosity with the alkyl chain length (logarithmic form). $n$ = 2 ■, 4 ▼, 6. $\eta_0$ = 1 Pa·s.

The VFT coefficients (Eq 2.44) obtained from the experimental viscosity-temperature data, $\eta(T)$, are presented in Table 5.28. The effect of the alkyl chain length on the obtained VFT coefficients is presented in Fig. 5.45 together with the graphical representation of the linearized VFT equation (Eq. 2.45).

**Table 5.29.** Fitting coefficients used to describe the temperature dependence of viscosity of the studied [$^1C_n{}^3C_1$im][FAP] homologue series.

| Ionic Liquid | $\frac{T_{\text{interval}}}{\text{K}}$ | $\frac{10^3 \cdot A_\eta}{\text{Pa} \cdot \text{s}}$ | $\frac{B_\eta}{\text{K}}$ | $\frac{C_\eta}{\text{K}}$ |
|---|---|---|---|---|
| [$^1C_2{}^3C_1$im][FAP] | 273 – 373 | 0.1526 ± 0.0017 | 846.6 ± 3.1 | 156.5 ± 0.2 |
| [$^1C_4{}^3C_1$im][FAP] | 278 – 373 | 0.1534 ± 0.0005 | 798.9 ± 0.8 | 168.4 ± 0.1 |
| [$^1C_6{}^3C_1$im][FAP] | 283 – 373 | 0.1192 ± 0.0020 | 873.9 ± 4.6 | 166.6 ± 0.3 |

The presented fitting coefficients were derived from the experimental $\eta(T)$ data (appendix) by applying the VFT fitting function, Eq. 2.44. The standard uncertainties related to the VFT coefficients were calculated to the confidence level of 0.95 ($k \approx 2$).

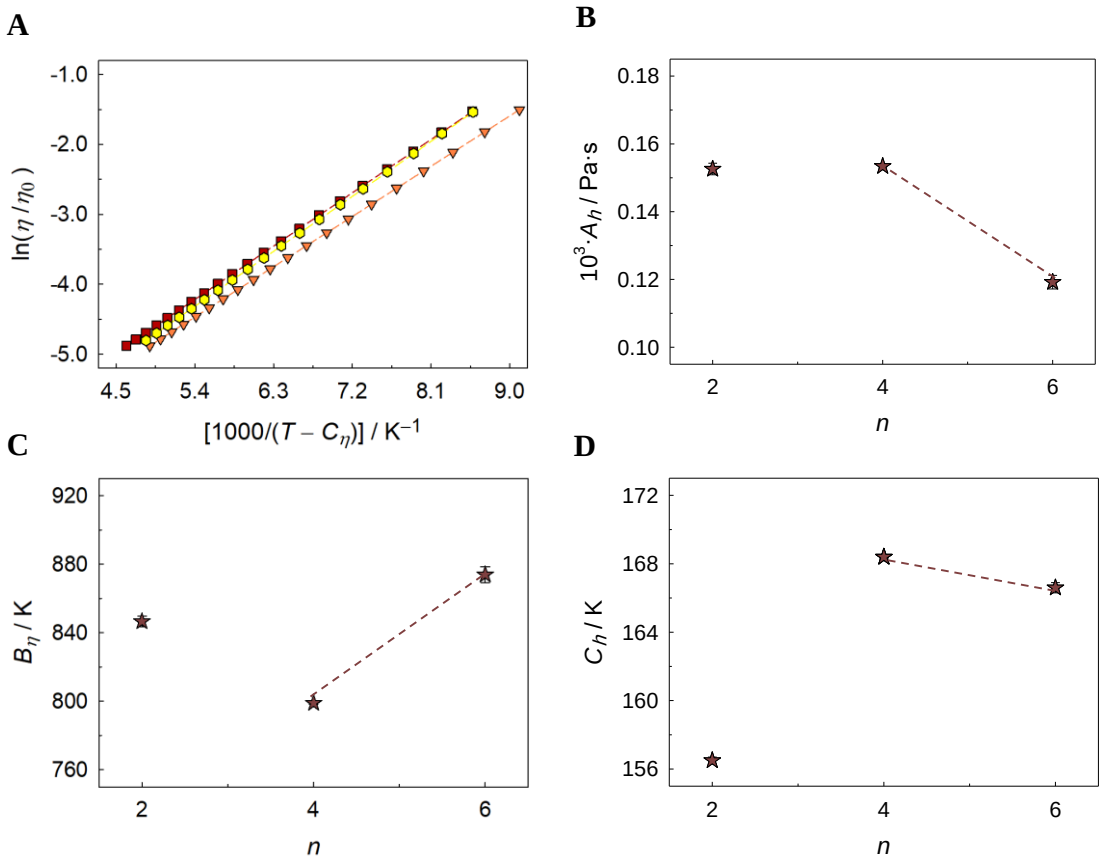



**Figure 5.45.** Impact of the alkyl chain length on the VFT coefficients for the viscosity of [$^1C_n{}^3C_1$im][FAP] series. **A**: Linearized VFT representation $n$ = 2 ■, 4 ▼, 6 ●; **B**: Pre-exponential coefficient, $A_\eta$; **C**: energy barrier-related coefficient, $B_\eta$; **D**: Vogel temperature, $C_\eta$. $\eta_0$ = 1 Pa·s

The viscosities at the reference temperature ($T$ = 298.15 K) are presented in Table 5.29 together with the energy barrier and strength parameter derived from Eq. 2.47 and Eq. 2.49 respectively. The temperature dependence of the viscosity-related energy barrier, $E_\eta$, and the effect of the alkyl chain length on $E_\eta$ and on the liquid fragility (strength parameter, $D_\eta$) are represented in Fig. 5.46.

**Table 5.29.** Viscosity and derived energy barrier of the studied [$^1C_n{}^3C_1$im][FAP] homologue series at the reference temperature ($T$ = 298.15 K), together with the strength parameter.

| Ionic Liquid | $\eta(T=298.15\ \text{K})$ / Pa · s | $E_\eta(T=298.15\ \text{K})$ / kJ · mol$^{-1}$ | $D_\eta$ |
|---|---|---|---|
| [$^1C_2{}^3C_1$im][FAP] | 0.06015 ± 0.00060 | 31.19 ± 0.14 | 5.410 ± 0.021 |
| [$^1C_4{}^3C_1$im][FAP] | 0.07242 ± 0.00072 | 35.07 ± 0.06 | 4.744 ± 0.006 |
| [$^1C_6{}^3C_1$im][FAP] | 0.09148 ± 0.00091 | 37.32 ± 0.26 | 5.245 ± 0.029 |

$\eta(T = 298.15\ \text{K})$ and $E_\eta(T = 298.15\ \text{K})$ were calculated from the fitting coefficients presented in Table 5.29 and by applying Eq. 2.44 and Eq. 2.47, respectively. The strength parameter was calculated by Eq. 2.49, $D_\eta = B_\eta / C_\eta$. The relative standard uncertainty associated with the viscosity measurements was estimated as $u(\eta)$ = 1.0% (Eq. 2.72); The standard uncertainty associated with the derived energy barrier, $u(E_\eta)$, and strength parameter , $u(D_\eta)$, was calculated by applying the propagation of uncertainty to Eq. 2.47 and Eq. 2.49, respectively.

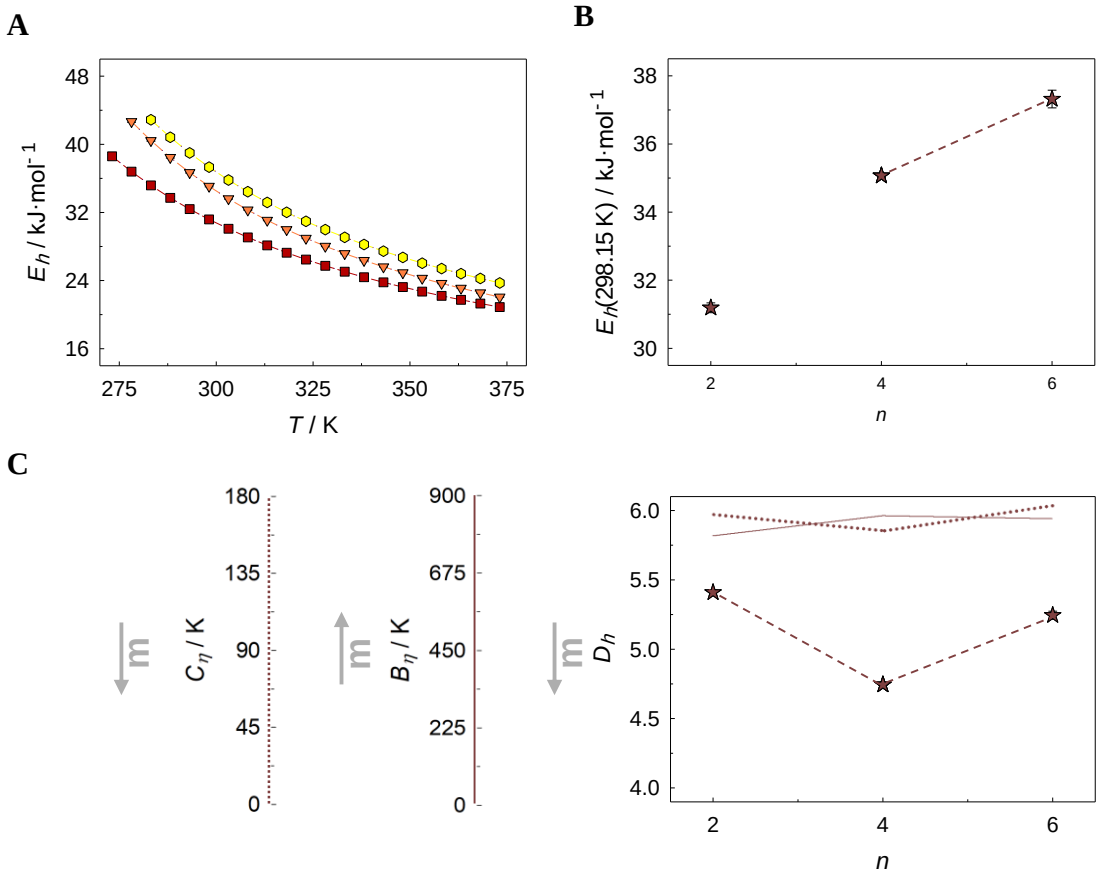



**Figure 5.46.** Graphical representation of the energy barrier and strength parameter derived from the experimental viscosity data of the [$^1C_n{}^3C_1$im][FAP] series. **A**: Temperature dependence of the derived energy barrier $n$ = 2 ■, 4 ▼, 6; **B**: Effect of the alkyl chain length on the energy barrier; **C**: Effect of the alkyl chain length on the liquid fragility ($B_\eta$ and $C_\eta$ scales are included as guide lines).

The deviation of the available viscosity data to the experimental results for the [$^1C_n{}^3C_1$im][FAP] series is presented in Fig. 5.47.

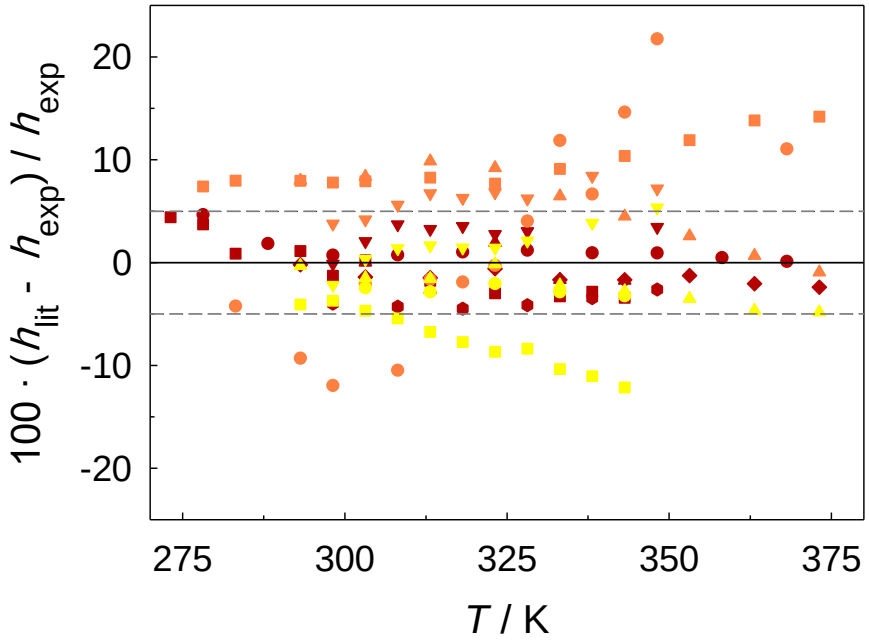



**Figure 5.47.** Deviation of the available viscosity data to the experimental results for the [$^1C_n{}^3C_1$im][FAP] series. ***n* = 2:** ● [111], ■ [89], ▲ [117], ▼ [118], ◆ [119], ⬢ [120]; ***n* = 4:** ● [121], ■ [122], ▲ [119], ▼ [118]. ***n* = 6:** ● [117], ■ [66], ▲ [119], ▼ [118].

A decent number of sources was found for all three ionic liquids. While the experimental results for *n* = 2 and 6 (apart of Li *et al.* [66] which as a pronounced temperature dependence) are in good agreement with the literature data there seems to be a significant deviation for n = 4.

#### 5.1.5.3. Electrical Conductivity

The resistance and reactance spectra obtained for the [$^1C_n{}^3C_1$im][FAP] ionic liquids through the ILDEM experiments are presented in Fig. 5.48.

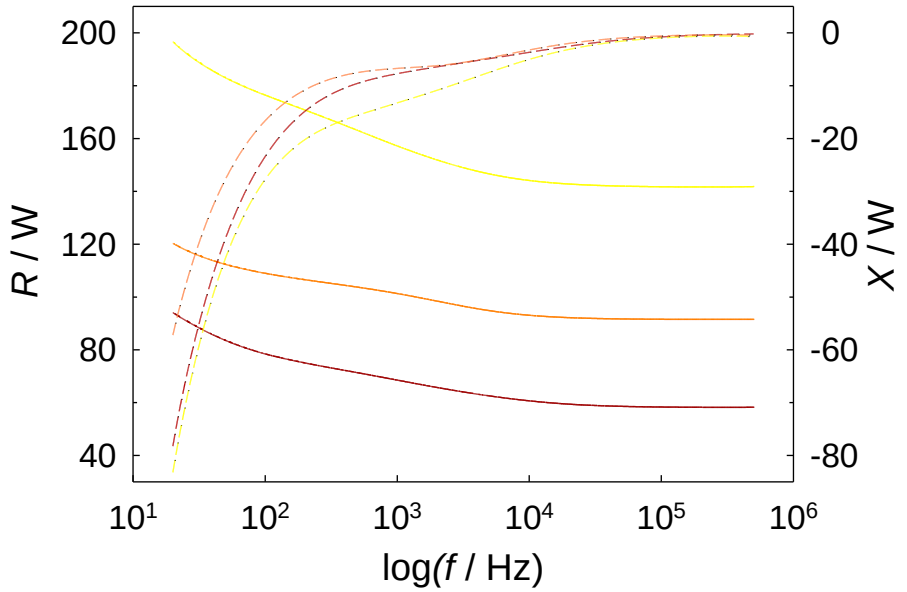



**Figure 5.48.** Typical resistance (straight line) and reactance (dashed line) spectra for the [$^1$C$_n$$^3$C$_1$im][FAP] series. $n$ = **2**, **4**, **6**.

The VFT coefficients (Eq 2.24) obtained from the experimental electrical conductivity-temperature data, $\sigma(T)$, are presented in Table 5.30.

**Table 5.30.** Fitting coefficients used to describe the temperature dependence of electrical conductivity of the studied [$^1$C$_n$$^3$C$_1$im][FAP] homologue series.

| Ionic Liquid | $\frac{A_\sigma}{\mathrm{S \cdot m^{-1}}}$ | $\frac{B_\sigma}{\mathrm{K}}$ | $\frac{C_\sigma}{\mathrm{K}}$ | $\frac{\sigma(T=298.15\ \mathrm{K})}{\mathrm{S \cdot m^{-1}}}$ |
|---|---|---|---|---|
| [$^1$C$_2$$^3$C$_1$im][FAP] | 49.96 ± 0.40 | 541.1 ± 2.1 | 178.3 ± 0.3 | 0.5468 ± 0.0082 |
| [$^1$C$_4$$^3$C$_1$im][FAP] | 45.6 ± 1.1 | 578.1 ± 6.0 | 183.2 ± 0.7 | 0.2981 ± 0.0045 |
| [$^1$C$_6$$^3$C$_1$im][FAP] | 46.61 ± 0.36 | 655.4 ± 2.0 | 181.1 ± 0.2 | 0.1725 ± 0.0026 |

The presented fitting coefficients were derived from the experimental $\sigma(T)$ data (appendix) by applying the VFT fitting function, Eq. 2.44. The standard uncertainties related to the VFT coefficients were calculated to the confidence level of 0.95 ($k \approx 2$). The relative standard uncertainty associated with the viscosity measurements was estimated as $u(\sigma)$ = 1.5% (Eq. 4.15).

The deviation of the available electrical conductivity data to the experimental results for the [$^1C_n{}^3C_1$im][FAP] series is presented in Fig. 5.49. No literature data was found for $n$ = 4, and only one literature source was found for $n$ = 2 and 6. The experimental results are in excellent agreement with the data published by Nazet *et al.* [111] and Li *et al.* [66].

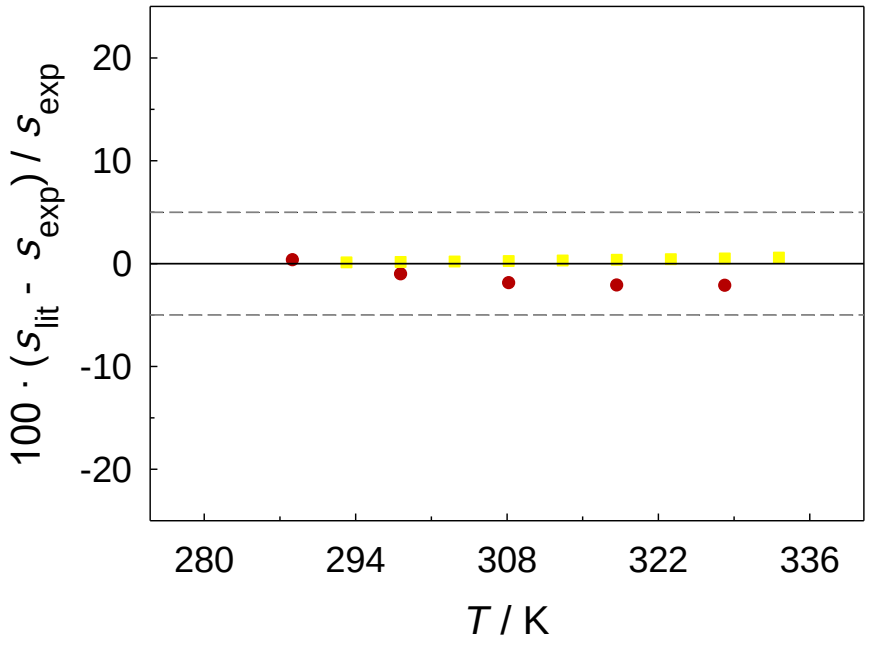



**Figure 5.49.** Deviation of the available electrical conductivity data to the experimental results for the [$^1C_n{}^3C_1$im][FAP] series. ***n* = 2:** ● [111]; ***n* = 6:** ● [66].

### 5.1.5.4. Molar Conductivity

The molar conductivity of the [$^1C_n{}^3C_1$im][FAP] ILs was calculated from the experimentally measured electrical conductivity and density data ILs. The molar conductivity is presented as a function of temperature and the number of carbons of the cation's alkyl chain in Fig. 5.50.

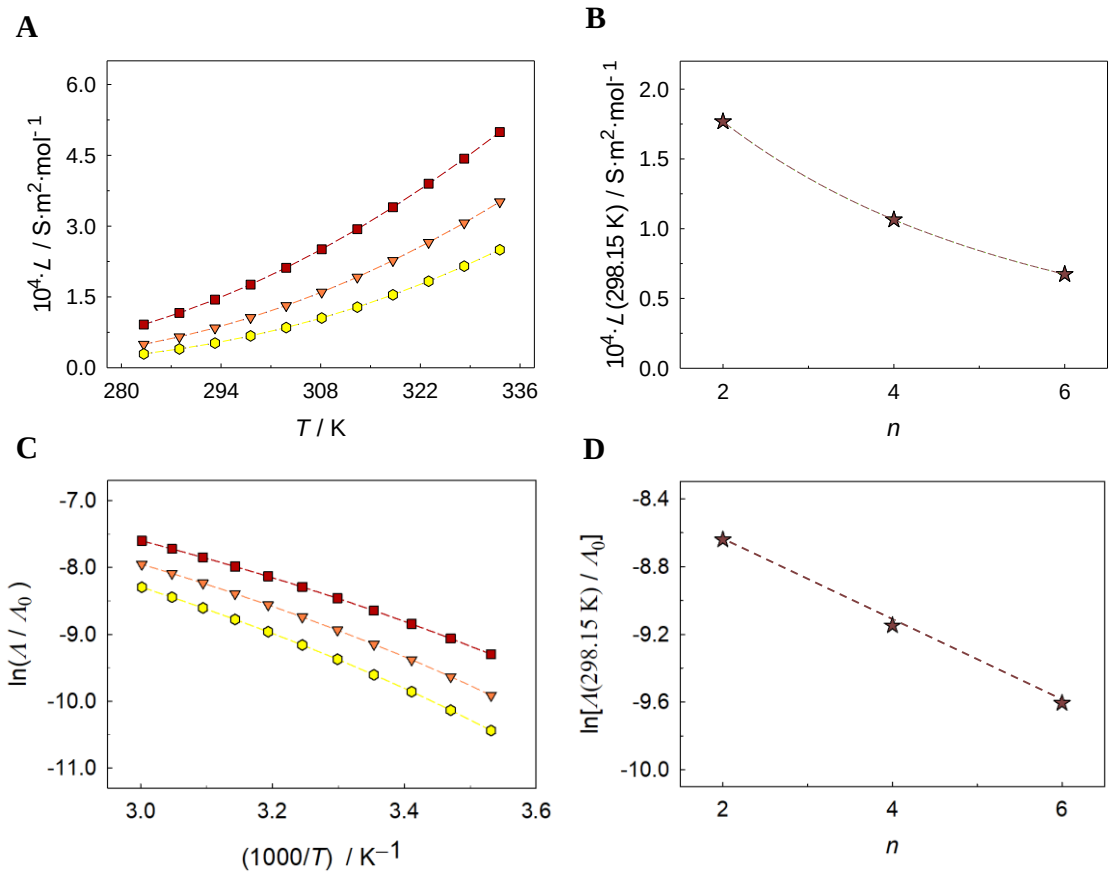



**Figure 5.50.** Molar conductivity of the [$^1$C$_n$$^3$C$_1$im][FAP] series as a function of temperature (A, C) and number of carbons on the alkyl chain of the cation (B, D). **A**: Temperature dependence of molar conductivity; **B**: Dependence of molar conductivity with the alkyl chain length; **C**: Temperature dependence of molar conductivity (Arrhenius representation); **D**: Dependence of molar conductivity with the alkyl chain length (logarithmic form). $n$ = 2 ■, 4 ▼, 6 ⬢. $\Lambda_0$ = 1 S·m$^2$·mol$^{-1}$

The VFT coefficients (Eq 2.44) obtained from the experimental molar conductivity-temperature data, $\eta(T)$, are presented in Table 5.31. The effect of the alkyl chain length on the obtained VFT coefficients is presented in Fig. 5.51, together with the graphical representation of the linearized VFT equation (Eq. 2.45).

**Table 5.31.** Fitting coefficients used to describe the temperature dependence of molar conductivity of the studied [$^1$C$_n$$^3$C$_1$im][FAP] homologue series.

| Ionic Liquid | $\frac{T_{\text{interval}}}{\text{K}}$ | $\frac{10^4 \cdot A_\Lambda}{\text{S} \cdot \text{m}^2 \cdot \text{mol}^{-1}}$ | $\frac{B_\Lambda}{\text{K}}$ | $\frac{C_\Lambda}{\text{K}}$ |
|---|---|---|---|---|
| [$^1$C$_2$$^3$C$_1$im][FAP] | 283 – 333 | 191.0 ± 2.1 | 573.4 ± 2.9 | 175.7 ± 0.3 |
| [$^1$C$_4$$^3$C$_1$im][FAP] | 283 – 333 | 191.6 ± 4.0 | 607.8 ± 5.5 | 181.1 ± 0.6 |
| [$^1$C$_6$$^3$C$_1$im][FAP] | 283 – 333 | 215.8 ± 1.5 | 687.0 ± 1.9 | 179.1 ± 0.2 |

The presented fitting coefficients were derived from the experimental $\Lambda(T)$ data (appendix) by applying the VFT fitting function, Eq. 2.44. The standard uncertainties related to the VFT coefficients were calculated to the confidence level of 0.95 ($k \approx 2$).

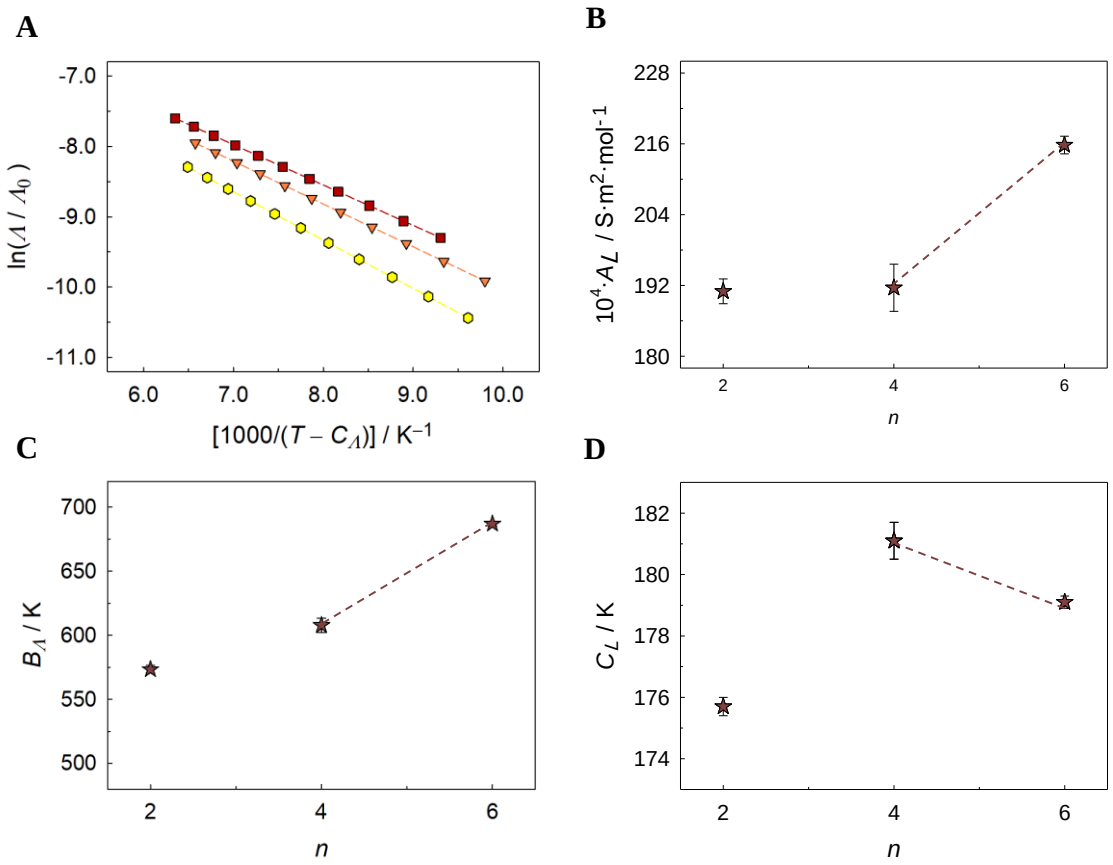



**Figure 5.51.** Impact of the alkyl chain length on the VFT coefficients for the molar conductivity of [$^1C_n{}^3C_1$im][FAP] series. **A**: Linearized VFT representation $n$ = 2 ■, 4 ▼, 6 ●; **B**: Pre-exponential coefficient, $A_\Lambda$; **C**: energy barrier-related coefficient, $B_\Lambda$; **D**: Vogel temperature, $C_\Lambda$. $\Lambda_0$ = 1 S·m$^2$·mol$^{-1}$.

The molar conductivities at the reference temperature ($T$ = 298.15 K) are presented in Table 5.32, together with the energy barrier and strength parameter derived from Eq. 2.47 and Eq. 2.49, respectively. The temperature dependence of the conductivity-related energy barrier, $E_\eta$, and the effect of the alkyl chain length on $E_\Lambda$ and on the liquid fragility (strength parameter, $D_\Lambda$) are represented in Fig. 5.52.

**Table 5.32.** Molar conductivity and derived energy barrier of the studied [$^1C_n{}^3C_1$im][FAP] homologue series at the reference temperature ($T$ = 298.15 K), together with the strength parameter.

| Ionic Liquid | $\frac{10^4 \cdot \Lambda(T=298.15\ \mathrm{K})}{\mathrm{S \cdot m^2 \cdot mol^{-1}}}$ | $\frac{E_\Lambda(T=298.15\ \mathrm{K})}{\mathrm{kJ \cdot mol^{-1}}}$ | $D_\Lambda$ |
|---|---|---|---|
| [$^1C_2{}^3C_1$im][FAP] | 1.768 ± 0.027 | 28.26 ± 0.20 | 3.264 ± 0.017 |
| [$^1C_4{}^3C_1$im][FAP] | 1.065 ± 0.016 | 32.79 ± 0.45 | 3.356 ± 0.032 |
| [$^1C_6{}^3C_1$im][FAP] | 0.673 ± 0.010 | 35.83 ± 0.16 | 3.836 ± 0.011 |

$\Lambda(T$ = 298.15 K) and $E_\Lambda(T$ = 298.15 K) were calculated from the fitting coefficients presented in Table 5.31 and by applying Eq. 2.44 and Eq. 2.47, respectively. The strength parameter was calculated by Eq. 2.49, $D_\Lambda = B_\Lambda / C_\Lambda$. The relative standard uncertainty associated with the viscosity measurements was estimated as $u(\Lambda)$ = 1.5% (Eq. 4.15); The standard uncertainty associated with the derived energy barrier, $u(E_\Lambda)$, and strength parameter, $u(D_\Lambda)$, was calculated by applying the propagation of uncertainty to Eq. 2.47 and Eq. 2.49, respectively.

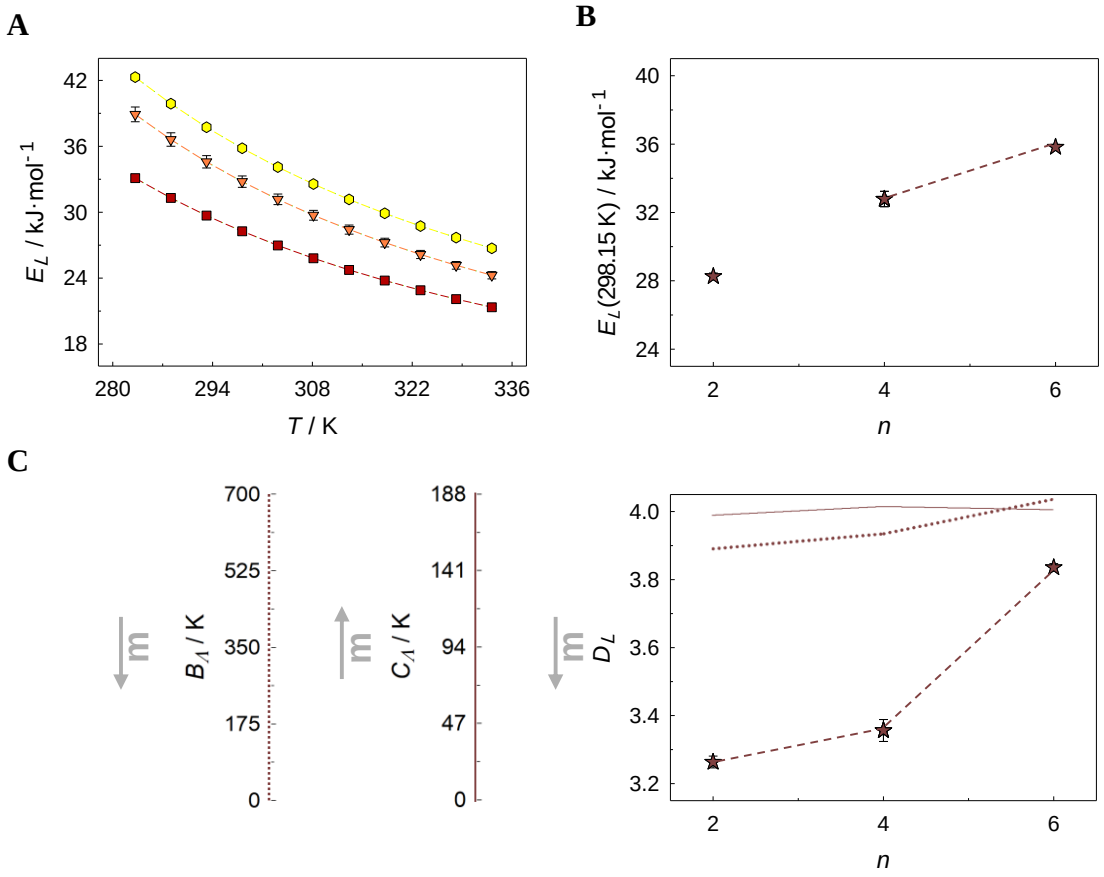



**Figure 5.52.** Graphical representation of the energy barrier and strength parameter derived from the experimental molar conductivity data of the [$^1C_n{}^3C_1$im][FAP] series. **A**: Temperature dependence of the derived energy barrier $n$ = 2 ■, 4 ▼, 6 ⬢; **B**: Effect of the alkyl chain length on the energy barrier; **C**: Effect of the alkyl chain length on the liquid fragility ($B_\Lambda$ and $C_\Lambda$ scales are included as guide lines).

### 5.1.6. [$^1C_n$py][$NTf_2$]Series

In this work, the density, viscosity, and electrical conductivity of the 1-alkylpyridinium bis(trifluoromethylsulfonyl)imide series, [$^1C_n$py][$NTf_2$] $n$ = 3 – 9 (Fig. 5.3).

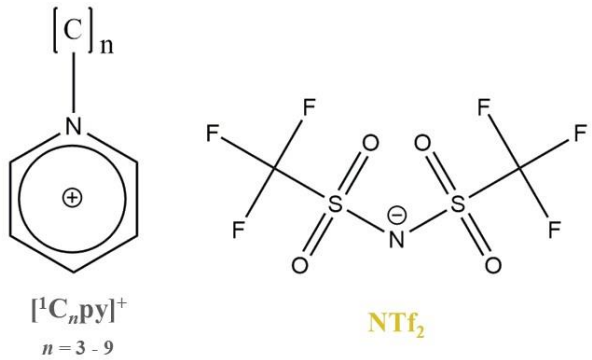



**Figure 5.53.** Structure of the studied [$^1C_n$py][$NTf_2$] ($n$ = 3 – 9) ionic liquids.

#### 5.1.6.1. Density

The resulting fitting coefficients from the temperature dependence of density of the $[^1C_n py][NTf_2]$ ILs (Eq. 2.4) are presented in Table 5.33. The densities at the reference temperature ($T$ = 298.15 K) are presented in Table 5.34, together with the molar volume and thermal expansion coefficient derived from Eq. 2.2 and Eq. 2.7 respectively. The graphical representation of density, thermal expansion coefficient, and molar volume as functions of temperature and number of carbons on the cations alkyl chain are presented in Fig 5.54.

**Table 5.33.** Fitting coefficients used to describe the temperature dependence of density of the studied $[^1C_n py][NTf_2]$ homologue series.

| Ionic Liquid | $\frac{T_{\text{interval}}}{\text{K}}$ | $\frac{10^7 \cdot a_2}{\text{K}^{-2}}$ | $\frac{10^4 \cdot a_1}{\text{K}^{-1}}$ | $\frac{a_0}{\text{K}}$ |
|---|---|---|---|---|
| $[^1C_3py][NTf_2]$ | 318 – 373 | 0.08 ± 0.12 | −6.548 ± 0.085 | 7.4865 ± 0.0015 |
| $[^1C_4py][NTf_2]$ | 293 – 373 | 0.007 ± 0.052 | −6.446 ± 0.035 | 7.4705 ± 0.0006 |
| $[^1C_5py][NTf_2]$ | 293 – 373 | 0.053 ± 0.055 | −6.507 ± 0.037 | 7.4477 ± 0.0006 |
| $[^1C_6py][NTf_2]$ | 293 – 373 | 0.071 ± 0.067 | −6.448 ± 0.044 | 7.4240 ± 0.0007 |
| $[^1C_7py][NTf_2]$ | 293 – 373 | 0.104 ± 0.069 | −6.428 ± 0.046 | 7.4033 ± 0.0008 |
| $[^1C_8py][NTf_2]$ | 293 – 373 | 0.078 ± 0.075 | −6.474 ± 0.050 | 7.3861 ± 0.0008 |
| $[^1C_9py][NTf_2]$ | 293 – 373 | 0.003 ± 0.053 | −6.546 ± 0.035 | 7.3731 ± 0.0006 |

The presented fitting coefficients were derived from the experimental $\rho(T)$ data (appendix) by applying a polynomial fitting function, $\ln[\rho(T)] = a_2T^2 + a_1T + a_0$ (Eq. 2.4). The standard uncertainties related to the fitting coefficients were calculated to the confidence level of 0.95 ($k \approx 2$).

**Table 5.34.** Density, thermal expansion coefficient, and molar volume at the reference temperature ($T$ = 298.15 K) for the studied $[^1C_n py][NTf_2]$ homologue series.

| Ionic Liquid | $\frac{\rho(298.15\ \text{K})}{\text{kg} \cdot \text{m}^{-3}}$ | $\frac{10^4 \cdot \alpha_\rho(298.15\ \text{K})}{\text{K}^{-1}}$ | $\frac{10^6 \cdot V_\text{m}(298.15\ \text{K})}{\text{m}^3 \cdot \text{mol}^{-1}}$ |
|---|---|---|---|
| $[^1C_3py][NTf_2]$ | 1468.4 ± 0.5 | 6.50 ± 0.09 | 274.0 ± 0.8 |
| $[^1C_4py][NTf_2]$ | 1448.6 ± 0.5 | 6.44 ± 0.04 | 287.4 ± 0.8 |
| $[^1C_5py][NTf_2]$ | 1414.0 ± 0.5 | 6.48 ± 0.04 | 304.4 ± 0.9 |
| $[^1C_6py][NTf_2]$ | 1383.5 ± 0.5 | 6.41 ± 0.04 | 321.2 ± 0.9 |
| $[^1C_7py][NTf_2]$ | 1356.4 ± 0.5 | 6.37 ± 0.05 | 338.0 ± 0.9 |
| $[^1C_8py][NTf_2]$ | 1331.1 ± 0.5 | 6.43 ± 0.05 | 354.9 ± 0.9 |
| $[^1C_9py][NTf_2]$ | 1310.2 ± 0.5 | 6.54 ± 0.04 | 371.3 ± 1.0 |

$\rho(T$ = 298.15 K) and $\alpha_\rho(T$ = 298.15 K) were calculated from the fitting coefficients presented in Table 5.33 and by applying Eq. 2.4 and Eq. 2.7 respectively. $V_\text{m}(298.15\ \text{K}) = M/\rho(298.15\ \text{K})$. The standard uncertainty associated with $\alpha_\rho$ and $V_\text{m}$ were calculated by applying the propagation of uncertainty to Eq. 2.7 and 2.2, respectively.

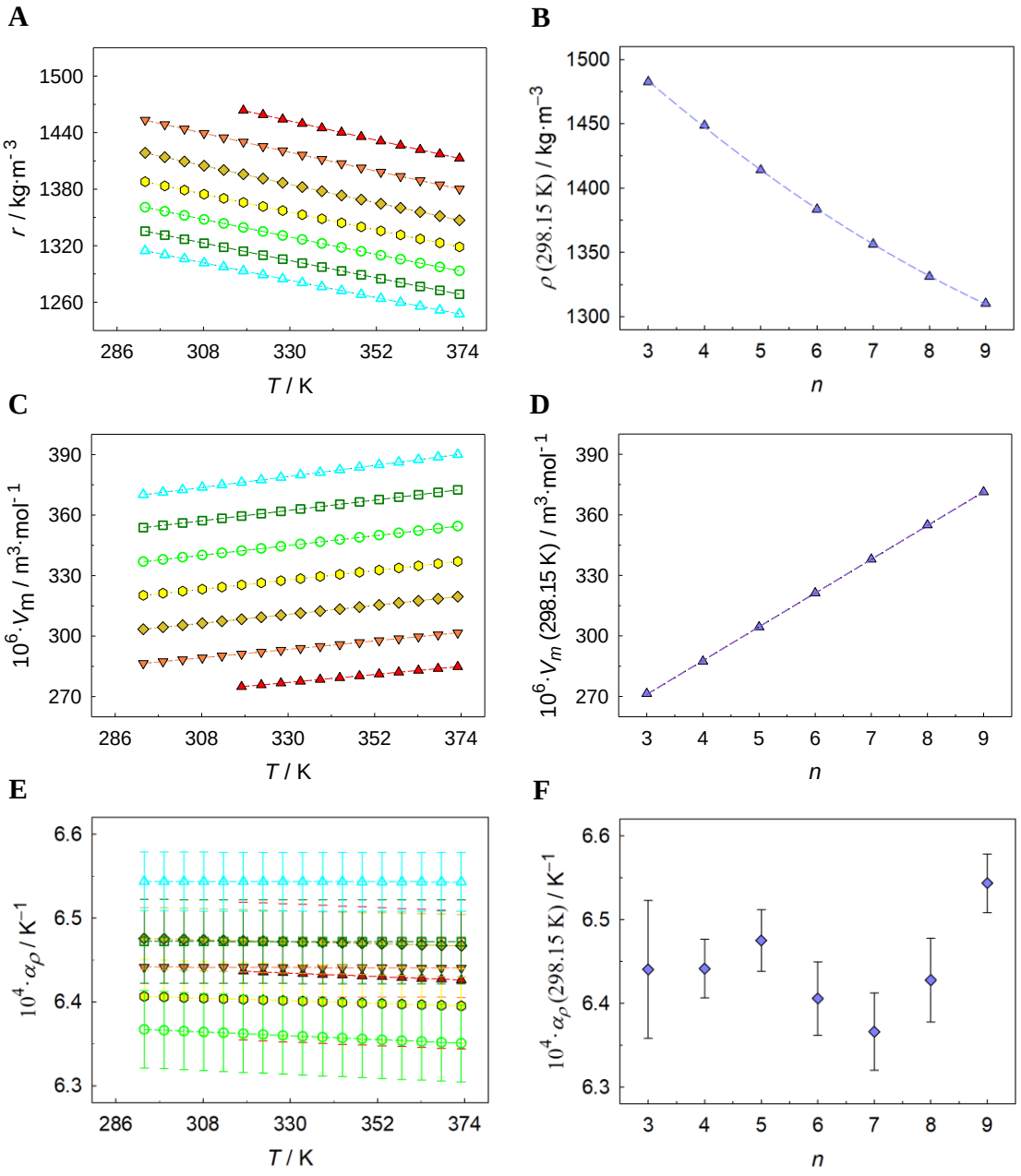



**Figure 5.54.** Density and derived properties of the [$^1C_n$py][$NTf_2$] series as a function of temperature (A, C, E) and number of carbons on the alkyl chain of the cation (B, D, F). **A**, **B**: Density; **C**, **D**: Molar volume; **E**, **F**: Thermal expansion coefficient. *n* = 3 ▲, 4 ▼, 5 ◆, 6 ⬢, 7 ○, 8 □, 9 △.

### 5.1.6.2. Viscosity

The obtained viscosity data for the [$^1C_n$py][$NTf_2$] ILs is presented as a function of temperature and the number of carbons of the cation's alkyl chain in Fig. 5.55.

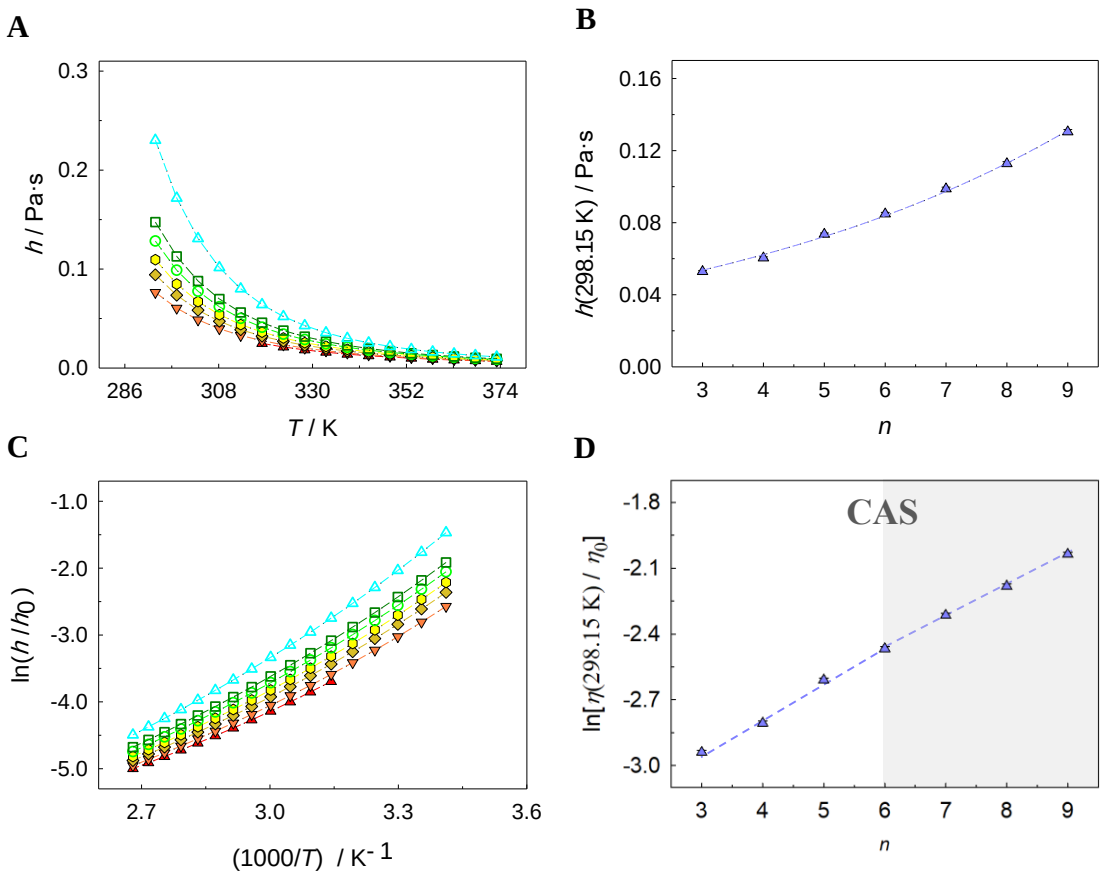



**Figure 5.55.** Viscosity of the [$^1C_n$py][$NTf_2$] series as a function of temperature (A, C) and number of carbons on the alkyl chain of the cation (B, D). **A**: Temperature dependence of viscosity; **B**: Dependence of viscosity with the alkyl chain length; **C**: Temperature dependence of viscosity (Arrhenius representation); **D**: Dependence of viscosity with the alkyl chain length (logarithmic form). $n$ = 3 ▲, 4 ▼, 5 ◆, 6 ⬢, 7 ○, 8 □, 9 △. $\eta_0$ = 1 Pa·s.

The VFT coefficients (Eq 2.44) obtained from the experimental viscosity-temperature data, $\eta(T)$, are presented in Table 5.35. The effect of the alkyl chain length on the obtained VFT coefficients is presented in Fig. 5.45 together with the graphical representation of the linearized VFT equation (Eq. 2.45).

**Table 5.35.** Fitting coefficients used to describe the temperature dependence of viscosity of the studied [$^1C_n$py][$NTf_2$] homologue series.

| Ionic Liquid | $\frac{T_{interval}}{K}$ | $\frac{10^3 \cdot A_\eta}{Pa \cdot s}$ | $\frac{B_\eta}{K}$ | $\frac{C_\eta}{K}$ |
|---|---|---|---|---|
| [$^1C_3$py][$NTf_2$] | 318 – 373 | 0.2133 ± 0.0011 | 693.8 ± 1.7 | 172.3 ± 0.2 |
| [$^1C_4$py][$NTf_2$] | 293 – 373 | 0.1725 ± 0.0014 | 759.5 ± 2.3 | 168.5 ± 0.2 |
| [$^1C_5$py][$NTf_2$] | 293 – 373 | 0.1490 ± 0.0020 | 807.1 ± 3.8 | 168.0 ± 0.3 |
| [$^1C_6$py][$NTf_2$] | 293 – 373 | 0.1230 ± 0.0034 | 874.8 ± 8.2 | 164.4 ± 0.7 |
| [$^1C_7$py][$NTf_2$] | 293 – 373 | 0.1067 ± 0.0038 | 929 ± 11 | 162.2 ± 0.9 |
| [$^1C_8$py][$NTf_2$] | 293 – 373 | 0.1024 ± 0.0035 | 949 ± 11 | 162.6 ± 0.9 |
| [$^1C_9$py][$NTf_2$] | 293 – 373 | 0.0784 ± 0.0044 | 1047 ± 17 | 162.0 ± 1.3 |

The presented fitting coefficients were derived from the experimental $\eta(T)$ data (appendix) by applying the VFT fitting function, Eq. 2.44. The standard uncertainties related to the VFT coefficients were calculated to the confidence level of 0.95 ($k \approx 2$).

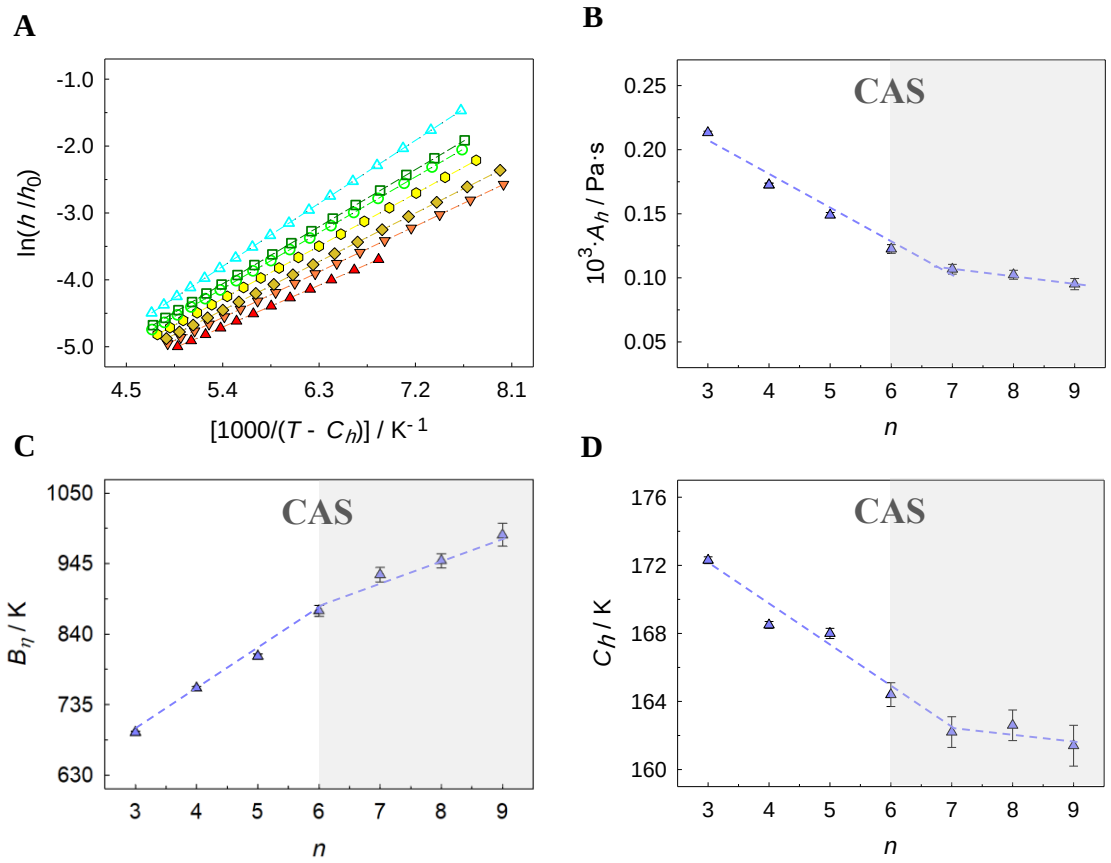



**Figure 5.56.** Impact of the alkyl chain length on the VFT coefficients for the viscosity of [$^1C_n$py][$NTf_2$] series. **A**: Linearized VFT representation $n$ = 3 ▲, 4 ▼, 5 ◆, 6 ⬢, 7 ○, 8 □, 9 △; **B**: Pre-exponential coefficient, $A_\eta$; **C**: energy barrier-related coefficient, $B_\eta$; **D**: Vogel temperature, $C_\eta$. $\eta_0$ = 1 Pa·s.

The viscosities at the reference temperature ($T$ = 298.15 K) are presented in Table 5.36, together with the energy barrier and strength parameter derived from Eq. 2.47 and Eq. 2.49 respectively. The temperature dependence of the viscosity-related energy

barrier, $E_\eta$, and the effect of the alkyl chain length on $E_\eta$ and the liquid fragility (strength parameter, $D_\eta$) are represented in Fig. 5.57.

**Table 5.36.** Viscosity and derived energy barrier of the studied [$^1C_n$py][$NTf_2$] homologue series at the reference temperature ($T$ = 298.15 K), together with the strength parameter.

| Ionic Liquid | $\eta(T=298.15\ K)$ / Pa·s | $E_\eta(T=298.15\ K)$ / kJ·mol$^{-1}$ | $D_\eta$ |
|---|---|---|---|
| [$^1C_3$py][$NTf_2$] | 0.05287 ± 0.00053 | 32.38 ± 0.13 | 4.027 ± 0.011 |
| [$^1C_4$py][$NTf_2$] | 0.06038 ± 0.00060 | 33.40 ± 0.14 | 4.507 ± 0.015 |
| [$^1C_5$py][$NTf_2$] | 0.07352 ± 0.00074 | 35.22 ± 0.23 | 4.804 ± 0.024 |
| [$^1C_6$py][$NTf_2$] | 0.08485 ± 0.00085 | 36.14 ± 0.51 | 5.321 ± 0.055 |
| [$^1C_7$py][$NTf_2$] | 0.09876 ± 0.00099 | 37.13 ± 0.65 | 5.725 ± 0.073 |
| [$^1C_8$py][$NTf_2$] | 0.1128 ± 0.0011 | 38.19 ± 0.66 | 5.839 ± 0.073 |
| [$^1C_9$py][$NTf_2$] | 0.1304 ± 0.0013 | 41.8 ± 1.1 | 6.46 ± 0.12 |

$\eta(T = 298.15\ K)$ and $E_\eta(T = 298.15\ K)$ were calculated from the fitting coefficients presented in Table 5.35 and by applying Eq. 2.44 and Eq. 2.47, respectively. The strength parameter was calculated by Eq. 2.49, $D_\eta = B_\eta/C_\eta$. The relative standard uncertainty associated with the viscosity measurements was estimated as $u(\eta)$ = 1.0% (Eq. 2.72); The standard uncertainty associated with the derived energy barrier, $u(E_\eta)$, and strength parameter, $u(D_\eta)$, was calculated by applying the propagation of uncertainty to Eq. 2.47 and Eq. 2.49, respectively.

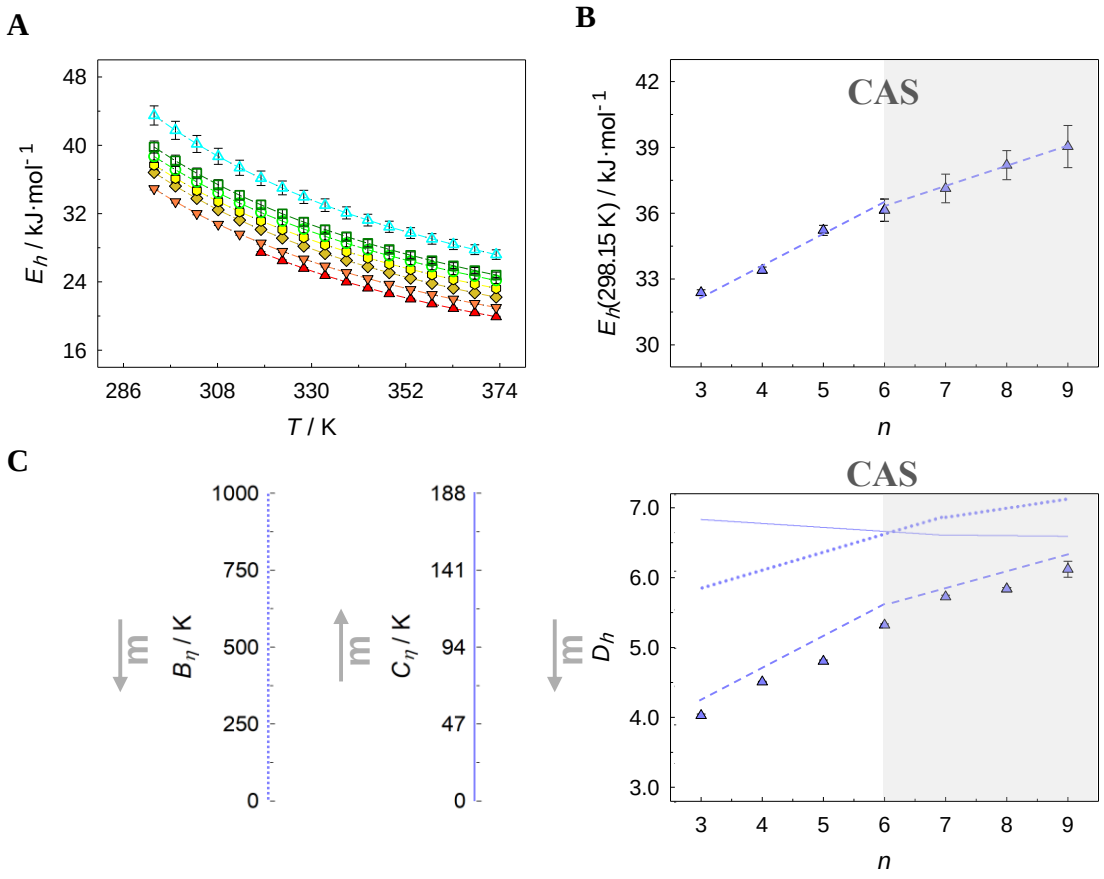



**Figure 5.57.** Graphical representation of the energy barrier and strength parameter derived from the experimental viscosity data of the [$^1C_n$py][$NTf_2$]. **A**: Temperature dependence of the derived energy barrier $n$ = 3 ▲, 4 ▼, 5 ◆, 6 ⬢, 7 ○, 8 □, 9 △; **B**: Effect of the alkyl chain length on the energy barrier; **C**: Effect of the alkyl chain length on the liquid fragility ($B_\eta$ and $C_\eta$ scales are included as guide lines).

The deviation of the available viscosity data to the experimental results of the [$^1C_n$py][$NTf_2$] series is presented in Fig. 5.58. As can be observed, some data show a clear temperature dependency [123, 124]. The data reported by Oliveira *et al.* (*n* = 4) [125], Yunus *et al.* (*n* = 4) [126], Nazet *et al*. (*n* = 4) [111], Wang *et al.* (*n* = 4) [127], Jin *et al.* (*n* = 8) [23] are in excellent agreement with the results obtained in this work (deviation <2%).

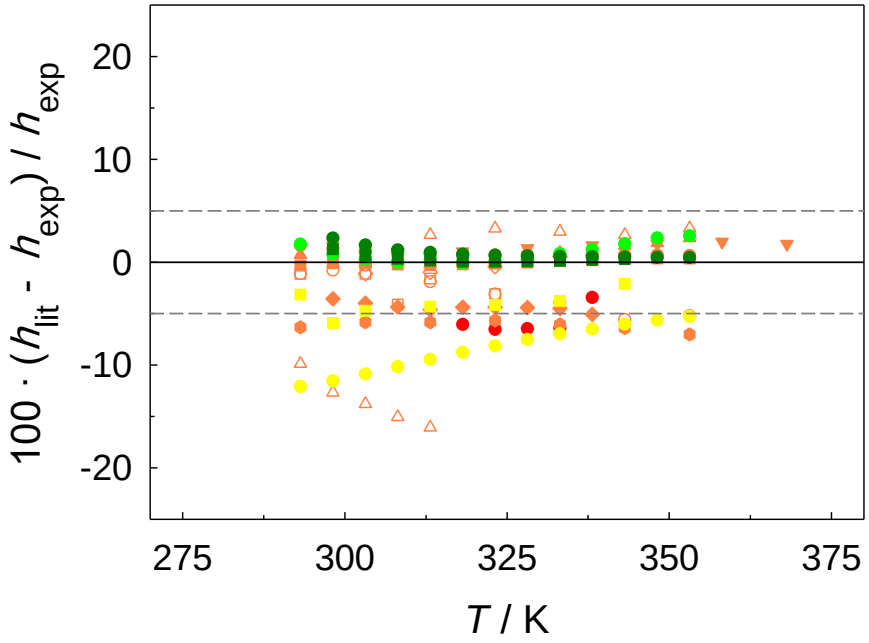



**Figure 5.58.** Deviation of the available viscosity data to the experimental results the [$^1C_n$py][$NTf_2$]. ***n* = 3:** ● [128]; ***n* = 4:** ● [125], ■ [126], ▲ [129], ▼ [130], ◆ [131], ⬢ [11], ○ [132], □ [133], △ [123], ▽ [134], ◇ [127]; ***n* = 6:** ● [124], ■ [135]; ***n* = 7:** ● [129]; ***n* = 8:** ● [125], ■ [126].

### 5.1.6.3. Electrical Conductivity

The resistance and reactance spectra obtained for the [$^1C_n$py][$NTf_2$] ionic liquids through the ILDEM experiments are presented in Fig. 5.59.

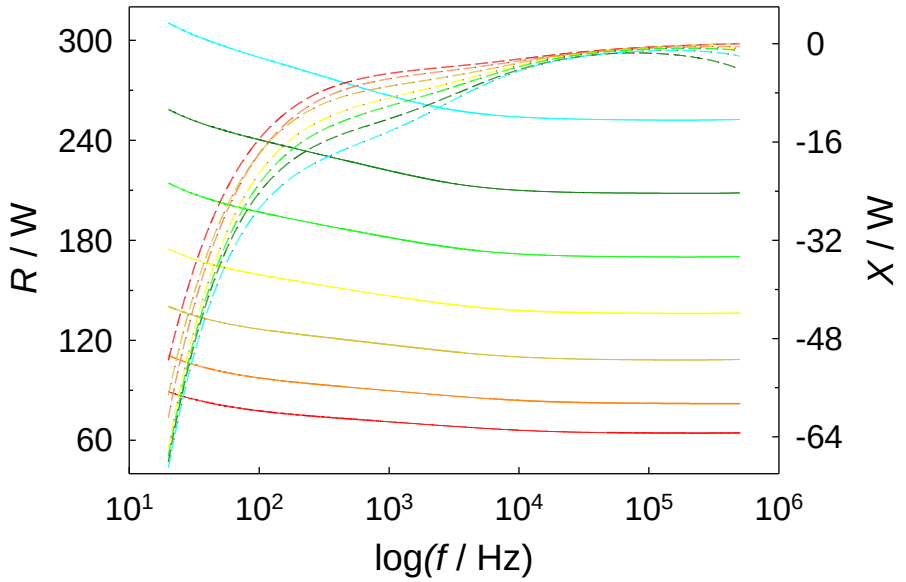



**Figure 5.59.** Typical resistance (straight line) and reactance (dashed line) spectra for the [$^1$C$_n$py][NTf$_2$] ionic liquids. **3**, **4**, **5**, **6**, **7**, **8**, **9**.

The VFT coefficients (Eq 2.24) obtained from the experimental electrical conductivity-temperature data, $\sigma(T)$, are presented in Table 5.37.

**Table 5.37.** Fitting coefficients used to describe the temperature dependence of electrical conductivity of the studied [$^1$C$_n$py][NTf$_2$] homologue series.

| Ionic Liquid | $\frac{A_\sigma}{S \cdot m^{-1}}$ | $\frac{B_\sigma}{K}$ | $\frac{C_\sigma}{K}$ | $\frac{\sigma(T=298.15\ K)}{S \cdot m^{-1}}$ |
|---|---|---|---|---|
| [$^1$C$_3$py][NTf$_2$] | 53.50 ± 0.68 | 554.4 ± 3.5 | 182.3 ± 0.4 | 0.4467 ± 0.0067 |
| [$^1$C$_4$py][NTf$_2$] | 55.53 ± 0.28 | 607.8 ± 1.4 | 179.6 ± 0.1 | 0.3295 ± 0.0049 |
| [$^1$C$_5$py][NTf$_2$] | 55.84 ± 0.60 | 651.8 ± 2.9 | 179.3 ± 0.3 | 0.2318 ± 0.0035 |
| [$^1$C$_6$py][NTf$_2$] | 55.50 ± 0.55 | 690.8 ± 2.7 | 178.4 ± 0.3 | 0.1734 ± 0.0026 |
| [$^1$C$_7$py][NTf$_2$] | 56.30 ± 0.79 | 735.0 ± 3.9 | 176.8 ± 0.4 | 0.1320 ± 0.0020 |
| [$^1$C$_8$py][NTf$_2$] | 57.77 ± 0.62 | 777.4 ± 3.0 | 175.4 ± 0.3 | 0.1026 ± 0.0015 |
| [$^1$C$_9$py][NTf$_2$] | 55.0 ± 1.3 | 798.4 ± 6.6 | 175.7 ± 0.6 | 0.08108 ± 0.0012 |

The presented fitting coefficients were derived from the experimental $\sigma(T)$ data (appendix) by applying the VFT fitting function, Eq. 2.44. The standard uncertainties related to the VFT coefficients were calculated to the confidence level of 0.95 ($k \approx 2$). The relative standard uncertainty associated with the viscosity measurements was estimated as $u(\sigma)$ = 1.5% (Eq. 4.15).

The deviation of the available electrical conductivity data to the experimental results of the [$^1$C$_n$py][NTf$_2$] series is presented in Fig. 5.60.

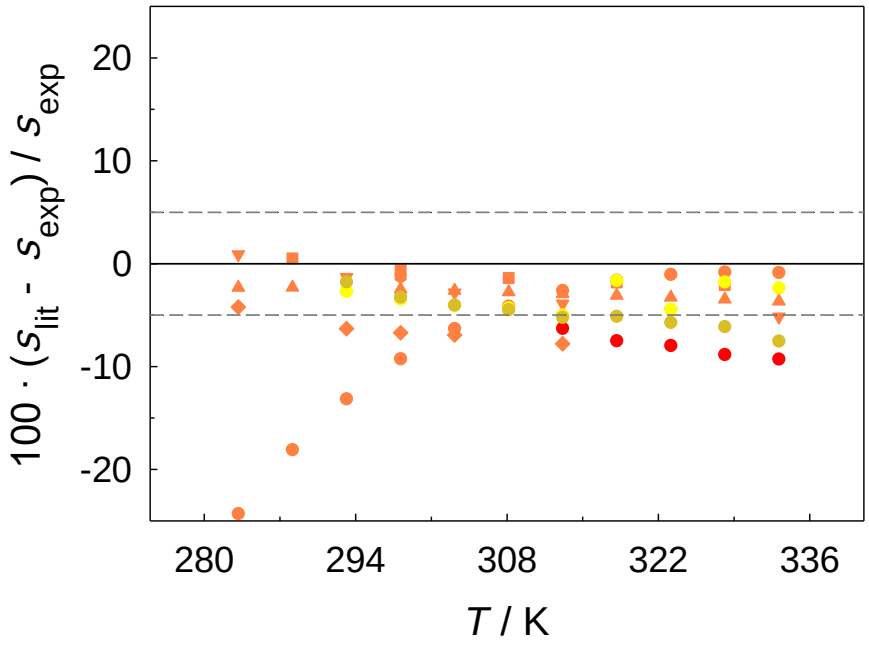



**Figure 5.60.** Deviation of the available electrical conductivity data to the experimental results for the [$^1$C$_n$py][NTf$_2$]. ***n* = 3:** ● [128]**;** ***n* = 4:** ● [136], ■ [130], ▲ [131], ▼[132], ◆[137], ⬢ [108]; ***n* = 5:** ● [131]; ***n* = 6:** ● [128].

Overall, the results are in relatively good agreement with the literature apart from the data reported by Reinado *et al.* [136] for [$^1$C$_4$py][NTf$_2$], which presents a strong temperature dependency and lower conductivity values that might be associated with polarization effects. No data was found for $n$ = 7 – 9.

#### 5.1.6.4. Molar Conductivity

The molar conductivity of the [$^1$C$_n$py][NTf$_2$] ILs was calculated from the experimentally measured electrical conductivity and density data of the ILs. The molar conductivity is presented as a function of temperature and the number of carbons of the cation's alkyl chain in Fig. 5.61.

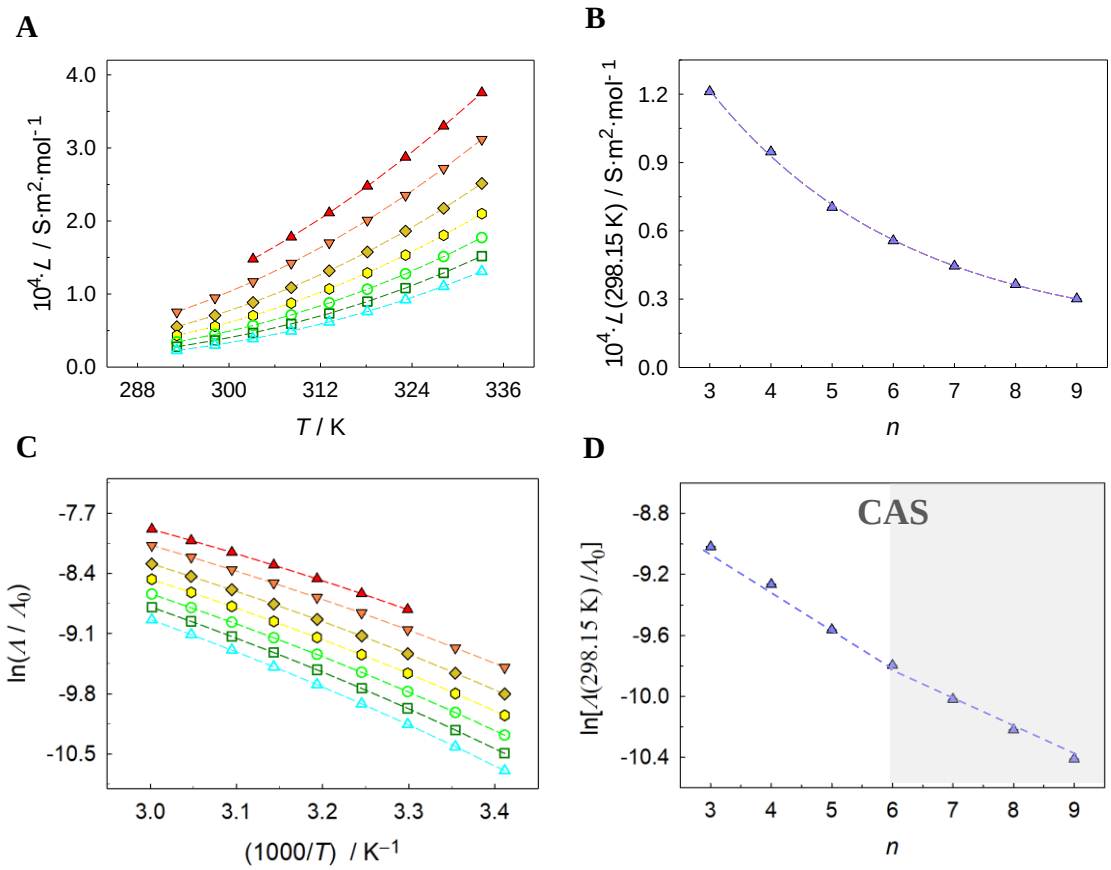



**Figure 5.61.** Molar conductivity of the [$^1$C$_n$py][NTf$_2$] series as a function of temperature (A, C) and number of carbons on the alkyl chain of the cation (B, D). **A**: Temperature dependence of molar conductivity; **B**: Dependence of molar conductivity with the alkyl chain length; **C**: Temperature dependence of molar conductivity (Arrhenius representation); **D**: Dependence of molar conductivity with the alkyl chain length (logarithmic form). $n$ = 3 ▲, 4 ▼, 5 ◆, 6 ●, 7 ○, 8 □, 9 △. $\Lambda_0$ = 1 S·m$^2$·mol$^{-1}$

The VFT coefficients (Eq 2.44) obtained from the experimental molar conductivity-temperature data, $\Lambda(T)$, are presented in Table 5.38. The effect of the alkyl chain length on the obtained VFT coefficients is presented in Fig. 5.62, together with the graphical representation of the linearized VFT equation (Eq. 2.45).

**Table 5.38.** Fitting coefficients used to describe the temperature dependence of molar conductivity of the studied [$^1C_n$py][NTf$_2$] homologue series.

| Ionic Liquid | $\frac{T_{interval}}{K}$ | $\frac{10^4 \cdot A_\Lambda}{S \cdot m^2 \cdot mol^{-1}}$ | $\frac{B_\Lambda}{K}$ | $\frac{C_\Lambda}{K}$ |
|---|---|---|---|---|
| [$^1C_3$py][NTf$_2$] | 303 – 333 | 175.8 ± 2.7 | 591.1 ± 4.3 | 179.4 ± 0.5 |
| [$^1C_4$py][NTf$_2$] | 293 – 333 | 191.9 ± 0.6 | 643.0 ± 0.8 | 177.1 ± 0.1 |
| [$^1C_5$py][NTf$_2$] | 293 – 333 | 204.5 ± 2.6 | 686.7 ± 3.5 | 177.1 ± 0.4 |
| [$^1C_6$py][NTf$_2$] | 293 – 333 | 214.3 ± 1.9 | 726.1 ± 2.5 | 176.2 ± 0.2 |
| [$^1C_7$py][NTf$_2$] | 293 – 333 | 228.9 ± 4.2 | 770.7 ± 5.2 | 174.7 ± 0.5 |
| [$^1C_8$py][NTf$_2$] | 293 – 333 | 248.2 ± 2.9 | 815.2 ± 3.4 | 173.2 ± 0.3 |
| [$^1C_9$py][NTf$_2$] | 293 – 333 | 246.3 ± 6.3 | 834.7 ± 7.4 | 173.7 ± 0.6 |

The presented fitting coefficients were derived from the experimental $\Lambda(T)$ data (appendix) by applying the VFT fitting function, Eq. 2.44. The standard uncertainties related to the VFT coefficients were calculated to the confidence level of 0.95 ($k \approx 2$).

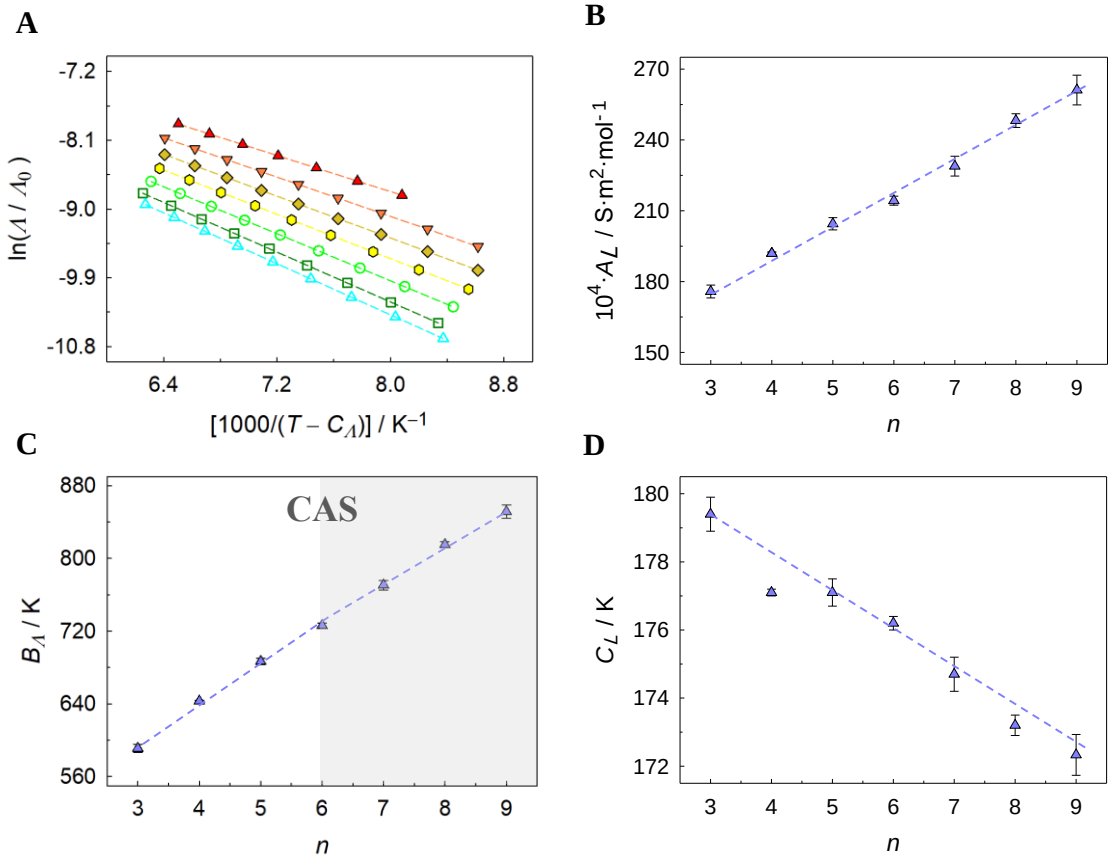



**Figure 5.62.** Impact of the alkyl chain length on the VFT coefficients for the molar conductivity of [$^1C_n$py][NTf$_2$] ILs. **A**: Linearized VFT representation $n$ = 3 ▲, 4 ▼, 5 ◆, 6 ●, 7 ○, 8 □, 9 △. **B**: Pre-exponential coefficient, $A_\Lambda$; **C**: energy barrier-related coefficient, $B_\Lambda$; **D**: Vogel temperature, $C_\Lambda$. $\Lambda_0$ = 1 S·m$^2$·mol$^{-1}$.

The molar conductivities at the reference temperature ($T$ = 298.15 K) are presented in Table 5.39, together with the energy barrier and strength parameter derived from Eq. 2.47 and Eq. 2.49, respectively. The temperature dependence of the

conductivity-related energy barrier, $E_\Lambda$, and the effect of the alkyl chain length on $E_\Lambda$ and on the liquid fragility (strength parameter, $D_\Lambda$) are represented in Fig. 5.63.

**Table 5.39.** Molar conductivity and derived energy barrier of the studied [$^1C_n$py][$NTf_2$] homologue series at the reference temperature ($T$ = 298.15 K), together with the strength parameter.

| Ionic Liquid | $10^4 \cdot \Lambda(T{=}298.15\ \mathrm{K})$ / S · m² · mol$^{-1}$ | $E_\Lambda(T{=}298.15\ \mathrm{K})$ / kJ · mol$^{-1}$ | $D_\Lambda$ |
|---|---|---|---|
| [$^1C_3$py][$NTf_2$] | 1.211 ± 0.018 | 30.98 ± 0.34 | 3.295 ± 0.026 |
| [$^1C_4$py][$NTf_2$] | 0.947 ± 0.014 | 32.43 ± 0.07 | 3.631 ± 0.005 |
| [$^1C_5$py][$NTf_2$] | 0.703 ± 0.011 | 34.64 ± 0.29 | 3.877 ± 0.022 |
| [$^1C_6$py][$NTf_2$] | 0.5562 ± 0.0083 | 36.09 ± 0.17 | 4.121 ± 0.015 |
| [$^1C_7$py][$NTf_2$] | 0.4450 ± 0.0067 | 37.38 ± 0.39 | 4.412 ± 0.032 |
| [$^1C_8$py][$NTf_2$] | 0.3642 ± 0.0055 | 38.59 ± 0.25 | 4.707 ± 0.021 |
| [$^1C_9$py][$NTf_2$] | 0.3010 ± 0.0045 | 39.83 ± 0.52 | 4.805 ± 0.046 |

$\Lambda(T = 298.15\ \mathrm{K})$ and $E_\Lambda(T = 298.15\ \mathrm{K})$ were calculated from the fitting coefficients presented in Table 5.38 and by applying Eq. 2.44 and Eq. 2.47, respectively. The strength parameter was calculated by Eq. 2.49, $D_\Lambda = B_\Lambda / C_\Lambda$. The relative standard uncertainty associated with the viscosity measurements was estimated as $u(\Lambda)$ = 1.5% (Eq. 4.15); The standard uncertainty associated with the derived energy barrier, $u(E_\Lambda)$, and strength parameter, $u(D_\Lambda)$, was calculated by applying the propagation of uncertainty to Eq. 2.47 and Eq. 2.49, respectively.

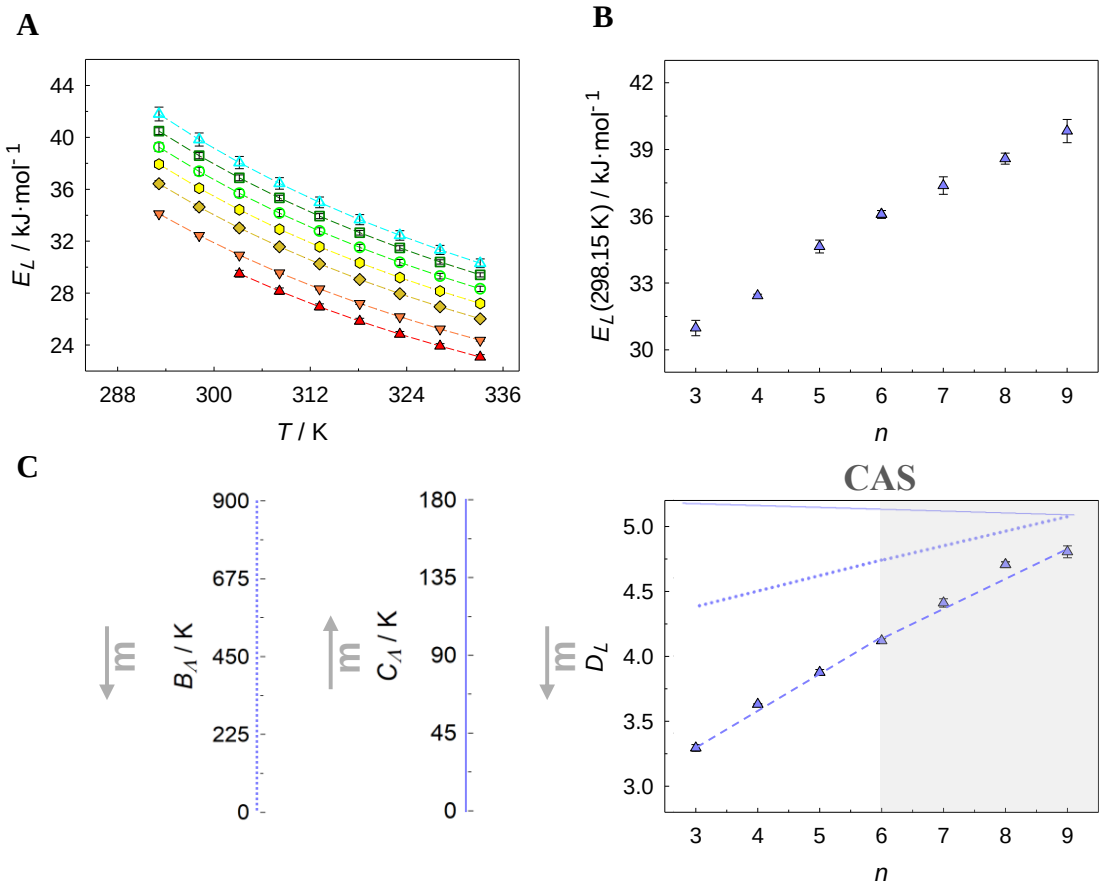



**Figure 5.63.** Graphical representation of the energy barrier and strength parameter derived from the experimental molar conductivity data of the [$^1C_n$py][$NTf_2$] ILs. **A**: Temperature dependence of the derived energy barrier $n$ = 3 ▲, 4 ▼, 5 ◆, 6 ⬢, 7 ○, 8 □, 9 △; **B**: Effect of the alkyl chain length on the energy barrier; **C**: Effect of the alkyl chain length on the liquid fragility ($B_\Lambda$ and $C_\Lambda$ scales are included as guide lines).

### 5.1.7. $[^1C_n C_1pyr][NTf_2]$ Series

In this work, the density, viscosity, and electrical conductivity of the 1-alkyl-1-methylpyrrolidinium bis(trifluoromethylsulfonyl)imide series, $[^1C_n{}^1C_1pyr][NTf_2]$ $n$ = 3, 4, 6, 8 (Fig. 5.64) were measured for different temperatures.

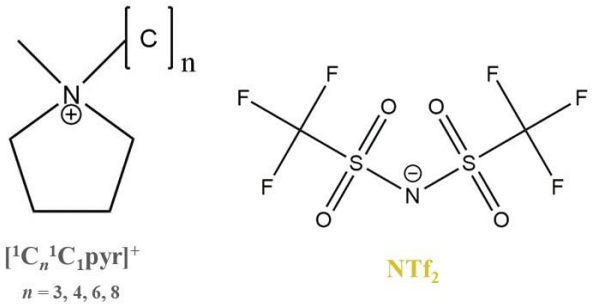



**Figure 5.64.** Structure of the studied $[^1C_n{}^1C_1pyr][NTf_2]$ ($n$ = 3, 4, 6, 8) ionic liquids.

#### 5.1.7.1. Density

The resulting fitting coefficients from the temperature dependence of density of the $[^1C_n{}^1C_1pyr][NTf_2]$ ILs (Eq. 2.4) are presented in Table 5.40. The densities at the reference temperature ($T$ = 298.15 K) are presented in Table 5.41, together with the molar volume and thermal expansion coefficient derived from Eq. 2.2 and Eq. 2.7 respectively. The graphical representation of density, thermal expansion coefficient, and molar volume as functions of temperature and number of carbons on the cations alkyl chain are presented in Fig 5.65.

**Table 5.40.** Fitting coefficients used to describe the temperature dependence of density of the studied $[^1C_n{}^1C_1pyr][NTf_2]$ homologue series.

| Ionic Liquid | $\frac{T_{\text{interval}}}{\text{K}}$ | $\frac{10^7 \cdot a_2}{\text{K}^{-2}}$ | $\frac{10^4 \cdot b_1}{\text{K}^{-1}}$ | $\frac{c_0}{\text{K}}$ |
|---|---|---|---|---|
| $[^1C_3{}^1C_1pyr][NTf_2]$ | 283 – 373 | 0.358 ± 0.063 | −6.518 ± 0.041 | 7.4552 ± 0.0007 |
| $[^1C_4{}^1C_1pyr][NTf_2]$ | 283 – 373 | 0.182 ± 0.056 | −6.433 ± 0.036 | 7.4301 ± 0.0006 |
| $[^1C_6{}^1C_1pyr][NTf_2]$ | 283 – 373 | 0.009 ± 0.051 | −6.348 ± 0.033 | 7.3869 ± 0.0005 |
| $[^1C_8{}^1C_1pyr][NTf_2]$ | 283 – 373 | −0.203 ± 0.060 | −6.246 ± 0.039 | 7.3501 ± 0.0006 |

The presented fitting coefficients were derived from the experimental $\rho(T)$ data (appendix) by applying a polynomial fitting function, $\ln[\rho(T)] = a_2T^2 + a_1T + a_0$ (Eq. 2.4). The standard uncertainties related to the fitting coefficients were calculated to the confidence level of 0.95 ($k \approx 2$).

**Table 5.41** Density, thermal expansion coefficient, and molar volume at the reference temperature ($T$ = 298.15 K) for the studied [$^1C_n{}^1C_1$pyr][$NTf_2$] homologue series.

| Ionic Liquid | $\rho$(298.15 K) / kg·m$^{-3}$ | $10^3 \cdot \alpha_p$(298.15 K) / K$^{-1}$ | $10^6 \cdot V_m$(298.15 K) / m$^3$·mol$^{-1}$ |
|---|---|---|---|
| [$^1C_3{}^1C_1$pyr][$NTf_2$] | 1428.0 ± 0.5 | 6.30 ± 0.04 | 286.0 ± 0.8 |
| [$^1C_4{}^1C_1$pyr][$NTf_2$] | 1394.0 ± 0.5 | 6.32 ± 0.04 | 303.0 ± 0.8 |
| [$^1C_6{}^1C_1$pyr][$NTf_2$] | 1336.4 ± 0.5 | 6.34 ± 0.03 | 337.1 ± 0.9 |
| [$^1C_8{}^1C_1$pyr][$NTf_2$] | 1289.6 ± 0.5 | 6.37 ± 0.04 | 373.4 ± 1.0 |

$\rho$($T$ = 298.15 K) and $\alpha_p$($T$ = 298.15 K) were calculated from the fitting coefficients presented in Table 5.40 and by applying Eq. 2.4 and Eq. 2.7 respectively. $V_m$(298.15 K)= $M/\rho$(298.15 K). The standard uncertainty associated with $\alpha_p$ and $V_m$ were calculated by applying the propagation of uncertainty to Eq. 2.7 and 2.2, respectively.

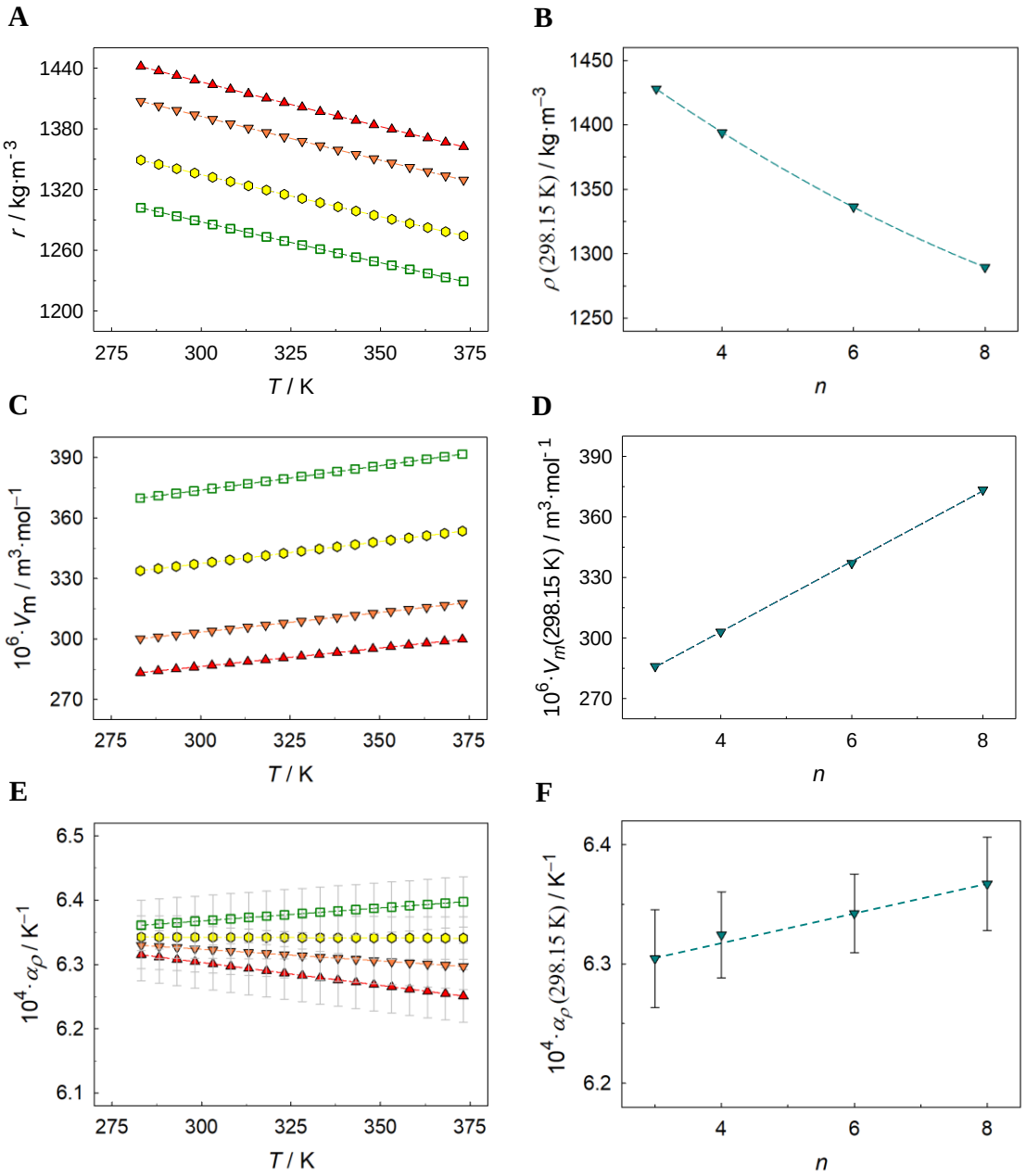



**Figure 5.65.** Density and derived properties of the [$^1C_n{}^1C_1$pyr][$NTf_2$] ILs as a function of temperature (A, C, E) and number of carbons on the alkyl chain of the cation (B, D, F). **A**, **B**: Density; **C**, **D**: Molar volume; **E**, **F**: Thermal expansion coefficient. $n$ = 3 ▲, 4 ▼, 6 ⬢, 8 □.

### 5.1.7.2. Viscosity

The obtained viscosity data for the $[^1C_n{}^1C_1pyr][NTf_2]$ ILs is presented as a function of temperature and the number of carbons of the cation's alkyl chain in Fig. 5.66.

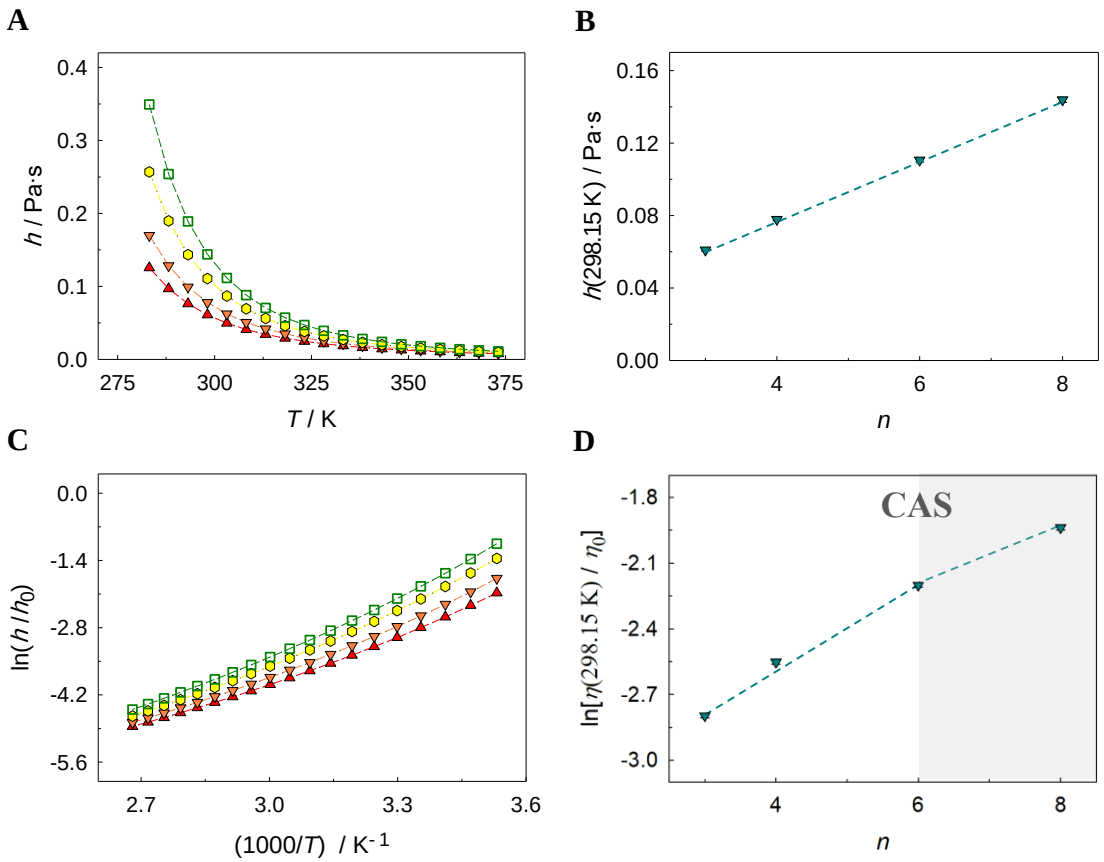



**Figure 5.66.** Viscosity of the $[^1C_n{}^1C_1pyr][NTf_2]$ series as a function of temperature (A, C) and number of carbons on the alkyl chain of the cation (B, D). **A**: Temperature dependence of viscosity; **B**: Dependence of viscosity with the alkyl chain length; **C**: Temperature dependence of viscosity (Arrhenius representation); **D**: Dependence of viscosity with the alkyl chain length (logarithmic form). $n$ = 3 ▲, 4 ▼, 6 ⬢, 8. $\eta_0$ = 1 Pa·s.

The VFT coefficients (Eq 2.44) obtained from the experimental viscosity-temperature data, $\eta(T)$, are presented in Table 5.42. The effect of the alkyl chain length on the obtained VFT coefficients is presented in Fig. 5.67 together with the graphical representation of the linearized VFT equation (Eq. 2.45).

**Table 5.42.** Fitting coefficients used to describe the temperature dependence of viscosity of the studied [$^1C_n{}^1C_1$pyr][$NTf_2$] homologue series.

| Ionic Liquid | $\frac{T_{interval}}{K}$ | $\frac{10^3 \cdot A_\eta}{Pa \cdot s}$ | $\frac{B_\eta}{K}$ | $\frac{C_\eta}{K}$ |
|---|---|---|---|---|
| [$^1C_3{}^1C_1$pyr][$NTf_2$] | 283 – 373 | 0.1906 ± 0.0012 | 778.4 ± 1.8 | 163.2 ± 0.2 |
| [$^1C_4{}^1C_1$pyr][$NTf_2$] | 283 – 373 | 0.1561 ± 0.0011 | 835.9 ± 1.7 | 163.6 ± 0.1 |
| [$^1C_6{}^1C_1$pyr][$NTf_2$] | 283 – 373 | 0.1052 ± 0.0030 | 966.1 ± 7.7 | 159.3 ± 0.5 |
| [$^1C_8{}^1C_1$pyr][$NTf_2$] | 283 – 373 | 0.0961 ± 0.0014 | 1014 ± 4.2 | 159.5 ± 0.3 |

The presented fitting coefficients were derived from the experimental $\eta(T)$ data (appendix) by applying the VFT fitting function, Eq. 2.44. The standard uncertainties related to the VFT coefficients were calculated to the confidence level of 0.95 ($k \approx 2$).

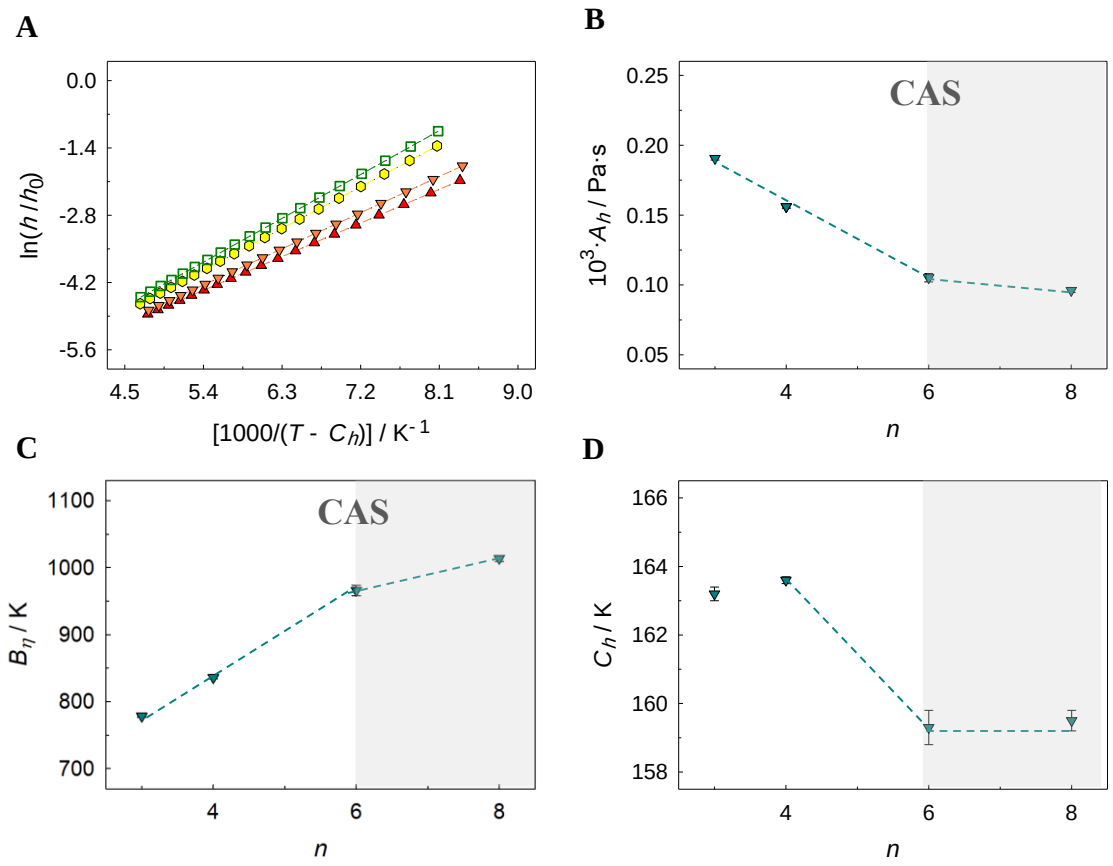



**Figure 5.67.** Impact of the alkyl chain length on the VFT coefficients for the viscosity of [$^1C_n{}^1C_1$pyr][$NTf_2$] series. **A**: Linearized VFT representation $n$ = 3 ▲, 4 ▼, 6 ●, 8 □; **B**: Pre-exponential coefficient, $A_\eta$; **C**: energy barrier-related coefficient, $B_\eta$; **D**: Vogel temperature, $C_\eta$. $\eta_0$ = 1 Pa·s.

The viscosities at the reference temperature ($T$ = 298.15 K) are presented in Table 5.43, together with the energy barrier and strength parameter derived from Eq. 2.47 and Eq. 2.49 respectively. The temperature dependence of the viscosity-related energy

barrier, $E_\eta$, and the effect of the alkyl chain length on $E_\eta$ and on the liquid fragility (strength parameter, $D_\eta$) are represented in Fig. 5.68.

**Table 5.43.** Viscosity and derived energy barrier of the studied [$^1C_n{}^1C_1$pyr][$NTf_2$] homologue series at the reference temperature ($T$ = 298.15 K), together with the strength parameter.

| Ionic Liquid | $\eta(T=298.15\ K)$ / Pa · s | $E_\eta(T=298.15\ K)$ / kJ · mol$^{-1}$ | $D_\eta$ |
|---|---|---|---|
| [$^1C_3{}^1C_1$pyr][$NTf_2$] | 0.06098 ± 0.00061 | 31.59 ± 0.12 | 4.770 ± 0.012 |
| [$^1C_4{}^1C_1$pyr][$NTf_2$] | 0.07789 ± 0.00078 | 34.13 ± 0.09 | 5.109 ± 0.011 |
| [$^1C_6{}^1C_1$pyr][$NTf_2$] | 0.1106 ± 0.0011 | 37.04 ± 0.40 | 6.065 ± 0.052 |
| [$^1C_8{}^1C_1$pyr][$NTf_2$] | 0.1439 ± 0.0014 | 38.97 ± 0.23 | 6.355 ± 0.029 |

$\eta(T = 298.15\ K)$ and $E_\eta(T = 298.15\ K)$ were calculated from the fitting coefficients presented in Table 5.422 and by applying Eq. 2.44 and Eq. 2.47, respectively. The strength parameter was calculated by Eq. 2.49, $D_\eta = B_\eta / C_\eta$. The relative standard uncertainty associated with the viscosity measurements was estimated as $u(\eta)$ = 1.0% (Eq. 2.72); The standard uncertainty associated with the derived energy barrier, $u(E_\eta)$, and strength parameter, $u(D_\eta)$, was calculated by applying the propagation of uncertainty to Eq. 2.47 and Eq. 2.49, respectively.

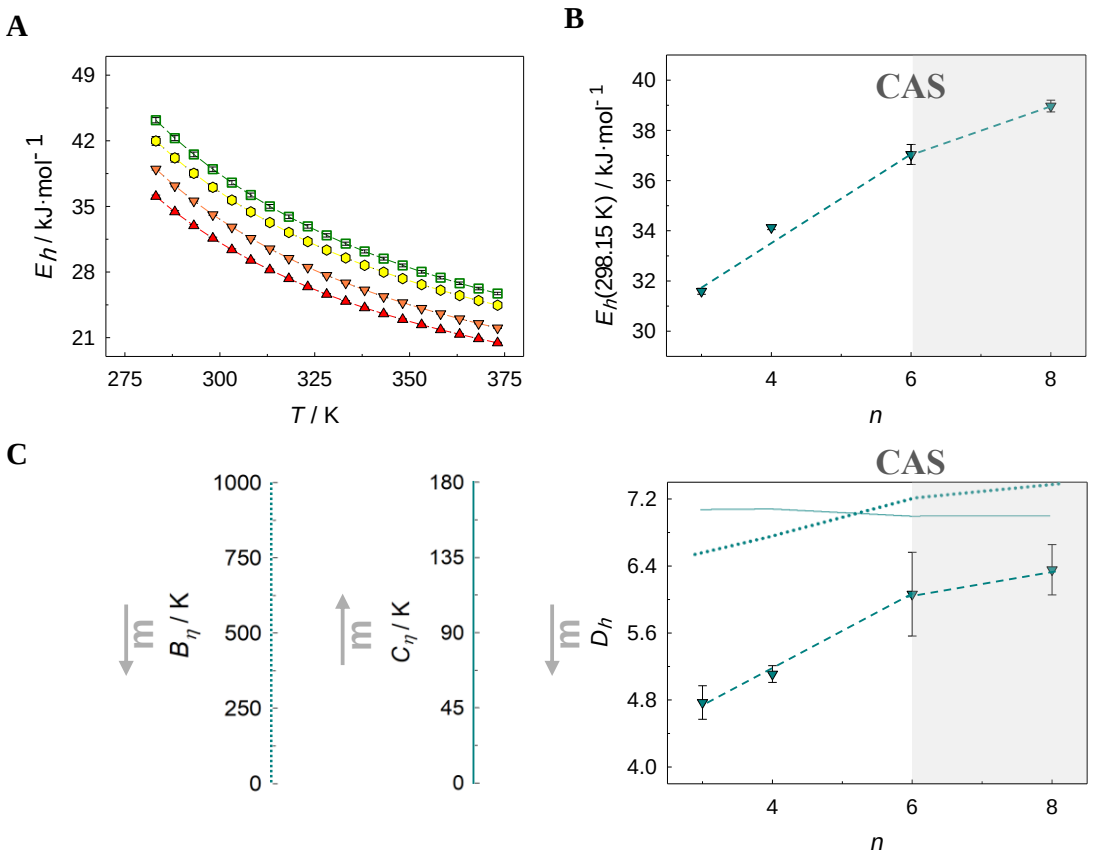



**Figure 5.68.** Graphical representation of the energy barrier and strength parameter derived from the experimental viscosity data of the [$^1C_n{}^1C_1$pyr][$NTf_2$] ionic liquids. **A**: Temperature dependence of the derived energy barrier $n$ = 3 ▲, 4 ▼, 6 ⬢, 8 □; **B**: Effect of the alkyl chain length on the energy barrier; **C**: Effect of the alkyl chain length on the liquid fragility ($B_\eta$ and $C_\eta$ scales are included as guide lines).

The deviation of the available viscosity data to the experimental results for the $[^1C_n{}^1C_1pyr][NTf_2]$ with the available literature is presented in Fig. 5.69. Several literature sources were found for the studied ILs, particularly for $[^1C_4{}^1C_1pyr][NTf_2]$. Overall, most of the data is within ± 5% relative to the experimental results. Still, there is a large amount of data with lower values, which might be due to the presence of water. Additionally, some cases show a clear temperature dependency [124, 138].

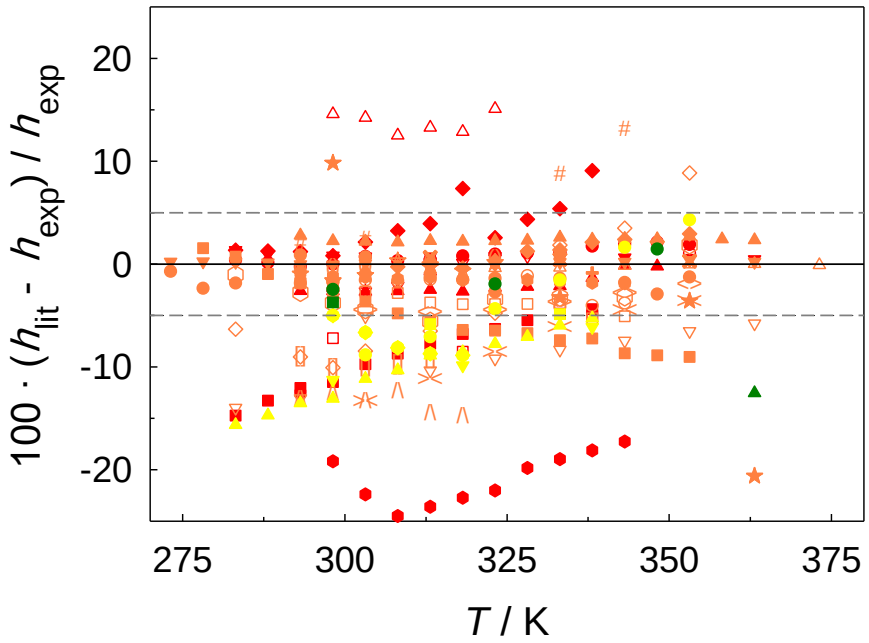



**Figure 5.69.** Deviation of the available viscosity data to the experimental results for the $[^1C_n{}^1C_1pyr][NTf_2]$ series. ***n* = 3** ● [124], ■ [23], ▲ [139], ▼ [140], ◆ [9], ⬢ [141], ○ [102], □ [142], △ [143], ▽ [144]; ***n* = 4** ● [145], ■ [146], ▲ [147], ▼ [145], ◆ [107], ⬢ [148], ○ [149], □ [80], △ [150], ▽ [12], ◇ [151], ⬡ [132], ★ [152], ☆ [153], >< [138], # [154], () [155], <> [156], /\ [134], [] [102], ✖ [142]; ***n* = 6** ● [138], ■ [102], ▲ [23], ▼ [142], ◆ [134]. ***n* = 8** ●[157], ■ [109], ▲ [158].

### 5.1.7.3. Electrical Conductivity

The resistance and reactance spectra obtained for the $[^1C_n{}^1C_1pyr][NTf_2]$ ionic liquids through the ILDEM experiments are presented in Fig. 5.70.

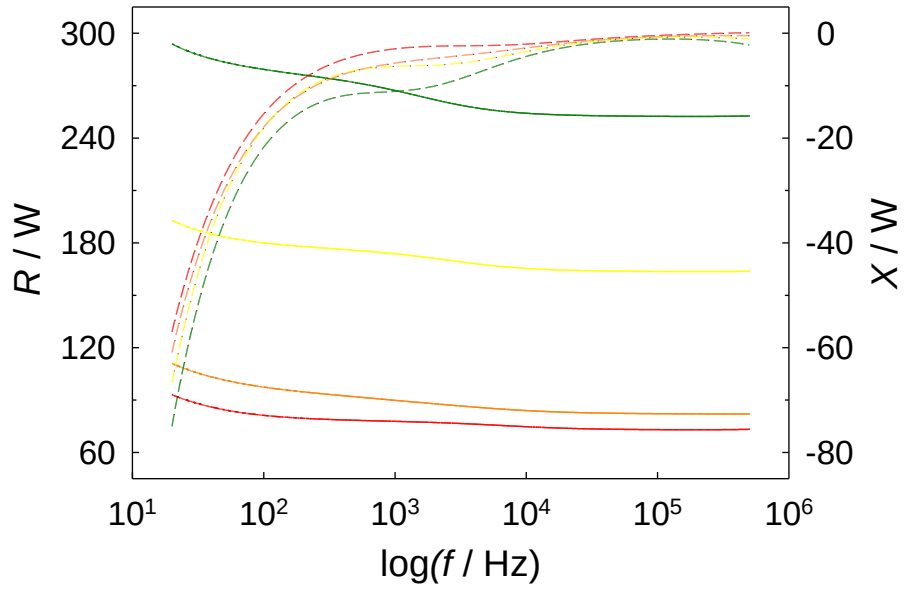



**Figure 5.70.** Typical resistance (straight line) and reactance (dashed line) spectra for the [$^1C_n{}^1C_1$pyr][$NTf_2$] ionic liquids. $n$ = **3**, **4**, **6**, **8**.

The VFT coefficients (Eq 2.24) obtained from the experimental electrical conductivity-temperature data, $\sigma(T)$, are presented in Table 5.44.

**Table 5.44.** Fitting coefficients used to describe the temperature dependence of electrical conductivity of the studied [$^1C_n{}^1C_1$pyr][$NTf_2$] homologue series.

| Ionic Liquid | $\frac{A_\sigma}{S \cdot m^{-1}}$ | $\frac{B_\sigma}{K}$ | $\frac{C_\sigma}{K}$ | $\frac{\sigma(T=298.15\ K)}{S \cdot m^{-1}}$ |
|---|---|---|---|---|
| [$^1C_3{}^1C_1$pyr][$NTf_2$] | 57.4 ± 1.7 | 615.3 ± 8.0 | 173.8 ± 0.9 | 0.4073 ± 0.0061 |
| [$^1C_4{}^1C_1$pyr][$NTf_2$] | 57.86 ± 0.28 | 658.0 ± 1.3 | 174.7 ± 0.1 | 0.2803 ± 0.0042 |
| [$^1C_6{}^1C_1$pyr][$NTf_2$] | 61.66 ± 0.66 | 763.0 ± 3.0 | 172.1 ± 0.3 | 0.1449 ± 0.0022 |
| [$^1C_8{}^1C_1$pyr][$NTf_2$] | 65.6 ± 1.6 | 861.7 ± 7.0 | 168.5 ± 0.6 | 0.08516 ± 0.0013 |

The presented fitting coefficients were derived from the experimental $\sigma(T)$ data (appendix) by applying the VFT fitting function, Eq. 2.44. The standard uncertainties related to the VFT coefficients were calculated to the confidence level of 0.95 ($k \approx 2$). The relative standard uncertainty associated with the viscosity measurements was estimated as $u(\sigma)$ = 1.5% (Eq. 4.15).

The deviation of the available electrical conductivity data to the experimental results for the [$^1C_n{}^1C_1$pyr][$NTf_2$] with the available literature is presented in Fig. 5.71.

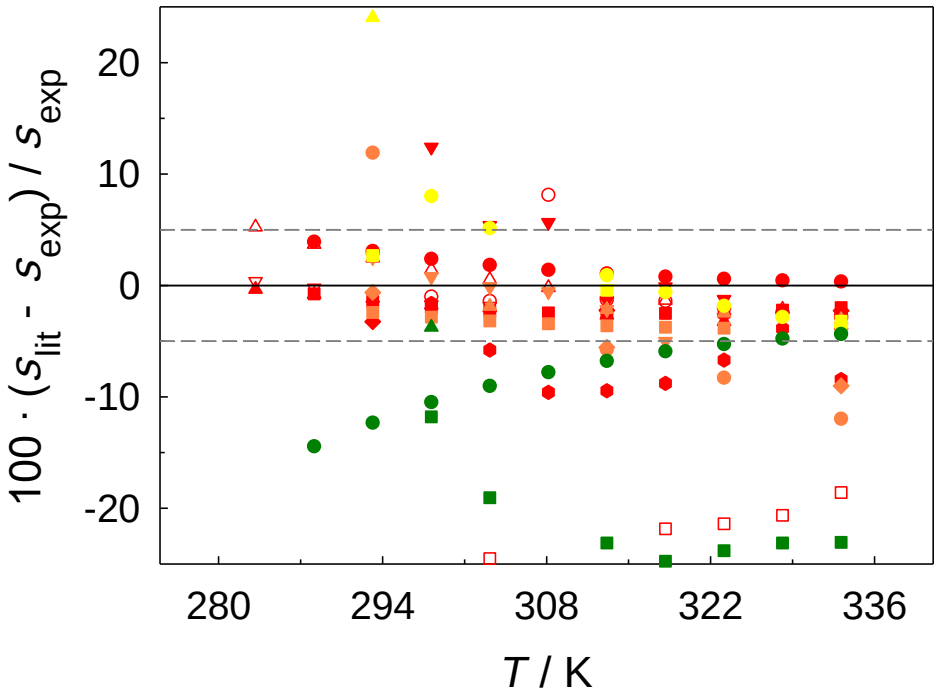



**Figure 5.71.** Deviation of the available electrical conductivity data to the experimental results for the [$^1C_nC_1$pyr][$NTf_2$] series. ***n* = 3:** ● [158], ■ [139], ▲ [140], ▼ [143], ◆ [102], ⬢ [157]; ***n* = 4:** ● [107], ■ [158], ▲ [159], ▼ [145], ◆ [160], ⬢ [155], ○ [161], □ [156], △ [102]; ***n* = 6:** ● [158], ■ [102], ▲ [23]; ***n* = 8:** ● [158], ■ [157], ▲ [109].

While there is some discrepancy between the available data, most of it is within ± 5% compared to the experimental results. The data for n = 3 and 4 are in excellent agreement with the present results overall. While there is not a large amount of coherent data for *n* = 8 (single temperature point [109] and strong temperature dependency [158]), the experimental results were found to fit well with the remaining ILs of the series.

#### 5.1.7.4. Molar Conductivity

The molar conductivity of the [$^1C_n{}^1C_1$pyr][$NTf_2$] ILs was calculated from the experimentally measured electrical conductivity and density data of the ILs. The molar conductivity is presented as a function of temperature and the number of carbons of the cation's alkyl chain in Fig. 5.72.

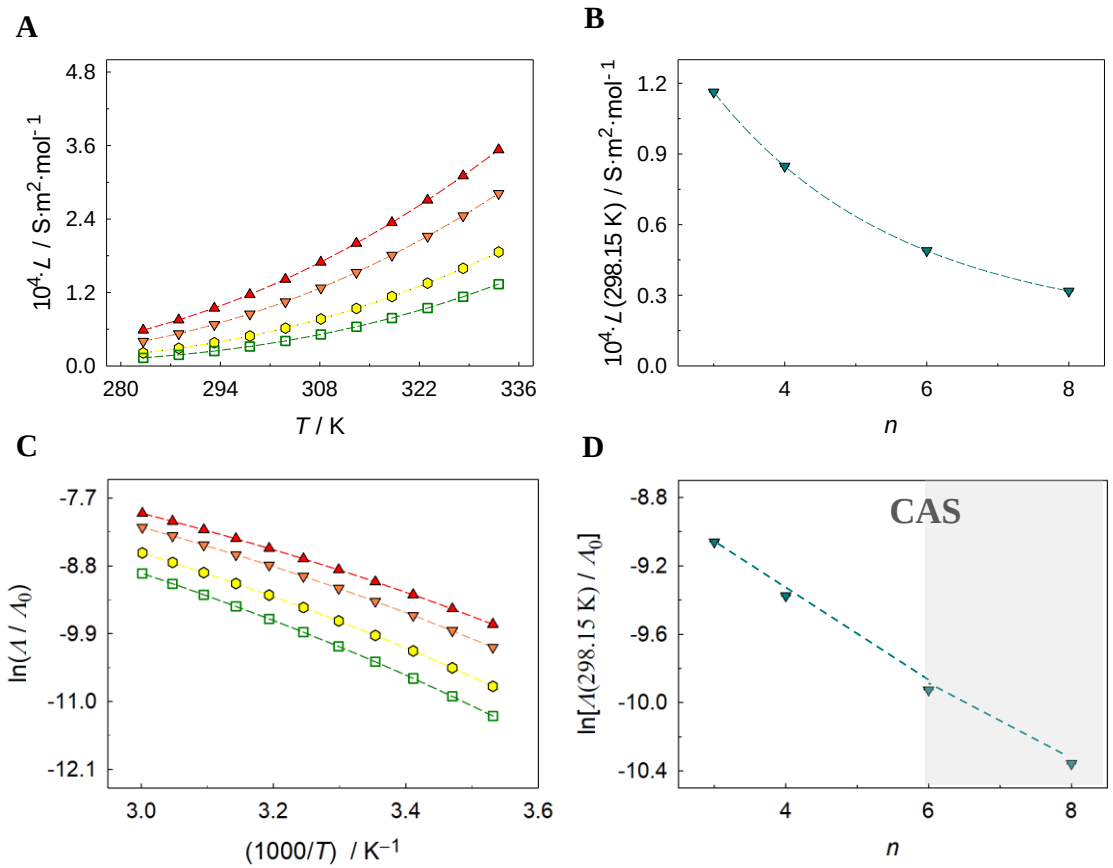



**Figure 5.72.** Molar conductivity of the [$^1C_n{}^1C_1$pyr][$NTf_2$] series as a function of temperature (A, C) and number of carbons on the alkyl chain of the cation (B, D). **A**: Temperature dependence of molar conductivity; **B**: Dependence of molar conductivity with the alkyl chain length; **C**: Temperature dependence of molar conductivity (Arrhenius representation); **D**: Dependence of molar conductivity with the alkyl chain length (logarithmic form). $n$ = 3 ▲, 4 ▼, 6 ⬢, 8 □. $\Lambda_0$ = 1 S·m$^2$·mol$^{-1}$

The VFT coefficients (Eq 2.44) obtained from the experimental molar conductivity-temperature data, $\Lambda(T)$, are presented in Table 5.45. The effect of the alkyl chain length on the obtained VFT coefficients is presented in Fig. 5.73 together with the graphical representation of the linearized VFT equation (Eq. 2.45).

**Table 5.45.** Fitting coefficients used to describe the temperature dependence of molar conductivity of the studied [$^1C_n{}^1C_1$pyr][$NTf_2$] homologue series.

| Ionic Liquid | $\frac{T_{interval}}{K}$ | $\frac{10^4 \cdot A_\Lambda}{S \cdot m^2 \cdot mol^{-1}}$ | $\frac{B_\Lambda}{K}$ | $\frac{C_\Lambda}{K}$ |
|---|---|---|---|---|
| [$^1C_3{}^1C_1$pyr][$NTf_2$] | 283 – 373 | 196.8 ± 6.1 | 650.9 ± 8.7 | 171.3 ± 0.9 |
| [$^1C_4{}^1C_1$pyr][$NTf_2$] | 283 – 373 | 210.0 ± 0.8 | 693.1 ± 1.1 | 172.4 ± 0.1 |
| [$^1C_6{}^1C_1$pyr][$NTf_2$] | 283 – 373 | 250.3 ± 2.7 | 800.0 ± 3.1 | 169.9 ± 0.3 |
| [$^1C_8{}^1C_1$pyr][$NTf_2$] | 283 – 373 | 296.6 ± 7.1 | 901.1 ± 7.1 | 166.4 ± 0.6 |

The presented fitting coefficients were derived from the experimental $\Lambda(T)$ data (appendix) by applying the VFT fitting function, Eq. 2.44. The standard uncertainties related to the VFT coefficients were calculated to the confidence level of 0.95 ($k \approx 2$).

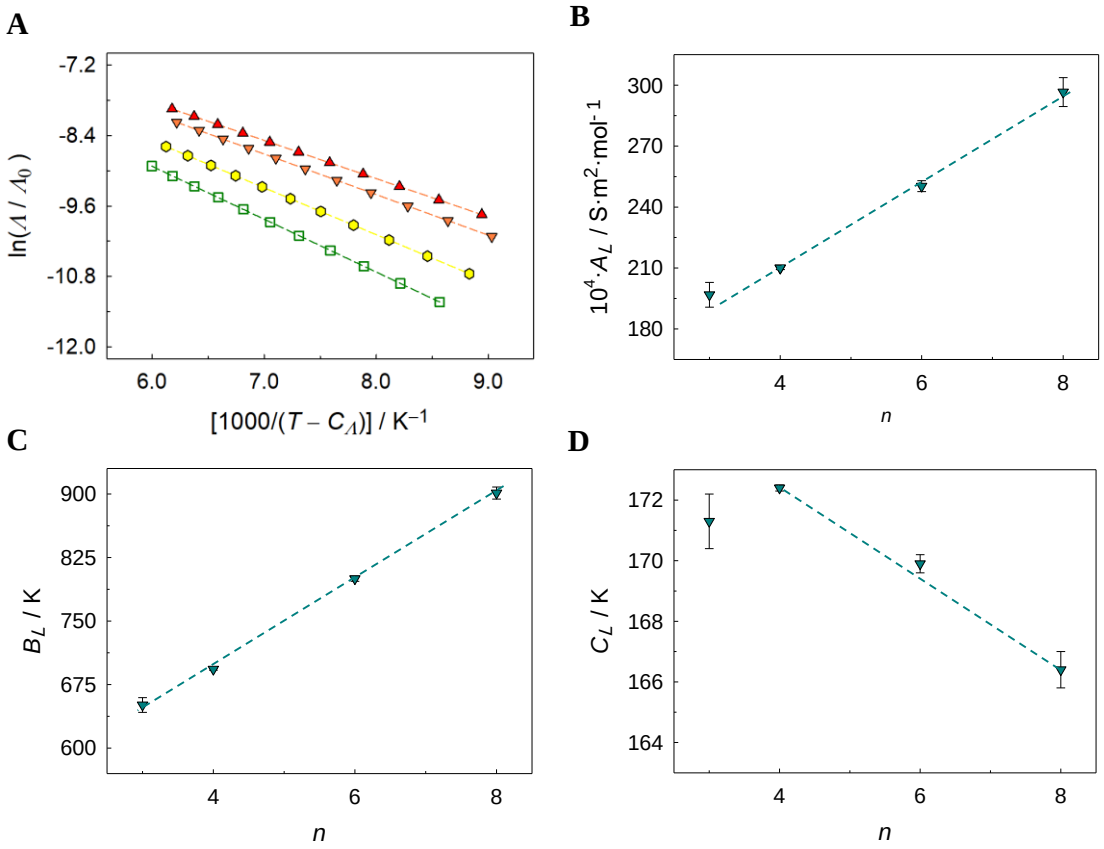



**Figure 5.73.** Impact of the alkyl chain length on the VFT coefficients for the molar conductivity of [$^1C_n{}^1C_1$pyr][$NTf_2$] series. **A**: Linearized VFT representation $n$ = 3 ▲, 4 ▼, 6 ●, 8 □; **B**: Pre-exponential coefficient, $A_\Lambda$; **C**: energy barrier-related coefficient, $B_\Lambda$; **D**: Vogel temperature, $C_\Lambda$. $\Lambda_0$ = 1 S·m$^2$·mol$^{-1}$

The molar conductivities at the reference temperature ($T$ = 298.15 K) are presented in Table 5.46, together with the energy barrier and strength parameter derived from Eq. 2.47 and Eq. 2.49 respectively. The temperature dependence of the molar conductivity-related energy barrier, $E_\Lambda$, and the effect of the alkyl chain length on $E_\Lambda$ and on the liquid fragility (strength parameter, $D_\Lambda$) are represented in Fig. 5.74.

**Table 5.46.** Molar conductivity and derived energy barrier of the studied [$^1C_n{}^1C_1$pyr][$NTf_2$] homologue series at the reference temperature ($T$ = 298.15 K), together with the strength parameter.

| Ionic Liquid | $10^4 \cdot \Lambda(T{=}298.15\ \mathrm{K})$ / $\mathrm{S \cdot m^2 \cdot mol^{-1}}$ | $E_\Lambda(T{=}298.15\ \mathrm{K})$ / $\mathrm{kJ \cdot mol^{-1}}$ | $D_\Lambda$ |
|---|---|---|---|
| [$^1C_3{}^1C_1$pyr][$NTf_2$] | 1.163 ± 0.017 | 29.90 ± 0.58 | 3.800 ± 0.055 |
| [$^1C_4{}^1C_1$pyr][$NTf_2$] | 0.848 ± 0.013 | 32.40 ± 0.07 | 4.020 ± 0.007 |
| [$^1C_6{}^1C_1$pyr][$NTf_2$] | 0.4891 ± 0.0073 | 35.95 ± 0.22 | 4.709 ± 0.020 |
| [$^1C_8{}^1C_1$pyr][$NTf_2$] | 0.3176 ± 0.0048 | 38.37 ± 0.46 | 5.415 ± 0.047 |

$\Lambda(T = 298.15\ \mathrm{K})$ and $E_\Lambda(T = 298.15\ \mathrm{K})$ were calculated from the fitting coefficients presented in Table 5.45 and by applying Eq. 2.44 and Eq. 2.47, respectively. The strength parameter was calculated by Eq. 2.49, $D_\Lambda = B_\Lambda / C_\Lambda$. The relative standard uncertainty associated with the viscosity measurements was estimated as $u(\Lambda)$ = 1.5% (Eq. 4.15); The standard uncertainty associated with the derived energy barrier, $u(E_\Lambda)$, and strength parameter, $u(D_\Lambda)$, was calculated by applying the propagation of uncertainty to Eq. 2.47 and Eq. 2.49, respectively.

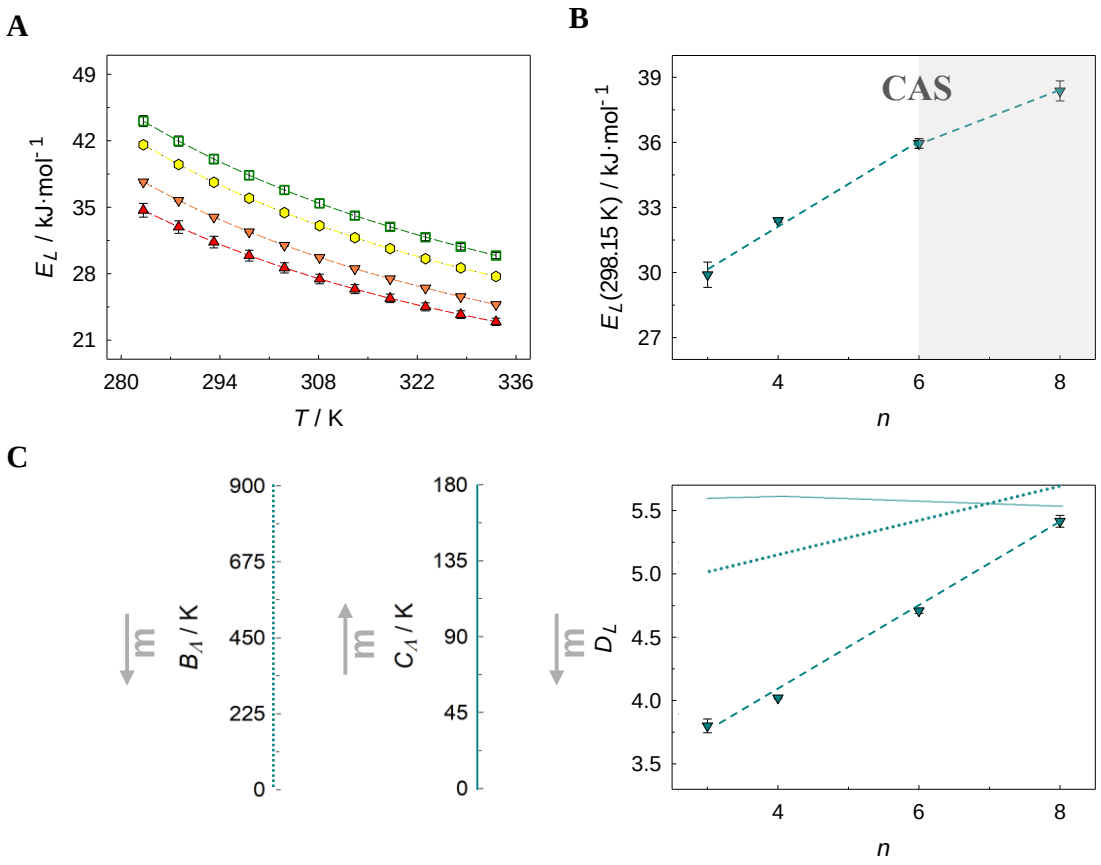



**Figure 5.74.** Graphical representation of the energy barrier and strength parameter derived from the experimental molar conductivity data of the [$^1C_n{}^1C_1$pyr][$NTf_2$] series. **A**: Temperature dependence of the derived energy barrier $n$ = 3 ▲, 4 ▼, 6 ●, 8 □; **B**: Effect of the alkyl chain length on the energy barrier; **C**: Effect of the alkyl chain length on the liquid fragility ($B_\Lambda$ and $C_\Lambda$ scales are included as guide lines).

### 5.1.8. Discussion Alkyl Chain Effect

The change in density and molar volume along the homologue series is compared with the alkanes in Fig. 5.75.

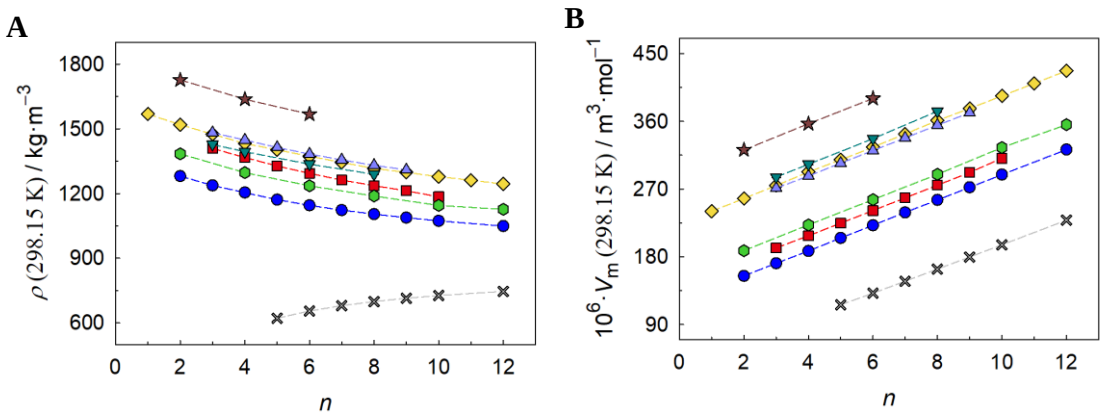



**Figure 5.75.** Effect of the alkyl chain length on the volumetric properties of the studied homologue series. **A**: Molar volume; **B:** Density. ● [$^1C_n{}^3C_1$im]$BF_4$, ■ [$^1C_n{}^3C_1$im]$PF_6$, ⬢ [$^1C_n{}^3C_1$im][OTf], ◆ [$^1C_n{}^3C_1$im][$NTf_2$], ★ [$^1C_n{}^3C_1$im][FAP], ▲ [$^1C_n$py][$NTf_2$]; ▼ [$^1C_n{}^1C_1$pyr][$NTf_2$]; ✖ n-alkanes.

The increment in molar volume per -$CH_2$- group for each series was found to be around 17 $cm^3 \cdot mol^{-1}$ (Table 5.47), which is similar to *n*-alkanes (16 $cm^3 \cdot mol^{-1}$). The density of the ionic liquids seems to be converging to the alkane behavior with the increase of the alkyl chain (~ 800 $kg \cdot m^{-3}$).

**Table 5.47.** Dependence of molar volume per methylene group for each homologue ionic liquid series.

| ILs Series | $\frac{10^6 \cdot a_{V1}}{m^3 \cdot mol^{-1}}$ | $\frac{10^6 \cdot a_{V0}}{m^3 \cdot mol^{-1}}$ |
|---|---|---|
| [$^1C_n{}^3C_1$im]$BF_4$ | 16.83 ± 0.02 | 120.8 ± 0.2 |
| [$^1C_n{}^3C_1$im]$PF_6$ [a] | 16.96 ± 0.11 | 140.0 ± 0.8 |
| [$^1C_n{}^3C_1$im][OTf] | 16.86 ± 0.15 | 154.7 ± 1.1 |
| [$^1C_n{}^3C_1$im][FAP] | 17.09 ± 0.18 | 288.1 ± 0.8 |
| [$^1C_n{}^3C_1$im][$NTf_2$] [b] | 17.17 ± 0.26 | 233.4 ± 1.0 |
| [$^1C_n$py][$NTf_2$] | 16.73 ± 0.05 | 220.9 ± 0.3 |
| [$^1C_n{}^1C_1$pyr][$NTf_2$] | 17.45 ± 0.20 | 233.2 ± 1.1 |
| *n*-alkanes [c] | 16.06 ± 0.06 | 35.3 ± 0.5 |

$a_{v1}$: increment per methylene (-$CH_2$-) group; $a_{v0}$: molar volume for *n* = 0. a: *n* = 3 – 9 [2]; b: [1]; c:

The resistance and reactance spectra presented previously (Fig. 5.9, 5.20, 5.31, 5.37, 5.48) show a shift to lower frequencies with the increase of the alkyl chain length. This is likely a consequence of the increased electrical resistivity and affects the appropriate range for frequency extrapolation. To analyze this effect, the point of minimum absolute reactance, $X_{min}$, was selected, and the effect of the number of carbons on the alkyl chain on $X_{min}$ and the respective frequency, $f_{min}$, are presented in Fig. 5.76.

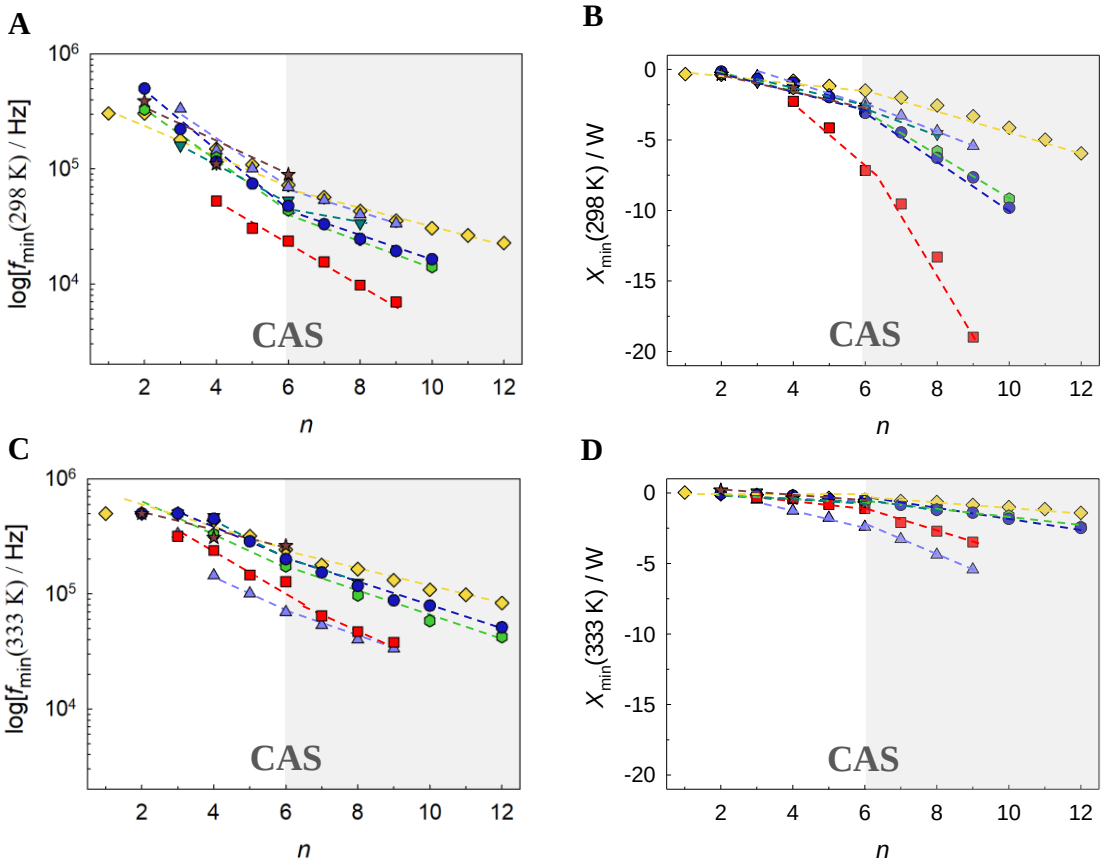



**Figure 5.76.** Effect of the alkyl chain on the reactance spectra. **A** and **C**: Frequency at absolute minimum reactance at $T$= 298 and 333 K, $f_{min}$; **B** and **D**: Absolute minimum reactance at $T$= 298 and 333 K, $X_{min}$; ●[$^1C_n{}^3C_1$im]$BF_4$, ■ [$^1C_n{}^3C_1$im]$PF_6$, ⬢ [$^1C_n{}^3C_1$im][OTf], ◆ [$^1C_n{}^3C_1$im][$NTf_2$], ★ [$^1C_n{}^3C_1$im][FAP], ▲ [$^1C_n$py][$NTf_2$]; ▼[$^1C_n{}^1C_1$pyr][$NTf_2$].

As observed, the effect of increasing the alkyl chain length is not only reflected in a decrease in $f_{min}$ and an increase in $|X_{min}|$ but also in a trendshift around $n$ = 6, which is likely associated with the intensification of nanostrucration of the ionic liquids.

The results presented in the previous sections concerning the effect of the alkyl chain on the transport properties of ILs are compiled in Fig. 5.77 with the representation of viscosity, molar conductivity, and the respective energy barrier and pre-exponential values for all the studied homologue series.

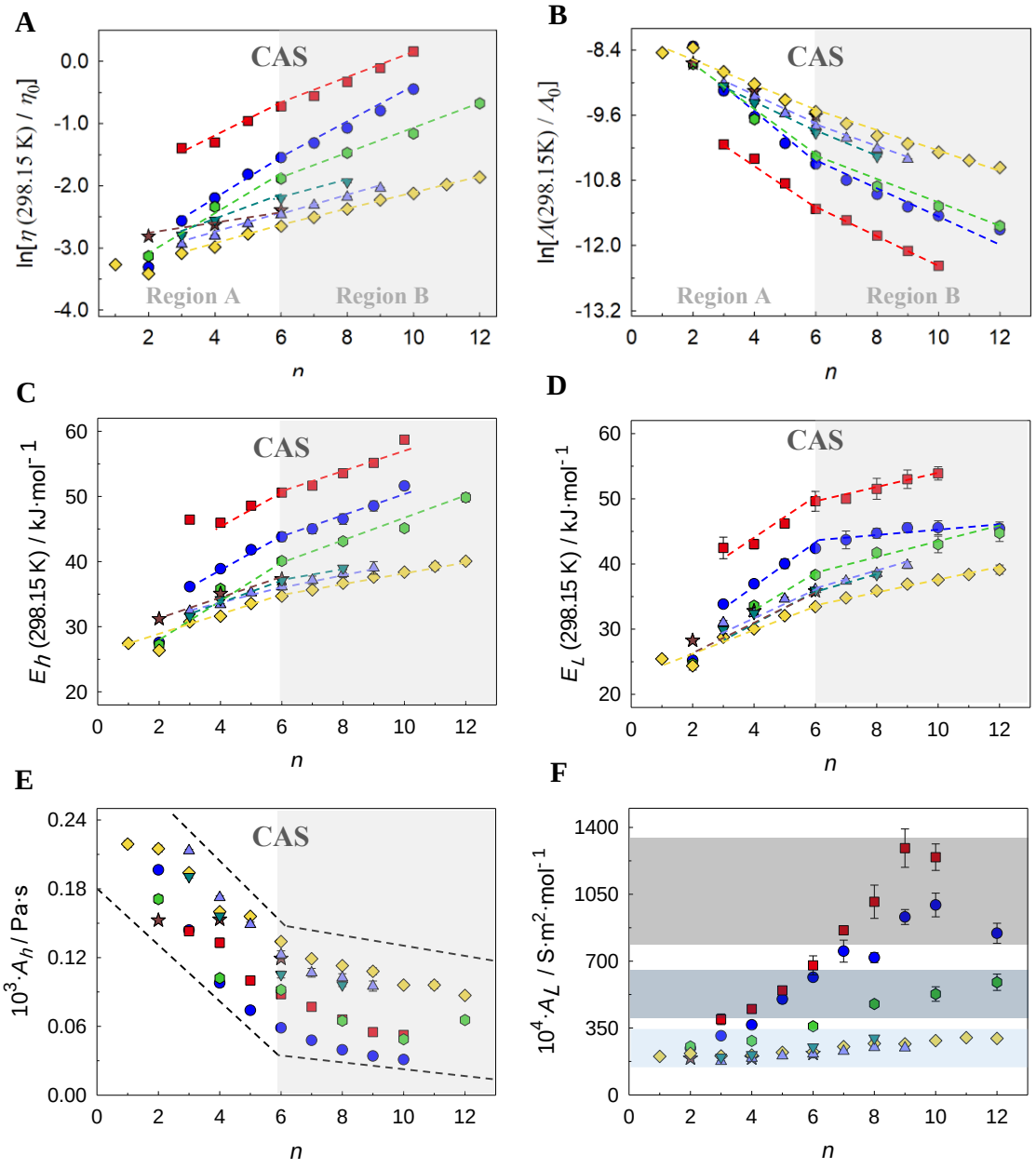



**Figure 5.77.** Effect of the alkyl chain of the transport properties of the studied homologue ionic liquids series. **A**: Viscosity (logarithmic form); **B**: Molar conductivity (logarithmic form); **C**: Energy barrier (viscosity); **D**: Energy barrier (molar conductivity); **E**: Pre-exponential coefficient (infinite temperature viscosity); **F**: Pre-exponential coefficient (infinite temperature molar conductivity). ●[$^1C_n{}^3C_1$im]$BF_4$, ■ [$^1C_n{}^3C_1$im]$PF_6$, ⬢ [$^1C_n{}^3C_1$im][OTf], ◆ [$^1C_n{}^3C_1$im][$NTf_2$], ★ [$^1C_n{}^3C_1$im][FAP], ▲ [$^1C_n$py][$NTf_2$]; ▼[$^1C_n{}^1C_1$pyr][$NTf_2$]. $\eta_0 = 1$ Pa·s; $\Lambda_0 = 1$ S·m$^2$·mol$^{-1}$.

For all homologue series, the viscosity was found to increase and the molar conductivity to decrease with the increase of the cation's alkyl chain length. This is expected and is in agreement with other similar studies from the literature, as the enlargement of the alkyl chain reduces the overall mobility of the liquid and increases its cohesive energy. This is corroborated by the increase of the derived energy barriers associated with viscous flow and ionic conduction along the homologue series. The increase of $E_\eta$ and $E_\Lambda$ is related to the increase in the potential of the dispersive (van der Waals) interactions due to the insertion of -$CH_2$- groups. On the same note, fragility decreases ($D_\eta$ and $D_\Lambda$ increases) along the homologue series as the overall interactional potential increases. The increase in the strength parameter is a result of the increase of $B_\eta$ and $B_\Lambda$ and the decrease of $C_\eta$ and $C_\Lambda$. However, $B_\eta$ and $B_\Lambda$ seem to be the dominant factors. Interestingly, the pre-exponential coefficients seem to present an opposite trend relative to viscosity and molar conductivity. $A_\eta$ and $A_\Lambda$ are mainly related to the shape, size, and dynamics of the ions overall. $A_\eta$ decreases with the increase of carbon atoms on the alkyl side chain, and $A_\Lambda$ tends to increase with the alkyl chain length. Based on this, the obtained results indicate that the elongation of the hydrocarbonated chain favors the mobility of fluid. Similar trends were also observed in other works for different ILs series, [$^1C_n{}^3C_1$im][$NTf_2$] [95, 162],[$^1Cn^3$C=Cim][Br] [163], [$^1C_n{}^3C_1$im][TCM] [164]. Furthermore, based on the results presented in Fig.5.77, while the values of $A_\eta$ seem to decrease somewhat equally for all series, there is a significant differentiation on the $A_\Lambda$ profile, as the increase seems to be much more drastic for the series with more spheric and smaller anions, $BF_4$ and $PF_6$. This highlights the increased complexity of the electric conductivity as transport properties when compared with viscosity due to the heterogeneity of charge distribution, which raises the importance of dimension-related factors such as ionic surface-volume ratio and anion-cation size ratio.

Fig 5.77 shows a trendshift on the profile of the transport properties with the cation's alkyl chain length. This trendshift is clearer for the derived properties ($E_\eta$, $E_\Lambda$, $A_\eta$, and $A_\Lambda$) and shows up when the number of carbons on the alkyl side chain is around 6 or 7 (CAS). As discussed in Chapter 1, this has been previously observed for different physicochemical properties, including solid-liquid equilibrium [165], volatility [166], heat capacity [167], and surface tension [168]. The so-called trendshift, which occurs in the observed properties of the ILs series (along the alkyl chain), has been interpreted as a consequence of the intensification of IL nanostructuration associated with the expansion of the polar tridimensional network due to the clustering of the hydrocarbonated chains [169-171]. In the present case, the trendshift is marked by a slowdown in the change rate on the properties. This slowdown is likely due to the transition from a liquid

with a strong ionic character (molten salt-like) to a fully nanostructured liquid dominated by the hydrophobic domain (alkane-like). The decrease in the trend of the energy barrier profile means a decrease in the contribution to the cohesive energy per -$CH_2$- group, which is coherent with what has been reported for other properties. Moreover, the fact that trendshift seems to be often found after n = 6 suggests that this number of carbons on the alkyl side chain which is often regarded as the turning point (CAS) seems to be more similar to the short chain ILs (Region A) than the longer chain ILs (Region B). In some cases, the shorter chain ILs (*n* = 1 - 3) behave as outliers. This has been previously reported for other physicochemical properties, including enthalpy of vaporization, and is usually attributed to the strong ionic character of these ionic liquids.

Additionally, Fig. 5.77 also highlights the impact of the nature of the ions as it reveals a somewhat clear differentiation between the series. The following trends were found for viscosity and molar conductivity:

***η*(298.15 K):**

$$[^1C_n{}^3C_1im]PF_6 > [^1C_n{}^3C_1im]BF_4 > [^1C_n{}^3C_1im][OTf] > [^1C_n{}^1C_1pyr][NTf_2] > > [^1C_n{}^3C_1im][FAP] > [^1C_npy][NTf_2] > [^1C_n{}^3C_1im][NTf_2]$$

***Λ*(298.15 K):**

$$[^1C_n{}^3C_1im][NTf_2] > [^1C_n{}^3C_1im][FAP] > [^1C_npy][NTf_2] > [^1C_n{}^1C_1pyr][NTf_2] > > [^1C_n{}^3C_1im][OTf] > [^1C_n{}^3C_1im]BF_4 > [^1C_n{}^3C_1im]PF_6$$

As expected, these trends are almost the reverse of each other, as the molar conductivity of an IL is mainly ruled by its viscosity. Although there are some exceptions, particularly the higher-than-expected molar conductivity of the $[^1C_n{}^3C_1im][FAP]$ series. Looking at Fig 5.77 A and 5.77 B, other exceptions can be found to the overall trend, such as the low viscosity and high molar conductivity of $[^1C_2{}^3C_1im]BF_4$ and $[^1C_2{}^3C_1im][OTf]$ series, which are comparable to the $NTf_2$ analog. The presented viscosity and molar conductivity trends are well described by the energy barrier. The larger $E_\eta$ and $E_\Lambda$ values (higher cohesive energies) were found for the smaller and more spheric anions, while the smaller values were found for the large and highly charge dispersed anions ($NTf_2$ and FAP). The energy barrier for the $[^1C_n{}^3C_1im][OTf]$ was found to be in the middle of the order, suggesting the existence of hydrogen bonding between the sulfonate group and the imidazolium ring. Furthermore, the pre-exponential coefficients also highlight the impact of the anion nature as the small and spheric anions seem to favor more dynamic systems (lower $A_\eta$ and higher $A_\Lambda$). This will be further discussed in the next sections.

The viscosity and molar conductivity data were used to construct the Walden Plots for the studied ILs (Fig. 5.78). While the Walden rule (Eq. 2.57) is an empirical relation and its use has been criticized, it is still a useful tool for comparing the viscosity-conductivity relationship between different compounds.

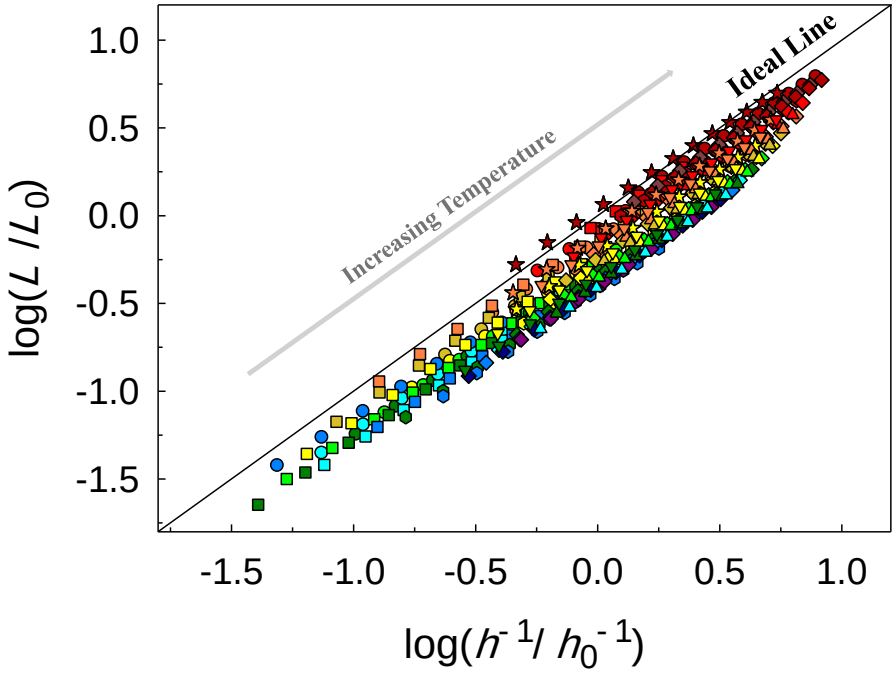



**Figure 5.78.** Walden plot of the studied homologue series based on the experimental viscosity and molar conductivity results. $n$ = **1**, **2**, **3**, **4**, **5**, **6**, **7**, **8**, **9**, **10**, **11**, **12**; ● $[^1C_n{}^3C_1im]BF_4$, ■ $[^1C_n{}^3C_1im]PF_6$, ⬢ $[^1C_n{}^3C_1im][OTf]$, ◆ $[^1C_n{}^3C_1im][NTf_2]$, ★ $[^1C_n{}^3C_1im][FAP]$, ▲ $[^1C_npy][NTf_2]$; ▼ $[^1C_n{}^1C_1pyr][NTf_2]$. $\eta_0$ = 1 Poise; $\Lambda_0$ = 1 S·cm$^2$·mol$^{-1}$.

Negative deviations to the “ideal line” indicate that the molar conductivity of the IL is lower than what should be expected from its viscosity, suggesting the occurrence of ionic association/aggregation. However, the correlation between these two transport properties (viscosity and molar conductivity) is significantly affected by the increased complexity of the electrical conductivity due to the differentiation in the charge distribution for the case of no spherical anions and cations. Fig 5.78 shows a larger negative deviation for long-chain ILs, which is coherent with the clustering of the alkyl chain. Additionally, from the constructed Walden Plot, the data for the pre-CAS ILs (n < 6,7) seems to be more dispersed, while there is more overlap for the data correspondent to the pos-CAS ILs (n > 6,7). To further explore this effect, the impact of the alkyl chain length on the deviation to the ideal Walden line, $\Delta w$ at the reference temperature ($T$ = 298.15 K) and the slope of the Walden lines, $\alpha_w$, is graphically presented on Fig 5.79.

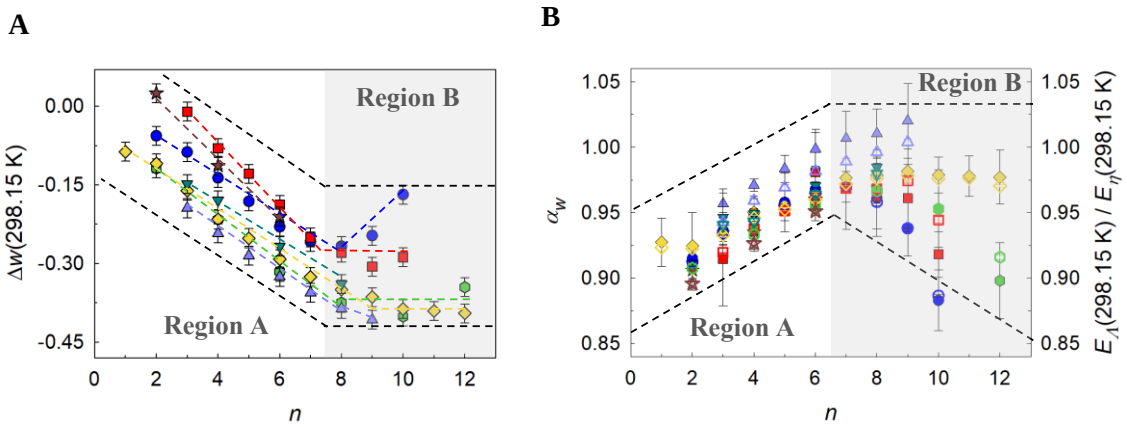



**Figure 5.79.** Viscosity – molar conductivity correlations for the studied homologue series. **A**: Deviation to the "ideal Walden line" (log $\Lambda$ – log $\eta^{-1}$) as a function of the number of carbons on the alkyl chain; **B**: Walden slope and Energy barrier ratio ($E_\Lambda/E_\eta$) as a function of the number of carbons on the alkyl chain. ● [$^1C_n{}^3C_1$im]$BF_4$, ■ [$^1C_n{}^3C_1$im]$PF_6$, ⬢ [$^1C_n{}^3C_1$im][OTf], ◆ [$^1C_n{}^3C_1$im][$NTf_2$], ★ [$^1C_n{}^3C_1$im][FAP], ▲ [$^1C_n$py][$NTf_2$]; ▼[$^1C_n{}^1C_1$pyr][$NTf_2$].

Fig. 5.79 also shows a trendshift on both the Δ*w* and $\alpha_w$ plots, highlighting a clear distinction between Region A and Region B. The trend highlighted in this figure presented a quantified approach to what was observed from the Walden Plot (Fig 5.78). The comparison between the viscosity and molar conductivity along the ionic liquid series highlights the increased complexity and differentiation of the electric conductivity due to the specific point interaction forces with the charge regions of the ILs. The trend is similar for all homologue series (Δ*w* decrease and $\alpha_w$, $E_\Lambda/E_\eta$ increases). The increase of $E_\Lambda/E_\eta$ suggests that the conductivity-associated energy barrier becomes similar to the viscosity-associated energy barrier with the increase of the alkyl chain in the polar region. The observed behavior of the studied ILs is in good agreement with previous studies by other authors [49, 94, 95, 172].

Fig. 5.80 presents the relationship between the derived energy barriers and the selected literature data for the enthalpy of vaporization (cohesive interaction).

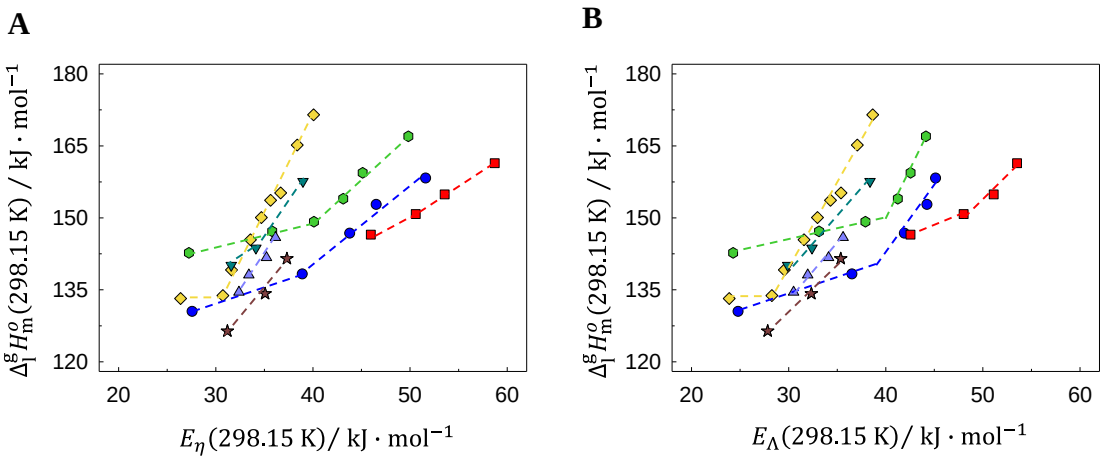



**Figure 5.80.** Correlation between the enthalpy of vaporization and energy barrier for the studied IL homologue series. **A**: Viscosity; **B**: Molar conductivity. ● [$^1C_n{}^3C_1$im]$BF_4$ [173], ■ [$^1C_n{}^3C_1$im]$PF_6$ [174], ⬢ [$^1C_n{}^3C_1$im][OTf] [175], ◆ [$^1C_n{}^3C_1$im][$NTf_2$] [166], ★ [$^1C_n{}^3C_1$im][FAP] [176], ▲ [$^1C_n$py][$NTf_2$] [177]; ▼[$^1C_n{}^1C_1$pyr][$NTf_2$] [178].

The observed profiles of the relation between $E_\eta$ and $E_\Lambda$ and enthalpy of vaporization are very similar, which is expected due to their interrelation and small difference (10 % maximum). A more clear and informative representation of this relationship can be achieved by looking at the ratio between the energy barrier and the enthalpy of vaporization as a function of the number of carbons on the alkyl chain (Fig. 5.81).

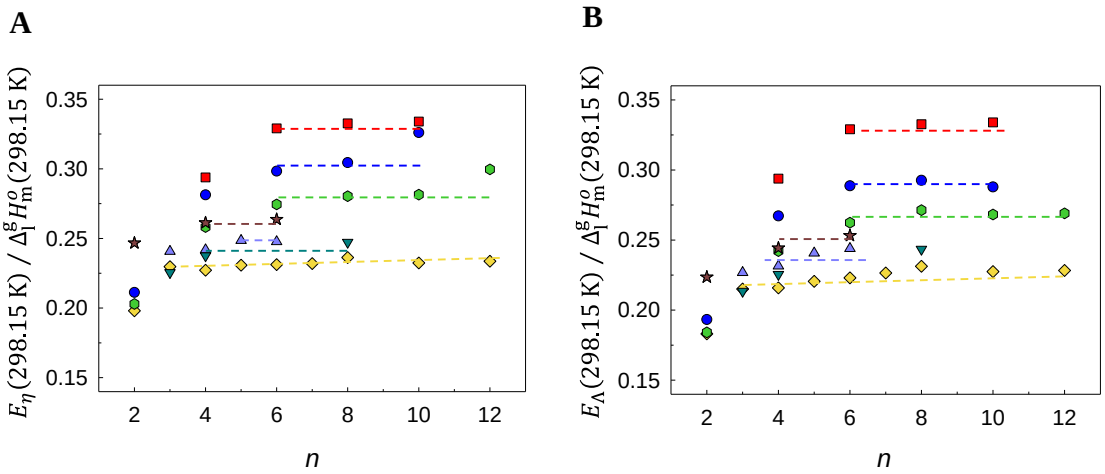



**Figure 5.81.** Ratio between energy barrier and enthalpy of vaporization (cohesive energy) for the studied ionic liquid homologue series. **A**: Viscosity; **B**: Molar conductivity. ● [$^1C_n{}^3C_1$im]$BF_4$ [173], ■ [$^1C_n{}^3C_1$im]$PF_6$ [174], ⬢ [$^1C_n{}^3C_1$im][OTf] [175], ◆ [$^1C_n{}^3C_1$im][$NTf_2$] [166], ★ [$^1C_n{}^3C_1$im][FAP] [176], ▲ [$^1C_n$py][$NTf_2$] [177]; ▼[$^1C_n{}^1C_1$pyr][$NTf_2$] [178].

It is observed that the ratio $E_{\eta,\Lambda}/\Delta_{\mathrm{l}}^{\mathrm{g}}H_{\mathrm{m}}^{0}$ ranges between 0.20 to 0.35 depending on the homologue series. This indicates that the energy barrier associated with viscous flow or ion conduction is a small fraction of the cohesive interaction of the liquid. For each family, the magnitude of the energy barrier is related to a constant fraction of the cohesive interaction, excluding the short-chain ILs (*n* = 2). In these cases (short-chain ILs), the energy barrier is a lower fraction of the cohesive interaction when compared to the rest of the series. The observed trend between the ILs series indicates that the spherical anions $BF_4^-$ and $PF_6^-$ show the highest fraction of the cohesive energy, and the more stretched and larger anions, $NTf_2$-based series, the lowest.

## 5.2. Effect of the Anion Nature

In the previous section, the impact of the nature of the anion on the transport properties was briefly discussed when comparing the behavior of the different studied homologue series. To further explore the effect of the anion the densities, viscosities and electrical conductivities of ten ionic liquids based on the 1-butyl-3-methylimidazolium cation, $[^1C_4{}^3C_1im][X]$ (Fig. 5.82) were measured at different temperatures. The results of five of these ILs were already presented in the previous section ($[^1C_4{}^3C_1im]BF_4$, $[^1C_4{}^3C_1im]PF_6$, $[^1C_4{}^3C_1im][OTf]$, $[^1C_4{}^3C_1im][NTf_2]$, and $[^1C_4{}^3C_1im][FAP]$. In this section, the experimental results obtained for the $[^1C_4{}^3C_1im]Ac$, $[^1C_4{}^3C_1im][DCA]$, ($[^1C_4{}^3C_1im][TFA]$, $[^1C_4{}^3C_1im][FSI]$, and $[^1C_4{}^3C_1im][BETI]$ will be presented and combined with the first set of $[^1C_4{}^3C_1im][X]$ ILs for the discussion on the effect of the anion on the transport properties and derived parameters.

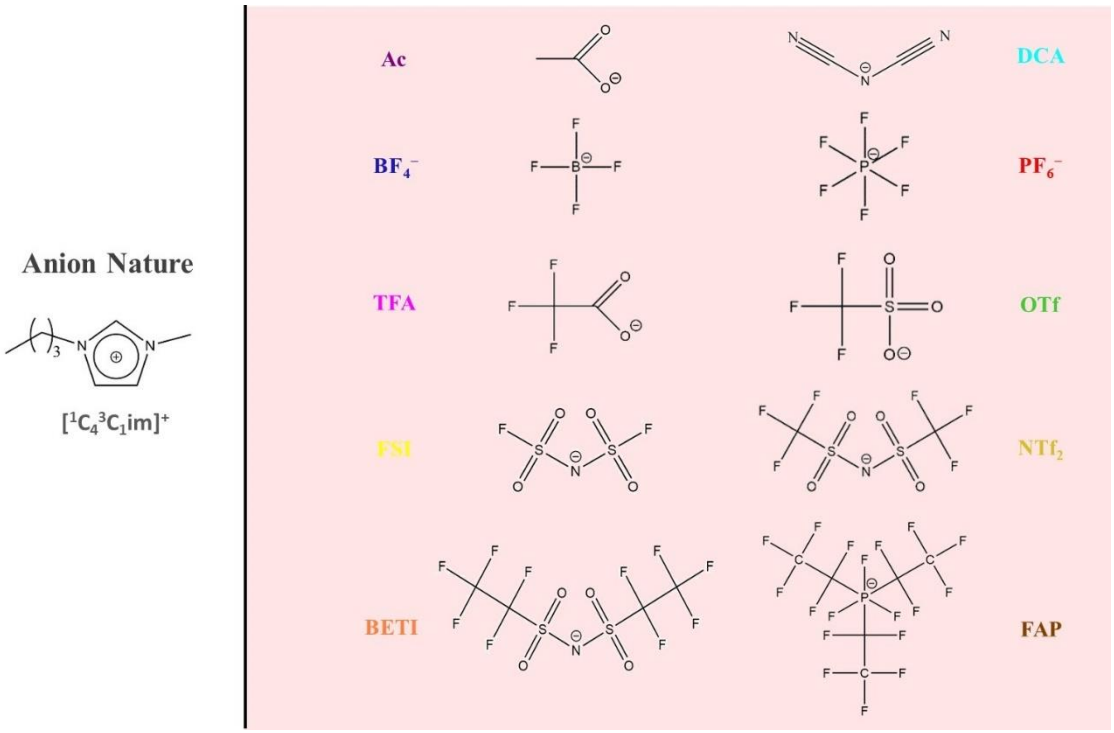



**Figure 5.82.** Ion structures of the $[^1C_4{}^3C_1im][X]$ ionic liquids involved in the study focused on the effect of the nature of the anion on the transport properties of ILs.

### 5.2.1. Density

The resulting fitting coefficients from the temperature dependence of density of the $[^1C_n{}^3C_1im][X]$ ILs (Eq. 2.4) are presented in Table 5.48. The densities at the reference temperature ($T$ = 298.15 K) are presented in Table 5.49, together with the molar volume and thermal expansion coefficient derived from Eq. 2.2 and Eq. 2.7 respectively.

**Table 5.48.** Fitting coefficients used to describe the temperature dependence of density of the studied $[^1C_4{}^3C_1im][X]$ ILs.

| Ionic Liquid | $\frac{T_{interval}}{K}$ | $\frac{10^7 \cdot a_2}{K^{-2}}$ | $\frac{10^4 \cdot a_1}{K^{-1}}$ | $\frac{a_0}{K}$ |
|---|---|---|---|---|
| $[^1C_4{}^3C_1im][Ac]$ | 298 – 373 | 0.623 ± 0.104 | −6.111 ± 0.069 | 7.1336 ± 0.0011 |
| $[^1C_4{}^3C_1im][DCA]$ | 273 – 373 | 1.510 ± 0.080 | −6.900 ± 0.052 | 7.1591 ± 0.0008 |
| $[^1C_4{}^3C_1im][TFA]$ | 293 – 373 | 0.514 ± 0.074 | −6.532 ± 0.048 | 7.2910 ± 0.0008 |
| $[^1C_4{}^3C_1im][FSI]$ | 273 – 373 | 0.987 ± 0.064 | −6.941 ± 0.041 | 7.4113 ± 0.0007 |
| $[^1C_4{}^3C_1im][BETI]$ | 273 – 373 | 0.701 ± 0.033 | −6.482 ± 0.021 | 7.5223 ± 0.0003 |

The presented fitting coefficients were derived from the experimental $\rho(T)$ data (appendix) by applying a polynomial fitting function, $\ln[\rho(T)] = a_2T^2 + a_1T + a_0$ (Eq. 2.4). The standard uncertainties related to the fitting coefficients were calculated to the confidence level of 0.95 ($k \approx 2$).

**Table 5.49.** Density, thermal expansion coefficient, and molar volume at the reference temperature ($T$ = 298.15 K) for the studied $[^1C_4{}^3C_1im][X]$ ILs.

| Ionic Liquid | $\frac{\rho(298.15\ K)}{kg \cdot m^{-3}}$ | $\frac{10^4 \cdot \alpha_\rho(298.15\ K)}{K^{-1}}$ | $\frac{10^6 \cdot V_m(298.15\ K)}{m^3 \cdot mol^{-1}}$ |
|---|---|---|---|
| $[^1C_4{}^3C_1im][Ac]$ | 1050.4 ± 0.5 | 5.74 ± 0.07 | 188.7 ± 0.4 |
| $[^1C_4{}^3C_1im][DCA]$ | 1060.8 ± 0.5 | 6.00 ± 0.05 | 193.5 ± 0.4 |
| $[^1C_4{}^3C_1im][TFA]$ | 1213.0 ± 0.5 | 6.23 ± 0.05 | 186.3 ± 0.5 |
| $[^1C_4{}^3C_1im][FSI]$ | 1357.1 ± 0.5 | 6.35 ± 0.04 | 235.3 ± 0.6 |
| $[^1C_4{}^3C_1im][BETI]$ | 1533.4 ± 0.5 | 6.06 ± 0.02 | 338.7 ± 1.0 |

$\rho(T = 298.15\ K)$ and $\alpha_\rho(T = 298.15\ K)$ were calculated from the fitting coefficients presented in Table 5.48 and by applying Eq. 2.4 and Eq. 2.7 respectively. $V_m(298.15\ K) = M/\rho(298.15\ K)$. The standard uncertainty associated with $\alpha_\rho$ and $V_m$ were calculated by applying the propagation of uncertainty to Eq. 2.7 and 2.2, respectively.

The graphical representation of density, thermal expansion coefficient, and molar volume as functions of temperature and graphical comparisons at $T$ = 298.15 K are presented in Fig. 5.83.

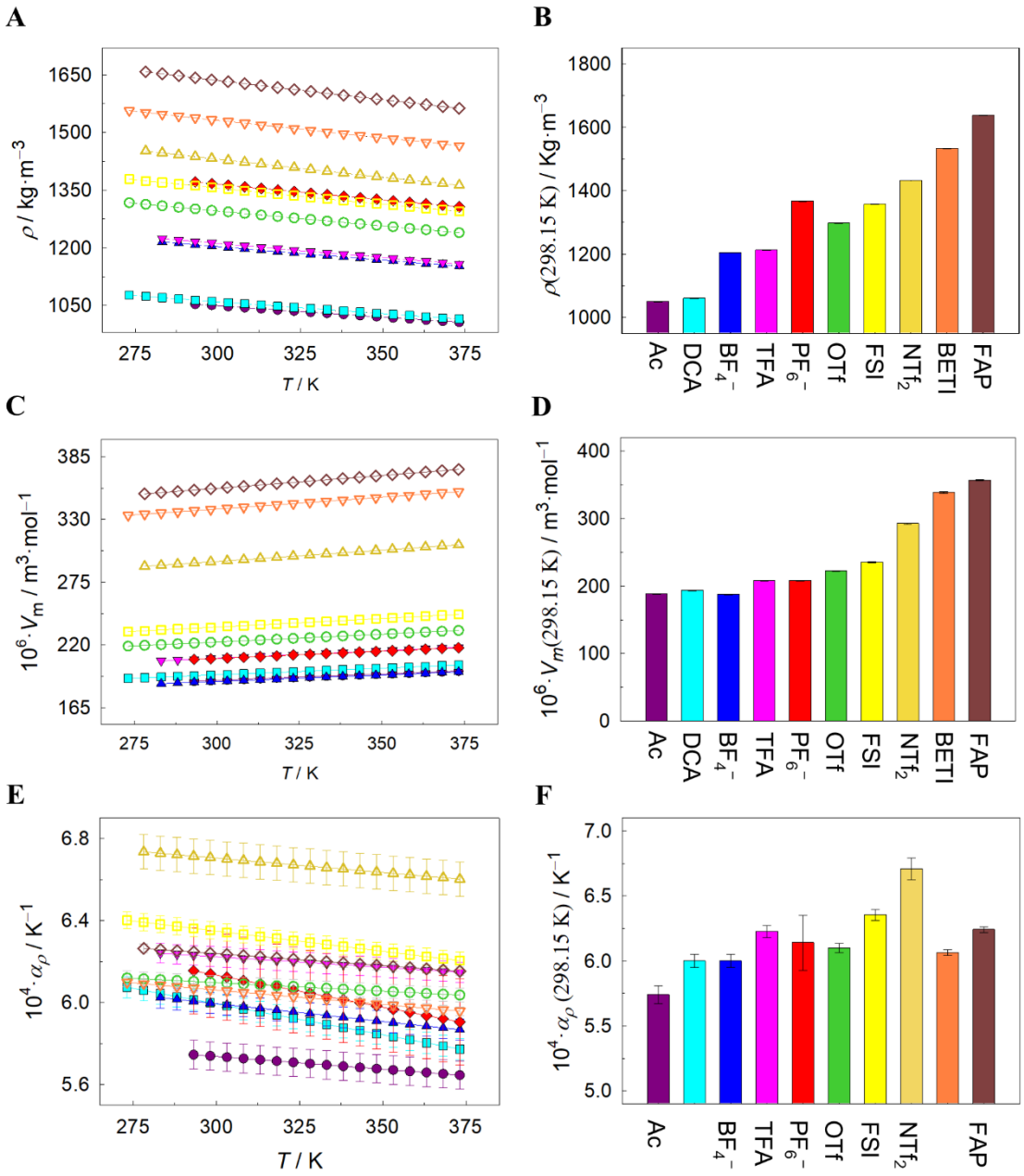



**Figure 5.83.** Density and derived properties of the [$^1C_4{}^3C_1$im][X] ILs as functions of temperature (A, C, E) and at reference temperature $T$ = 298.15 K (B, D, F). **A**, **B**: Density; **C**, **D**: Molar volume; **E**, **F**: Thermal expansion coefficient. ● [$^1C_4{}^3C_1$im][Ac]; ■ [$^1C_4{}^3C_1$im][DCA]; ▲ [$^1C_4{}^3C_1$im][$BF_4$]; ▼ [$^1C_4{}^3C_1$im][TFA]; ◆ [$^1C_4{}^3C_1$im][$PF_6$]; ○ [$^1C_4{}^3C_1$im][OTf]; □ [$^1C_4{}^3C_1$im][FSI]; △ [$^1C_4{}^3C_1$im][$NTf_2$] ▽ [$^1C_4{}^3C_1$im][BETI]; ◇ [$^1C_4{}^3C_1$im][FAP].

### 5.2.2. Viscosity

The VFT coefficients (Eq 2.44) obtained from the experimental viscosity-temperature data, $\eta(T)$, are presented in Table 5.50 and in Fig. 5.84.

**Table 5.50.** Fitting coefficients used to describe the temperature dependence of viscosity of the studied $[^1C_4{}^3C_1im][X]$ ILs.

| Ionic Liquid | $\frac{T_{interval}}{K}$ | $\frac{10^3 \cdot A_\eta}{Pa \cdot s}$ | $\frac{B_\eta}{K}$ | $\frac{C_\eta}{K}$ |
|---|---|---|---|---|
| $[^1C_4{}^3C_1im][Ac]$ | 298 – 373 | 0.0730 ± 0.0022 | 973.1 ± 7.1 | 189.7 ± 0.4 |
| $[^1C_4{}^3C_1im][DCA]$ | 273 – 373 | 0.2138 ± 0.0009 | 627.4 ± 1.0 | 171.6 ± 0.1 |
| $[^1C_4{}^3C_1im][TFA]$ | 293 – 373 | 0.1266 ± 0.0015 | 825.1 ± 3.2 | 169.6 ± 0.3 |
| $[^1C_4{}^3C_1im][FSI]$ | 273 – 373 | 0.2022 ± 0.0004 | 719.8 ± 0.5 | 156.7 ± 0.1 |
| $[^1C_4{}^3C_1im][BETI]$ | 273 – 373 | 0.0720 ± 0.0026 | 1036 ± 9.0 | 158.0 ± 0.6 |

The presented fitting coefficients were derived from the experimental $\eta(T)$ data (appendix) by applying the VFT fitting function, Eq. 2.44. The standard uncertainties related to the VFT coefficients were calculated to the confidence level of 0.95 ($k \approx 2$).

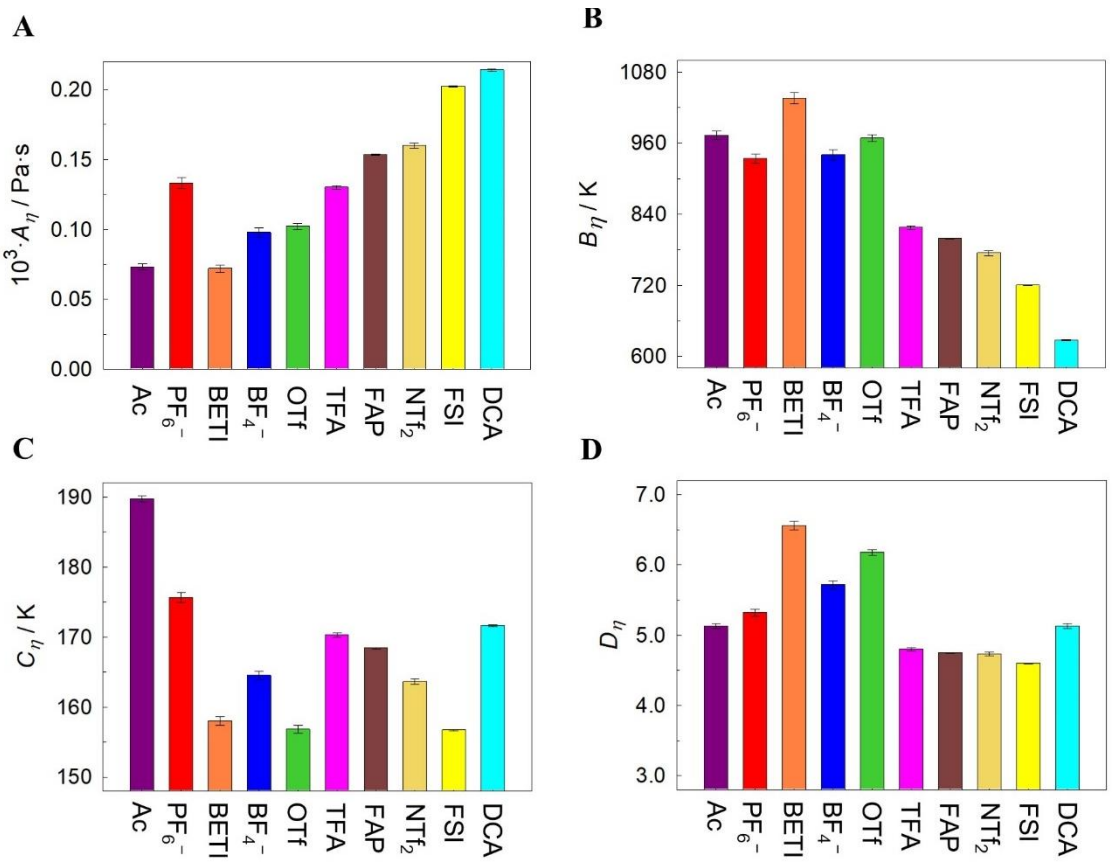



**Figure 5.84.** Effect of the anion on the VFT coefficients derived from the experimental molar conductivity-temperature data of the $[^1C_4{}^3C_1im][X]$ ILs. **A**: VFT pre-exponential coefficient, $A_\eta$, (viscosity at infinite temperature); **B**: VFT energy-related coefficient, $B_\eta$; **C**: Vogel temperature, $C_\eta$; **D**: Strength parameter, $D_\eta$.

The viscosities at the reference temperature ($T$ = 298.15 K) are presented in Table 5.51, together with the energy barrier and strength parameter derived from Eq. 2.47 and Eq. 2.49 respectively. The temperature dependence of viscosity and the derived energy barrier, $E_\eta$, are represented in Fig. 5.85.

**Table 5.51.** Viscosity and derived energy barrier of the studied [$^1C_4{}^3C_1$im][X] ILs at the reference temperature ($T$ = 298.15 K), together with the strength parameter.

| Ionic Liquid | $\eta(T$=298.15 K) / Pa · s | $E_\eta(T$=298.15 K) / kJ · mol$^{-1}$ | $D_\eta$ |
|---|---|---|---|
| [$^1C_4{}^3C_1$im][Ac] | 0.5757 ± 0.0058 | 61.15 ± 0.63 | 5.130 ± 0.039 |
| [$^1C_4{}^3C_1$im][DCA] | 0.03042 ± 0.00030 | 28.96 ± 0.07 | 3.656 ± 0.006 |
| [$^1C_4{}^3C_1$im][TFA] | 0.07762 ± 0.00078 | 36.90 ± 0.22 | 4.865 ± 0.021 |
| [$^1C_4{}^3C_1$im][FSI] | 0.03279 ± 0.00033 | 26.59 ± 0.04 | 4.593 ± 0.004 |
| [$^1C_4{}^3C_1$im][BETI] | 0.1169 ± 0.0012 | 38.98 ± 0.48 | 6.557 ± 0.062 |

$\eta(T$ = 298.15 K) and $E_\eta(T$ = 298.15 K) were calculated from the fitting coefficients presented in Table 5.50 and by applying Eq. 2.44 and Eq. 2.47, respectively. The strength parameter was calculated by Eq. 2.49, $D_\eta = B_\eta / C_\eta$. The relative standard uncertainty associated with the viscosity measurements was estimated as $u(\eta)$ = 1.0% (Eq. 2.72); The standard uncertainty associated with the derived energy barrier, $u(E_\eta)$, and strength parameter, $u(D_\eta)$, was calculated by applying the propagation of uncertainty to Eq. 2.47 and Eq. 2.49, respectively.

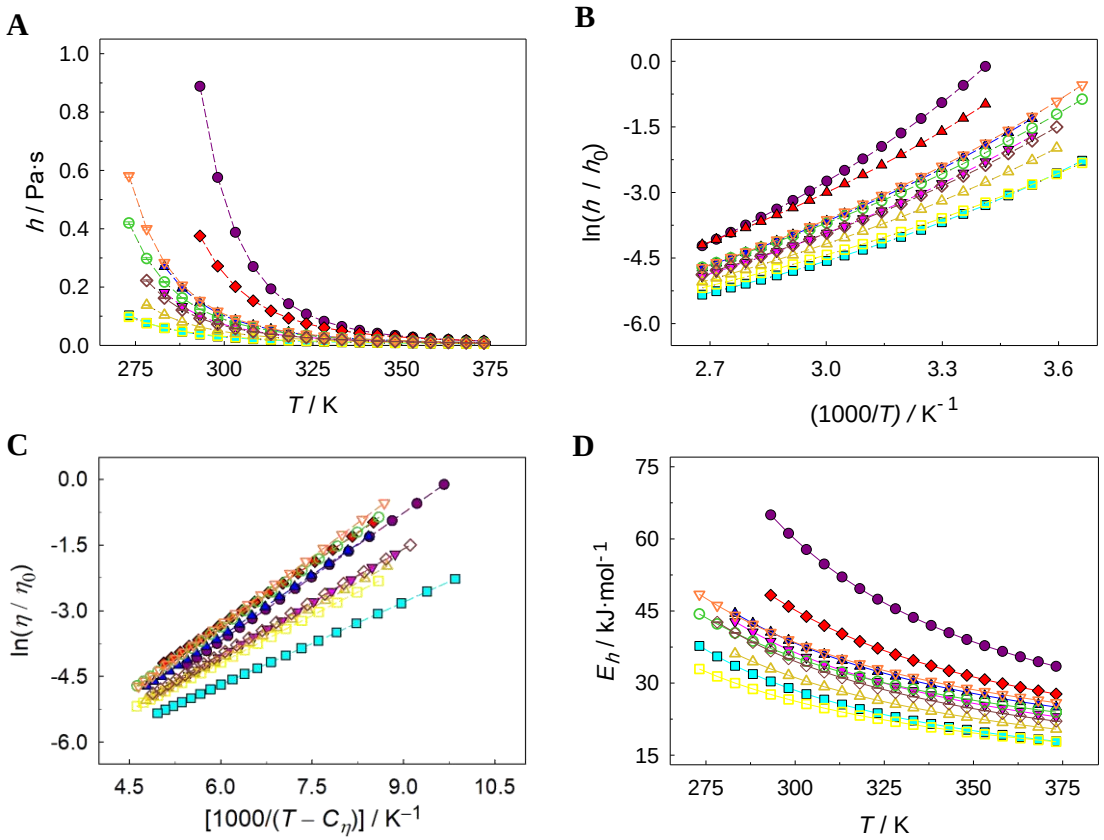



**Figure 5.85.** Temperature dependence of the viscosity and derived energy barrier of the studied [$^1C_4{}^3C_1$im][X] ILs. **A**: viscosity; **B**: Arrhenius representation; **C**: VFT representation; **D**: Energy barrier. ● [$^1C_4{}^3C_1$im][Ac]; ■ [$^1C_4{}^3C_1$im][DCA]; ▲ [$^1C_4{}^3C_1$im][$BF_4$]; ▼ [$^1C_4{}^3C_1$im][TFA]; ◆ [$^1C_4{}^3C_1$im][$PF_6$]; ○ [$^1C_4{}^3C_1$im][OTf]; □ [$^1C_4{}^3C_1$im][FSI]; △ [$^1C_4{}^3C_1$im][$NTf_2$] ▽ [$^1C_4{}^3C_1$im][BETI]; ◇ [$^1C_4{}^3C_1$im][FAP]. $\eta_0$ = 1 Pa·s.

The deviation of the available viscosity data to the experimental results for the [$^1C_4{}^3C_1$im][X] presented in this section is presented in Fig. 5.86.

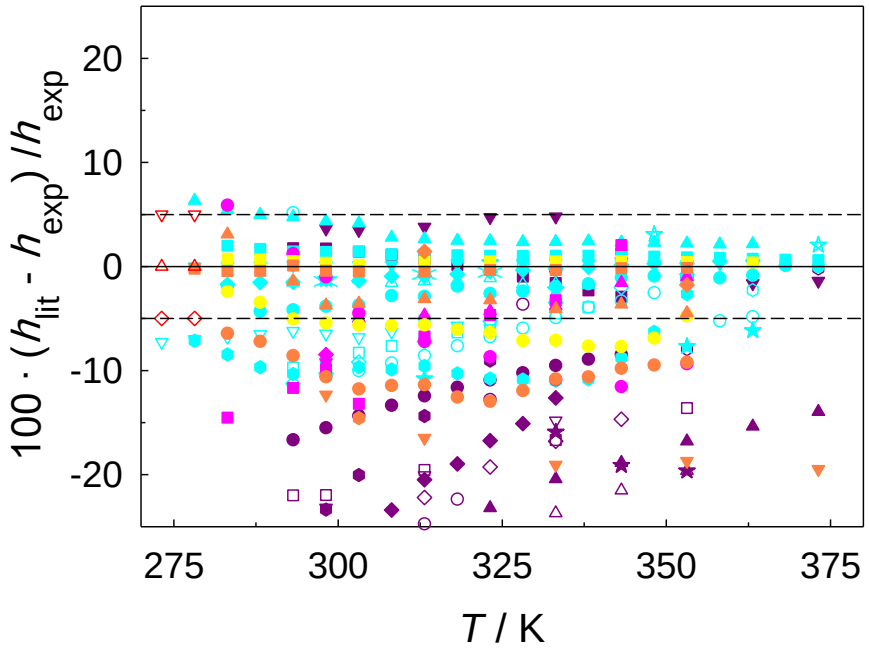



**Figure 5.86.** Deviation of the available viscosity data to the experimental results for the [$^1C_4{}^3C_1$im][X] ionic liquids. **[$^1C_4{}^3C_1$im][Ac]:** ● [179], ■ [180], ▲ [181], ▼ [182], ◆ [183], ⬢ [135], ○ [54], □ [184], △ [185], ▽ [186], ◇ [187], ⬡ [188], ★ [189]; **[$^1C_4{}^3C_1$im][DCA]:** ● [190], ■ [191], ▲ [192], ▼ [4], ◆ [5], ⬢ [78], ○ [193], □ [194], △ [80], ▽ [195], ◇ [196], ⬡ [75], ★ [197], ☆ [198], >< [199]; **[$C_4C_1$im][TFA]:** ● [29], ■ [135], ▲ [200], ▼ [201], ◆ [202]; **[$^1C_4{}^3C_1$im][FSI]:** ● [78], ■ [111]; **[$^1C_4{}^3C_1$im][BETI]:** ● [78], ■ [111], ▲ [29], ▼ [152], ◆ [203], ⬢ [204].

There is a large amount of data in the literature for these ILs, particularly [$^1C_4{}^3C_1$im][Ac] and [$^1C_4{}^3C_1$im][DCA] while there is a good number of datasets within ± 2% relative to the results obtained in this work, there are also a lot of points showing significant negative deviations. This is likely associated with the presence of water, and as expected, it is very clear for [$^1C_4{}^3C_1$im][Ac] and [$^1C_4{}^3C_1$im][TFA], as the acetate group is very reactive with water.

### 5.2.3. Electrical Conductivity

The VFT coefficients (Eq 2.44) obtained from the experimental electrical conductivity-temperature data, $\sigma(T)$, are presented in Table 5.52 together with the electrical conductivity at the reference temperature ($T$ = 298.15 K)

**Table 5.52.** Fitting coefficients used to describe the temperature dependence of electrical conductivity of the studied [$^1$C$_4$$^3$C$_1$im][X] ILs.

| Ionic Liquid | $A_\sigma$ / S·m$^{-1}$ | $B_\sigma$ / K | $C_\sigma$ / K | $\sigma(T$=298.15 K) / S·m$^{-1}$ |
|---|---|---|---|---|
| [$^1$C$_4$$^3$C$_1$im][Ac] | 277.8 ± 35 | 973 ± 33 | 184.8 ± 2.3 | 0.0520 ± 0.0008 |
| [$^1$C$_4$$^3$C$_1$im][DCA] | 112.6 ± 1.6 | 576.9 ± 3.9 | 173.3 ± 0.5 | 1.1086 ± 0.0166 |
| [$^1$C$_4$$^3$C$_1$im][TFA] | 104.8 ± 1.1 | 723.2 ± 2.9 | 173.8 ± 0.3 | 0.3123 ± 0.0047 |
| [$^1$C$_4$$^3$C$_1$im][FSI] | 71.72 ± 0.45 | 587.8 ± 1.8 | 166.6 ± 0.2 | 0.8224 ± 0.0123 |
| [$^1$C$_4$$^3$C$_1$im][BETI] | 71.97 ± 0.93 | 771.0 ± 3.6 | 173.8 ± 0.3 | 0.1460 ± 0.0022 |

The presented fitting coefficients were derived from the experimental $\sigma(T)$ data (appendix) by applying the VFT fitting function, Eq. 2.44. The standard uncertainties related to the VFT coefficients were calculated to the confidence level of 0.95 ($k \approx 2$). The relative standard uncertainty associated with the viscosity measurements was estimated as $u(\sigma)$ = 1.5% (Eq.4.15).

The deviation of the available electrical conductivity data to the experimental results for the [$^1$C$_4$$^3$C$_1$im][X] presented in this section is presented in Fig. 5.87.

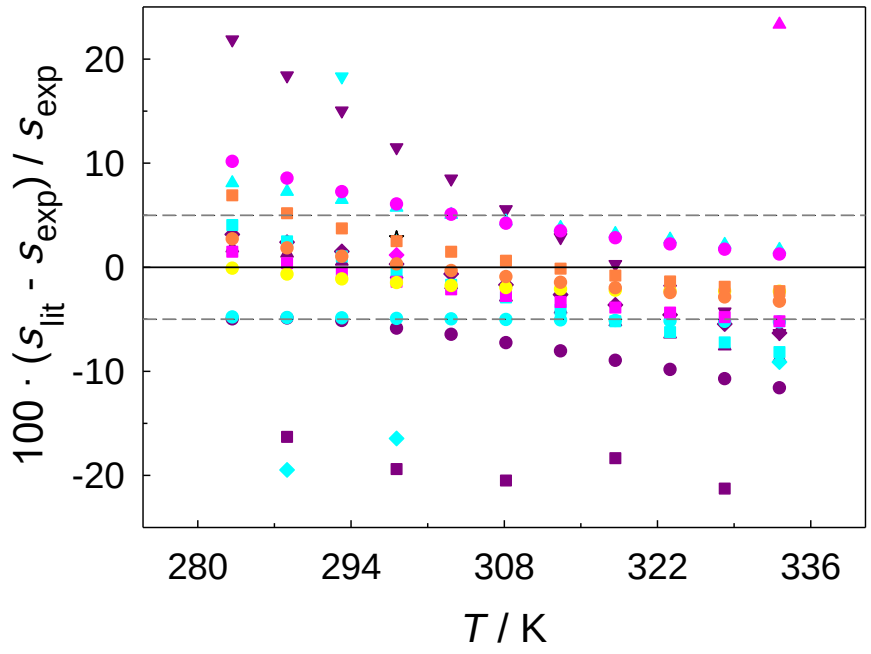



**Figure 5.87.** Deviation of the available electrical conductivity data to the experimental results for the [$^1$C$_4$$^3$C$_1$im][X] ionic liquids. **[$^1$C$_4$$^3$C$_1$im][Ac]:** ● [205], ■ [187], ▲ [54], ▼ [186], ◆ [179]; **[$^1$C$_4$$^3$C$_1$im][DCA]:** ● [61], ■ [194], ▲ [195], ▼ [206], ◆ [93]; **[C$_4$C$_1$im][TFA]**: ● [61], ■ [29], ▲ [63], ▼ [91], ◆ [201]; **[$^1$C$_4$$^3$C$_1$im][FSI]:** ● [111]; **[$^1$C$_4$$^3$C$_1$im][BETI]:** ● [111], ■ [29].

Some literature data was found for the electrical conductivity of these five ionic liquids, although it is still a much lower number compared to viscosity. While there are some disparities, a good part of the data is within ± 5% relative to the results obtained in this work. Positive deviations (higher conductivities) might be due to a higher water content of the IL sample, while negative deviations (lower conductivities) might be associated with the effect of solution polarization.

### 5.2.4. Molar Conductivity

The VFT coefficients (Eq 2.44) obtained from the experimental molar conductivity-temperature data, $\Lambda(T)$, are presented in Table 5.53 and in Fig. 5.88.

**Table 5.53.** Fitting coefficients used to describe the temperature dependence of molar conductivity of the studied [$^1C_4{}^3C_1$im][X] ILs.

| Ionic Liquid | $\frac{T_{\text{interval}}}{\text{K}}$ | $\frac{10^4 \cdot A_\Lambda}{\text{S} \cdot \text{m}^2 \cdot \text{mol}^{-1}}$ | $\frac{B_\Lambda}{\text{K}}$ | $\frac{C_\Lambda}{\text{K}}$ |
|---|---|---|---|---|
| [$^1C_4{}^3C_1$im][Ac] | 283 – 333 | 611.4 ± 77.2 | 1001 ± 34 | 183.6 ± 2.3 |
| [$^1C_4{}^3C_1$im][DCA] | 283 – 333 | 258.2 ± 4.2 | 610.2 ± 4.6 | 170.8 ± 0.5 |
| [$^1C_4{}^3C_1$im][TFA] | 283 – 333 | 259.9 ± 3.4 | 757.6 ± 3.7 | 171.7 ± 0.3 |
| [$^1C_4{}^3C_1$im][FSI] | 283 – 333 | 203.9 ± 1.4 | 626.9 ± 2.0 | 163.5 ± 0.2 |
| [$^1C_4{}^3C_1$im][BETI] | 283 – 333 | 290.1 ± 3.4 | 805.2 ± 3.3 | 171.9 ± 0.3 |

The presented fitting coefficients were derived from the experimental $\Lambda(T)$ data (appendix) by applying the VFT fitting function, Eq. 2.44. The standard uncertainties related to the VFT coefficients were calculated to the confidence level of 0.95 ($k \approx 2$).

The molar conductivities at the reference temperature ($T$ = 298.15 K) are presented in Table 5.54, together with the energy barrier and strength parameter derived from Eq. 2.47 and Eq. 2.49, respectively. The temperature dependence of molar conductivity and the derived energy barrier, $E_\Lambda$, are represented in Fig. 5.89.

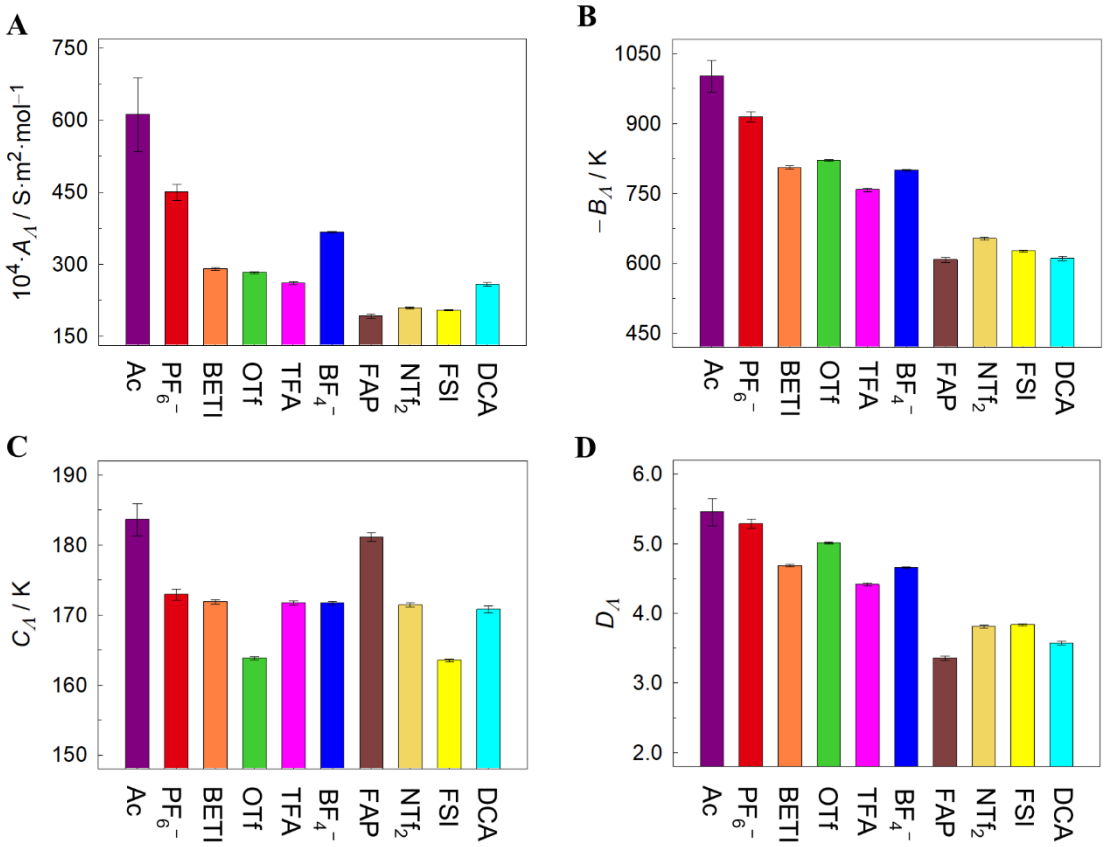



**Figure 5.88.** Effect of the anion on the VFT coefficients derived from the experimental molar conductivity-temperature data of the [$^1C_4{}^3C_1$im][X] ILs. **A**: Pre-exponential coefficient ($A_\Lambda$); **B**: energy barrier-related coefficient ($B_\Lambda$); **C**: Vogel temperature ($C_\Lambda$); **D**: Strength parameter ($D_\Lambda$).

**Table 5.54.** Molar conductivity and derived energy barrier of the studied [$^1C_4{}^3C_1$im][X] ILs at the reference temperature ($T$ = 298.15 K), together with the strength parameter.

| Ionic Liquid | $10^4 \cdot \Lambda(T{=}298.15\ \mathrm{K})$ / S · m² · mol⁻¹ | $E_\Lambda(T{=}298.15\ \mathrm{K})$ / kJ · mol⁻¹ | $D_\Lambda$ |
|---|---|---|---|
| [$^1C_4{}^3C_1$im][Ac] | 98.00 ± 0.05 | 56.38 ± 2.97 | 5.452 ± 0.197 |
| [$^1C_4{}^3C_1$im][DCA] | 2143 ± 2 | 27.81 ± 0.30 | 3.573 ± 0.029 |
| [$^1C_4{}^3C_1$im][TFA] | 649.9 ± 0.4 | 35.02 ± 0.24 | 4.412 ± 0.023 |
| [$^1C_4{}^3C_1$im][FSI] | 1938 ± 2 | 25.56 ± 0.11 | 3.834 ± 0.013 |
| [$^1C_4{}^3C_1$im][BETI] | 492.8 ± 0.2 | 37.34 ± 0.23 | 4.684 ± 0.021 |

$\Lambda(T = 298.15\ \mathrm{K})$ and $E_\Lambda(T = 298.15\ \mathrm{K})$ were calculated from the fitting coefficients presented in Table 5.53 and by applying Eq. 2.44 and Eq. 2.47, respectively. The strength parameter was calculated by Eq. 2.49, $D_\Lambda = B_\Lambda / C_\Lambda$. The relative standard uncertainty associated with the viscosity measurements was estimated as $u(\Lambda)$ = 1.5% (Eq. 4.15); The standard uncertainty associated with the derived energy barrier, $u(E_\Lambda)$, and strength parameter, $u(D_\Lambda)$, was calculated by applying the propagation of uncertainty to Eq. 2.47 and Eq. 2.49, respectively.

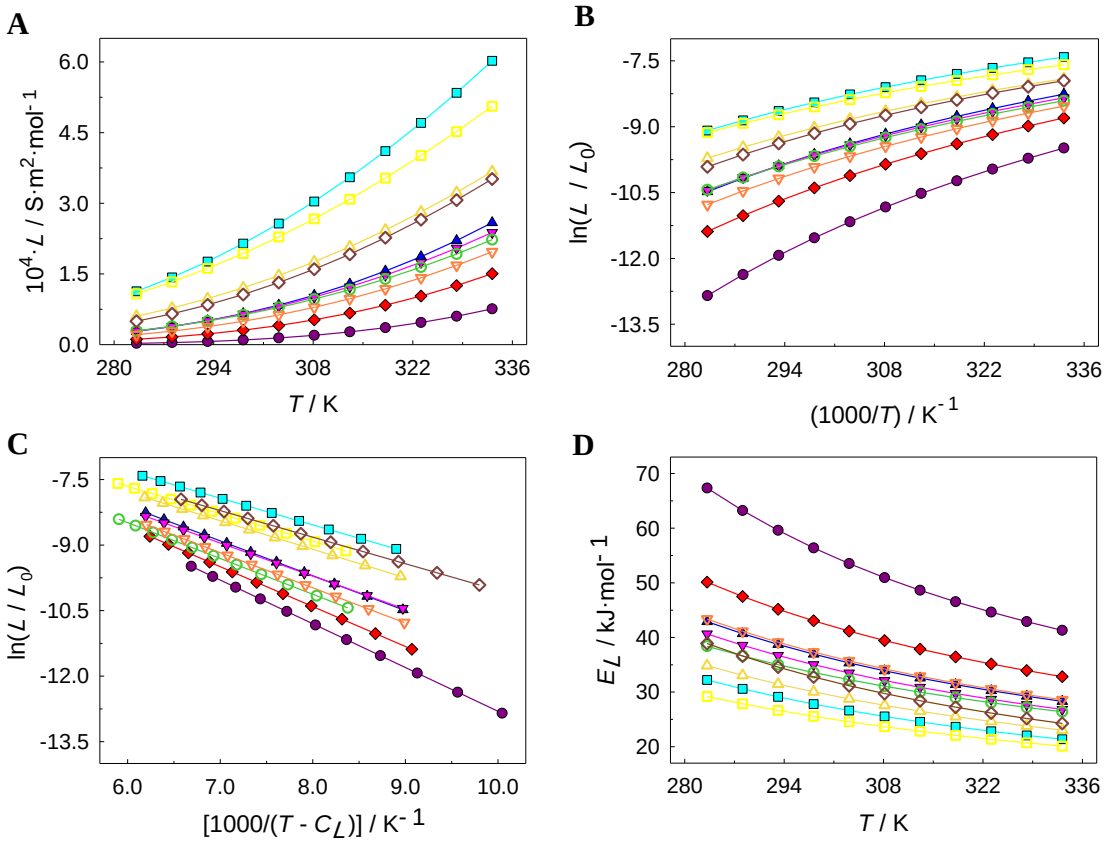



**Figure 5.89.** Temperature dependence of the molar conductivity and derived energy barrier of the studied $[^1C_4{}^3C_1im][X]$ ILs. **A**: Molar Conductivity; **B**: Arrhenius representation; **C**: VFT representation; **D**: Energy barrier. ● $[^1C_4{}^3C_1im][Ac]$; ■ $[^1C_4{}^3C_1im][DCA]$; ▲ $[^1C_4{}^3C_1im][BF_4]$; ▼ $[^1C_4{}^3C_1im][TFA]$; ◆ $[^1C_4{}^3C_1im][PF_6]$; ○ $[^1C_4{}^3C_1im][OTf]$; □ $[^1C_4{}^3C_1im][FSI]$; △ $[^1C_4{}^3C_1im][NTf_2]$ ▽ $[^1C_4{}^3C_1im][BETI]$; ◇ $[^1C_4{}^3C_1im][FAP]$. $\Lambda_0$ = 1 S·m²·mol⁻¹.

### 5.2.5. Discussion

A graphical summary of the results obtained for the measured transport properties and respective derived parameters is presented in Fig. 5.90.

Based on the obtained experimental results, the viscosity and molar conductivity of the studied ILs at the reference temperature of 298.15 K follow the order:

***η*(298.15 K):**

$$Ac > PF_6^- > BETI > BF_4^- > OTf > TFA > FAP > NTf_2 > FSI > DCA$$

***Λ*(298.15 K):**

$$Ac < PF_6^- < BETI < OTf < TFA < BF_4^- < FAP < NTf_2 < FSI < DCA$$

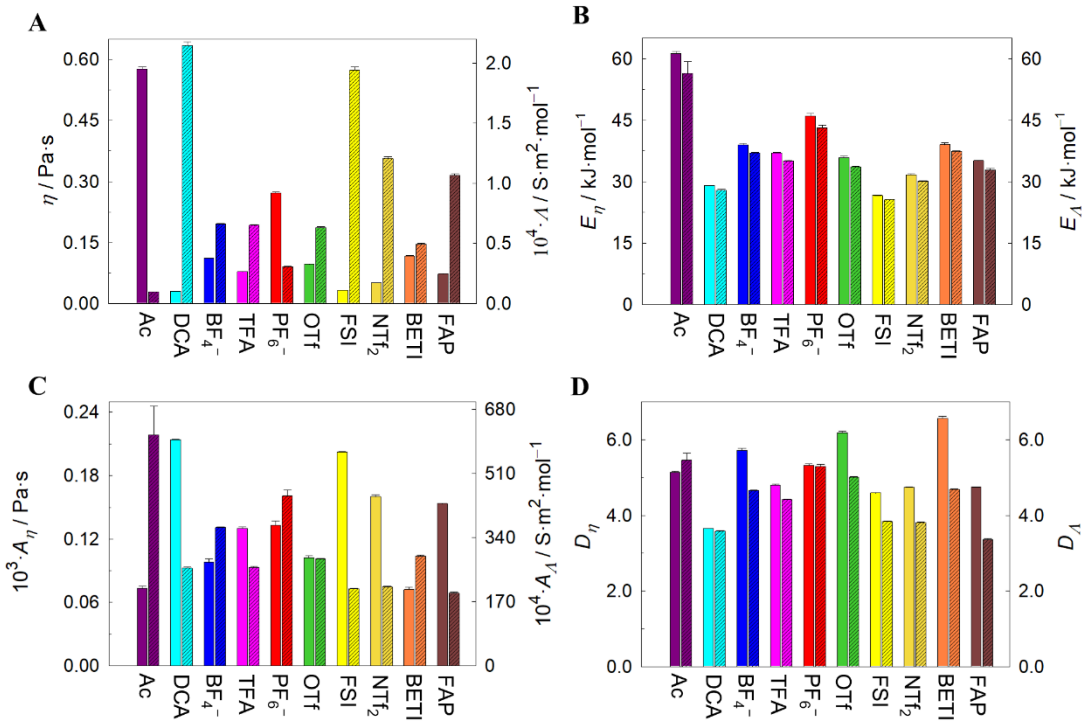



**Figure 5.90.** Graphical summary of the results obtained for the measured transport properties and respective derived parameters of the $[^1C_4{}^3C_1im][X]$ ILs. **A**: Viscosity and molar conductivity; **B**: Energy barrier; **C**: Pre-exponential coefficient; **D**: Strength parameter. **Plain bars**: viscosity (left); **Dashed bars**: molar conductivity (right).

As expected, besides some exceptions ($BF_4^-$, OTf, TFA), these orders are the reverse of each other, indicating that the molar conductivity is mainly described by the viscosity of the system. These orders are in good agreement with previous works based on the $[^1C_4{}^3C_1im]^+$ cation [29, 54, 55, 61, 111, 207, 208], as well as other works focused on other imidazolium-based cations with different alkyl chain sizes, $[^1C_2{}^3C_1im]^+$ [50, 53, 111] and $[^1C_6{}^3C_1im]^+$ [41]. Some previous works suggested that it should be expected for the molar conductivity to be lower for ILs with larger anions as these systems are usually related to lower mobilities [54, 209]. However, as can be seen by looking at the obtained trend, there is no direct relation between the electrical conductivity of the IL and the size of the anions. The presented trend seems to be better described by the interactions and cohesive energy, as the higher viscosities and lower molar conductivity values are observed for the Ac (strong hydrogen donor) and $PF_6^-$ (low charge dispersion) while larger anions with a higher degree of charge dispersion such as FAP, $NTf_2$, and FSI were found to present higher molar conductivities. This observation is in good agreement with trends reported in other works [29, 41, 53, 61, 90, 208]. Based on this, the two main factors opposing the primary reasoning of larger ion dimensions leading to lower

mobilities are: the presence of strong/localized interactions; charge delocalization [208]. This is in agreement with the dual effect of superficial electrical charge density and the level of dynamics suggested by Vila *et al.* [53]. At a first glance, BETI might seem an outlier to this trend as it presents the third lowest molar conductivity amongst the studied ILs. However, by comparing its $\Lambda_{298.15K}$ with the values of the structurally similar $NTf_2$ and FSI anion, a strong correlation between the molar conductivity and the number of carbons in the perfluoroalkyl chain (~ $-0.72 \times 10^{-4}$ $S \cdot m^2 \cdot mol^{-1}$ per $-CF_2-$ increment) was found.

From the results obtained in this work, the following order for both energy barriers, $E_\eta$ and $E_\Lambda$, at the reference temperature of 298.15 K was derived:

**$E_\eta$(298.15 K) and $E_\Lambda$(298.15 K) :**

$$FSI < DCA < NTf_2 < FAP < OTf < TFA < BF_4^- < BETI < PF_6^- < Ac$$

By interpreting the conduction mechanism as an activated process, $E_\Lambda$ can be thought of as the energy needed to promote ion conduction. Therefore, this property should be a good indicator of the cohesive energy of the ionic liquid, which in turn is related to the strength of interactions and the order of the liquid phase. Overall, this is coherent with the presented trend, as Ac, due to its chemical characteristics, is likely to interact strongly with H(C2). Furthermore, the small, symmetric, and sphere-like anions such as $BF_4^-$ and $PF_6^-$ should yield stronger electrostatic interactions compared to the larger and highly charged delocalized anions, such as $NTf_2$ and FAP. The presence of the perfluoroalkyl chain favors charge dispersion, which leads to less strongly localized systems, thus smoothing the potential energy valleys and reducing the energy barrier [90, 208]. Meanwhile, mid-size anions with decent donor ability, OTf, and TFA can be found in the middle of the trend. The BETI anion seems to be an exception to this reasoning, being placed between $BF_4^-$ and $PF_6^-$. However, the same relative order was identified by calculating the $E_\Lambda$($T$=298.15 K) based on the VFT coefficients from the work of Tokuda *et al.* [29] and the review of Nancarrow *et al.* [207]. The high value of the energy barrier for BETI-based IL is related to the strong dispersive interactions due to the increase of the fluorinated chain. Looking at the VFT coefficients, the following order was found for the pre-exponential coefficient, $A_\Lambda$:

***$A_\eta$*:**

$$DCA > FSI > NTf_2 > FAP > PF_6^- > TFA > OTf > BF_4^- > Ac > BETI$$

***$A_\Lambda$*:**

$$FAP < FSI < NTf_2 < DCA < TFA < OTf < BETI < BF_4^- < PF_6^- < Ac$$

While overall, these two orders are similar (in reverse), there are some exceptions. The coefficients $A_\eta$ and $A_\Lambda$ can be interpreted as the viscosity and molar conductivity in conditions where the energy barrier is already overcome. Virtually, the coefficients $A_\Lambda$ reflect the contribution of electrical conductivity without the impact of the cohesive interaction, and therefore, the magnitude of $A_\Lambda$ is related to the size, shape, and dynamics of the anions. Overall, lower $A_\eta$ and higher $A_\Lambda$ values were obtained for smaller and more regular-shaped anions with higher dynamics ($BF_4^-$, $PF_6^-$, Ac). On the other hand, higher $A_\eta$ and lower $A_\Lambda$ values for larger and more sterically hindered anions (FSI, $NTf_2$, FAP). These results highlight the cohesive energy – size/shape/dynamics balance that essentially rules the transport properties of the ionic liquids and are strongly correlated with the interpretation of Leys *et al.* [208]. Interestingly, [$^1C_4{}^3C_1$im][BETI] (the second largest anion) seems to be an outlier as it presents low $A_\eta$ and high $A_\Lambda$ (indicates high mobility). Considering the anionic family FSI, $NTf_2$, and BETI, it is observed that $A_\eta$ decreases and $A_\Lambda$ increases with the increase of the perfluoroalkyl chain, which is consistent with the results from the study of the effect of the cations alkyl chain (previous section). Therefore, the derived results for [$^1C_4{}^3C_1$im][BETI] might be related to surface-volume or cation-anion size ratios.

Additionally, the VFT coefficients can be related to the liquid fragility as introduced by Angell *et al.* [210]. Glass-forming liquids are divided into strong and fragile, depending on how their properties are affected by changes in temperature. The fragility-related parameter, $D_\Lambda = |B_\Lambda / C_\Lambda|$, is inversely related to the fragility (higher $D_\Lambda$ parameter indicates lower fragility of the liquid). Our derived experimental results listed in Table 5.51 as well as the values fores [$^1C_4{}^3C_1$im][X] presented previously, were found to be below 6, which is in agreement with the expected fragile behavior of the ionic liquids [211, 212]. Overall, the anions that promote stronger interactions were found to yield lower fragilities (higher $D_\Lambda$ value). The following trend was found for $D_\Lambda$ value:

**$D_\eta$ (higher to lower fragility):**

$$FSI < NTf_2 < FAP < TFA < Ac < DCA < PF_6^- < BF_4^- < OTf < BETI$$

**$D_\Lambda$ (higher to lower fragility):**

$$FAP < DCA < FSI < NTf_2 < TFA < BF_4^- < BETI < OTf < PF_6^- < Ac$$

While overall, there are some similarities (in reverse order) between these two orders, they are not exactly the same. This might be due to a differentiation between viscosity and molar conductivity temperature dependences or differences in the experimental temperature range. Since the viscosity measurements were performed in a broader temperature range, the interpretation of the anion effect on the IL fragility will be done based on the viscosity results. Moreover, being a mechanical property, viscosity-derived data should be expected to provide a more accurate insight into the liquid fragility. Fragility can also be interpreted as a measurement of the deviation from the regular Arrhenius behavior [211, 212]. This deviation is associated with the dependence of the energy barrier on temperature. The temperature dependence of the energy barrier (Eq. 2.47) is only dependent on the $C_\eta$ coefficient, as higher $C_\eta$ leads to a higher temperature dependence of the energy barrier, $E_\eta$ ($T$). Based on the obtained results, [$^1C_4{}^3C_1$im][Ac] presents by far the highest value of $C_\eta$ (189.7 K). The remaining ILs can be subdivided into 3 groups. [$^1C_4{}^3C_1$im][FAP], [$^1C_4{}^3C_1$im][TFA], [$^1C_4{}^3C_1$im][DCA], and [$^1C_4{}^3C_1$im][$PF_6$] were found to present higher $C_\Lambda$ coefficients after their acetate analogue (168 – 176 K). On the other hand, [$^1C_4{}^3C_1$im][FSI], [$^1C_4{}^3C_1$im][BETI], and [$^1C_4{}^3C_1$im][OTf] lower $C_\eta$ coefficients (156 – 158 K). The remaining ILs present intermediate $C_\eta$ coefficients (163 – 165 K). The higher $C_\eta$ coefficients are also typically well-correlated with higher glass transition temperatures and higher liquid fragility (decrease of $D_\eta$ parameter). However, in this series, the IL with the highest $C_\eta$ value, [$^1C_4{}^3C_1$im][Ac], presents one of the lowest fragilities (high $D_\eta$) of the series due to the compensation of the $B_\eta$ coefficient. The high value of $B_\eta$ of this IL is a reflection of the strong cohesive interactions in [$^1C_4{}^3C_1$im][Ac], particularly the effect of the hydrogen bond between the imidazolium and the acetate group.

The experimental viscosity and molar conductivity data were used to construct Walden plots (Fig. 5.91) for the [$^1C_4{}^3C_1$im][X] ILs.

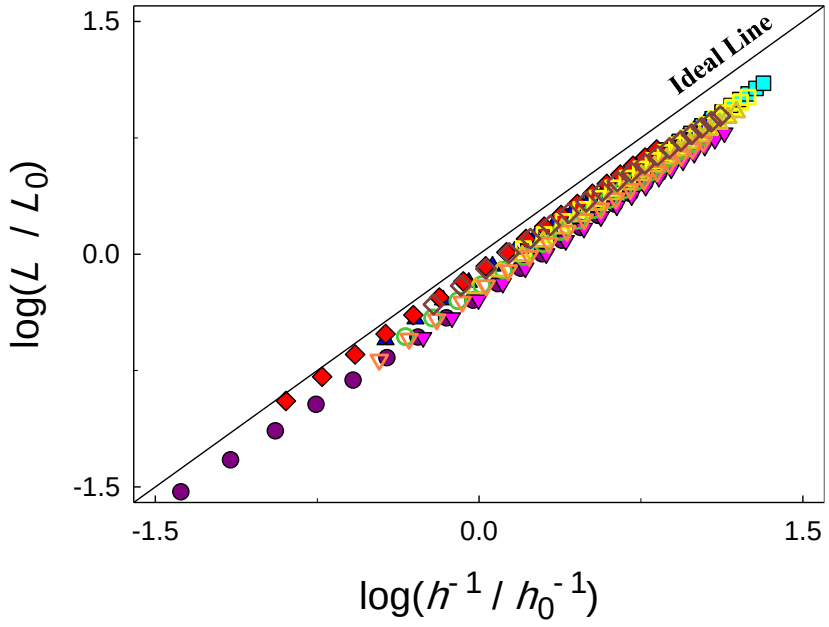



**Figure 5.91.** Walen plot for the [$^1C_4{}^3C_1$im][X] ILs based on the experimental viscosity and molar conductivity results. ● [$^1C_4{}^3C_1$im][Ac]; ■ [$^1C_4{}^3C_1$im][DCA]; ▲ [$^1C_4{}^3C_1$im][$BF_4$]; ▼ [$^1C_4{}^3C_1$im][TFA]; ◆ [$^1C_4{}^3C_1$im][$PF_6$]; ○ [$^1C_4{}^3C_1$im][OTf]; □ [$^1C_4{}^3C_1$im][FSI]; △ [$^1C_4{}^3C_1$im][$NTf_2$] ▽ [$^1C_4{}^3C_1$im][BETI]; ◇ [$^1C_4{}^3C_1$im][FAP]. $\eta_0$ = 1 Poise; $\Lambda_0$ = 1 S·cm$^2$·mol$^{-1}$.

As expected, all [$^1C_4{}^3C_1$im][X] ionic liquids show a negative deviation to the "ideal Walden line". Moreover, Figure 5.91 reveals a slight impact of the anion nature on the correlation between viscosity and molar conductivity. To further explore this effect deviation to the ideal Walden line, Δ*w* at the reference temperature (*T* = 298.15 K) and the slope of the Walden lines, $\alpha_w$, are graphically presented in Fig 5.92.

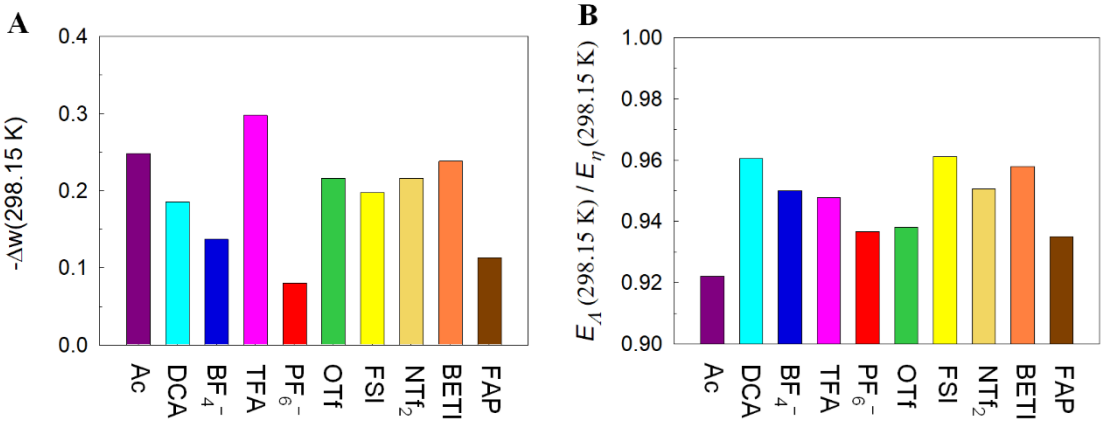



**Figure 5.92.** Relationship between viscosity and molar conductivity for the [$^1C_4{}^3C_1$im][X] ILs. **A:** Deviation to the "ideal Walden line" (log $\Lambda$ – log $\eta^{-1}$) at the reference temperature (*T* = 298.15 K); **B:** Energy barrier ratio ($E_\Lambda/E_\eta$) at the reference temperature (*T* = 298.15 K).

Based on the results, ILs with spheric anions ($PF_6^-$, $BF_4^-$, and FAP) present the least deviation from the “ideal Walden line”) which suggests a stronger correlation between viscosity and molar conductivity. The remaining ILs that present larger deviations from the “ideal Walden line” can be divided into two groups:

1. Anions with a more branched shape/structure and high charge distribution: DCA, FSI, $NTf_2$, and BETI
2. Anions with high hydrogen bonding ability:
   Ac, TFA, and OTf

This highlights the loss of sphericity and charge dispersions as factors for a more complex ion-conducing mechanism when compared to the simpler sphere model. Furthermore, it also supports the presence of ion aggregation/association, which leads to a decrease in molar conductivity.

## 5.3. Effect of the Cation Nature

This section is divided into three works:

1. Nature of the cationic ring (imidazolium vs. pyridinium vs. pyrrolidinium)
2. Isomerization of the pyridinium ring
3. C2-methylation of the imidazolium ring

### 5.3.1. Effect of the Nature of the Cationic Ring

The effect of the nature of the cationic ring was explored by studying the transport properties of 1-butyl-3-methylimidazolium $[^1C_4{}^3C_1im]^+$, 1-butylpyridinium $[^1C_4py]^+$, 1-butyl-1-methylpyrrolidinium $[^1C_4{}^1C_1pyr]^+$. The cation effect is further explored by pairing the selected cations with three different anions, $NTf_2$, OTf, and FAP (Fig. 5.93). In this section the data for $[^1C_4py][OTf]$, $[^1C_4{}^1C_1pyr][OTf]$, and $[^1C_4{}^1C_1pyr][FAP]$ will be presented and combined with the remaining selected ILs from Fig. 5.93 which were already described in the previous sections.

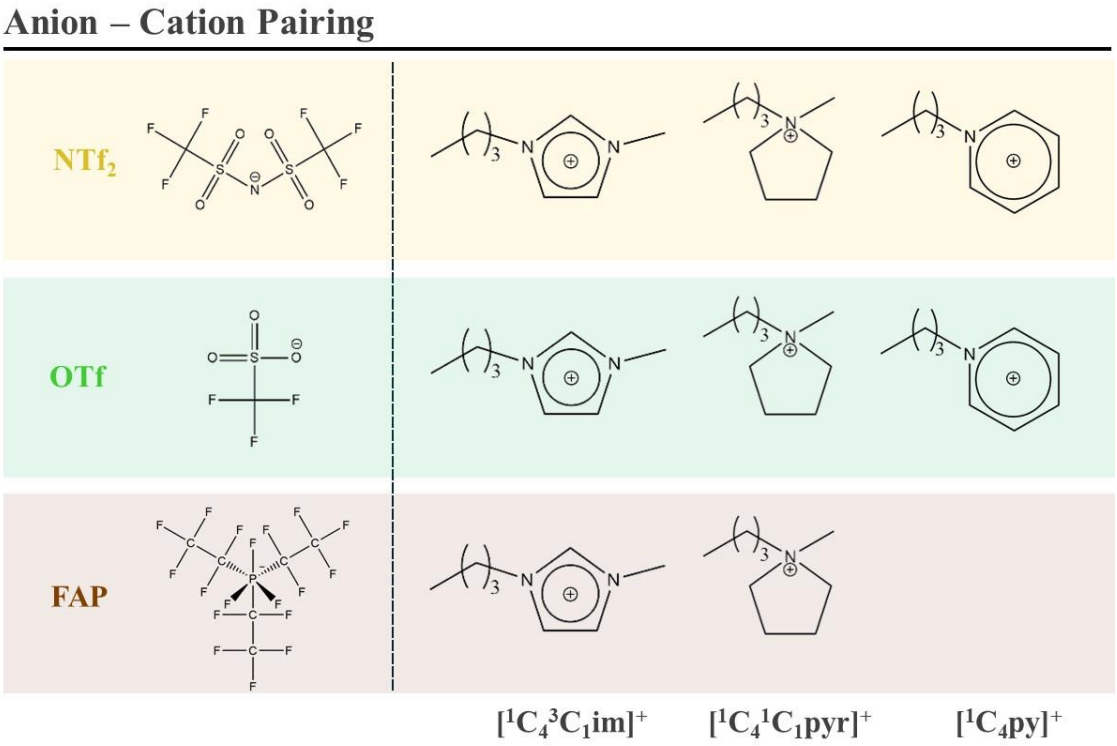



**Figure 5.93.** Schematic representation of the study strategy on the effect of the cation-anion pairing.

#### 5.3.1.1. Density

The derived fitting coefficients from the temperature dependence of the density of the selected ILs (Eq. 2.4) are presented in Table 5.55. The densities at the reference temperature ($T$ = 298.15 K) are presented in Table 5.56, together with the molar volume and thermal expansion coefficient derived from Eq. 2.2 and Eq. 2.7 respectively. The graphical representation of density, thermal expansion coefficient, and molar volume as functions of temperature and at the reference temperature (T = 298.15 K) are presented in Fig 5.94.

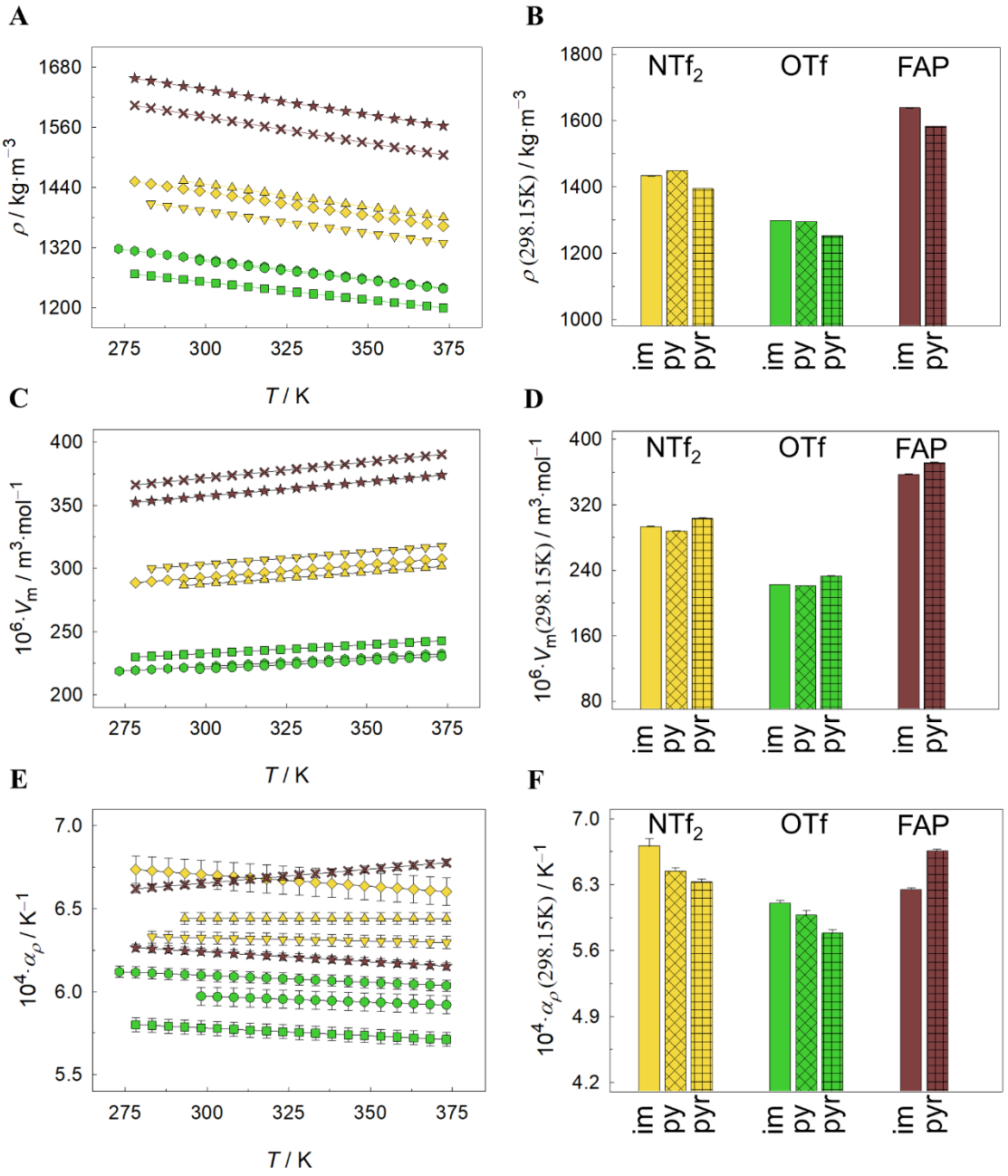



**Figure 5.94.** Density and derived properties of the selected imidazolium, pyridinium, and pyrrolidinium ILs as functions of temperature (A, C, E) and at the reference temperature, $T$ = 298.15 K, (B, D, F). **A**, **B**: Density; **C**, **D**: Molar volume; **E**, **F**: Thermal expansion coefficient. ◆ [$^1$C$_4$$^3$C$_1$im][NTf$_2$], ▲ [$^1$C$_4$py][NTf$_2$], ▼ [$^1$C$_4$$^1$C$_1$pyr][NTf$_2$] , ⬢ [$^1$C$_4$$^3$C$_1$im][OTf], ● [$^1$C$_4$py][OTf], ■ [$^1$C$_4$$^1$C$_1$pyr][OTf], ★ [$^1$C$_4$$^3$C$_1$im][FAP], ✖[$^1$C$_4$$^1$C$_1$pyr][FAP].

**Table 5.55.** Fitting coefficients used to describe the temperature dependence of density of [$^1$C$_4$py][OTf], [$^1$C$_4$$^1$C$_1$pyr][OTf], and [$^1$C$_4$$^1$C$_1$pyr][FAP].

| Ionic Liquid | $\frac{T_{\text{interval}}}{\text{K}}$ | $\frac{10^7 \cdot a_2}{\text{K}^{-2}}$ | $\frac{10^4 \cdot a_1}{\text{K}^{-1}}$ | $\frac{a_0}{\text{K}}$ |
|---|---|---|---|---|
| [$^1$C$_4$py][OTf] | 298 − 373 | 0.348 ± 0.082 | −6.180 ± 0.055 | 7.5921 ± 0.0004 |
| [$^1$C$_4$$^1$C$_1$pyr][OTf] | 278 − 373 | 0.469 ± 0.064 | −6.062 ± 0.042 | 7.3094 ± 0.0007 |
| [$^1$C$_4$$^1$C$_1$pyr][FAP] | 278 − 373 | −0.830 ± 0.032 | −6.158 ± 0.021 | 7.5578 ± 0.0003 |

The presented fitting coefficients were derived from the experimental $\rho(T)$ data (appendix) by applying a polynomial fitting function, $\ln[\rho(T)] = a_2T^2 + a_1T + a_0$ (Eq. 2.4). The standard uncertainties related to the fitting coefficients were calculated to the confidence level of 0.95 ($k \approx 2$).

**Table 5.56.** Density, thermal expansion coefficient, and molar volume at the reference temperature ($T$ = 298.15 K) of [$^1$C$_4$py][OTf], [$^1$C$_4$$^1$C$_1$pyr][OTf], and [$^1$C$_4$$^1$C$_1$pyr][FAP].

| Ionic Liquid | $\frac{\rho(298.15\ \text{K})}{\text{kg} \cdot \text{m}^{-3}}$ | $\frac{10^4 \cdot \alpha_\rho(298.15\ \text{K})}{\text{K}^{-1}}$ | $\frac{10^6 \cdot V_\text{m}(298.15\ \text{K})}{\text{m}^3 \cdot \text{mol}^{-1}}$ |
|---|---|---|---|
| [$^1$C$_4$py][OTf] | 1294.2 ± 0.5 | 5.97 ± 0.006 | 220.4 ± 0.6 |
| [$^1$C$_4$$^1$C$_1$pyr][OTf] | 1252.4 ± 0.5 | 5.78 ± 0.004 | 232.6 ± 0.6 |
| [$^1$C$_4$$^1$C$_1$pyr][FAP] | 1582.6 ± 0.5 | 6.65 ± 0.002 | 371.1 ± 1.2 |

$\rho(T = 298.15\ \text{K})$ and $\alpha_\rho(T = 298.15\ \text{K})$ were calculated from the fitting coefficients presented in Table 5.55 and by applying Eq. 2.4 and Eq. 2.7 respectively. $V_\text{m}(298.15\ \text{K}) = M/\rho(298.15\ \text{K})$. The standard uncertainty associated with $\alpha_\rho$ and $V_\text{m}$ were calculated by applying the propagation of uncertainty to Eq. 2.7 and 2.2, respectively.

#### 5.3.1.2. Viscosity

The VFT coefficients (Eq 2.44) obtained from the experimental viscosity-temperature data, $\eta(T)$, for the selected ILs are presented in Table 5.57.

**Table 5.57.** Fitting coefficients used to describe the temperature dependence of viscosity of [$^1$C$_4$py][OTf], [$^1$C$_4$$^1$C$_1$pyr][OTf], and [$^1$C$_4$$^1$C$_1$pyr][FAP].

| Ionic Liquid | $\frac{T_{\text{interval}}}{\text{K}}$ | $\frac{10^3 \cdot A_\eta}{\text{Pa} \cdot \text{s}}$ | $\frac{B_\eta}{\text{K}}$ | $\frac{C_\eta}{\text{K}}$ |
|---|---|---|---|---|
| [$^1$C$_4$py][OTf] | 298 − 373 | 0.1462 ± 0.0056 | 843 ± 11 | 174.3 ± 0.2 |
| [$^1$C$_4$$^1$C$_1$pyr][OTf] | 278 − 373 | 0.1283 ± 0.0007 | 966.8 ± 1.5 | 163.3 ± 0.1 |
| [$^1$C$_4$$^1$C$_1$pyr][FAP] | 278 − 373 | 0.1161 ± 0.0014 | 945.4 ± 2.9 | 172.4 ± 0.2 |

The presented fitting coefficients were derived from the experimental $\eta(T)$ data (appendix) by applying the VFT fitting function, Eq. 2.44. The standard uncertainties related to the VFT coefficients were calculated to the confidence level of 0.95 ($k \approx 2$).

The viscosities at the reference temperature ($T$ = 298.15 K) for the selected ILs are presented in Table 5.58, together with the energy barrier and strength parameter derived from Eq. 2.47 and Eq. 2.49, respectively.

**Table 5.58.** Viscosity and derived energy barrier of [$^1$C$_4$py][OTf], [$^1$C$_4$$^1$C$_1$pyr][OTf], and [$^1$C$_4$$^1$C$_1$pyr][FAP] ILs at the reference temperature ($T$ = 298.15 K), together with the strength parameter.

| Ionic Liquid | $\eta(T=298.15\ \text{K})$ / Pa · s | $E_\eta(T=298.15\ \text{K})$ / kJ · mol$^{-1}$ | $D_\eta$ |
|---|---|---|---|
| [$^1$C$_4$py][OTf] | 0.1326 ± 0.0013 | 40.64 ± 0.54 | 4.839 ± 0.062 |
| [$^1$C$_4$$^1$C$_1$pyr][OTf] | 0.1667 ± 0.0017 | 39.30 ± 0.08 | 5.92 ± 0.10 |
| [$^1$C$_4$$^1$C$_1$pyr][FAP] | 0.2137 ± 0.0021 | 44.19 ± 0.20 | 5.484 ± 0.018 |

$\eta(T = 298.15\ \text{K})$ and $E_\eta(T = 298.15\ \text{K})$ were calculated from the fitting coefficients presented in Table 5.57 and by applying Eq. 2.44 and Eq. 2.47, respectively. The strength parameter was calculated by Eq. 2.49, $D_\eta = B_\eta / C_\eta$. The relative standard uncertainty associated with the viscosity measurements was estimated as $u(\eta)$ = 1.0% (Eq. 2.72); The standard uncertainty associated with the derived energy barrier, $u(E_\eta)$, and strength parameter, $u(D_\eta)$, was calculated by applying the propagation of uncertainty to Eq. 2.47 and Eq. 2.49, respectively.

The temperature dependence of the viscosity and derived properties is presented in Fig. 5.95.

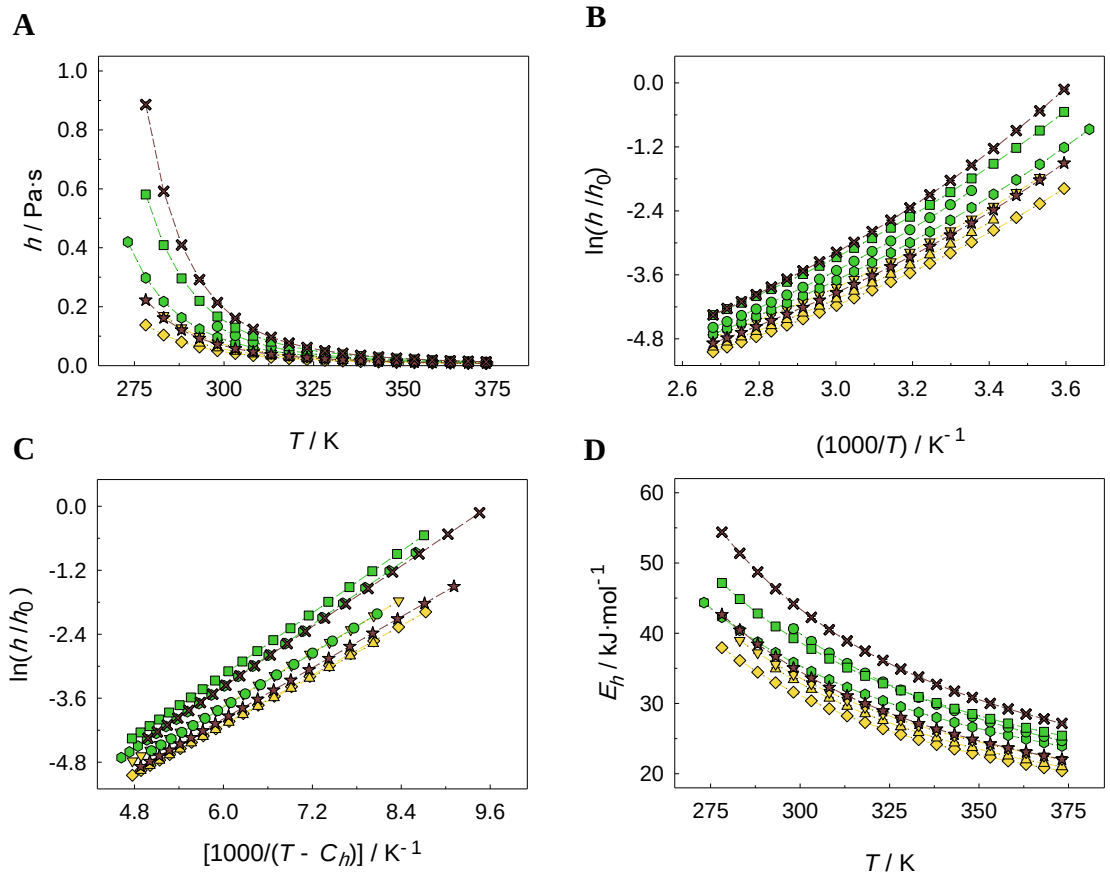



**Figure 5.95.** Temperature dependence of viscosity for the selected imidazolium, pyridinium, and pyrrolidinium. **A**: viscosity, **B**: Arrhenius representation; **C**: VFT representation; **D**: Energy barrier. ◆ [$^1$C$_4$$^3$C$_1$im][NTf$_2$], ▲ [$^1$C$_4$py][NTf$_2$] , ▼ [$^1$C$_4$$^1$C$_1$pyr][NTf$_2$] , ⬢ [$^1$C$_4$$^3$C$_1$im][OTf], ● [$^1$C$_4$py][OTf], ■ [$^1$C$_4$$^1$C$_1$pyr][OTf], ★ [$^1$C$_4$$^3$C$_1$im][FAP], ✖[$^1$C$_4$$^1$C$_1$pyr][FAP]. $\eta_0$ = 1 Pa·s.

The deviation of the available viscosity data to the experimental results for [$^1$C$_4$py][OTf], [$^1$C$_4$$^1$C$_1$pyr][OTf], and [$^1$C$_4$$^1$C$_1$pyr][FAP] is presented in Fig. 5.96.

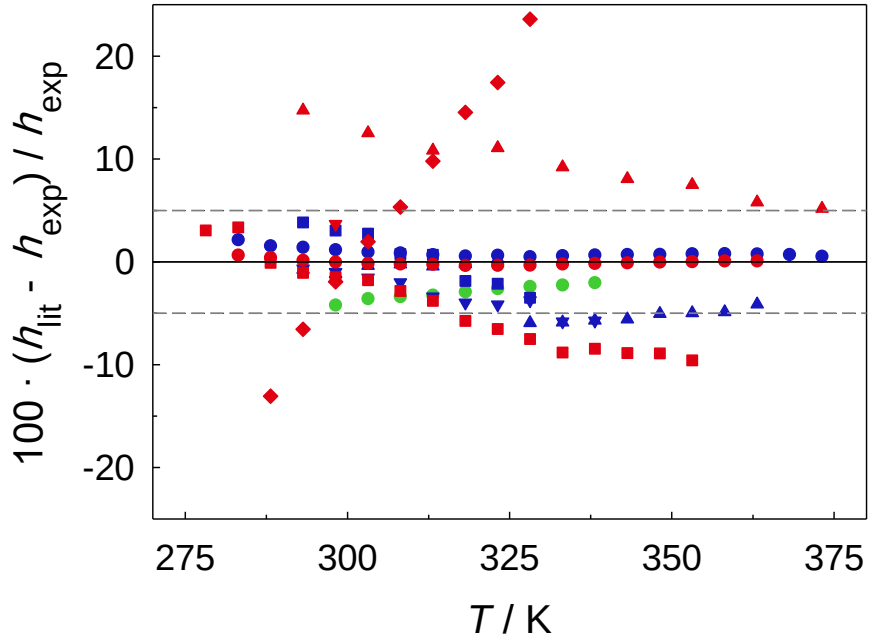



**Figure 5.96.** Deviation of the available viscosity data to the experimental results for [$^1$C$_4$py][OTf], [$^1$C$_4$$^1$C$_1$pyr][OTf], and [$^1$C$_4$$^1$C$_1$pyr][FAP]. **[$^1$C$_4$py][OTf]:** ● [213]; **[$^1$C$_4$$^1$C$_1$pyr][OTf]:** ● [214], ■ [146], ▲ [215], ▼ [80]; **[$^1$C$_4$$^1$C$_1$pyr][FAP]:** ● [214]; ■ [146]; ▲ [216]; ▼ [217]; ◆ [218].

Overall, most of the data is in good agreement with the experimental results, particularly the data reported by Gaciño *et al.* [214] for [$^1$C$_4$$^1$C$_1$pyr][OTf] and [$^1$C$_4$$^1$C$_1$pyr][FAP]. On the other hand, some data for [$^1$C$_4$$^1$C$_1$pyr][FAP] seems to have strong temperature dependence [78, 216, 218].

#### 5.3.1.3. Electrical Conductivity

The VFT coefficients (Eq 2.24) obtained from the experimental electrical conductivity-temperature data, $\sigma(T)$, are presented in Table 5.59.

**Table 5.59.** Fitting coefficients used to describe the temperature dependence of electrical conductivity of [$^1$C$_4$py][OTf], [$^1$C$_4$$^1$C$_1$pyr][OTf], and [$^1$C$_4$$^1$C$_1$pyr][FAP].

| Ionic Liquid | $A_\sigma$ / S · m$^{-1}$ | $B_\sigma$ / K | $C_\sigma$ / K | $\sigma(T$=298.15 K) / S · m$^{-1}$ |
|---|---|---|---|---|
| [$^1$C$_4$py][OTf] | 106.0 ± 1.8 | 782.8 ± 4.9 | 173.2 ± 0.5 | 0.2016 ± 0.0030 |
| [$^1$C$_4$$^1$C$_1$pyr][OTf] | 101.9 ± 1.1 | 803.2 ± 3.2 | 169.7 ± 0.3 | 0.1961 ± 0.0029 |
| [$^1$C$_4$$^3$C$_1$im][FAP] | 62.56 ± 0.49 | 694.4 ± 4.2 | 185.4 ± 0.4 | 0.1323 ± 0.0020 |

The presented fitting coefficients were derived from the experimental $\sigma(T)$ data (appendix) by applying the VFT fitting function, Eq. 2.44. The standard uncertainties related to the VFT coefficients were calculated to the confidence level of 0.95 ($k \approx 2$). The relative standard uncertainty associated with the viscosity measurements was estimated as $u(\sigma)$ = 1.5% (Eq. 4.15).

The deviation of the available electrical conductivity data to the experimental results for [$^1$C$_4$py][OTf], [$^1$C$_4$$^1$C$_1$pyr][OTf], and [$^1$C$_4$$^1$C$_1$pyr][FAP] is presented in Fig. 5.97. Only one literature source was found for each ionic liquid. Overall, the results are reasonably in good agreement with the experimental data. The discrepancies might arise from the difference in the measuring method, sample purity, or polarization effects.

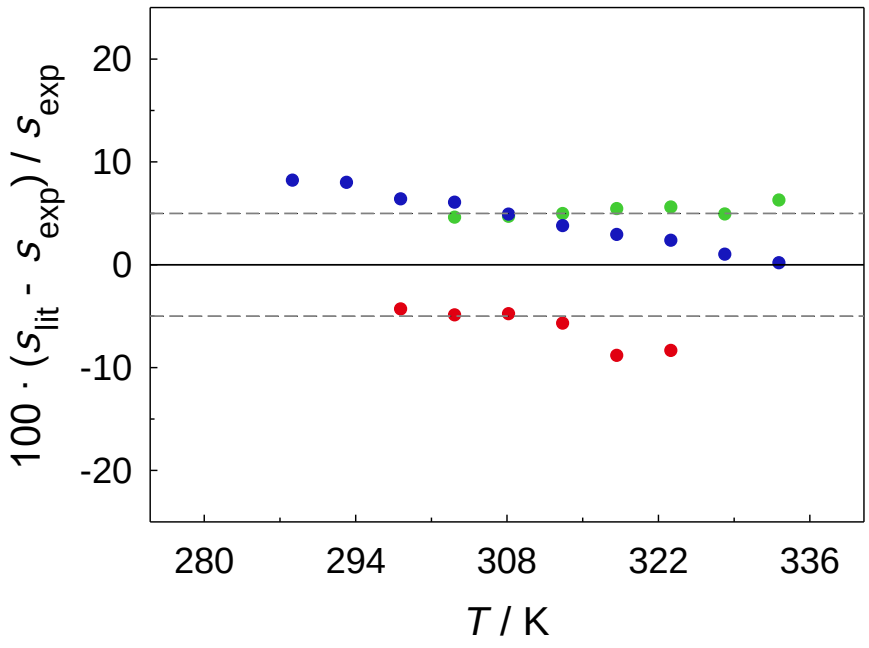



**Figure 5.97.** Deviation of the available electrical conductivity data to the experimental results for [$^1$C$_4$py][OTf], [$^1$C$_4$$^1$C$_1$pyr][OTf], and [$^1$C$_4$$^1$C$_1$pyr][FAP]. **[$^1$C$_4$py][OTf]:** ● [213]; **[$^1$C$_4$$^1$C$_1$pyr][OTf]:** ● [219]; **[$^1$C$_4$$^1$C$_1$pyr][FAP]:** ● [220].

#### 5.3.1.4. Molar Conductivity

The VFT coefficients (Eq 2.44) obtained from the experimental molar conductivity-temperature data, $\Lambda(T)$, for the selected ILs are presented in Table 5.60.

**Table 5.60.** Fitting coefficients used to describe the temperature dependence of molar conductivity of [$^1$C$_4$py][OTf], [$^1$C$_4$$^1$C$_1$pyr][OTf], and [$^1$C$_4$$^1$C$_1$pyr][FAP].

| Ionic Liquid | $\frac{T \text{ range}}{\text{K}}$ | $\frac{10^4 \cdot A_\Lambda}{\text{S} \cdot \text{m}^2 \cdot \text{mol}^{-1}}$ | $\frac{B_\Lambda}{\text{K}}$ | $\frac{C_\Lambda}{\text{K}}$ |
|---|---|---|---|---|
| [$^1$C$_4$py][OTf] | 298 − 333 | 281.0 ± 5.4 | 820.3 ± 5.7 | 171.0 ± 0.5 |
| [$^1$C$_4$$^1$C$_1$pyr][OTf] | 283 − 333 | 281.7 ± 3.8 | 838.2 ± 4.0 | 167.7 ± 0.3 |
| [$^1$C$_4$$^1$C$_1$pyr][FAP] | 283 − 333 | 239.3 ± 3.5 | 721.1 ± 3.8 | 183.9 ± 0.3 |

The presented fitting coefficients were derived from the experimental $\Lambda(T)$ data (appendix) by applying the VFT fitting function, Eq. 2.44. The standard uncertainties related to the VFT coefficients were calculated to the confidence level of 0.95 ($k \approx 2$).

The molar conductivities at the reference temperature ($T$ = 298.15 K) for the selected ILs are presented in Table 5.61, together with the energy barrier and strength parameter derived from Eq. 2.47 and Eq. 2.49, respectively.

**Table 5.61.** Molar conductivity and derived energy barrier of [$^1$C$_4$py][OTf], [$^1$C$_4$$^1$C$_1$pyr][OTf], and [$^1$C$_4$$^1$C$_1$pyr][FAP] at the reference temperature ($T$ = 298.15 K), together with the strength parameter.

| Ionic Liquid | $\frac{10^4 \cdot \Lambda(T\text{=}298.15\text{ K})}{\text{S} \cdot \text{m}^2 \cdot \text{mol}^{-1}}$ | $\frac{E_\Lambda(T\text{=}298.15\text{ K})}{\text{kJ} \cdot \text{mol}^{-1}}$ | $D_\Lambda$ |
|---|---|---|---|
| [$^1$C$_4$py][OTf] | 0.4435 ± 0.0067 | 37.50 ± 0.39 | 4.797 ± 0.036 |
| [$^1$C$_4$$^1$C$_1$pyr][OTf] | 0.4563 ± 0.0068 | 36.41 ± 0.24 | 4.998 ± 0.025 |
| [$^1$C$_4$$^1$C$_1$pyr][FAP] | 0.4344 ± 0.0065 | 40.83 ± 0.30 | 3.921 ± 0.022 |

$\Lambda(T$ = 298.15 K) and $E_\Lambda(T$ = 298.15 K) were calculated from the fitting coefficients presented in Table 5.60 and by applying Eq. 2.44 and Eq. 2.47, respectively. The strength parameter was calculated by Eq. 2.49, $D_\Lambda = B_\Lambda / C_\Lambda$. The relative standard uncertainty associated with the viscosity measurements was estimated as $u(\Lambda)$ = 1.5% (Eq. 4.15); The standard uncertainty associated with the derived energy barrier, $u(E_\Lambda)$, and strength parameter, $u(D_\Lambda)$, was calculated by applying the propagation of uncertainty to Eq. 2.47 and Eq. 2.49, respectively.

The temperature dependence of the molar conductivity and derived properties is presented in Fig. 5.98.

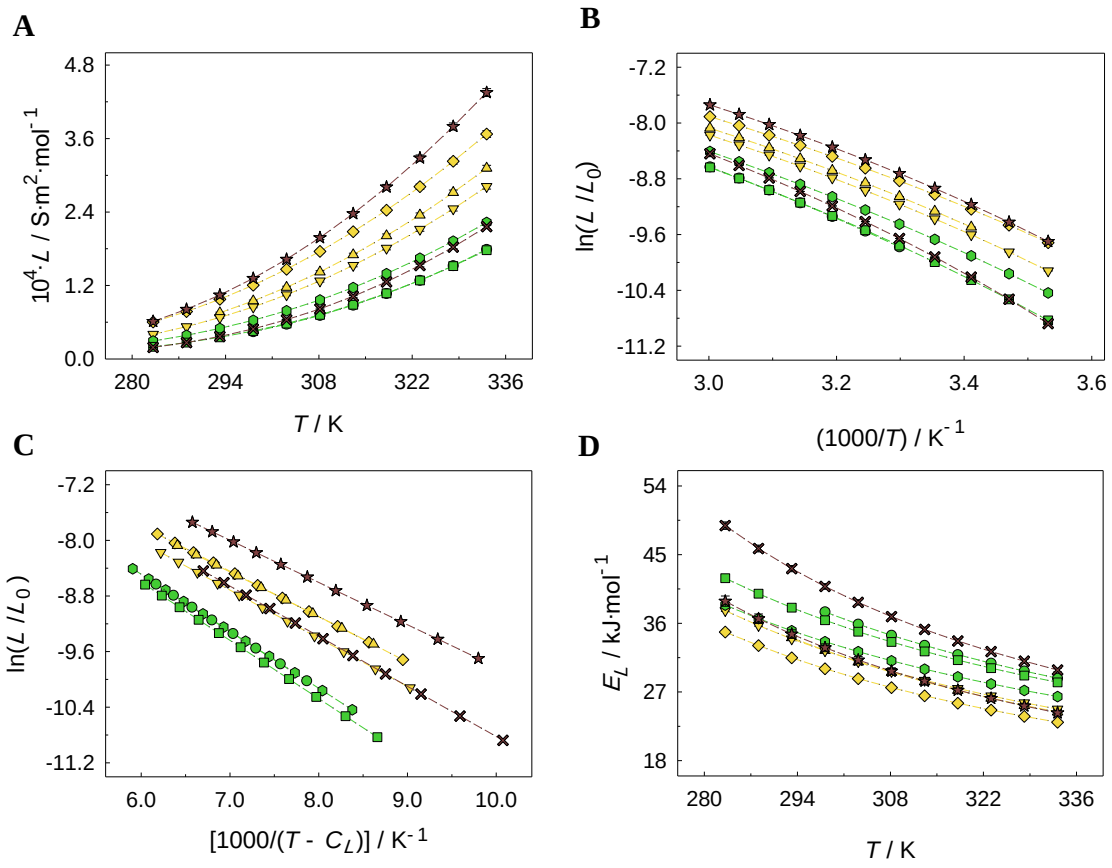



**Figure 5.98.** Temperature dependence of molar conductivity for the selected imidazolium, pyridinium, and pyrrolidinium. **A**: viscosity, **B**: Arrhenius representation; **C**: VFT representation; **D**: Energy barrier. ◆ [$^1$C$_4$$^3$C$_1$im][NTf$_2$], ▲ [$^1$C$_4$py][NTf$_2$] , ▼ [$^1$C$_4$$^1$C$_1$pyr][NTf$_2$] , ⬢ [$^1$C$_4$$^3$C$_1$im][OTf], ● [$^1$C$_4$py][OTf], ■ [$^1$C$_4$$^1$C$_1$pyr][OTf], ★ [$^1$C$_4$$^3$C$_1$im][FAP], ✖[$^1$C$_4$$^1$C$_1$pyr][FAP]. $\Lambda_0$ = 1 S·m$^2$·mol$^{-1}$.

### 5.3.1.5. Discussion

The graphical comparison of the viscosity and molar conductivity properties between the selected imidazolium, pyridinium, and pyrrolidinium are presented in Fig. 5.99 and Fig. 5.100, respectively.

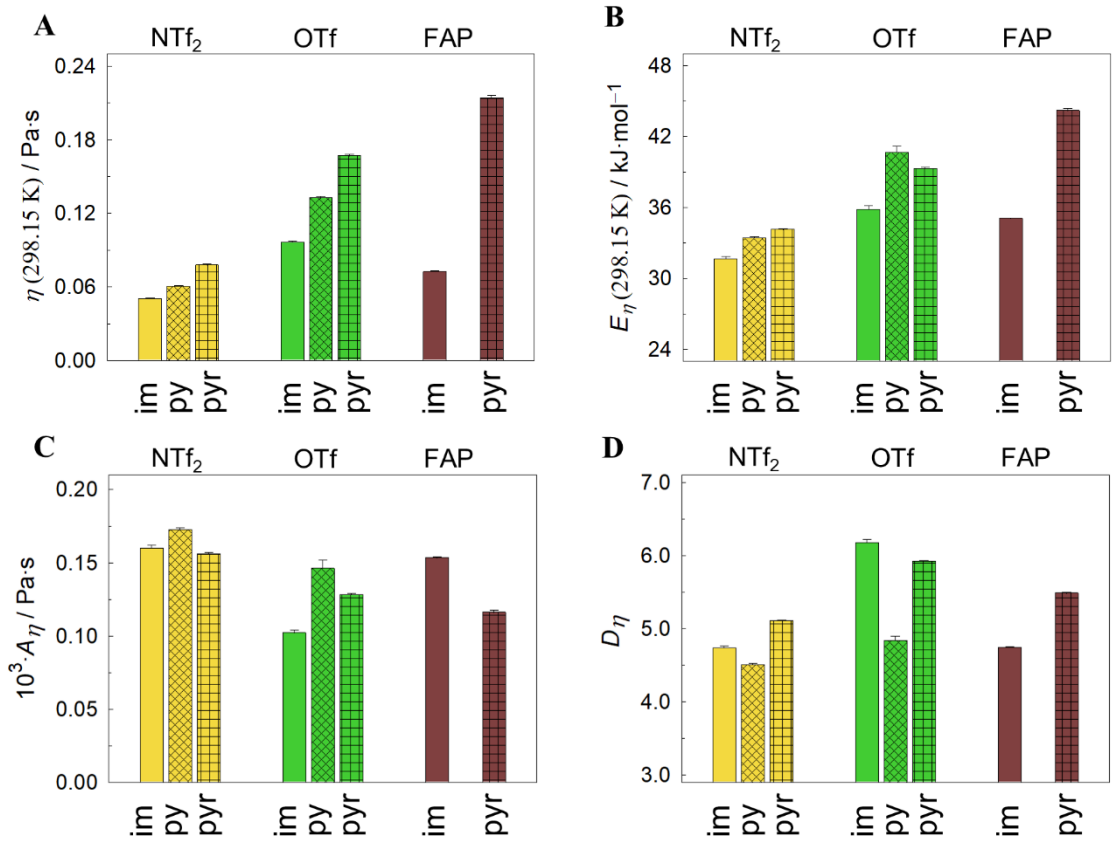



**Figure 5.99.** Viscosity and derived properties for the selected imidazolium, pyridinium, and pyrrolidinium. **A**: Viscosity; **B**: Energy barriers; **C**: Pre-exponential coefficient; **D**: Strength parameter.

Based on the results, the following trends are observed for viscosity and molar conductivity:

***η*(298.15 K):**

$$[^1C_4{}^3C_1im][NTf_2] < [^1C_4py][NTf_2] < [^1C_4{}^3C_1im][FAP] < [^1C_4{}^1C_1pyr][NTf_2] < [^1C_4{}^3C_1im][OTf] < [^1C_4py][OTf] < [^1C_4{}^1C_1pyr][OTf] < [^1C_4{}^1C_1pyr][FAP]$$

***Λ*(298.15 K):**

$$[^1C_4{}^3C_1im][NTf_2] > [^1C_4{}^3C_1im][FAP] > [^1C_4py][NTf_2] > [^1C_4{}^1C_1pyr][NTf_2] > [^1C_4{}^3C_1im][OTf] > [^1C_4{}^1C_1pyr][OTf] > [^1C_4py][OTf] > [^1C_4{}^1C_1pyr][FAP]$$

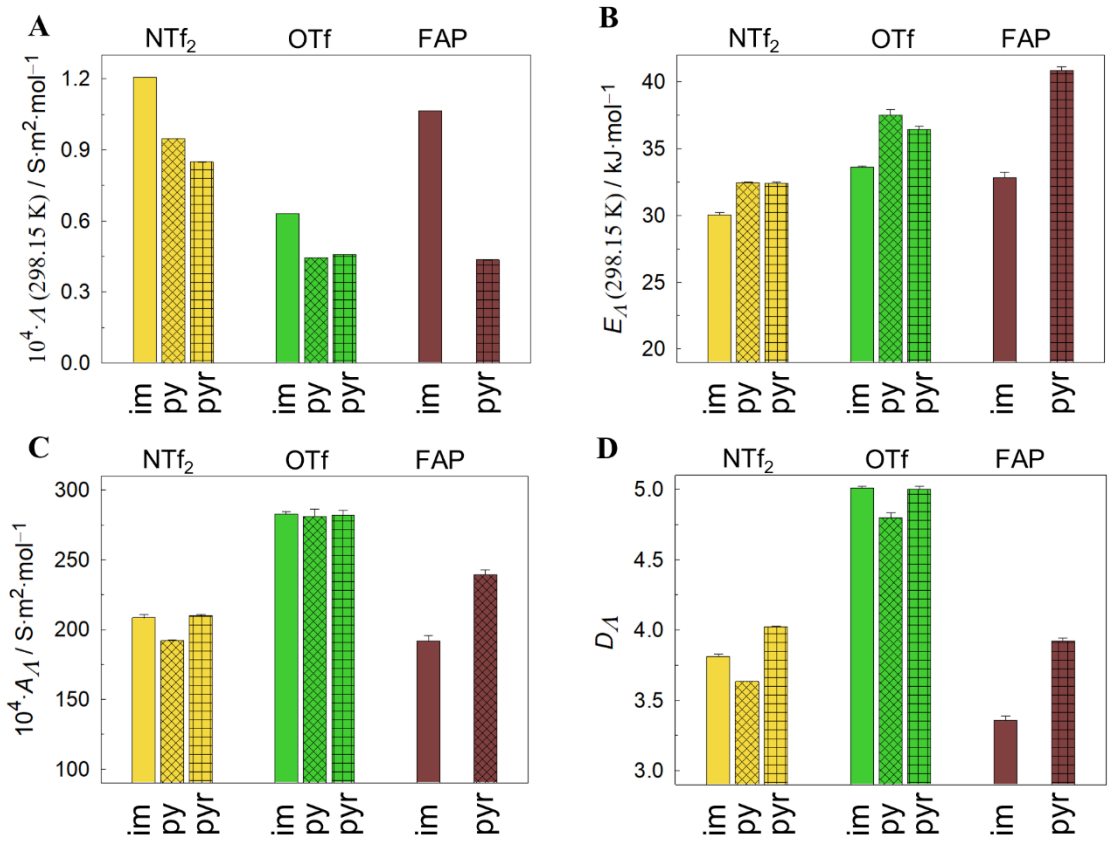



**Figure 5.100.** Molar conductivity and derived properties for the selected imidazolium, pyridinium, and pyrrolidinium. **A**: Molar conductivity; **B**: Energy barrier; **C**: Pre-exponential coefficient; **D**: Strength parameter.

Based on the results, the following trends are observed for the derived energy barriers:

***E*$_\eta$(298.15 K):**

$$[^1C_4{}^3C_1im][OTf] < [^1C_4py][NTf_2] < [^1C_4{}^3C_1im][FAP] < [^1C_4{}^3C_1im][NTf_2] <$$
$$< [^1C_4{}^1C_1pyr][OTf] < [^1C_4{}^1C_1pyr][NTf_2] < [^1C_4py][OTf] < [^1C_4{}^1C_1pyr][FAP]$$

***E*$_\Lambda$(298.15 K):**

$$[^1C_4{}^3C_1im][NTf_2] < [^1C_4{}^1C_1pyr][NTf_2] \sim [^1C_4py][NTf_2] < [^1C_4{}^3C_1im][FAP] <$$
$$< [^1C_4{}^3C_1im][OTf] < [^1C_4{}^1C_1pyr][OTf] < [^1C_4py][OTf] < [^1C_4{}^1C_1pyr][FAP]$$

Overall, for each anionic group, the imidazolium-based ILs were found to present the lowest viscosity and higher molar conductivities, while the pyrrolidinium ILs showed the highest viscosities and lowest molar conductivities. This is consistent with the literature

[44, 132, 207]. This is corroborated by the lower energy barriers of the imidazolium ILs, which are associated with its high charge dispersion (aromatic ring and two nitrogen atoms). Conversely, the higher energy barrier of the pyridinium systems is due to the higher degree of charge localization on this cationic ring (non-aromatic and a single nitrogen atom). However, this is not the case for the OTf ILs, as [$^1C_4$py][OTf] presents the highest energy barrier. This is likely due to the strong dispersive interactions between the sulfonate group "$S(O)_2O$" and the aromatic pyridinium ring. The pre-exponential coefficients suggest lower dynamics for the pyridinium systems (highest $A_\eta$ and lowest $A_\Lambda$), which might be related to the larger dimension of this ring (6-atoms ring). Furthermore, the results show that the impact of the anion seems to be more significant than the changes in the cationic structure. This can be easily seen by comparing the transport properties between the $NTf_2$ and OTf ionic liquids, as all ILs from the former group present lower viscosity and higher molar conductivities [29, 207]. However, there is a strong difference between the transport properties of the FAP ILs, as[$^1C_4{}^3C_1$im][FAP] displays transport properties comparable with the $NTf_2$ ILs while [$^1C_4{}^1C_1$pyr][FAP] presents the highest viscosity and lowest molar conductivity of the whole series. FAP is an anion with relatively higher charge localization (P atom) although the charge region is not easily accessible due to the perfluoroalkyl chains. Based on that, it is plausible that differences between the charge distribution in the imidazolium and pyridinium rings would result in a significant differentiation in the cohesive interaction of the liquid as is reflected on the derived energy barriers. These results highlight the relevance of the nature of the ion pair and the anion-cation interactions on the transport properties of ionic liquids.

The experimental viscosity and molar conductivity data were used to construct Walden plots (Fig. 5.101) for the selected imidazolium, pyridinium, and pyrrolidinium ILs. Additionally, the ideal Walden line, $\Delta w$ at the reference temperature ($T$ = 298.15 K) and the slope of the Walden lines, $\alpha_w$, are graphically presented in Fig 5.102.

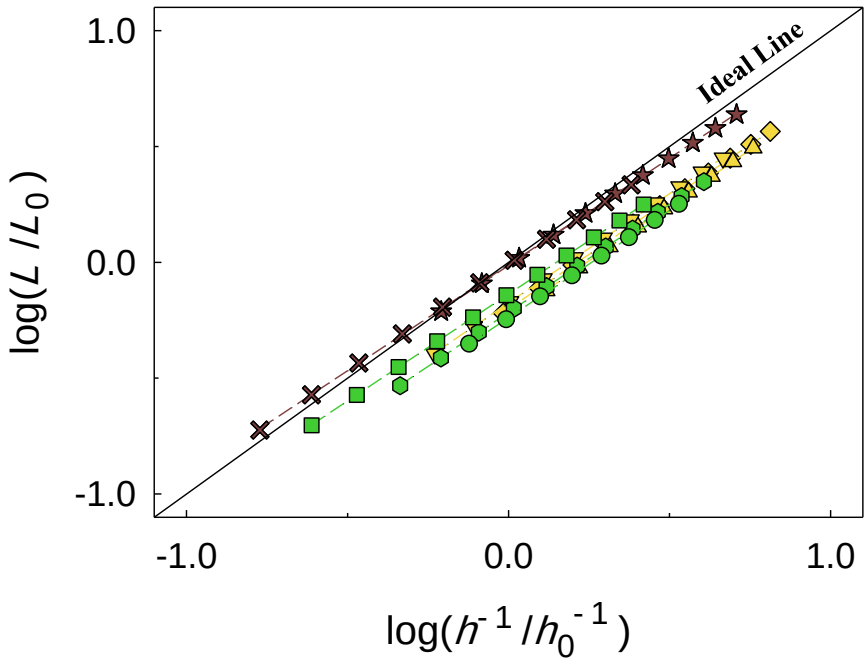



**Figure 5.101.** Walden plot for the selected imidazolium, pyridinium, and pyrrolidinium ILs based on the experimental viscosity and molar conductivity data. ◆ [$^1C_4{}^3C_1$im][$NTf_2$], ▲ [$^1C_4$py][$NTf_2$], ▼ [$^1C_4{}^1C_1$pyr][$NTf_2$], ⬢ [$^1C_4{}^3C_1$im][OTf], ● [$^1C_4$py][OTf], ■ [$^1C_4{}^1C_1$pyr][OTf], ★ [$^1C_4{}^3C_1$im][FAP], ✖[$^1C_4{}^1C_1$pyr][FAP]. $\eta_0$ = 1 Poise; $\Lambda_0$ = 1 S·cm$^2$·mol$^{-1}$.

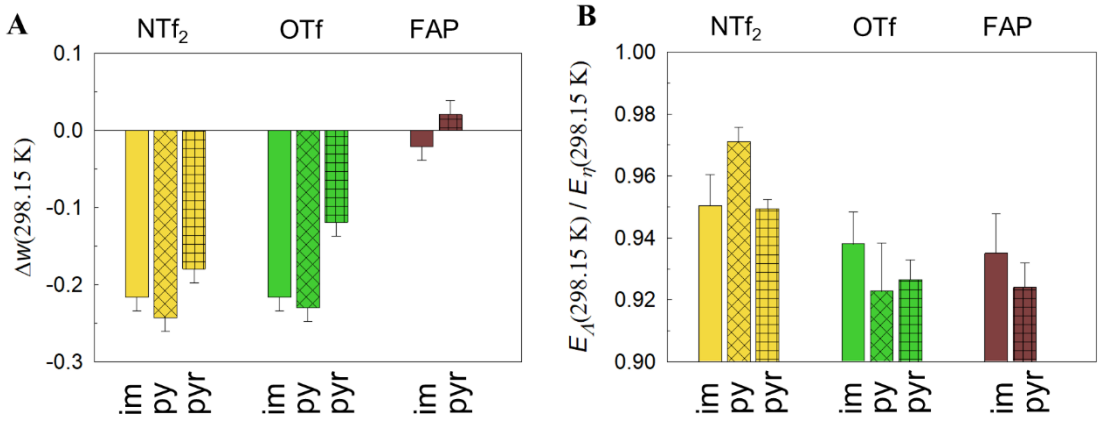



**Figure 5.102.** Viscosity-molar conductivity correlations for the selected imidazolium, pyridinium, and pyrrolidinium. **A**: Deviation to the "ideal Walden line" (log $\Lambda$ – log $\eta$); B: Energy barrier ratio ($E_\Lambda/E_\eta$).

The Walden plot shows a stronger viscosity-molar conductivity correlation for the FAP ILs compared to the $NTf_2$ and OTf compounds. This means that while the two FAP anions present vastly different transport properties, in both systems the molar conductivity is excellently described by the viscosity of the liquid. This is likely due to the sphere-like shape of the FAP anion and its strong charge localization and is consistent with what has been reported by Nazet *et al.* [111]. Additionally, there is a visible differentiation between the Δw of the non-aromatic pyrrolidinium compared to the aromatic imidazolium

and pyridinium rings. This is in agreement with the higher ionicity values for the pyrrolidinium-based ILs determined by Tokuda *et al.* [132].

### 5.3.2. C2-Methylation on the Imidazolium Ring

This section is dedicated to the study of the effect of C2 methylation of the imidazolium ring on the transport properties of bis(trifluoromethylsulfonyl)imide ionic liquids. The density, viscosity, and molar conductivity of three C2-methylated ILs, $[^1C_n{}^2C_1{}^3C_1im][NTf_2]$ $n$ = 2 – 4, will be presented in this section and compared with the protonated analogues and isomers as described in Fig. 5.103. The impact of C2-methylation on physicochemical properties has been previously explored in the literature, and it has been reported to drastically affect the transport properties, solid-liquid equilibrium, and vaporization thermodynamics. From these works, two hypotheses have emerged:

1. **Enthalpy-based hypothesis:** The methylation at the C2 position prevents hydrogen bonding in the preferable interaction site of the imidazolium ring.

2. **Entropy-based hypothesis:** The methylation at the C2 position hinders the movement of the anion around the cation, reducing the number of conformers for the ionic pair.

The results obtained in this work will be discussed based on these two hypotheses.

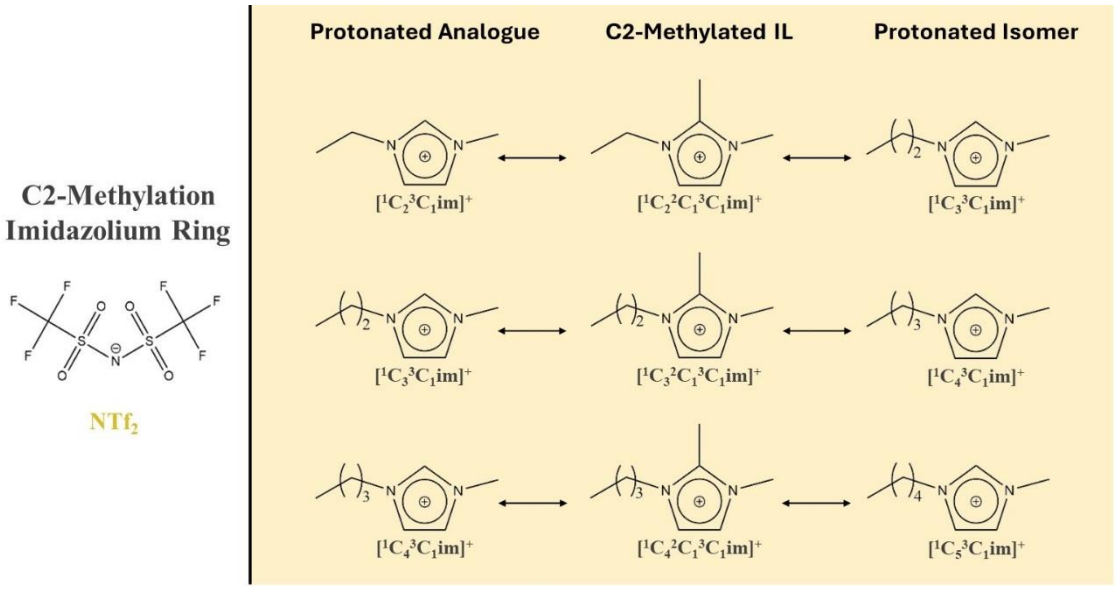



**Figure 5.103.** Schematic representation of the study of the impact of C2-methylation on transport properties of ILs.

#### 5.3.2.1. Density

The resulting fitting coefficients from the temperature dependence of density of the $[^1C_n{}^2C_1{}^3C_1im][NTf_2]$ ILs (Eq. 2.4) are presented in Table 5.62. The densities at the reference temperature ($T$ = 298.15 K) are presented in Table 5.63, together with the molar volume and thermal expansion coefficient derived from Eq. 2.2 and Eq. 2.7 respectively. The graphical representation of density, thermal expansion coefficient, and molar volume as functions of temperature and number of carbons on the cations alkyl chain are presented in Fig 5.104.

**Table 5.62.** Fitting coefficients used to describe the temperature dependence of density of the studied C2-methylated $[^1C_n{}^2C_1{}^3C_1im][NTf_2]$ ILs.

| Ionic Liquid | $\frac{T_{\text{interval}}}{\text{K}}$ | $\frac{10^7 \cdot a_2}{\text{K}^{-2}}$ | $\frac{10^4 \cdot a_1}{\text{K}^{-1}}$ | $\frac{a_0}{\text{K}}$ |
|---|---|---|---|---|
| $[^1C_2{}^2C_1{}^3C_1im][NTf_2]$ | 293 − 373 | −0.50 ± 0.10 | −6.128 ± 0.069 | 7.4947 ± 0.0011 |
| $[^1C_3{}^2C_1{}^3C_1im][NTf_2]$ | 283 − 373 | −0.328 ± 0.039 | −6.317 ± 0.026 | 7.4740 ± 0.0004 |
| $[^1C_4{}^2C_1{}^3C_1im][NTf_2]$ | 283 − 373 | −0.11 ± 0.11 | −6.476 ± 0.070 | 7.4517 ± 0.0011 |

The presented fitting coefficients were derived from the experimental $\rho(T)$ data (appendix) by applying a polynomial fitting function, $\ln[\rho(T)] = a_2T^2 + a_1T + a_0$ (Eq. 2.4). The standard uncertainties related to the fitting coefficients were calculated to the confidence level of 0.95 ($k \approx 2$).

**Table 5.63.** Density, thermal expansion coefficient, and molar volume at the reference temperature ($T$ = 298.15 K) for the studied C2-methylated $[^1C_n{}^2C_1{}^3C_1im][NTf_2]$ ILs.

| Ionic Liquid | $\frac{\rho(298.15\ \text{K})}{\text{kg} \cdot \text{m}^{-3}}$ | $\frac{10^4 \cdot \alpha_\rho(298.15\ \text{K})}{\text{K}^{-1}}$ | $\frac{10^6 \cdot V_\text{m}(298.15\ \text{K})}{\text{m}^3 \cdot \text{mol}^{-1}}$ |
|---|---|---|---|
| $[^1C_2{}^2C_1{}^3C_1im][NTf_2]$ | 1491.5 ± 0.5 | 6.43 ± 0.07 | 271.8 ± 0.8 |
| $[^1C_3{}^2C_1{}^3C_1im][NTf_2]$ | 1455.0 ± 0.5 | 6.51 ± 0.03 | 288.2 ± 0.8 |
| $[^1C_4{}^2C_1{}^3C_1im][NTf_2]$ | 1418.9 ± 0.5 | 6.54 ± 0.07 | 305.4 ± 0.9 |

$\rho(T = 298.15\ \text{K})$ and $\alpha_\rho(T = 298.15\ \text{K})$ were calculated from the fitting coefficients presented in Table 5.62 and by applying Eq. 2.4 and Eq. 2.7 respectively. $V_\text{m}(298.15\ \text{K}) = M/\rho(298.15\ \text{K})$. The standard uncertainty associated with $\alpha_\rho$ and $V_\text{m}$ were calculated by applying the propagation of uncertainty to Eq. 2.7 and 2.2, respectively.

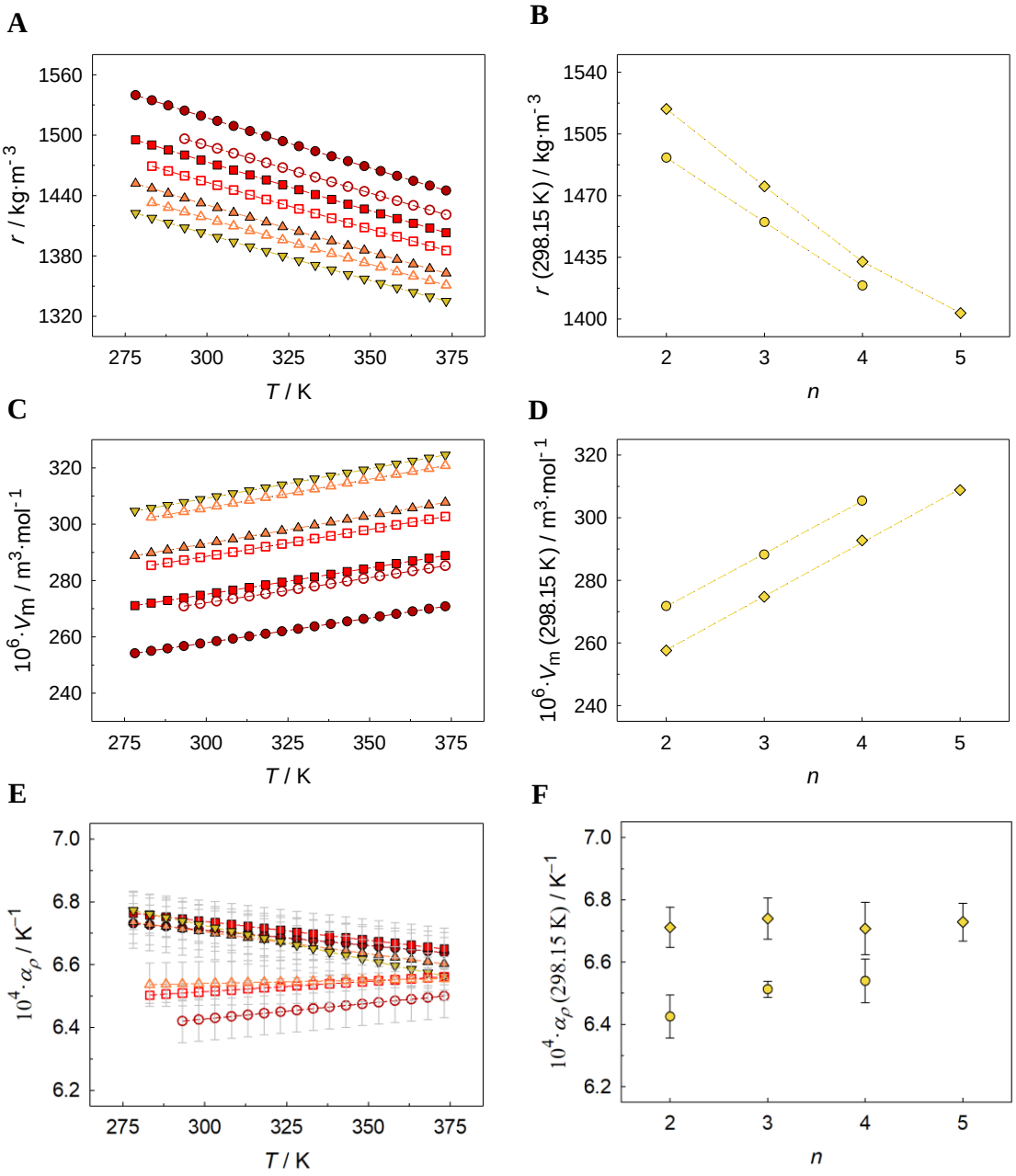



**Figure 5.104.** Density and derived properties of the $[^1C_n{}^2C_1{}^3C_1im][NTf_2]$ ILs and their protonated analogues and isomers as functions of temperature (A, C, E) and number of carbons on the alkyl chain of the cation (B, D, F). **A**, **B**: Density; **C**, **D**: Molar volume; **E**, **F**: Thermal expansion coefficient. **A**, **C**, and **E**: ● $[^1C_2{}^3C_1im][NTf_2]$; ■ $[^1C_3{}^3C_1im][NTf_2]$, ▼ $[^1C_4{}^3C_1im][NTf_2]$, ▲ $[^1C_5{}^3C_1im][NTf_2]$, ○ $[^1C_2{}^2C_1{}^3C_1im][NTf_2]$, □ $[^1C_3{}^2C_1{}^3C_1im][NTf_2]$, △ $[^1C_3{}^2C_1{}^3C_1im][NTf_2]$. **B**, **D**, and **F**: ◆ $[^1C_n{}^3C_1im][NTf_2]$; ● $[^1C_n{}^2C_1{}^3C_1im][NTf_2]$.

#### 5.3.2.2. Viscosity

The VFT coefficients (Eq 2.44) of the $[^1C_n{}^2C_1{}^3C_1im][NTf_2]$ ILs obtained from the experimental viscosity-temperature data, $\eta(T)$, for the selected ILs are presented in Table 5.64.

**Table 5.64.** Fitting coefficients used to describe the temperature dependence of viscosity of the studied C2-methylated $[^1C_n{}^2C_1{}^3C_1im][NTf_2]$ ILs.

| Ionic Liquid | $\frac{T_{\text{interval}}}{\text{K}}$ | $\frac{10^3 \cdot A_\eta}{\text{Pa} \cdot \text{s}}$ | $\frac{B_\eta}{\text{K}}$ | $\frac{C_\eta}{\text{K}}$ |
|---|---|---|---|---|
| $[^1C_2{}^2C_1{}^3C_1im][NTf_2]$ | 293 − 373 | 0.1715 ± 0.0005 | 821.7 ± 0.8 | 162.0 ± 0.1 |
| $[^1C_3{}^2C_1{}^3C_1im][NTf_2]$ | 283 − 373 | 0.1567 ± 0.0010 | 811.2 ± 1.6 | 171.6 ± 0.1 |
| $[^1C_4{}^2C_1{}^3C_1im][NTf_2]$ | 283 − 373 | 0.1432 ± 0.0010 | 828.3 ± 1.6 | 172.3 ± 0.1 |

The presented fitting coefficients were derived from the experimental $\eta(T)$ data (appendix) by applying the VFT fitting function, Eq. 2.44. The standard uncertainties related to the VFT coefficients were calculated to the confidence level of 0.95 ($k \approx 2$).

The viscosities at the reference temperature ($T$ = 298.15 K) for the selected ILs are presented in Table 5.65, together with the energy barrier and strength parameter derived from Eq. 2.47 and Eq. 2.49, respectively.

**Table 5.65.** Viscosity and derived energy barrier of the studied C2-methylated $[^1C_n{}^2C_1{}^3C_1im][NTf_2]$ ILs at the reference temperature ($T$ = 298.15 K), together with the strength parameter.

| Ionic Liquid | $\frac{\eta(T=298.15\ \text{K})}{\text{Pa} \cdot \text{s}}$ | $\frac{E_\eta(T=298.15\ \text{K})}{\text{kJ} \cdot \text{mol}^{-1}}$ | $D_\eta$ |
|---|---|---|---|
| $[^1C_2{}^2C_1{}^3C_1im][NTf_2]$ | 0.07167 ± 0.00072 | 32.76 ± 0.06 | 5.072 ± 0.006 |
| $[^1C_3{}^2C_1{}^3C_1im][NTf_2]$ | 0.09527 ± 0.00095 | 37.44 ± 0.09 | 4.727 ± 0.010 |
| $[^1C_4{}^2C_1{}^3C_1im][NTf_2]$ | 0.1034 ± 0.0010 | 38.64 ± 0.10 | 4.807 ± 0.011 |

$\eta(T$ = 298.15 K) and $E_\eta(T$ = 298.15 K) were calculated from the fitting coefficients presented in Table 5.64 and by applying Eq. 2.44 and Eq. 2.47, respectively. The strength parameter was calculated by Eq. 2.49, $D_\eta = B_\eta / C_\eta$. The relative standard uncertainty associated with the viscosity measurements was estimated as $u(\eta)$ = 1.0% (Eq. 2.72); The standard uncertainty associated with the derived energy barrier, $u(E_\eta)$, and strength parameter, $u(D_\eta)$, was calculated by applying the propagation of uncertainty to Eq. 2.47 and Eq. 2.49, respectively.

The temperature dependence of the viscosity and derived properties is presented in Fig. 5.105.

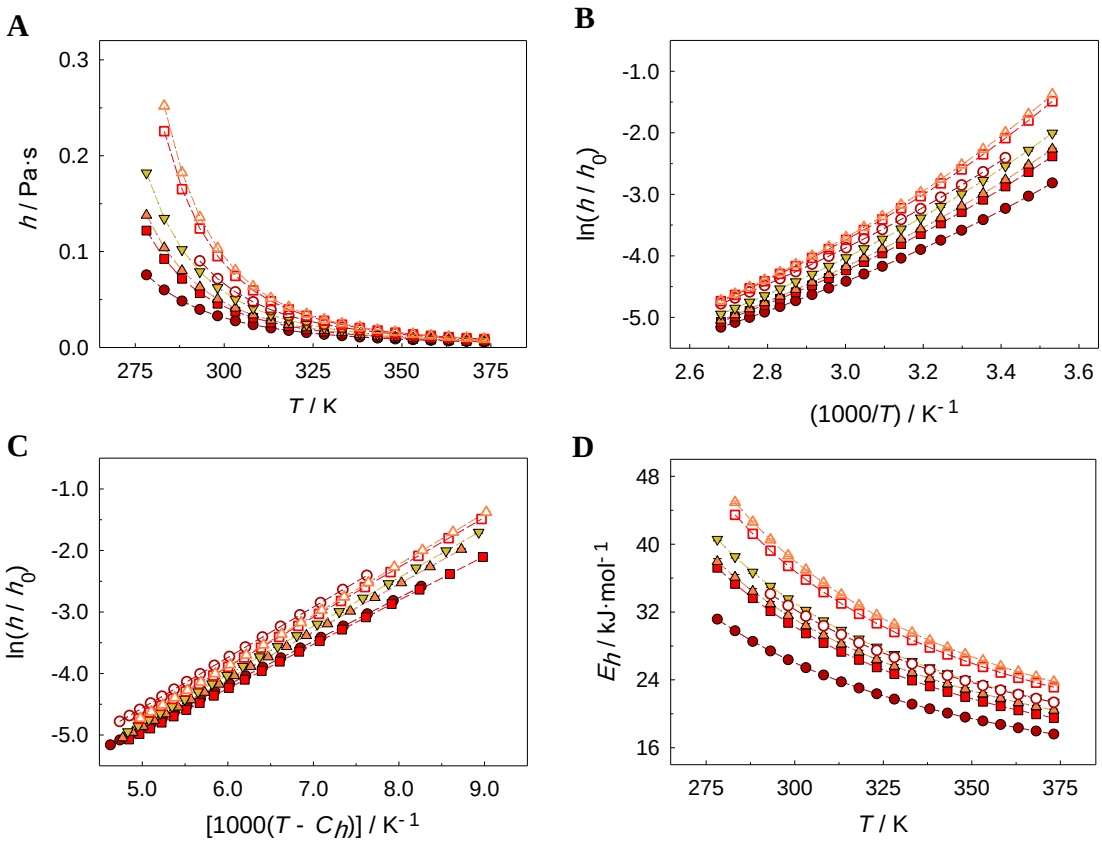



**Figure 5.105.** Temperature dependence of viscosity and derived energy barrier for the $[^1C_n{}^2C_1{}^3C_1im][NTf_2]$ ILs and their protonated analogues and isomers. **A**: viscosity, **B**: Arrhenius representation; **C**: VFT representation; **D**: Energy barrier. ● $[^1C_2{}^3C_1im][NTf_2]$; ■ $[^1C_3{}^3C_1im][NTf_2]$, ▼ $[^1C_4{}^3C_1im][NTf_2]$, ▲ $[^1C_5{}^3C_1im][NTf_2]$, ○ $[^1C_2{}^2C_1{}^3C_1im][NTf_2]$, □ $[^1C_3{}^2C_1{}^3C_1im][NTf_2]$, △ $[^1C_3{}^2C_1{}^3C_1im][NTf_2]$. $\eta_0$ = 1 Pa·s.

The deviation of the available viscosity data to the experimental results for the $[^1C_n{}^2C_1{}^3C_1im][NTf_2]$ ILs is presented in Fig. 5.106. Most of the data is in excellent agreement with the results obtained in this work, particularly Mou *et al.* ($n$ = 2) [221] and Gaciño *et al.* ($n$ = 2) [214]. On the other hand, the data by Fletcher *et al.* [218] seems to present a strong temperature dependency going into large positive deviation with the increase in temperature.

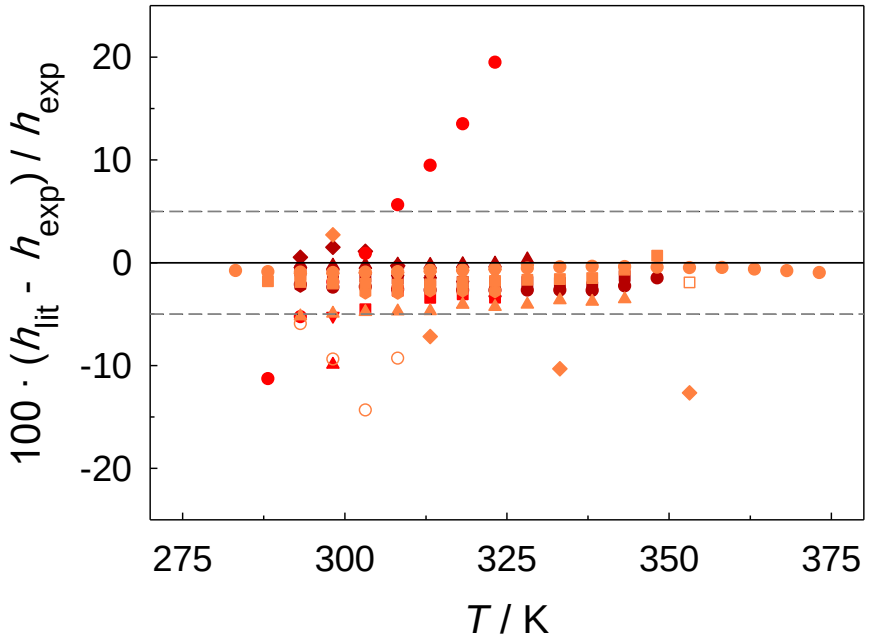



**Figure 5.106.** Deviation of the available viscosity data to the experimental results for the [$^1C_n{}^2C_1{}^3C_1$im][$NTf_2$] ILs. ***n* = 2:** ●[222], ■[223], ▲ [221], ▼ [100], ◆ [9], ⬢ [91]; ***n* = 3:** ● [218]; ■ [100]; ▲ [202], ▼ [224]; ***n* = 4:** ●[214], ▲ [223], ▼ [221], ◆[152]; ⬢[100], ○ [225], □ [203].

### 5.3.2.3. Electrical Conductivity

The VFT coefficients (Eq 2.24) of the [$^1C_n{}^3C_1$im][$NTf_2$] ILs obtained from the experimental electrical conductivity-temperature data, $\sigma(T)$, are presented in Table 5.66.

**Table 5.66.** Fitting coefficients used to describe the temperature dependence of electrical conductivity of the studied [$^1C_n{}^2C_1{}^3C_1$im][$NTf_2$] ILs.

| Ionic Liquid | $\frac{A_\sigma}{S \cdot m^{-1}}$ | $\frac{B_\sigma}{K}$ | $\frac{C_\sigma}{K}$ | $\frac{\sigma(T=298.15\ K)}{S \cdot m^{-1}}$ |
|---|---|---|---|---|
| [$^1C_2{}^2C_1{}^3C_1$im][$NTf_2$] | 72.9 ± 1.4 | 661.1 ± 5.7 | 170.9 ± 0.6 | 0.4043 ± 0.0061 |
| [$^1C_3{}^2C_1{}^3C_1$im][$NTf_2$] | 73.5 ± 1.2 | 667.9 ± 4.0 | 179.1 ± 0.6 | 0.2689 ± 0.0040 |
| [$^1C_4{}^2C_1{}^3C_1$im][$NTf_2$] | 66.4 ± 1.0 | 668.9 ± 3.9 | 181.2 ± 0.4 | 0.2178 ± 0.0032 |

The presented fitting coefficients were derived from the experimental $\sigma(T)$ data (appendix) by applying the VFT fitting function, Eq. 2.44. The standard uncertainties related to the VFT coefficients were calculated to the confidence level of 0.95 ($k \approx 2$). The relative standard uncertainty associated with the viscosity measurements was estimated as $u(\sigma)$ = 1.5% (Eq. 4.15).

The deviation of the available electrical conductivity data to the experimental results for the [$^1C_n{}^2C_1{}^3C_1$im][$NTf_2$] ILs is presented in Fig. 5.107.

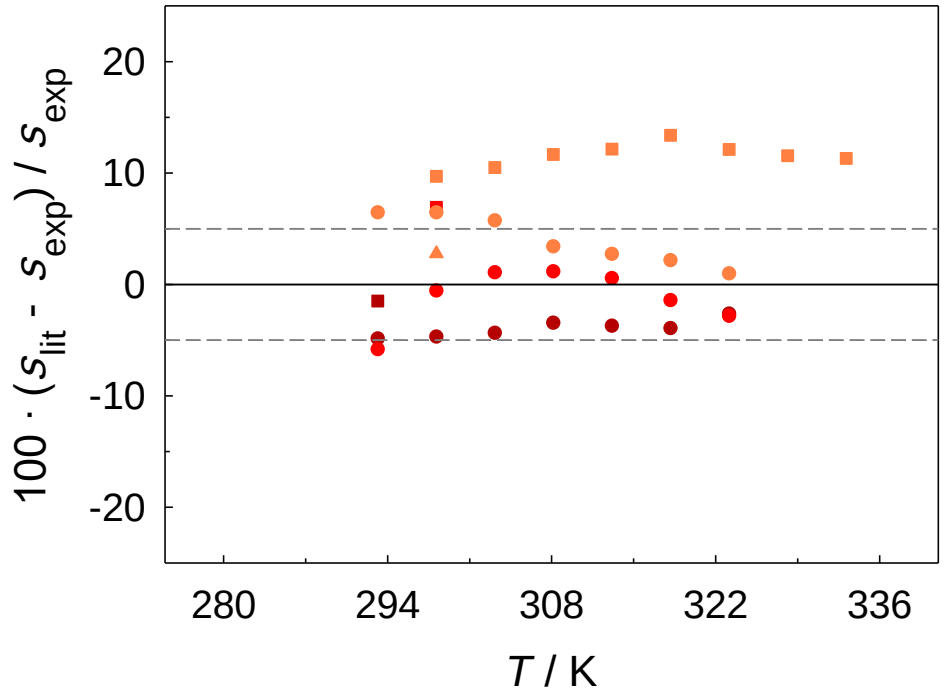



**Figure 5.107.** Deviation of the available electrical conductivity data to the experimental results for the [$^1C_n{}^2C_1{}^3C_1$im][$NTf_2$] ILs. ***n* = 2:** ● [100], ■ [91]. ***n* = 3:** ● [100], ■ [226]; ***n* = 4:** ● [100], ■ [227], ▲ [108].

Most data are within ± 5% relative to the results obtained in this work. The data reported by Zhang *et al.* [227] for [$^1C_4{}^2C_1{}^3C_1$im][$NTf_2$] show a significant positive deviation, which might be associated with a high water content in the sample.

#### 5.3.2.4. Molar Conductivity

The VFT coefficients (Eq 2.44) of the [$^1C_n{}^3C_1$im][$NTf_2$] ILs obtained from the experimental molar conductivity-temperature data, $\Lambda(T)$, for the selected ILs are presented in Table 5.67.

**Table 5.67.** Fitting coefficients used to describe the temperature dependence of molar conductivity of the studied C2-methylated [$^1C_n{}^2C_1{}^3C_1$im][$NTf_2$] ILs.

| Ionic Liquid | $\frac{T_{\text{interval}}}{\text{K}}$ | $\frac{10^4 A_\Lambda}{\text{S}\cdot\text{m}^2\cdot\text{mol}^{-1}}$ | $\frac{B_\Lambda}{\text{K}}$ | $\frac{C_\Lambda}{\text{K}}$ |
|---|---|---|---|---|
| [$^1C_2{}^2C_1{}^3C_1$im][$NTf_2$] | 293 − 333 | 241.8 ± 5.1 | 702.0 ± 6.2 | 168.0 ± 0.7 |
| [$^1C_3{}^2C_1{}^3C_1$im][$NTf_2$] | 283 − 333 | 242.0 ± 2.8 | 690.0 ± 3.1 | 178.1 ± 0.3 |
| [$^1C_4{}^2C_1{}^3C_1$im][$NTf_2$] | 283 − 333 | 244.6 ± 3.1 | 704.4 ± 3.6 | 178.9 ± 0.3 |

The presented fitting coefficients were derived from the experimental $\Lambda(T)$ data (appendix) by applying the VFT fitting function, Eq. 2.44. The standard uncertainties related to the VFT coefficients were calculated to the confidence level of 0.95 ($k \approx 2$).

The molar conductivities at the reference temperature ($T$ = 298.15 K) for the selected ILs are presented in Table 5.68, together with the energy barrier and strength parameter derived from Eq. 2.47 and Eq. 2.49, respectively. The temperature dependence of the viscosity and derived properties is presented in Fig. 5.108.

**Table 5.68.** Molar conductivity and derived energy barrier of the studied C2-methylated [$^1C_n{}^2C_1{}^3C_1$im][$NTf_2$] ILs at the reference temperature ($T$ = 298.15 K), together with the strength parameter.

| Ionic Liquid | $\Lambda(T$=298.15 K) / S · m² · mol$^{-1}$ | $E_\Lambda(T$=298.15 K) / kJ · mol$^{-1}$ | $D_\Lambda$ |
|---|---|---|---|
| [$^1C_2{}^2C_1{}^3C_1$im][$NTf_2$] | 1.0989 ± 0.0006 | 30.63 ± 0.43 | 4.179 ± 0.041 |
| [$^1C_3{}^2C_1{}^3C_1$im][$NTf_2$] | 0.7721 ± 0.0004 | 35.39 ± 0.24 | 3.874 ± 0.019 |
| [$^1C_4{}^2C_1{}^3C_1$im][$NTf_2$] | 0.6654 ± 0.0003 | 36.61 ± 0.26 | 3.937 ± 0.021 |

$\Lambda(T$ = 298.15 K) and $E_\Lambda(T$ = 298.15 K) were calculated from the fitting coefficients presented in Table 5.67 and by applying Eq. 2.44 and Eq. 2.47, respectively. The strength parameter was calculated by Eq. 2.49, $D_\Lambda = B_\Lambda / C_\Lambda$. The relative standard uncertainty associated with the viscosity measurements was estimated as $u(\Lambda)$ = 1.5% (Eq. 4.15); The standard uncertainty associated with the derived energy barrier, $u(E_\Lambda)$, and strength parameter, $u(D_\Lambda)$, was calculated by applying the propagation of uncertainty to Eq. 2.47 and Eq. 2.49, respectively.

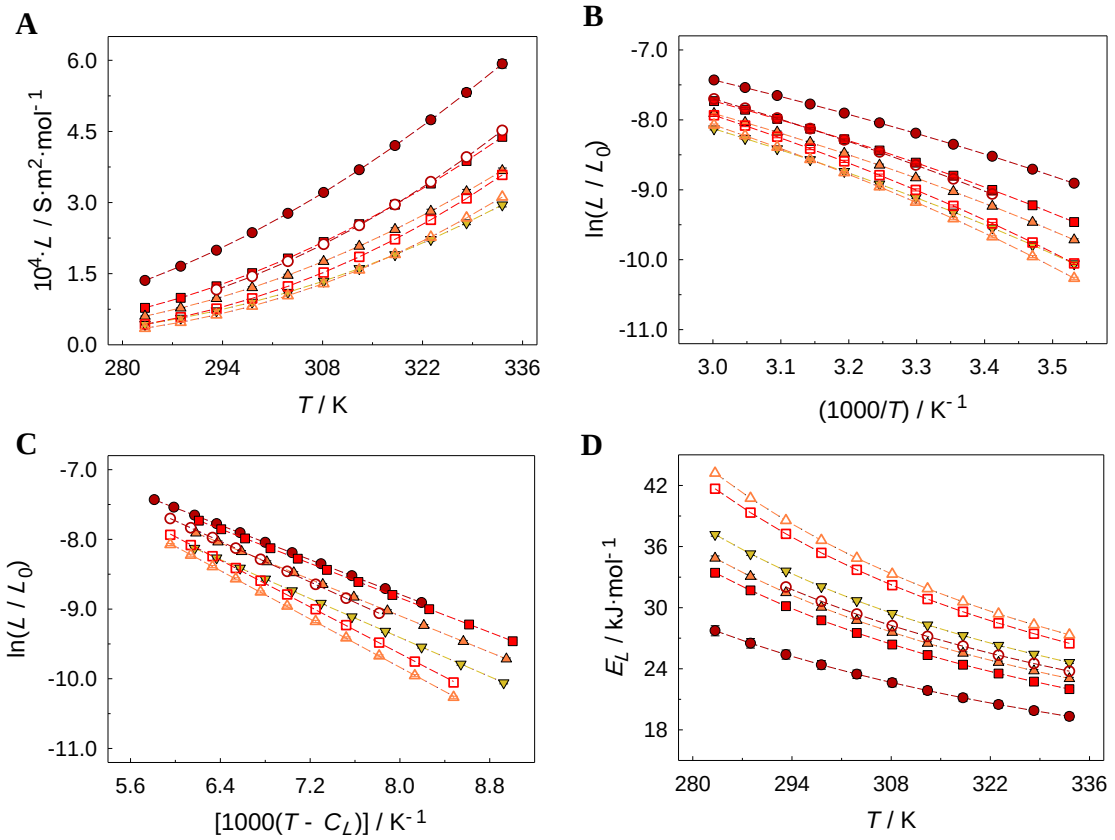



**Figure 5.108.** Temperature dependence of molar conductivity and derived energy barrier for the [$^1C_n{}^2C_1{}^3C_1$im][$NTf_2$] ILs and their protonated analogues and isomers. **A**: viscosity, **B**: Arrhenius representation; **C**: VFT representation; **D**: Energy barrier. $\Lambda_0$ = 1 S·m²·mol$^{-1}$. ● [$^1C_2{}^3C_1$im][$NTf_2$]; ■ [$^1C_3{}^3C_1$im][$NTf_2$], ▼ [$^1C_4{}^3C_1$im][$NTf_2$], ▲ [$^1C_5{}^3C_1$im][$NTf_2$], ○ [$^1C_2{}^2C_1{}^3C_1$im][$NTf_2$], □ [$^1C_3{}^2C_1{}^3C_1$im][$NTf_2$], △[$^1C_4{}^2C_1{}^3C_1$im][$NTf_2$].

### 5.3.2.5. Discussion

The measured transport properties and respective derived parameters of the $[^1C_n{}^2C_1{}^3C_1im][NTf_2]$ ILs and their protonated analogues and isomers are presented in Fig. 5.109 as functions of the number of carbons on alkyl side chain of the imidazolium cation (position 1). A schematic diagram of the effect of C2-methylation on the transport properties and derived parameters is presented in Fig. 5.110.

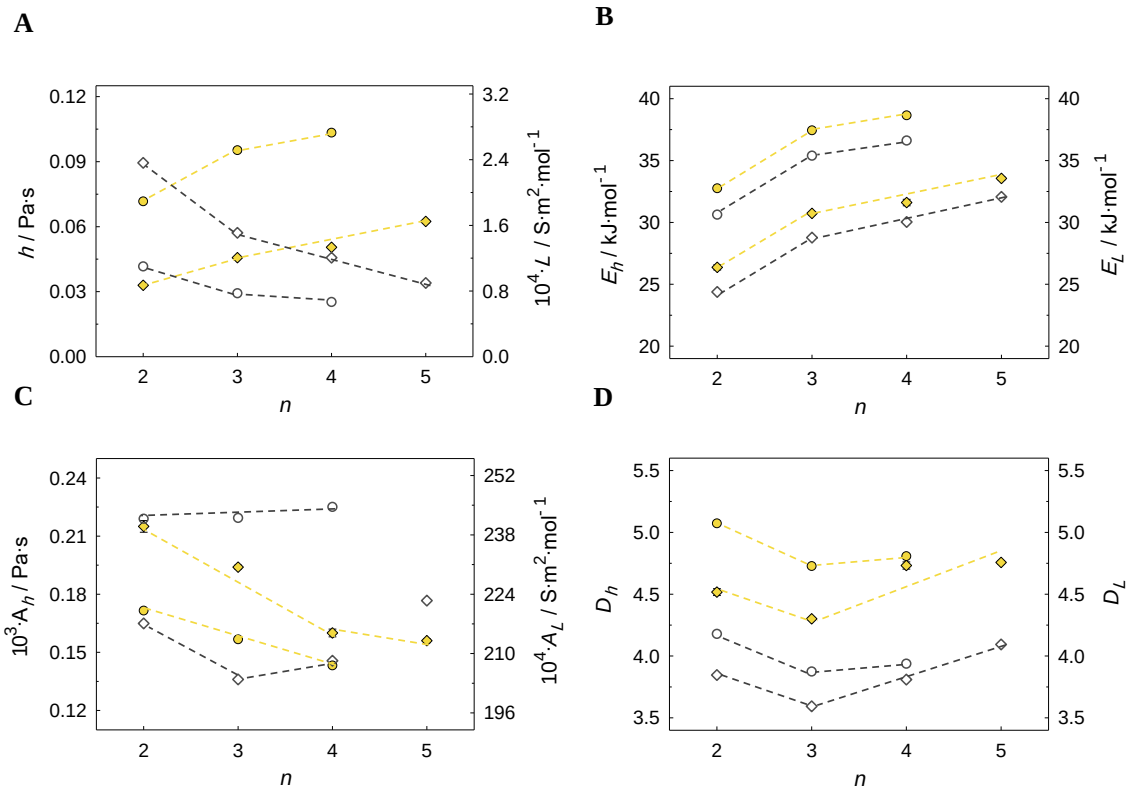



**Figure 5.109.** Transport properties and derived parameters of the $[^1C_n{}^2C_1{}^3C_1im][NTf_2]$ ILs and their protonated analogues and isomers as functions of the number of carbons on the alkyl side chain of the imidazolium cation (position 1). **A**: Viscosity and molar conductivity; **B**: Energy barrier; **C**: Pre-exponential coefficient; **D**: Strength parameter (fragility). ◆ $[^1C_n{}^3C_1im][NTf_2]$ ILs; ● $[^1C_n{}^2C_1{}^3C_1im][NTf_2]$ ILs; filled symbols: viscosity; unfilled symbols: molar conductivity.

The effect of the alkyl chain length on the $[^1C_n{}^2C_1{}^3C_1im][NTf_2]$ homologues series is reflected in an increase in energy barrier and viscosity and a decrease in molar conductivity and fragility. This is consistent with what was observed for the other homologue series in section 5.1 and is due to the strengthening of the van der Waals interactions. Additionally, the outlier behavior for the short-chain ILs is also observed for $[^1C_2{}^2C_1{}^3C_1im][NTf_2]$. The results show that the methylation at the position 2 of the imidazolium ring has a drastic impact on the transport properties of these ionic liquids.

The C2-methylated ILs present higher viscosities and lower molar conductivities (in some cases twice the viscosity and half the molar conductivity, Fig. 5.110) than the respective C2-protonated analogues and isomers. This has been previously reported in the literature [91, 100, 223] and is consistent with the higher energy barriers derived for the [$^1C_n{}^2C_1{}^3C_1$im][$NTf_2$] ILs. As expected the differences are more severe when using the analogues as the reference of comparison due to the difference in molar mass. The pre-exponential coefficients seem to take a reverse trend of the corresponding transport property, as the C2-methylated ILs present lower $A_\eta$ and higher $A_\Lambda$. This is similar to what has been observed for the effect of the alkyl chain length and is likely related to the surface-volume ratio.

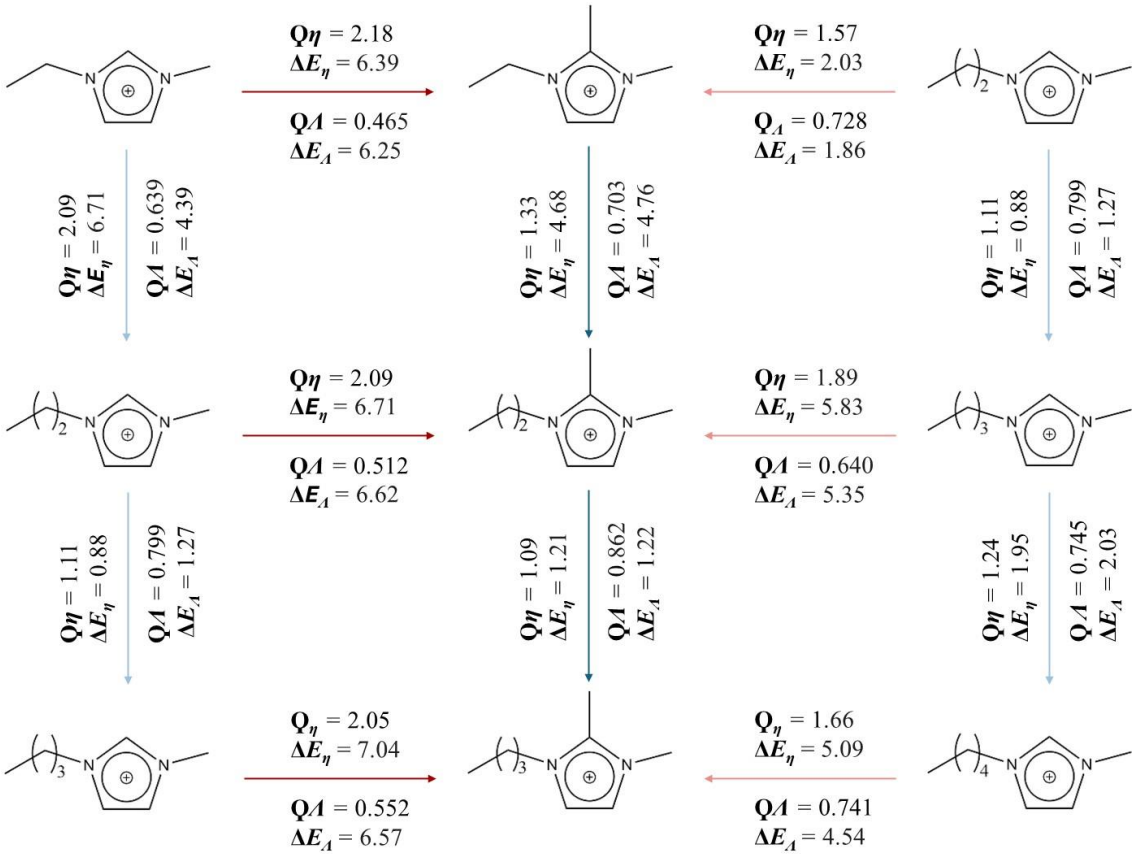



**Figure 5.110.** Schematic diagram of the effect of C2-methylation on the transport properties and derived parameters. The arrows represent the comparison between IL1 and IL2 (arrow point). Δ = IL2 – IL1; Q = IL2/IL1.

The derived strength parameter and energy barriers suggest an increase in cohesive energy upon C2-methylation. However in a previous work concerning the effect of C2-methylation on the thermodynamic properties of bis(trifluoromethylsulfonyl)imide it

was reported that the impact of this structural change was entropically driven as there were no significant differences in the enthalpy of vaporization (for isomers) [228]. On the other hand, in a more recent work on the vaporization of trifluoromethanesulfonate ILs it was observed that the hydrogen bonding between the sulfonate group "C=(O)$_2$O" and the acidic H(2) hydrogen of the imidazolium ring has a significant contribution to the cohesive energy of the liquid [229].

Fig 5.111 presents the relationship between the derived energy barriers and the selected literature data for enthalpy of vaporization (cohesive interaction).

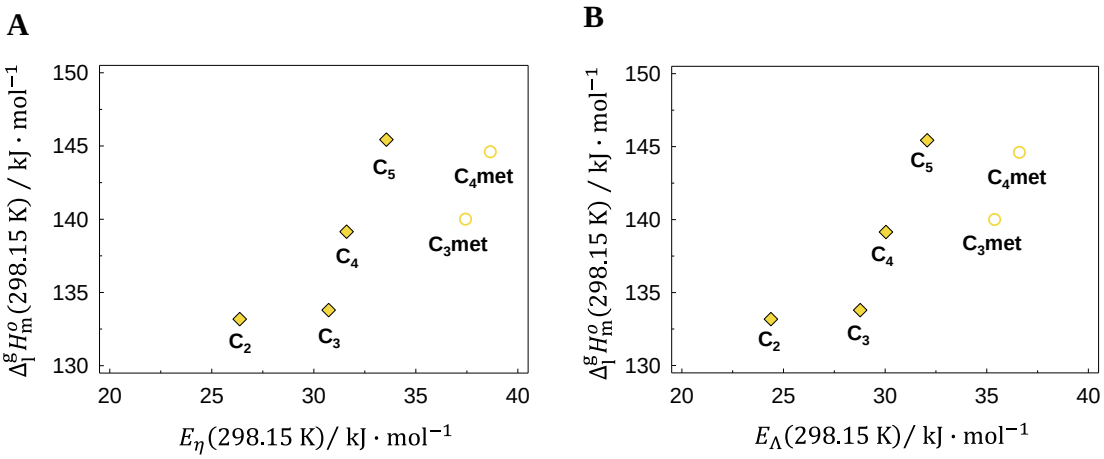



**Figure 5.111.** Correlation between the transport properties energy barrier and the enthalpy of vaporization for the [$^1$C$_n$$^2$C$_1$$^3$C$_1$im][NTf$_2$] [228] ◆ and [$^1$C$_n$$^3$C$_1$im][NTf$_2$] [166] ○ ILs. **A**: viscosity; **B**: molar conductivity.

A more clear and informative representation of this relationship can be achieved by looking at the ratio between the energy barrier and the enthalpy of vaporization as a function of the number of carbons on the alkyl chain (Fig. 5.112).

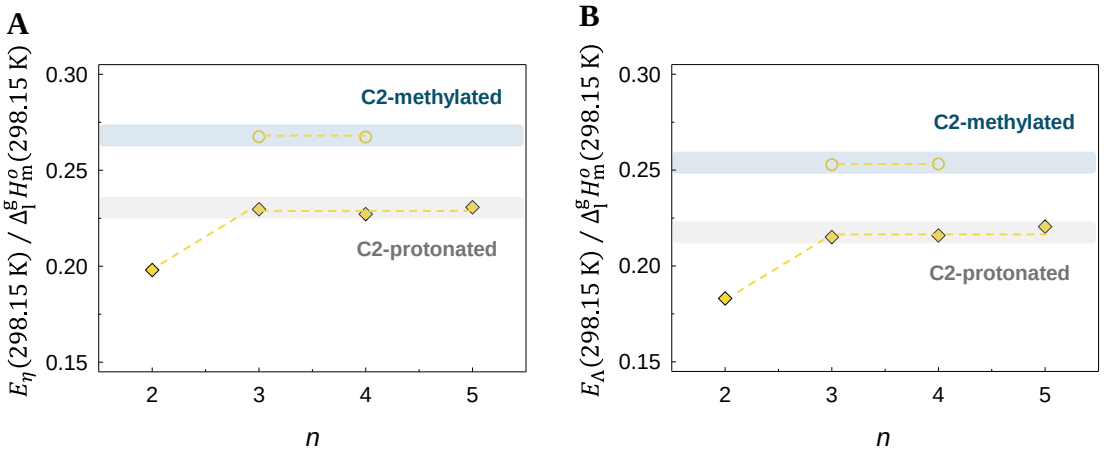



**Figure 5.112.** Ratio between energy barrier and enthalpy of vaporization (cohesive interaction) for the [$^1$C$_n$$^2$C$_1$$^3$C$_1$im][NTf$_2$] ○ [228] and [$^1$C$_n$$^3$C$_1$im][NTf$_2$] ◆ [166] ILs. **A**: Viscosity; **B**: Molar conductivity.

As observed the energy barrier associated with transport properties of $[^1C_n{}^2C_1{}^3C_1im][NTf_2]$ corresponds to a higher fraction of cohesive interaction of the liquid. Since this potential is associated with ion transport and dynamic flow of the liquid it is possible that this higher fraction is due to a more hindered ion motion due to the presence of the bulkier methyl group "-$CH_3$". This is consistent with the decrease of liquid entropy hypothesis that has been previously supported by experimental vaporization data [228] and computational calculations of the anion-around cation rotation [228, 230, 231].

The viscosity and molar conductivity data were used to construct Walden plot (Fig. 5.113) for the $[^1C_n{}^2C_1{}^3C_1im][NTf_2]$ ILs and their protonated analogues and isomers.

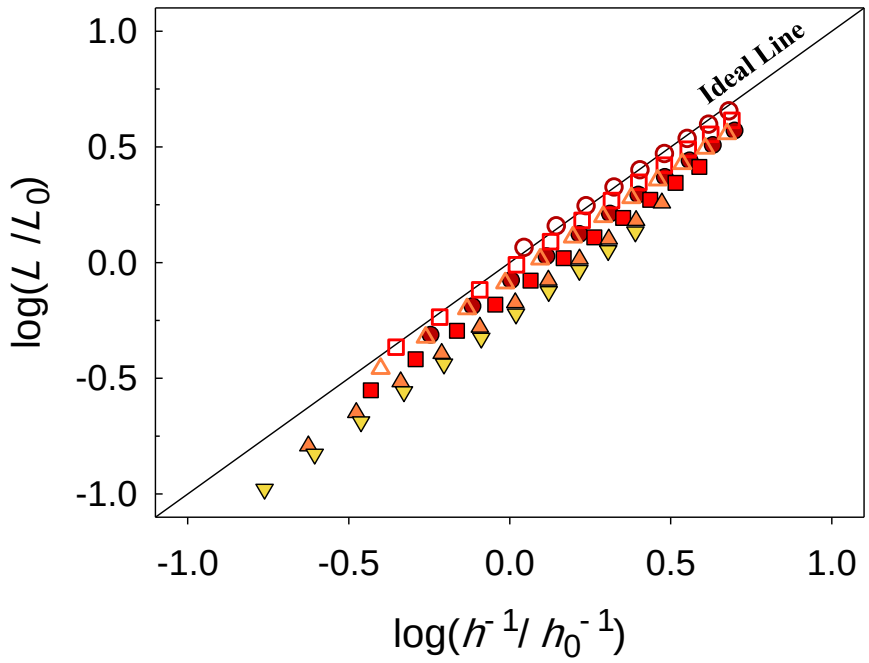



**Figure 5.113.** Walden plot for the $[^1C_n{}^2C_1{}^3C_1im][NTf_2]$ ILs and their protonated analogues and isomers. ● $[^1C_2{}^3C_1im][NTf_2]$; ■ $[^1C_3{}^3C_1im][NTf_2]$, ▼ $[^1C_4{}^3C_1im][NTf_2]$, ▲ $[^1C_5{}^3C_1im][NTf_2]$, ○ $[^1C_2{}^2C_1{}^3C_1im][NTf_2]$, □ $[^1C_3{}^2C_1{}^3C_1im][NTf_2]$, △ $[^1C_3{}^2C_1{}^3C_1im][NTf_2]$. $\eta_0$ = 1 Poise; $\Lambda_0$ = 1 S·cm$^2$·mol$^{-1}$.

To further explore this effect deviation to the ideal Walden line, $\Delta w$ at the reference temperature ($T$ = 298.15 K) and the slope of the Walden lines, $\alpha_w$, are graphically presented on Fig 5.114.

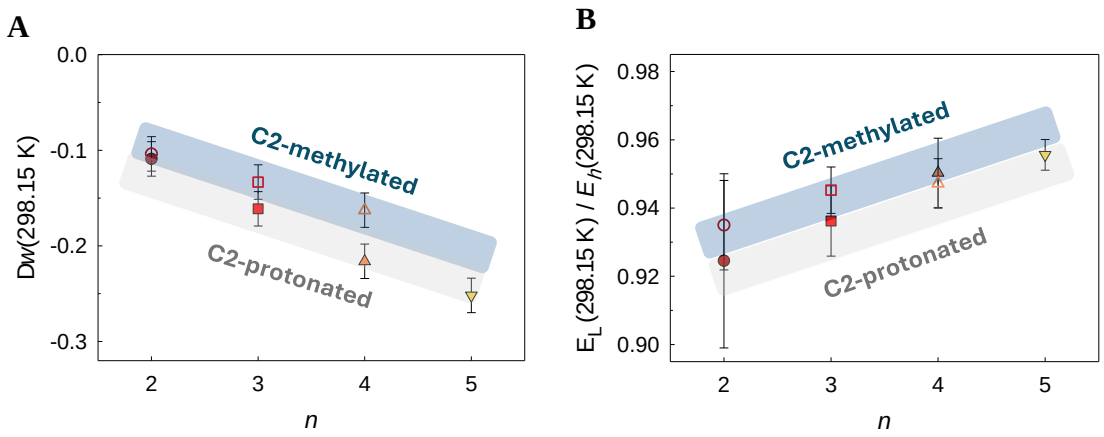



**Figure 5.114.** Viscosity – molar conductivity correlations for the $[^1C_n{}^2C_1{}^3C_1im][NTf_2]$ ILs and their protonated analogues and isomers. **A**: Deviation to the "ideal Walden line" ($\log \Lambda - \log \eta^{-1}$) as a function of the number of carbons on the alkyl chain; **B**: Walden slope and Energy barrier ratio ($E_\Lambda / E_\eta$) as a function of the number of carbons on the alkyl chain. ● $[^1C_2{}^3C_1im][NTf_2]$; ■ $[^1C_3{}^3C_1im][NTf_2]$, ▼ $[^1C_4{}^3C_1im][NTf_2]$, ▲ $[^1C_5{}^3C_1im][NTf_2]$, ○ $[^1C_2{}^2C_1{}^3C_1im][NTf_2]$, □ $[^1C_3{}^2C_1{}^3C_1im][NTf_2]$, △ $[^1C_3{}^2C_1{}^3C_1im][NTf_2]$.

The C2-methylated ILs show a slightly closer proximity to the "ideal line" compared to the C2-protonated ILs. This suggests that the removal of the acidic hydrogen at the position 2 of the imidazolium ring somehow yields a positive impact on the better viscosity-molar conductivity correlation. Furthermore, it is observed an increasing deviation to the "ideal line" with the increase of the alkyl chain of the cation, as has been already described in section 5.1.

### 5.3.3. Isomerization of the Pyridinium Ring

This section is dedicated to the study of the effect of isomerization of the pyridinium ring on the transport properties of bis(trifluoromethylsulfonyl)imide ionic liquids. The density, viscosity, and molar conductivity of $[^1C_3{}^2C_1py][NTf_2]$ and $[^1C_3{}^3C_1py][NTf_2]$ will be presented in this section and compared with $[^1C_4py][NTf_2]$ (Fig. 5.115).

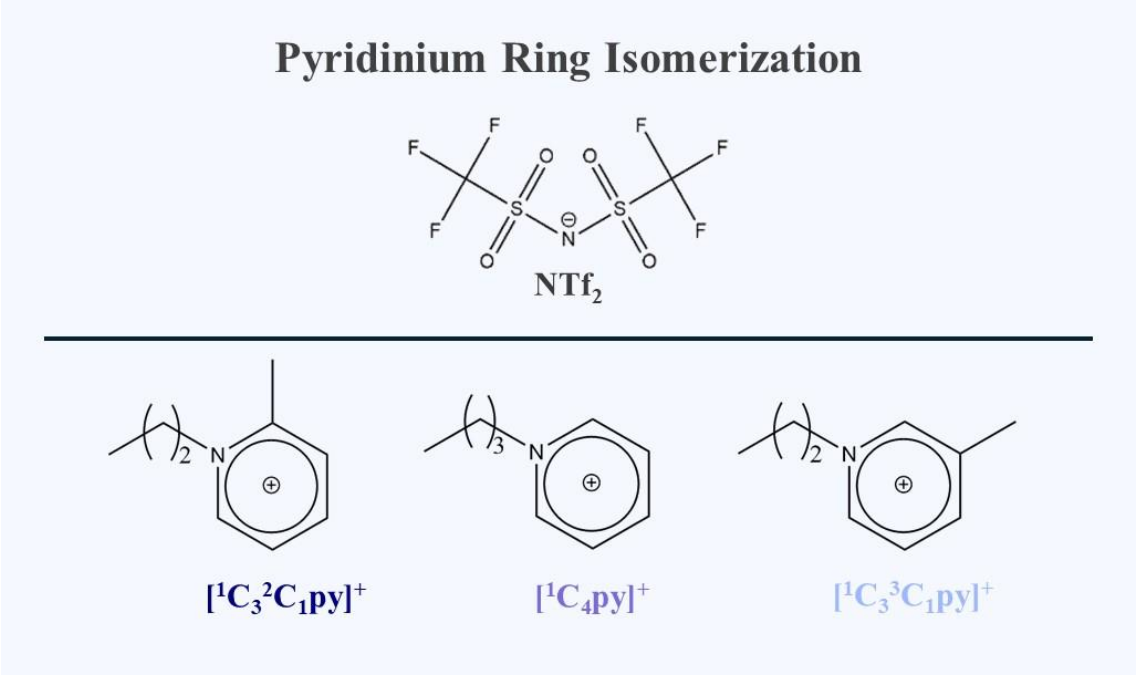



**Figure 5.115.** Schematic representation of the study on the effect of the isomerization of the pyridinium ring on the transport properties of ILs.

#### 5.3.3.1. Density

The resulting fitting coefficients from the temperature dependence of density of the $[^1C_3{}^2C_1py][NTf_2]$ and $[^1C_3{}^3C_1py][NTf_2]$ (Eq. 2.4) are presented in Table 5.69. The densities at the reference temperature ($T$ = 298.15 K) are presented in Table 5.70 together with the molar volume and thermal expansion coefficient derived from Eq. 2.2 and Eq. 2.7 respectively. The graphical representation of density, thermal expansion coefficient, and molar volume as functions of temperature and the reference temperature ($T$ = 298.15 K) are presented in Fig 5.116.

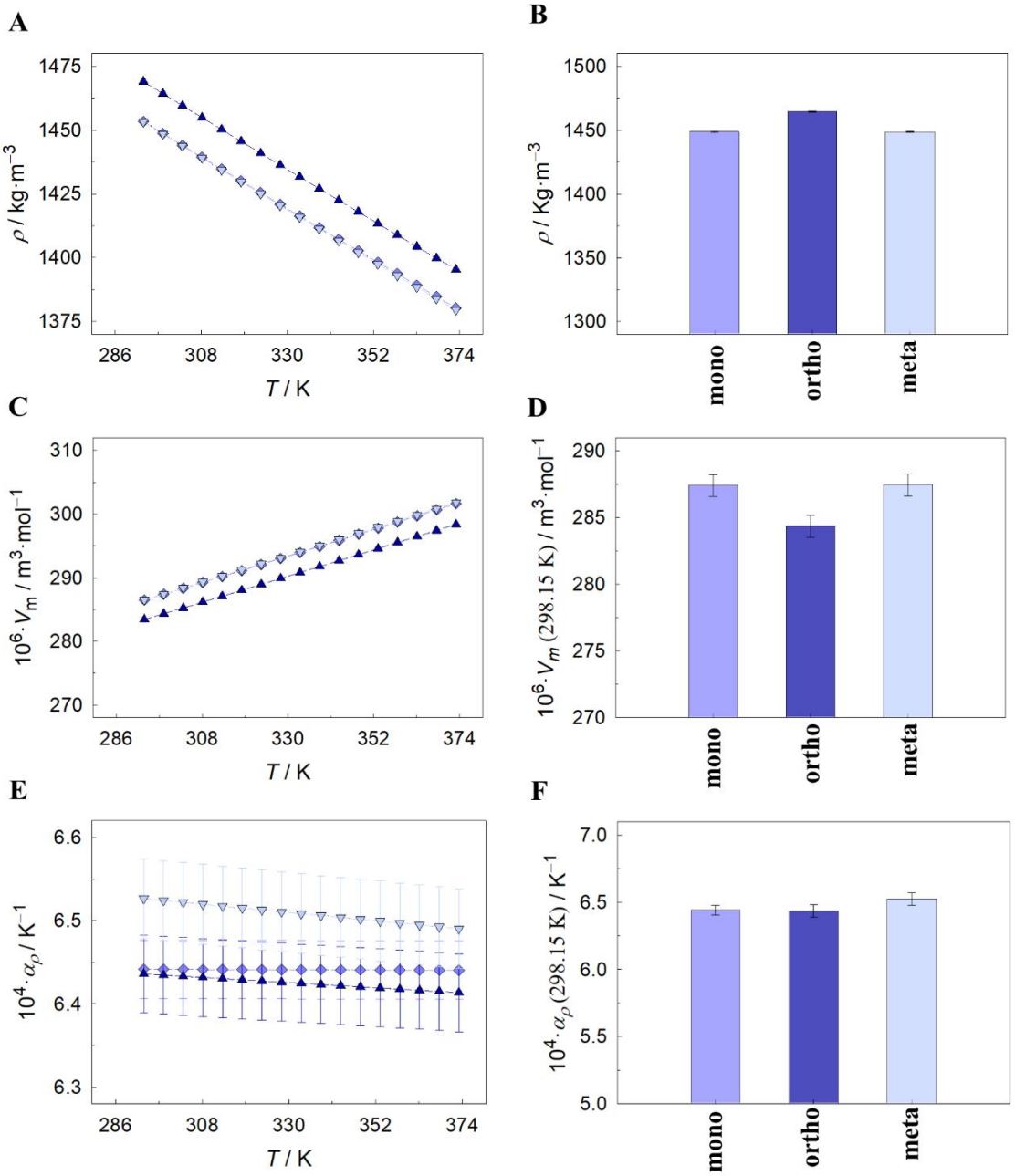



**Figure 5.116.** Density and derived properties of the selected pyridinium isomers as functions of temperature (A, C, E) and at the reference temperature, $T$ = 298.15 K, (B, D, F). **A**, **B**: Density; **C**, **D**: Molar volume; **E**, **F**: Thermal expansion coefficient. ◆ [$^1$C$_4$py][NTf$_2$] (unsubstituted), ▲ [$^1$C$_3$$^2$C$_1$py][NTf$_2$] (ortho) , ▼ [$^1$C$_3$$^3$C$_1$py][NTf$_2$] (meta).

**Table 5.69.** Fitting coefficients used to describe the temperature dependence of density of the studied pyridinium isomers ILs.

| Ionic Liquid | $\frac{T_{\text{interval}}}{\text{K}}$ | $\frac{10^7 \cdot a_2}{\text{K}^{-2}}$ | $\frac{10^4 \cdot a_1}{\text{K}^{-1}}$ | $\frac{a_0}{\text{K}}$ |
|---|---|---|---|---|
| $[^1C_3{}^2C_1py][NTf_2]$ | 293 − 373 | 0.141 ± 0.070 | −6.518 ± 0.047 | 7.4822 ± 0.0008 |
| $[^1C_3{}^3C_1py][NTf_2]$ | 293 − 373 | 0.226 ± 0.072 | −6.659 ± 0.048 | 7.4748 ± 0.0008 |

The presented fitting coefficients were derived from the experimental $\rho(T)$ data (appendix) by applying a polynomial fitting function, $\ln[\rho(T)] = a_2T^2 + a_1T + a_0$ (Eq. 2.4). The standard uncertainties related to the fitting coefficients were calculated to the confidence level of 0.95 ($k \approx 2$).

**Table 5.70.** Density, thermal expansion coefficient, and molar volume at the reference temperature ($T$ = 298.15 K) for the studied pyridinium isomers ILs.

| Ionic Liquid | $\frac{\rho(298.15\ \text{K})}{\text{kg} \cdot \text{m}^{-3}}$ | $\frac{10^4 \cdot \alpha_\rho(298.15\ \text{K})}{\text{K}^{-1}}$ | $\frac{10^6 \cdot V_\text{m}(298.15\ \text{K})}{\text{m}^3 \cdot \text{mol}^{-1}}$ |
|---|---|---|---|
| $[^1C_3{}^2C_1py][NTf_2]$ | 1464.3 ± 0.5 | 6.43 ± 0.05 | 284.4 ± 0.8 |
| $[^1C_3{}^3C_1py][NTf_2]$ | 1448.5 ± 0.5 | 6.52 ± 0.05 | 287.5 ± 0.8 |

$\rho(T = 298.15\ \text{K})$ and $\alpha_\rho(T = 298.15\ \text{K})$ were calculated from the fitting coefficients presented in Table 5.69 and by applying Eq. 2.4 and Eq. 2.7 respectively. $V_\text{m}(298.15\ \text{K}) = M/\rho(298.15\ \text{K})$. The standard uncertainty associated with $\alpha_\rho$ and $V_\text{m}$ were calculated by applying the propagation of uncertainty to Eq. 2.7 and 2.2 respectively.

#### 5.3.3.2. Viscosity

The VFT coefficients (Eq 2.44) of $[^1C_3{}^2C_1py][NTf_2]$ and $[^1C_3{}^3C_1py][NTf_2]$ ILs obtained from the experimental viscosity-temperature data, $\eta(T)$, for the selected ILs are presented in Table 5.71.

**Table 5.71.** Fitting coefficients used to describe the temperature dependence of viscosity of the studied pyridinium isomers.

| Ionic Liquid | $\frac{T_{\text{interval}}}{\text{K}}$ | $\frac{10^3 \cdot A_\eta}{\text{Pa} \cdot \text{s}}$ | $\frac{B_\eta}{\text{K}}$ | $\frac{C_\eta}{\text{K}}$ |
|---|---|---|---|---|
| $[^1C_3{}^2C_1py][NTf_2]$ | 293 − 373 | 0.1880 ± 0.0006 | 741.6 ± 0.9 | 176.5 ± 0.1 |
| $[^1C_3{}^3C_1py][NTf_2]$ | 293 − 373 | 0.1894 ± 0.0007 | 710.2 ± 1.0 | 172.9 ± 0.1 |

The presented fitting coefficients were derived from the experimental $\eta(T)$ data (appendix) by applying the VFT fitting function, Eq. 2.44. The standard uncertainties related to the VFT coefficients were calculated to the confidence level of 0.95 ($k \approx 2$).

The viscosities at the reference temperature ($T$ = 298.15 K) for $[^1C_3{}^2C_1py][NTf_2]$ and $[^1C_3{}^3C_1py][NTf_2]$ are presented in Table 5.72 together with the energy barrier and strength parameter derived from Eq. 2.47 and Eq. 2.49 respectively.

**Table 5.72.** Viscosity and derived energy barrier of the studied pyridinium isomers at the reference temperature ($T$ = 298.15 K), together with the strength parameter.

| Ionic Liquid | $\eta(T=298.15\ \text{K})$ / Pa · s | $E_\eta(T=298.15\ \text{K})$ / kJ · mol$^{-1}$ | $D_\eta$ |
|---|---|---|---|
| [$^1$C$_3^2$C$_1$py][NTf$_2$] | 0.0837 ± 0.0008 | 37.07 ± 0.07 | 4.201 ± 0.006 |
| [$^1$C$_3^3$C$_1$py][NTf$_2$] | 0.0550 ± 0.0006 | 33.48 ± 0.07 | 4.107 ± 0.006 |

$\eta$($T$ = 298.15 K) and $E_\eta$($T$ = 298.15 K) were calculated from the fitting coefficients presented in Table 5.71 and by applying Eq. 2.44 and Eq. 2.47, respectively. The strength parameter was calculated by Eq. 2.49, $D_\eta = B_\eta / C_\eta$. The relative standard uncertainty associated with the viscosity measurements was estimated as $u(\eta)$ = 1.0% (Eq. 2.72); The standard uncertainty associated with the derived energy barrier, $u(E_\eta)$, and strength parameter , $u(D_\eta)$, was calculated by applying the propagation of uncertainty to Eq. 2.47 and Eq. 2.49, respectively.

The temperature dependence of the viscosity and derived properties of [$^1$C$_3^2$C$_1$py][NTf$_2$] and [$^1$C$_3^3$C$_1$py][NTf$_2$] and the 1-alkylpyridinium isomer is presented in Fig. 5.117.

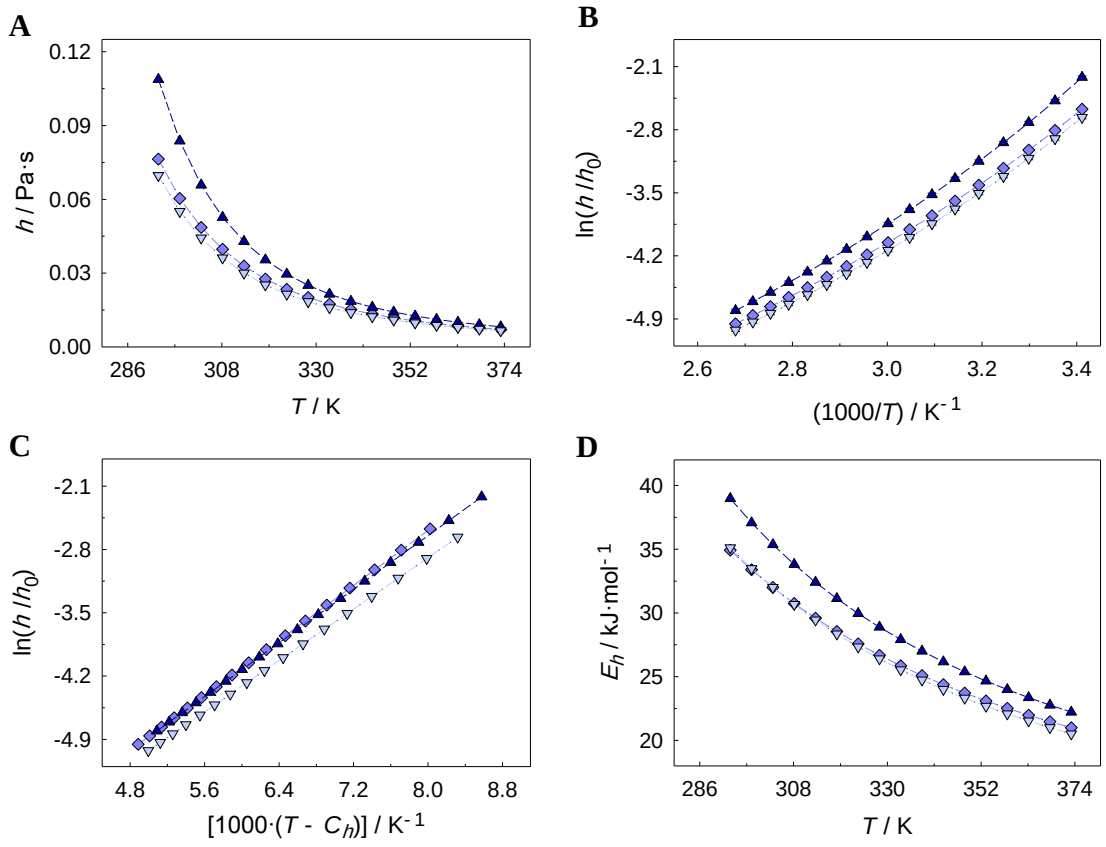



**Figure 5.117.** Temperature dependence of viscosity for the pyridinium isomers. **A**: viscosity, **B**: Arrhenius representation; **C**: VFT representation; **D**: Energy barrier. ◆ [$^1$C$_4$py][NTf$_2$] (unsubstituted), ▲ [$^1$C$_3^2$C$_1$py][NTf$_2$] (ortho) , ▼ [$^1$C$_3^3$C$_1$py][NTf$_2$] (meta). $\eta_0$ = 1 Pa·s

The deviation of the available viscosity literature data to the experimental results for the pyridinium isomers is presented in Fig. 5.118. Overall the available data lies within ± 5% relative to the results obtained in this work. The results reported by Gárcia-Mardones *et al.* (ortho) [232], Oliveira *et al.* (meta) [125], and Bhattacharjee *et al.* (meta)[233] are in excellent agreement with the present work.

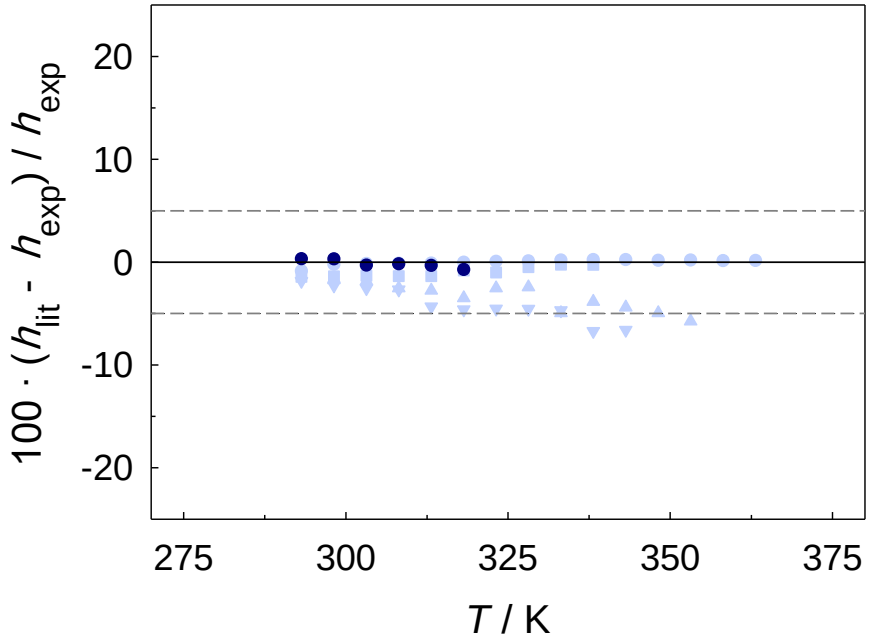



**Figure 5.118.** Deviation of the available viscosity literature data to the experimental results for the pyridinium isomers. **[$^1$C$_3$$^2$C$_1$py][NTf$_2$] (ortho):** ● [232]; **[$^1$C$_3$$^3$C$_1$py][NTf$_2$] (meta):** ● [125], ■ [233], ▲ [234]; ▼ [80].

### 5.3.3.3. Electrical Conductivity

The VFT coefficients (Eq 2.24) of [$^1$C$_3$$^2$C$_1$py][NTf$_2$] and [$^1$C$_3$$^3$C$_1$py][NTf$_2$] obtained from the experimental electrical conductivity-temperature data, $\sigma(T)$, are presented in Table 5.73.

**Table 5.73.** Fitting coefficients used to describe the temperature dependence of electrical conductivity of the studied pyridinium isomers.

| Ionic Liquid | $\frac{A_\sigma}{S \cdot m^{-1}}$ | $\frac{B_\sigma}{K}$ | $\frac{C_\sigma}{K}$ | $\frac{\sigma(T=298.15\ K)}{S \cdot m^{-1}}$ |
|---|---|---|---|---|
| [$^1$C$_3$$^2$C$_1$py][NTf$_2$] | 57.19 ± 0.37 | 601.1 ± 1.7 | 185.4 ± 0.2 | 0.2767 ± 0.0042 |
| [$^1$C$_3$$^3$C$_1$py][NTf$_2$] | 54.35 ± 0.44 | 570.7 ± 2.1 | 182.1 ± 0.2 | 0.3976 ± 0.0060 |

The presented fitting coefficients were derived from the experimental $\sigma(T)$ data (appendix) by applying the VFT fitting function, Eq. 2.44. The standard uncertainties related to the VFT coefficients were calculated to the confidence level of 0.95 ($k \approx 2$). The relative standard uncertainty associated with the viscosity measurements was estimated as $u(\sigma) = 1.5\%$ (Eq. 4.15).

The deviation of the available viscosity literature data to the experimental results for the pyridinium isomers are presented in Fig. 5.119. Only one literature source was found for

each ionic liquid and both were found to lie within ± 5% relative to the results obtained in this work.

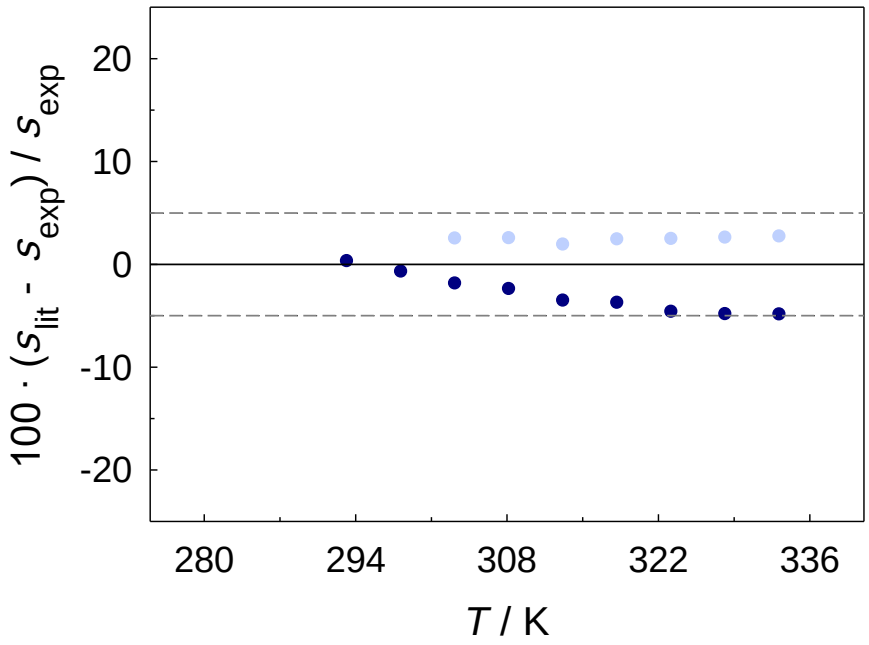



**Figure. 5.119.** Deviation of the available electrical conductivity literature data to the experimental results for the pyridinium isomers. **[$^1$C$_3$$^2$C$_1$py][NTf$_2$] (ortho):** ● ; **[$^1$C$_3$$^3$C$_1$py][NTf$_2$] (meta):** ● [234].

### 5.3.3.4. Molar Conductivity

The VFT coefficients (Eq 2.44) of [$^1$C$_3$$^2$C$_1$py][NTf$_2$] and [$^1$C$_3$$^3$C$_1$py][NTf$_2$] ILs obtained from the experimental molar conductivity-temperature data, $\Lambda(T)$, for the selected ILs are presented in Table 5.74.

**Table 5.74.** Fitting coefficients used to describe the temperature dependence of molar conductivity of the studied pyridinium isomers.

| Ionic Liquid | $\frac{T_{\text{interval}}}{\text{K}}$ | $\frac{10^4 \cdot A_\Lambda}{\text{S} \cdot \text{m}^2 \cdot \text{mol}^{-1}}$ | $\frac{B_\Lambda}{\text{K}}$ | $\frac{C_\Lambda}{\text{K}}$ |
|---|---|---|---|---|
| [$^1$C$_3$$^2$C$_1$py][NTf$_2$] | 293 − 333 | 194.3 ± 1.3 | 633.7 ± 1.8 | 183.2 ± 0.2 |
| [$^1$C$_3$$^3$C$_1$py][NTf$_2$] | 293 − 333 | 188.0 ± 2.1 | 605.5 ± 3.0 | 179.5 ± 0.3 |

The presented fitting coefficients were derived from the experimental $\Lambda(T)$ data (appendix) by applying the VFT fitting function, Eq. 2.44. The standard uncertainties related to the VFT coefficients were calculated to the confidence level of 0.95 ($k \approx 2$).

The molar conductivity at the reference temperature ($T$ = 298.15 K) for [$^1C_3{}^2C_1$py][$NTf_2$] and [$^1C_3{}^3C_1$py][$NTf_2$] are presented in Table 5.75 together with the energy barrier and strength parameter derived from Eq. 2.47 and Eq. 2.49 respectively.

**Table 5.75.** Molar conductivity and derived energy barrier of the studied pyridinium isomers at the reference temperature ($T$ = 298.15 K), together with the strength parameter.

| Ionic Liquid | $10^4 \cdot \Lambda(T{=}298.15\ \mathrm{K})$ / S · m² · mol$^{-1}$ | $E_\Lambda(T{=}298.15\ \mathrm{K})$ / kJ · mol$^{-1}$ | $D_\Lambda$ |
|---|---|---|---|
| [$^1C_3{}^2C_1$py][$NTf_2$] | 0.784 ± 0.012 | 35.45 ± 0.16 | 3.459 ± 0.011 |
| [$^1C_3{}^3C_1$py][$NTf_2$] | 1.142 ± 0.017 | 31.79 ± 0.23 | 3.373 ± 0.018 |

$\Lambda(T = 298.15\ \mathrm{K})$ and $E_\Lambda(T = 298.15\ \mathrm{K})$ were calculated from the fitting coefficients presented in Table 5.74 and by applying Eq. 2.44 and Eq. 2.47, respectively. The strength parameter was calculated by Eq. 2.49, $D_\Lambda = B_\Lambda / C_\Lambda$. The relative standard uncertainty associated with the viscosity measurements was estimated as $u(\Lambda)$ = 1.5% (Eq. 4.15); The standard uncertainty associated with the derived energy barrier, $u(E_\Lambda)$, and strength parameter , $u(D_\Lambda)$, was calculated by applying the propagation of uncertainty to Eq. 2.47 and Eq. 2.49, respectively.

The temperature dependence of the molar conductivity and derived properties of [$^1C_3{}^2C_1$py][$NTf_2$] and [$^1C_3{}^3C_1$py][$NTf_2$] and the 1-alkylpyridinium isomer is presented in Fig. 5.120.

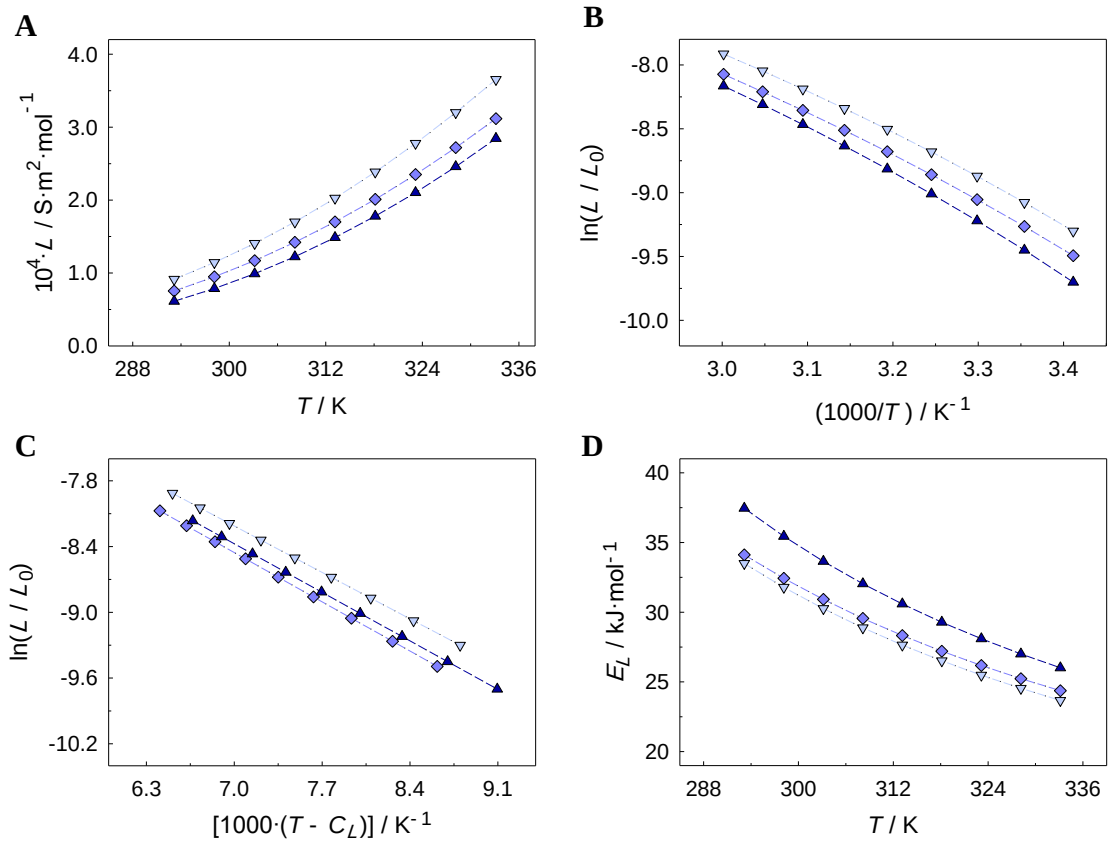



**Figure 5.120.** Temperature dependence of molar conductivity for the pyridinium isomers. **A**: viscosity, **B**: Arrhenius representation; **C**: VFT representation; **D**: Energy barrier. ◆ [$^1C_4$py][$NTf_2$] (unsubstituted), ▲ [$^1C_3{}^2C_1$py][$NTf_2$] (ortho) , ▼ [$^1C_3{}^3C_1$py][$NTf_2$] (meta). $\Lambda_0$ = 1 S·m$^2$·mol$^{-1}$.

#### 5.3.3.5. Discussion

A graphical summary of the results obtained for the measured transport properties and respective derived parameters of the pyridinium isomers is presented in Fig. 5.121. A schematic diagram of the effect of pyridinium isomerization on the transport properties and derived parameters is presented in Fig. 5.122.

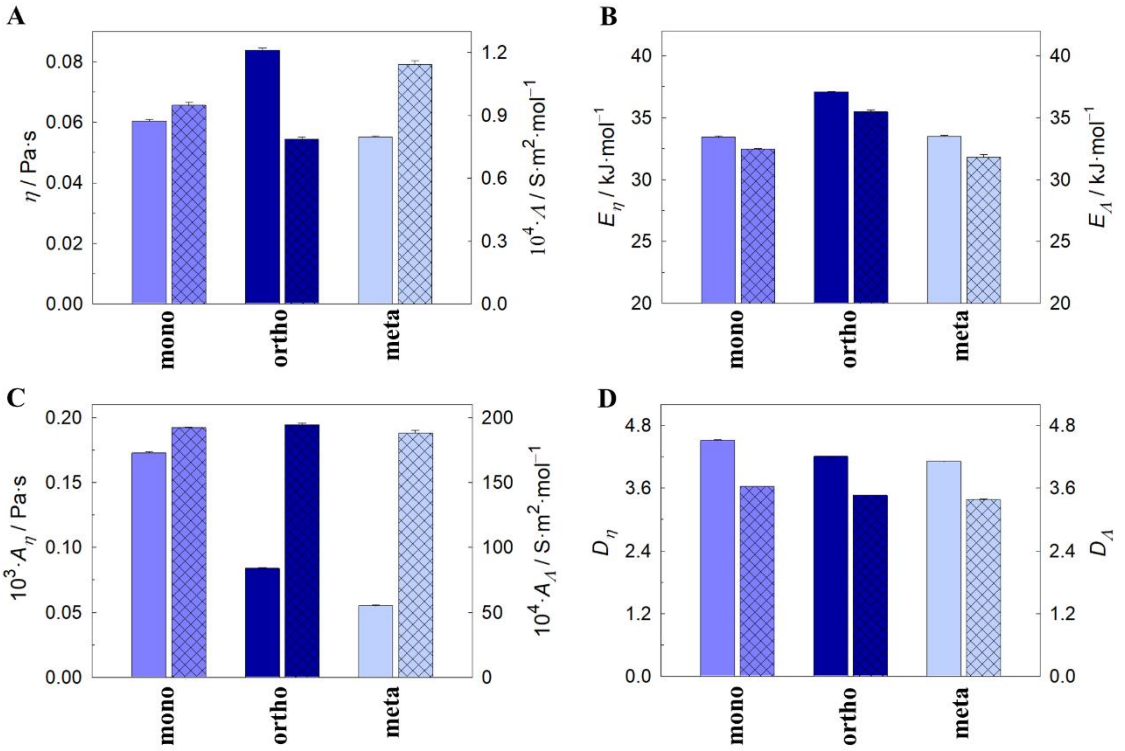



**Figure 5.121.** Graphical summary of the results obtained for the measured transport properties and respective derived parameters of the pyridinium isomers, **[$^1$C$_4$py][NTf$_2$] (unsubstituted)**, **[$^1$C$_3$$^2$C$_1$py][NTf$_2$] (ortho)**, **[$^1$C$_3$$^3$C$_1$py][NTf$_2$] (meta)**. **A**: Viscosity and molar conductivity; **B**: Energy barrier; **C**: Pre-exponential coefficient; **D**: Strength parameter. **Plain bars**: viscosity (left); **Dashed bars**: molar conductivity (right).

Based on the results, the isomerization to the ortho conformation was found to result in an increase in viscosity and a decrease in molar conductivity. On the other hand, the inverse effect was observed for the isomerization to the meta conformation. This is supported by the derived values of energy barrier as [$^1$C$_3$$^2$C$_1$py][NTf$_2$] presents the highest and [$^1$C$_3$$^3$C$_1$py][NTf$_2$] the lowest. For reference, the viscosity of the meta isomer is comparable to $\eta$([$^1$C$_3$py][NTf$_2$]), while the viscosity of the ortho isomer is comparable to $\eta$([$^1$C$_6$py][NTf$_2$]). This suggests that the proximity of the alkyl side chains hinders the dynamic flow and ion transport. This is somewhat supported by the density data as the higher density of [$^1$C$_3$$^2$C$_1$py][NTf$_2$] suggests a more cohesive “packing”. Furthermore, it

seems that the presence of two spaced chains creates a more symmetric shape. Rocha *et al.*. [1] have already demonstrated that cation symmetry reduces the viscosity of imidazolium bis(trifluoromethylsulfonyl)imide ionic liquids. This is also consistent with work published by Oliveira *et al.* [125]. In this work the authors reported that [$^1C_4{}^3C_1$py][$NTf_2$] (meta isomer) compared to [$^1C_4{}^4C_1$py][$NTf_2$] (para isomer). Overall, the pre-exponential coefficients seem to be somewhat similar for the three isomers, and the same can be said for the viscosity-molar conductivity correlation (Walden plot, Fig. 5.123).

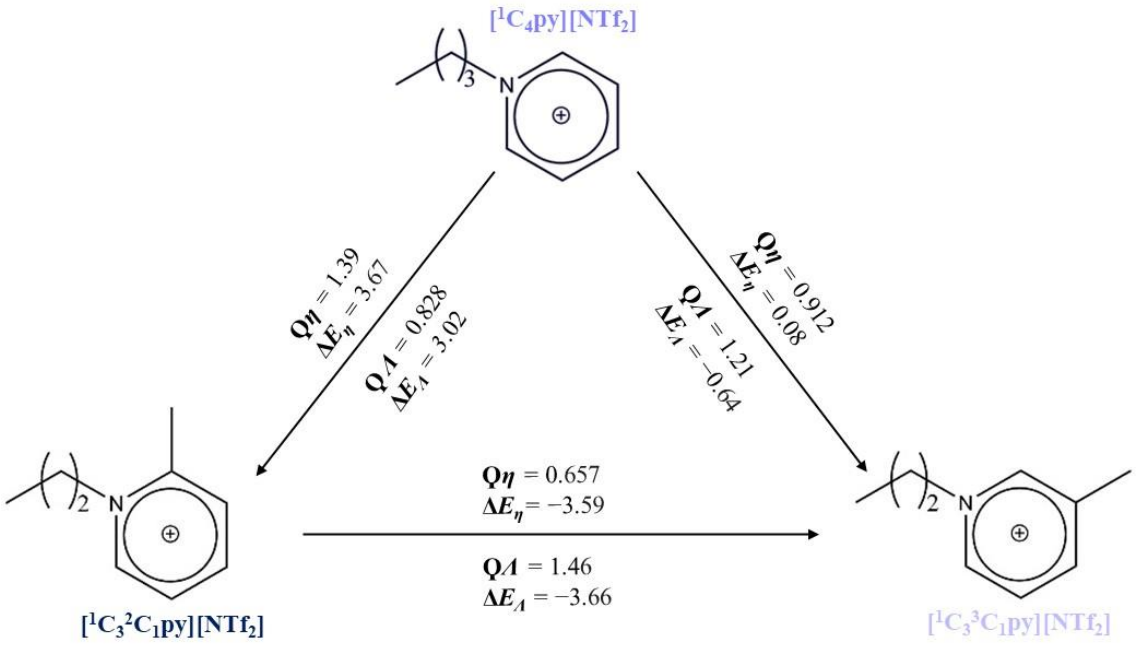



**Figure 5.122.** Schematic diagram of the effect of isomerization of the pyridinium ring on the transport properties and derived parameters. The arrows represent the comparison between IL1 and IL2 (arrow point). Δ = IL2 – IL1; Q = IL2/IL1.

The viscosity and molar conductivity data were used to construct the Walden plot (Fig. 5.123) for the pyridinium isomers.

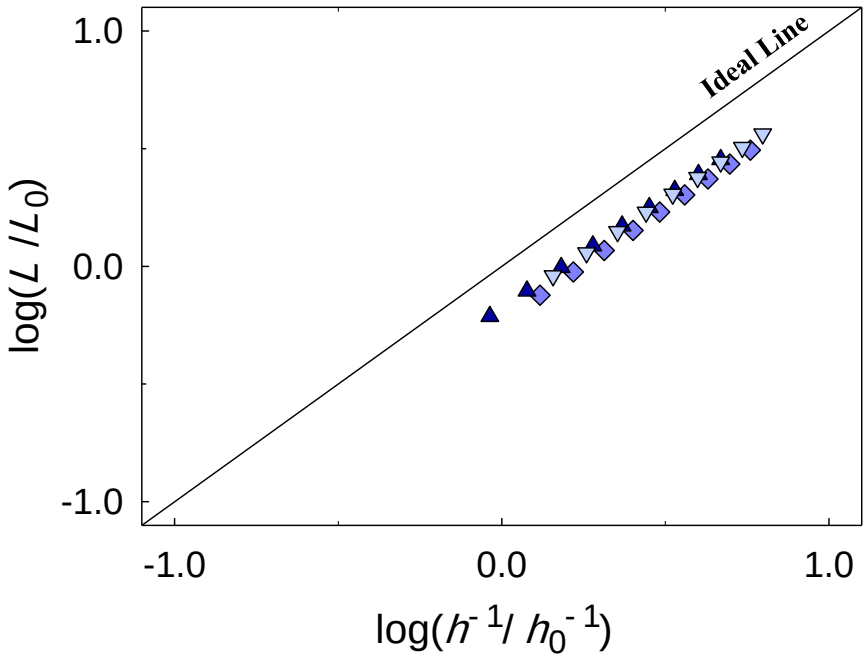



**Figure 5.123.** Walden plot for the pyridinium isomers based on experimental viscosity and molar conductivity data. ◆ [$^1$C$_4$py][NTf$_2$] (unsubstituted), ▲ [$^1$C$_3$$^2$C$_1$py][NTf$_2$] (ortho) , ▼ [$^1$C$_3$$^3$C$_1$py][NTf$_2$] (meta). $\eta_0$ = 1 Poise; $\Lambda_0$ = 1 S·cm$^2$·mol$^{-1}$.

Fig 5.124 presents the relationship between the derived energy barriers and the selected literature data for the enthalpy of vaporization (cohesive interaction).

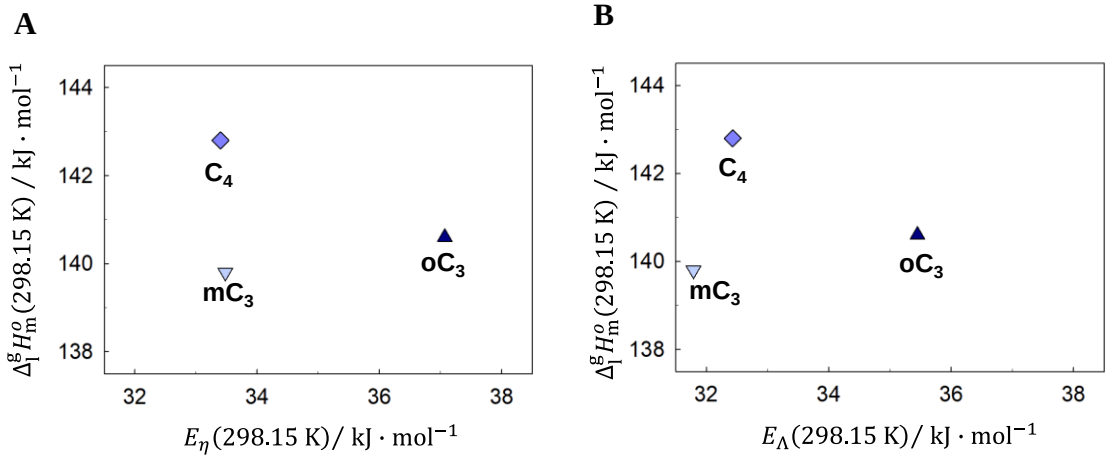



**Figure 5.124.** Correlation between the transport properties energy barrier and the enthalpy of vaporization for the pyridinium isomers. **A**: viscosity; **B**: molar conductivity. ◆ [$^1$C$_4$py][NTf$_2$] (unsubstituted) [235], ▲ [$^1$C$_3$$^2$C$_1$py][NTf$_2$] (ortho) [236] , ▼ [$^1$C$_3$$^3$C$_1$py][NTf$_2$] (meta) [236].

A more clear and informative representation of this relationship can be achieved by looking at the ratio between the energy barrier and the enthalpy of vaporization as a function of the number of carbons on the alkyl chain (Fig. 5.125).

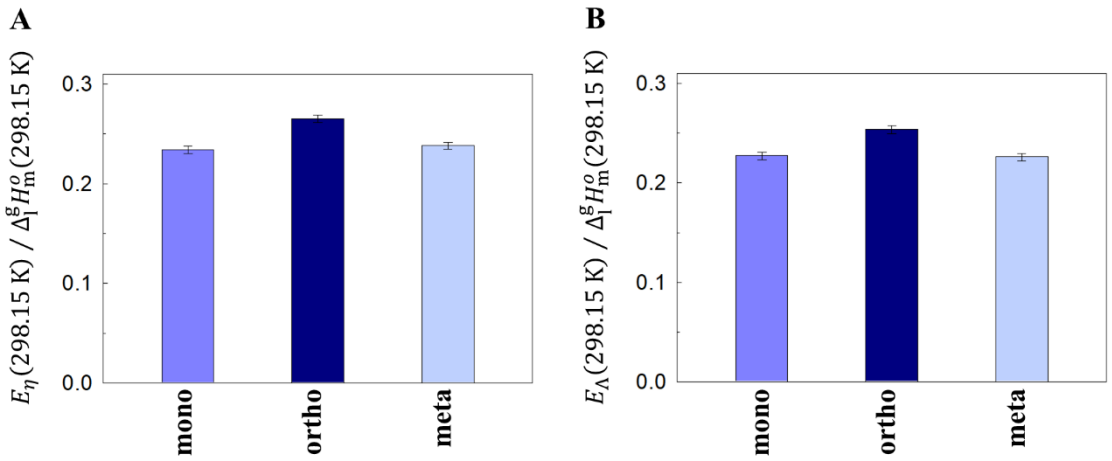



**Figure 5.125.** Ratio between energy barrier and enthalpy of vaporization (cohesive interaction) for the pyridinium isomers. **A**: viscosity; **B**: molar conductivity. ◆ [$^1$C$_4$py][NTf$_2$] (unsubstituted) [235], ▲ [$^1$C$_3{}^2$C$_1$py][NTf$_2$] (ortho) [236] , ▼ [$^1$C$_3{}^3$C$_1$py][NTf$_2$] (meta) [236].

In previous work, the cohesive interaction (enthalpy of vaporization) of the pyridinium bis(trifluoromethylsulfonyl)imide was found not to be significantly affected by the isomerization (ortho, meta, para) but instead to be usually higher for the monosubstituted isomer [236]. Based on that, the energy barrier associated with the transport properties of [$^1$C$_3{}^2$C$_1$py][NTf$_2$] corresponds to a higher fraction of cohesive interaction of the liquid. On a similar basis to what was proposed on the methylation effect, since this potential is associated with ion transport and dynamic flow of the liquid, this higher fraction may be due to a more hindered ion motion due to the more compact packing and proximity of the alkyl chains.

# References

[1] M.A.A. Rocha, C.M.S.S. Neves, M.G. Freire, O. Russina, A. Triolo, J.A.P. Coutinho, L.M.N.B.F. Santos, J. Phys. Chem. B 117 (2013) 10889. https://doi.org/10.1021/jp406374a

[2] M.A.A. Rocha, F.M.S. Ribeiro, A.I.M.C.L. Ferreira, J.A.P. Coutinho, L.M.N.B.F. Santos, J. Mol. Liq. 188 (2013) 196. https://doi.org/10.1016/j.molliq.2013.09.031

[3] C. Schreiner, S. Zugmann, R. Hartl, H.J. Gores, J. Chem. Eng. Data 55 (2010) 1784. https://doi.org/10.1021/je900878j

[4] C.M.S.S. Neves, K.A. Kurnia, J.A.P. Coutinho, I.M. Marrucho, J.N.C. Lopes, M.G. Freire, L.P.N. Rebelo, J. Phys. Chem. B 117 (2013) 10271. https://doi.org/10.1021/jp405913b

[5] H.F.D. Almeida, J.N. Canongia Lopes, L.P.N. Rebelo, J.A.P. Coutinho, M.G. Freire, I.M. Marrucho, J. Chem. Eng. Data 61 (2016) 2828. https://doi.org/10.1021/acs.jced.6b00178

[6] J.-Y. Wu, Y.-P. Chen, C.-S. Su, Journal of the Taiwan Institute of Chemical Engineers 45 (2014) 2205. https://doi.org/10.1016/j.jtice.2014.04.012

[7] K.R. Harris, M. Kanakubo, L.A. Woolf, Journal of Chemical and Engineering Data 51 (2006) 1161. https://doi.org/10.1021/je060082s

[8] D. Tomida, S. Kenmochi, T. Tsukada, K. Qiao, Q. Bao, C. Yokoyama, Int. J. Thermophys. 33 (2012) 959. https://doi.org/10.1007/s10765-012-1233-x

[9] S. Seki, T. Kobayashi, Y. Kobayashi, K. Takei, H. Miyashiro, K. Hayamizu, S. Tsuzuki, T. Mitsugi, Y. Umebayashi, J. Mol. Liq. 152 (2010) 9. https://doi.org/10.1016/j.molliq.2009.10.008

[10] D. Song, J. Chen, J. Chem. Eng. Data 59 (2014) 257. https://doi.org/10.1021/je400332j

[11] A. Noda, K. Hayamizu, M. Watanabe, J. Phys. Chem. B 105 (2001) 4603. https://doi.org/10.1021/jp004132q

[12] M. Shamsipur, A.A.M. Beigi, M. Teymouri, S.M. Pourmortazavi, M. Irandoust, J. Mol. Liq. 157 (2010) 43. https://doi.org/10.1016/j.molliq.2010.08.005

[13] O. Ciocirlan, O. Croitoru, O. Iulian, J. Chem. Thermodyn. 101 (2016) 285. https://doi.org/10.1016/j.jct.2016.06.015

[14] S. Zhang, X. Li, H. Chen, J. Wang, J. Zhang, M. Zhang, J. Chem. Eng. Data 49 (2004) 760. https://doi.org/10.1021/je030191w

[15] X. He, Q. Shao, W. Kong, L. Yu, X. Zhang, Y. Deng, Fluid Phase Equilib. 366 (2014) 9. https://doi.org/10.1016/j.fluid.2014.01.003

[16] E. Vercher, F.J. Llopis, V. González-Alfaro, P.J. Miguel, V. Orchillés, A. Martínez-Andreu, J. Chem. Thermodyn. 90 (2015) 174. https://doi.org/10.1016/j.jct.2015.06.036

[17] X.-H. Fan, Y.-P. Chen, C.-S. Su, J. Chem. Eng. Data 61 (2016) 920. https://doi.org/10.1021/acs.jced.5b00753

[18] V. Narsimlu, K.C.S. Reddy, T.V. Krishna, T.M. Mohan, V.S. Rao, J. Chem. Thermodyn. 139 (2019) 105891. https://doi.org/10.1016/j.jct.2019.105891

[19] E. Rilo, J. Vila, M. García, L.M. Varela, O. Cabeza, J. Chem. Eng. Data 55 (2010) 5156. https://doi.org/10.1021/je100687x

[20] K.R. Harris, M. Kanakubo, L.A. Woolf, J. Chem. Eng. Data 52 (2007) 2425. https://doi.org/10.1021/je700370z

[21] M. Atilhan, J. Jacquemin, D. Rooney, M. Khraisheh, S. Aparicio, Industrial & Engineering Chemistry Research 52 (2013) 16774. https://doi.org/10.1021/ie403065u

[22] J. Salgado, T. Regueira, L. Lugo, J. Vijande, J. Fernández, J. García, J. Chem. Thermodyn. 70 (2014) 101. https://doi.org/10.1016/j.jct.2013.10.027

[23] H. Jin, B. O'Hare, J. Dong, S. Arzhantsev, G.A. Baker, J.F. Wishart, A.J. Benesi, M. Maroncelli, J. Phys. Chem. B 112 (2008) 81. https://doi.org/10.1021/jp076462h

[24] K. Iwasaki, K. Yoshii, T. Tsuda, S. Kuwabata, J. Mol. Liq. 246 (2017) 236. https://doi.org/10.1016/j.molliq.2017.09.067

[25] J. Gao, N.J. Wagner, J. Mol. Liq. 223 (2016) 678. https://doi.org/10.1016/j.molliq.2016.08.084

[26] V.A. Nikitina, A. Nazet, T. Sonnleitner, R. Buchner, J. Chem. Eng. Data 57 (2012) 3019. https://doi.org/10.1021/je300603d

[27] L.M. Galán Sánchez, G.W. Meindersma, A.B. de Haan, Chem. Eng. Res. Des. 85 (2007) 31. https://doi.org/10.1205/cherd06124

[28] K.R. Seddon, A. Stark, M.-J. Torres, Clean Solvents, American Chemical Society, 2002, p. 34-49. https://doi.org/doi:10.1021/bk-2002-0819.ch004

10.1021/bk-2002-0819.ch004

[29] H. Tokuda, K. Hayamizu, K. Ishii, M.A.B.H. Susan, M. Watanabe, J. Phys. Chem. B 108 (2004) 16593. https://doi.org/10.1021/jp047480r

[30] W. Ahmad, A. Al-Ajmi, G.R. Vakili-Nezhaad, J. Solution Chem. 48 (2019) 578. https://doi.org/10.1007/s10953-019-00868-0

[31] Y.A. Sanmamed, D. González-Salgado, J. Troncoso, C.A. Cerdeiriña, L. Romaní, Fluid Phase Equilib. 252 (2007) 96. https://doi.org/10.1016/j.fluid.2006.12.016

[32] I. Bahadur, M. Kgomotso, E.E. Ebenso, G. Redhi, RSC Advances 6 (2016) 104708. https://doi.org/10.1039/C6RA15476J

[33] X. Yang, Y. Fang, J. Chem. Eng. Data 64 (2019) 722. https://doi.org/10.1021/acs.jced.8b00965

[34] Y. Yin, C. Zhu, Y. Ma, J. Chem. Thermodyn. 102 (2016) 413. https://doi.org/10.1016/j.jct.2016.07.041

[35] B. Sarkoohaki, M. Karimkhani, M. Almasi, A. Najafloo, S. Mansouri, J. Solution Chem. 49 (2020) 405. https://doi.org/10.1007/s10953-020-00967-3

[36] T.-Y. Wu, B.-K. Chen, L. Hao, K.-F. Lin, I.W. Sun, Journal of the Taiwan Institute of Chemical Engineers 42 (2011) 914. https://doi.org/10.1016/j.jtice.2011.04.006

[37] K.R. Harris, M. Kanakubo, J. Chem. Eng. Data 66 (2021) 4618. https://doi.org/10.1021/acs.jced.1c00628

[38] A. Ahosseini, A.M. Scurto, Int. J. Thermophys. 29 (2008) 1222. https://doi.org/10.1007/s10765-008-0497-7

[39] A.A. Miran Beigi, M. Abdouss, M. Yousefi, S.M. Pourmortazavi, A. Vahid, J. Mol. Liq. 177 (2013) 361. https://doi.org/10.1016/j.molliq.2012.10.025

[40] F. Kermanpour, H.Z. Niakan, J. Chem. Thermodyn. 48 (2012) 129. https://doi.org/10.1016/j.jct.2011.12.008

[41] H. Ning, M. Hou, Q. Mei, Y. Liu, D. Yang, B. Han, Science China Chemistry 55 (2012) 1509. https://doi.org/10.1007/s11426-012-4655-1

[42] F. Kermanpour, T. Sharifi, Thermochim. Acta 527 (2012) 211. https://doi.org/10.1016/j.tca.2011.10.030

[43] B. Mokhtarani, M.M. Mojtahedi, H.R. Mortaheb, M. Mafi, F. Yazdani, F. Sadeghian, J. Chem. Eng. Data 53 (2008) 677. https://doi.org/10.1021/je700521t

[44] L.G. Sánchez, J.R. Espel, F. Onink, G.W. Meindersma, A.B.d. Haan, J. Chem. Eng. Data 54 (2009) 2803. https://doi.org/10.1021/je800710p

[45] J. Restolho, A.P. Serro, J.L. Mata, B. Saramago, J. Chem. Eng. Data 54 (2009) 950. https://doi.org/10.1021/je800727f

[46] J. Fuller, R.T. Carlin, R.A. Osteryoung, J. Electrochem. Soc. 144 (1997) 3881. https://doi.org/10.1149/1.1838106

[47] J. Leys, M. Wübbenhorst, C. Preethy Menon, R. Rajesh, J. Thoen, C. Glorieux, P. Nockemann, B. Thijs, K. Binnemans, S. Longuemart, J. Chem. Phys. 128 (2008). https://doi.org/10.1063/1.2827462

[48] J. Vila, P. Ginés, J.M. Pico, C. Franjo, E. Jiménez, L.M. Varela, O. Cabeza, Fluid Phase Equilib. 242 (2006) 141. https://doi.org/10.1016/j.fluid.2006.01.022

[49] A. Stoppa, O. Zech, W. Kunz, R. Buchner, J. Chem. Eng. Data 55 (2010) 1768. https://doi.org/10.1021/je900789j

[50] Y.-H. Yu, A.N. Soriano, M.-H. Li, J. Chem. Thermodyn. 41 (2009) 103. https://doi.org/10.1016/j.jct.2008.07.013

[51] T. Nishida, Y. Tashiro, M. Yamamoto, J. Fluorine Chem. 120 (2003) 135. https://doi.org/10.1016/S0022-1139(02)00322-6

[52] K.R. Harris, M. Kanakubo, N. Tsuchihashi, K. Ibuki, M. Ueno, J. Phys. Chem. B 112 (2008) 9830. https://doi.org/10.1021/jp8021375

[53] J. Vila, L.M. Varela, O. Cabeza, Electrochim. Acta 52 (2007) 7413. https://doi.org/10.1016/j.electacta.2007.06.044

[54] S.A. Pandit, M.A. Rather, S.A. Bhat, G.M. Rather, M.A. Bhat, J. Solution Chem. 45 (2016) 1641. https://doi.org/10.1007/s10953-016-0514-6

[55] Y.-H. Yu, A.N. Soriano, M.-H. Li, Thermochim. Acta 482 (2009) 42. https://doi.org/10.1016/j.tca.2008.10.015

[56] K.R. Harris, M. Kanakubo, J. Phys. Chem. B 120 (2016) 12937. https://doi.org/10.1021/acs.jpcb.6b10341

[57] M. Kanakubo, K.R. Harris, N. Tsuchihashi, K. Ibuki, M. Ueno, Fluid Phase Equilib. 261 (2007) 414. https://doi.org/10.1016/j.fluid.2007.06.019

[58] J. Vila, B. Fernández-Castro, E. Rilo, J. Carrete, M. Domínguez-Pérez, J.R. Rodríguez, M. García, L.M. Varela, O. Cabeza, Fluid Phase Equilib. 320 (2012) 1. https://doi.org/10.1016/j.fluid.2012.02.006

[59] R. Wang, X. Qi, S. Liu, Y. He, Y. Deng, J. Mol. Liq. 221 (2016) 339. https://doi.org/10.1016/j.molliq.2016.05.092

[60] C.M.S.S. Neves, M.L.S. Batista, A.F.M. Cláudio, L.M.N.B.F. Santos, I.M. Marrucho, M.G. Freire, J.A.P. Coutinho, J. Chem. Eng. Data 55 (2010) 5065. https://doi.org/10.1021/je100638g

[61] O. Zech, A. Stoppa, R. Buchner, W. Kunz, J. Chem. Eng. Data 55 (2010) 1774. https://doi.org/10.1021/je900793r

[62] J.A. Widegren, E.M. Saurer, K.N. Marsh, J.W. Magee, J. Chem. Thermodyn. 37 (2005) 569. https://doi.org/10.1016/j.jct.2005.04.009

[63] W. Li, Z. Zhang, B. Han, S. Hu, Y. Xie, G. Yang, J. Phys. Chem. B 111 (2007) 6452. https://doi.org/10.1021/jp071051m

[64] P.A.Z. Suarez, S. Einloft, J.E.L. Dullius, R.F. de Souza, J. Dupont, J. Chim. Phys. 95 (1998) 1626.

[65] Y. Geng, S. Chen, T. Wang, D. Yu, C. Peng, H. Liu, Y. Hu, J. Mol. Liq. 143 (2008) 100. https://doi.org/10.1016/j.molliq.2008.06.014

[66] J.-G. Li, Y.-F. Hu, S. Ling, J.-Z. Zhang, J. Chem. Eng. Data 56 (2011) 3068. https://doi.org/10.1021/je200073x

[67] K. Nakamura, T. Shikata, Chemphyschem 11 (2010) 285. https://doi.org/10.1002/cphc.200900642

[68] K.R. Harris, J. Phys. Chem. B 120 (2016) 12135. https://doi.org/10.1021/acs.jpcb.6b08381

[69] M.G. Freire, A.R.R. Teles, M.A.A. Rocha, B. Schröder, C.M.S.S. Neves, P.J. Carvalho, D.V. Evtuguin, L.M.N.B.F. Santos, J.A.P. Coutinho, J. Chem. Eng. Data 56 (2011) 4813. https://doi.org/10.1021/je200790q

[70] Y. Wei, W. Zhang, X. Zhang, H. Yang, Q. Zhang, J. Solution Chem. 48 (2019) 125. https://doi.org/10.1007/s10953-019-00842-w

[71] H. Rodríguez, J.F. Brennecke, J. Chem. Eng. Data 51 (2006) 2145. https://doi.org/10.1021/je0602824

[72] N. Anwar, Riyazuddeen, J. Chem. Eng. Data 63 (2018) 269. https://doi.org/10.1021/acs.jced.7b00429

[73] U. Fatima, Riyazuddeen, M.J. Alam, S. Ahmad, Fluid Phase Equilib. 508 (2020) 112447. https://doi.org/10.1016/j.fluid.2019.112447

[74] B.E. Mbondo Tsamba, S. Sarraute, M. Traïkia, P. Husson, J. Chem. Eng. Data 59 (2014) 1747. https://doi.org/10.1021/je400841s

[75] R. Yusoff, M.K. Aroua, A. Shamiri, A. Ahmady, N.S. Jusoh, N.F. Asmuni, L.C. Bong, S.H. Thee, J. Chem. Eng. Data 58 (2013) 240. https://doi.org/10.1021/je300628e

[76] O. Nordness, L.D. Simoni, M.A. Stadtherr, J.F. Brennecke, J. Phys. Chem. B 123 (2019) 1348. https://doi.org/10.1021/acs.jpcb.8b11892

[77] J.M. Vuksanovic, M.S. Calado, G.R. Ivanis, M.L. Kijevcanin, S.P. Serbanovic, Z.P. Visak, Fluid Phase Equilib. 352 (2013) 100. https://doi.org/10.1016/j.fluid.2013.05.013

[78] S. Kakinuma, T. Ishida, H. Shirota, J. Phys. Chem. B 121 (2017) 250. https://doi.org/10.1021/acs.jpcb.6b11009

[79] M.S. Páez, Y.A. Vega, C.M. Romero, J. Mol. Liq. 243 (2017) 78.

[80] R.G. Seoane, S. Corderí, E. Gómez, N. Calvar, E.J. González, E.A. Macedo, Á. Domínguez, Industrial & Engineering Chemistry Research 51 (2012) 2492. https://doi.org/10.1021/ie2029255

[81] D. Soldatović, J. Vuksanović, I. Radović, Z. Višak, M. Kijevčanin, J. Chem. Thermodyn. 109 (2017) 137. https://doi.org/10.1016/j.jct.2017.02.007

[82] A. Yadav, A. Guha, A. Pandey, M. Pal, S. Trivedi, S. Pandey, J. Chem. Thermodyn. 116 (2018) 67. https://doi.org/10.1016/j.jct.2017.08.032

[83] M.-L. Ge, R.-S. Zhao, Y.-F. Yi, Q. Zhang, L.-S. Wang, J. Chem. Eng. Data 53 (2008) 2408. https://doi.org/10.1021/je8003832

[84] N. Anwar, Riyazuddeen, J. Solution Chem. 45 (2016) 1077. https://doi.org/10.1007/s10953-016-0490-x

[85] U. Fatima, Riyazuddeen, N. Anwar, J. Chem. Eng. Data 63 (2018) 4288. https://doi.org/10.1021/acs.jced.8b00176

[86] M.L.S. Batista, L.I.N. Tomé, C.M.S.S. Neves, J.R.B. Gomes, J.A.P. Coutinho, J. Mol. Liq. 192 (2014) 26. https://doi.org/10.1016/j.molliq.2013.10.014

[87] S.N. Khan, S.M. Hailegiorgis, Z. Man, A.M. Shariff, S. Garg, J. Mol. Liq. 229 (2017) 221. https://doi.org/10.1016/j.molliq.2016.12.056

[88] D. Warmińska, I. Cichowska-Kopczyńska, J. Chem. Thermodyn. 171 (2022) 106789. https://doi.org/10.1016/j.jct.2022.106789

[89] K.R. Harris, M. Kanakubo, J. Chem. Eng. Data 61 (2016) 2399. https://doi.org/10.1021/acs.jced.6b00021

[90] M.S. Calado, J.C.F. Diogo, J.L. Correia da Mata, F.J.P. Caetano, Z.P. Visak, J.M.N.A. Fareleira, Int. J. Thermophys. 34 (2013) 1265. https://doi.org/10.1007/s10765-013-1491-2

[91] P. Bonhôte, A.-P. Dias, N. Papageorgiou, K. Kalyanasundaram, M. Grätzel, Inorg. Chem. 35 (1996) 1168. https://doi.org/10.1021/ic951325x

[92] E.I. Cooper, E.J.M. O'Sullivan, ECS Proceedings Volumes 1992-16 (1992) 386. https://doi.org/10.1149/199216.0386pv

[93] J. Asenbauer, N. Ben Hassen, B.D. McCloskey, J.M. Prausnitz, Electrochim. Acta 247 (2017) 1038. https://doi.org/10.1016/j.electacta.2017.07.053

[94] N.R. Pitawela, S.K. Shaw, ACS Measurement Science Au 1 (2021) 117. https://doi.org/10.1021/acsmeasuresciau.1c00015

[95] H. Tokuda, K. Hayamizu, K. Ishii, M.A.B.H. Susan, M. Watanabe, J. Phys. Chem. B 109 (2005) 6103. https://doi.org/10.1021/jp044626d

[96] S. Papović, S. Gadžurić, M. Bešter-Rogač, B. Jović, M. Vraneš, J. Chem. Thermodyn. 116 (2018) 330. https://doi.org/10.1016/j.jct.2017.10.004

[97] T. Makino, M. Kanakubo, Y. Masuda, T. Umecky, A. Suzuki, Fluid Phase Equilib. 362 (2014) 300. https://doi.org/10.1016/j.fluid.2013.10.031

[98] L.M. Ramenskaya, E.P. Grishina, N.O. Kudryakova, J. Mol. Liq. 272 (2018) 759. https://doi.org/10.1016/j.molliq.2018.10.005

[99] S. Bansal, N. Kaur, G.R. Chaudhary, S.K. Mehta, A.S. Ahluwalia, J. Chem. Eng. Data 59 (2014) 3988. https://doi.org/10.1021/je500502a

[100] S. Papović, S. Gadžurić, M. Bešter-Rogač, M. Vraneš, J. Chem. Thermodyn. 102 (2016) 367. https://doi.org/10.1016/j.jct.2016.07.039

[101] A. Hofmann, M. Migeot, T. Hanemann, J. Chem. Eng. Data 61 (2016) 114. https://doi.org/10.1021/acs.jced.5b00338

[102] G. Annat, M. Forsyth, D.R. MacFarlane, J. Phys. Chem. B 116 (2012) 8251. https://doi.org/10.1021/jp3012602

[103] S. Papović, M. Vraneš, S. Gadžurić, J. Chem. Thermodyn. 91 (2015) 360. https://doi.org/10.1016/j.jct.2015.07.048

[104] K.R. Harris, M. Kanakubo, Phys. Chem. Chem. Phys. 17 (2015) 23977. https://doi.org/10.1039/C5CP04277A

[105] H. Srour, M. Traïkia, B. Fenet, H. Rouault, M.F. Costa Gomes, C.C. Santini, P. Husson, J. Solution Chem. 44 (2015) 495. https://doi.org/10.1007/s10953-014-0280-2

[106] M. Kanakubo, K.R. Harris, N. Tsuchihashi, K. Ibuki, M. Ueno, J. Chem. Eng. Data 60 (2015) 1495. https://doi.org/10.1021/acs.jced.5b00071

[107] M. Vranes, S. Dozic, V. Djeric, S. Gadzuric, J. Chem. Eng. Data 57 (2012) 1072. https://doi.org/10.1021/je2010837

[108] T. Yamaguchi, T. Kikuzawa, J. Mol. Liq. 284 (2019) 252. https://doi.org/10.1016/j.molliq.2019.04.015

[109] J.M. Andanson, N. Papaiconomou, P.A. Cable, M. Traïkia, I. Billard, P. Husson, Phys. Chem. Chem. Phys. 19 (2017) 28834. https://doi.org/10.1039/C7CP05886A

[110] Y. Yoshimura, S. Hattori, K. Kitawaki, T. Mori, K. Kaneko, T. Takekiyo, A. Shimizu, J. Solution Chem. 50 (2021) 995. https://doi.org/10.1007/s10953-021-01098-z

[111] A. Nazet, S. Sokolov, T. Sonnleitner, T. Makino, M. Kanakubo, R. Buchner, J. Chem. Eng. Data 60 (2015) 2400. https://doi.org/10.1021/acs.jced.5b00285

[112] J.E. Morales-Ugarte, C.C. Santini, R. Bouchet, A. Benayad, J. Phys. Chem. B 124 (2020) 7625. https://doi.org/10.1021/acs.jpcb.0c04090

[113] K.R. Harris, M. Kanakubo, J. Mol. Liq. 358 (2022) 119109. https://doi.org/10.1016/j.molliq.2022.119109

[114] M.E. Kandil, K.N. Marsh, A.R.H. Goodwin, J. Chem. Eng. Data 52 (2007) 2382. https://doi.org/10.1021/je7003484

[115] F. Santos, C. Nieto de Castro, P. Mota, International Journal of Thermophysics - INT J THERMOPHYS 31 (2010) 1869. https://doi.org/10.1007/s10765-009-0584-4

[116] D.W. Bruce, C.P. Cabry, J.N.C. Lopes, M.L. Costen, L. D'Andrea, I. Grillo, B.C. Marshall, K.G. McKendrick, T.K. Minton, S.M. Purcell, S. Rogers, J.M. Slattery, K. Shimizu, E. Smoll, M.A. Tesa-Serrate, J. Phys. Chem. B 121 (2017) 6002. https://doi.org/10.1021/acs.jpcb.7b01654

[117] K. Li, W. Wu, L. Peng, H. Zhang, J. Mol. Liq. 337 (2021) 116240. https://doi.org/10.1016/j.molliq.2021.116240

[118] G.B. Dutt, J. Phys. Chem. B 114 (2010) 8971. https://doi.org/10.1021/jp1039282

[119] D. Almantariotis, S. Stevanovic, O. Fandiño, A.S. Pensado, A.A.H. Padua, J.Y. Coxam, M.F. Costa Gomes, J. Phys. Chem. B 116 (2012) 7728. https://doi.org/10.1021/jp304501p

[120] M. Wlazło, A. Marciniak, T.M. Letcher, J. Solution Chem. 44 (2015) 413. https://doi.org/10.1007/s10953-014-0274-0

[121] C.A. Nieto de Castro, A.P.d.C. Ribeiro, A.O. Figueiras, E. Langa, S.I.C. Vieira, M.J.V. Lourenço, Â.F.S.d. Santos, F.J. Vieira dos Santos, I.M.S. Lampreia, P. Goodrich, C. Hardacre, J. Chem. Eng. Data 66 (2021) 1717. https://doi.org/10.1021/acs.jced.0c01017

[122] J. Safarov, F. Lesch, K. Suleymanli, A. Aliyev, A. Shahverdiyev, E. Hassel, I. Abdulagatov, J. Chem. Eng. Data 62 (2017) 3620. https://doi.org/10.1021/acs.jced.7b00618

[123] M. Larriba, S. García, J. García, J.S. Torrecilla, F. Rodríguez, J. Chem. Eng. Data 56 (2011) 3589. https://doi.org/10.1021/je2004462

[124] S. Seki, N. Serizawa, S. Ono, K. Takei, K. Hayamizu, S. Tsuzuki, Y. Umebayashi, J. Chem. Eng. Data 64 (2019) 433. https://doi.org/10.1021/acs.jced.8b00334

[125] F.S. Oliveira, M.G. Freire, P.J. Carvalho, J.A.P. Coutinho, J.N.C. Lopes, L.P.N. Rebelo, I.M. Marrucho, J. Chem. Eng. Data 55 (2010) 4514. https://doi.org/10.1021/je100377k

[126] N.M. Yunus, M.I. Abdul Mutalib, Z. Man, M.A. Bustam, T. Murugesan, J. Chem. Thermodyn. 42 (2010) 491. https://doi.org/10.1016/j.jct.2009.11.004

[127] X. Wang, S. Zeng, J. Wang, D. Shang, X. Zhang, J. Liu, Y. Zhang, Industrial & Engineering Chemistry Research 57 (2018) 1284. https://doi.org/10.1021/acs.iecr.7b04477

[128] Q.-S. Liu, M. Yang, P.-P. Li, S.-S. Sun, U. Welz-Biermann, Z.-C. Tan, Q.-G. Zhang, J. Chem. Eng. Data 56 (2011) 4094. https://doi.org/10.1021/je200534b

[129] S. Zeng, J. Wang, L. Bai, B. Wang, H. Gao, D. Shang, X. Zhang, S. Zhang, Energy & Fuels 29 (2015) 6039. https://doi.org/10.1021/acs.energyfuels.5b01274

[130] A. Nazet, S. Sokolov, T. Sonnleitner, S. Friesen, R. Buchner, J. Chem. Eng. Data 62 (2017) 2549. https://doi.org/10.1021/acs.jced.7b00060

[131] Q.-S. Liu, P.-F. Yan, M. Yang, Z.-C. Tan, C.-P. Li, U. Welz-Biermann, Acta Physico-Chimica Sinica 27 (2011) 2762.

[132] H. Tokuda, K. Ishii, M.A.B.H. Susan, S. Tsuzuki, K. Hayamizu, M. Watanabe, J. Phys. Chem. B 110 (2006) 2833. https://doi.org/10.1021/jp053396f

[133] B. Bittner, R.J. Wrobel, E. Milchert, J. Chem. Thermodyn. 55 (2012) 159. https://doi.org/10.1016/j.jct.2012.06.018

[134] D. Warmińska, I. Cichowska-Kopczyńska, J. Mol. Liq. 304 (2020) 112754. https://doi.org/10.1016/j.molliq.2020.112754

[135] J.M. Crosthwaite, M.J. Muldoon, J.K. Dixon, J.L. Anderson, J.F. Brennecke, J. Chem. Thermodyn. 37 (2005) 559. https://doi.org/10.1016/j.jct.2005.03.013

[136] C. Reinado, A. Pelegrina, M. Sánchez-Rubio, H. Artigas, C. Lafuente, J. Chem. Eng. Data 67 (2022) 636. https://doi.org/10.1021/acs.jced.1c00925

[137] Q.-G. Zhang, S.-S. Sun, S. Pitula, Q.-S. Liu, U. Welz-Biermann, J.-J. Zhang, J. Chem. Eng. Data 56 (2011) 4659. https://doi.org/10.1021/je200616t

[138] O.U. Ahmed, F.S. Mjalli, A.-W. Talal, Y. Al-Wahaibi, I.M. Al Nashef, J. Solution Chem. 47 (2018) 468. https://doi.org/10.1007/s10953-018-0732-1

[139] Q. Liu, L. Zhao, L. Ma, J. Chu, J. Wang, Y. Zang, J. Chem. Eng. Data 65 (2020) 4780. https://doi.org/10.1021/acs.jced.0c00187

[140] T. Makino, M. Kanakubo, T. Umecky, A. Suzuki, T. Nishida, J. Takano, Fluid Phase Equilib. 360 (2013) 253. https://doi.org/10.1016/j.fluid.2013.09.036

[141] B. González, E.J. González, J. Chem. Thermodyn. 68 (2014) 109. https://doi.org/10.1016/j.jct.2013.08.021

[142] A.R.C. Morais, L.M. Alaras, D.L. Baek, R.V. Fox, M.B. Shiflett, A.M. Scurto, J. Chem. Eng. Data 64 (2019) 4658. https://doi.org/10.1021/acs.jced.8b01237

[143] Q. Huang, T.C. Lourenço, L.T. Costa, Y. Zhang, E.J. Maginn, B. Gurkan, J. Phys. Chem. B 123 (2019) 516. https://doi.org/10.1021/acs.jpcb.8b08859

[144] J.M. Klein, H. Squire, W. Dean, B.E. Gurkan, J. Phys. Chem. B 124 (2020) 6348. https://doi.org/10.1021/acs.jpcb.0c03296

[145] K.R. Harris, L.A. Woolf, M. Kanakubo, T. Rüther, J. Chem. Eng. Data 56 (2011) 4672. https://doi.org/10.1021/je2006049

[146] S. Kakinuma, H. Shirota, J. Phys. Chem. B 123 (2019) 1307. https://doi.org/10.1021/acs.jpcb.8b10269

[147] A.S.M.C. Rodrigues, H.F.D. Almeida, M.G. Freire, J.A. Lopes-da-Silva, J.A.P. Coutinho, L.M.N.B.F. Santos, Fluid Phase Equilib. 423 (2016) 190. https://doi.org/10.1016/j.fluid.2016.04.009

[148] A.B. Pereiro, H.I.M. Veiga, J.M.S.S. Esperança, A. Rodríguez, J. Chem. Thermodyn. 41 (2009) 1419. https://doi.org/10.1016/j.jct.2009.06.020

[149] M. Ramos-Estrada, I.Y. López-Cortés, G.A. Iglesias-Silva, F. Pérez-Villaseñor, J. Chem. Eng. Data 63 (2018) 4425. https://doi.org/10.1021/acs.jced.8b00537

[150] Y. Hiraga, S. Hagiwara, Y. Sato, R.L. Smith, Jr., J. Chem. Eng. Data 63 (2018) 972. https://doi.org/10.1021/acs.jced.7b00773

[151] T. Song, O. Morales-Collazo, J.F. Brennecke, J. Chem. Eng. Data 64 (2019) 4956. https://doi.org/10.1021/acs.jced.9b00750

[152] H. Liu, E. Maginn, A.E. Visser, N.J. Bridges, E.B. Fox, Industrial & Engineering Chemistry Research 51 (2012) 7242. https://doi.org/10.1021/ie300222a

[153] S. Papović, M. Vraneš, A. Tot, I. Szilágyi, B. Katana, K. Alenezi, S. Gadžurić, J. Chem. Eng. Data 65 (2020) 68. https://doi.org/10.1021/acs.jced.9b00738

[154] Y. Deng, P. Husson, A.-M. Delort, P. Besse-Hoggan, M. Sancelme, M.F. Costa Gomes, J. Chem. Eng. Data 56 (2011) 4194. https://doi.org/10.1021/je2006743

[155] A.R. Neale, C. Schütter, P. Wilde, P. Goodrich, C. Hardacre, S. Passerini, A. Balducci, J. Jacquemin, J. Chem. Eng. Data 62 (2017) 376. https://doi.org/10.1021/acs.jced.6b00718

[156] R. Zarrougui, M. Dhahbi, D. Lemordant, Ionics 17 (2011) 343. https://doi.org/10.1007/s11581-010-0511-5

[157] J. Salminen, N. Papaiconomou, R.A. Kumar, J.-M. Lee, J. Kerr, J. Newman, J.M. Prausnitz, Fluid Phase Equilib. 261 (2007) 421. https://doi.org/10.1016/j.fluid.2007.06.031

[158] A.M. Fleshman, N.A. Mauro, J. Mol. Liq. 279 (2019) 23. https://doi.org/10.1016/j.molliq.2019.01.108

[159] O. Borodin, G.A. Giffin, A. Moretti, J.B. Haskins, J.W. Lawson, W.A. Henderson, S. Passerini, The Journal of Physical Chemistry C 122 (2018) 20108. https://doi.org/10.1021/acs.jpcc.8b05573

[160] M. Nahra, E. Chainet, L. Svecova, L. Cointeaux, I. Billard, Fluid Phase Equilib. 415 (2016) 101. https://doi.org/10.1016/j.fluid.2016.01.043

[161] T. Vogl, P. Goodrich, J. Jacquemin, S. Passerini, A. Balducci, The Journal of Physical Chemistry C 120 (2016) 8525. https://doi.org/10.1021/acs.jpcc.6b01945

[162] R. Khalil, N. Chaabene, M. Azar, I.B. Malham, M. Turmine, Fluid Phase Equilib. 503 (2020) 112316. https://doi.org/10.1016/j.fluid.2019.112316

[163] M. Vraneš, S. Rackov, S. Papović, R. Tomaš, B. Pilić, J. Chem. Eng. Data 67 (2022) 3329. https://doi.org/10.1021/acs.jced.2c00377

[164] L.F. Zubeir, M.A.A. Rocha, N. Vergadou, W.M.A. Weggemans, L.D. Peristeras, P.S. Schulz, I.G. Economou, M.C. Kroon, Phys. Chem. Chem. Phys. 18 (2016) 23121. https://doi.org/10.1039/C6CP01943A

[165] A.S.M.C. Rodrigues, L.M.N.B.F. Santos, ChemPhysChem 17 (2016) 1512. https://doi.org/10.1002/cphc.201501128

[166] M.A.A. Rocha, C.F.R.A.C. Lima, L.R. Gomes, B. Schröder, J.A.P. Coutinho, I.M. Marrucho, J.M.S.S. Esperança, L.P.N. Rebelo, K. Shimizu, J.N.C. Lopes, L.M.N.B.F. Santos, J. Phys. Chem. B 115 (2011) 10919. https://doi.org/10.1021/jp2049316

[167] M.A.A. Rocha, M. Bastos, J.A.P. Coutinho, L.M.N.B.F. Santos, J. Chem. Thermodyn. 53 (2012) 140. https://doi.org/10.1016/j.jct.2012.04.025

[168] H.F.D. Almeida, M.G. Freire, A.M. Fernandes, J.A. Lopes-da-Silva, P. Morgado, K. Shimizu, E.J.M. Filipe, J.N. Canongia Lopes, L.M.N.B.F. Santos, J.A.P. Coutinho, Langmuir 30 (2014) 6408. https://doi.org/10.1021/la501308q

[169] J.N.A. Canongia Lopes, A.A.H. Pádua, J. Phys. Chem. B 110 (2006) 3330. https://doi.org/10.1021/jp056006y

[170] K. Shimizu, M.F. Costa Gomes, A.A.H. Pádua, L.P.N. Rebelo, J.N. Canongia Lopes, Journal of Molecular Structure: THEOCHEM 946 (2010) 70. https://doi.org/10.1016/j.theochem.2009.11.034

[171] M.F. Gomes, J.N. Lopes, A.A. Padua, Top. Curr. Chem. 290 (2010) 161. https://doi.org/10.1007/128_2009_2

[172] A.T. De La Hoz, U.G. Brauer, K.M. Miller, J. Phys. Chem. B 118 (2014) 9944. https://doi.org/10.1021/jp505592t

[173] D.H. Zaitsau, A.V. Yermalayeu, T.J.S. Schubert, S.P. Verevkin, J. Mol. Liq. 242 (2017) 951. https://doi.org/10.1016/j.molliq.2017.07.094

[174] D.H. Zaitsau, A.V. Yermalayeu, V.N. Emel'Yanenko, S. Butler, T. Schubert, S.P. Verevkin, J. Phys. Chem. B 120 (2016) 7949. https://doi.org/10.1021/acs.jpcb.6b06081

[175] D.H. Zaitsau, A.V. Yermalayeu, V.N. Emel'yanenko, S.P. Verevkin, Chem. Eng. Technol. 41 (2018) 1604. https://doi.org/10.1002/ceat.201700454

[176] D.H. Zaitsau, S.P. Verevkin, J. Mol. Liq. 287 (2019). https://doi.org/10.1016/j.molliq.2019.110959

[177] D.H. Zaitsau, A.V. Yermalayeu, V.N. Emel'yanenko, S.P. Verevkin, U. Welz-Biermann, T. Schubert, Science China Chemistry 55 (2012) 1525. https://doi.org/10.1007/s11426-012-4662-2

[178] D.H. Zaitsau, A.V. Yermalayeu, V.N. Emel'Yanenko, A. Heintz, S.P. Verevkin, C. Schick, S. Berdzinski, V. Strehmel, J. Mol. Liq. 192 (2014) 171. https://doi.org/10.1016/j.molliq.2013.07.018

[179] J.M.M. Araújo, A.B. Pereiro, F. Alves, I.M. Marrucho, L.P.N. Rebelo, J. Chem. Thermodyn. 57 (2013) 1. https://doi.org/10.1016/j.jct.2012.07.022

[180] Y. Bai, S. Zeng, L. Bai, H. Gao, Z. Zhou, X. Zhang, Industrial & Engineering Chemistry Research 59 (2020) 16751. https://doi.org/10.1021/acs.iecr.0c02727

[181] Y. Hiraga, A. Kato, Y. Sato, R.L. Smith, Jr., J. Chem. Eng. Data 60 (2015) 876. https://doi.org/10.1021/je5009679

[182] S. Stevanovic, A. Podgoršek, A.A.H. Pádua, M.F. Costa Gomes, J. Phys. Chem. B 116 (2012) 14416. https://doi.org/10.1021/jp3100377

[183] S. Balchandani, B. Mandal, S. Dharaskar, Fluid Phase Equilib. 521 (2020) 112643. https://doi.org/10.1016/j.fluid.2020.112643

[184] J. Safarov, M. Geppert-Rybczyńska, I. Kul, E. Hassel, Fluid Phase Equilib. 383 (2014) 144. https://doi.org/10.1016/j.fluid.2014.10.015

[185] A. Haghtalab, A. Shojaeian, J. Chem. Thermodyn. 68 (2014) 128. https://doi.org/10.1016/j.jct.2013.09.001

[186] M. Kanakubo, T. Makino, T. Umecky, J. Mol. Liq. 217 (2016) 112. https://doi.org/10.1016/j.molliq.2016.02.018

[187] A. Xu, Y. Zhang, Z. Li, J. Wang, J. Chem. Eng. Data 57 (2012) 3102. https://doi.org/10.1021/je300507h

[188] S. Fendt, S. Padmanabhan, H.W. Blanch, J.M. Prausnitz, J. Chem. Eng. Data 56 (2011) 31. https://doi.org/10.1021/je1007235

[189] F. Feuzing, J.-P. Mbakidi, F. Lazar, L. Marchal, E. Leroy, S. Bouquillon, J. Mol. Liq. 370 (2023) 120983. https://doi.org/10.1016/j.molliq.2022.120983

[190] M. Engelmann, H. Schmidt, J. Safarov, J. Nocke, E. Hassel, Acta Chimica Slovaca 5 (2012). https://doi.org/10.2478/v10188-012-0014-2

[191] M. Tariq, J.M.S.S. Esperança, L.P.N. Rebelo, X. Paredes, F.J.V. Santos, C.A. Nieto de Castro, J. Mol. Liq. 337 (2021) 116482. https://doi.org/10.1016/j.molliq.2021.116482

[192] P.J. Carvalho, T. Regueira, L.M.N.B.F. Santos, J. Fernandez, J.A.P. Coutinho, J. Chem. Eng. Data 55 (2010) 645. https://doi.org/10.1021/je900632q

[193] K. Paduszyński, M. Okuniewski, U. Domańska, J. Phys. Chem. B 117 (2013) 7034. https://doi.org/10.1021/jp401937p

[194] Y. Zheng, Y. Zheng, Q. Wang, Z. Wang, J. Chem. Eng. Data 66 (2021) 480. https://doi.org/10.1021/acs.jced.0c00754

[195] N. Zec, M. Bešter-Rogač, G. Marolt, M. Vraneš, S. Gadžurić, J. Chem. Thermodyn. 101 (2016) 293. https://doi.org/10.1016/j.jct.2016.06.017

[196] M. Larriba, P. Navarro, J. García, F. Rodríguez, Industrial & Engineering Chemistry Research 52 (2013) 2714. https://doi.org/10.1021/ie303357s

[197] C.K. Foo, C.Y. Leo, R. Aramesh, M.K. Aroua, N. Aghamohammadi, M.S. Shafeeyan, A. Shamiri, J. Mol. Liq. 209 (2015) 596. https://doi.org/10.1016/j.molliq.2015.05.041

[198] M.B. Shiflett, B.A. Elliott, A. Yokozeki, Fluid Phase Equilib. 316 (2012) 147. https://doi.org/10.1016/j.fluid.2011.11.030

[199] M. Mirzaei, A.R. Badiei, B. Mokhtarani, A. Sharifi, J. Mol. Liq. 232 (2017) 462. https://doi.org/10.1016/j.molliq.2017.02.104

[200] I. Otero, L.F. Lepre, A. Dequidt, P. Husson, M.F. Costa Gomes, J. Phys. Chem. B 121 (2017) 9725. https://doi.org/10.1021/acs.jpcb.7b06452

[201] Z. Chen, Y. Huo, P. Long, H. Shen, J.-M. Lee, Phys. Chem. Chem. Phys. 19 (2017) 5389. https://doi.org/10.1039/C6CP08876G

[202] A. Kadyan, S. Pandey, J. Phys. Chem. B 121 (2017) 1081. https://doi.org/10.1021/acs.jpcb.6b12122

[203] M. Musiał, S. Bair, S. Cheng, Z. Wojnarowska, M. Paluch, J. Mol. Liq. 331 (2021) 115772. https://doi.org/10.1016/j.molliq.2021.115772

[204] D. Morgan, L. Ferguson, P. Scovazzo, Industrial & Engineering Chemistry Research 44 (2005) 4815. https://doi.org/10.1021/ie048825v

[205] A. Pinkert, K.L. Ang, K.N. Marsh, S. Pang, Phys. Chem. Chem. Phys. 13 (2011) 5136. https://doi.org/10.1039/C0CP02222E

[206] Y. Yoshida, O. Baba, G. Saito, J. Phys. Chem. B 111 (2007) 4742. https://doi.org/10.1021/jp067055t

[207] P. Nancarrow, A. Al-Othman, D.K. Mital, S. Döpking, Energy 220 (2021) 119761. https://doi.org/10.1016/j.energy.2021.119761

[208] J. Leys, R.N. Rajesh, P.C. Menon, C. Glorieux, S. Longuemart, P. Nockemann, M. Pellens, K. Binnemans, J. Chem. Phys. 133 (2010). https://doi.org/10.1063/1.3455892

[209] L. Yu, B.S. Pizio, T.D. Vaden, J. Phys. Chem. B 116 (2012) 6553. https://doi.org/10.1021/jp301883e

[210] C.A. Angell, Proceedings of the National Academy of Sciences 92 (1995) 6675. https://doi.org/10.1073/pnas.92.15.6675

[211] A. Martinelli, A. Matic, P. Jacobsson, L. Börjesson, A. Fernicola, B. Scrosati, J. Phys. Chem. B 113 (2009) 11247. https://doi.org/10.1021/jp905783t

[212] C. Austen Angell, Y. Ansari, Z. Zhao, Faraday Discuss. 154 (2012) 9. https://doi.org/10.1039/C1FD00112D

[213] I. Bandrés, D.F. Montaño, I. Gascón, P. Cea, C. Lafuente, Electrochim. Acta 55 (2010) 2252. https://doi.org/10.1016/j.electacta.2009.11.073

[214] F.M. Gaciño, T. Regueira, L. Lugo, M.J.P. Comuñas, J. Fernández, J. Chem. Eng. Data 56 (2011) 4984. https://doi.org/10.1021/je200883w

[215] M. Okuniewski, K. Paduszyński, U. Domańska, J. Chem. Eng. Data 61 (2016) 1296. https://doi.org/10.1021/acs.jced.5b00931

[216] S. Stevanovic, M.F. Costa Gomes, J. Chem. Thermodyn. 59 (2013) 65. https://doi.org/10.1016/j.jct.2012.11.010

[217] G. McHale, C. Hardacre, R. Ge, N. Doy, R.W.K. Allen, J.M. MacInnes, M.R. Bown, M.I. Newton, Anal. Chem. 80 (2008) 5806. https://doi.org/10.1021/ac800490q

[218] S.I. Fletcher, F.B. Sillars, N.E. Hudson, P.J. Hall, J. Chem. Eng. Data 55 (2010) 778. https://doi.org/10.1021/je900405j

[219] M. Havlová, V. Dohnal, J. Chem. Eng. Data 67 (2022) 2108. https://doi.org/10.1021/acs.jced.2c00096

[220] C.S.M. Kang, X. Zhang, D.R. MacFarlane, The Journal of Physical Chemistry C 123 (2019) 21376. https://doi.org/10.1021/acs.jpcc.9b06000

[221] L. Mou, Y. Chai, G. Yang, Q. Xia, Q. Liu, Q. Zheng, Q. Zhang, J. Chem. Thermodyn. 130 (2019) 183. https://doi.org/10.1016/j.jct.2018.10.015

[222] Q. Liu, L. Ma, S. Wang, Z. Ni, X. Fu, J. Wang, Q. Zheng, J. Mol. Liq. 325 (2021) 114573. https://doi.org/10.1016/j.molliq.2020.114573

[223] M. Musiał, M. Kuczak, A. Mrozek-Wilczkiewicz, R. Musiol, E. Zorębski, M. Dzida, ACS Sustainable Chemistry & Engineering 6 (2018) 7960. https://doi.org/10.1021/acssuschemeng.8b01317

[224] M.E.V. Valkenburg, R.L. Vaughn, M. Williams, J.S. Wilkes, Thermochim. Acta 425 (2005) 181. https://doi.org/10.1016/j.tca.2004.11.013

[225] S. Katsuta, Y. Shiozawa, K. Imai, Y. Kudo, Y. Takeda, J. Chem. Eng. Data 55 (2010) 1588. https://doi.org/10.1021/je900694m

[226] A.B. McEwen, H.L. Ngo, K. LeCompte, J.L. Goldman, J. Electrochem. Soc. 146 (1999) 1687. https://doi.org/10.1149/1.1391827

[227] H. Zhang, X. Cui, P. Li, T. Feng, H. Feng, J. Mol. Liq. 365 (2022) 120193. https://doi.org/10.1016/j.molliq.2022.120193

[228] A.S.M.C. Rodrigues, C.F.R.A.C. Lima, J.A.P. Coutinho, L.M.N.B.F. Santos, Phys. Chem. Chem. Phys. 19 (2017) 5326. https://doi.org/10.1039/C6CP08451F

[229] C.F.P. Miranda, A.I.M.C. Lobo Ferreira, L.M.N.B.F. Santos, J. Mol. Liq. 353 (2022) 118772. https://doi.org/10.1016/j.molliq.2022.118772

[230] P.A. Hunt, J. Phys. Chem. B 111 (2007) 4844. https://doi.org/10.1021/jp067182p

[231] E.I. Izgorodina, R. Maganti, V. Armel, P.M. Dean, J.M. Pringle, K.R. Seddon, D.R. MacFarlane, J. Phys. Chem. B 115 (2011) 14688. https://doi.org/10.1021/jp208573y

[232] M. García-Mardones, I. Bandrés, M.C. López, I. Gascón, C. Lafuente, J. Solution Chem. 41 (2012) 1836. https://doi.org/10.1007/s10953-012-9906-4

[233] A. Bhattacharjee, P.J. Carvalho, J.A.P. Coutinho, Fluid Phase Equilib. 375 (2014) 80. https://doi.org/10.1016/j.fluid.2014.04.029

[234] Q.-S. Liu, P.-P. Li, U. Welz-Biermann, J. Chen, X.-X. Liu, J. Chem. Thermodyn. 66 (2013) 88. https://doi.org/10.1016/j.jct.2013.06.008

[235] M.A.A. Rocha, L.M.N.B.F. Santos, Chem. Phys. Lett. 585 (2013) 59. https://doi.org/10.1016/j.cplett.2013.08.095

[236] A.S.M.C. Rodrigues, University of Porto, University of Porto Open Repository 2017.

# Chapter 6

## Conclusions and Achievments

**6.1.** ILDEM

**6.2.** Structure – Property Relationships

**6.3.** Reflections and Future Perspectives

**References**

# 6. Conclusions and Achievements

This chapter presents the main conclusions and achievements of this work, highlighting their contribution to the field. Furthermore, some possibilities for future work are proposed.

## 6.1. ILDEM

This work marked the start of a new line in this research group focusing on the study of the transport properties of ionic liquids, particularly electrical conductivity. With this aim, an apparatus and measuring methodology centered on a high-precision LCR meter were developed [1].

**Frequency Effects & Resistance Extrapolation**

The impact of polarization can be graphically observed by the high resistance values at low frequencies, which reflect the blocking of the current path due to the formation of an ion layer on the electrode-electrolyte interface. However, the $R(1/f) = a/f + R_\infty$ extrapolation method upon proper adequate frequency range selection seems to appropriately correct for this undesired effect, as the present results are in agreement with the recommended and other properly treated data. Overall, the study of different systems at different temperatures demonstrated a shift of the spectra towards higher frequencies for more conductive systems. This is likely associated with the change of relaxation time of the conductive/electrochemical processes and highlights the importance of scanning the impedance of a system in a wide range of frequencies.

**Temperature Control**

A good temperature control is fundamental for high-accuracy measurements of electrical conductivity. In this work, this was achieved by designing and constructing an aluminum air bath chamber with Peltier heating-cooling and internal ventilation. The applied air bath methodology results in excellent temperature control (± 0.005 K) comparable to oil baths. This is mainly due to the high thermal inertia of the chamber as well as to the homogeneous heat distribution and placement of the temperature sensors. Additionally, the utilization of a dry air bath offers a cleaner and more practical alternative to the oil baths while also preventing the stray capacitance effects typically associated with water baths [2, 3]. However, the high thermal inertia of the chamber and the cell (PEEK block) leads to long thermal stabilization periods (0.5 – 1h).

### Cell Design

Two electrical conductivity cells were developed during this work: dip-in cell and coin cell. The first is an adaptation of a 2-pole Metrohm commercial probe attached to a glass tube by a specially designed PEEK holder. This holder was designed to fix the position of the conductivity probe in the sample and to connect the sample vessel with vacuum and $N_2$(g) lines. The in-situ degasification and atmospheric control, paired with the traditional purification processes before the measurements, contributed to stable and reproducible results. Additionally, the fixed position of the probe and delimited space around the electrodes seem to effectively prevent electric field effects [2, 4]. On the other hand, while the current cell design yields excellent results, it uses a decent amount of IL sample (7.5 $cm^3$). The coin cell uses a “sandwich” type configuration where the two electrode discs are pressed against a PEEK spacer. This cell has the advantages of only using around 0.140 $cm^3$ and being easier to clean. On the other hand, this configuration is more susceptible to the presence of air bubbles, which affect the accuracy of the results. Four types of electrodes were tested with this cell: stainless steel 316, stainless steel coated with titanium nitride, nickel, and platinum. Results in agreement with the recommended data were obtained using all types of electrodes. Furthermore, the good performance of the coin cell with stainless steel electrodes demonstrates the possibility of the development of viable and affordable conductivity cells, compared to the more expensive and difficult-to-maintain black platinum electrode cells. A summary of the main features of the ILDEM apparatus are presented in Fig. 6.1.

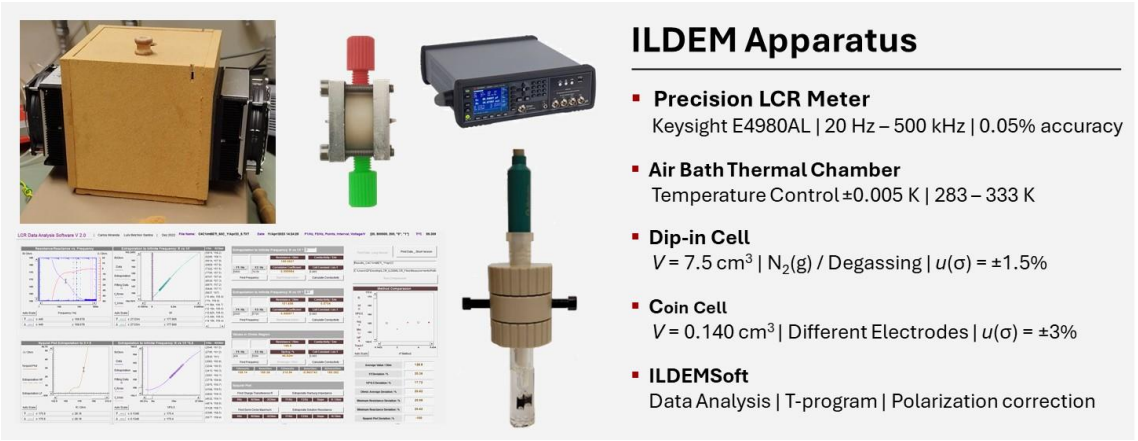



**Figure 6.1.** Summary of the characteristics of the ILDEM Apparatus.

## 6.2. Structure Effect on the Transport Properties of Ionic Liquids

The second part of this work was dedicated to the study of the effect of ion structure on the transport properties of ionic liquids. The main objectives of this study were:

- To explore the saturation and dynamics of ionic liquids;
- Create fundamental knowledge to be applied in electrochemistry areas;

The work conducted was a systematic study based on the measurement of density, viscosity, and electrical conductivity and involved the 60 ILs with different cationic and anionic features in order to explore:

- The effect of the alkyl chain of the cation;
- The effect of the nature of the anion;
- The effect of the nature of the cation.

A summary of the main conclusions and achievements of the systematic study on the effect of structure on the transport properties of ionic liquids is presented in Fig. 6.2.

**Nanostructuration**

In this work, the effect of the length of the alkyl chain of the cation was explored for seven homologue series: $[^1C_n{}^3C_1im]BF_4$, $[^1C_n{}^3C_1im]PF_6$, $[^1C_n{}^3C_1im][OTf]$, $[^1C_n{}^3C_1im][FAP]$, $[^1C_n{}^3C_1im][NTf_2]$, $[^1C_n{}^1C_1pyr][NTf_2]$, and $[^1C_n{}^1C_1pyr][NTf_2]$. The results revealed a trendshift (around $n$ = 6) in the transport properties and derived parameters, including energy barrier, fragility, and pre-exponential coefficient. This is a consequence of the intensification of nanostructuration of ionic liquids, reflecting the transition of a liquid with strong ionic character to a nanostructured liquid, where the polar network is permeated by the nonpolar alkyl chains. The trendshift is marked by a decrease in slope and is due to the balance between the electrostatic and van der Waals interactions.

**Cohesive Interaction vs. Shape**

The study with different ions highlighted the importance of different characteristics, such as charge dispersion, size, shape, and dynamics on the transport properties of the ionic liquids. Systems with more centralized charge regions, such as $BF_4^-$ and $PF_6^-$ were found to yield higher energy barriers, highlighting the higher cohesive energy of these liquids. Similarly, the same was observed by changing the cationic headgroup, as the more localized pyrrolidinium ring typically presented higher energy barriers. Furthermore, changes of cationic structures, namely the C2 methylation of the imidazolium ring and isomerization of the pyridinium ring, were also found to be reflected on the derived energy barriers. This is expected as these structural changes affect the

charge distribution and the movement of the anion around the cation. On the other hand, the pre-exponential coefficient was shown to be a good indication of the dynamics of the ions. Overall, lower $A_\Lambda$ and higher $A_\eta$ values were obtained for larger and more sterically hindered anions. While higher $A_\Lambda$ and lower $A_\eta$ values were found for smaller and more regular-shaped anions with higher dynamics ($BF_4^-$, $PF_6^-$, Ac).

**Correlation Between Viscosity and Molar Conductivity**

As a transport property, the molar conductivity is deeply influenced by the viscosity. However, this work showed that the structural changes, particularly the alkyl chain length and the nature of the anion, impact the correlation between these two transport properties. This was evaluated based on the Walden rule and stronger correlations were found for short-chain ILs and spheric anions with localized charges ($BF_4^-$, $PF_6^-$, FAP). Deviations to the Walden rule are usually associated with ionicity and ion association. Although the validity of this approach has been previously criticized in the past. A more sober interpretation would be based on the differentiation between the ion conduction and viscous flow mechanisms. The effect of charge dispersion on the correlation highlights the higher complexity of the ion conduction. In summary, the Walden rule works well for less complex structures that approach the simple model for electrolytes (small ionic spheres).

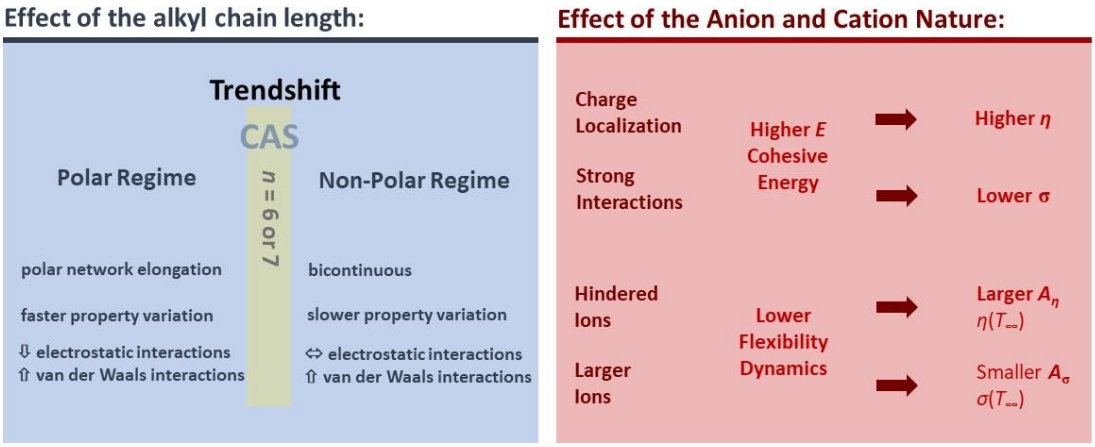



**Figure 6.2.** Summary of the conclusions on the effect of structure on the transport properties of ionic liquids.

## 6.3. Reflections and Future Perspectives

This work was the product of a new research line in this research group, and we believe that it produced a wide set of useful and high-accuracy data for the viscosity and electrical conductivity of ionic liquids, as well as important insight into the nanostructuration and liquid dynamics of these compounds.

From a personal point of view, the development of a new apparatus/methodology was a challenging yet enriching experience, as it allowed me to develop competencies in different areas of knowledge, including programming, electronics, and technical drawing, as well as understanding, exploring, and applying new concepts.

The initial motivation for designing and developing the coin cell was to measure the electrical conductivity of mixtures of ionic liquids with alkaline salts and molecular solvents, such as glymes (oligoethers). However, due to the need for high-accurate data and a proper understanding of the effect of molecular effects on the transport properties, this project ended up being focused on the pure ionic liquids. Based on that, the study of the more complex binary and ternary systems would be a clear follow-up to continue the work initiated during this thesis. On the other hand, it would also be interesting to study newer and more unconventional ionic liquids, such as fluorinated [5] and silicon-based [6] ILs.

# References

[1] C.F.P. Miranda, L.M.N.B.F. Santos, J. Mol. Liq. 423 (2025) 126916. https://doi.org/10.1016/j.molliq.2025.126916

[2] J. Braunstein, G.D. Robbing, J. Chem. Educ. 48 (1971) 52. https://doi.org/10.1021/ed048p52

[3] G. Jones, R.C. Josephs, Journal of the American Chemical Society 50 (1928) 1049. https://doi.org/10.1021/ja01391a016

[4] G. Jones, G.M. Bollinger, Journal of the American Chemical Society 53 (1931) 1207. https://doi.org/10.1021/ja01355a002

[5] A.B. Pereiro, J.M.M. Araújo, S. Martinho, F. Alves, S. Nunes, A. Matias, C.M.M. Duarte, L.P.N. Rebelo, I.M. Marrucho, ACS Sustainable Chemistry & Engineering 1 (2013) 427. https://doi.org/10.1021/sc300163n

[6] R.M.A. Silva, H. Montes-Campos, A.I.M.C. Lobo Ferreira, E. Bakis, L.M.N.B.F. Santos, J. Phys. Chem. B 128 (2024) 3742. https://doi.org/10.1021/acs.jpcb.3c08333

# Appendix

**Appendix A.** Pinout and Electrical Configurations

**Appendix B.** Experimental Results

# Appendix A: Pinout and Electric Configuration

This appendix presents the pinout of some electronic configurations related to the ILDEM apparatus.

## Peltier Assemblies

Since the used Peltier assemblies operate at a voltage of 12 V and the used power source applies a voltage of 24 V, these modules were wired in series. A small box was constructed to encapsulate this electrical assembly. The pinout and images of the wiring configuration are presented in Fig. A.1.

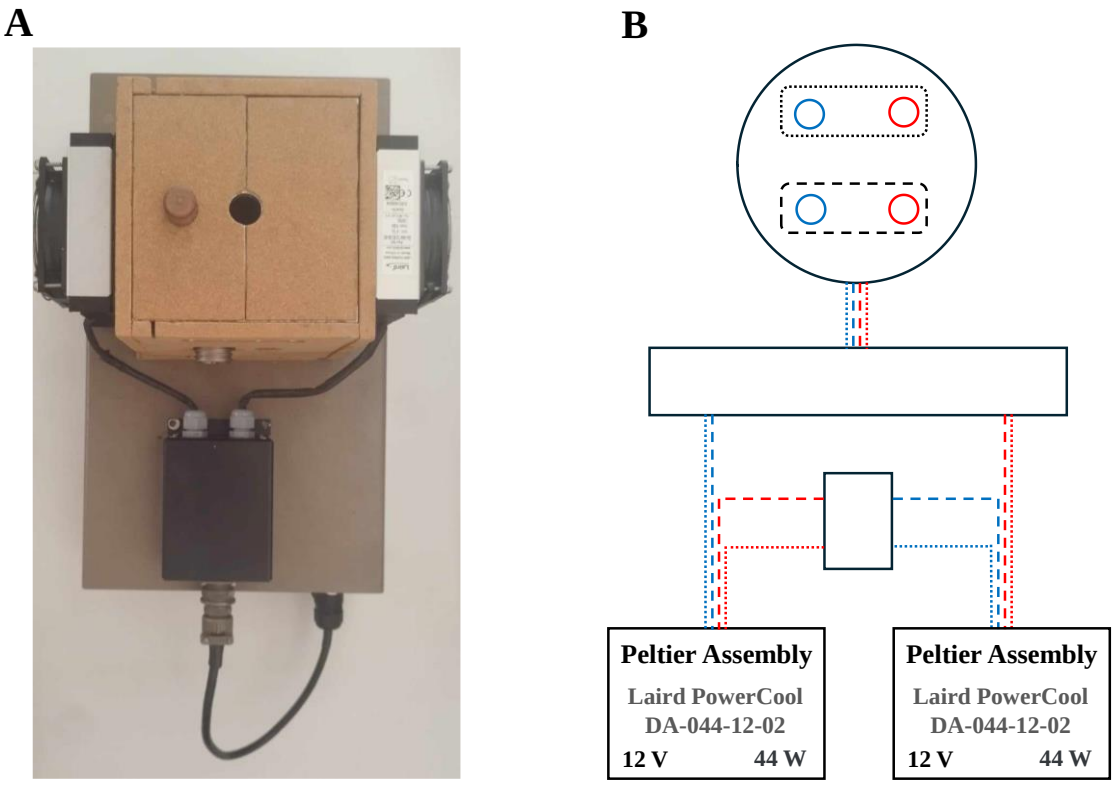



**Figure A.1.** Schematic representation and images of the Peltier wiring configuration. **A:** Overall Peltier connection; **B:** Pinout of the wiring configuration. Dashed lines: Peltier elements; Dotted lines: Peltier's ventilators; Positive (+); Negative (−). The circular shapes represent the cable plugs, and the rectangular shapes represent the wire connectors.

## Temperature Sensors

The pinout and images of the inside of the thermal chamber with highlights to the devices powered/connected via this cable are presented in Fig. A.2.

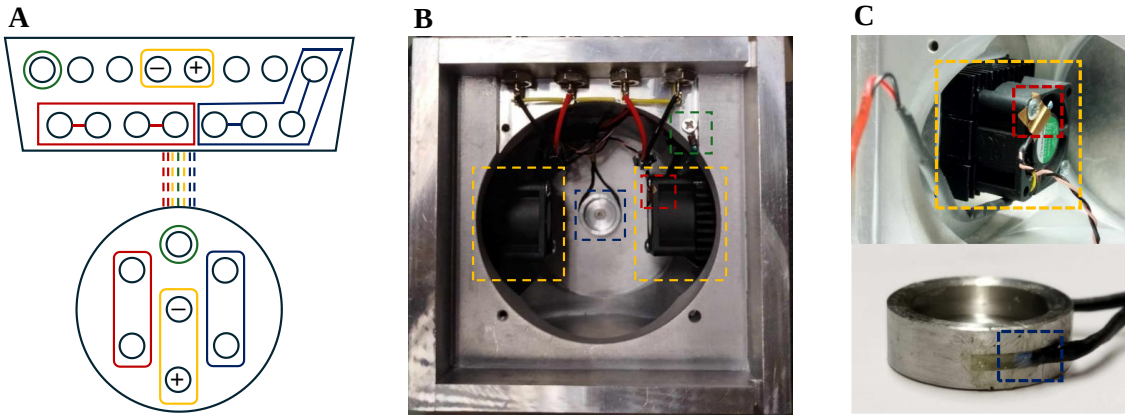



**Figure A.2.** Representation Control Box – Thermal Chamber connection with highlight to the powered/connected devices. **A:** Wiring pinout; **B:** Interior of the Thermal Chamber; **C:** Images focused on the Pt100 temperature sensors. Ground; Internal ventilators; OEM TEC – Pt100; Digital Meter – Pt100. + and – represent the positive and negative terminals, respectively. The colored links between the pins represent the electrical pairings.

The temperature sensors are connected to the Data-logger. The images of the cable installation on the Data-logger board can be found in Fig. A.3 together with the respective schematic representations.

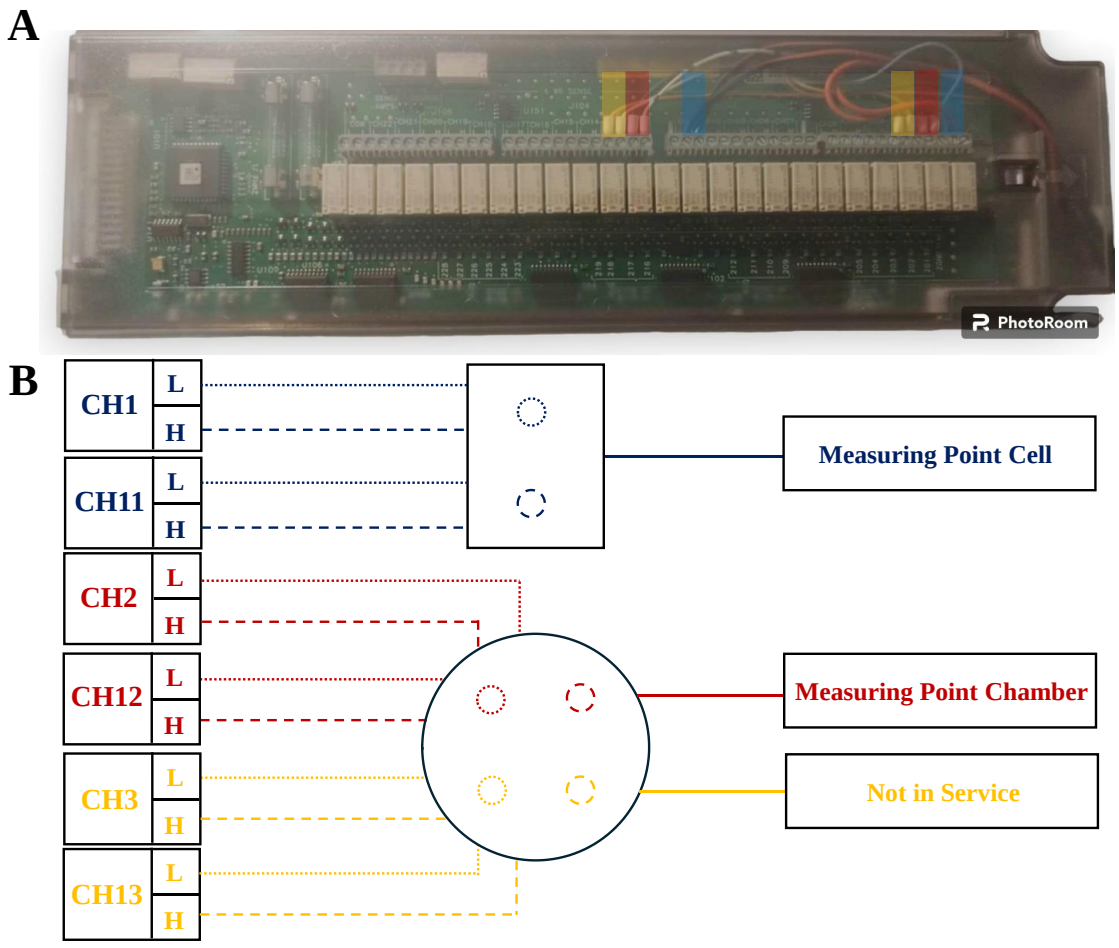



**Figure A.3.** Installation of the wiring installation on the Data Logger board. **A:** Image; **B:** Schematic representation.

# Appendix B: Experimental Results

This appendix presents the experimental results associated with the density, viscosity, and electrical conductivity measurements of the studied ionic liquids.

**Table B.1.** Experimental values for electrical conductivity and molar conductivity for $[^1C_1{}^3C_1im][NTf_2]$.

| ILDEM | | |
|---|---|---|
| $\frac{T}{K}$ | $\frac{\sigma}{S \cdot m^{-1}}$ | $\frac{10^4 \Lambda}{S \cdot m^2 \cdot mol^{-1}}$ |
| 293.42 | 0.7563 | 1.8127 |
| 298.33 | 0.8992 | 2.1623 |
| 303.24 | 1.0549 | 2.5450 |
| 308.16 | 1.2231 | 2.9605 |
| 313.07 | 1.4036 | 3.4085 |
| 317.97 | 1.5959 | 3.8881 |
| 322.88 | 1.7997 | 4.3990 |
| 327.77 | 2.0144 | 4.9398 |
| 332.64 | 2.2391 | 5.5085 |

$u(T)$ = ± 0.02 K; $u(\sigma)$ = 1.5% (Eq. 4.15); $u(\Lambda)$ = 1.5% (Eq. 4.15)

**Table B.2.** Experimental values for electrical conductivity and molar conductivity for $[^1C_2{}^3C_1im][NTf_2]$.

| ILDEM | | |
|---|---|---|
| $\frac{T}{K}$ | $\frac{\sigma}{S \cdot m^{-1}}$ | $\frac{10^4 \Lambda}{S \cdot m^2 \cdot mol^{-1}}$ |
| 283.61 | 0.5395 | 1.3762 |
| 288.51 | 0.6550 | 1.6763 |
| 293.40 | 0.7821 | 2.0082 |
| 298.29 | 0.9216 | 2.3741 |
| 303.19 | 1.0730 | 2.7732 |
| 308.10 | 1.2364 | 3.2061 |
| 313.00 | 1.4113 | 3.6717 |
| 317.90 | 1.5973 | 4.1692 |
| 322.80 | 1.7933 | 4.6962 |
| 327.68 | 2.0047 | 5.2669 |
| 332.57 | 2.2195 | 5.8504 |

$u(T)$ = ± 0.02 K; $u(\sigma)$ = 1.5% (Eq. 4.15); $u(\Lambda)$ = 1.5% (Eq. 4.15)

**Table B.3.** Experimental values for electrical conductivity and molar conductivity for [$^1C_1{}^3C_3$im][$NTf_2$].

| ILDEM | | |
|---|---|---|
| $\frac{T}{K}$ | $\frac{\sigma}{S \cdot m^{-1}}$ | $\frac{10^4 \Lambda}{S \cdot m^2 \cdot mol^{-1}}$ |
| 283.64 | 0.2926 | 0.7961 |
| 288.50 | 0.3684 | 1.0056 |
| 293.39 | 0.4552 | 1.2467 |
| 298.28 | 0.5530 | 1.5195 |
| 303.20 | 0.6620 | 1.8251 |
| 308.11 | 0.7821 | 2.1633 |
| 313.02 | 0.9131 | 2.5340 |
| 317.93 | 1.0547 | 2.9367 |
| 322.82 | 1.2064 | 3.3701 |
| 327.71 | 1.3681 | 3.8343 |
| 332.59 | 1.5393 | 4.3283 |

$u(T)$ = ± 0.02 K; $u(\sigma)$ = 1.5% (Eq. 4.15); $u(\Lambda)$ = 1.5% (Eq. 4.15)

**Table B.4.** Experimental values for electrical conductivity and molar conductivity for [$^1C_4{}^3C_1$im][$NTf_2$].

| ILDEM | | |
|---|---|---|
| $\frac{T}{K}$ | $\frac{\sigma}{S \cdot m^{-1}}$ | $\frac{10^4 \Lambda}{S \cdot m^2 \cdot mol^{-1}}$ |
| 283.70 | 0.2136 | 0.6193 |
| 288.56 | 0.2713 | 0.7892 |
| 293.44 | 0.3382 | 0.9868 |
| 298.32 | 0.4143 | 1.2129 |
| 303.21 | 0.4998 | 1.4681 |
| 308.11 | 0.5949 | 1.7531 |
| 313.02 | 0.6994 | 2.0679 |
| 317.91 | 0.8132 | 2.4124 |
| 322.80 | 0.9362 | 2.7862 |
| 327.69 | 1.0680 | 3.1889 |
| 332.56 | 1.2084 | 3.6197 |

$u(T)$ = ± 0.02 K; $u(\sigma)$ = 1.5% (Eq. 4.15); $u(\Lambda)$ = 1.5% (Eq. 4.15)

**Table B.5.** Experimental values for electrical conductivity and molar conductivity for [$^1C_1{}^3C_5$im][$NTf_2$].

| ILDEM | | |
|---|---|---|
| $\frac{T}{K}$ | $\frac{\sigma}{S \cdot m^{-1}}$ | $\frac{10^4 \Lambda}{S \cdot m^2 \cdot mol^{-1}}$ |
| 283.46 | 0.1430 | 0.4373 |
| 288.38 | 0.1850 | 0.5677 |
| 293.29 | 0.2345 | 0.7218 |
| 298.21 | 0.2918 | 0.9013 |
| 303.16 | 0.3574 | 1.1075 |
| 308.10 | 0.4312 | 1.3407 |
| 313.04 | 0.5135 | 1.6017 |
| 317.97 | 0.6040 | 1.8904 |
| 322.90 | 0.7029 | 2.2071 |
| 327.82 | 0.8098 | 2.5511 |
| 332.74 | 0.9245 | 2.9221 |

$u(T)$ = ± 0.02 K; $u(\sigma)$ = 1.5% (Eq. 4.15); $u(\Lambda)$ = 1.5% (Eq. 4.15)

**Table B.6.** Experimental values for electrical conductivity and molar conductivity for [$^1C_6{}^3C_1$im][$NTf_2$].

| ILDEM | | |
|---|---|---|
| $\frac{T}{K}$ | $\frac{\sigma}{S \cdot m^{-1}}$ | $\frac{10^4 \Lambda}{S \cdot m^2 \cdot mol^{-1}}$ |
| 283.57 | 0.1063 | 0.3430 |
| 288.44 | 0.1388 | 0.4493 |
| 293.33 | 0.1773 | 0.5758 |
| 298.24 | 0.2224 | 0.7247 |
| 303.14 | 0.2745 | 0.8974 |
| 308.05 | 0.3335 | 1.0938 |
| 313.95 | 0.3998 | 1.3156 |
| 317.85 | 0.4735 | 1.5632 |
| 322.75 | 0.5542 | 1.8356 |
| 327.65 | 0.6420 | 2.1334 |
| 332.53 | 0.7367 | 2.4561 |

$u(T)$ = ± 0.02 K; $u(\sigma)$ = 1.5% (Eq. 4.15); $u(\Lambda)$ = 1.5% (Eq. 4.15)

**Table B.7.** Experimental values for electrical conductivity and molar conductivity for [$^1$C$_7$$^3$C$_1$im][NTf$_2$].

| ILDEM | | |
|---|---|---|
| $\frac{T}{K}$ | $\frac{\sigma}{\mathrm{S{\cdot}m^{-1}}}$ | $\frac{10^4\Lambda}{\mathrm{S{\cdot}m^2{\cdot}mol^{-1}}}$ |
| 283.66 | 0.0794 | 0.2700 |
| 288.54 | 0.1046 | 0.3565 |
| 293.42 | 0.1348 | 0.4611 |
| 298.32 | 0.1705 | 0.5854 |
| 303.22 | 0.2122 | 0.7307 |
| 308.13 | 0.2600 | 0.8983 |
| 313.03 | 0.3141 | 1.0887 |
| 317.94 | 0.3746 | 1.3028 |
| 322.83 | 0.4414 | 1.5403 |
| 327.72 | 0.5148 | 1.8025 |
| 332.62 | 0.5949 | 2.0896 |

$u(T)$ = ± 0.02 K; $u(\sigma)$ = 1.5% (Eq. 4.15); $u(\Lambda)$ = 1.5% (Eq. 4.15)

**Table B.8.** Experimental values for electrical conductivity and molar conductivity for [$^1$C$_1$$^3$C$_8$im][NTf$_2$].

| ILDEM | | |
|---|---|---|
| $\frac{T}{K}$ | $\frac{\sigma}{\mathrm{S{\cdot}m^{-1}}}$ | $\frac{10^4\Lambda}{\mathrm{S{\cdot}m^2{\cdot}mol^{-1}}}$ |
| 283.66 | 0.0607 | 0.2105 |
| 288.53 | 0.0806 | 0.2805 |
| 293.41 | 0.1047 | 0.3659 |
| 298.31 | 0.1336 | 0.4682 |
| 303.21 | 0.1674 | 0.5887 |
| 308.11 | 0.2065 | 0.7287 |
| 313.02 | 0.2512 | 0.8891 |
| 317.94 | 0.3015 | 1.0709 |
| 322.84 | 0.3576 | 1.2742 |
| 327.73 | 0.4195 | 1.4998 |
| 332.60 | 0.4873 | 1.7479 |

$u(T)$ = ± 0.02 K; $u(\sigma)$ = 1.5% (Eq. 4.15); $u(\Lambda)$ = 1.5% (Eq. 4.15)

**Table B.9.** Experimental values for electrical conductivity and molar conductivity for [$^1C_1{}^3C_9$im][$NTf_2$].

| ILDEM | | |
|---|---|---|
| $\frac{T}{K}$ | $\frac{\sigma}{S \cdot m^{-1}}$ | $\frac{10^4 \Lambda}{S \cdot m^2 \cdot mol^{-1}}$ |
| 283.66 | 0.0478 | 0.1785 |
| 288.54 | 0.0639 | 0.2394 |
| 293.42 | 0.0836 | 0.3142 |
| 298.32 | 0.1073 | 0.4046 |
| 303.22 | 0.1353 | 0.5119 |
| 308.13 | 0.1680 | 0. 6375 |
| 313.03 | 0.2054 | 0.7822 |
| 317.94 | 0.2479 | 0.9470 |
| 322.83 | 0.2953 | 1.1320 |
| 327.72 | 0.3479 | 1.3379 |
| 332.62 | 0.4057 | 1.5652 |

$u(T)$ = ± 0.02 K; $u(\sigma)$ = 1.5% (Eq. 4.15); $u(\Lambda)$ = 1.5% (Eq. 4.15)

**Table B.10.** Experimental values for electrical conductivity and molar conductivity for [$^1C_{10}{}^3C_1$im][$NTf_2$].

| ILDEM | | |
|---|---|---|
| $\frac{T}{K}$ | $\frac{\sigma}{S \cdot m^{-1}}$ | $\frac{10^4 \Lambda}{S \cdot m^2 \cdot mol^{-1}}$ |
| 283.66 | 0.0387 | 0.1508 |
| 288.54 | 0.0520 | 0.2034 |
| 293.43 | 0.0683 | 0.2681 |
| 298.33 | 0.0880 | 0.3467 |
| 303.22 | 0.1115 | 0.4406 |
| 308.13 | 0.1389 | 0.5508 |
| 313.03 | 0.1705 | 0.6785 |
| 317.93 | 0.2066 | 0.8246 |
| 322.83 | 0.2470 | 0.9895 |
| 327.71 | 0.2921 | 1.1738 |
| 332.60 | 0.3418 | 1.3782 |

$u(T)$ = ± 0.02 K; $u(\sigma)$ = 1.5% (Eq. 4.15); $u(\Lambda)$ = 1.5% (Eq. 4.15)

**Table B.11.** Experimental values for electrical conductivity and molar conductivity for [$^1C_1{}^3C_{11}$im][$NTf_2$].

| ILDEM | | |
|---|---|---|
| $\frac{T}{K}$ | $\frac{\sigma}{S \cdot m^{-1}}$ | $\frac{10^4 \Lambda}{S \cdot m^2 \cdot mol^{-1}}$ |
| 283.47 | 0.0308 | 0.1250 |
| 288.43 | 0.0419 | 0.1708 |
| 293.34 | 0.0556 | 0.2272 |
| 298.27 | 0.0722 | 0.2961 |
| 303.20 | 0.0921 | 0.3791 |
| 308.15 | 0.1156 | 0.4774 |
| 313.09 | 0.1428 | 0.5920 |
| 317.03 | 0.1740 | 0.7236 |
| 322.96 | 0.2093 | 0.8734 |
| 327.88 | 0.2489 | 1.0418 |
| 332.80 | 0.2927 | 1.2295 |

$u(T)$ = ± 0.02 K; $u(\sigma)$ = 1.5% (Eq. 4.15); $u(\Lambda)$ = 1.5% (Eq. 4.15)

**Table B.12.** Experimental values for electrical conductivity and molar conductivity for [$^1C_{12}{}^3C_1$im][$NTf_2$].

| ILDEM | | |
|---|---|---|
| $\frac{T}{K}$ | $\frac{\sigma}{S \cdot m^{-1}}$ | $\frac{10^4 \Lambda}{S \cdot m^2 \cdot mol^{-1}}$ |
| 293.39 | 0.0469 | 0.1996 |
| 298.29 | 0.0610 | 0.2606 |
| 303.19 | 0.0780 | 0.3342 |
| 308.09 | 0.0981 | 0.4217 |
| 312.99 | 0.1215 | 0.5244 |
| 317.89 | 0.1485 | 0.6428 |
| 322.78 | 0.1790 | 0.7777 |
| 327.67 | 0.2133 | 0.9295 |
| 332.54 | 0.2513 | 1.0989 |

$u(T)$ = ± 0.02 K; $u(\sigma)$ = 1.5% (Eq. 4.15); $u(\Lambda)$ = 1.5% (Eq. 4.15)

**Table B.13.** Experimental values for density, viscosity, electrical conductivity, and molar conductivity for [$^{1}C_{2}^{2}C_{1}^{3}C_{1}$im][$NTf_2$].

| SVM 3001 | | | ILDEM | | |
|---|---|---|---|---|---|
| $\frac{T}{K}$ | $\frac{\rho}{kg \cdot m^{-3}}$ | $\frac{10^3 \eta}{Pa \cdot s}$ | $\frac{T}{K}$ | $\frac{\sigma}{S \cdot m^{-1}}$ | $\frac{10^4 \Lambda}{S \cdot m^2 \cdot mol^{-1}}$ |
| 293.15 | 1496.3 | 90.018 | 293.12 | 0.3266 | 0.8847 |
| 298.15 | 1491.5 | 71.517 | 298.14 | 0.4040 | 1.0979 |
| 303.15 | 1486.7 | 57.758 | 303.14 | 0.4920 | 1.3414 |
| 308.15 | 1481.9 | 47.336 | 308.13 | 0.5904 | 1.6148 |
| 313.15 | 1477.2 | 39.312 | 313.15 | 0.6993 | 1.9188 |
| 318.15 | 1472.4 | 33.038 | 318.15 | 0.8185 | 2.2532 |
| 323.15 | 1467.7 | 28.066 | 323.14 | 0.9486 | 2.6197 |
| 328.15 | 1462.9 | 24.076 | 328.12 | 1.0889 | 3.0169 |
| 333.15 | 1458.2 | 20.838 | 333.09 | 1.2381 | 3.4413 |
| 338.15 | 1453.5 | 18.183 | | | |
| 343.15 | 1448.9 | 15.984 | | | |
| 348.15 | 1444.2 | 14.149 | | | |
| 353.15 | 1439.5 | 12.604 | | | |
| 358.15 | 1434.9 | 11.297 | | | |
| 363.15 | 1430.2 | 10.182 | | | |
| 368.15 | 1425.6 | 9.2240 | | | |
| 373.15 | 1420.9 | 8.3985 | | | |

$u(T)$ = ± 0.02 K; $u(\rho)$ = ± 0.5 kg·m$^3$ (Eq. 2.90); $u(\eta)$ = 1% (Eq. 2.90); $u(\sigma)$ = 1.5% (Eq. 4.15); $u(\Lambda)$ = 1.5% (Eq. 4.15)

**Table B.14.** Experimental values for density, viscosity, electrical conductivity, and molar conductivity for [$^1C_1{}^2C_1{}^3C_3$im][$NTf_2$].

| SVM 3001 | | | ILDEM | | |
|---|---|---|---|---|---|
| $\frac{T}{K}$ | $\frac{\rho}{\text{kg·m}^{-3}}$ | $\frac{10^3\eta}{\text{Pa·s}}$ | $\frac{T}{K}$ | $\frac{\sigma}{\text{S·m}^{-1}}$ | $\frac{10^4\Lambda}{\text{S·m}^2\text{·mol}^{-1}}$ |
| 283.15 | 1469.9 | 224.79 | 283.18 | 0.1197 | 0.3417 |
| 288.15 | 1464.5 | 164.67 | 288.15 | 0.1604 | 0.4593 |
| 293.15 | 1459.7 | 123.69 | 293.15 | 0.2096 | 0.6022 |
| 298.15 | 1455.0 | 95.020 | 298.13 | 0.2679 | 0.7722 |
| 303.15 | 1450.3 | 74.470 | 303.13 | 0.3360 | 0.9716 |
| 308.15 | 1445.6 | 59.417 | 308.12 | 0.4142 | 1.2016 |
| 313.15 | 1440.8 | 48.172 | 313.12 | 0.5024 | 1.4623 |
| 318.15 | 1436.1 | 39.620 | 318.12 | 0.6009 | 1.7547 |
| 323.15 | 1431.5 | 33.011 | 323.11 | 0.7099 | 2.0797 |
| 328.15 | 1426.8 | 27.830 | 328.09 | 0.8285 | 2.4351 |
| 333.15 | 1422.1 | 23.712 | 333.06 | 0.9567 | 2.8210 |
| 338.15 | 1417.5 | 20.400 | | | |
| 343.15 | 1412.9 | 17.705 | | | |
| 348.15 | 1408.3 | 15.491 | | | |
| 353.15 | 1403.7 | 13.656 | | | |
| 358.15 | 1399.1 | 12.122 | | | |
| 363.15 | 1394.5 | 10.831 | | | |
| 368.15 | 1389.9 | 9.7350 | | | |
| 373.15 | 1385.3 | 8.8000 | | | |

$u(T)$ = ± 0.02 K; $u(\rho)$ = ± 0.5 kg·m$^3$ (Eq. 2.90); $u(\eta)$ = 1% (Eq. 2.90); $u(\sigma)$ = 1.5% (Eq. 4.15); $u(\Lambda)$ = 1.5% (Eq. 4.15)

**Table B.15.** Experimental values for density, viscosity, electrical conductivity, and molar conductivity for [$^1C_4{}^2C_1{}^3C_1$im][$NTf_2$].

| SVM 3001 | | | ILDEM | | |
|---|---|---|---|---|---|
| $\frac{T}{K}$ | $\frac{\rho}{\text{kg·m}^{-3}}$ | $\frac{10^3\eta}{\text{Pa·s}}$ | $\frac{T}{K}$ | $\frac{\sigma}{\text{S·m}^{-1}}$ | $\frac{10^4\Lambda}{\text{S·m}^2\text{·mol}^{-1}}$ |
| 283.15 | 1433.0 | 251.23 | 293.15 | 0.1686 | 0.5133 |
| 288.15 | 1428.3 | 182.10 | 298.15 | 0.2175 | 0.6643 |
| 293.15 | 1423.5 | 135.45 | 303.15 | 0.2748 | 0.8421 |
| 298.15 | 1418.9 | 103.19 | 308.13 | 0.3412 | 1.0490 |
| 303.15 | 1414.2 | 80.238 | 313.13 | 0.4166 | 1.2850 |
| 308.15 | 1409.6 | 63.552 | 318.13 | 0.5014 | 1.5516 |
| 313.15 | 1405.0 | 51.177 | 323.12 | 0.5957 | 1.8495 |
| 318.15 | 1400.5 | 41.832 | 328.10 | 0.6988 | 2.1766 |
| 323.15 | 1395.9 | 34.655 | 333.08 | 0.8111 | 2.5347 |
| 328.15 | 1391.3 | 29.061 | | | |
| 333.15 | 1386.8 | 24.641 | | | |
| 338.15 | 1382.3 | 21.103 | | | |
| 343.15 | 1377.8 | 18.240 | | | |
| 348.15 | 1373.3 | 15.900 | | | |
| 353.15 | 1368.8 | 13.967 | | | |
| 358.15 | 1364.3 | 12.358 | | | |
| 363.15 | 1359.8 | 11.008 | | | |
| 368.15 | 1355.3 | 9.866 | | | |
| 373.15 | 1350.9 | 8.8951 | | | |

$u(T)$ = ± 0.02 K; $u(\rho)$ = ± 0.5 kg·m$^3$ (Eq. 2.90); $u(\eta)$ = 1% (Eq. 2.90); $u(\sigma)$ = 1.5% (Eq. 4.15); $u(\Lambda)$ = 1.5% (Eq. 4.15)

**Table B.16.** Experimental values for density, viscosity, electrical conductivity, and molar conductivity for $[^1C_2{}^3C_1im]BF_4$.

| SVM 3001 | | | ILDEM | | |
|---|---|---|---|---|---|
| $\frac{T}{K}$ | $\frac{\rho}{kg \cdot m^{-3}}$ | $\frac{10^3 \eta}{Pa \cdot s}$ | $\frac{T}{K}$ | $\frac{\sigma}{S \cdot m^{-1}}$ | $\frac{10^4 \Lambda}{S \cdot m^2 \cdot mol^{-1}}$ |
| 283.15 | 1292.5 | 68.057 | 283.53 | 0.8959 | 1.3726 |
| 288.15 | 1288.6 | 54.324 | 288.42 | 1.0949 | 1.6824 |
| 293.15 | 1284.7 | 44.118 | 293.34 | 1.3175 | 2.0303 |
| 298.15 | 1280.9 | 36.374 | 298.26 | 1.5640 | 2.4173 |
| 303.15 | 1277.1 | 30.392 | 303.19 | 1.8336 | 2.8422 |
| 308.15 | 1273.4 | 25.702 | 308.13 | 2.1261 | 3.3053 |
| 313.15 | 1269.6 | 21.972 | 313.06 | 2.4411 | 3.8061 |
| 318.15 | 1265.9 | 18.964 | 317.99 | 2.7775 | 4.3432 |
| 323.15 | 1262.1 | 16.514 | 322.92 | 3.1349 | 4.9163 |
| 328.15 | 1258.5 | 14.492 | 327.84 | 3.5129 | 5.5250 |
| 333.15 | 1254.8 | 12.813 | 332.75 | 3.9094 | 6.1664 |
| 338.15 | 1251.1 | 11.406 | | | |
| 343.15 | 1247.5 | 10.219 | | | |
| 348.15 | 1243.9 | 9.2079 | | | |
| 353.15 | 1240.2 | 8.3418 | | | |
| 358.15 | 1236.6 | 7.5953 | | | |
| 363.15 | 1233.1 | 6.9481 | | | |
| 368.15 | 1229.5 | 6.3842 | | | |
| 373.15 | 1225.9 | 5.8916 | | | |

$u(T)$ = ± 0.02 K; $u(\rho)$ = ± 0.5 kg·m$^3$ (Eq. 2.90); $u(\eta)$ = 1% (Eq. 2.90); $u(\sigma)$ = 1.5% (Eq. 4.15); $u(\Lambda)$ = 1.5% (Eq. 4.15)

**Table B.17.** Experimental values for density, viscosity, electrical conductivity, and molar conductivity for $[^1C_1{}^3C_3im]BF_4$.

| SVM 3001 | | | ILDEM | | |
|---|---|---|---|---|---|
| $\frac{T}{K}$ | $\frac{\rho}{\text{kg·m}^{-3}}$ | $\frac{10^3\eta}{\text{Pa·s}}$ | $\frac{T}{K}$ | $\frac{\sigma}{\text{S·m}^{-1}}$ | $\frac{10^4\Lambda}{\text{S·m}^2\text{·mol}^{-1}}$ |
| 283.15 | 1248.9 | 175.78 | 288.46 | 0.3857 | 0.6568 |
| 288.15 | 1245.1 | 130.43 | 293.36 | 0.4962 | 0.8475 |
| 293.15 | 1241.4 | 98.971 | 298.29 | 0.6255 | 1.0714 |
| 298.15 | 1237.7 | 76.694 | 303.22 | 0.7745 | 1.3306 |
| 303.15 | 1234.0 | 60.571 | 308.15 | 0.9438 | 1.6262 |
| 308.15 | 1230.4 | 48.664 | 313.07 | 1.1338 | 1.9593 |
| 313.15 | 1226.7 | 39.699 | 318.00 | 1.3444 | 2.3300 |
| 318.15 | 1223.1 | 32.838 | 322.92 | 1.5756 | 2.7386 |
| 323.15 | 1219.5 | 27.508 | 327.83 | 1.8278 | 3.1862 |
| 328.15 | 1215.9 | 23.309 | 332.74 | 2.1004 | 3.6720 |
| 333.15 | 1212.3 | 19.957 | | | |
| 338.15 | 1208.3 | 17.251 | | | |
| 343.15 | 1205.3 | 15.042 | | | |
| 348.15 | 1201.7 | 13.221 | | | |
| 353.15 | 1198.2 | 11.708 | | | |
| 358.15 | 1194.7 | 10.439 | | | |
| 363.15 | 1191.3 | 9.3677 | | | |
| 368.15 | 1187.8 | 8.4558 | | | |
| 373.15 | 1184.3 | 7.6760 | | | |

$u(T)$ = ± 0.02 K; $u(\rho)$ = ± 0.5 kg·m$^3$ (Eq. 2.90); $u(\eta)$ = 1% (Eq. 2.90); $u(\sigma)$ = 1.5% (Eq. 4.15); $u(\Lambda)$ = 1.5% (Eq. 4.15)

**Table B.18.** Experimental values for density, viscosity, electrical conductivity, and molar conductivity for $[^1C_4{}^3C_1im]BF_4$.

| SVM 3001 | | | ILDEM | | |
|---|---|---|---|---|---|
| $\frac{T}{K}$ | $\frac{\rho}{kg \cdot m^{-3}}$ | $\frac{10^3 \eta}{Pa \cdot s}$ | $\frac{T}{K}$ | $\frac{\sigma}{S \cdot m^{-1}}$ | $\frac{10^4 \Lambda}{S \cdot m^2 \cdot mol^{-1}}$ |
| 278.15 | 1216.7 | 381.76 | 283.64 | 0.1558 | 0.2898 |
| 283.15 | 1213.0 | 269.94 | 288.52 | 0.2094 | 0.3906 |
| 288.15 | 1209.4 | 195.95 | 293.43 | 0.2750 | 0.5145 |
| 293.15 | 1205.8 | 145.69 | 298.33 | 0.3537 | 0.6637 |
| 298.15 | 1202.2 | 110.72 | 303.24 | 0.4465 | 0.8402 |
| 303.15 | 1198.7 | 85.829 | 308.16 | 0.5542 | 1.0460 |
| 308.15 | 1195.2 | 67.737 | 313.08 | 0.6775 | 1.2825 |
| 313.15 | 1191.6 | 54.333 | 318.00 | 0.8169 | 1.5509 |
| 318.15 | 1188.1 | 44.231 | 322.92 | 0.9727 | 1.8521 |
| 323.15 | 1184.6 | 36.492 | 327.82 | 1.1452 | 2.1869 |
| 328.15 | 1181.2 | 30.480 | 332.72 | 1.3345 | 2.5559 |
| 333.15 | 1177.7 | 25.746 | | | |
| 338.15 | 1174.3 | 21.970 | | | |
| 343.15 | 1170.9 | 18.928 | | | |
| 348.15 | 1167.5 | 16.448 | | | |
| 353.15 | 1164.1 | 14.409 | | | |
| 358.15 | 1160.7 | 12.716 | | | |
| 363.15 | 1157.3 | 11.300 | | | |
| 368.15 | 1153.9 | 10.107 | | | |
| 373.15 | 1150.5 | 9.0966 | | | |

$u(T)$ = ± 0.02 K; $u(\rho)$ = ± 0.5 kg·m$^3$ (Eq. 2.90); $u(\eta)$ = 1% (Eq. 2.90); $u(\sigma)$ = 1.5% (Eq. 4.15); $u(\Lambda)$ = 1.5% (Eq. 4.15)

**Table B.19.** Experimental values for density, viscosity, electrical conductivity, and molar conductivity for $[^1C_1{}^3C_5im]BF_4$.

| SVM 3001 | | | ILDEM | | |
|---|---|---|---|---|---|
| $\frac{T}{K}$ | $\frac{\rho}{kg \cdot m^{-3}}$ | $\frac{10^3 \eta}{Pa \cdot s}$ | $\frac{T}{K}$ | $\frac{\sigma}{S \cdot m^{-1}}$ | $\frac{10^4 \Lambda}{S \cdot m^2 \cdot mol^{-1}}$ |
| 283.15 | 1182.1 | 423.36 | 283.59 | 0.0819 | 0.1664 |
| 288.15 | 1178.5 | 300.80 | 288.49 | 0.1136 | 0.2314 |
| 293.15 | 1175.0 | 219.07 | 293.39 | 0.1513 | 0.3092 |
| 298.15 | 1171.5 | 163.18 | 298.31 | 0.1990 | 0.4078 |
| 303.15 | 1168.0 | 124.06 | 303.23 | 0.2564 | 0.5270 |
| 308.15 | 1164.6 | 96.098 | 308.09 | 0.3248 | 0.6695 |
| 313.15 | 1161.1 | 75.718 | 313.09 | 0.4049 | 0.8371 |
| 318.15 | 1157.7 | 60.598 | 318.01 | 0.4975 | 1.0315 |
| 323.15 | 1154.2 | 49.194 | 322.94 | 0.6031 | 1.2542 |
| 328.15 | 1150.8 | 40.462 | 327.83 | 0.7215 | 1.5047 |
| 333.15 | 1147.4 | 33.682 | 332.73 | 0.8531 | 1.7844 |
| 338.15 | 1144.1 | 28.350 | | | |
| 343.15 | 1140.7 | 24.107 | | | |
| 348.15 | 1137.3 | 20.692 | | | |
| 353.15 | 1134.0 | 17.918 | | | |
| 358.15 | 1130.6 | 15.641 | | | |
| 363.15 | 1127.3 | 13.756 | | | |
| 368.15 | 1124.0 | 12.184 | | | |
| 373.15 | 1120.6 | 10.863 | | | |

$u(T) = \pm 0.02$ K; $u(\rho) = \pm 0.5$ kg·m$^3$ (Eq. 2.90); $u(\eta) = 1\%$ (Eq. 2.90); $u(\sigma) = 1.5\%$ (Eq. 4.15); $u(\Lambda) = 1.5\%$ (Eq. 4.15).

**Table B.20.** Experimental values for density, viscosity, electrical conductivity, and molar conductivity for $[^1C_6{}^3C_1im]BF_4$.

| SVM 3001 | | | ILDEM | | |
|---|---|---|---|---|---|
| $\frac{T}{K}$ | $\frac{\rho}{kg \cdot m^{-3}}$ | $\frac{10^3 \eta}{Pa \cdot s}$ | $\frac{T}{K}$ | $\frac{\sigma}{S \cdot m^{-1}}$ | $\frac{10^4 \Lambda}{S \cdot m^2 \cdot mol^{-1}}$ |
| 283.15 | 1156.0 | 579.17 | 283.57 | 0.0492 | 0.1081 |
| 288.15 | 1152.5 | 405.47 | 288.46 | 0.0688 | 0.1516 |
| 293.15 | 1149.0 | 291.01 | 293.36 | 0.0938 | 0.2075 |
| 298.15 | 1145.6 | 213.76 | 298.27 | 0.1252 | 0.2778 |
| 303.15 | 1142.1 | 160.37 | 303.20 | 0.1638 | 0.3644 |
| 308.15 | 1138.7 | 122.68 | 308.12 | 0.2104 | 0.4695 |
| 313.15 | 1135.3 | 95.508 | 313.04 | 0.2658 | 0.5947 |
| 318.15 | 1131.9 | 75.573 | 318.96 | 0.3307 | 0.7423 |
| 323.15 | 1128.5 | 60.692 | 322.88 | 0.4059 | 0.9138 |
| 328.15 | 1125.1 | 49.413 | 327.80 | 0.4921 | 1.1112 |
| 333.15 | 1121.8 | 40.737 | 332.70 | 0.5889 | 1.3336 |
| 338.15 | 1118.4 | 33.977 | | | |
| 343.15 | 1115.1 | 28.642 | | | |
| 348.15 | 1111.8 | 24.386 | | | |
| 353.15 | 1108.5 | 20.953 | | | |
| 358.15 | 1105.2 | 18.158 | | | |
| 363.15 | 1101.9 | 15.860 | | | |
| 368.15 | 1098.6 | 13.957 | | | |
| 373.15 | 1095.3 | 12.365 | | | |

$u(T) = \pm 0.02$ K; $u(\rho) = \pm 0.5$ kg·m$^3$ (Eq. 2.90); $u(\eta) = 1\%$ (Eq. 2.90); $u(\sigma) = 1.5\%$ (Eq. 4.15); $u(\Lambda) = 1.5\%$ (Eq. 4.15).

**Table B.21.** Experimental values for density, viscosity, electrical conductivity, and molar conductivity for $[^1C_7{}^3C_1im]BF_4$.

| SVM 3001 | | | ILDEM | | |
|---|---|---|---|---|---|
| $\frac{T}{K}$ | $\frac{\rho}{kg \cdot m^{-3}}$ | $\frac{10^3 \eta}{Pa \cdot s}$ | $\frac{T}{K}$ | $\frac{\sigma}{S \cdot m^{-1}}$ | $\frac{10^4 \Lambda}{S \cdot m^2 \cdot mol^{-1}}$ |
| 283.15 | 1132.9 | 746.51 | 283.58 | 0.0332 | 0.0785 |
| 288.15 | 1129.4 | 518.31 | 288.46 | 0.0468 | 0.1110 |
| 293.15 | 1126.0 | 369.07 | 293.36 | 0.0643 | 0.1532 |
| 298.15 | 1122.6 | 268.86 | 298.28 | 0.0866 | 0.2067 |
| 303.15 | 1119.2 | 200.10 | 303.21 | 0.1141 | 0.2734 |
| 308.15 | 1115.8 | 151.84 | 308.13 | 0.1478 | 0.3551 |
| 313.15 | 1112.4 | 117.29 | 313.06 | 0.1882 | 0.4536 |
| 318.15 | 1109.1 | 92.086 | 317.98 | 0.2364 | 0.5713 |
| 323.15 | 1105.7 | 73.399 | 322.89 | 0.2929 | 0.7100 |
| 328.15 | 1102.4 | 59.321 | 327.80 | 0.3579 | 0.8730 |
| 333.15 | 1099.1 | 48.560 | 332.70 | 0.4309 | 1.0509 |
| 338.15 | 1095.8 | 40.221 | | | |
| 343.15 | 1092.5 | 33.681 | | | |
| 348.15 | 1089.2 | 28.493 | | | |
| 353.15 | 1085.9 | 24.331 | | | |
| 358.15 | 1082.7 | 20.960 | | | |
| 363.15 | 1079.4 | 18.204 | | | |
| 368.15 | 1076.2 | 15.934 | | | |
| 373.15 | 1072.9 | 14.049 | | | |

$u(T) = \pm 0.02$ K; $u(\rho) = \pm 0.5$ kg·m$^3$ (Eq. 2.90); $u(\eta) = 1\%$ (Eq. 2.90); $u(\sigma) = 1.5\%$ (Eq. 4.15); $u(\Lambda) = 1.5\%$ (Eq. 4.15).

**Table B.22.** Experimental values for density, viscosity, electrical conductivity, and molar conductivity for $[^1C_1{}^3C_8im]BF_4$.

| SVM 3001 | | | ILDEM | | |
|---|---|---|---|---|---|
| $\frac{T}{K}$ | $\frac{\rho}{\text{kg·m}^{-3}}$ | $\frac{10^3\eta}{\text{Pa·s}}$ | $\frac{T}{K}$ | $\frac{\sigma}{\text{S·m}^{-1}}$ | $\frac{10^4\Lambda}{\text{S·m}^2\text{·mol}^{-1}}$ |
| 283.15 | 1114.1 | 978.78 | 283.57 | 0.0233 | 0.0590 |
| 288.15 | 1110.7 | 672.34 | 288.45 | 0.0331 | 0.0841 |
| 293.15 | 1107.3 | 473.37 | 293.35 | 0.0459 | 0.1169 |
| 298.15 | 1103.9 | 341.33 | 298.26 | 0.0622 | 0.1589 |
| 303.15 | 1100.5 | 251.54 | 303.19 | 0.0826 | 0.2117 |
| 308.15 | 1097.1 | 189.05 | 308.12 | 0.1076 | 0.2768 |
| 313.15 | 1093.8 | 144.70 | 313.04 | 0.1379 | 0.3558 |
| 318.15 | 1090.5 | 112.62 | 317.97 | 0.1741 | 0.4505 |
| 323.15 | 1087.1 | 89.013 | 322.89 | 0.2168 | 0.5625 |
| 328.15 | 1083.8 | 71.365 | 327.79 | 0.2661 | 0.6926 |
| 333.15 | 1080.6 | 57.972 | 332.71 | 0.3225 | 0.8418 |
| 338.15 | 1077.3 | 47.670 | | | |
| 343.15 | 1074.0 | 39.641 | | | |
| 348.15 | 1070.8 | 33.312 | | | |
| 353.15 | 1067.5 | 28.266 | | | |
| 358.15 | 1064.3 | 24.203 | | | |
| 363.15 | 1061.0 | 20.900 | | | |
| 368.15 | 1057.8 | 18.192 | | | |
| 373.15 | 1054.6 | 15.956 | | | |

$u(T)$ = ± 0.02 K; $u(\rho)$ = ± 0.5 kg·m$^3$ (Eq. 2.90); $u(\eta)$ = 1% (Eq. 2.90); $u(\sigma)$ = 1.5% (Eq. 4.15); $u(\Lambda)$ = 1.5% (Eq. 4.15).

**Table B.23.** Experimental values for density, viscosity, electrical conductivity, and molar conductivity for $[^1C_1{}^3C_9im]BF_4$.

| SVM 3001 | | | ILDEM | | |
|---|---|---|---|---|---|
| $\frac{T}{K}$ | $\frac{\rho}{kg \cdot m^{-3}}$ | $\frac{10^3 \eta}{Pa \cdot s}$ | $\frac{T}{K}$ | $\frac{\sigma}{S \cdot m^{-1}}$ | $\frac{10^4 \Lambda}{S \cdot m^2 \cdot mol^{-1}}$ |
| 283.15 | 1097.8 | 1347.8 | 283.53 | 0.0170 | 0.0458 |
| 288.15 | 1094.4 | 911.25 | 288.43 | 0.0243 | 0.0658 |
| 293.15 | 1091.0 | 632.12 | 293.36 | 0.0340 | 0.0922 |
| 298.15 | 1087.6 | 449.56 | 298.30 | 0.0464 | 0.1263 |
| 303.15 | 1084.2 | 327.02 | 303.24 | 0.0621 | 0.1695 |
| 308.15 | 1080.9 | 242.82 | 308.20 | 0.0815 | 0.2232 |
| 313.15 | 1077.5 | 183.74 | 313.16 | 0.1051 | 0.2888 |
| 318.15 | 1074.2 | 141.48 | 318.11 | 0.1335 | 0.3681 |
| 323.15 | 1070.9 | 110.69 | 323.06 | 0.1674 | 0.4630 |
| 328.15 | 1067.6 | 87.893 | 328.00 | 0.2072 | 0.5747 |
| 333.15 | 1064.3 | 70.759 | 332.93 | 0.2528 | 0.7032 |
| 338.15 | 1061.1 | 57.690 | | | |
| 343.15 | 1057.8 | 47.594 | | | |
| 348.15 | 1054.6 | 39.693 | | | |
| 353.15 | 1051.4 | 33.441 | | | |
| 358.15 | 1048.1 | 28.438 | | | |
| 363.15 | 1044.9 | 24.400 | | | |
| 368.15 | 1041.7 | 21.108 | | | |
| 373.15 | 1038.5 | 18.403 | | | |

$u(T) = \pm 0.02$ K; $u(\rho) = \pm 0.5$ kg·m$^3$ (Eq. 2.90); $u(\eta) = 1\%$ (Eq. 2.90); $u(\sigma) = 1.5\%$ (Eq. 4.15); $u(\Lambda) = 1.5\%$ (Eq. 4.15).

**Table B.24.** Experimental values for density, viscosity, electrical conductivity, and molar conductivity for $[^1C_{10}{}^3C_1im]BF_4$.

| SVM 3001 | | | ILDEM | | |
|---|---|---|---|---|---|
| $\frac{T}{K}$ | $\frac{\rho}{kg \cdot m^{-3}}$ | $\frac{10^3 \eta}{Pa \cdot s}$ | $\frac{T}{K}$ | $\frac{\sigma}{S \cdot m^{-1}}$ | $\frac{10^4 \Lambda}{S \cdot m^2 \cdot mol^{-1}}$ |
| 283.15 | 1083.0 | 2032.6 | 283.53 | 0.0170 | 0.0458 |
| 288.15 | 1079.5 | 1336.2 | 288.43 | 0.0243 | 0.0658 |
| 293.15 | 1076.1 | 904.97 | 293.36 | 0.0340 | 0.0922 |
| 298.15 | 1072.7 | 629.85 | 298.30 | 0.0464 | 0.1263 |
| 303.15 | 1069.3 | 449.14 | 303.24 | 0.0621 | 0.1695 |
| 308.15 | 1066.0 | 327.63 | 308.20 | 0.0815 | 0.2232 |
| 313.15 | 1062.6 | 243.90 | 313.16 | 0.1051 | 0.2888 |
| 318.15 | 1059.3 | 185.07 | 318.11 | 0.1335 | 0.3681 |
| 323.15 | 1056.0 | 142.77 | 323.06 | 0.1674 | 0.4630 |
| 328.15 | 1052.7 | 111.95 | 328.00 | 0.2072 | 0.5747 |
| 333.15 | 1049.4 | 89.069 | 332.93 | 0.2528 | 0.7032 |
| 338.15 | 1046.2 | 71.831 | | | |
| 343.15 | 1042.9 | 58.657 | | | |
| 348.15 | 1039.7 | 48.455 | | | |
| 353.15 | 1036.5 | 40.460 | | | |
| 358.15 | 1033.2 | 34.122 | | | |
| 363.15 | 1030.0 | 29.046 | | | |
| 368.15 | 1026.8 | 24.943 | | | |
| 373.15 | 1023.6 | 21.595 | | | |

$u(T)$ = ± 0.02 K; $u(\rho)$ = ± 0.5 kg·m$^3$ (Eq. 2.90); $u(\eta)$ = 1% (Eq. 2.90); $u(\sigma)$ = 1.5% (Eq. 4.15); $u(\Lambda)$ = 1.5% (Eq. 4.15).

**Table B.25.** Experimental values for density, viscosity, electrical conductivity, and molar conductivity for $[^1C_{12}{}^3C_1im]BF_4$.

| SVM 3001 | | ILDEM | | |
|---|---|---|---|---|
| $\frac{T}{K}$ | $\frac{\rho}{kg \cdot m^{-3}}$ | $\frac{T}{K}$ | $\frac{\sigma}{S \cdot m^{-1}}$ | $\frac{10^4 \Lambda}{S \cdot m^2 \cdot mol^{-1}}$ |
| 323.15 | 1032.3 | 322.81 | 0.0930 | 0.2035 |
| 328.15 | 1029.0 | 327.75 | 0.1156 | 0.2538 |
| 333.15 | 1025.7 | 332.63 | 0.1417 | 0.3121 |
| 338.15 | 1022.5 | | | |
| 343.15 | 1019.2 | | | |
| 348.15 | 1016.0 | | | |
| 353.15 | 1012.8 | | | |
| 358.15 | 1009.5 | | | |
| 363.15 | 1006.3 | | | |
| 368.15 | 1003.1 | | | |
| 373.15 | 999.9 | | | |

$u(T)$ = ± 0.02 K; $u(\rho)$ = ± 0.5 kg·m$^3$ (Eq. 2.90); $u(\eta)$ = 1% (Eq. 2.90); $u(\sigma)$ = 1.5% (Eq. 4.15); $u(\Lambda)$ = 1.5% (Eq. 4.15).

**Table B.26.** Experimental values for density, viscosity, electrical conductivity, and molar conductivity for $[^1C_1{}^3C_3im]PF_6$.

| SVM 3001 | | | ILDEM | | |
|---|---|---|---|---|---|
| $\frac{T}{K}$ | $\frac{\rho}{kg \cdot m^{-3}}$ | $\frac{10^3 \eta}{Pa \cdot s}$ | $\frac{T}{K}$ | $\frac{\sigma}{S \cdot m^{-1}}$ | $\frac{10^4 \Lambda}{S \cdot m^2 \cdot mol^{-1}}$ |
| 318.15 | 1392.4 | 84.509 | 313.07 | 0.4397 | 0.8504 |
| 323.15 | 1388.2 | 67.723 | 318.00 | 0.5439 | 1.0551 |
| 328.15 | 1383.8 | 55.058 | 322.91 | 0.6632 | 1.2905 |
| 333.15 | 1379.7 | 45.357 | 327.81 | 0.7974 | 1.5562 |
| 338.15 | 1375.5 | 37.817 | 332.69 | 0.9468 | 1.8531 |
| 343.15 | 1371.3 | 31.883 | | | |
| 348.15 | 1367.2 | 27.155 | | | |
| 353.15 | 1363.0 | 23.347 | | | |
| 358.15 | 1358.9 | 20.248 | | | |
| 363.15 | 1354.8 | 17.714 | | | |
| 368.15 | 1350.6 | 15.604 | | | |
| 373.15 | 1346.5 | 13.845 | | | |

$u(T)$ = ± 0.02 K; $u(\rho)$ = ± 0.5 kg·m$^3$ (Eq. 2.90); $u(\eta)$ = 1% (Eq. 2.90); $u(\sigma)$ = 1.5% (Eq. 4.15); $u(\Lambda)$ = 1.5% (Eq. 4.15).

**Table B.27.** Experimental values for electrical conductivity and molar conductivity for $[^1C_4{}^3C_1im]PF_6$.

| ILDEM | | |
|---|---|---|
| $\frac{T}{K}$ | $\frac{\sigma}{S \cdot m^{-1}}$ | $\frac{10^4 \Lambda}{S \cdot m^2 \cdot mol^{-1}}$ |
| 283.62 | 0.0572 | 0.1179 |
| 288.50 | 0.0806 | 0.1665 |
| 293.41 | 0.1107 | 0.2294 |
| 298.31 | 0.1483 | 0.3082 |
| 303.23 | 0.1945 | 0.4056 |
| 308.15 | 0.2503 | 0.5234 |
| 313.08 | 0.3164 | 0.6637 |
| 317.99 | 0.3944 | 0.8297 |
| 322.92 | 0.4827 | 1.0185 |
| 327.82 | 0.5836 | 1.2352 |
| 332.73 | 0. 6972 | 1.4800 |

$u(T)$ = ± 0.02 K; $u(\sigma)$ = 1.5% (Eq. 4.15); $u(\Lambda)$ = 1.5% (Eq. 4.15)

**Table B.28.** Experimental values for electrical conductivity and molar conductivity for $[^1C_1{}^3C_5im]PF_6$.

| ILDEM | | |
|---|---|---|
| $\frac{T}{K}$ | $\frac{\sigma}{S \cdot m^{-1}}$ | $\frac{10^4 \Lambda}{S \cdot m^2 \cdot mol^{-1}}$ |
| 283.69 | 0.0315 | 0.0700 |
| 288.51 | 0.0452 | 0.1009 |
| 293.36 | 0.0633 | 0.1416 |
| 298.22 | 0.0865 | 0.1941 |
| 303.10 | 0.1155 | 0.2602 |
| 307.98 | 0.1514 | 0.3420 |
| 312.88 | 0.1947 | 0.4411 |
| 317.77 | 0.2461 | 0.5593 |
| 322.65 | 0.3063 | 0.6982 |
| 327.52 | 0.3757 | 0.8590 |
| 332.40 | 0.4551 | 1.0437 |

$u(T)$ = ± 0.02 K; $u(\sigma)$ = 1.5% (Eq. 4.15); $u(\Lambda)$ = 1.5% (Eq. 4.15)

**Table B.29.** Experimental values for electrical conductivity and molar conductivity for $[^1C_6{}^3C_1im]PF_6$.

| ILDEM | | |
|---|---|---|
| $\frac{T}{K}$ | $\frac{\sigma}{S \cdot m^{-1}}$ | $\frac{10^4 \Lambda}{S \cdot m^2 \cdot mol^{-1}}$ |
| 283.66 | 0.0195 | 0.0465 |
| 288.52 | 0.0285 | 0.0682 |
| 293.41 | 0.0405 | 0.0973 |
| 298.32 | 0.0562 | 0.1356 |
| 303.23 | 0.0763 | 0.1847 |
| 308.14 | 0.1013 | 0.2459 |
| 313.06 | 0.1322 | 0.3219 |
| 317.97 | 0.1696 | 0.4143 |
| 322.88 | 0.2142 | 0.5246 |
| 327.78 | 0.2659 | 0.6534 |
| 332.67 | 0.3253 | 0.8016 |

$u(T)$ = ± 0.02 K; $u(\sigma)$ = 1.5% (Eq. 4.15); $u(\Lambda)$ = 1.5% (Eq. 4.15)

**Table B.30.** Experimental values for electrical conductivity and molar conductivity for $[^1C_7{}^3C_1im]PF_6$.

| ILDEM | | |
|---|---|---|
| $\frac{T}{K}$ | $\frac{\sigma}{S \cdot m^{-1}}$ | $\frac{10^4 \Lambda}{S \cdot m^2 \cdot mol^{-1}}$ |
| 283.64 | 0.0129 | 0.0331 |
| 288.50 | 0.0191 | 0.0490 |
| 293.38 | 0.0274 | 0.0706 |
| 298.27 | 0.0384 | 0.0993 |
| 303.24 | 0.0526 | 0.1365 |
| 308.08 | 0.0705 | 0.1834 |
| 312.99 | 0.0928 | 0.2419 |
| 317.90 | 0.1200 | 0.3138 |
| 322.81 | 0.1528 | 0.4009 |
| 327.73 | 0.1920 | 0.5054 |
| 332.64 | 0.2379 | 0. 6280 |

$u(T)$ = ± 0.02 K; $u(\sigma)$ = 1.5% (Eq. 4.15); $u(\Lambda)$ = 1.5% (Eq. 4.15)

**Table B.31.** Experimental values for electrical conductivity and molar conductivity for $[^1C_1{}^3C_8im]PF_6$.

| ILDEM | | |
|---|---|---|
| $\frac{T}{K}$ | $\frac{\sigma}{S \cdot m^{-1}}$ | $\frac{10^4 \Lambda}{S \cdot m^2 \cdot mol^{-1}}$ |
| 283.65 | 0.0088 | 0.0239 |
| 288.50 | 0.0131 | 0.0258 |
| 293.38 | 0.0190 | 0.0523 |
| 298.28 | 0.0270 | 0.0743 |
| 303.18 | 0.0374 | 0.1032 |
| 308.12 | 0.0507 | 0.1404 |
| 313.03 | 0.0674 | 0.1872 |
| 317.93 | 0.0880 | 0.2452 |
| 322.83 | 0.1132 | 0.3164 |
| 327.74 | 0.1433 | 0.4016 |
| 332.64 | 0.1784 | 0.5015 |

$u(T)$ = ± 0.02 K; $u(\sigma)$ = 1.5% (Eq. 4.15); $u(\Lambda)$ = 1.5% (Eq. 4.15)

**Table B.32.** Experimental values for electrical conductivity and molar conductivity for $[^1C_1{}^3C_9im]PF_6$.

| ILDEM | | |
|---|---|---|
| $\frac{T}{K}$ | $\frac{\sigma}{S \cdot m^{-1}}$ | $\frac{10^4 \Lambda}{S \cdot m^2 \cdot mol^{-1}}$ |
| 293.44 | 0.0134 | 0.0391 |
| 298.34 | 0.0192 | 0.0562 |
| 303.24 | 0.0269 | 0.0788 |
| 308.15 | 0.0368 | 0.1082 |
| 313.05 | 0.0493 | 0.1455 |
| 317.95 | 0.0650 | 0.1923 |
| 322.88 | 0.0843 | 0.2502 |
| 327.77 | 0.1077 | 0.3206 |
| 332.65 | 0.1352 | 0.4036 |

$u(T)$ = ± 0.02 K; $u(\sigma)$ = 1.5% (Eq. 4.15); $u(\Lambda)$ = 1.5% (Eq. 4.15)

**Table B.33.** Experimental values for density, viscosity, electrical conductivity, and molar conductivity for $[^1C_{10}{}^3C_1im]PF_6$.

| SVM 3001 | | | ILDEM | | |
|---|---|---|---|---|---|
| $\frac{T}{K}$ | $\frac{\rho}{kg \cdot m^{-3}}$ | $\frac{10^3 \eta}{Pa \cdot s}$ | $\frac{T}{K}$ | $\frac{\sigma}{S \cdot m^{-1}}$ | $\frac{10^4 \Lambda}{S \cdot m^2 \cdot mol^{-1}}$ |
| 318.15 | 1171.1 | 296.45 | 303.23 | 0.0202 | 0.0605 |
| 323.15 | 1167.4 | 222.95 | 308.15 | 0.0278 | 0.0835 |
| 328.15 | 1163.8 | 170.57 | 313.07 | 0.0376 | 0.1131 |
| 333.15 | 1160.2 | 132.63 | 317.98 | 0.0497 | 0.1502 |
| 338.15 | 1156.6 | 104.69 | 322.88 | 0.0647 | 0.1962 |
| 343.15 | 1153.0 | 83.795 | 327.77 | 0.0830 | 0.2523 |
| 348.15 | 1149.4 | 67.942 | 332.66 | 0.1048 | 0.3196 |
| 353.15 | 1145.8 | 55.753 | | | |
| 358.15 | 1142.2 | 46.264 | | | |
| 363.15 | 1138.7 | 38.792 | | | |
| 368.15 | 1135.1 | 32.846 | | | |
| 373.15 | 1131.5 | 28.067 | | | |

$u(T)$ = ± 0.02 K; $u(\rho)$ = ± 0.5 kg·m$^3$ (Eq. 2.90); $u(\eta)$ = 1% (Eq. 2.90); $u(\sigma)$ = 1.5% (Eq. 4.15); $u(\Lambda)$ = 1.5% (Eq. 4.15).

**Table B.34.** Experimental values for density, viscosity, electrical conductivity, and molar conductivity for [$^{1}C_{2}^{3}C_{1}$im][OTf].

| SVM 3001 | | | ILDEM | | |
|---|---|---|---|---|---|
| $\frac{T}{K}$ | $\frac{\rho}{\text{kg·m}^{-3}}$ | $\frac{10^{3}\eta}{\text{Pa·s}}$ | $\frac{T}{K}$ | $\frac{\sigma}{\text{S·m}^{-1}}$ | $\frac{10^{4}\Lambda}{\text{S·m}^{2}\text{·mol}^{-1}}$ |
| 273.15 | 1405.4 | 131.90 | 283.72 | 0.5478 | 1.0209 |
| 278.15 | 1401.1 | 102.29 | 288.58 | 0.6637 | 1.2406 |
| 283.15 | 1396.8 | 80.500 | 293.49 | 0.7933 | 1.4873 |
| 188.15 | 1392.5 | 64.812 | 298.39 | 0.9367 | 1.7613 |
| 293.15 | 1388.3 | 52.913 | 303.29 | 1.0940 | 2.0632 |
| 298.15 | 1384.2 | 43.762 | 308.21 | 1.2652 | 2.3932 |
| 303.15 | 1380.0 | 36.540 | 313.12 | 1.4501 | 2.7511 |
| 308.15 | 1375.8 | 30.943 | 318.03 | 1.6488 | 3.1374 |
| 313.15 | 1371.7 | 26.459 | 321.93 | 1.8611 | 3.5519 |
| 318.15 | 1367.5 | 22.825 | 327.83 | 2.0867 | 3.9942 |
| 323.15 | 1363.4 | 19.852 | 332.73 | 2.3253 | 4.4641 |
| 328.15 | 1359.3 | 17.395 | | | |
| 333.15 | 1355.2 | 15.348 | | | |
| 338.15 | 1351.1 | 13.630 | | | |
| 343.15 | 1347.1 | 12.176 | | | |
| 348.15 | 1343.0 | 10.939 | | | |
| 353.15 | 1339.0 | 9.8794 | | | |
| 358.15 | 1335.0 | 8.9659 | | | |
| 363.15 | 1331.0 | 8.1747 | | | |
| 368.15 | 1327.0 | 7.4860 | | | |
| 373.15 | 1323.0 | 6.8849 | | | |

$u(T)$ = ± 0.02 K; $u(\rho)$ = ± 0.5 kg·m$^{3}$ (Eq. 2.90); $u(\eta)$ = 1% (Eq. 2.90); $u(\sigma)$ = 1.5% (Eq. 4.15); $u(\Lambda)$ = 1.5% (Eq. 4.15).

**Table B.35.** Experimental values for density, viscosity, electrical conductivity, and molar conductivity for [$^1C_4{}^3C_1$im][OTf].

| SVM 3001 | | | ILDEM | | |
|---|---|---|---|---|---|
| $\frac{T}{K}$ | $\frac{\rho}{\text{kg·m}^{-3}}$ | $\frac{10^3\eta}{\text{Pa·s}}$ | $\frac{T}{K}$ | $\frac{\sigma}{\text{S·m}^{-1}}$ | $\frac{10^4\Lambda}{\text{S·m}^2\text{·mol}^{-1}}$ |
| 273.15 | 1317.3 | 418.62 | 283.65 | 0.1370 | 0.3018 |
| 278.15 | 1313.2 | 297.60 | 288.54 | 0.1785 | 0.3943 |
| 283.15 | 1309.2 | 217.02 | 293.43 | 0.2282 | 0.5057 |
| 288.15 | 1305.2 | 161.95 | 298.34 | 0.2865 | 0.6367 |
| 293.15 | 1301.2 | 123.52 | 303.25 | 0.3541 | 0.7893 |
| 298.15 | 1297.3 | 96.066 | 308.17 | 0.4314 | 0.9645 |
| 303.15 | 1293.3 | 76.017 | 313.09 | 0.5185 | 1.1628 |
| 308.15 | 1289.4 | 61.103 | 318.01 | 0.6158 | 1.3851 |
| 313.15 | 1285.5 | 49.795 | 322.92 | 0.7236 | 1.6324 |
| 318.15 | 1281.6 | 41.114 | 327.82 | 0.8414 | 1.9039 |
| 323.15 | 1277.7 | 34.347 | 332.73 | 0.9702 | 2.2019 |
| 328.15 | 1273.8 | 29.002 | | | |
| 333.15 | 1269.9 | 24.731 | | | |
| 338.15 | 1266.1 | 21.281 | | | |
| 343.15 | 1262.3 | 18.466 | | | |
| 348.15 | 1258.5 | 16.148 | | | |
| 353.15 | 1254.7 | 14.222 | | | |
| 358.15 | 1250.9 | 12.611 | | | |
| 363.15 | 1247.1 | 11.251 | | | |
| 368.15 | 1243.3 | 10.099 | | | |
| 373.15 | 1239.5 | 9.11777 | | | |

$u(T)$ = ± 0.02 K; $u(\rho)$ = ± 0.5 kg·m$^3$ (Eq. 2.90); $u(\eta)$ = 1% (Eq. 2.90); $u(\sigma)$ = 1.5% (Eq. 4.15); $u(\Lambda)$ = 1.5% (Eq. 4.15).

**Table B.36.** Experimental values for density, viscosity, electrical conductivity, and molar conductivity for [$^{1}C_{6}{}^{3}C_{1}$im][OTf].

| SVM 3001 | | | ILDEM | | |
|---|---|---|---|---|---|
| $\frac{T}{K}$ | $\frac{\rho}{\text{kg·m}^{-3}}$ | $\frac{10^{3}\eta}{\text{Pa·s}}$ | $\frac{T}{K}$ | $\frac{\sigma}{\text{S·m}^{-1}}$ | $\frac{10^{4}\Lambda}{\text{S·m}^{2}\text{·mol}^{-1}}$ |
| 293.15 | 1239.7 | 200.68 | 293.38 | 0.0966 | 0.2465 |
| 298.15 | 1235.9 | 151.71 | 298.31 | 0.1256 | 0.3215 |
| 303.15 | 1232.0 | 116.53 | 303.26 | 0.1603 | 0.4116 |
| 308.15 | 1228.2 | 91.392 | 308.19 | 0.2011 | 0.5180 |
| 313.15 | 1224.4 | 72.796 | 313.13 | 0.2484 | 0.6417 |
| 318.15 | 1220.6 | 58.813 | 318.06 | 0.3027 | 0.7844 |
| 323.15 | 1216.9 | 48.138 | 322.99 | 0.3643 | 0.9469 |
| 328.15 | 1213.1 | 39.879 | 327.92 | 0.4336 | 1.1305 |
| 333.15 | 1209.4 | 33.397 | 332.84 | 0.5107 | 1.3356 |
| 338.15 | 1205.6 | 28.259 | | | |
| 343.15 | 1201.9 | 24.138 | | | |
| 348.15 | 1198.2 | 20.797 | | | |
| 353.15 | 1194.5 | 18.065 | | | |
| 358.15 | 1190.8 | 15.810 | | | |
| 363.15 | 1187.1 | 13.933 | | | |
| 368.15 | 1183.5 | 12.361 | | | |
| 373.15 | 1179.8 | 11.035 | | | |

$u(T)$ = ± 0.02 K; $u(\rho)$ = ± 0.5 kg·m$^{3}$ (Eq. 2.90); $u(\eta)$ = 1% (Eq. 2.90); $u(\sigma)$ = 1.5% (Eq. 4.15); $u(\Lambda)$ = 1.5% (Eq. 4.15).

**Table B.37.** Experimental values for density, viscosity, electrical conductivity, and molar conductivity for [$^1C_1{}^3C_8$im][OTf].

| SVM 3001 | | | ILDEM | | |
|---|---|---|---|---|---|
| $\frac{T}{K}$ | $\frac{\rho}{\text{kg·m}^{-3}}$ | $\frac{10^3\eta}{\text{Pa·s}}$ | $\frac{T}{K}$ | $\frac{\sigma}{\text{S·m}^{-1}}$ | $\frac{10^4\Lambda}{\text{S·m}^2\text{·mol}^{-1}}$ |
| 283.15 | 1200.2 | 610.68 | 283.68 | 0.0257 | 0.0738 |
| 288.15 | 1196.5 | 429.45 | 288.55 | 0.0356 | 0.1025 |
| 293.15 | 1192.7 | 310.37 | 293.42 | 0.0483 | 0.1395 |
| 298.15 | 1189.0 | 229.37 | 298.31 | 0.0641 | 0.1857 |
| 303.15 | 1185.3 | 173.00 | 303.21 | 0.0834 | 0.2423 |
| 308.15 | 1181.6 | 132.92 | 308.13 | 0.1067 | 0.3110 |
| 313.15 | 1177.9 | 103.88 | 313.03 | 0.1343 | 0.3927 |
| 318.15 | 1174.2 | 82.443 | 317.95 | 0.1666 | 0.4886 |
| 323.15 | 1170.6 | 66.365 | 322.86 | 0.2041 | 0.6004 |
| 328.15 | 1166.9 | 54.123 | 327.74 | 0.2469 | 0.7285 |
| 333.15 | 1163.3 | 44.670 | 332.63 | 0.2954 | 0.8743 |
| 338.15 | 1159.7 | 37.278 | | | |
| 343.15 | 1156.1 | 31.429 | | | |
| 348.15 | 1152.5 | 26.750 | | | |
| 353.15 | 1148.9 | 22.970 | | | |
| 358.15 | 1145.3 | 19.886 | | | |
| 363.15 | 1141.7 | 17.348 | | | |
| 368.15 | 1138.2 | 15.246 | | | |
| 373.15 | 1134.6 | 13.489 | | | |

$u(T)$ = ± 0.02 K; $u(\rho)$ = ± 0.5 kg·m$^3$ (Eq. 2.90); $u(\eta)$ = 1% (Eq. 2.90); $u(\sigma)$ = 1.5% (Eq. 4.15); $u(\Lambda)$ = 1.5% (Eq. 4.15).

**Table B.38.** Experimental values for density, viscosity, electrical conductivity, and molar conductivity for [$^1C_{10}{}^3C_1$im][OTf].

| SVM 3001 | | | ILDEM | | |
|---|---|---|---|---|---|
| $\frac{T}{K}$ | $\frac{\rho}{\text{kg·m}^{-3}}$ | $\frac{10^3\eta}{\text{Pa·s}}$ | $\frac{T}{K}$ | $\frac{\sigma}{\text{S·m}^{-1}}$ | $\frac{10^4\Lambda}{\text{S·m}^2\text{·mol}^{-1}}$ |
| 283.15 | 1166.7 | 869.52 | 293.39 | 0.0293 | 0.0949 |
| 288.15 | 1163.0 | 603.44 | 298.28 | 0.0393 | 0.1278 |
| 293.15 | 1159.3 | 429.61 | 303.19 | 0.0517 | 0.1686 |
| 298.15 | 1155.6 | 313.02 | 308.10 | 0.0667 | 0.2182 |
| 303.15 | 1151.9 | 232.88 | 313.01 | 0.0846 | 0.2779 |
| 308.15 | 1148.2 | 176.62 | 317.92 | 0.1058 | 0.3486 |
| 313.15 | 1144.6 | 136.33 | 322.83 | 0.1306 | 0.4314 |
| 318.15 | 1140.9 | 106.92 | 327.71 | 0.1591 | 0.5274 |
| 323.15 | 1137.7 | 85.104 | 332.59 | 0.1920 | 0.6382 |
| 328.15 | 1133.7 | 68.671 | | | |
| 333.15 | 1130.1 | 56.104 | | | |
| 338.15 | 1126.5 | 46.372 | | | |
| 343.15 | 1123.0 | 38.740 | | | |
| 348.15 | 1119.4 | 32.688 | | | |
| 353.15 | 1115.8 | 27.836 | | | |
| 358.15 | 1112.3 | 23.908 | | | |
| 363.15 | 1108.7 | 20.700 | | | |
| 368.15 | 1105.2 | 18.058 | | | |
| 373.15 | 1101.6 | 15.866 | | | |

$u(T)$ = ± 0.02 K; $u(\rho)$ = ± 0.5 kg·m$^3$ (Eq. 2.90); $u(\eta)$ = 1% (Eq. 2.90); $u(\sigma)$ = 1.5% (Eq. 4.15); $u(\Lambda)$ = 1.5% (Eq. 4.15).

**Table B.39.** Experimental values for density, viscosity, electrical conductivity, and molar conductivity for [$^1C_{12}{}^3C_1$im][OTf].

| SVM 3001 | | | ILDEM | | |
|---|---|---|---|---|---|
| $\frac{T}{K}$ | $\frac{\rho}{\text{kg·m}^{-3}}$ | $\frac{10^3\eta}{\text{Pa·s}}$ | $\frac{T}{K}$ | $\frac{\sigma}{\text{S·m}^{-1}}$ | $\frac{10^4\Lambda}{\text{S·m}^2\text{·mol}^{-1}}$ |
| 318.15 | 1112.0 | 157.55 | 318.00 | 0.0708 | 0.2551 |
| 323.15 | 1108.4 | 123.19 | 322.94 | 0.0883 | 0.3192 |
| 328.15 | 1104.8 | 97.741 | 327.86 | 0.1087 | 0.3941 |
| 333.15 | 1101.2 | 78.586 | 332.76 | 0.1324 | 0.4813 |
| 338.15 | 1097.2 | 63.985 | | | |
| 343.15 | 1094.2 | 52.699 | | | |
| 348.15 | 1090.6 | 43.877 | | | |
| 353.15 | 1087.1 | 36.904 | | | |
| 358.15 | 1083.6 | 31.325 | | | |
| 363.15 | 1080.1 | 26.824 | | | |
| 368.15 | 1076.6 | 23.156 | | | |
| 373.15 | 1073.1 | 20.141 | | | |

$u(T)$ = ± 0.02 K; $u(\rho)$ = ± 0.5 kg·m$^3$ (Eq. 2.90); $u(\eta)$ = 1% (Eq. 2.90); $u(\sigma)$ = 1.5% (Eq. 4.15); $u(\Lambda)$ = 1.5% (Eq. 4.15).

**Table B.40.** Experimental values for density, viscosity, electrical conductivity, and molar conductivity for [$^{1}C_{2}^{3}C_{1}$im][FAP].

| SVM 3001 | | | ILDEM | | |
|---|---|---|---|---|---|
| $\frac{T}{K}$ | $\frac{\rho}{\text{kg·m}^{-3}}$ | $\frac{10^{3}\eta}{\text{Pa·s}}$ | $\frac{T}{K}$ | $\frac{\sigma}{\text{S·m}^{-1}}$ | $\frac{10^{4}\Lambda}{\text{S·m}^{2}\text{·mol}^{-1}}$ |
| 273.15 | 1738.3 | 216.43 | 283.73 | 0.2950 | 0.9416 |
| 278.15 | 1732.3 | 160.51 | 288.57 | 0.3701 | 1.1848 |
| 283.15 | 1726.3 | 122.13 | 293.44 | 0.4554 | 1.4623 |
| 288.15 | 1720.3 | 94.754 | 298.32 | 0.5514 | 1.7760 |
| 293.15 | 1714.4 | 74.852 | 303.19 | 0.6570 | 2.1225 |
| 298.15 | 1708.5 | 60.066 | 308.07 | 0.7731 | 2.5051 |
| 303.15 | 1702.5 | 48.987 | 312.95 | 0.8991 | 2.9222 |
| 308.15 | 1696.6 | 40.499 | 317.83 | 1.0346 | 3.3727 |
| 313.15 | 1690.8 | 33.896 | 322.71 | 1.1795 | 3.8567 |
| 318.15 | 1685.0 | 28.686 | 327.59 | 1.3330 | 4.3718 |
| 323.15 | 1679.1 | 24.522 | 332.46 | 1.4951 | 4.9181 |
| 328.15 | 1673.3 | 21.157 | | | |
| 333.15 | 1667.5 | 18.405 | | | |
| 338.15 | 1661.7 | 16.137 | | | |
| 343.15 | 1655.9 | 14.248 | | | |
| 348.15 | 1650.2 | 12.663 | | | |
| 353.15 | 1644.4 | 11.322 | | | |
| 358.15 | 1638.7 | 10.181 | | | |
| 363.15 | 1632.9 | 9.2025 | | | |
| 368.15 | 1627.2 | 8.3605 | | | |
| 373.15 | 1621.5 | 7.6316 | | | |

$u(T)$ = ± 0.02 K; $u(\rho)$ = ± 0.5 kg·m$^{3}$ (Eq. 2.90); $u(\eta)$ = 1% (Eq. 2.90); $u(\sigma)$ = 1.5% (Eq. 4.15); $u(\Lambda)$ = 1.5% (Eq. 4.15).

**Table B.41.** Experimental values for density, viscosity, electrical conductivity, and molar conductivity for [$^{1}C_{4}{}^{3}C_{1}$im][FAP].

| SVM 3001 | | | ILDEM | | |
|---|---|---|---|---|---|
| $\frac{T}{K}$ | $\frac{\rho}{\text{kg·m}^{-3}}$ | $\frac{10^{3}\eta}{\text{Pa·s}}$ | $\frac{T}{K}$ | $\frac{\sigma}{\text{S·m}^{-1}}$ | $\frac{10^{4}\Lambda}{\text{S·m}^{2}\text{·mol}^{-1}}$ |
| 278.15 | 1642.9 | 222.24 | 283.74 | 0.1454 | 0.5142 |
| 283.15 | 1637.2 | 161.89 | 288.59 | 0.1890 | 0.6704 |
| 288.15 | 1631.5 | 121.05 | 293.46 | 0.2403 | 0.8550 |
| 293.15 | 1625.9 | 92.631 | 298.33 | 0.2999 | 1.0703 |
| 298.15 | 1620.2 | 72.363 | 303.21 | 0.3680 | 1.3173 |
| 303.15 | 1614.6 | 57.583 | 308.10 | 0.4446 | 1.5964 |
| 308.15 | 1609.0 | 46.583 | 312.99 | 0.5297 | 1.9077 |
| 313.15 | 1603.4 | 38.227 | 317.87 | 0.6225 | 2.2487 |
| 318.15 | 1597.8 | 31.802 | 322.74 | 0.7233 | 2.6208 |
| 323.15 | 1592.3 | 26.772 | 327.62 | 0.8320 | 3.0238 |
| 328.15 | 1586.7 | 22.782 | 332.55 | 0.9485 | 3.4578 |
| 333.15 | 1581.2 | 19.576 | | | |
| 338.15 | 1575.7 | 16.971 | | | |
| 343.15 | 1570.2 | 14.832 | | | |
| 348.15 | 1564.7 | 13.060 | | | |
| 353.15 | 1559.3 | 11.581 | | | |
| 358.15 | 1553.8 | 10.335 | | | |
| 363.15 | 1548.4 | 9.2774 | | | |
| 368.15 | 1542.9 | 8.3745 | | | |
| 373.15 | 1537.5 | 7.6008 | | | |

$u(T)$ = ± 0.02 K; $u(\rho)$ = ± 0.5 kg·m$^{3}$ (Eq. 2.90); $u(\eta)$ = 1% (Eq. 2.90); $u(\sigma)$ = 1.5% (Eq. 4.15); $u(\Lambda)$ = 1.5% (Eq. 4.15).

**Table B.42.** Experimental values for density, viscosity, electrical conductivity, and molar conductivity for [$^{1}C_{6}{}^{3}C_{1}$im][FAP].

| SVM 3001 | | | ILDEM | | |
|---|---|---|---|---|---|
| $\frac{T}{K}$ | $\frac{\rho}{\text{kg·m}^{-3}}$ | $\frac{10^{3}\eta}{\text{Pa·s}}$ | $\frac{T}{K}$ | $\frac{\sigma}{\text{S·m}^{-1}}$ | $\frac{10^{4}\Lambda}{\text{S·m}^{2}\text{·mol}^{-1}}$ |
| 283.15 | 1568.0 | 215.33 | 283.77 | 0.0786 | 0.3042 |
| 288.15 | 1562.5 | 158.35 | 288.60 | 0.1046 | 0.4060 |
| 293.15 | 1557.1 | 119.17 | 293.46 | 0.1361 | 0.5296 |
| 298.15 | 1551.6 | 91.593 | 298.30 | 0.1733 | 0.6767 |
| 303.15 | 1546.2 | 71.761 | 303.17 | 0.2167 | 0.8488 |
| 308.15 | 1540.8 | 57.206 | 308.04 | 0.2664 | 1.0464 |
| 313.15 | 1535.5 | 46.326 | 312.92 | 0.3224 | 1.2703 |
| 318.15 | 1530.1 | 38.045 | 317.79 | 0.3850 | 1.5215 |
| 323.15 | 1524.7 | 31.646 | 322.66 | 0.4541 | 1.8002 |
| 328.15 | 1519.4 | 26.631 | 327.53 | 0.5297 | 2.1063 |
| 333.15 | 1514.1 | 22.648 | 332.39 | 0.6116 | 2.4394 |
| 338.15 | 1508.8 | 19.449 | | | |
| 343.15 | 1503.5 | 16.848 | | | |
| 348.15 | 1498.2 | 14.713 | | | |
| 353.15 | 1493.0 | 12.945 | | | |
| 358.15 | 1487.7 | 11.468 | | | |
| 363.15 | 1482.5 | 10.228 | | | |
| 368.15 | 1477.2 | 9.1761 | | | |
| 373.15 | 1472.0 | 8.2792 | | | |

$u(T)$ = ± 0.02 K; $u(\rho)$ = ± 0.5 kg·m$^{3}$ (Eq. 2.90); $u(\eta)$ = 1% (Eq. 2.90); $u(\sigma)$ = 1.5% (Eq. 4.15); $u(\Lambda)$ = 1.5% (Eq. 4.15).

**Table B.43.** Experimental values for density, viscosity, electrical conductivity, and molar conductivity for [$^1C_4{}^3C_1$im][FSI].

| SVM 3001 | | | ILDEM | | |
|---|---|---|---|---|---|
| $\frac{T}{K}$ | $\frac{\rho}{\text{kg·m}^{-3}}$ | $\frac{10^3\eta}{\text{Pa·s}}$ | $\frac{T}{K}$ | $\frac{\sigma}{\text{S·m}^{-1}}$ | $\frac{10^4\Lambda}{\text{S·m}^2\text{·mol}^{-1}}$ |
| 273.15 | 1379.0 | 97.728 | 283.65 | 0.4735 | 1.1040 |
| 278.15 | 1374.5 | 75.791 | 288.53 | 0.5790 | 1.3542 |
| 283.15 | 1370.1 | 59.948 | 293.41 | 0.6972 | 1.6356 |
| 288.15 | 1365.8 | 48.272 | 298.31 | 0.8281 | 1.9487 |
| 293.15 | 1361.4 | 39.496 | 303.21 | 0.9717 | 2.2939 |
| 298.15 | 1357.1 | 32.780 | 308.12 | 1.1278 | 2.6706 |
| 303.15 | 1352.8 | 27.557 | 313.03 | 1.2961 | 3.0787 |
| 308.15 | 1348.5 | 23.433 | 317.93 | 1.4763 | 3.5177 |
| 313.15 | 1344.3 | 20.133 | 322.82 | 1.6674 | 3.9852 |
| 318.15 | 1340.0 | 17.461 | 327.73 | 1.8696 | 4.4823 |
| 323.15 | 1335.8 | 15.272 | 332.65 | 2.0825 | 5.0084 |
| 328.15 | 1331.6 | 13.461 | | | |
| 333.15 | 1327.5 | 11.950 | | | |
| 338.15 | 1323.3 | 10.678 | | | |
| 343.15 | 1319.2 | 9.5999 | | | |
| 348.15 | 1315.1 | 8.6784 | | | |
| 353.15 | 1311.0 | 7.8858 | | | |
| 358.15 | 1306.9 | 7.2001 | | | |
| 363.15 | 1302.8 | 6.6038 | | | |
| 368.15 | 1298.7 | 6.0825 | | | |
| 373.15 | 1294.6 | 5.6253 | | | |

$u(T)$ = ± 0.02 K; $u(\rho)$ = ± 0.5 kg·m$^3$ (Eq. 2.90); $u(\eta)$ = 1% (Eq. 2.90); $u(\sigma)$ = 1.5% (Eq. 4.15); $u(\Lambda)$ = 1.5% (Eq. 4.15).

**Table B.44.** Experimental values for density, viscosity, electrical conductivity, and molar conductivity for [$^1C_4{}^3C_1$im][BETI].

| SVM 3001 | | | ILDEM | | |
|---|---|---|---|---|---|
| $\frac{T}{K}$ | $\frac{\rho}{\text{kg·m}^{-3}}$ | $\frac{10^3\eta}{\text{Pa·s}}$ | $\frac{T}{K}$ | $\frac{\sigma}{\text{S·m}^{-1}}$ | $\frac{10^4\Lambda}{\text{S·m}^2\text{·mol}^{-1}}$ |
| 273.15 | 1540.8 | 580.86 | 283.68 | 0.0646 | 0.2168 |
| 278.15 | 1535.5 | 400.12 | 288.52 | 0.0866 | 0.2915 |
| 283.15 | 1530.2 | 283.46 | 293.38 | 0.1137 | 0.3838 |
| 288.15 | 1524.9 | 206.04 | 298.24 | 0.1464 | 0.4957 |
| 293.15 | 1519.7 | 153.30 | 303.12 | 0.1850 | 0.6282 |
| 298.15 | 1514.5 | 116.47 | 308.00 | 0.2299 | 0.7829 |
| 303.15 | 1509.3 | 90.205 | 312.91 | 0.2815 | 0.9615 |
| 308.15 | 1504.1 | 71.091 | 317.80 | 0.3399 | 1.1644 |
| 313.15 | 1498.9 | 56.921 | 322.68 | 0.4052 | 1.3922 |
| 318.15 | 1493.7 | 46.238 | 327.56 | 0.4776 | 1.6457 |
| 323.15 | 1488.5 | 38.058 | 332.44 | 0.5571 | 1.9253 |
| 328.15 | 1483.4 | 31.708 | | | |
| 333.15 | 1478.2 | 26.708 | | | |
| 338.15 | 1473.1 | 22.729 | | | |
| 343.15 | 1468.0 | 19.521 | | | |
| 348.15 | 1462.9 | 16.912 | | | |
| 353.15 | 1457.8 | 14.768 | | | |
| 358.15 | 1452.7 | 12.991 | | | |
| 363.15 | 1447.6 | 11.509 | | | |
| 368.15 | 1442.6 | 10.262 | | | |
| 373.15 | 1437.5 | 9.2064 | | | |

$u(T)$ = ± 0.02 K; $u(\rho)$ = ± 0.5 kg·m$^3$ (Eq. 2.90); $u(\eta)$ = 1% (Eq. 2.90); $u(\sigma)$ = 1.5% (Eq. 4.15); $u(\Lambda)$ = 1.5% (Eq. 4.15).

**Table B.45.** Experimental values for density, viscosity, electrical conductivity, and molar conductivity for [$^{1}C_{4}{}^{3}C_{1}$im][Ac].

| SVM 3001 | | | ILDEM | | |
|---|---|---|---|---|---|
| $\frac{T}{K}$ | $\frac{\rho}{\text{kg·m}^{-3}}$ | $\frac{10^{3}\eta}{\text{Pa·s}}$ | $\frac{T}{K}$ | $\frac{\sigma}{\text{S·m}^{-1}}$ | $\frac{10^{4}\Lambda}{\text{S·m}^{2}\text{·mol}^{-1}}$ |
| 293.15 | 1055.8 | 884.46 | 283.45 | 0.0146 | 0.0273 |
| 298.15 | 1052.8 | 574.07 | 288.38 | 0.0233 | 0.0437 |
| 303.15 | 1049.7 | 386.47 | 293.32 | 0.0357 | 0.0672 |
| 308.15 | 1046.7 | 268.91 | 298.27 | 0.0527 | 0.0995 |
| 313.15 | 1043.7 | 192.67 | 303.22 | 0.0753 | 0.1425 |
| 318.15 | 1040.8 | 141.68 | 308.19 | 0.1045 | 0.1984 |
| 323.15 | 1037.8 | 106.65 | 313.15 | 0.1413 | 0.2690 |
| 328.15 | 1034.8 | 81.985 | 318.11 | 0.1878 | 0.3585 |
| 333.15 | 1031.9 | 64.215 | 323.06 | 0.2448 | 0.4687 |
| 338.15 | 1029.0 | 51.166 | 328.01 | 0.3125 | 0.6000 |
| 343.15 | 1026.1 | 41.404 | 332.93 | 0.3899 | 0.7507 |
| 348.15 | 1023.2 | 33.979 | | | |
| 353.15 | 1020.3 | 28.244 | | | |
| 358.15 | 1017.4 | 23.755 | | | |
| 363.15 | 1014.5 | 20.194 | | | |
| 368.15 | 1011.6 | 17.338 | | | |
| 373.15 | 1008.7 | 15.027 | | | |

$u(T)$ = ± 0.02 K; $u(\rho)$ = ± 0.5 kg·m$^{3}$ (Eq. 2.90); $u(\eta)$ = 1% (Eq. 2.90); $u(\sigma)$ = 1.5% (Eq. 4.15); $u(\Lambda)$ = 1.5% (Eq. 4.15).

**Table B.46.** Experimental values for density, viscosity, electrical conductivity, and molar conductivity for [$^1C_4{}^3C_1$im][TFA].

| SVM 3001 | | | ILDEM | | |
|---|---|---|---|---|---|
| $\frac{T}{K}$ | $\frac{\rho}{\text{kg·m}^{-3}}$ | $\frac{10^3\eta}{\text{Pa·s}}$ | $\frac{T}{K}$ | $\frac{\sigma}{\text{S·m}^{-1}}$ | $\frac{10^4\Lambda}{\text{S·m}^2\text{·mol}^{-1}}$ |
| 283.15 | 1224.4 | 181.32 | 283.69 | 0.1451 | 0.2433 |
| 288.15 | 1220.5 | 133.55 | 288.58 | 0.1921 | 0.3231 |
| 293.15 | 1216.7 | 100.76 | 293.46 | 0.2486 | 0.4194 |
| 298.15 | 1212.9 | 77.674 | 298.35 | 0.3153 | 0.5336 |
| 303.15 | 1209.2 | 61.052 | 303.25 | 0.3928 | 0.6668 |
| 308.15 | 1205.4 | 48.827 | 308.15 | 0.4814 | 0.8198 |
| 313.15 | 1201.7 | 39.667 | 313.05 | 0.5817 | 0.9936 |
| 318.15 | 1197.9 | 32.681 | 317.96 | 0.6939 | 1.1889 |
| 323.15 | 1194.2 | 27.271 | 322.84 | 0.8181 | 1.4059 |
| 328.15 | 1190.5 | 23.021 | 327.74 | 0.9548 | 1.6459 |
| 333.15 | 1186.9 | 19.639 | 332.64 | 1.1038 | 1.9084 |
| 338.15 | 1183.2 | 16.915 | | | |
| 343.15 | 1179.6 | 14.698 | | | |
| 348.15 | 1175.9 | 12.875 | | | |
| 353.15 | 1172.3 | 11.363 | | | |
| 358.15 | 1168.7 | 10.098 | | | |
| 363.15 | 1165.1 | 9.0331 | | | |
| 368.15 | 1161.5 | 8.1288 | | | |
| 373.15 | 1157.9 | 7.3515 | | | |

$u(T)$ = ± 0.02 K; $u(\rho)$ = ± 0.5 kg·m$^3$ (Eq. 2.90); $u(\eta)$ = 1% (Eq. 2.90); $u(\sigma)$ = 1.5% (Eq. 4.15); $u(\Lambda)$ = 1.5% (Eq. 4.15).

**Table B.47.** Experimental values for density, viscosity, electrical conductivity, and molar conductivity for [$^1C_4{}^3C_1$im][DCA].

| SVM 3001 | | | ILDEM | | |
|---|---|---|---|---|---|
| $\frac{T}{K}$ | $\frac{\rho}{\text{kg·m}^{-3}}$ | $\frac{10^3\eta}{\text{Pa·s}}$ | $\frac{T}{K}$ | $\frac{\sigma}{\text{S·m}^{-1}}$ | $\frac{10^4\Lambda}{\text{S·m}^2\text{·mol}^{-1}}$ |
| 273.15 | 1077.1 | 103.00 | 283.68 | 0.6028 | 1.1562 |
| 278.15 | 1073.8 | 77.076 | 288.58 | 0.7540 | 1.4505 |
| 283.15 | 1070.5 | 59.174 | 293.48 | 0.9254 | 1.7853 |
| 288.15 | 1067.3 | 46.504 | 298.37 | 1.1169 | 2.1612 |
| 293.15 | 1064.0 | 37.278 | 303.27 | 1.3289 | 2.5789 |
| 298.15 | 1060.9 | 30.411 | 308.18 | 1.5613 | 3.0390 |
| 303.15 | 1057.7 | 25.197 | 313.09 | 1.8138 | 3.5407 |
| 308.15 | 1054.5 | 21.163 | 318.00 | 2.0862 | 4.0843 |
| 313.15 | 1051.4 | 17.996 | 322.89 | 2.3782 | 4.6696 |
| 318.15 | 1048.3 | 15.470 | 327.79 | 2.6885 | 5.2941 |
| 323.15 | 1045.2 | 13.430 | 332.70 | 3.0156 | 5.9555 |
| 328.15 | 1042.1 | 11.764 | | | |
| 333.15 | 1039.0 | 10.388 | | | |
| 338.15 | 1036.0 | 9.2423 | | | |
| 343.15 | 1033.0 | 8.2785 | | | |
| 348.15 | 1030.0 | 7.4612 | | | |
| 353.15 | 1026.9 | 6.7633 | | | |
| 358.15 | 1024.0 | 6.1630 | | | |
| 363.15 | 1021.0 | 5.6437 | | | |
| 368.15 | 1018.0 | 5.1921 | | | |
| 373.15 | 1015.0 | 4.7982 | | | |

$u(T)$ = ± 0.02 K; $u(\rho)$ = ± 0.5 kg·m$^3$ (Eq. 2.90); $u(\eta)$ = 1% (Eq. 2.90); $u(\sigma)$ = 1.5% (Eq. 4.15); $u(\Lambda)$ = 1.5% (Eq. 4.15).

**Table B.48.** Experimental values for density, viscosity, electrical conductivity, and molar conductivity for [$^1$C$_3$py][NTf$_2$].

| SVM 3001 | | | ILDEM | | |
|---|---|---|---|---|---|
| $\frac{T}{K}$ | $\frac{\rho}{\text{kg·m}^{-3}}$ | $\frac{10^3\eta}{\text{Pa·s}}$ | $\frac{T}{K}$ | $\frac{\sigma}{\text{S·m}^{-1}}$ | $\frac{10^4\Lambda}{\text{S·m}^2\text{·mol}^{-1}}$ |
| 318.15 | 1463.6 | 24.805 | 303.27 | 0.5416 | 1.4745 |
| 323.15 | 1458.8 | 21.189 | 308.18 | 0.6485 | 1.7739 |
| 328.15 | 1454.1 | 18.285 | 313.09 | 0.7687 | 2.1062 |
| 333.15 | 1449.5 | 15.923 | 318.00 | 0.8984 | 2.4695 |
| 338.15 | 1444.8 | 13.982 | 322.89 | 1.0379 | 2.8621 |
| 343.15 | 1440.2 | 12.369 | 327.79 | 1.1875 | 3.2852 |
| 348.15 | 1435.6 | 11.020 | 332.70 | 1.3465 | 3.7370 |
| 353.15 | 1431.0 | 9.8818 | | | |
| 358.15 | 1426.4 | 8.9129 | | | |
| 363.15 | 1421.8 | 8.0830 | | | |
| 368.15 | 1417.2 | 7.3683 | | | |
| 373.15 | 1412.7 | 6.7497 | | | |

$u(T)$ = ± 0.02 K; $u(\rho)$ = ± 0.5 kg·m$^3$ (Eq. 2.90); $u(\eta)$ = 1% (Eq. 2.90); $u(\sigma)$ = 1.5% (Eq. 4.15); $u(\Lambda)$ = 1.5% (Eq. 4.15).

**Table B.49.** Experimental values for density, viscosity, electrical conductivity, and molar conductivity for [$^1$C$_4$py][NTf$_2$].

| SVM 3001 | | | ILDEM | | |
|---|---|---|---|---|---|
| $\frac{T}{K}$ | $\frac{\rho}{\text{kg·m}^{-3}}$ | $\frac{10^3\eta}{\text{Pa·s}}$ | $\frac{T}{K}$ | $\frac{\sigma}{\text{S·m}^{-1}}$ | $\frac{10^4\Lambda}{\text{S·m}^2\text{·mol}^{-1}}$ |
| 293.15 | 1453.3 | 76.449 | 293.23 | 0.2637 | 0.7555 |
| 298.15 | 1448.7 | 60.459 | 298.17 | 0.3294 | 0.9468 |
| 303.15 | 1444.0 | 48.645 | 303.11 | 0.4043 | 1.1658 |
| 308.15 | 1439.4 | 39.735 | 308.05 | 0.4886 | 1.4133 |
| 313.15 | 1434.7 | 32.923 | 312.99 | 0.5824 | 1.6900 |
| 318.15 | 1430.1 | 27.613 | 317.93 | 0.6854 | 1.9953 |
| 323.15 | 1425.5 | 23.429 | 322.87 | 0.7975 | 2.3290 |
| 328.15 | 1420.9 | 20.087 | 327.80 | 0.9184 | 2.6906 |
| 333.15 | 1416.3 | 17.382 | 332.72 | 1.0478 | 3.0794 |
| 338.15 | 1411.8 | 15.171 | | | |
| 343.15 | 1407.3 | 13.346 | | | |
| 348.15 | 1402.8 | 11.827 | | | |
| 353.15 | 1398.2 | 10.552 | | | |
| 358.15 | 1393.8 | 9.4715 | | | |
| 363.15 | 1389.3 | 8.5512 | | | |
| 368.15 | 1384.8 | 7.7617 | | | |
| 373.15 | 1380.3 | 7.0814 | | | |

$u(T)$ = ± 0.02 K; $u(\rho)$ = ± 0.5 kg·m$^3$ (Eq. 2.90); $u(\eta)$ = 1% (Eq. 2.90); $u(\sigma)$ = 1.5% (Eq. 4.15); $u(\Lambda)$ = 1.5% (Eq. 4.15).

**Table B.50.** Experimental values for density, viscosity, electrical conductivity, and molar conductivity for [$^1C_5$py][$NTf_2$].

| SVM 3001 | | | ILDEM | | |
|---|---|---|---|---|---|
| $\frac{T}{K}$ | $\frac{\rho}{\text{kg·m}^{-3}}$ | $\frac{10^3\eta}{\text{Pa·s}}$ | $\frac{T}{K}$ | $\frac{\sigma}{\text{S·m}^{-1}}$ | $\frac{10^4\Lambda}{\text{S·m}^2\text{·mol}^{-1}}$ |
| 293.15 | 1418.7 | 94.340 | 293.11 | 0.1817 | 0.5513 |
| 298.15 | 1414.1 | 73.683 | 298.09 | 0.2308 | 0.7025 |
| 303.15 | 1409.5 | 58.577 | 303.08 | 0.2879 | 0.8791 |
| 308.15 | 1404.9 | 47.320 | 308.07 | 0.3531 | 1.0817 |
| 313.15 | 1400.4 | 38.787 | 313.05 | 0.4267 | 1.3114 |
| 318.15 | 1395.9 | 32.215 | 318.04 | 0.5086 | 1.5681 |
| 323.15 | 1391.4 | 27.080 | 323.03 | 0.5986 | 1.8516 |
| 328.15 | 1386.9 | 23.013 | 328.01 | 0.6966 | 2.1617 |
| 333.15 | 1382.4 | 19.754 | 332.98 | 0.8028 | 2.4993 |
| 338.15 | 1377.9 | 17.111 | | | |
| 343.15 | 1373.5 | 14.946 | | | |
| 348.15 | 1369.1 | 13.156 | | | |
| 353.15 | 1364.4 | 11.663 | | | |
| 358.15 | 1360.2 | 10.409 | | | |
| 363.15 | 1355.8 | 9.3457 | | | |
| 368.15 | 1351.4 | 8.4386 | | | |
| 373.15 | 1347.1 | 7.6649 | | | |

$u(T)$ = ± 0.02 K; $u(\rho)$ = ± 0.5 kg·m$^3$ (Eq. 2.90); $u(\eta)$ = 1% (Eq. 2.90); $u(\sigma)$ = 1.5% (Eq. 4.15); $u(\Lambda)$ = 1.5% (Eq. 4.15).

**Table B.51.** Experimental values for density, viscosity, electrical conductivity, and molar conductivity for [$^1C_6$py][$NTf_2$].

| SVM 3001 | | | ILDEM | | |
|---|---|---|---|---|---|
| $\frac{T}{K}$ | $\frac{\rho}{\text{kg·m}^{-3}}$ | $\frac{10^3\eta}{\text{Pa·s}}$ | $\frac{T}{K}$ | $\frac{\sigma}{\text{S·m}^{-1}}$ | $\frac{10^4\Lambda}{\text{S·m}^2\text{·mol}^{-1}}$ |
| 293.15 | 1386.2 | 109.44 | 293.11 | 0.1345 | 0.4307 |
| 298.15 | 1381.8 | 85.029 | 298.09 | 0.1727 | 0.5547 |
| 303.15 | 1377.3 | 67.174 | 303.07 | 0.2174 | 0.7005 |
| 308.15 | 1372.8 | 53.905 | 308.06 | 0.2692 | 0.8702 |
| 313.15 | 1368.3 | 43.895 | 313.05 | 0.3280 | 1.0637 |
| 318.15 | 1359.5 | 36.216 | 318.03 | 0.3940 | 1.2818 |
| 323.15 | 1355.1 | 30.261 | 323.02 | 0.4672 | 1.5249 |
| 328.15 | 1355.1 | 25.567 | 327.99 | 0.5476 | 1.7930 |
| 333.15 | 1350.7 | 21.824 | 332.96 | 0.6352 | 2.0864 |
| 338.15 | 1346.3 | 18.804 | | | |
| 343.15 | 1342.0 | 16.342 | | | |
| 348.15 | 1337.6 | 14.316 | | | |
| 353.15 | 1333.3 | 12.633 | | | |
| 358.15 | 1328.9 | 11.225 | | | |
| 363.15 | 1324.6 | 10.038 | | | |
| 368.15 | 1320.3 | 9.0295 | | | |
| 373.15 | 1316.0 | 8.1675 | | | |

$u(T)$ = ± 0.02 K; $u(\rho)$ = ± 0.5 kg·m$^3$ (Eq. 2.90); $u(\eta)$ = 1% (Eq. 2.90); $u(\sigma)$ = 1.5% (Eq. 4.15); $u(\Lambda)$ = 1.5% (Eq. 4.15).

**Table B.52.** Experimental values for density, viscosity, electrical conductivity, and molar conductivity for [$^1C_7$py][$NTf_2$].

| SVM 3001 | | | ILDEM | | |
|---|---|---|---|---|---|
| $\frac{T}{K}$ | $\frac{\rho}{\text{kg·m}^{-3}}$ | $\frac{10^3\eta}{\text{Pa·s}}$ | $\frac{T}{K}$ | $\frac{\sigma}{\text{S·m}^{-1}}$ | $\frac{10^4\Lambda}{\text{S·m}^2\text{·mol}^{-1}}$ |
| 293.15 | 1358.3 | 127.86 | 293.09 | 0.1013 | 0.3413 |
| 298.15 | 1353.9 | 98.716 | 298.07 | 0.1311 | 0.4431 |
| 303.15 | 1349.5 | 77.497 | 303.06 | 0.1665 | 0.5645 |
| 308.15 | 1345.1 | 61.804 | 308.04 | 0.2079 | 0.7071 |
| 313.15 | 1340.8 | 49.988 | 313.03 | 0.2553 | 0.8711 |
| 318.15 | 1336.4 | 41.013 | 318.01 | 0.3089 | 1.0574 |
| 323.15 | 1332.1 | 34.068 | 322.99 | 0.3689 | 1.2667 |
| 328.15 | 1327.8 | 28.627 | 327.97 | 0.4352 | 1.4991 |
| 333.15 | 1323.5 | 24.309 | 332.93 | 0.5080 | 1.7554 |
| 338.15 | 1319.2 | 20.841 | | | |
| 343.15 | 1314.9 | 18.027 | | | |
| 348.15 | 1310.7 | 15.721 | | | |
| 353.15 | 1306.4 | 13.815 | | | |
| 358.15 | 1302.2 | 12.225 | | | |
| 363.15 | 1297.9 | 10.891 | | | |
| 368.15 | 1293.7 | 9.7624 | | | |
| 373.15 | 1289.5 | 8.8025 | | | |

$u(T)$ = ± 0.02 K; $u(\rho)$ = ± 0.5 kg·m$^3$ (Eq. 2.90); $u(\eta)$ = 1% (Eq. 2.90); $u(\sigma)$ = 1.5% (Eq. 4.15); $u(\Lambda)$ = 1.5% (Eq. 4.15).

**Table B.53.** Experimental values for density, viscosity, electrical conductivity, and molar conductivity for [$^1C_8$py][$NTf_2$].

| SVM 3001 | | | ILDEM | | |
|---|---|---|---|---|---|
| $\frac{T}{K}$ | $\frac{\rho}{\text{kg·m}^{-3}}$ | $\frac{10^3\eta}{\text{Pa·s}}$ | $\frac{T}{K}$ | $\frac{\sigma}{\text{S·m}^{-1}}$ | $\frac{10^4\Lambda}{\text{S·m}^2\text{·mol}^{-1}}$ |
| 298.15 | 1329.3 | 112.91 | 293.08 | 0.0783 | 0.2770 |
| 303.15 | 1325.0 | 88.137 | 298.06 | 0.1022 | 0.3627 |
| 308.15 | 1320.7 | 69.893 | 303.04 | 0.1309 | 0.4661 |
| 313.15 | 1316.4 | 56.236 | 308.03 | 0.1646 | 0.5880 |
| 318.15 | 1312.1 | 45.872 | 313.02 | 0.2036 | 0.7296 |
| 323.15 | 1307.8 | 37.888 | 318.01 | 0.2481 | 0.8919 |
| 328.15 | 1303.5 | 31.671 | 323.00 | 0.2983 | 1.0758 |
| 333.15 | 1299.3 | 26.761 | 327.97 | 0.3541 | 1.2812 |
| 338.15 | 1295.1 | 22.837 | 332.94 | 0.4157 | 1.5089 |
| 343.15 | 1290.9 | 19.667 | | | |
| 348.15 | 1286.7 | 17.082 | | | |
| 353.15 | 1282.5 | 14.950 | | | |
| 358.15 | 1278.3 | 13.182 | | | |
| 363.15 | 1274.1 | 11.701 | | | |
| 368.15 | 1270.0 | 10.454 | | | |
| 373.15 | 1265.8 | 9.3957 | | | |

$u(T)$ = ± 0.02 K; $u(\rho)$ = ± 0.5 kg·m$^3$ (Eq. 2.90); $u(\eta)$ = 1% (Eq. 2.90); $u(\sigma)$ = 1.5% (Eq. 4.15); $u(\Lambda)$ = 1.5% (Eq. 4.15).

**Table B.54.** Experimental values for density, viscosity, electrical conductivity, and molar conductivity for [$^1C_9$py][$NTf_2$].

| SVM 3001 | | | ILDEM | | |
|---|---|---|---|---|---|
| $\frac{T}{K}$ | $\frac{\rho}{\text{kg·m}^{-3}}$ | $\frac{10^3\eta}{\text{Pa·s}}$ | $\frac{T}{K}$ | $\frac{\sigma}{\text{S·m}^{-1}}$ | $\frac{10^4\Lambda}{\text{S·m}^2\text{·mol}^{-1}}$ |
| 293.15 | 1310.2 | 171.26 | 293.10 | 0.0613 | 0.2267 |
| 298.15 | 1305.9 | 130.76 | 298.09 | 0.0806 | 0.2993 |
| 303.15 | 1301.7 | 101.46 | 303.07 | 0.1040 | 0.3874 |
| 308.15 | 1297.4 | 79.955 | 308.05 | 0.1319 | 0.4929 |
| 313.15 | 1293.2 | 63.959 | 313.04 | 0.1642 | 0.6156 |
| 318.15 | 1288.9 | 51.882 | 318.03 | 0.2014 | 0.7576 |
| 323.15 | 1284.7 | 42.634 | 323.02 | 0.2434 | 0.9186 |
| 328.15 | 1280.5 | 35.450 | 327.99 | 0.2906 | 1.1003 |
| 333.15 | 1276.3 | 29.807 | 332.96 | 0.3428 | 1.3025 |
| 338.15 | 1272.2 | 25.325 | | | |
| 343.15 | 1268.0 | 21.715 | | | |
| 348.15 | 1263.9 | 18.783 | | | |
| 353.15 | 1259.8 | 16.377 | | | |
| 358.15 | 1255.6 | 14.386 | | | |
| 363.15 | 1251.5 | 12.725 | | | |
| 368.15 | 1247.4 | 11.330 | | | |
| 373.15 | 1243.3 | 10.151 | | | |

$u(T)$ = ± 0.02 K; $u(\rho)$ = ± 0.5 kg·m$^3$ (Eq. 2.90); $u(\eta)$ = 1% (Eq. 2.90); $u(\sigma)$ = 1.5% (Eq. 4.15); $u(\Lambda)$ = 1.5% (Eq. 4.15).

**Table B.55.** Experimental values for density, viscosity, electrical conductivity, and molar conductivity for [$^1C_3{}^2C_1$py][$NTf_2$].

| SVM 3001 | | | ILDEM | | |
|---|---|---|---|---|---|
| $\frac{T}{K}$ | $\frac{\rho}{\mathrm{kg\cdot m^{-3}}}$ | $\frac{10^3\eta}{\mathrm{Pa\cdot s}}$ | $\frac{T}{K}$ | $\frac{\sigma}{\mathrm{S\cdot m^{-1}}}$ | $\frac{10^4\Lambda}{\mathrm{S\cdot m^2\cdot mol^{-1}}}$ |
| 293.15 | 1469.0 | 108.75 | 293.09 | 0.2151 | 0.6097 |
| 298.15 | 1464.2 | 83.739 | 298.07 | 0.2751 | 0.7822 |
| 303.15 | 1459.5 | 65.806 | 303.05 | 0.3449 | 0.9838 |
| 308.15 | 1454.8 | 52.689 | 308.04 | 0.4247 | 1.2154 |
| 313.15 | 1450.2 | 42.859 | 313.02 | 0.5144 | 1.4768 |
| 318.15 | 1445.5 | 35.377 | 318.01 | 0.6141 | 1.7687 |
| 323.15 | 1440.9 | 29.585 | 322.99 | 0.7236 | 2.0907 |
| 328.15 | 1436.2 | 25.042 | 327.97 | 0.5429 | 2.4432 |
| 333.15 | 1431.6 | 21.419 | 332.94 | 0.9717 | 2.8256 |
| 338.15 | 1427.1 | 18.499 | | | |
| 343.15 | 1422.5 | 16.118 | | | |
| 348.15 | 1417.9 | 14.158 | | | |
| 353.15 | 1413.4 | 12.528 | | | |
| 358.15 | 1408.9 | 11.163 | | | |
| 363.15 | 1404.3 | 10.010 | | | |
| 368.15 | 1399.8 | 9.0290 | | | |
| 373.15 | 1395.3 | 8.1894 | | | |

$u(T)$ = ± 0.02 K; $u(\rho)$ = ± 0.5 kg·m$^3$ (Eq. 2.90); $u(\eta)$ = 1% (Eq. 2.90); $u(\sigma)$ = 1.5% (Eq. 4.15); $u(\Lambda)$ = 1.5% (Eq. 4.15).

**Table B.56.** Experimental values for density, viscosity, electrical conductivity, and molar conductivity for [$^{1}C_{3}{}^{3}C_{1}$py][$NTf_2$].

| SVM 3001 | | | ILDEM | | |
|---|---|---|---|---|---|
| $\frac{T}{K}$ | $\frac{\rho}{\mathrm{kg{\cdot}m^{-3}}}$ | $\frac{10^{3}\eta}{\mathrm{Pa{\cdot}s}}$ | $\frac{T}{K}$ | $\frac{\sigma}{\mathrm{S{\cdot}m^{-1}}}$ | $\frac{10^{4}\Lambda}{\mathrm{S{\cdot}m^{2}{\cdot}mol^{-1}}}$ |
| 293.15 | 1453.2 | 69.691 | 293.09 | 0.3171 | 0.9114 |
| 298.15 | 1448.5 | 55.057 | 298.06 | 0.3966 | 1.1400 |
| 303.15 | 1443.7 | 44.283 | 303.03 | 0.4857 | 1.4006 |
| 308.15 | 1439.0 | 36.191 | 308.03 | 0.5855 | 1.6939 |
| 313.15 | 1434.4 | 30.009 | 313.02 | 0.6959 | 2.0199 |
| 318.15 | 1429.7 | 25.203 | 318.01 | 0.8165 | 2.3776 |
| 323.15 | 1425.0 | 21.414 | 322.99 | 0.9470 | 2.7666 |
| 328.15 | 1420.4 | 18.389 | 327.97 | 1.0874 | 3.1871 |
| 333.15 | 1415.8 | 15.939 | 332.94 | 1.2372 | 3.6379 |
| 338.15 | 1411.2 | 13.936 | | | |
| 343.15 | 1046.6 | 12.281 | | | |
| 348.15 | 1402.1 | 10.911 | | | |
| 353.15 | 1397.5 | 9.7508 | | | |
| 358.15 | 1393.0 | 8.7674 | | | |
| 363.15 | 1388.5 | 7.9282 | | | |
| 368.15 | 1383.9 | 7.2080 | | | |
| 373.15 | 1379.4 | 6.5853 | | | |

$u(T)$ = ± 0.02 K; $u(\rho)$ = ± 0.5 kg·m$^3$ (Eq. 2.90); $u(\eta)$ = 1% (Eq. 2.90); $u(\sigma)$ = 1.5% (Eq. 4.15); $u(\Lambda)$ = 1.5% (Eq. 4.15).

**Table B.57.** Experimental values for density, viscosity, electrical conductivity, and molar conductivity for [$^1$C$_4$py][OTf].

| SVM 3001 | | | ILDEM | | |
|---|---|---|---|---|---|
| $\frac{T}{K}$ | $\frac{\rho}{\text{kg·m}^{-3}}$ | $\frac{10^3\eta}{\text{Pa·s}}$ | $\frac{T}{K}$ | $\frac{\sigma}{\text{S·m}^{-1}}$ | $\frac{10^4\Lambda}{\text{S·m}^2\text{·mol}^{-1}}$ |
| 298.15 | 1294..2 | 132.59 | 298.15 | 0.2010 | 0.4431 |
| 303.15 | 1290.3 | 101.46 | 303.11 | 0.2557 | 0.5653 |
| 308.15 | 1286.5 | 79.643 | 308.12 | 0.3198 | 0.7092 |
| 313.15 | 1282.6 | 63.538 | 313.13 | 0.3936 | 0.8755 |
| 318.15 | 1278.8 | 51.478 | 318.14 | 0.4776 | 1.0654 |
| 323.15 | 1275.0 | 42.278 | 323.14 | 0.5719 | 1.2795 |
| 328.15 | 1271.2 | 35.158 | 328.13 | 0.6767 | 1.5186 |
| 333.15 | 1267.5 | 29.517 | 333.11 | 0.7922 | 1.7830 |
| 338.15 | 1263.7 | 25.133 | | | |
| 343.15 | 1260.0 | 21.567 | | | |
| 348.15 | 1256.2 | 18.670 | | | |
| 353.15 | 1252.5 | 16.295 | | | |
| 358.15 | 1248.8 | 14.329 | | | |
| 363.15 | 1245.1 | 12.689 | | | |
| 368.15 | 1241.4 | 11.311 | | | |
| 373.15 | 1237.7 | 10.145 | | | |

$u(T)$ = ± 0.02 K; $u(\rho)$ = ± 0.5 kg·m$^3$ (Eq. 2.90); $u(\eta)$ = 1% (Eq. 2.90); $u(\sigma)$ = 1.5% (Eq. 4.15); $u(\Lambda)$ = 1.5% (Eq. 4.15).

**Table B.58.** Experimental values for density, viscosity, electrical conductivity, and molar conductivity for [$^1C_3{}^1C_1$pyr][$NTf_2$].

| SVM 3001 | | | ILDEM | | |
|---|---|---|---|---|---|
| $\frac{T}{K}$ | $\frac{\rho}{kg \cdot m^{-3}}$ | $\frac{10^3 \eta}{Pa \cdot s}$ | $\frac{T}{K}$ | $\frac{\sigma}{S \cdot m^{-1}}$ | $\frac{10^4 \Lambda}{S \cdot m^2 \cdot mol^{-1}}$ |
| 283.15 | 1441.6 | 125.50 | 283.63 | 0.2114 | 0.5991 |
| 288.15 | 1437.0 | 96.870 | 288.51 | 0.2685 | 0.7632 |
| 293.15 | 1432.5 | 76.179 | 293.39 | 0.3343 | 0.9532 |
| 298.15 | 1428.0 | 60.998 | 298.27 | 0.4092 | 1.1703 |
| 303.15 | 1423.5 | 49.633 | 303.17 | 0.4934 | 1.4155 |
| 308.15 | 1419.0 | 40.970 | 308.05 | 0.5868 | 1.6886 |
| 313.15 | 1414.5 | 34.251 | 312.94 | 0.6893 | 1.9897 |
| 318.15 | 1410.1 | 28.971 | 317.91 | 0.8009 | 2.3191 |
| 323.15 | 1405.7 | 24.762 | 322.71 | 0.9214 | 2.6761 |
| 328.15 | 1401.3 | 21.368 | 327.60 | 1.0504 | 3.0602 |
| 333.15 | 1396.9 | 18.597 | 332.49 | 1.1180 | 3.4717 |
| 338.15 | 1392.5 | 16.316 | | | |
| 343.15 | 1388.2 | 14.419 | | | |
| 348.15 | 1383.8 | 12.826 | | | |
| 353.15 | 1379.5 | 11.481 | | | |
| 358.15 | 1375.2 | 10.337 | | | |
| 363.15 | 1370.9 | 9.3568 | | | |
| 368.15 | 1366.6 | 8.5124 | | | |
| 373.15 | 1362.3 | 7.7822 | | | |

$u(T)$ = ± 0.02 K; $u(\rho)$ = ± 0.5 kg·m$^3$ (Eq. 2.90); $u(\eta)$ = 1% (Eq. 2.90); $u(\sigma)$ = 1.5% (Eq. 4.15); $u(\Lambda)$ = 1.5% (Eq. 4.15).

**Table B.59.** Experimental values for density, viscosity, electrical conductivity, and molar conductivity for [$^1C_4{}^1C_1$pyr][$NTf_2$].

| SVM 3001 | | | ILDEM | | |
|---|---|---|---|---|---|
| $\frac{T}{K}$ | $\frac{\rho}{\text{kg·m}^{-3}}$ | $\frac{10^3\eta}{\text{Pa·s}}$ | $\frac{T}{K}$ | $\frac{\sigma}{\text{S·m}^{-1}}$ | $\frac{10^4\Lambda}{\text{S·m}^2\text{·mol}^{-1}}$ |
| 273.15 | 1416.3 | 321.28 | 283.62 | 0.1374 | 0.4125 |
| 278.15 | 1411.8 | 230.42 | 288.49 | 0.1779 | 0.5358 |
| 283.15 | 1407.3 | 169.75 | 293.36 | 0.2256 | 0.6816 |
| 288.15 | 1402.8 | 128.23 | 298.26 | 0.2810 | 0.8516 |
| 293.15 | 1398.4 | 98.933 | 303.14 | 0.3442 | 1.0463 |
| 298.15 | 1394.0 | 77.839 | 308.04 | 0.4156 | 1.2673 |
| 303.15 | 1389.6 | 62.269 | 312.93 | 0.4950 | 1.5141 |
| 308.15 | 1385.2 | 50.629 | 317.83 | 0.5825 | 1.7872 |
| 313.15 | 1380.8 | 41.721 | 322.72 | 0.6781 | 2.0870 |
| 318.15 | 1376.5 | 34.833 | 327.60 | 0.7816 | 2.4129 |
| 323.15 | 1372.1 | 29.407 | 332.48 | 0.8930 | 2.7653 |
| 328.15 | 1367.8 | 25.084 | | | |
| 333.15 | 1363.5 | 21.600 | | | |
| 338.15 | 1359.3 | 18.759 | | | |
| 343.15 | 1355.0 | 16.426 | | | |
| 348.15 | 1350.7 | 14.486 | | | |
| 353.15 | 1346.5 | 12.861 | | | |
| 358.15 | 1342.2 | 11.491 | | | |
| 363.15 | 1338.0 | 10.328 | | | |
| 368.15 | 1333.7 | 9.3326 | | | |
| 373.15 | 1329.5 | 8.4768 | | | |

$u(T)$ = ± 0.02 K; $u(\rho)$ = ± 0.5 kg·m$^3$ (Eq. 2.90); $u(\eta)$ = 1% (Eq. 2.90); $u(\sigma)$ = 1.5% (Eq. 4.15); $u(\Lambda)$ = 1.5% (Eq. 4.15).

**Table B.60.** Experimental values for density, viscosity, electrical conductivity, and molar conductivity for [$^1C_6{}^1C_1$pyr][$NTf_2$].

| SVM 3001 | | | ILDEM | | |
|---|---|---|---|---|---|
| $\frac{T}{K}$ | $\frac{\rho}{\text{kg·m}^{-3}}$ | $\frac{10^3\eta}{\text{Pa·s}}$ | $\frac{T}{K}$ | $\frac{\sigma}{\text{S·m}^{-1}}$ | $\frac{10^4\Lambda}{\text{S·m}^2\text{·mol}^{-1}}$ |
| 278.15 | 1353.5 | 356.74 | 283.69 | 0.0664 | 0.2217 |
| 283.15 | 1349.2 | 257.46 | 288.56 | 0.0882 | 0.2953 |
| 288.15 | 1344.9 | 190.08 | 293.43 | 0.1146 | 0.3851 |
| 293.15 | 1340.7 | 143.51 | 298.29 | 0.1460 | 0.4922 |
| 298.15 | 1336.4 | 110.56 | 303.18 | 0.1830 | 0.6188 |
| 303.15 | 1332.4 | 86.748 | 308.06 | 0.2257 | 0.7656 |
| 308.15 | 1328.0 | 69.199 | 312.96 | 0.2742 | 0.9330 |
| 313.15 | 1323.8 | 56.029 | 317.85 | 0.3288 | 1.1223 |
| 318.15 | 1319.6 | 45.987 | 322.74 | 0.3897 | 1.3343 |
| 323.15 | 1315.4 | 38.213 | 327.63 | 0.4568 | 1.5689 |
| 328.15 | 1311.2 | 32.113 | 332.50 | 0.5302 | 1.8266 |
| 333.15 | 1307.1 | 27.266 | | | |
| 338.15 | 1303.0 | 23.371 | | | |
| 343.15 | 1298.9 | 20.206 | | | |
| 348.15 | 1294.7 | 17.612 | | | |
| 353.15 | 1290.6 | 15.464 | | | |
| 358.15 | 1286.6 | 13.672 | | | |
| 363.15 | 1282.5 | 12.166 | | | |
| 368.15 | 1278.4 | 10.892 | | | |
| 373.15 | 1274.3 | 9.8086 | | | |

$u(T)$ = ± 0.02 K; $u(\rho)$ = ± 0.5 kg·m$^3$ (Eq. 2.90); $u(\eta)$ = 1% (Eq. 2.90); $u(\sigma)$ = 1.5% (Eq. 4.15); $u(\Lambda)$ = 1.5% (Eq. 4.15).

**Table B.61.** Experimental values for density, viscosity, electrical conductivity, and molar conductivity for [$^{1}C_{8}{}^{1}C_{1}$pyr][$NTf_2$].

| SVM 3001 | | | ILDEM | | |
|---|---|---|---|---|---|
| $\frac{T}{K}$ | $\frac{\rho}{\mathrm{kg\cdot m^{-3}}}$ | $\frac{10^3\eta}{\mathrm{Pa\cdot s}}$ | $\frac{T}{K}$ | $\frac{\sigma}{\mathrm{S\cdot m^{-1}}}$ | $\frac{10^4\Lambda}{\mathrm{S\cdot m^2\cdot mol^{-1}}}$ |
| 283.15 | 1301.9 | 348.06 | 283.67 | 0.0372 | 0.1375 |
| 288.15 | 1297.8 | 253.12 | 288.60 | 0.0503 | 0.1865 |
| 293.15 | 1293.6 | 188.70 | 293.48 | 0.0664 | 0.2472 |
| 298.15 | 1289.5 | 143.54 | 298.35 | 0.0860 | 0.3212 |
| 303.15 | 1285.4 | 111.25 | 303.23 | 0.1094 | 0.4098 |
| 308.15 | 1281.3 | 87.746 | 308.11 | 0.1370 | 0.5148 |
| 313.15 | 1277.2 | 70.242 | 313.01 | 0.1689 | 0.6367 |
| 318.15 | 1273.2 | 57.030 | 317.90 | 0.2052 | 0.7759 |
| 323.15 | 1269.1 | 46.904 | 322.79 | 0.2463 | 0.9343 |
| 328.15 | 1265.1 | 39.040 | 327.67 | 0.2923 | 1.1122 |
| 333.15 | 1261.1 | 32.847 | 332.54 | 0.3432 | 1.3099 |
| 338.15 | 1257.1 | 27.910 | | | |
| 343.15 | 1253.1 | 23.935 | | | |
| 348.15 | 1249.1 | 20.699 | | | |
| 353.15 | 1245.1 | 18.044 | | | |
| 358.15 | 1241.1 | 15.844 | | | |
| 363.15 | 1237.2 | 14.007 | | | |
| 368.15 | 1233.2 | 12.455 | | | |
| 373.15 | 1229.2 | 11.159 | | | |

$u(T)$ = ± 0.02 K; $u(\rho)$ = ± 0.5 kg·m$^3$ (Eq. 2.90); $u(\eta)$ = 1% (Eq. 2.90); $u(\sigma)$ = 1.5% (Eq. 4.15); $u(\Lambda)$ = 1.5% (Eq. 4.15).

**Table B.62.** Experimental values for density, viscosity, electrical conductivity, and molar conductivity for [$^1$C$_4$$^1$C$_1$pyr][OTf].

| SVM 3001 | | | ILDEM | | |
|---|---|---|---|---|---|
| $\frac{T}{K}$ | $\frac{\rho}{\text{kg·m}^{-3}}$ | $\frac{10^3\eta}{\text{Pa·s}}$ | $\frac{T}{K}$ | $\frac{\sigma}{\text{S·m}^{-1}}$ | $\frac{10^4\Lambda}{\text{S·m}^2\text{·mol}^{-1}}$ |
| 278.15 | 1267.0 | 581.23 | 283.75 | 0.0889 | 0.2050 |
| 283.15 | 1263.3 | 408.90 | 288.62 | 0.1187 | 0.2746 |
| 288.15 | 1259.6 | 296.20 | 293.49 | 0.1549 | 0.3594 |
| 293.15 | 1256.0 | 219.82 | 298.38 | 0.1983 | 0.4612 |
| 298.15 | 1252.4 | 166.77 | 303.28 | 0.2493 | 0.5815 |
| 303.15 | 1248.7 | 129.05 | 308.19 | 0.3085 | 0.7217 |
| 308.15 | 1245.1 | 101.64 | 313.10 | 0.3763 | 0.8829 |
| 313.15 | 1241.5 | 81.346 | 318.02 | 0.4530 | 1.0659 |
| 318.15 | 1238.0 | 66.053 | 322.92 | 0.5388 | 1.2713 |
| 323.15 | 1234.4 | 54.330 | 327.83 | 0.6338 | 1.4998 |
| 328.15 | 1230.9 | 45.218 | 332.72 | 0.7386 | 1.7526 |
| 333.15 | 1227.4 | 38.043 | | | |
| 338.15 | 1223.8 | 32.322 | | | |
| 343.15 | 1220.3 | 27.714 | | | |
| 348.15 | 1216.8 | 23.964 | | | |
| 353.15 | 1213.4 | 20.883 | | | |
| 358.15 | 1209.9 | 18.330 | | | |
| 363.15 | 1206.4 | 16.198 | | | |
| 368.15 | 1202.9 | 14.402 | | | |
| 373.15 | 1199.5 | 12.883 | | | |

$u(T)$ = ± 0.02 K; $u(\rho)$ = ± 0.5 kg·m$^3$ (Eq. 2.90); $u(\eta)$ = 1% (Eq. 2.90); $u(\sigma)$ = 1.5% (Eq. 4.15); $u(\Lambda)$ = 1.5% (Eq. 4.15).

**Table B.63.** Experimental values for density, viscosity, electrical conductivity, and molar conductivity for [$^1C_4{}^1C_1$pyr][FAP].

| SVM 3001 | | | ILDEM | | |
|---|---|---|---|---|---|
| $\frac{T}{K}$ | $\frac{\rho}{\text{kg·m}^{-3}}$ | $\frac{10^3\eta}{\text{Pa·s}}$ | $\frac{T}{K}$ | $\frac{\sigma}{\text{S·m}^{-1}}$ | $\frac{10^4\Lambda}{\text{S·m}^2\text{·mol}^{-1}}$ |
| 278.15 | 1642.9 | 222.24 | 283.76 | 0.0485 | 0.1757 |
| 283.15 | 1637.2 | 161.89 | 288.60 | 0.0674 | 0.2452 |
| 288.15 | 1631.5 | 121.05 | 293.48 | 0.0912 | 0.3326 |
| 293.15 | 1625.9 | 92.631 | 298.36 | 0.1204 | 0.4401 |
| 298.15 | 1620.2 | 72.363 | 303.25 | 0.1554 | 0.5698 |
| 303.15 | 1614.6 | 57.583 | 308.15 | 0.1966 | 0.7231 |
| 308.15 | 1609.0 | 46.583 | 313.05 | 0.2444 | 0.9010 |
| 313.15 | 1603.4 | 38.227 | 317.94 | 0.2988 | 1.1046 |
| 318.15 | 1597.8 | 31.802 | 322.82 | 0.3600 | 1.3349 |
| 323.15 | 1592.3 | 26.772 | 327.70 | 0.4282 | 1.5920 |
| 328.15 | 1586.7 | 22.782 | 332.60 | 0.5033 | 1.8765 |
| 333.15 | 1581.2 | 19.576 | | | |
| 338.15 | 1575.7 | 16.971 | | | |
| 343.15 | 1570.2 | 14.832 | | | |
| 348.15 | 1564.7 | 13.060 | | | |
| 353.15 | 1559.3 | 11.581 | | | |
| 358.15 | 1153.8 | 10.335 | | | |
| 363.15 | 1548.4 | 9.2774 | | | |
| 368.15 | 1542.9 | 8.3745 | | | |
| 373.15 | 1537.5 | 7.6008 | | | |

$u(T)$ = ± 0.02 K; $u(\rho)$ = ± 0.5 kg·m$^3$ (Eq. 2.90); $u(\eta)$ = 1% (Eq. 2.90); $u(\sigma)$ = 1.5% (Eq. 4.15); $u(\Lambda)$ = 1.5% (Eq. 4.15).